MODELING AND VALIDATION OF A SUBSCALE AEROBATIC AIRCRAFT CONFIGURATION IN SPIN

BY

ADAM M. RAGHEB

DISSERTATION

Submitted in partial fulfillment of the requirements
for the degree of Doctor of Philosophy in Aerospace Engineering
in the Graduate College of the
University of Illinois at Urbana-Champaign, 2016

Urbana, Illinois

Doctoral Committee:

Professor Michael S. Selig, Director of Research and Chair
Professor Gregory S. Elliott
Assistant Professor Phillip J. Ansell
Assistant Professor Leonardo P. Chamorro

Abstract

An approach for modeling the stall/spin regime of single engine aircraft is presented. A three-pronged approach is taken that involves the following components: flight testing, the development of a new analytical model for calculating the forces on a stalled spinning wing, and validation of that model through wind tunnel tests. Significantly, these results are combined to form a new code, SpinSim, which assists with the six-degree-of-freedom (6DOF) simulation of the aerodynamics and flight dynamics of an aircraft. This code places particular emphasis on the simulation of the stall/spin regime.

The flight-testing phase of this research was conducted using a radio-controlled unmanned aerial vehicle (UAV) that was flown into a wide variety of different stall/spin configurations. This UAV was equipped with onboard instrumentation and fitted with a data acquisition system specifically configured for this spin research. A large number of spins were flown, and the data were used in the development of the analytical model and 6DOF simulations. Four proposed ventral fin configurations were implemented, and their beneficial effects on the spin and recovery characteristics were demonstrated and explained.

The SpinSim analytical model considers the normal force on a stalled spinning wing as a function of the aircraft pitch, the spin parameter, and the wing aspect ratio. The proposed first-principles-based approach allows for a standard flight model to be corrected for the three-dimensional flow effects and structures inherent in the spin regime. This approach demonstrates a significant improvement to the current state of the art. Notably, this model is based on the following: (1) the centrifugal pumping of the fluid in the elliptical trapped wing wake and (2) its eventual ejection at the wing tip.

Also, wind tunnel tests were conducted to validate the analytical model, which revealed that the aspect ratio causes an increased effect on the wing normal force as the pitch angle is decreased. It is also concluded that the normal force coefficient is proportional to the spin parameter squared and that no Reynolds number effects exist within the range of Reynolds numbers tested. At values of the spin parameter in excess of unity, a maximum wing normal force coefficient limit appears to exist. This normal force coefficient limit increases in value for higher aspect ratio wings.

The 6DOF simulations maintain a low computational cost in order to serve as a useful design tool for stall/spin studies. Such simulations incorporate the results of the flight and wind tunnel tests as well as the new analytical

model. Simulations of the UAV in stall/spin situations showed strong agreement with the flight test data, especially in regard to the angular rates, spin radii, and aerodynamic angles. By using the proposed analytical model, SpinSim extends the range of the modelable parameter space that would otherwise require hazardous piloted testing or expensive dynamically-scaled model testing. Also, SpinSim functions as a tool to aid in the design-for-spin of airplanes and successfully captures the first-order effects attributable to the yawing motion of a stalled spinning wing.

To Isabel and my parents.

Acknowledgments

The research and accomplishments to be found in this document are the result of effort, support, and assistance from many different individuals.

First, I am thankful for the aerodynamic and technical guidance that my PhD adviser, Prof. Michael Selig, provided to me. I gained exposure to flight testing, wind tunnel testing, and analytical model development, in particular. Moreover, I learned a great deal about aircraft simulations and airfoil design, as well as the art of presenting, organizing, and analyzing data. My experience as a PhD candidate afforded me the opportunity to develop my presentation, data analysis, and coding skills under the guidance of Prof. Selig. I am also particularly grateful for the privilege of working with and learning a great deal about novel concepts for utility-scale wind turbines, one of his many areas of expertise.

I also wish to thank my Master's adviser, Prof. Gregory Elliott for his guidance during my initial studies in graduate school. He helped to instill a high level of intellectual curiosity in me. While a member of his research group, I learned a great deal about flow diagnostics, design and machining of parts, experimental design, and high energy lasers. I am very thankful for my time and experiences in the COIL lab. In particular, I learned about an interesting field of study with broad applications beyond aerospace and aviation.

Gratitude must also be given to the members of our research group, without whom the experimental tests would not be possible. Specifically, I wish to thank Or Dantsker for lending his excellent RC piloting skills to fly the 35%-scale Extra 260 Aero Testbed and for helping me to learn about RC aircraft. I also wish to thank Gavin Ananda and Dr. Rob Deters for teaching me about the operation of the wind tunnel and propeller rig as well as assisting me with its setup. Dr. Brent Pomeroy deserves my gratitude for his assistance with MATLAB and for the help he provided me regarding good coding practices. Thanks to him for being receptive to spontaneous discussions and sharing ideas. Finally, I wish to thank Dr. Giovanni Fiore for his company in 327H and for the chats we had together.

Finally, I wish to thank Gail Jonkouski and Dr. Elaine Wood for their great assistance with helping me edit this document. Gratitude must also be given to Dr. Andreia L. Sousa for her mentoring. I also wish to thank my friends, family, and others for supporting me through this lengthy effort and for helping me when necessary. This goal could not have been achieved without each and every person's help.

Table of Contents

List of Tables viii

List of Figures ix

Nomenclature xvi

Chapter 1 Introduction 1

Chapter 2 Goals and Objectives 8

Chapter 3 Flight Testing 10
3.1 Test Aircraft Description 10
3.2 Ventral Fin Configurations 11
3.3 Data Acquisition Equipment 13
3.4 Data Reduction Techniques 16
3.5 Flight Testing Results 21
3.5.1 Baseline Spin and Repeatability 27
3.5.2 Direction of Spin 28
3.5.3 Pro-Spin Aileron Deflection 28
3.5.4 Anti-Spin Aileron Deflection 30
3.5.5 Increased Control Surface Deflections with and without Ailerons 32
3.5.6 Inverted Spin with and without Ailerons 35
3.5.7 Effect of Motor Power / Throttle 37
3.5.8 Effect of Ventral Fins 1, 2, and 3 40
3.6 Discussion of Ventral Fin Spin-Exit Observations 45
3.7 Reduction of Flight Test Data for 6DOF Simulation Validation 45
3.7.1 Method Validation Using Direct SpinSim Spiral Flight Data 45
3.7.2 Aero Testbed Gliding "Mush" Flight Data Results 52
3.8 Summary of Flight Testing 57

Chapter 4 Wind Tunnel Testing 60
4.1 Experimental Setup 60
4.1.1 Wind Tunnel Corrections 63
4.1.2 Motion Control and Data Acquisition 64
4.2 Wing Test Article Properties 65
4.3 Results and Discussion 66
4.3.1 Reynolds Number Effects 67
4.3.2 Aspect Ratio Effects 68
4.3.3 Airfoil Geometry Effects 70
4.3.4 High Spin Parameter Effects 72
4.3.5 Airfoil and High Spin Parameter Effects 73
4.3.6 Experiments for Re = 7,500 74
4.3.7 Additional Experiments for Re = 11,000 and Re = 15,000 75

4.3.8 Experiments for Re = 22,000 . . . 76
4.3.9 Tests of Two Approximate GA Aircraft Wing Planforms . . . 76
4.3.10 Experiments for Flat Plates of Varying Aspect Ratio . . . 81
4.4 Summary of Wind Tunnel Testing . . . 81

Chapter 5 Force Modeling Methodology of SpinSim . . . 84
5.1 Introduction . . . 84
5.2 Basis for the Theory Behind the Proposed Analytical Model . . . 84
5.3 Analytical Spin Correction and Wing Model . . . 87
5.4 Wing Aerodynamic Data and Development . . . 96
5.5 Fuselage . . . 106
5.6 Vertical Tail . . . 110
5.7 Horizontal Tail . . . 112
5.8 Shielding Methodology for Vertical Stabilizer and Aft Fuselage . . . 113
5.9 Modeling Results . . . 117
5.9.1 SpinSim Simulation of Wing-Only Wind Tunnel Tests . . . 118
5.9.2 Full Airplane C_N Comparisons . . . 120
5.9.3 Comparison of Proposed Analytical Wing Model to Current State of the Art . . . 127
5.9.4 Comparison of Calculated Airplane Coefficients to Experimental Data . . . 131
5.10 Summary of SpinSim Force Modeling Methodology . . . 136

Chapter 6 Six Degree of Freedom (6DOF) SpinSim Simulations . . . 137
6.1 Aircraft Equations of Motion . . . 137
6.1.1 Select Corrections Made to 6DOF Integrating Code . . . 139
6.1.2 Elevator Deflection Trimmed Flight Trade Studies . . . 142
6.1.3 Integration Tolerance Parametric Studies . . . 143
6.1.4 Integration Methodology Parameter Study . . . 151
6.1.5 Demonstration of Initial Condition Insensitivity . . . 158
6.2 Comparison of SpinSim 6DOF Simulations and Aero Testbed Extra 260 Flight Test Results . . . 173
6.2.1 Aero Testbed Results: Case A . . . 173
6.2.2 Aero Testbed Results: Case B . . . 178
6.2.3 Aero Testbed Results: Case C . . . 183
6.2.4 Aero Testbed Results: Case D . . . 184
6.2.5 SpinSim Flight Simulations and Total Angular Velocity Parameter . . . 192
6.2.6 SpinSim Results: Case A . . . 192
6.2.7 SpinSim Results: Case B . . . 199
6.2.8 SpinSim Results: Case C . . . 205
6.2.9 SpinSim Results: Case D . . . 212
6.3 Summary of 6DOF SpinSim Spin Simulations . . . 214

Chapter 7 Conclusions and Recommendations . . . 219
7.1 Conclusions . . . 219
7.1.1 Flight Testing . . . 220
7.1.2 Wind Tunnel Testing . . . 221
7.1.3 Analytical Modeling and Simulations . . . 222
7.2 Recommendations . . . 222

References . . . 225

List of Tables

3.1 Physical Properties of the 35%-Scale Extra 260 UIUC Aero Testbed Aircraft 12
3.2 Physical Properties of the Spin-Reduction Ventral Fin Configurations 12
3.3 Maximum Control Surface Deflection Angles 16
3.4 Throttle Settings and Approximate RPM Range in Spin 23
3.5 Spin Configuration Naming Convention 23
3.6 Summary of Individual Spin Parameters 25

4.1 Aspect Ratio Study – Wing and Blade Information and Dimensions 65
4.2 Cross-Sectional Shape Study – Wing and Blade Information and Dimensions 66
4.3 Approximate General Aviation Wing Planform Study – Wing Information and Dimensions 81

5.1 Drag and Bubble Dimensions of Varying Aspect Ratio Flat Plates Normal to the Flow (Data from Ref. [90]) 86

6.1 Control Surface Deflection Combinations of Spin Cases A, B, C, and D 173

List of Figures

1.1 An illustration of the spin parameter variables (McCormick [43]). 3
1.2 Comparison of (a) strip theory predictions and (b) strip theory predictions with post-stall spinning correction to experimentally-acquired C_N versus ω data for α values of 30, 50, 70, and 90 deg (McCormick [46]). 5
1.3 Plot of experimentally-acquired C_N versus ω data for α values between 55 and 90 deg (Hultberg [38]). 5

3.1 Photograph of the 35%-scale Extra 260 UIUC Aero Testbed aircraft. 11
3.2 Depiction of the ventral fin installation by (a) a photograph of Fin 1 installed on the testbed aircraft, and (b) a CAD drawing of the four fins. 13
3.3 Photograph of the instrumentation system on the Extra 260 UIUC Aero Testbed aircraft (left/nose). . . 14
3.4 Plot of the pitot probe calibration data points (red) with linear curve fit (blue) superimposed. 16
3.5 Spin trajectories for representative spin using the (a) direct IMU data, and (b) IMU trajectory with average windfield subtracted (aircraft magnified three times actual size and drawn every 0.40 s). . . . 18
3.6 Plot of IMU direct position (red) and position integrated from IMU velocities (blue) with projected paths on ground. 20
3.7 Renderings of the spins using graphics from FS One: a) T0R1E1A0-Lft-Up, b) T0R1E1A0-Rght-Up, c) T0R1E1A1-Lft-Up, d) T0R1E1A1-Lft-Up-(cross ail), e) T0R2E2A0-Lft-Up, f) T0R2E2A2-Lft-Up, g) T0R2E2A0-Rght-Up, h) T0R2E2A2-Rght-Up, i) T0R1E1A0-Rght-Inv, j) T0R1E1A1-Rght-Up, and k) T0R1E1A1-Lft-Inv. 24
3.8 Spin trajectories for (a) T0R2E2A2-Lft-Up, and (b) T0R1E1A0-Lft-Inv spins with windfield subtracted (aircraft magnified four times actual size and drawn every 0.50 s). 26
3.9 Repeatability test: two T0R1E1A0-Lft-Up spins performed on different days. 27
3.10 Repeatability test: two T0R1E1A0-Lft-Up spins performed on different days. 28
3.11 Effect of spin direction: T0R1E1A0-Lft-Up and T0R1E1A0-Rght-Up spins performed on two different flights. 29
3.12 Effect of pro-spin aileron input: T0R1E1A0-Lft-Up and T0R1E1A1-Lft-Up spins performed on two different days. 30
3.13 Effect of anti-spin aileron input: T0R1E1A0-Lft-Up and T0R1E1A1-Lft-Up-(cross ail) spins performed on two different days. 31
3.14 Effect of high deflection angles: T0R1E1A0-Lft-Up and T0R2E2A0-Lft-Up spins performed on two different days. 32
3.15 Effect of pro-spin aileron input at high deflection angles: T0R2E2A0-Lft-Up and T0R2E2A2-Lft-Up spins performed on two different days. 33
3.16 Effect of pro-spin aileron input at high deflection angles: T0R2E2A0-Rght-Up and T0R2E2A2-Rght-Up spins performed on two different days. 34
3.17 Effect of spin direction at high deflection angles: T0R2E2A2-Rght-Up and T0R2E2A2-Lft-Up spins performed on two different days. 34
3.18 Effect of inverted spin: T0R1E1A0-Lft-Up and T0R1E1A0-Lft-Inv spins performed on two different days. 35
3.19 Effect of inverted spin with pro-spin ailerons: T0R1E1A1-Rght-Up and T0R1E1A1-Rght-Inv spins performed on two different flights. 36
3.20 Effect of throttle setting: T0R1E1A0-Lft-Up and T1R1E1A0-Lft-Up spins performed on the same flight. 38

3.21 Effect of throttle setting: T0R1E1A0-Lft-Up and T2R1E1A0-Lft-Up spins performed on the same flight. 38
3.22 Effect of throttle setting: T0R1E1A0-Rght-Up and T2R1E1A0-Rght-Up spins performed on the same flight. . . . 39
3.23 Effect of throttle setting with pro-spin ailerons: T0R1E1A1-Lft-Up and T1R1E1A1-Lft-Up spins performed on the same flight. . . . 40
3.24 Effect of throttle setting with pro-spin ailerons: T0R1E1A1-Rght-Up and T1R1E1A1-Rght-Up spins performed on the same flight. . . . 41
3.25 Effect of throttle setting with anti-spin ailerons: T0R1E1A1-Lft-Up-(cross ail) and T1R1E1A1-Lft-Up-(cross ail) spins performed on two different days. . . . 42
3.26 Effect of Ventral Fin 1: T0R1E1A1-Lft-Up and T0R1E1A1-Lft-Up-(Fin 1) spins performed on two different days. . . . 42
3.27 Effect of Ventral Fin 2: T0R1E1A1-Lft-Up and T0R1E1A1-Lft-Up-(Fin 2) spins performed on two different days. . . . 43
3.28 Effect of Ventral Fin 3: T0R1E1A1-Lft-Up and T0R1E1A1-Lft-Up-(Fin 3) spins performed on two different days. . . . 43
3.29 Effect of Ventral Fin 3 with non-zero throttle: T1R1E1A1-Lft-Up and T1R1E1A1-Lft-Up-(Fin 3) spins performed on two different days. . . . 44
3.30 Effect of Ventral Fin 3 with neutral ailerons: T0R1E1A0-Lft-Up and T0R1E1A0-Lft-Up-(Fin 3) spins performed on two different days. . . . 44
3.31 Trajectory of SpinSim-simulated righthand spiral of Aero Testbed with 5 deg up elevator deflection and 15 deg right rudder. . . . 46
3.32 Plot of integrated and direct aircraft Euler angles for a righthand spiral flight. . . . 48
3.33 Plot of aircraft velocities in the earth-fixed reference frame for a righthand spiral flight. . . . 49
3.34 Plot of aircraft u, v, and w velocity components in the body-fixed reference frame for a righthand spiral. 50
3.35 Plot of aircraft α, β, and V for a righthand spiral. . . . 51
3.36 Plot of integrated and IMU direct Aero Testbed Euler angles for a mush flight. . . . 53
3.37 Results from assumed installation error corrections of a) $\theta - 5$ deg and $\psi + 5$ deg, b) $\theta + 5$ deg and $\psi - 5$ deg, c) $\theta - 5$ deg and $\psi - 5$ deg, d) $\theta + 5$ deg and $\psi + 5$ deg. . . . 55
3.38 Plot of calculated Aero Testbed Euler angle rates for a mush flight. . . . 56
3.39 Plot of direct Aero Testbed velocities in the earth-fixed reference frame for a mush flight. . . . 57
3.40 Plot of Aero Testbed u, v, and w velocity components in the body-fixed reference frame for a mush flight. . . . 58
3.41 Plot of Aero Testbed α, β, and V for a mush flight. . . . 59

4.1 University of Illinois 2.8 $\times$ 4.0 ft low-speed low-turbulence wind tunnel. . . . 61
4.2 Experimental setup for drag force measurement (fairing not shown). . . . 61
4.3 Spinning wing balance enclosed in fairing. . . . 61
4.4 Diagram of experimental spinning wing setup showing the orientation of the freestream velocity, wing location, orientation of θ, motor location, and direction of D. . . . 62
4.5 Diagram depicting relative orientations of V_∞, D, and C_N from Eq. 4.1. . . . 62
4.6 Isometric view of the fairing, sting, and spinning wing in the wind tunnel test section. . . . 63
4.7 CAD rendering of the $\mathcal{AR} = 4.85$ wing of Table 4.1 at 30, 60, and 90 degree orientations, left to right. . 66
4.8 Plot of C_N versus ω for three different Re values at $\theta = 90$ deg for a symmetric wing with (a) $\mathcal{AR} =$ 6.50, and (b) a flat plate with $\mathcal{AR} = 5.00$. . . . 67
4.9 Plot of C_N versus ω for a symmetric wing at three different Re values at $\theta = 60$ deg for a wing with $\mathcal{AR} = 2.55$. . . . 67
4.10 Plot of C_N versus ω for five different $\mathcal{AR}$ values for a symmetric wing at $Re = 15{,}000$ and (a) $\theta = 30$ deg, (b) $\theta = 60$ deg, and (c) $\theta = 90$ deg. . . . 69
4.11 Plot of C_N versus ω for five different $\mathcal{AR}$ values for a symmetric wing at $Re = 11{,}000$ and (a) $\theta = 30$ deg, (b) $\theta = 60$ deg, and (c) $\theta = 90$ deg. . . . 70
4.12 Plot of C_N versus ω or five different Re values at $\theta = 90$ deg for (a) a symmetric wing with $\mathcal{AR} = 6.30$, and (b) a flat-bottom wing with $\mathcal{AR} = 5.97$. . . . 71
4.13 Plot of C_N versus ω for flat-bottomed wings of four different $\mathcal{AR}$ values and $\theta = 90$ deg at various Re values. . . . 72

4.14 Plot of C_N versus ω for three different θ values at $Re = 11{,}000$ for (a) a flat-bottom wing, and (b) a symmetric wing. . . . 73
4.15 Plot of C_N versus ω for five different $\mathcal{AR}$ values at $Re = 7{,}500$ and $\theta = 30$ deg for (a) early tests, and (b) later tests. . . . 74
4.16 Plot of C_N versus ω for five different $\mathcal{AR}$ values at $Re = 7{,}500$ and $\theta = 60$ deg for (a) early tests, and (b) later tests. . . . 75
4.17 Plot of C_N versus ω for five different $\mathcal{AR}$ values at $Re = 7{,}500$ and $\theta = 90$ deg for (a) early tests, and (b) later tests. . . . 76
4.18 Plot of C_N versus ω for five different $\mathcal{AR}$ values at $Re = 11{,}000$ and $\theta = 30$ deg. . . . 77
4.19 Plot of C_N versus ω for five different $\mathcal{AR}$ values at $Re = 11{,}000$ and $\theta = 60$ deg. . . . 77
4.20 Plot of C_N versus ω for five different $\mathcal{AR}$ values at $Re = 11{,}000$ and $\theta = 90$ deg. . . . 77
4.21 Plot of C_N versus ω for five different $\mathcal{AR}$ values at $Re = 15{,}000$ and $\theta = 30$ deg. . . . 78
4.22 Plot of C_N versus ω for five different $\mathcal{AR}$ values at $Re = 15{,}000$ and $\theta = 60$ deg. . . . 78
4.23 Plot of C_N versus ω for five different $\mathcal{AR}$ values at $Re = 15{,}000$ and $\theta = 90$ deg. . . . 78
4.24 Plot of C_N versus ω for five different $\mathcal{AR}$ values at $Re = 22{,}000$ and $\theta = 30$ deg. . . . 79
4.25 Plot of C_N versus ω for five different $\mathcal{AR}$ values at $Re = 22{,}000$ and $\theta = 60$ deg. . . . 79
4.26 Plot of C_N versus ω for five different $\mathcal{AR}$ values at $Re = 22{,}000$ and $\theta = 90$ deg. . . . 79
4.27 Plot of C_N versus ω for an approximate Piper Archer wing planform at five different Re values at $\theta = 90$ deg. . . . 80
4.28 Plot of C_N versus ω for an approximate Cessna 172 wing planform at five different Re values at $\theta = 90$ deg. . . . 80
4.29 Illustration of approximate Piper Cherokee wing planform as tested in this study (leading edge on top). 80
4.30 Illustration of approximate Cessna 172 wing planform as tested in this study (leading edge on top). . . . 80
4.31 Plot of C_N versus ω for an $\mathcal{AR} = 1$ flat plate at four different Re values at $\theta = 90$ deg. . . . 82
4.32 Plot of C_N versus ω for an $\mathcal{AR} = 2$ flat plate at three different Re values at $\theta = 90$ deg. . . . 82
4.33 Plot of C_N versus ω for an $\mathcal{AR} = 5$ flat plate at three different Re values at $\theta = 90$ deg. . . . 83
4.34 Plot of C_N versus ω for an $\mathcal{AR} = 10$ flat plate at three different Re values at $\theta = 90$ deg. . . . 83

5.1 Plot of spanwise flow velocity w on rotating flat plate wings of $\mathcal{AR} = 2$ and 4 at $\alpha = 48$ deg (Carr [50]). 85
5.2 Plot of streamlines for a wind turbine airfoil at $\alpha \approx 25$ deg (Hu [89]). . . . 85
5.3 Illustration of a 2D flat plate (a) without, and (b) with the influence of rotational effects present. . . . 88
5.4 Plots of the (a) semi-ellipse of trapped flow behind a wing section with flow at $\alpha = 90$ deg, bottom to top, and (b) weighting function $w_1(i)$ used for ΔC_N in Eq. 5.3. . . . 90
5.5 Plot of entrainment factor weighting function $w_2(y)$ versus normalized wing spanwise y location for five different aspect ratios. . . . 91
5.6 Plot of entrainment factor at wing tip versus wing aspect ratio, as determined by minimizing the RMS error between computational and experimental data. . . . 92
5.7 Plot of buildup of C_N corrected for spin based on C_N from strip theory ($C_{N,st}$) and ΔC_N from centrifugal pumping components. . . . 93
5.8 Illustration of the classic sprinkler problem modified for this research. . . . 94
5.9 Plot of correction factor η versus flap deflection angle δ_f (McCormick [43]). . . . 97
5.10 $C_{l_{max}}$ increment ratio as a function of c_f/c (McCormick [43]). . . . 97
5.11 Plot of experimental C_L and C_D data, calculated and experimental $C_{M,c/4}$ data, and the x_{cp}/c location used for determining the moment, all as a function of α. . . . 99
5.12 Plot of experimental C_l and C_d airfoil data from Sheldahl and Klimas [98], calculated and experimental $C_{m,c/4}$ data, and the x_{cp} location used for determining the moment, all as a function of α. . . . 100
5.13 Plot of experimental C_L and C_D data from Koenig [104] for an $\mathcal{AR} = 2$ tail surface, calculated and experimental $C_{M,c/4}$ data, and the x_{cp} location used for determining the moment, all as a function of α. 101
5.14 Plot of experimental C_L and C_D data from Koenig [104] for an $\mathcal{AR} = 6$ tail surface, calculated and experimental $C_{M,c/4}$ data, and the x_{cp} location used for determining the moment, all as a function of α. 102
5.15 Comparison of undeflected airfoil chord length c and the effective chord length c_{eff} of an airfoil with deflected control surfaces. . . . 102
5.16 Root airfoil section of the Extra 260 Aero Testbed aircraft. . . . 102
5.17 C_l lookup table data used for wing airfoil over the range $-180 \leq \alpha \leq 180$ deg. . . . 103

5.18 C_d lookup table data used for wing airfoil over the range $-180 \leq \alpha \leq 180$ deg. 103
5.19 $C_{m,c/4}$ lookup table data used for wing airfoil over the range $-180 \leq \alpha \leq 180$ deg. 104
5.20 Plot of C_l/C_d for wing airfoil over the range $-180 \leq \alpha \leq 180$ deg. 104
5.21 Illustration of the convention used to define C_x, C_y, and ϕ for the aft fuselage lookup tables (Polhamus [25]). 106
5.22 C_x lookup table data used for aft fuselage over the range $-180 \leq \alpha \leq 180$ deg. 106
5.23 C_y lookup table data used for aft fuselage over the range $-180 \leq \alpha \leq 180$ deg. 107
5.24 C_x lookup table data used for forward fuselage over the range $-180 \leq \alpha \leq 180$ deg. 107
5.25 C_y lookup table data used for forward fuselage over the range $-180 \leq \alpha \leq 180$ deg. 108
5.26 C_A lookup table data used for full fuselage over the range $-0.9 < \omega < 0.9$ at seven values of α. . . . 108
5.27 C_Y lookup table data used for full fuselage over the range $-0.9 < \omega < 0.9$ at seven values of α. . . . 109
5.28 C_N lookup table data used for full fuselage over the range $-0.9 < \omega < 0.9$ at seven values of α. . . . 109
5.29 C_m lookup table data used for full fuselage over the range $-0.9 < \omega < 0.9$ at seven values of α. . . . 109
5.30 C_n lookup table data used for full fuselage over the range $-0.9 < \omega < 0.9$ at seven values of α. 110
5.31 C_L lookup table data used for the vertical stabilizer over the range $-180 \leq \alpha \leq 180$ deg. 111
5.32 C_D lookup table data used for the vertical stabilizer over the range $-180 \leq \alpha \leq 180$ deg. 111
5.33 $C_{M,c/4}$ lookup table data used for the vertical stabilizer over the range $-180 \leq \alpha \leq 180$ deg. 112
5.34 Plot of C_L/C_D for the vertical stabilizer over the range $-180 \leq \alpha \leq 180$ deg. 112
5.35 C_L lookup table data used for the horizontal stabilizer over the range $-180 \leq \alpha \leq 180$ deg. 114
5.36 C_D lookup table data used for the horizontal stabilizer over the range $-180 \leq \alpha \leq 180$ deg. 114
5.37 $C_{M,c/4}$ lookup table data used for the horizontal stabilizer over the range $-180 \leq \alpha \leq 180$ deg. 115
5.38 Plot of C_L/C_D for the horizontal stabilizer over the range $-180 \leq \alpha \leq 180$ deg. 115
5.39 Flow shadow map used to model the vertical stabilizer of the Extra 260 Aero Testbed aircraft. 116
5.40 Plot of C_N versus ω for the $\mathcal{AR} = 2.55$ wing of Table 4.1 at three experimentally-measured *Re* values compared with analytically-modeled results using SpinSim. 118
5.41 Plot of C_N versus ω for the $\mathcal{AR} = 3.85$ wing of Table 4.1 at three experimentally-measured *Re* values compared with analytically-modeled results using SpinSim. 119
5.42 Plot of C_N versus ω for the $\mathcal{AR} = 4.85$ wing of Table 4.1 at three experimentally-measured *Re* values compared with analytically-modeled results using SpinSim. 119
5.43 Plot of C_N versus ω for the $\mathcal{AR} = 6.50$ wing of Table 4.1 at three experimentally-measured *Re* values compared with analytically-modeled results using SpinSim. 120
5.44 Plot of C_N versus ω for the $\mathcal{AR} = 8.33$ wing of Table 4.1 at three experimentally-measured *Re* values compared with analytically-modeled results using SpinSim. 120
5.45 Plot of C_N versus ω for $R_s = 0$ at four analytically-modeled θ values compared with the rotary balance data of the low-wing general aviation full-airplane configuration of Ref. [38] with $\mathcal{AR} = 5.9$ and $\lambda = 1$. 121
5.46 Plot of C_N versus ω for $R_s = 0$ at four analytically-modeled θ values compared with the rotary balance data of the low-wing single-engine trainer full-airplane configuration of Ref. [37] with $\mathcal{AR} = 6.21$ and $\lambda = 0.5$. 122
5.47 Plot of C_N versus ω for $R_s = 0$ at four analytically-modeled θ values compared with the rotary balance data of the low-wing general aviation full-airplane configuration of Ref. [31] with $\mathcal{AR} = 7.24$ and $\lambda = 0.67$. 123
5.48 Plot of C_N versus ω for $R_s = 0$ at four analytically-modeled θ values compared with the rotary balance data of the high-wing general aviation full-airplane configuration of Ref. [41] with $\mathcal{AR} = 7.4$ and $\lambda = 1$. 123
5.49 Plot of C_N versus ω for $R_s = 0$ at four analytically-modeled θ values compared with the rotary balance data of the low-wing general aviation full-airplane configuration of Ref. [33] with $\mathcal{AR} = 5.9$ and $\lambda = 1$. 124
5.50 Plot of C_N versus ω for $R_s = 0$ at four analytically-modeled θ values compared with the rotary balance data of the high-wing general aviation full-airplane configuration of Ref. [36] with $\mathcal{AR} = 7.37$ and $\lambda = 0.70$. 124
5.51 Plot of C_N versus ω for $R_s = 0$ at four analytically-modeled θ values compared with the rotary balance data of the low-wing general aviation full-airplane configuration of Ref. [42] with $\mathcal{AR} = 7.37$ and $\lambda = 0.70$. 125
5.52 Plot of C_N versus ω for $R_s = 0$ at four analytically-modeled θ values compared with the rotary balance data of the low-wing general aviation full-airplane configuration of Ref. [40] with $\mathcal{AR} = 7.4$ and $\lambda = 1$. 125

5.53 Plot of C_N versus ω for $R_s = 0$ at four analytically-modeled θ values compared with the rotary balance data of the low-wing general aviation full-airplane configuration of Ref. [30] with $\mathcal{AR} = 7.24$ and $\lambda = 0.67$. 126
5.54 Plot of C_N versus ω for $R_s = 0$ at four analytically-modeled θ values compared with the rotary balance data of the high-wing general aviation full-airplane configuration of Ref. [39] with $\mathcal{AR} = 5.9$ and $\lambda = 1$. 126
5.55 Comparison of RMS error values of SpinSim C_N correction (Eq. 5.8) and the current state of the art (Eq. 1.2) in predicting C_N over the five experimental rotary balance data sets of (a) CR-2972, (c) CR-3098, (e) CR-3100, (g) CR-3200, and (i) CR-3246. 128
5.56 Comparison of RMS error values of SpinSim C_N correction (Eq. 5.8) and the current state of the art (Eq. 1.2) in predicting C_N over the five experimental rotary balance data sets of (b) CR-3097, (d) CR-3099, (f) CR-3101, (h) CR-3201, and (j) CR-3247. 129
5.57 Comparison of average RMS error values of SpinSim C_N correction (Eq. 5.8) and the current state of the art (Eq. 1.2) across all ten experimental rotary balance data sets. 130
5.58 Comparison of component breakdown simulation corrected with proposed centrifugal pumping model used to correct wing forces to the experimental data set of Ref. [40] for the aircraft normal force coefficient C_N. 132
5.59 Comparison of component breakdown simulation corrected with proposed centrifugal pumping model used to correct wing forces to the experimental data set of Ref. [40] for the aircraft axial force coefficient C_A. 133
5.60 Comparison of component breakdown simulation corrected with proposed centrifugal pumping model used to correct wing forces to the experimental data set of Ref. [40] for the aircraft side force coefficient C_Y. 133
5.61 Comparison of component breakdown simulation corrected with proposed centrifugal pumping model used to correct wing forces to the experimental data set of Ref. [40] for the aircraft roll moment coefficient C_l. 134
5.62 Comparison of component breakdown simulation corrected with proposed centrifugal pumping model used to correct wing forces to the experimental data set of Ref. [40] for the aircraft pitch moment coefficient C_m. 134
5.63 Comparison of component breakdown simulation corrected with proposed centrifugal pumping model used to correct wing forces to the experimental data set of Ref. [40] for the aircraft yaw moment coefficient C_n. 135

6.1 Graphic depicting the Euler angles of an aircraft (CH Robotics [107]). 140
6.2 Screenshot of modified code for defining ψ. 140
6.3 Plot of ψ prior to necessary modifications. 141
6.4 Plot of δ_e versus trim C_L from SpinSim for flight test c.g. location, and a c.g. location moved 0.055 m aft. 142
6.5 Plot of δ_e versus trim V_{trim} from SpinSim for flight test c.g. location, and a c.g. location moved 0.055 m aft. 143
6.6 Comparison of u, v, and w velocity components for SpinSim simulation of the Aero Testbed in a left spin with pro-spin ailerons and integration tolerances of 10^{-7} and 10^{-4}. 145
6.7 Comparison of p, q, and r angular rates for SpinSim simulation of the Aero Testbed in a left spin with pro-spin ailerons and integration tolerances of 10^{-7} and 10^{-4}. 146
6.8 Comparison of trajectories for SpinSim simulation of the Aero Testbed in a left spin with pro-spin ailerons and integration tolerances of 10^{-7} and 10^{-4}. 147
6.9 Comparison of ϕ, θ, and ψ Euler angles for SpinSim simulation of the Aero Testbed in a left spin with pro-spin ailerons and integration tolerances of 10^{-7} and 10^{-4}. 148
6.10 Comparison of airspeed, Mach number, and q for SpinSim simulation of the Aero Testbed in a left spin with pro-spin ailerons and integration tolerances of 10^{-7} and 10^{-4}. 149
6.11 Comparison of airspeed, Mach number, and q for SpinSim simulation of the Aero Testbed in a left spin with pro-spin ailerons and integration tolerances of 10^{-7} and 10^{-4}. 150
6.12 Comparison of u, v, and w velocity components for SpinSim simulation of the Aero Testbed in a left spin with pro-spin ailerons and *ode*45 and RK4 integration routines. 152

6.13 Comparison of p, q, and r angular rates for SpinSim simulation of the Aero Testbed in a left spin with pro-spin ailerons and *ode*45 and RK4 integration routines. 153
6.14 Comparison of trajectories for SpinSim simulation of the Aero Testbed in a left spin with pro-spin ailerons and *ode*45 and RK4 integration routines. 154
6.15 Comparison of ϕ, θ, and ψ Euler angles for SpinSim simulation of the Aero Testbed in a left spin with pro-spin ailerons and *ode*45 and RK4 integration routines. 155
6.16 Comparison of airspeed, Mach number, and q for SpinSim simulation of the Aero Testbed in a left spin with pro-spin ailerons and *ode*45 and RK4 integration routines. 156
6.17 Comparison of airspeed, Mach number, and q for SpinSim simulation of the Aero Testbed in a left spin with pro-spin ailerons and *ode*45 and RK4 integration routines. 157
6.18 Comparison of u, v, and w velocity components for SpinSim simulation of the Aero Testbed in a left spin with pro-spin ailerons for baseline spin and $r = -90$ deg/s initial condition. 159
6.19 Comparison of p, q, and r angular rates for SpinSim simulation of the Aero Testbed in a left spin with pro-spin ailerons for baseline spin and $r = -90$ deg/s initial condition. 160
6.20 Comparison of trajectories for SpinSim simulation of the Aero Testbed in a left spin with pro-spin ailerons for baseline spin and $r = -90$ deg/s initial condition. 161
6.21 Comparison of ϕ, θ, and ψ Euler angles for SpinSim simulation of the Aero Testbed in a left spin with pro-spin ailerons for baseline spin and $r = -90$ deg/s initial condition. 163
6.22 Comparison of airspeed, Mach number, and q for SpinSim simulation of the Aero Testbed in a left spin with pro-spin ailerons for baseline spin and $r = -90$ deg/s initial condition. 164
6.23 Comparison of aerodynamic and flight path angles for SpinSim simulation of the Aero Testbed in a left spin with pro-spin ailerons for baseline spin and $r = -90$ deg/s initial condition. 165
6.24 Comparison of u, v, and w velocity components for SpinSim simulation of the Aero Testbed in a left spin with pro-spin ailerons for baseline spin and $r = -90$ deg/s and $\alpha = 32.8$ deg initial condition. . . 167
6.25 Comparison of p, q, and r angular rates for SpinSim simulation of the Aero Testbed in a left spin with pro-spin ailerons for baseline spin and $r = -90$ deg/s and $\alpha = 32.8$ deg initial condition. 168
6.26 Comparison of trajectories for SpinSim simulation of the Aero Testbed in a left spin with pro-spin ailerons for baseline spin and $r = -90$ deg/s and $\alpha = 32.8$ deg initial condition. 169
6.27 Comparison of ϕ, θ, and ψ Euler angles for SpinSim simulation of the Aero Testbed in a left spin with pro-spin ailerons for baseline spin and $r = -90$ deg/s and $\alpha = 32.8$ deg initial condition. 170
6.28 Comparison of airspeed, Mach number, and q for SpinSim simulation of the Aero Testbed in a left spin with pro-spin ailerons for baseline spin and $r = -90$ deg/s and $\alpha = 32.8$ deg initial condition. . . 171
6.29 Comparison of aerodynamic and flight path angles for SpinSim simulation of the Aero Testbed in a left spin with pro-spin ailerons for baseline spin and $r = -90$ deg/s and $\alpha = 32.8$ deg initial condition. 172
6.30 Plot of integrated and IMU direct Aero Testbed Euler angles for a Case A spin. 174
6.31 Plot of direct Aero Testbed velocities in the earth-fixed reference frame for a Case A spin. 175
6.32 Plot of Aero Testbed u, v, and w velocity components in the body-fixed reference frame for a Case A spin. 176
6.33 Plot of Aero Testbed α, β, and V for a Case A spin. 177
6.34 Plot of integrated and IMU direct Aero Testbed Euler angles for a Case B spin. 178
6.35 Plot of direct Aero Testbed velocities in the earth-fixed reference frame for a Case B spin. 179
6.36 Plot of Aero Testbed u, v, and w velocity components in the body-fixed reference frame for a Case B spin. 181
6.37 Plot of Aero Testbed α, β, and V for a Case B spin. 182
6.38 Plot of integrated and IMU direct Aero Testbed Euler angles for a Case C spin. 184
6.39 Plot of direct Aero Testbed velocities in the earth-fixed reference frame for a Case C spin. 185
6.40 Plot of Aero Testbed u, v, and w velocity components in the body-fixed reference frame for a Case C spin. 186
6.41 Plot of Aero Testbed α, β, and V for a Case C spin. 187
6.42 Plot of integrated and direct Aero Testbed Euler angles for a Case D spin. 188
6.43 Plot of IMU direct Aero Testbed velocities in the earth-fixed reference frame for a Case D spin. 189
6.44 Plot of Aero Testbed u, v, and w velocity components in the body-fixed reference frame for a Case D spin. 190
6.45 Plot of Aero Testbed α, β, and V for a Case D spin. 191

6.46 Comparison plots of altitude, descent rate, and spin parameter of a Case A spin for Aero Testbed flight test and SpinSim simulation. . . . 193
6.47 Comparison plots of angular rates of a Case A spin for Aero Testbed flight test and SpinSim simulation. 194
6.48 Comparison plots of Case A spin trajectories with airplane plotted every second at a 1:1 scale for Aero Testbed flight test and SpinSim simulation. . . . 195
6.49 Body inertial velocities of SpinSim simulation of the Aero Testbed in a Case A spin. . . . 196
6.50 Trajectory of SpinSim simulation of the Aero Testbed in a Case A spin. . . . 196
6.51 Angular rates of SpinSim simulation of the Aero Testbed in a Case A spin. . . . 197
6.52 Angular orientation of SpinSim simulation of the Aero Testbed in a Case A spin. . . . 197
6.53 Airspeed, Mach number, and q of SpinSim simulation of the Aero Testbed in a Case A spin. . . . 198
6.54 Aerodynamic and flight path angles of SpinSim simulation of the Aero Testbed in a Case A spin. . . . 198
6.55 Comparison plots of altitude, descent rate, and spin parameter of a Case B spin for Aero Testbed flight test and SpinSim simulation. . . . 199
6.56 Comparison plots of angular rates of a Case B spin for Aero Testbed flight test and SpinSim simulation. 200
6.57 Comparison plots of Case B spin trajectories with airplane plotted every second at a 1:1 scale for Aero Testbed flight test and SpinSim simulation. . . . 201
6.58 Body inertial velocities of SpinSim simulation of the Aero Testbed in a Case B spin. . . . 202
6.59 Trajectory of SpinSim simulation of the Aero Testbed in a Case B spin. . . . 202
6.60 Angular rates of SpinSim simulation of the Aero Testbed in a Case B spin. . . . 203
6.61 Angular orientation of SpinSim simulation of the Aero Testbed in a Case B spin. . . . 203
6.62 Airspeed, Mach number, and q of SpinSim simulation of the Aero Testbed in a Case B spin. . . . 204
6.63 Aerodynamic and flight path angles of SpinSim simulation of the Aero Testbed in a Case B spin. . . . 204
6.64 Comparison plots of altitude, descent rate, and spin parameter of a Case C spin for Aero Testbed flight test and SpinSim simulation. . . . 205
6.65 Comparison plots of angular rates of a Case C spin for Aero Testbed flight test and SpinSim simulation. 206
6.66 Comparison plots of Case C spin trajectories with airplane plotted every second at a 1:1 scale for Aero Testbed flight test and SpinSim simulation. . . . 208
6.67 Body inertial velocities of SpinSim simulation of the Aero Testbed in a Case C spin. . . . 209
6.68 Trajectory of SpinSim simulation of the Aero Testbed in a Case C spin. . . . 209
6.69 Angular rates of SpinSim simulation of the Aero Testbed in a Case C spin. . . . 210
6.70 Angular orientation of SpinSim simulation of the Aero Testbed in a Case C spin. . . . 210
6.71 Airspeed, Mach number, and q of SpinSim simulation of the Aero Testbed in a Case C spin. . . . 211
6.72 Aerodynamic and flight path angles of SpinSim simulation of the Aero Testbed in a Case C spin. . . . 211
6.73 Comparison plots of altitude, descent rate, and spin parameter of a Case D spin for Aero Testbed flight test and SpinSim simulation. . . . 212
6.74 Comparison plots of angular rates of a Case D spin for Aero Testbed flight test and SpinSim simulation. 213
6.75 Comparison plots of a Case D spin trajectories with airplane plotted every second at a 1:1 scale for Aero Testbed flight test and SpinSim simulation. . . . 215
6.76 Body inertial velocities of SpinSim simulation of the Aero Testbed in a Case D spin. . . . 216
6.77 Trajectory of SpinSim simulation of the Aero Testbed in a Case D spin. . . . 216
6.78 Angular rates of SpinSim simulation of the Aero Testbed in a Case D spin. . . . 217
6.79 Angular orientation of SpinSim simulation of the Aero Testbed in a Case D spin. . . . 217
6.80 Airspeed, Mach number, and q of SpinSim simulation of the Aero Testbed in a Case D spin. . . . 218
6.81 Aerodynamic and flight path angles of SpinSim simulation of the Aero Testbed in a Case D spin. . . . 218

Nomenclature

a	=	acceleration
A	=	area of swept disc of wing in spin
b	=	wing span
c	=	chord length
$\bar{c}$	=	wing mean aerodynamic chord
C	=	test section cross-sectional area
C_A	=	axial force coefficient (F_A/qS_W)
C_d	=	sectional drag coefficient
C_D	=	drag force coefficient (D/qS_W)
C_l	=	rolling moment coefficient (M_l/qS_Wb), or sectional lift coefficient
C_L	=	lift force coefficient (L/qS_W)
ΔC_l	=	change in rolling moment coefficient due to spin ($C_{l,\omega} - C_{l,\omega=0}$)
C_N	=	normal force coefficient (F_N/qS_W)
ΔC_N	=	change in normal force coefficient due to spin ($C_{N,\omega} - C_{N,\omega=0}$)
C_m	=	pitching moment coefficient ($M_m/qS_W\bar{c}$)
$C_{m,c/4}$	=	airfoil pitching moment coefficient about the quarter chord
$C_{M,c/4}$	=	horizontal and vertical stabilizer pitching moment coefficient about the quarter chord
C_n	=	yawing moment coefficient (M_n/qS_Wb)
C_X, C_Y, C_Z	=	aircraft body-axis force coefficients (F_X/qS_W, F_Y/qS_W, F_Z/qS_W)
D	=	drag force
F	=	force acting on object
F_A	=	axial force
$F_{Coriolis}$	=	Coriolis force
F_N	=	normal force
F_X, F_Y, F_Z	=	aircraft body-axis forces

g = gravitational constant

h_n = airplane neutral point

I_{xx}, I_{yy}, I_{zz} = roll, pitch, and yaw mass moments of inertia

$(I_{xx} - I_{yy})/mb^2$ = inertia yawing moment parameter ("*IYMP*")

$(I_{yy} - I_{zz})/mb^2$ = inertia rolling moment parameter ("*IRMP*")

$(I_{zz} - I_{xx})/mb^2$ = inertia pitching moment parameter ("*IPMP*")

J = advance ratio $(1/\omega)$

$k_{fairing}$ = velocity correction factor due to fairing

L = lift

L, M, N = roll, pitch, and yaw moments

m = airplane mass

$\dot{m}$ = mass flow rate

M = mass

N = normal force

n = number of blades

p, q, r = roll, pitch, and yaw rates

q = dynamic pressure

Q = spinning wing torque

r = position vector of object

R_g = radius of gyration

R_s = spin radius

Re = Reynolds number based on mean aerodynamic chord $(V\bar{c}/\nu)$

Ro = Rossby number

S = reference area

S_W = wing reference area

t = airfoil thickness

u, v, w = aircraft velocity in body-fixed coordinate system

V = inertial speed

$V_{c_{fairing}}$ = weighted average of velocities across spinning wing area

V_C = free flow velocity

V_X, V_Y, V_Z = aircraft velocity in earth-fixed coordinate system

V_∞ = freestream velocity

$[x,y,z]_{c/4_{wing,i},cg}$ = vector from i^{th} wing panel quarter chord to airplane c.g.

$[x,y,z]_{fuse_i,cg}$ = vector from i^{th} fuselage section to airplane c.g.

$[x,y,z]_{MAC_{hstab},cg}$ = vector from horizontal stabilizer MAC quarter chord to airplane c.g.

$[x,y,z]_{MAC_{vstab},cg}$ = vector from vertical stabilizer MAC quarter chord to airplane c.g.

$x_{c/4}$ = x-location of wing quarter chord

x_{cg} = x-location of aircraft center of gravity

x_{cp} = x-location of wing center of pressure

x = aircraft longitudinal axis

y = aircraft lateral axis

Y_S = normalized wing spanwise location of stalled region ($2y_s/b_W$)

y_s = spanwise location of stalled region

z = aircraft vertical axis

Symbols

α = angle of attack, or ratio of spinning wing swept area to test section cross-sectional area (A/C)

$\alpha_{N,2}$ = end angle of attack for post-stall drag weighting function

$\alpha_{P,1}$ = beginning angle of attack for post-stall drag weighting function

β = sideslip angle

γ = flightpath angle

δ_a = aileron deflection, positive for left roll [$(\delta_{a_{right}} - \delta_{a_{left}})/2$]

δ_e = elevator deflection

δ_r = rudder deflection

θ = pitch angle

λ = taper ratio

μ = airplane relative density ($W/\rho SgB$), or kinematic viscosity

μs = microseconds (10^{-6}s)

ν = kinematic viscosity

ρ = air density

θ = pitch angle

σ_{blade} = blade solidity

ϕ, θ, ψ = roll, pitch, and heading angles

τ = drag force coefficient of spinning wing ($D/\rho AV_\infty^2$)

ω	=	spin parameter (positive for nose-right spin) ($\Omega b/2V$)
Ω	=	angular velocity about axis of spin
Ω	=	total angular velocity of airplane ($\sqrt{p^2+q^2+r^2}$)
$\mathcal{AR}$	=	aspect ratio

Subscripts

A	=	property of the (full-scale) airplane
B	=	property of the non-inertial (rotating) reference frame
eff	=	effective
H	=	property of the horizontal stabilizer
i	=	property of the discretized wing section
I	=	property of the inertial (non-rotating) reference frame
M	=	property of the (scale) model
s	=	outboard extent of stalled region
T	=	property of the vertical stabilizer
W	=	property of the wing
Wr	=	property of the wing root
Wt	=	property of the wing tip

Acronyms

6DOF	=	six degree of freedom
AHRS	=	attitude and heading reference system
ARF	=	almost ready-to-fly
BWB	=	blended-wing-body
CG, c.g.	=	center of gravity
EOM	=	equations of motion
FSTD	=	flight simulator training device
GA	=	general aviation
GPS	=	global positioning system
HAWT	=	horizontal axis wind turbine
IMU	=	inertial measurement unit

LEV	=	leading edge vortex
MAV	=	micro air vehicle
MEMS	=	microelectromechanical systems
NACA	=	National Advisory Committee for Aeronautics
NTSB	=	National Transportation Safety Board
PIV	=	particle image velocimetry
RC	=	radio controlled
RPM	=	revolutions per minute
TDPF	=	tail damping power factor
TEV	=	trailing edge vortex
TV	=	trailing vortex
UAV	=	unmanned aerial vehicle
UPRT	=	upset prevention and recovery training

Chapter 1

Introduction

Research into the aerodynamics of stall/spin remains a topic of ongoing interest since as early as the 1930s [1–3]. Notably, accidents in which stall/spin are cited account for about 7% of total pilot-related single-engine accidents; yet, these accidents represent a staggering 65–70% of the total number of fatalities [4]. The only deadlier causal factor cited in accidents is weather, which is cited in only 5–6% of total pilot-related single-engine accidents, but it is a factor in 65–75% of the fatalities. For the purpose of clarity, multiple causal factors are often cited in aircraft accidents [4]. In some cases, continued visual flight into clouds results in a fatal stall/spin accident. Significantly, then, improvements to aircraft stall/spin behaviors hold great potential to improve safety and thus serve as a motivation for this research. Advancing the understanding of the aerodynamics of stall/spin and improving the ability to model the complex wing aerodynamics and the resulting dynamic airplane motion holds the potential to save lives because of the deadly nature of accidental spins.

In 2013, the Federal Aviation Administration (FAA) released a final rule that renewed interest in the study of stall/spin. The rule mandates the incorporation of an extended envelope into Flight Simulator Training Devices (FSTDs) within five years of its release. This extended envelope forms part of the training for Upset Prevention and Recovery Training (UPRT) [5]. A subsequent proposed update in 2014 to this final rule states that if a simulator that is used for post-stall flight training is inaccurate in the upset regime, the pilot may learn control strategies in the simulator that are inappropriate or potentially dangerous [6]. In order to train pilots to use appropriate and safe control strategies, a flight simulator must be accurate; this is the reason why a need exists for increased accuracy flight simulators, especially in the spin regime.

A spin is defined as the complicated motion that is exhibited by an aircraft rapidly descending at an angle of attack greater than stall and less than 90 deg, while rotating around a vertical axis [7]. In general, the rotation of the aircraft center of gravity (c.g.) follows a helical or spiral-like pattern around this vertical spin axis. In particular, Ward and Strganac define a spin as the "sustained yawing and rolling rotation at angles of attack above the stall angle of attack" [8]. A spin, in which the aircraft is stalled and at a relatively constant speed, differs from a spiral. In the case of a spiral, the airplane demonstrates increasing airspeed and is not necessarily stalled [9]. It is suggested

"stall/spin problems represent one of the last technical frontiers in the aviation field and have significant impact on the general-aviation (GA) industry" [10].

The existing methodology for determining spin characteristics, both for general aviation aircraft and transport aircraft, uses a combination of rotary balance and static wind tunnel data to create a dynamic model of the aircraft [11–14]. In some isolated cases, the rotary derivatives are estimated from the static data [15]. Such an estimation of rotary derivatives from the static data is contrary to Bihrle's 1976 paper [16], which concluded that rotary balance data are needed when creating a "useful analytical model for spin." These rotary balance data were acquired at Reynolds numbers as low as $Re = 140{,}000$ when on a 14% scale model [17]. Strong agreement was observed in an AGARD study [18] between rotary balance results taken at $Re = 6\text{–}7.5 \times 10^6$ and full scale tests, for which the Reynolds numbers are an order of magnitude larger than those measured by the NASA rotary balance experimental hardware. The NASA rotary balance hardware is capable of operating at a maximum of $Re = 1.3 \times 10^5$ [19]. While typical full-scale spin Reynolds numbers are on the order of 2.5×10^6 [19], free-flying spin tunnel tests are conducted at Reynolds numbers of around 50,000 [20]. The study of stalls and spins presents a challenging problem because of the high angles of attack involved and the associated highly-separated flow [21–24]. Additionally, any extrapolation of data from spin tunnel or radio-controlled (RC) model tests to full-scale aircraft is difficult on account of critical Reynolds number effects [21, 25, 26].

Less typically, full-scale tests are performed with a pilot at the controls. These tests are risky, and in the case of the Cessna 162 Skycatcher, two of the early prototypes were lost during spin-related testing. After the first crash, a new aircraft was built that had a redesigned tail with reduced sweep and increased area [27]. The tail was redesigned in an attempt to improve the spin recovery characteristics, but it did not fully solve the spin problem. Production airframes were modified by reducing the travel of the ailerons and elevator, extending the rudder further down the tail, and adding a large ventral fin [28]. A dorsal fin was also tested in one of the interim configurations, but it was not included on the production aircraft [27]. Other aircraft that lost prototypes during spin flight testing include the Lancair 400, Gippsland GA-8 Airvan, and the Airplane Factory Sling [29].

Spin testing began as early as the biplane era of the early 1930s [1] when the National Advisory Committee for Aeronautics (NACA) staff first dropped dynamically-scaled models from the top of a 105-ft balloon hangar in order to study ways to improve the spin characteristics of the NB–1 seaplane trainer and the O2–E observation airplane [2]. The free-drop method [1] did not yield a long-enough time series of data for satisfactory tests, and by 1932, researchers in the United Kingdom constructed the first operational vertical spin tunnel with a 12-ft diameter circular test section [3]. More recently, NASA studied the stall/spin characteristics of general aviation aircraft in great depth in the late 1970s and early 1980s, and a large amount of rotary balance data was generated from these experiments [30–42]. All of these rotary balance data showed that, as the spin rate increased, the wing normal force coefficient C_N increased roughly proportional to the square of the spin parameter ω, defined as

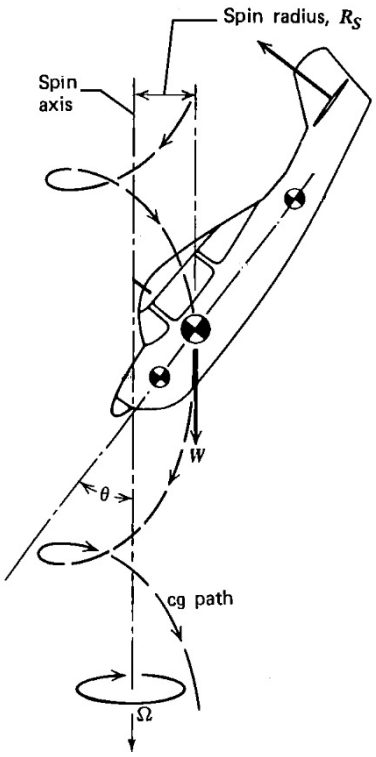

Figure 1.1: An illustration of the spin parameter variables (McCormick [43]).

$$\omega = \frac{\Omega b}{2V} \tag{1.1}$$

where b is the wing span, Ω is the angular velocity about the spin axis, and V_∞ is the freestream velocity. Figure 1.1, taken from Ref. [43], depicts the spin parameter variables.

Typically, low values of ω correspond to a steep spin with the aircraft pitched with its nose toward the ground, while ω values above 0.9 correspond to a flatter spin mode, where the nose is pointing in a nearly-horizontal direction [43]. The spin parameter may be thought of as equal to the tip speed ratio, or TSR [44], a number used in the analysis of wind turbines, and boomerangs [45]. In the propeller and helicopter fields of study the advance ratio J is used. The advance ratio is defined as the ratio of the freestream velocity to the product of the rotational speed and the propeller diameter and is equal to the inverse of the tip speed ratio. Flight spin parameter values typically do not exceed $|\omega| = 1$; thus, the NASA general aviation rotary balance tests in the 1970s and 1980s were conducted for $|\omega| \leq 1$.

In 1981, McCormick [46] showed that "a simple strip analysis ... underestimates the magnitude of the wing's normal force coefficient and also fails, qualitatively, to predict the effect of spin rate on C_N" and proposed a "centrifugal pumping" effect that creates a spanwise pressure gradient [46]. McCormick [46] states that because flow is separated above a spinning wing and "for some distance beyond, ... the fluid in the separated region is moving with the wing

in the form of a solid body rotation" and "hence, a radial pressure gradient must exist." The additional drag behind a stalled spinning wing was quantified with the "approximate method" of Ref. [46] by

$$\Delta C_N = \frac{\omega^2}{3}(1+Y_S^2) \tag{1.2}$$

where Y_S is the normalized spanwise location ($2y_s/b_W$) outside of which the wing is stalled. For the case of a fully-stalled wing, Eq. 1.2 simplifies to Eq. 1.3.

$$\Delta C_N = \frac{2\omega^2}{3} \tag{1.3}$$

Pamadi and Taylor [24, 47] incorporate the correction factor of Eq. 1.2 into their method for estimating the forces and moments on a steadily spinning airplane. Since the publication of their papers in 1984 and 1987, no updates to the predictions of the normal force on a spinning wing are evident in the literature. This ΔC_N term was "a relatively simple expression ... which agrees reasonably well with experiment" [46]. Figure 1.2, taken from Refs. [24, 46], indicates the necessity of a correction for a stalled spinning wing. Equations 1.2 and 1.3 assume no wing tip ejection of the trapped fluid in the wake. Referenced by McCormick [46] in creating Eqs. 1.2 and 1.3, the rotary balance experiments were those of Bihrle et al. [33]. Data from later NASA rotary balance data sets also confirm the existence of the additional drag. One such data set is that of Ref. [38], which shows at $\alpha = 90$ deg and $\omega = 0$, $\Delta C_N = 0$. When $\omega = 0.85$, ΔC_N increased to approximately 2.75. Figure 1.3 taken from Hultberg and Mulcay [38] depicts a representative plot of C_N versus ω for large angles of attack.

Interestingly, the increased C_N on a wing in spin is a phenomenon that is also observed in the insect and micro air vehicle (MAV) fields of research. Experimental investigations into insect and flapping-wing flight provided insight into the structures and forces associated with wings in spin. Experiments by Lentink and Dickinson [48] showed that a unidirectionally translating fly wing model in a tank filled with either oil or water produced a maximum C_D of around 1.5 in the regime $110 < Re < 14{,}000$. When the wing motion was changed to unidirectionally revolving (akin to an airplane spin), C_D values of between 3 and 4 were measured. In the experiments, the wings and plates were attached at one of the tips, as opposed to having the wing centered on the rotational axis. Numerical simulations support the trends of higher coefficent data found in these experiments. Garmann [49] analyzed flat plates ($\mathcal{AR} = 1$, 2, and 4) and showed local sectional lift coefficients of around $C_l = 2.5$ and wing drag coefficients of $C_D \approx 3.0$. Also, quite significantly, the recent computational studies of Garmann as well as the experimental particle image velocimetry (PIV) studies of Carr et al. [50] showed that fluid from the trapped wake is indeed ejected radially at the tip.

Centrifugal pumping models were proposed where the rotating blade (or in the case of a spin, the wing) pumped the separated air outward radially [51, 52]. Generally, these models subject the separated flow to centrifugal loading, which is proportional to $\Omega^2 r$ [51]. In all cases, these models note that the greatest effect is observed near the wing or

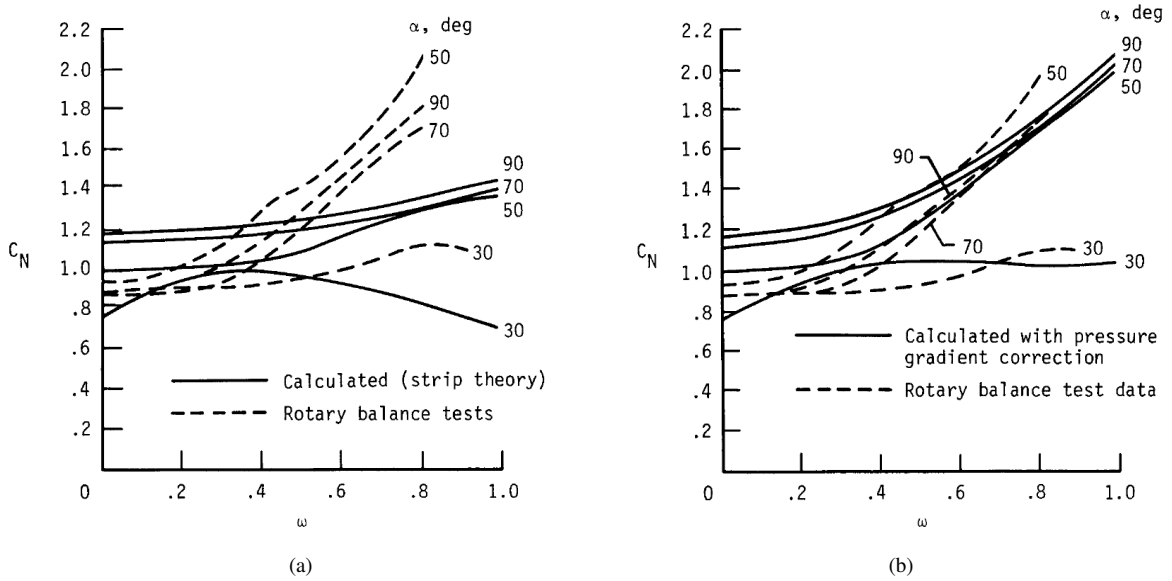

Figure 1.2: Comparison of (a) strip theory predictions and (b) strip theory predictions with post-stall spinning correction to experimentally-acquired C_N versus ω data for α values of 30, 50, 70, and 90 deg (McCormick [46]).

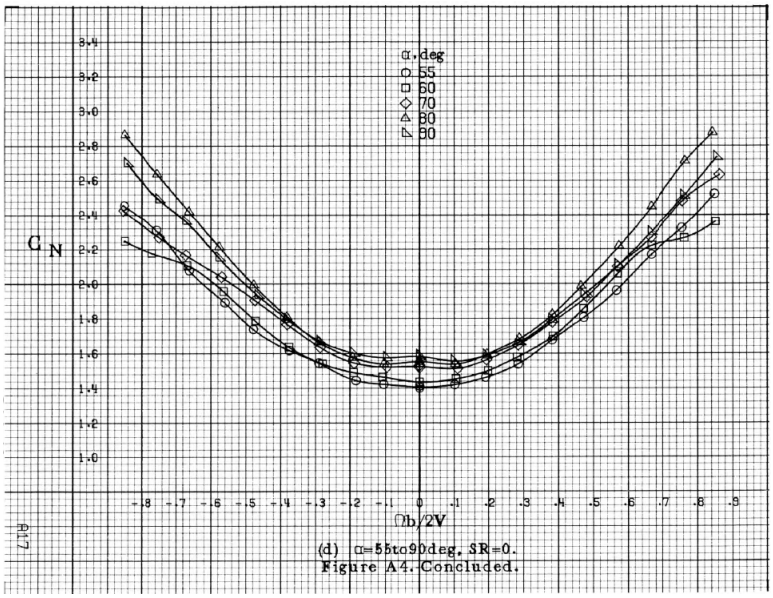

Figure 1.3: Plot of experimentally-acquired C_N versus ω data for α values between 55 and 90 deg (Hultberg [38]).

blade root [51, 53–56]. One such root effect is stall delay, which is used to explain the increased power and bending moment that exists on the inboard section of wind turbines [51]. In the case of stall delay, the outward radial flow, which is caused by 3D rotation effects and a high blade solidity ratio (defined as the ratio of the local chord length to the distance from the rotation center), causes airfoil $C_{l,max}$ values to exceed 2D measurements [51]. It should be

noted, however, that stall delay is not entirely applicable to the deep stall/spin regime studied here. Instead, stall delay is more so geared toward lower angles of attack near and just above the airfoil stall angle of attack.

In general, the centrifugal pumping loads on the boundary layer and stalled flow accelerate the flow outward radially [52], and, in the case of the stalled flow, some of the fluid departs from the area of the wake at the trailing edge if the chordwise pressure gradient is unable to counteract the Coriolis forces. This departure of the fluid reduces the fluid volume within the stalled region, as the Coriolis forces do not counteract the "centrifugal effects" [52]. The Coriolis force is the result of transforming Newton's laws from an inertial (non-rotating) reference frame into a non-inertial (rotating) frame of reference (i.e., a spinning airplane in this case) and it acts perpendicular to the velocity of the fluid and to the rotation axis of the body. The derivation of the fundamental equation that describes the Coriolis force begins with a definition of the velocity in the inertial reference frame, as given by

$$V_I = \frac{dr}{dt_I} = \Omega \times r \tag{1.4}$$

where dr/dt_I is the time derivative of r in the inertial reference frame, Ω is the angular velocity about the axis of rotation, and r is the position vector of the object. If the object has a non-zero velocity V_B in the non-inertial reference frame, Eq. 1.4 becomes

$$V_I = \frac{dr}{dt_I} = V_B + \Omega \times r \tag{1.5}$$

Noting that $V_B = dr/dt_B$ (time derivative of r in the non-inertial reference frame), Eq. 1.5 becomes

$$V_I = \frac{dr}{dt_I} = \frac{dr}{dt_B} + \Omega \times r \tag{1.6}$$

From Eq. 1.6 it becomes apparent that the general relationship of time derivatives in the inertial and non-inertial reference frames for a general vector is

$$\frac{d[\,]}{dt_I} = \frac{d[\,]}{dt_B} + \Omega \times [\,] \tag{1.7}$$

where $[\,]$ represents a general vector. Applying the time derivative of Eq. 1.7 to the velocity vector of Eq. 1.5 to get the acceleration in the inertial reference frame a_I yields

$$a_I = \left(\frac{d}{dt_B} + \Omega\times\right)(V_B + \Omega \times r) \tag{1.8}$$

Applying the cross products and noting that $a_B = d^2r/dt_B^2$, Eq. 1.8 becomes

$$a_I = a_B + \Omega \times (\Omega \times r) + 2\Omega \times V_B \tag{1.9}$$

Applying Newton's second law (i.e., $F = ma$) to Eq. 1.9 by multiplying both sides by the object mass m and solving for ma_B gives the equation of motion for the object in the non-inertial reference frame

$$ma_B = F - m\Omega \times (\Omega \times r) - 2m\Omega \times V_B \tag{1.10}$$

where ma_B is the apparent force on the object and F is the force acting on the object. The second term $(-m\Omega \times (\Omega \times r))$ represents the centrifugal acceleration, and the final term represents the Coriolis force, i.e.,

$$F_{Coriolis} = -2m\Omega \times V_B \tag{1.11}$$

In the case of a stalled wing in yaw, the velocity of the fluid is toward the wing tip, and the rotation axis of the body is vertical. Thus, the Coriolis force would push the fluid toward the wing trailing edge. If an insufficient chordwise pressure gradient exists, the flow in the boundary layer or separated wake may depart the wing at the trailing edge.

It should also be noted that far into the stall region, estimates of the sectional lift and drag coefficients are mostly not dependent on the airfoil shape and Reynolds number. The wing aspect ratio and planform geometry are the primary factors that determine the lift and drag characteristics of a wing well beyond stall [56]. For the purposes of preliminary design and analysis [54], "simplified methods are needed that capture the first-order effects due to rotation" [51]. These methods to capture the first-order effects due to rotation are precisely the topic of this research.

Chapter 2

Goals and Objectives

The overall goal of this research is to use experimental and analytical tools to advance the understanding of the aerodynamics of a stalled wing and airplane in spin. This research aims to develop a force prediction computer code with a first-principles-based analytical model that advances the current state of the art. Experimental studies of stalled wings in spin were previously lacking, and this research offers a way to characterize the behavior of wings in spin and the forces encountered beyond those predicted by strip theory. It is demonstrated that uncorrected strip theory underpredicts the aerodynamic forces on wings in spin, especially at high spin parameter values of $|\omega| \geq 0.5$. Room for improvement exists; thus, effort will be put toward the development of an improved force model for wings in spin. It is of particular interest to establish the normal forces on a wing in spin, as this parameter plays a large part in defining the spin radius of an airplane. Consequently, an improved model for a stalled wing in spin would yield a significant enhancement in the accuracy of spin modeling. The specific objectives of this research include the following:

1. Increase the understanding of the forces on an airplane in spin using flight testing to determine the motions of an airplane and its wing in spin.
2. Evaluate the effects of different ventral fin geometries to develop an understanding of how to improve the spin characteristics of an airplane.
3. Develop an analytical model to quantify the additional force due to centrifugal pumping and flow entrainment experienced by wings in spin.
4. Develop a methodology for testing wings in spin in a horizontal wind tunnel, perform wind tunnel tests to increase understanding of the forces on stalled wings in spin, and validate the newly developed analytical model with the experimental wind tunnel data.
5. Create a force prediction code to calculate the forces on an airplane in spin, and incorporate the aforementioned analytical model into airplane force predictions. Use this force prediction code to produce 6DOF trajectory simulations, and validate select spin control configurations against the flight test data acquired in this research.

Achieving these objectives will add to the knowledge of wings in spin and 6DOF spin simulations. Also, it will improve upon the state of the art and allow for the creation of better spin simulation codes and correction models.

Because the stall/spin regime is such a deadly one, any improvements to the state of the art in understanding and modeling stall/spin hold great potential to save many lives.

Chapter 3

Flight Testing

For the flight test portion of the experimental components of this research, a radio controlled testbed aircraft was flown with an onboard instrumentation suite specifically configured and adapted for this spin analysis. This airplane was flown at Eli Field in Monticello, IL. A flight test program that included a large number of spins with a number of different control deflection combinations and ventral fin additions was flown. The onboard instrumentation suite centered on an inertial measurement unit (IMU), which recorded the time histories of the trajectory, velocity, acceleration, and angular rates of the aircraft as it executed various maneuvers.

3.1 Test Aircraft Description

The Aero Testbed aircraft used in the flight tests was developed [57] from a commercially available almost ready-to-fly (ARF) 35%-scale Extra 260 produced by Horizon Hobby's Hangar 9 division [58]. Table 3.1 lists the physical properties of the airplane. The airplane had a wingspan of 105 in (266.7 cm) and a weight of 37.51 lb (17.01 kg) when flown. A photograph of the Extra 260 UIUC Aero Testbed aircraft is shown in Fig. 3.1. Based on the mean aerodynamic chord, the airplane had a nominal cruise Reynolds number range of 7–9$\times 10^5$ at a C_L of 0.3–0.5. When in a spin condition, the wing tip Reynolds number was in the vicinity of 5×10^5. The tapered wing had a 10.5%-thick symmetric airfoil, a taper ratio of 0.45, and an aspect ratio of 5.50. The horizontal and vertical tail surfaces consisted of symmetric airfoils with a t/c of 11%, and both the wing and horizontal tail had zero dihedral and zero incidence. To reduce vibrations and avoid inflight changes to the weight and c.g. that would be generated by using a gas-powered engine on the aircraft, the Aero Testbed was powered by a Hacker A150-8 electric motor fitted with a Mejzlik 27x12TH propeller. To counteract the left-turning tendency, which was caused by the propeller wake swirl, the motor was angled at 2.5 deg to the right, and there was zero downward thrust (i.e., motor was not angled down). A 14-cell, 51.8V, 10,000-mAh lithium polymer (LiPo) battery provided a power source for the motor. This power source provided approximately 8 min of flight time when performing spins and as much as 12 min of flight time when performing primarily at a steady cruise flight with gentle climbs and glides.

Figure 3.1: Photograph of the 35%-scale Extra 260 UIUC Aero Testbed aircraft.

3.2 Ventral Fin Configurations

In an attempt to identify the flight configurations that would mitigate stall/spin situations, a total of four different flat-plate ventral fins were tested on the airplane to determine which tail and aft fuselage geometries most significantly affect the spin condition. A ventral fin is an additional tail surface mounted below the fuselage. Figure 3.2(a) presents a photograph of the ventral fin installation on the testbed aircraft. The fins were affixed to the airframe with four bolts that threaded into an equal number of blind nuts. These nuts were affixed to the internal structure of the aircraft tail. The aforementioned attaching method was devised to allow for rapid and repeatable installation and removal of the ventral fins at the flying field. Specifically, the fins were constructed of 1/8-in birch plywood that was glued and buttressed with 1/2-in basswood triangle stock. Lightening holes were made to Fins 2, 3, and 4 to keep the weight similar to that of Fin 1. Then, covering was applied to maintain the smooth flat-plate surface. The properties of the four ventral fins are presented in Table 3.2, and a drawing of the four fins is presented in Fig. 3.2(b). The row in Table 3.2 entitled "(sub hstab)" refers to the area of the fin that is located beneath the horizontal stabilizer, as opposed to the area of the ventral fin that extends forward of the leading edge of the horizontal stabilizer. The inclusion of this measurement was prompted by the geometries used in calculating the tail damping power factor ($TDPF$) [59] and from the results of Ref. [60], which demonstrated significant spin damping by the area beneath the horizontal stabilizer at ω values similar to those experienced by the Aero Testbed. The four ventral fins were sized to determine whether it was the total area of the fin that was important, or whether it was only the area below the horizontal stabilizer that

Table 3.1: Physical Properties of the 35%-Scale Extra 260 UIUC Aero Testbed Aircraft

Aircraft		
Length	245.9 cm	(96.8 in)
Nose/Tail length ratio	0.44	
Mass / Weight	17.01 kg	(37.51 lb)
CG location ($\%\bar{c}$)	35.2% $\bar{c}$	
Roll moment of inertia (I_{xx})	1.53 kg-m^2	(1.13 slug-ft^2)
Pitch moment of inertia (I_{yy})	4.86 kg-m^2	(3.58 slug-ft^2)
Yaw moment of inertia (I_{zz})	6.06 kg-m^2	(4.47 slug-ft^2)
Wing		
Span (b)	266.7 cm	(105.0 in)
Area (S_W)	13,118.2 cm^2	(2033.3 in^2)
Root chord (c_{Wr})	66.7 cm	(26.3 in)
Tip chord (c_{Wt})	30.2 cm	(11.9 in)
Taper ratio (λ)	0.45	
Mean aerodynamic chord ($\bar{c}$)	50.7 cm	(20.0 in)
Airfoil t/c	10.5%	
Airfoil	Symmetrical	
Aspect ratio ($\mathcal{R}$)	5.50	
Incidence angle	0.0 deg	
Dihedral	0.0 deg	
Sweep	$<$ 1 deg	
Vertical Stabilizer		
Area (S_V)	1,379.4 cm^2	(213.8 in^2)
Rudder Area	990.3 cm^2	(153.5 in^2)
Airfoil t/c	11%	
Airfoil	Symmetrical	
Horizontal Stabilizer		
Area (S_H)	2,895.0 cm^2	(448.7 in^2)
Elevator area	1,315.0 cm^2	(203.8 in^2)
Root chord (c_{Hr})	36.6 cm	(14.4 in)
Tip chord (c_{Ht})	20.3 cm	(8.0 in)
Airfoil t/c	11.0%	
Airfoil	Symmetrical	
Aspect ratio ($\mathcal{R}$)	4.90	
Incidence angle	0.0 deg	
Dihedral	0.0 deg	

Table 3.2: Physical Properties of the Spin-Reduction Ventral Fin Configurations

	Fin 1		Fin 2		Fin 3		Fin 4	
Height	6.4 cm	(2.5 in)	6.4 cm	(2.5 in)	8.9 cm	(3.5 in)	8.9 cm	(3.5 in)
Length	24.8 cm	(9.75 in)	36.6 cm	(14.4 in)	24.8 cm	(9.75 in)	36.6 cm	(14.4 in)
Area	137.4 cm^2	(21.3 in^2)	200.0 cm^2	(31.0 in^2)	180.6 cm^2	(28.0 in^2)	261.4 cm^2	(40.5 in^2)
(sub hstab)	137.4 cm^2	(21.3 in^2)	157.3 cm^2	(24.4 in^2)	180.6 cm^2	(28.0 in^2)	220.2 cm^2	(34.1 in^2)
Weight	85.1 g	(3.0 oz)	93.6 g	(3.3 oz)	90.7 g	(3.2 oz)	93.6 g	(3.3 oz)

improved the spin characteristics. As an example, Fins 2 and 3 have similar areas with Fin 2 being slightly larger, but Fin 3 has all of its area located beneath the horizontal stabilizer and has slightly more area beneath the stabilizer than Fin 2.

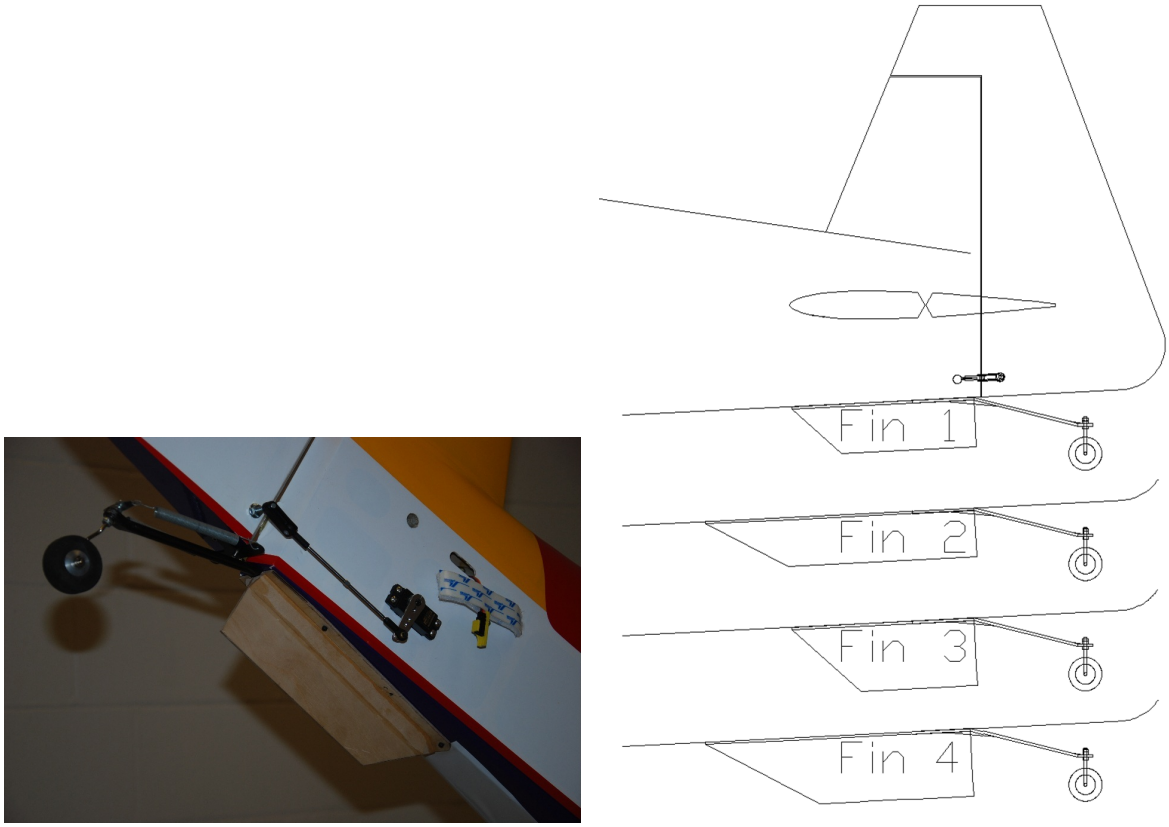

(a) (b)

Figure 3.2: Depiction of the ventral fin installation by (a) a photograph of Fin 1 installed on the testbed aircraft, and (b) a CAD drawing of the four fins.

3.3 Data Acquisition Equipment

During the test flights, the trajectory and orientation of the aircraft were recorded using an Xsens MTi-G IMU which contains a global positioning system-aided (GPS) microelectromechanical systems-based (MEMS) IMU. For trajectory tracking, the GPS signal is augmented by barometric pressure and inertial measurements to produce 3D location and velocity data superior to that of a standalone GPS receiver. The airplane is fitted with a single GPS antenna located atop the fuselage directly aft of the canopy (see Fig. 3.1). The IMU, located near the aircraft c.g., is programmed to automatically correct the GPS location data based on the offset between the IMU and the GPS antenna. The data from the onboard Attitude and Heading Reference System (AHRS) and navigation processor undergo onboard real-time digital signal processing to produce filtered data based on the linking of the GPS, inertial, and barometric pressure recording devices [61]. Control surface positions, motor power settings, and motor revolutions per minute (RPM) values are recorded by an Eagle Tree recording system [62]. A photograph of the electronics system is shown in Fig. 3.3.

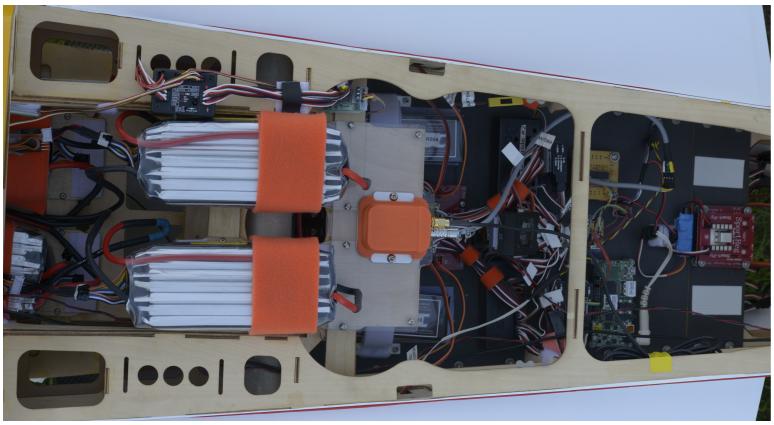

Figure 3.3: Photograph of the instrumentation system on the Extra 260 UIUC Aero Testbed aircraft (left/nose).

While the velocity and orientation information is recorded in the earth-reference frame, the acceleration and angular rate data are recorded in the body-fixed reference frame of the aircraft. When the motor power setting is increased, the electric motor induces a change in the local magnetic field. This change in the local magnetic field creates a change in the heading observed by the IMU, but it does not change the angular rates and GPS position. The proximity of the IMU to the batteries is necessary in order to locate the IMU as close as possible to the airplane c.g. This location was chosen because it would give the highest accuracy measurements of the angular rates, accelerations, and orientation of the aircraft. The consequence of this location is that the measured heading ψ will slew when power is applied. To reduce this effect, all of the spins were conducted at a constant motor power setting, with the majority of the spins conducted at a zero power setting.

The specified maximum operating altitude of the XSens MTi-G IMU is 18 km, the maximum operating velocity is 600 m/s, and the GPS resolution is 2.0–2.5 m, depending on satellite coverage [61]. The dynamic accuracy of the IMU is 1-deg root mean squared (RMS) in roll and pitch and 2-deg RMS in heading. The GPS data is updated at a rate of 4 Hz, and the position and velocity is updated at 120 Hz [61]. The orientation and position of the IMU is estimated by means of an extended Kalman filter, which is referred to as the Xsens Kalman Filter 6DOF GPS (XKF-6G). Since the GPS updates at 4 Hz, and the inertial sensors update at 120 Hz, the data from the inertial sensors are integrated to predict the position, velocity, and orientation. Because of small errors in the measurements, the orientation estimates will experience a growing error of approximately 3–4 deg/min. This growing error, or drift, is corrected using the GPS receiver. The result is a system that is able to estimate the position and velocity at a rapid update rate with minimal latency relative to a GPS-only system (like the Eagle Tree). As a result, small, rapid displacements can be quantified [61]. Altitude estimates from the GPS are supplemented by the internal barometer because of the inherent low accuracy of the GPS in sensing vertical position. The barometer is used only to sense the change in altitude because the pressure varies daily [61].

The aircraft is also instrumented with a pitot-static airspeed measuring system. The pitot probe geometry allows it to record accurate dynamic pressures at flow angles up to 20 deg. Because of the high angles of attack experienced in a spin, the static pressure is not measured on the pitot probe. Instead, the static pressure is measured from inside the aircraft. This solution was determined to be the best-possible method to measure the static pressure given the constraints of the aircraft and hardware. The pitot probe and static tube are connected to a miniature amplified output pressure sensor. The device is 0.62×0.50 in and is temperature compensated, producing a linear output to the measured pressure in the pressure ranges used for these flight tests. The 20cmH2O-D1-4V-MINI pressure sensor has an operating pressure range of -0.2 to 20 cm water, and it is temperature compensated between 5 and 50 deg C [63].

The IMU- and pitot probe-logged data were transferred through a Paparazzi UAV autopilot board and recorded at 5 Hz on a Gumstix microcomputer running the Linux Ubuntu operating system. This system operated independently of the other two electrical systems on the aircraft. The second electrical system ran the RC receiver, servos, and the Eagle Tree recording device. The third and final electrical system powered the electric motor described in detail earlier in this section.

Some processing of the IMU-direct data was necessary. Times were recorded in microseconds (10^{-6} s) as a 32-bit signed integer. As such, the largest recordable value was 2,147,483,647 μs, or approximately 2,147 s. When the IMU was run for longer periods than this duration, after 2,147,483,647 μs the time would start at $-2{,}147{,}483{,}647$ μs, and count toward zero. Because no IMU runs lasted longer than $2 \times 2,147,483,647$ μs, and the as-recorded time was not suitable for plotting because many IMU runs lasted between 2,147 and 4,294 s, a simple time correction was implemented, as shown in Eq. 3.1

$$T = \begin{cases} \frac{t}{10^{-6}} & 0 \leq t < 2147483647 \\ \frac{t+2*2147483647+1}{10^{-6}} & -2147483647 < t < 0 \end{cases} \tag{3.1}$$

where t is the uncorrected, as-recorded IMU time in μs, and T is the corrected and plotted time in s. A similar correction was applied to the heading, ψ, which was recorded by the IMU over the range $-\pi < \psi \leq \pi$ rad, and was corrected to $0 < \psi \leq 2\pi$ rad.

By subjecting the pitot probe to a known freestream velocity, and recording the raw voltage reading, a calibration curve for the pitot probe was determined. The fit is shown in Fig. 3.4. This freestream velocity was measured using both static and rolling rig devices. The constants were $m = 0.7305$ and $b = 3.0855$, and they converted the voltage recorded by the IMU from the differential pressure sensor to an airspeed. Temperature and pressure were different on each test day, and the average value of the KCMI and KDEC airport METAR data was used to provide the values. This average was used as Eli Field is located nearly halfway between the two METAR recording stations. Figure 3.4 shows the data and linear curve fit used as the calibration curve.

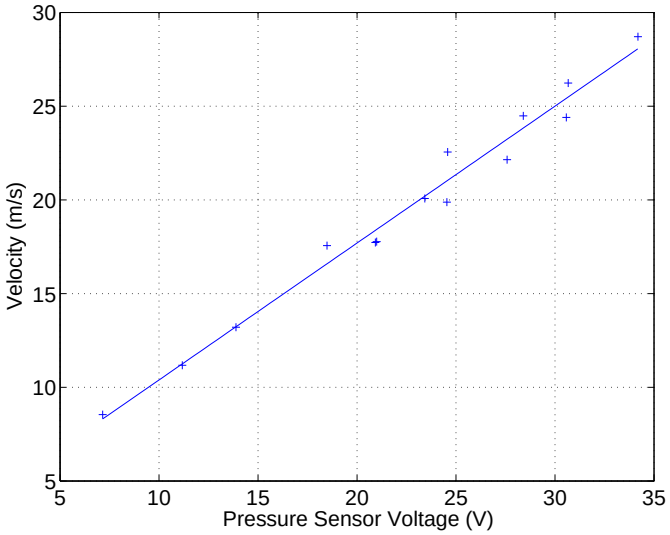

Figure 3.4: Plot of the pitot probe calibration data points (red) with linear curve fit (blue) superimposed.

Table 3.3: Maximum Control Surface Deflection Angles

Control Surface	Low Deflection (deg)	High Deflection (deg)
Rudder (δ_r)	± 29	± 40
Elevator (δ_e)	± 14	± 46
Ailerons (δ_a)	± 22	± 34

The terms "IMU *Re*" and "*Re*," as presented in this document, were determined from the IMU trajectory and pitot-probe velocities, respectively. Because the IMU trajectory-derived Reynolds number included the effects of the windfield and the wing tip pitot-probe velocity readings were only accurate over the range $-20 \leq \alpha_{Wt} \leq 20$ deg, only a side-by-side comparison of these two values would shed light on the actual Reynolds number values experienced by the aircraft.

During flight testing, two control surface deflection settings were used. These are, henceforth, referred to as the low deflection angles and the high, or aerobatic, deflection angles. Table 3.3 summarizes the deflection angles of the rudder, elevator, and ailerons for both the low and high deflection angle settings. In summary, the low deflection angle magnitudes for the rudder, elevator, and ailerons are 29, 14, and 22 deg, respectively. The high control surface deflection angles are 40, 46, and 34 deg for the rudder, elevator, and ailerons, respectively.

3.4 Data Reduction Techniques

The velocity, as recorded by the instrumentation, must be corrected. This is because of the fact that the pitot probe is located on the left wing tip, while the IMU is located near the c.g. of the airplane, and the airplane spins about a helix with a non-zero radius (i.e., airplane c.g. does not pass through spin axis). This velocity correction involves

the geometric distance from the airplane centerline and the spin radius. The geometric distance from the airplane centerline was measured to be 133.48 cm (52.55 in).

When conducting flight tests, it was observed that the winds aloft would produce a drift in the spin trajectory that would differ from day to day. To generate proper spin trajectories, the winds aloft were calculated in the data-processing software and subtracted to produce a near-vertical spin trajectory. The closer to straight and vertical that the post-processed trajectory was, the better the quality of the generated trajectory plots. An estimate of $U(z)$, the average wind velocity at height z, may be determined through the use of a logarithmic profile (which is commonly used in meteorological studies to approximate the atmospheric boundary layer) as presented below [64]

$$U(z) = U_{ref} \frac{log(z/z_0)}{log(z_{ref}/z_0)} \tag{3.2}$$

where U_{ref} is the wind velocity at reference height z_{ref}, and z_0 is the aerodynamic roughness length. The aerodynamic roughness length is an experimentally derived constant determined by the type of surface over which the wind is blowing (i.e., over a city or an open field) [64]. For open fields, like those near the Aero Testbed flying site, an aerodynamic roughness length of $z_0 = 0.05$ m provides a good match to the actual wind profile [64, 65]. With $z_0 = 0.05$ m and based on a reference velocity of $U_{ref} = 15$ m/s at $z_{ref} = 5$ m, the average wind velocity at $z = 300$ m, an altitude typical of the beginning of an experimental spin, is estimated to be $U(300) = 28.3$ m/s. With the same values of z_0 and z_{ref}, but with $U_{ref} = 10$ m/s, the average wind velocity is estimated to be $U(300) = 18.9$ m/s.

An estimation of the winds during each spin was performed by selecting a time range of data to plot, and then defining a time slice at the beginning and end of the data set. This time slice allowed for the spin entry and exit to be plotted while not including those data points in the wind calculation. For the data between the start and end time slices, the *x*- and *y*-displacement of the aircraft from the beginning of the spin to the end was calculated. Using these distances, the altitude data, and the time stamp, and, assuming that the axis of the spin helix was vertical, the average windfield was calculated. The average windfield was then subtracted from the entire data set (i.e., the spin *and* the entry and exit time slices) based on the *x*-*y*-*z* location and the time since data set start, and the results were plotted. This process was performed for both the IMU-direct *x*-*y*-*z* data as well as the post-processed data, which will be described later in this section. This process was selected as it provided a good balance between accuracy and time required to implement. On days where the windfield was constant and consistent, good trajectory plots were generated where the airplane c.g. followed a vertical or near-vertical path during the developed spin. On gusty days, or ones where different windfields existed at different altitudes, the resulting trajectory plots were not as clean or straight.

Figure 3.5(a) depicts the direct IMU trajectory information from a representative Aero Testbed spin, while Fig. 3.5(b) depicts that same spin trajectory with an average windfield removed. An average wind vector was determined for each spin and was subtracted from the direct IMU data. It should be noted that data referred to as direct IMU data or IMU-

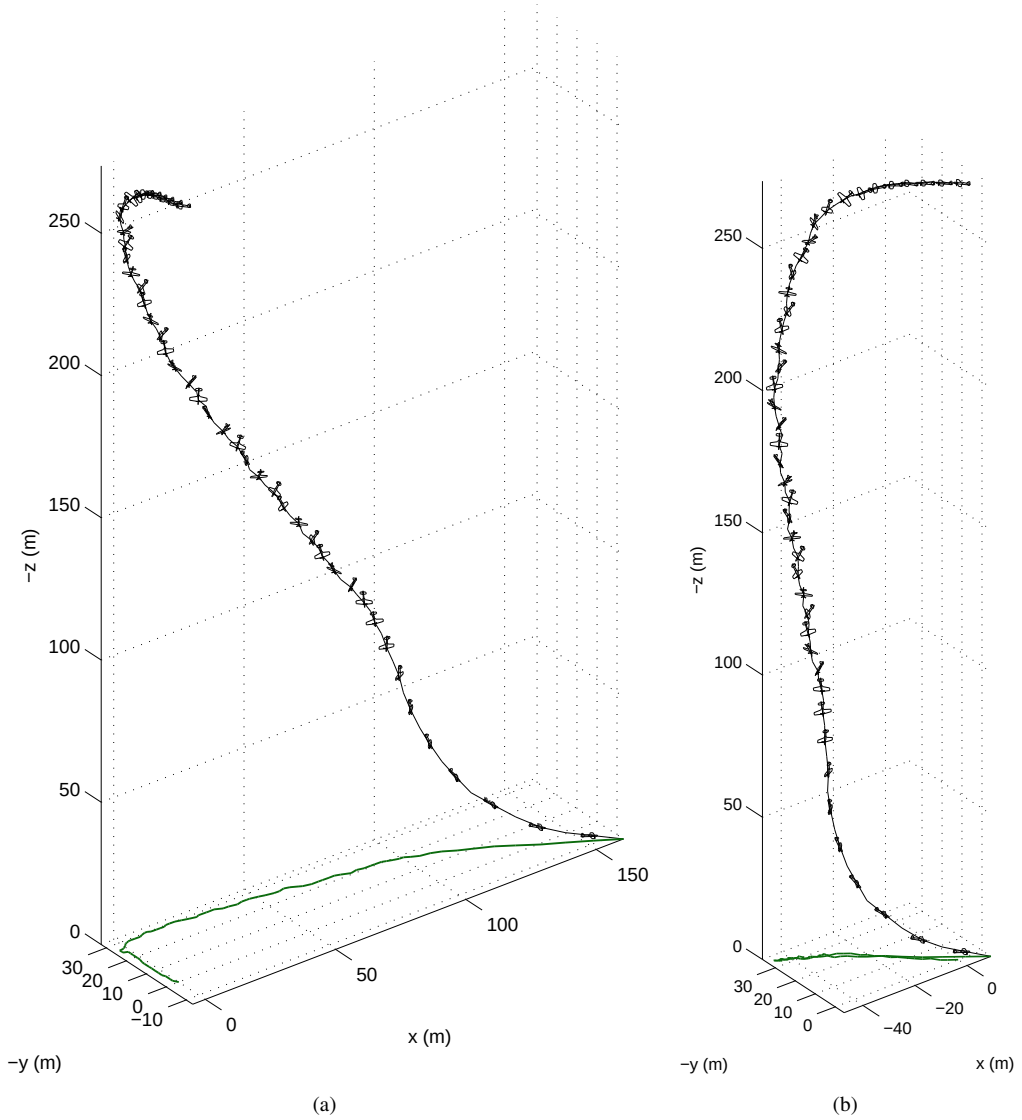

Figure 3.5: Spin trajectories for representative spin using the (a) direct IMU data, and (b) IMU trajectory with average windfield subtracted (aircraft magnified three times actual size and drawn every 0.40 s).

direct data refer to readings that were output directly from the IMU. When the windfield was removed from a data set, or an integration was performed, the direct IMU data set is then referred to as processed or integrated IMU data, respectively. The use of a windfield averaged over the course of a spin, as opposed to subtracting instantaneous wind velocities, is why the plotted trajectories with the windfield subtracted are not perfectly straight. Instantaneous wind velocities were not used because there was no instrumentation to measure them. The fact that the trajectory with the windfield subtracted is much straighter than that of the direct IMU data demonstrates that the windfield approximation used was appropriate. In order to minimize the influence of the winds aloft and to have calm and steady winds rather than strong and gusty winds, flights were conducted near sunset on low-wind days over a period of five months.

Additional post-processing of the IMU data was necessary in order to acquire accurate position information from the IMU. When stationary, the IMU was observed to demonstrate an actual resolution of 0.5 m in the *x*- and *y*-coordinates (the IMU hardware specification sheet shows 2–2.5 m resolution), which is too large of an error because the radii of the various spins were calculated to be on the order of the measured IMU resolution of approximately 0.5 m. The combination of the GPS resolution as recorded by the IMU, the small spin radii of the airplane, and the winds aloft prevented the spin radius from being accurately measured from the direct IMU position information, which is driven primarily by the GPS signal.

Instead of using the as-recorded *x*-*y*-*z* location of the IMU, for each spin, the *x*-, *y*-, and *z*-velocities were integrated using a 4-step backward difference Adams-Bashforth method [66], as summarized by

$$k = 1 : [x,y,z]_{n+1} = [x,y,z]_n + h[V_X,V_Y,V_Z]_n \tag{3.3}$$

$$k = 2 : [x,y,z]_{n+1} = [x,y,z]_n + \frac{h}{2}(3[V_X,V_Y,V_Z]_n - [V_X,V_Y,V_Z]_{n-1}) \tag{3.4}$$

$$k = 3 : [x,y,z]_{n+1} = [x,y,z]_n + \frac{h}{12}(23[V_X,V_Y,V_Z]_n - 16[V_X,V_Y,V_Z]_{n-1} + 5[V_X,V_Y,V_Z]_{n-2}) \tag{3.5}$$

$$k \geq 4 : [x,y,z]_{n+1} = [x,y,z]_n + \frac{h}{24}(55[V_X,V_Y,V_Z]_n - 59[V_X,V_Y,V_Z]_{n-1} + 37[V_X,V_Y,V_Z]_{n-2} - 9[V_X,V_Y,V_Z]_{n-3}) \tag{3.6}$$

where h is the timestep, $[V_X,V_Y,V_Z]$ are the *x*-, *y*-, and *z*-velocities, and $[x,y,z]$ are the *x*-, *y*-, and *z*-coordinates. This integration method smoothed the data and allowed a 3D helix to become readily seen, as shown in Fig. 3.6. Despite the fact that the velocities reported by the MTi-G IMU are derived from the GPS data, which was shown to have insufficient resolution, the reported velocities are adequately corrected internally by integrating the accelerometer data, which allows the velocity data to produce a helical path in *x*-*y*-*z* when integrated. This velocity-derived helical shape is contrasted with the IMU direct *x*-*y*-*z* data from the GPS. All spin trajectories presented, henceforth, have the average wind subtracted and the Adams-Bashforth integration applied.

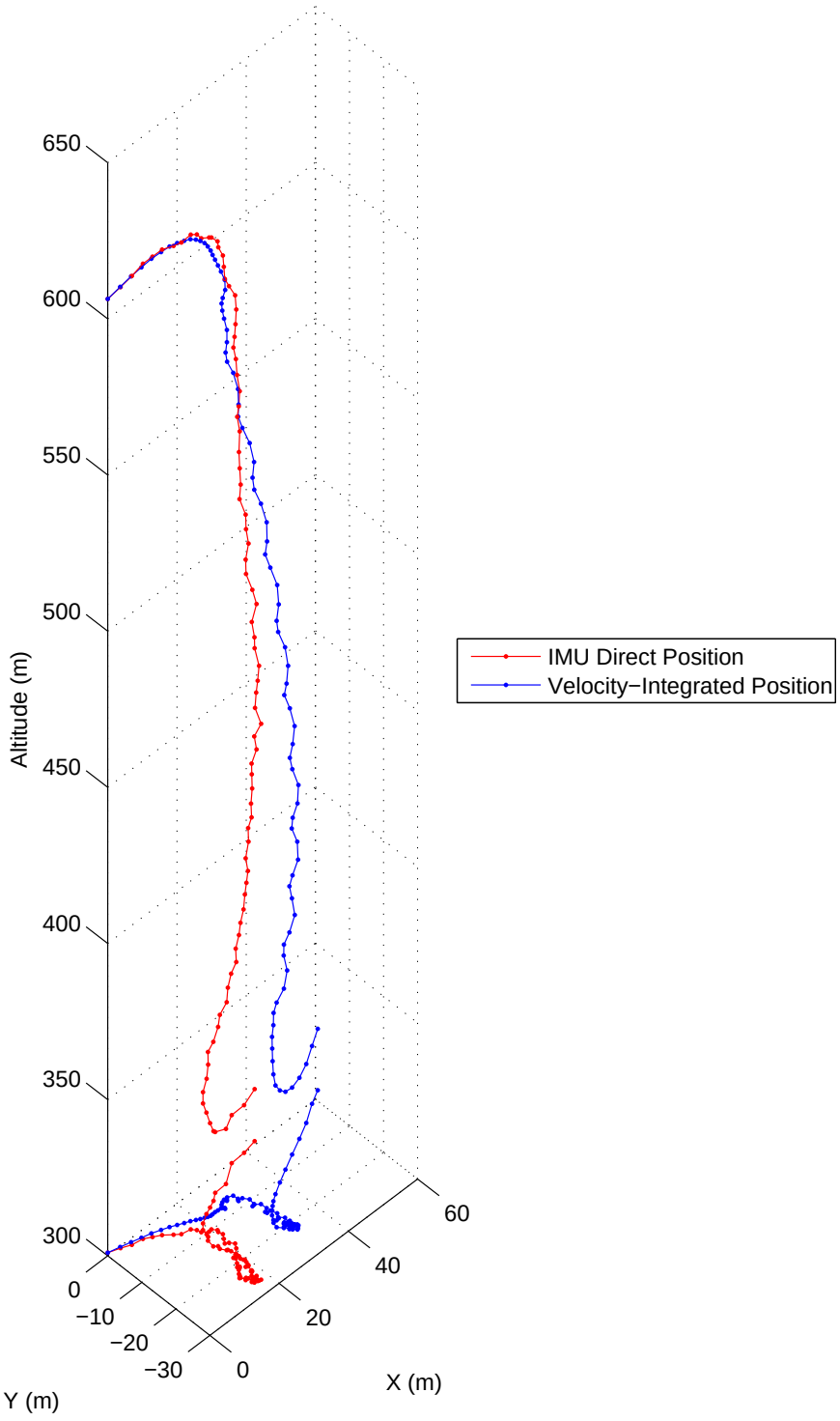

Figure 3.6: Plot of IMU direct position (red) and position integrated from IMU velocities (blue) with projected paths on ground.

3.5 Flight Testing Results

Results from a total of 24 different flight test spins generated in this work are presented. A spin occurs when an airplane is simultaneously stalled and yawed, resulting in one wing stalling before the other. As will be demonstrated, the spin has large values for both the yaw and roll rates, even without aileron deflection. The loss of lift from an uneven stall results in a roll in the direction of yaw. As the airplane rolls, the angle of attack on the more-stalled wing increases further as it plunges down, further decreasing lift and increasing drag. It is this increased drag that creates a yawing moment that keeps an airplane in a spin, even if the rudder deflection is returned to neutral. In the case of the Aero Testbed, however, deflection of the elevator and rudder were necessary to maintain a spin. The less-stalled wing (e.g., the right wing in a left spin) remains stalled, but, because it is less deeply stalled, it generates more lift and less drag than the more deeply stalled wing. Like any other stall, the nose of the aircraft drops down, and once yaw and roll rates increase, the aircraft pitch stabilizes at a large downward angle. This uneven stalling of the wings is the reason that even without aileron deflection, a high roll rate is experienced. Given the same rudder deflection, with and without deflected ailerons, differing, but large yaw rates were experienced, which will be shown in later subsections.

Because of the large number of spin configuration variables, a naming convention was constructed. For each spin, the rudder, elevator, and aileron deflections and directions, the motor power setting, and the installed ventral fin (if any), were defined. The motor power setting is customarily called the throttle setting in an airplane, and will be referred to as such. The construction of the naming convention allows for all of the information about the spin configuration to be conveyed to the reader with a string of letters, numbers, and dashes. The naming convention is organized according to four sections, each of which is separated by a dash. The first section describes the throttle, rudder, elevator, and aileron settings in the conventional "TREA" order. Three possible throttle settings exist — "T0," "T1," and "T2." The approximate RPM values for each of these three settings are summarized in Table 3.4. Two settings for the rudder and elevator exist, and they are designated "R1" and "R2," and "E1" and "E2," respectively. "R1" and "E1" refer to the low deflection angles of Table 3.3, respectively. No "R0" or "E0" settings (zero values) exist because all spins were performed with the rudder and elevator deflected. The ailerons, however, have a possible "A0" setting, which corresponds to no deflection. The "A1" and "A2" aileron settings, similar to those for the rudder and elevator, refer to the low and high deflection angles, respectively (see Table 3.3).

The second section of the naming convention consists of either a "Lft" or "Rght." This section is used to denote the direction in which the rudder was deflected in the aircraft reference frame. The third section of the naming convention defines whether the spin is an upright spin, or an inverted spin, denoted as "Up" and "Inv," respectively. For an upright spin, a "Lft-Up" indicates a rudder deflection to the left and a corresponding upward deflection of the elevator. In the case of an inverted spin, a "Lft-Inv" indicates a left rudder deflection and a downward deflection of the elevator, in the aircraft reference frame. When the spin is viewed from outside the airplane by an observer unaware of whether the

plane is upright or inverted, upright and inverted "Lft" spins will exhibit a rudder deflection that yaws the nose to the left and to the right, respectively, and an elevator deflection that pitches the nose away from the earth in both cases. In short, the naming convention is based on the control surface deflections in the aircraft frame of reference.

The fourth and final section of the naming convention is not present for all spins. It is surrounded by parentheses, and serves as an additional note regarding the spin. If the ailerons were deflected in an anti-spin manner (i.e., right roll commanded in a left spin), a "cross ail" entry would be present within the parentheses. This term indicates that the airplane is in a cross-controlled situation. If no indication is present and an "A0" is not present in the first section of the name, then the ailerons are deflected in a pro-spin manner. An example of this instance would be a left roll commanded in a left spin. The other factor indicated by the fourth section would be the presence of a ventral fin. The terms "Fin 1," "Fin 2," and "Fin 3" denote that ventral fins 1, 2, or 3, respectively, were present for that spin.

As an example, T2R1E1A1-Lft-Up-(cross ail) indicates that the spin configuration had a throttle setting of 750–1200 RPM, the rudder, elevator, and ailerons deflected at low deflection angles, in a left/upright spin, with the ailerons deflected in an anti-spin manner. The naming convention, as described above, is summarized in Table 3.5. FS One^{TM} RC flight simulator [67] renderings of the airplane with various control surface combinations are presented in Fig. 3.7 for reference.

The average bank angle, average pitch, standard deviation of pitch, roll and yaw rates, vertical velocity, Reynolds number, and spin parameter ω, were calculated for each of the spins. The spin radius R_s was measured by analyzing the flight test trajectory data with the average wind subtracted and the Adams-Bashforth integration applied. Each individual spin trajectory was plotted in MATLAB, and five representative pairs of points along the helical trajectory were visually selected. Five values for the diameter of the helical spin trajectory were then calculated based on the x- and y-coordinates of each of the respective pairs of points. The five diameter values were then averaged, and the spin radius R_s was calculated by dividing the average spin diameter by two. The data are summarized in Table 3.6. All aerodynamic values were calculated for the temperature and pressure specific to the day and time of the flight test. Table 3.6 begins with the T0R1E1A0-Lft-Up spin, which was defined as the baseline spin and used to demonstrate the repeatability of flight test results. The T0R1E1A0-Lft-Up spin represents the most-common configuration for which an airplane would typically enter an inadvertent stall/spin situation. The T0R1E1A0-Lft-Up spin would be encountered on a downwind-to-base or base-to-final traffic pattern turn that was overshot, where the pilot initiates an attempt to correct the overshoot by attempting to tighten the turn. The left rudder deflection was selected because a standard airport traffic pattern calls for left hand turns [68]. Notably, all spins performed in this series of flight tests were forced spins. After demonstrating the repeatability of the flight test results, the effects of changing the direction (rudder deflection) of the spin, adding pro- or anti-spin aileron deflections, increasing the control surface deflections, inverting the spin, increasing the motor power setting, and adding three different ventral fins for spin mitigation, are thoroughly investigated.

Table 3.4: Throttle Settings and Approximate RPM Range in Spin

Throttle Setting	Approximate RPM Range in Spin
T0	50–200
T1	340–840
T2	750–1200
Maximum	6900

Table 3.5: Spin Configuration Naming Convention

Throttle-Rudder-Elevator-Aileron Input	Spin Direction	Aircraft Orientation	Additional Note
T $\begin{pmatrix}0\\1\\2\end{pmatrix}$ R $\begin{pmatrix}1\\2\end{pmatrix}$ E $\begin{pmatrix}1\\2\end{pmatrix}$ A $\begin{pmatrix}0\\1\\2\end{pmatrix}$	– $\begin{pmatrix}\text{Lft}\\\text{Rght}\end{pmatrix}$	– $\begin{pmatrix}\text{Up}\\\text{Inv}\end{pmatrix}$	– $\begin{pmatrix}\text{cross ail}\\\text{Fin 1}\\\text{Fin 2}\\\text{Fin 3}\end{pmatrix}$

All of the flight test data figures in this section display two sets of V and Re values in an effort to present a comprehensive understanding of the aerodynamics of each spin. The set of values calculated from the direct IMU data are presented as "IMU V" and "IMU Re." These values are based on the motion of the c.g. of the aircraft as recorded by the IMU. The weakness of these data is that the x-y velocity calculated by the IMU includes the effects of the windfield and may not always accurately represent the true airspeed. The consistency of the IMU Reynolds number values, which are based on the wing MAC, between the three T0R1E1A0-Lft-Up spins of Figs. 3.9–3.10, shows that the flight test technique of planning flights near sunset on low-wind days, as mentioned before, was successful in achieving reasonably calm windfields on any given flight test day. The right column features values labeled "V" and "Re," which are derived from the pitot-static probe. The velocity recorded by the pitot static probe, however, must be corrected from the wing tip velocity to the airplane c.g. velocity. Further, if the wing tip α is beyond $\pm$20 deg, the reading is unreliable.

Figure 3.8 presents 3D spin trajectories for a T0R2E2A2-Lft-Up spin and a T0R1E1A0-Lft-Inv spin with the average windfield subtracted. Figure 3.8(a) provides an example of a spin where the windfield subtraction method did not produce a completely vertical spin axis. This spin, however, did exhibit a nearly vertical spin trajectory over the approximate range of $275 \geq -z \geq 200$ m. This lack of a vertical spin axis for the whole spin trajectory shows that the windfield was not constant during the flight test. On the other hand, Fig. 3.8(b) depicts a spin where the average windfield subtraction method worked well. Over the 450 m descent of the spin, a near vertical trajectory is depicted for the final 350 m. The straightness of the spin trajectory shows that the windfield was constant during the final 350 m of this spin and was only slightly different over the first 100 m descended during the spin.

(a) (b) (c)

(d) (e) (f)

(g) (h) (i)

(j) (k)

Figure 3.7: Renderings of the spins using graphics from FS One: a) T0R1E1A0-Lft-Up, b) T0R1E1A0-Rght-Up, c) T0R1E1A1-Lft-Up, d) T0R1E1A1-Lft-Up-(cross ail), e) T0R2E2A0-Lft-Up, f) T0R2E2A2-Lft-Up, g) T0R2E2A0-Rght-Up, h) T0R2E2A2-Rght-Up, i) T0R1E1A0-Rght-Inv, j) T0R1E1A1-Rght-Up, and k) T0R1E1A1-Lft-Inv.

Table 3.6: Summary of Individual Spin Parameters

Spin	ϕ_{avg} (deg)	θ_{avg} (deg)	σ_θ	p_{avg} (deg/s)	r_{avg} (deg/s)	V_Z (m/s)	Re	ω	R_s (m)	Fig.
T0R1E1A0-Lft-Up	0.7	−56.6	3.6	−238.1	−158.9	−15.9	0.65×10^6	−0.20	0.6	3.9, 3.10
T0R1E1A0-Lft-Up	1.0	−55.8	4.8	−232.7	−157.4	−14.8	0.58×10^6	−0.22	0.6	3.9
T0R1E1A0-Lft-Up	0.2	−57.4	3.3	−235.3	−150.3	−15.7	*n/a*	−0.20	0.6	3.10
T0R1E1A0-Rght-Up	−1.3	−56.7	5.3	239.6	157.9	−16.8	0.65×10^6	0.16	0.6	3.11
T0R1E1A1-Lft-Up	−60.6	−59.1	10.9	−355.1	−101.0	−25.4	1.03×10^6	−0.08	0.5	3.12
T0R1E1A1-Lft-Up-(cross ail)	13.1	−46.4	2.0	−186.9	−174.5	−14.0	0.50×10^6	−0.28	1.0	3.13
T0R2E2A0-Lft-Up	−11.2	−48.1	5.6	−134.7	−119.2	−14.2	1.01×10^6	−0.10	0.9	3.14
T0R2E2A2-Lft-Up*	−53.5	−40.8	14.5	−182.8	−77.9	−14.0	0.55×10^6	−0.64	0.8	3.15, 3.17
T0R2E2A0-Rght-Up	16.7	−53.8	4.6	182.2	129.3	−16.4	0.64×10^6	0.16	0.6	3.16
T0R2E2A2-Rght-Up*	47.1	−38.7	17.4	178.4	86.3	−15.7	0.55×10^6	0.71	0.8	3.16, 3.17
T0R1E1A0-Lft-Inv	−12.3	−63.2	12.8	266.3	−106.1	−21.1	0.83×10^6	−0.10	0.9	3.18
T0R1E1A1-Rght-Up	56.6	−59.3	13.5	383.9	107.8	−24.7	1.01×10^6	0.08	0.6	3.19
T0R1E1A1-Rght-Inv	−2.9	−56.6	12.5	259.5	154.6	−20.9	0.84×10^6	0.11	0.6	3.19
T1R1E1A0-Lft-Up	−4.6	−57.3	3.8	−234.8	−151.6	−16.9	0.64×10^6	−0.19	0.6	3.20
T2R1E1A0-Lft-Up	−12.3	−59.7	3.9	−264.2	−152.6	−19.6	0.77×10^6	−0.16	0.6	3.21
T2R1E1A0-Rght-Up	−4.4	−57.1	6.6	248.7	161.3	−17.7	0.68×10^6	0.19	0.5	3.22
T1R1E1A1-Lft-Up	−59.1	−61.3	4.5	−365.3	−104.5	−23.5	0.85×10^6	−0.10	0.7	3.23
T1R1E1A1-Rght-Up	57.4	−63.0	7.5	396.5	111.0	−25.2	0.90×10^6	0.10	1.0	3.24
T1R1E1A1-Lft-Up-(cross ail)	5.2	−39.8	3.6	−147.0	−178.3	−16.0	0.56×10^6	−0.25	0.8	3.25
T0R1E1A1-Lft-Up-(Fin 1)	−58.5	−60.6	3.6	−352.8	−104.0	−24.2	0.96×10^6	−0.10	0.7	3.26
T0R1E1A1-Lft-Up-(Fin 2)	−58.5	−58.3	11.8	−357.0	−104.8	−25.0	0.98×10^6	−0.06	0.9	3.27
T0R1E1A1-Lft-Up-(Fin 3)	−52.2	−53.2	17.3	−352.8	−102.7	−28.5	1.08×10^6	−0.07	1.0	3.28
T1R1E1A1-Lft-Up-(Fin 3)	−47.4	−48.3	20.1	−352.5	−103.1	−30.1	1.12×10^6	−0.07	0.9	3.29
T0R1E1A0-Lft-Up-(Fin 3)	−1.3	−57.4	9.0	−233.1	−145.8	−17.6	0.62×10^6	−0.13	0.7	3.30

*gyrating spin

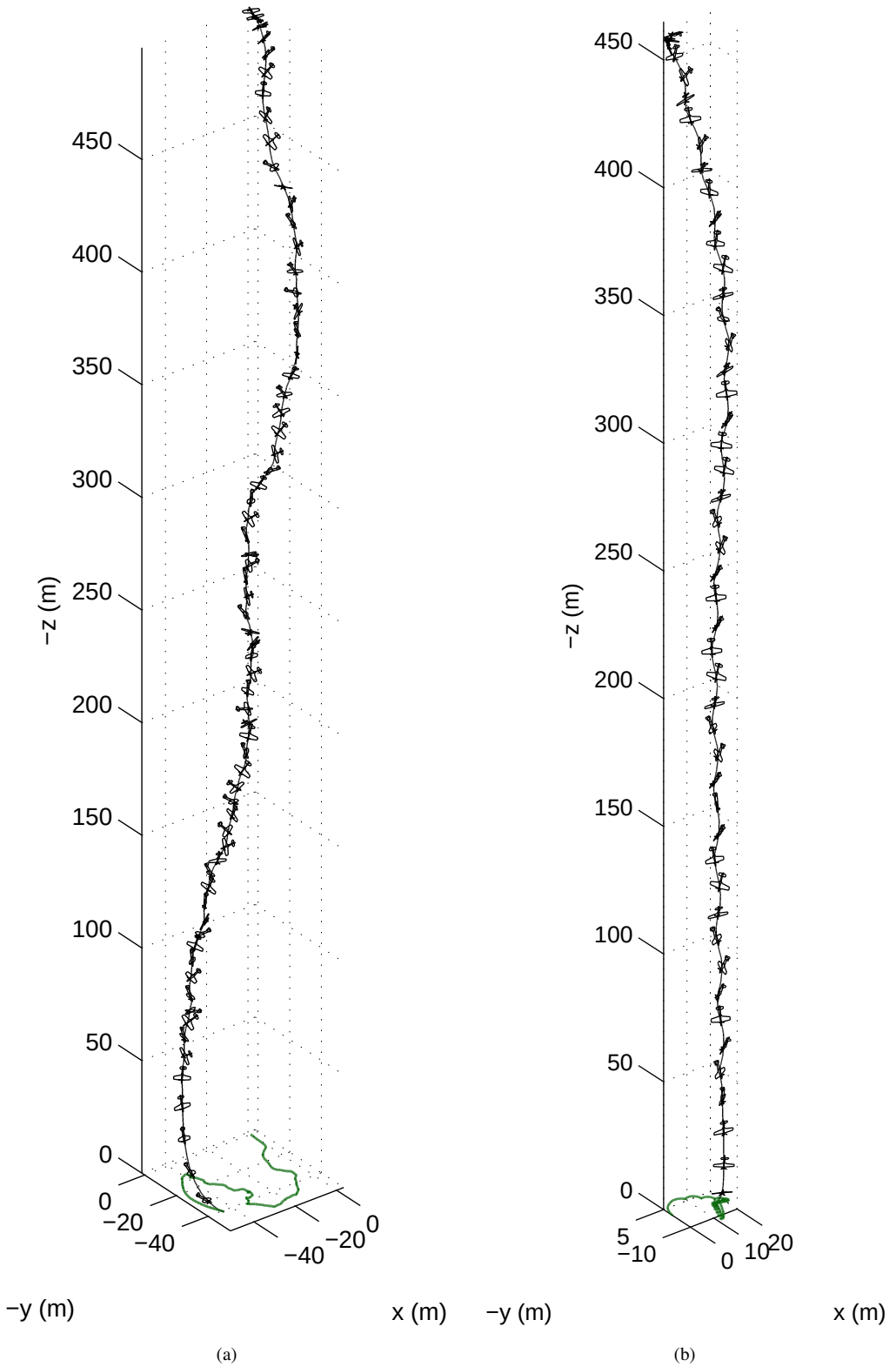

Figure 3.8: Spin trajectories for (a) T0R2E2A2-Lft-Up, and (b) T0R1E1A0-Lft-Inv spins with windfield subtracted (aircraft magnified four times actual size and drawn every 0.50 s).

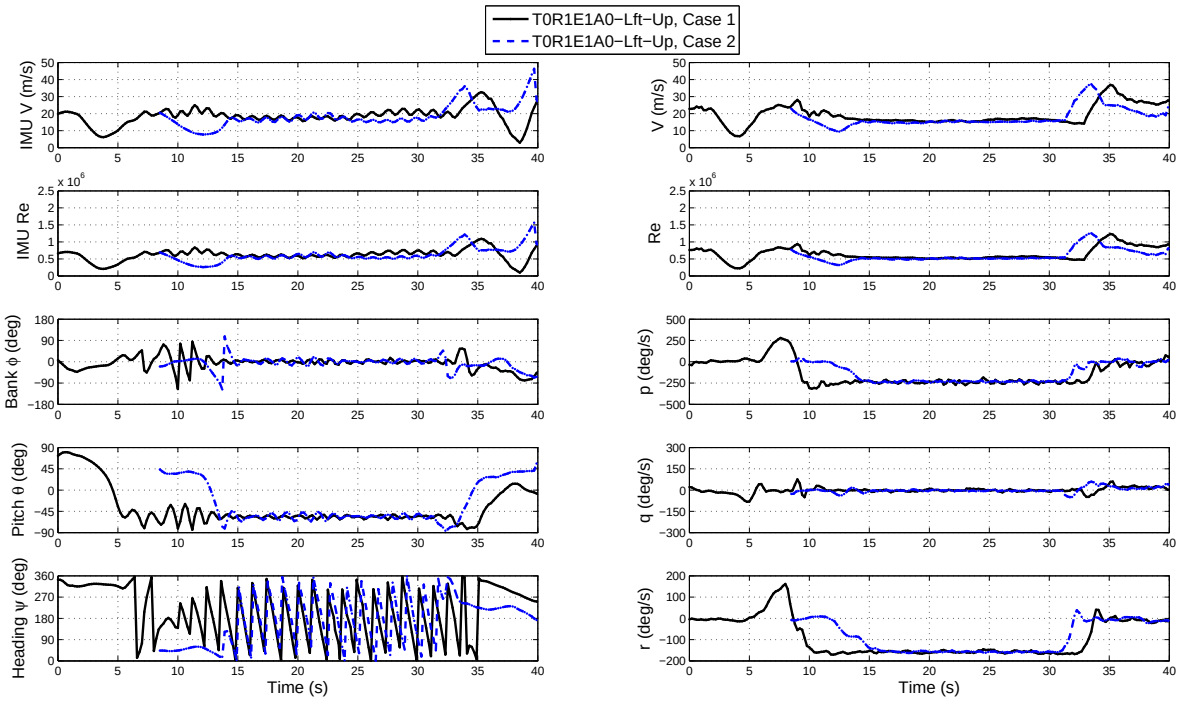

Figure 3.9: Repeatability test: two T0R1E1A0-Lft-Up spins performed on different days.

3.5.1 Baseline Spin and Repeatability

Figures 3.9 and 3.10 compare three T0R1E1A0-Lft-Up spins that were flown on three different days. Two different T0R1E1A0-Lft-Up spins (dashed blue line) are compared with the baseline spin (solid black line). It should be noted that the velocity and Reynolds number, as calculated from the pitot probe data, are slightly lower than the values calculated from the IMU data. This lower velocity recorded by the pitot probe may be due to a high local angle of attack at the wing tip. As previously mentioned, the pitot probe is able to record dynamic pressures at flow angles up to 20 deg. If the local alpha at the wing tip is greater than 20 deg, the pitot probe is unable to accurately measure the dynamic pressure and the measured velocity will be lower than the actual velocity. The Reynolds number and velocity as determined by the pitot-static system are approximately the same for both spins in Fig. 3.9, as shown in the upper right corner of the figures. This strong agreement between the two spin data sets shows the repeatability of the data. No pitot probe data (V and Re) is presented for Case 3 of Fig. 3.10 because the spin was flown early in the flight test program and prior to the installation of a pitot probe on the testbed aircraft. The plots of bank, pitch, as well as the roll, pitch, and yaw rates, are approximately equal for all three of the T0R1E1A0-Lft-Up spins. This consistency demonstrates the repeatability of flight test results with the testbed aircraft. This repeatability is reinforced by the data of Table 3.6, where the vertical velocity of the spins was between 14.8 and 15.9 m/s.

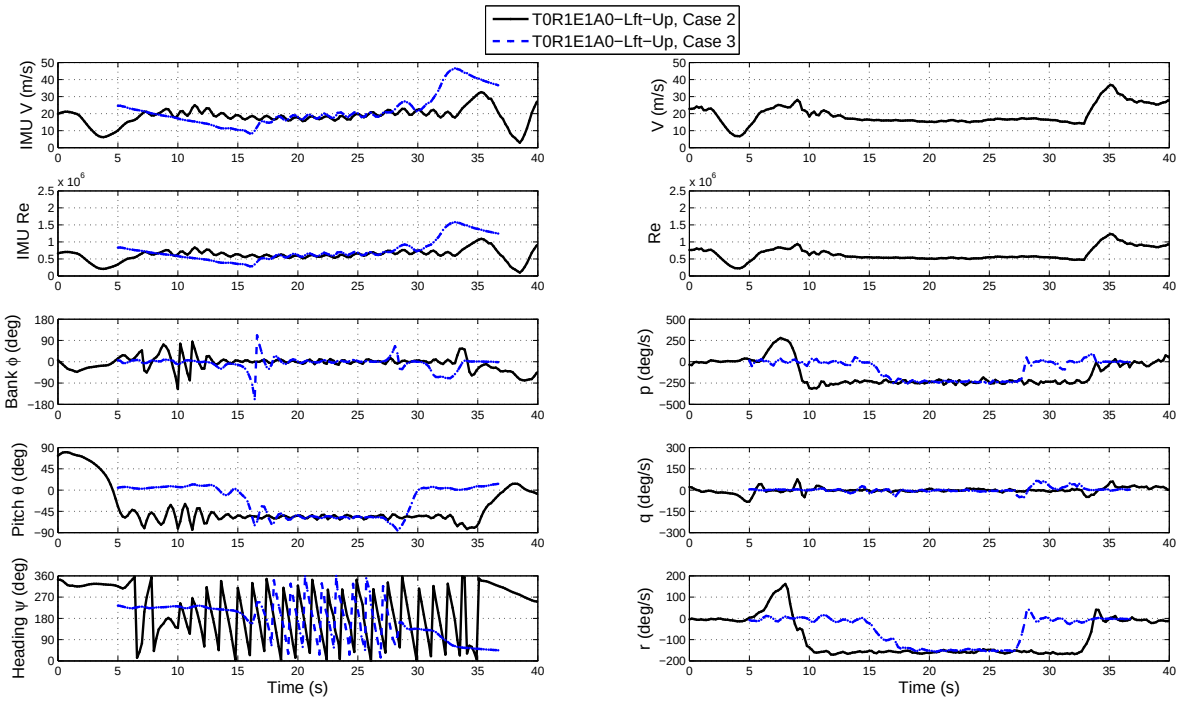

Figure 3.10: Repeatability test: two T0R1E1A0-Lft-Up spins performed on different days.

3.5.2 Direction of Spin

As demonstrated in Fig. 3.11, no significant differences between a T0R1E1A0-Lft-Up and T0R1E1A0-Rght-Up spin were observed. This similarity between the left and right spins shows that while the propeller is windmilling during the spin, the effects of its spiral wake and small gyroscopic moments have no appreciable effect on the spin. The spin parameter for the T0R1E1A0-Rght-Up spin was 0.16, which agrees in regard to the magnitude, 0.20 and 0.22, of two of the T0R1E1A0-Lft-Up spins. The difference in sign is due to the different rudder deflection directions. Likewise, the bank and yaw rates were approximately equal and opposite, with magnitudes of approximately 238 and 154 deg/s, respectively. The vertical velocity was slightly greater in magnitude, at 16.8 m/s for the T0R1E1A0-Rght-Up spin when compared with the T0R1E1A0-Lft-Up spin average value of 15.5 m/s.

3.5.3 Pro-Spin Aileron Deflection

Deflecting the ailerons in a pro-spin manner was observed to increase the magnitude of the bank angle from approximately zero (wings level) to -60.6 deg, while not significantly affecting the pitch angle. As seen in Fig. 3.12, the addition of pro-spin ailerons increased the Reynolds number as well as the magnitude of the roll rate. The magnitude of the roll rate increased because the pro-spin aileron deflection aided the wing in rolling by deflecting the aileron down on the upward moving wing and deflecting the aileron up on the downward plunging wing. These aileron deflections increased the camber of the sections of the upward moving wing where the right aileron was located and

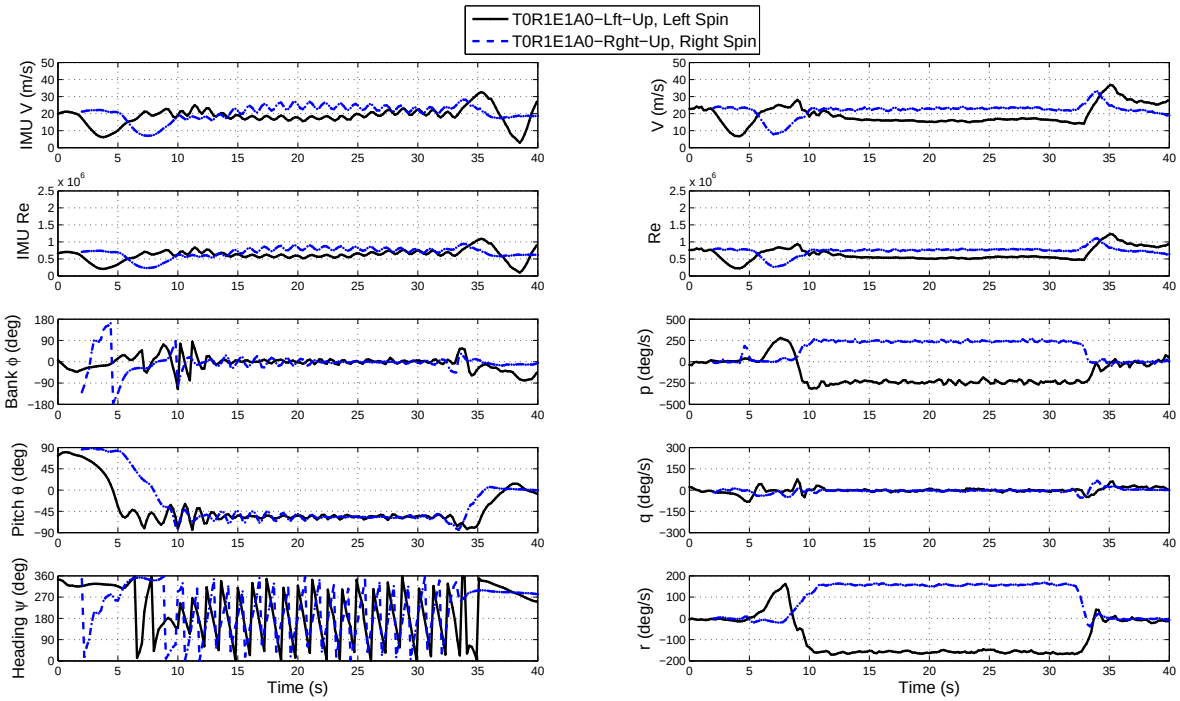

Figure 3.11: Effect of spin direction: T0R1E1A0-Lft-Up and T0R1E1A0-Rght-Up spins performed on two different flights.

increased the camber of the sections in the negative direction of the downward plunging wing where the left aileron was located. The T0R1E1A0-Lft-Up pitch rate of zero was increased to over 150 deg/s for the T0R1E1A1-Lft-Up spin, while the yaw rate was decreased in magnitude from approximately -155 to -101.0 deg/s. A corresponding decrease in the magnitude of the spin parameter resulted from this lower yaw rate, reducing the value from -0.22 to -0.08, as presented in Table 3.6. Because of this lower yaw rate, the time required for a recovery from the spin yaw rate to a zero yaw rate decreased through the addition of pro-spin ailerons. A downside to the addition of pro-spin ailerons is an increased descent rate. This increased descent rate is evident in Table 3.6, where the descent rate increases from 16.8 m/s for the T0R1E1A0-Rght-Up spin to 24.7 m/s for the T0R1E1A1-Rght-Up spin. A similar increase, from approximately 16 m/s to 25.4 m/s, was noted for the T0R1E1A0-Lft-Up and T0R1E1A1-Lft-Up spins, respectively. Since the rudder deflection is the same for both the pro-spin and neutral aileron spins, it is hypothesized that the reduction in the magnitude of the yaw rate is due to an increased amount of angular momentum in the roll axis that resists yaw motion. The result of a lower yaw rate is less drag from the tail section, which may explain the significant increase in the descent rate. The increased descent rate of the pro-spin aileron spins, when compared with the neutral aileron spins, coupled with the decreased yaw rate, reduces the magnitude of the spin parameter for both the left and right spins, from around 0.20 to 0.08.

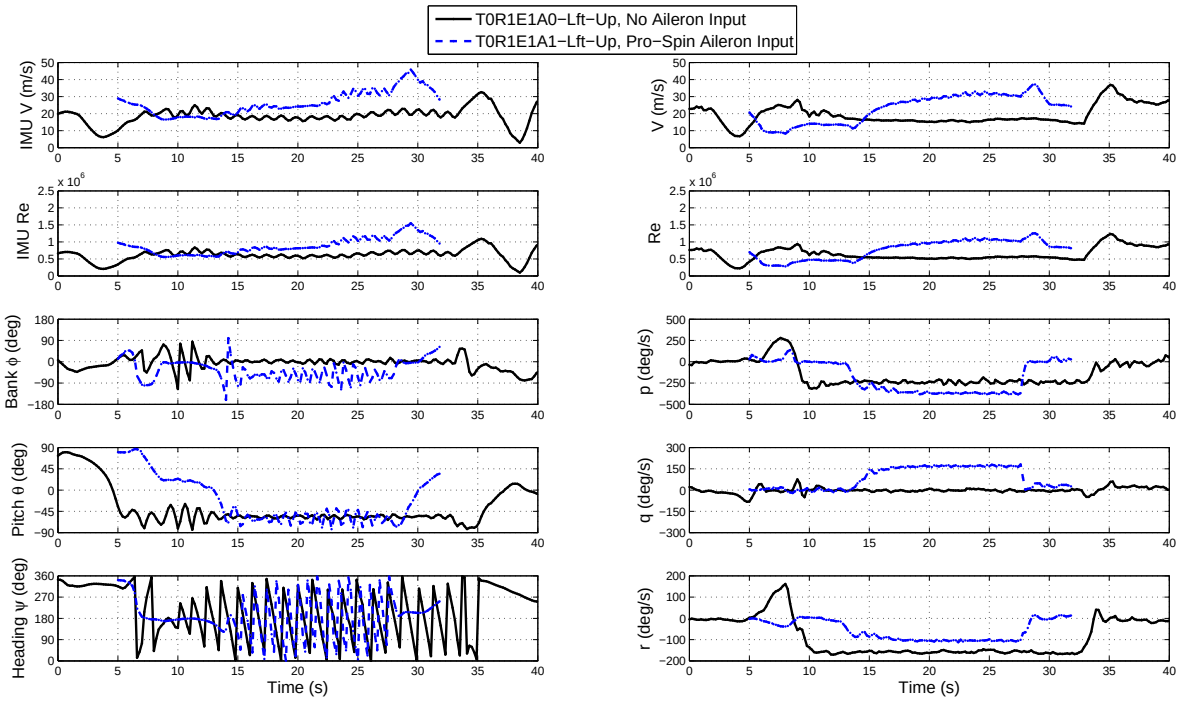

Figure 3.12: Effect of pro-spin aileron input: T0R1E1A0-Lft-Up and T0R1E1A1-Lft-Up spins performed on two different days.

3.5.4 Anti-Spin Aileron Deflection

Figure 3.13 demonstrates the effects of adding anti-spin aileron deflection to a T0R1E1A0-Lft-Up spin configuration. The typical reaction of an untrained pilot to the entry of a stall/spin situation is to command anti-spin ailerons. This action further exacerbates the spin, however, by placing the airplane in a cross-controlled situation. The "cross ail" moniker denotes this spin configuration. By stalling the left wing more deeply, in a left spin situation, for example, the airplane appears to enter a more stable and seemingly less recoverable spin mode. The more stable spin mode is evidenced by the decreased oscillation magnitude in the bank and pitch as well as the decreased speed of recoveries to the bank, pitch, and roll rates. Ultimately, in this spin configuration, the addition of anti-spin aileron causing decreased speed recoveries is a significant result and may be caused by the increased yaw rate. This decrease in the recovery rate illustrates why proper spin training is essential. Without proper training, the reaction of an untrained pilot to a stall/spin situation would be to command anti-spin ailerons (i.e., turn the control column opposite the spin). This incorrect recovery technique would, in fact, worsen the spin. The addition of anti-spin ailerons yielded a slight increase in the magnitude of the yaw rate to -174.5 deg/s, which would be caused by the increased yaw moment stemming from further deepening the stall of the more-stalled wing and reducing the severity of the stall on the less-stalled wing. The spin parameter was consequently increased in magnitude from -0.20 to -0.28, while the vertical velocity was decreased in magnitude to -14.0 m/s by the anti-spin aileron deflection. It is hypothesized that this reduction is due to

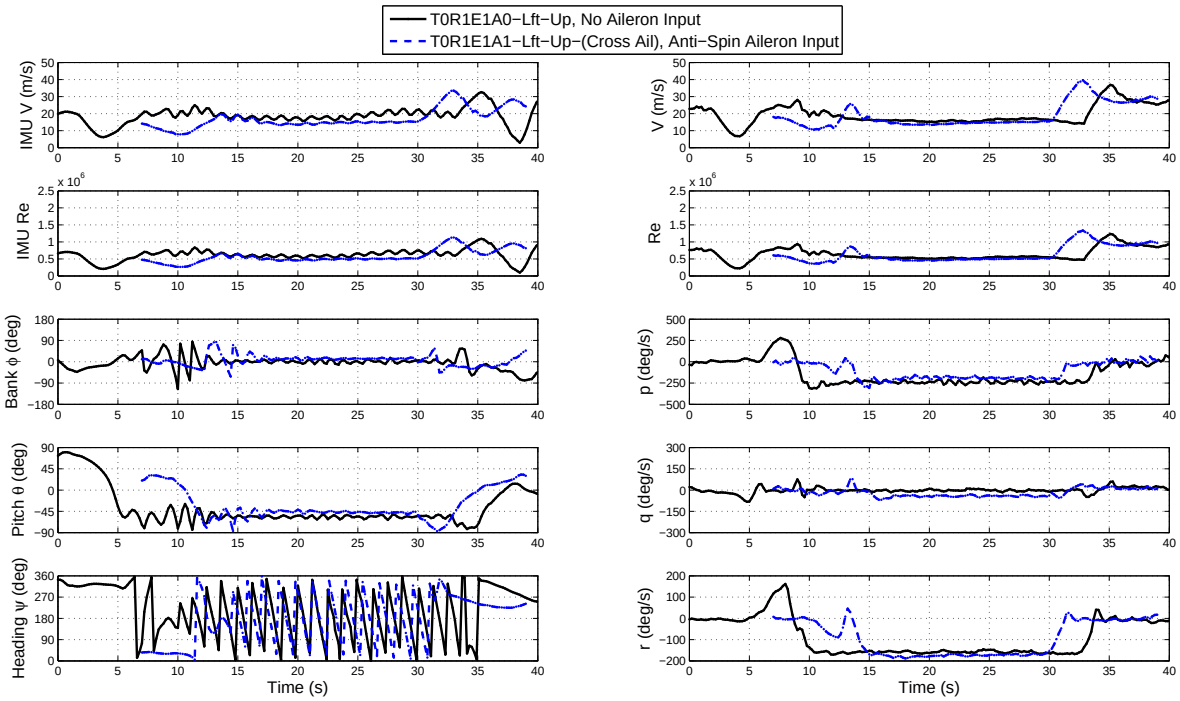

Figure 3.13: Effect of anti-spin aileron input: T0R1E1A0-Lft-Up and T0R1E1A1-Lft-Up-(cross ail) spins performed on two different days.

the 15 deg reduction in the magnitude of pitch, which positions the aircraft, generally, in a higher drag orientation with respect to the freestream. The increased yaw rate also helps to increase the drag of the airplane, which also contributes to its reduced descent rate (caused by increased aircraft C_D).

Despite numerous attempts on different days with different pressures and temperatures, the airplane would always exit a right spin when anti-spin (left roll) ailerons were applied. It should be noted that, with the installation of any of the ventral fins, the addition of anti-spin ailerons to the left spin would cause the airplane to exit the spin. In short, this aggravated spin was only able to be performed in a left spin and with no ventral fin installed. The most-likely reason for the aircraft exiting a right spin when left ailerons were commanded would be because of airframe asymmetries. These airframe asymmetries would have been either accidental or included to counteract the left turning tendencies of a single engine propeller airplane. The motor was offset 2.5 deg to the right to counteract such forces under power. Another potential reason for the airplane exiting a right spin when left roll is commanded may be due to the windmilling propeller shedding a vortex and acting like a nacelle chine. When a left aileron roll is commanded in a right hand spin, the windmilling propeller, which rotates clockwise when viewed from the cockpit, shed a spiraling vortex from its tip that impinges on the bottom of the left wing and the top of the right wing. When a left roll is commanded by the ailerons, the left aileron is deflected upward, and the right aileron is deflected downward. The presence of the shed vortex of the propeller adds energy to the flow as it passes over the aileron, which, in both cases, is directed away from the shed vortex, reducing the amount of or preventing separation over a small portion of the

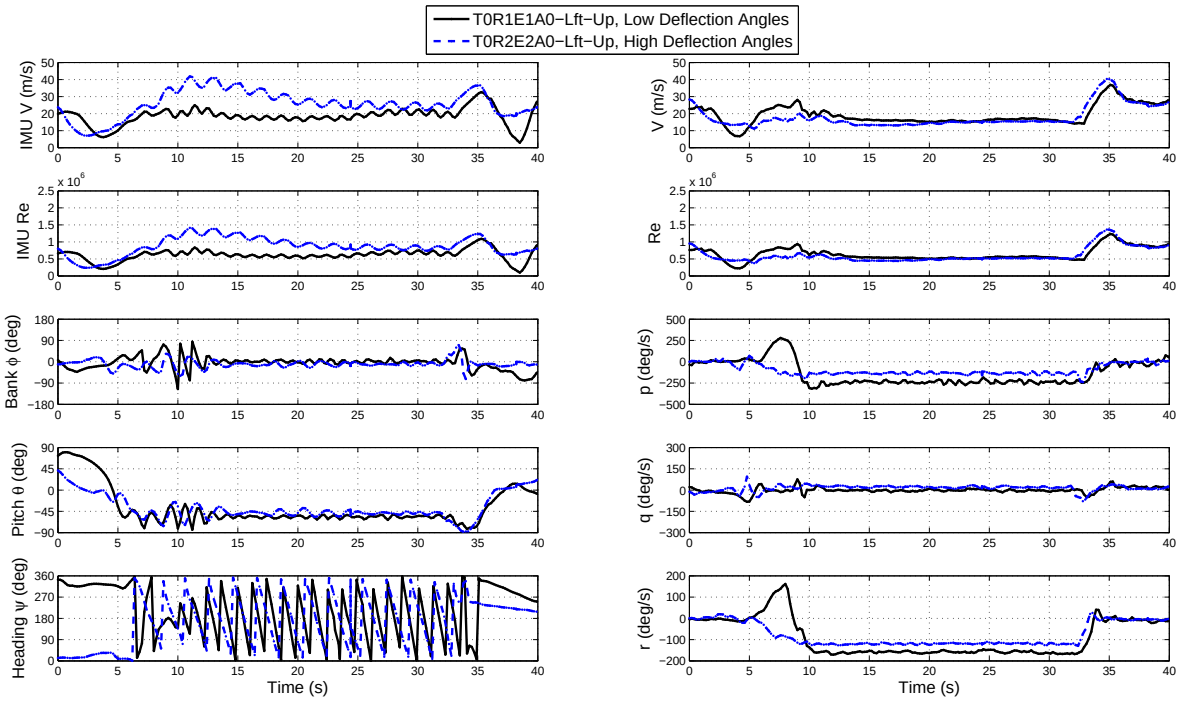

Figure 3.14: Effect of high deflection angles: T0R1E1A0-Lft-Up and T0R2E2A0-Lft-Up spins performed on two different days.

wing. This reduction or prevention of separation provides enough control authority to halt the rolling motion of the spin, and thus, to exit the spin.

3.5.5 Increased Control Surface Deflections with and without Ailerons

It was observed that increasing the control surface deflections from the low deflection angles to the high deflection angles (see Table 3.3) reduced the magnitude of the roll and yaw rates with neutral ailerons. Increasing the control surface deflection angles of a spin with neutral ailerons reduced the angular rate magnitudes from $p = -235$ deg/s and $r = -150$ deg/s to $p = -134.7$ deg/s and $r = -119.2$ deg/s. Also, a minor effect on the pitch rate is evidenced in Fig. 3.14. The average pitch angle was reduced in magnitude, from $\theta = -57$ to -48 deg, but no significant changes to the recovery were observed or experienced.

The addition of pro-spin ailerons to a high deflection angle spin (T0R2E2A0-Lft-Up to T0R2E2A2-Lft-Up spin) significantly altered the motion of the spin. As shown in Fig. 3.15, a periodic, multi-modal, unsteady gyration was introduced to the spin motion. This gyration was initiated through the addition of ailerons to a high-deflection-angle spin. A similar multi-modal behavior was observed during the testing of the Boeing X-48 BWB [69]. The periodic motion of the Aero Testbed exhibited a period of approximately 2.5 s in varied wind conditions. The period remained almost unchanged for spins to the right, as shown in Fig. 3.16. When the right and left high deflection pro-spin aileron spins are compared, as shown in Fig. 3.17, it becomes evident that the spin to the left has a slightly longer

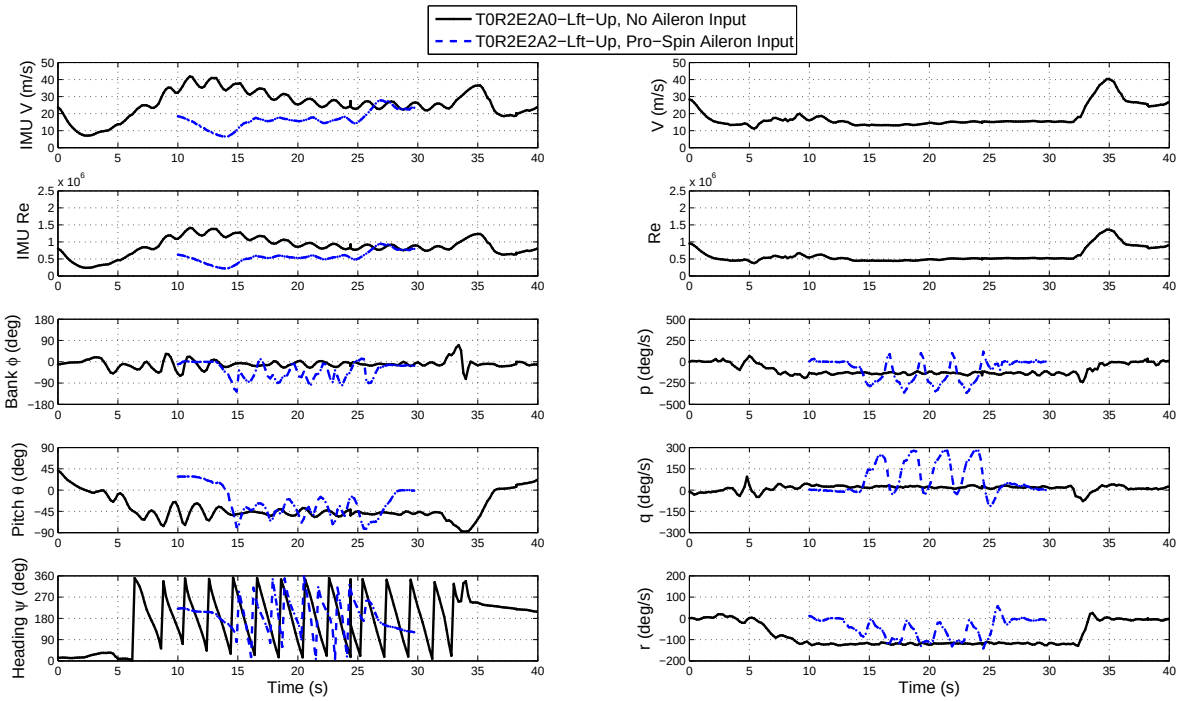

Figure 3.15: Effect of pro-spin aileron input at high deflection angles: T0R2E2A0-Lft-Up and T0R2E2A2-Lft-Up spins performed on two different days.

period than the right spin. Although this difference is minor, it is most likely due to a slight asymmetry in the airframe construction. Airframe asymmetry is hypothesized to be the reason, especially on account of the fact that the atmospheric conditions were nearly identical between the two flights. Moreover, there was not a significant difference noticed for low-deflection spins to the left or right. The temperature on both days on which these spins occurred was 29 deg C, and the pressure difference was only 0.01 mmHg. Both the left and right spins exhibit the same double peak for the yaw rate and pitch. The yaw rate was approximately equal and opposite for the left and right spins. No pitot-static data is presented in Fig. 3.17 because these spins were flown prior to the installation of the pitot probe on the Aero Testbed.

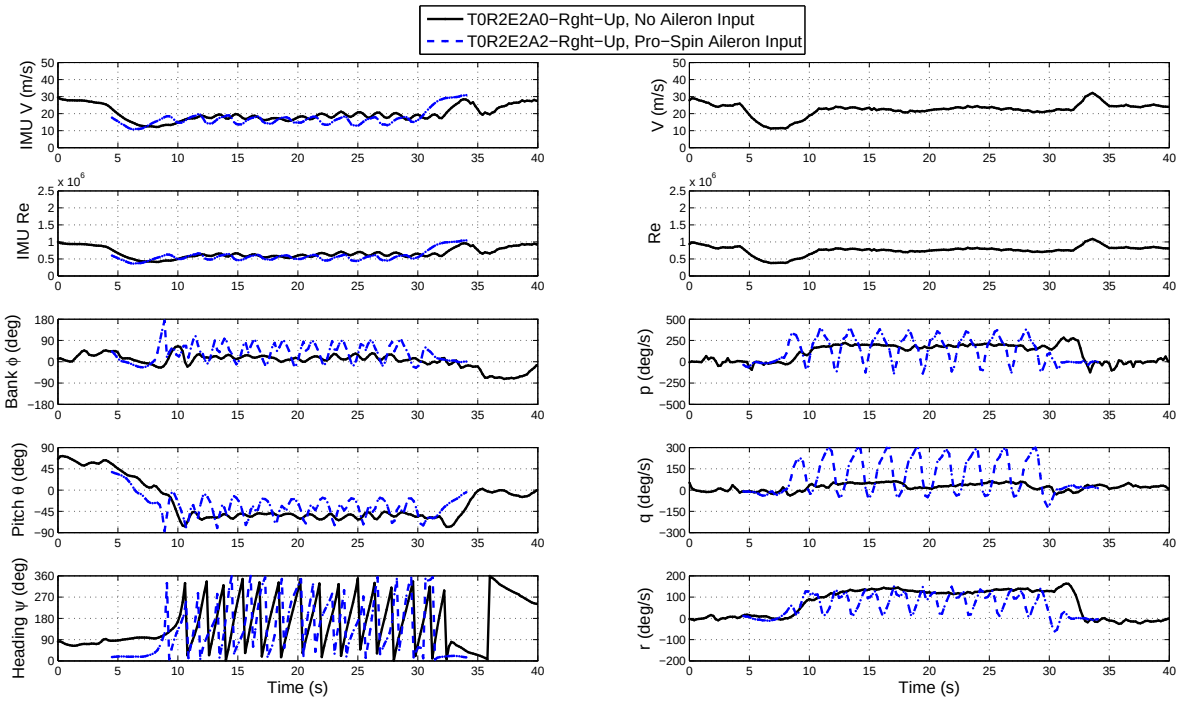

Figure 3.16: Effect of pro-spin aileron input at high deflection angles: T0R2E2A0-Rght-Up and T0R2E2A2-Rght-Up spins performed on two different days.

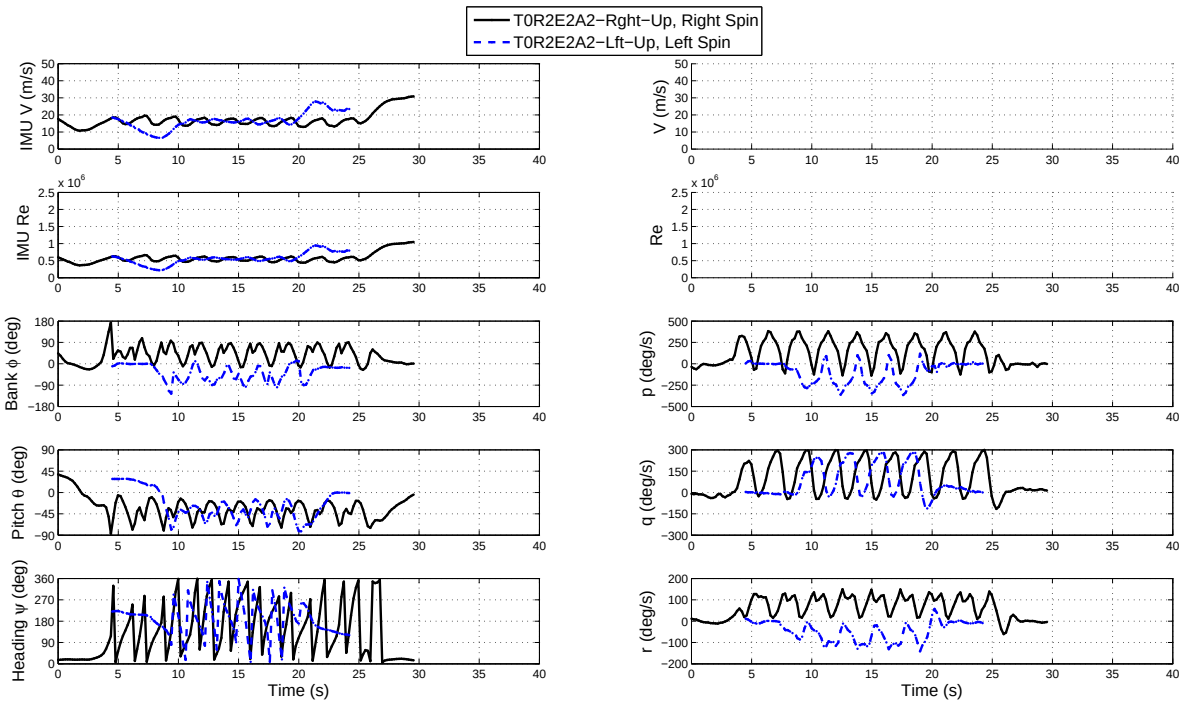

Figure 3.17: Effect of spin direction at high deflection angles: T0R2E2A2-Rght-Up and T0R2E2A2-Lft-Up spins performed on two different days.

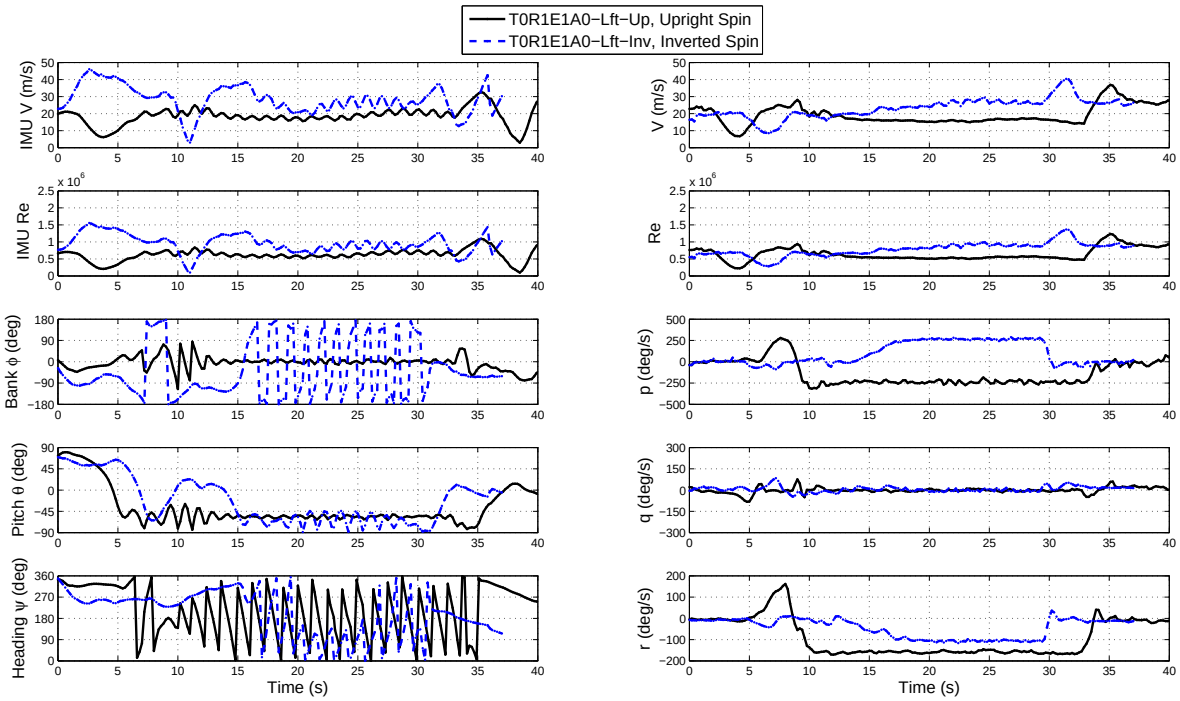

Figure 3.18: Effect of inverted spin: T0R1E1A0-Lft-Up and T0R1E1A0-Lft-Inv spins performed on two different days.

Both the right and left high deflection spins with pro-spin ailerons demonstrated the same highly regular periodic gyration motion. This motion was characterized by a period of approximately 2.5 s, a buildup in pitch rate followed by a steep drop-off from the maximum, and a double peak in the yaw rate for each period. It should be noted that, according to the definition of spin in Ref. [8], these "gyrating spins" are not even spins, as the yawing and rolling motion is not sustained and the roll rate p changes sign within each period of the motion.

3.5.6 Inverted Spin with and without Ailerons

Inverting the spin for an aileron neutral spin reduces the yaw rate and destabilizes the spin. This destabilization of the spin is evidenced by the larger oscillations in bank and pitch in Fig. 3.18. The larger amount of vertical stabilizer area, which is now "beneath" the horizontal stabilizer in an inverted spin, acts as a sort of keel for the airplane, thus reducing the yaw rate. An increased area of vertical stabilizer out of the wake of the horizontal stabilizer allows for faster recoveries from the spin. As evidenced before, the reduction in the yaw rate is accompanied by an increase in the descent rate and *Re*. This increase in *Re* occurs without a significant change in the pitch, indicating that the difference in drag is due to sideforce on the vertical tail and not because of the angle of attack of the fuselage or wing. The pitch angle is increased slightly in the negative direction, and recoveries that are more rapid are apparent for the bank and heading rates, as well as for the pitch angle. Additionally, as shown in the beginning phase of the spin, the bank and

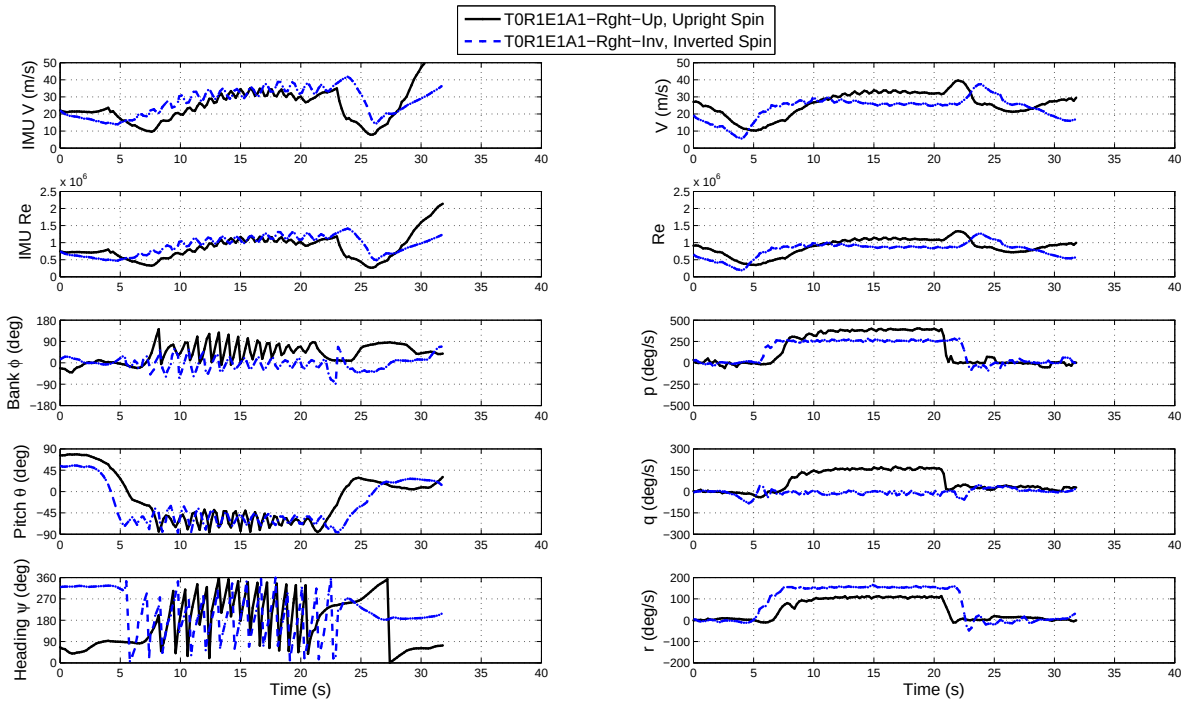

Figure 3.19: Effect of inverted spin with pro-spin ailerons: T0R1E1A1-Rght-Up and T0R1E1A1-Rght-Inv spins performed on two different flights.

yaw rates approach their maximum near steady-state values at a slower rate, as compared with the level flight case. It should also be noted that the direction of the bank changes. This bank direction change is an artifact of the inverted orientation of the spin entry. The rudder is deflected in the same direction for both spins in the aircraft reference frame, but in the level spin, the left wing stalls and drops, which creates a roll to the left. In the inverted spin case, when observed from the airplane frame of reference, the left wing stalls while inverted, which creates a roll to the right. This inverted spin was studied because it offered a close approximation to the inverting of the tail geometry, as well as to changing the shape of the aft fuselage from a flat-bottom round-top geometry to a round-bottom flat-top geometry. The round-bottom fuselage geometry is preferable, as described in the literature [70–72]. These inverted spins were studied because the testbed airplane has zero dihedral, zero incidence angle between the wing and horizontal stabilizer, and symmetric airfoils for both the wing and the horizontal stabilizer. Because of these geometric features, no effects from dihedral or different airfoils would be encountered. Notably, when upright, the horizontal stabilizer is located 3.1 cm (1.2 in) above the wing; when inverted, the horizontal stabilizer is located 3.1 cm (1.2 in) beneath the wing.

While Fig. 3.18 addresses the inverting of an aileron neutral spin, Fig. 3.19 shows the effects of inverting a spin with pro-spin ailerons. In this case, inverting the pro-spin aileron spin reduces the measured pitch rate to zero, reduces the bank rate slightly, and increases the yaw rate. The average bank is reduced slightly, while no appreciable change to the pitch is observed. The combination of reduced bank rate and increased yaw rate may be attributable to the new vertical tail "geometry," where the increased vertical tail area beneath the horizontal stabilizer acts as a stabilizing

keel. Meanwhile, the increased rudder area increases the moment and the effectiveness of the rudder. Inverting the T1R1E1A0-Lft-Up spin also reduces the spin parameter by nearly 50% from $\omega = -0.20$ for the T0R1E1A0-Lft-Up spin to $\omega = -0.10$ for the T0R1E1A0-Lft-Inv spin.

3.5.7 Effect of Motor Power / Throttle

As demonstrated in Fig. 3.20, increasing the throttle from an idle setting (T0), to one that will produce an RPM of 340–840 (T1), has no appreciable effect on a spin with neutral ailerons. This observation of no appreciable effect on the spin when slightly increasing the throttle setting is verified by the data of Table 3.6. In Table 3.6, the T0R1E1A0-Lft-Up and T1R1E1A0-Lft-Up spins demonstrate spin parameters of -0.20 and -0.19, respectively. The pitch, roll rate, yaw rate, and Reynolds number values also do not change appreciably, but the descent rate was observed to increase to 16.9 m/s in Table 3.6. The descent rate for the T1R1E1A0-Lft-Up spin configuration was, however, nearly equal to the descent rate for the T0R1E1A0-Rght-Up spin. An observation to be made between the T0R1E1A0-Lft-Up and T1R1E1A0-Lft-Up spins is the slight reduction in the rate of recovery of the yaw rate for the T1R1E1A0-Lft-Up spin. Increasing the motor power to a setting which would produce an RPM of 750–1200 (T2), as shown in Fig. 3.21, increased the Reynolds number, pitch rate, and slowed the recovery from the steady-state spin yaw rate in a left hand spin. Noting that the slowed recovery from the spin yaw rate was less pronounced in Fig. 3.20, it is hypothesized that this change is not due to the aerodynamic effects of the propeller. Instead, this change may be due to the gyroscopic effects of the rotating propeller. A rotating propeller produces an increasingly left turning tendency as the motor power setting is raised, and additionally, it resists a change in orientation because of gyroscopic forces. This hypothesis is, in-theory, confirmed in Fig. 3.22, where no significant changes to a right-hand spin are observed, aside from a slight increase in the recovery from the spin yaw rate. If aerodynamics were the primary factor in any changes, one would expect a more rapid recovery in both directions, because of an increased dynamic pressure on the control surfaces. A reduced recovery rate in a left spin, and an increased recovery rate in a right spin, clearly indicates that gyroscopic effects are the main driver behind the changes. The increase in *Re* and the descent rate is simply due to the addition of thrust, which propels the aircraft earthward at a greater velocity when the pitch is negative.

Additional changes introduced when progressing from the T0R1E1A0-Lft-Up to T1R1E1A0-Lft-Up and T2R1E1A0-Lft-Up spins include an increase in the negative direction of the bank angle, from approximately 0 to -4.6 deg and -12.3 deg, respectively. The pitch angle of the T2R1E1A0-Lft-Up spin is also increased in the negative direction, to -59.7 deg, and the roll rate is increased by approximately 12%. The descent rate of the T2R1E1A0-Lft-Up spin is increased from the T0R1E1A0-Lft-Up spin to 19.6 m/s. Consequently, the spin parameter decreases in magnitude.

When power is added to a spin with pro-spin ailerons, as depicted in Fig. 3.23, the only appreciable effect is the apparent stabilization of the spin. This stabilization of the spin may be evidenced by the decreased oscillations in the

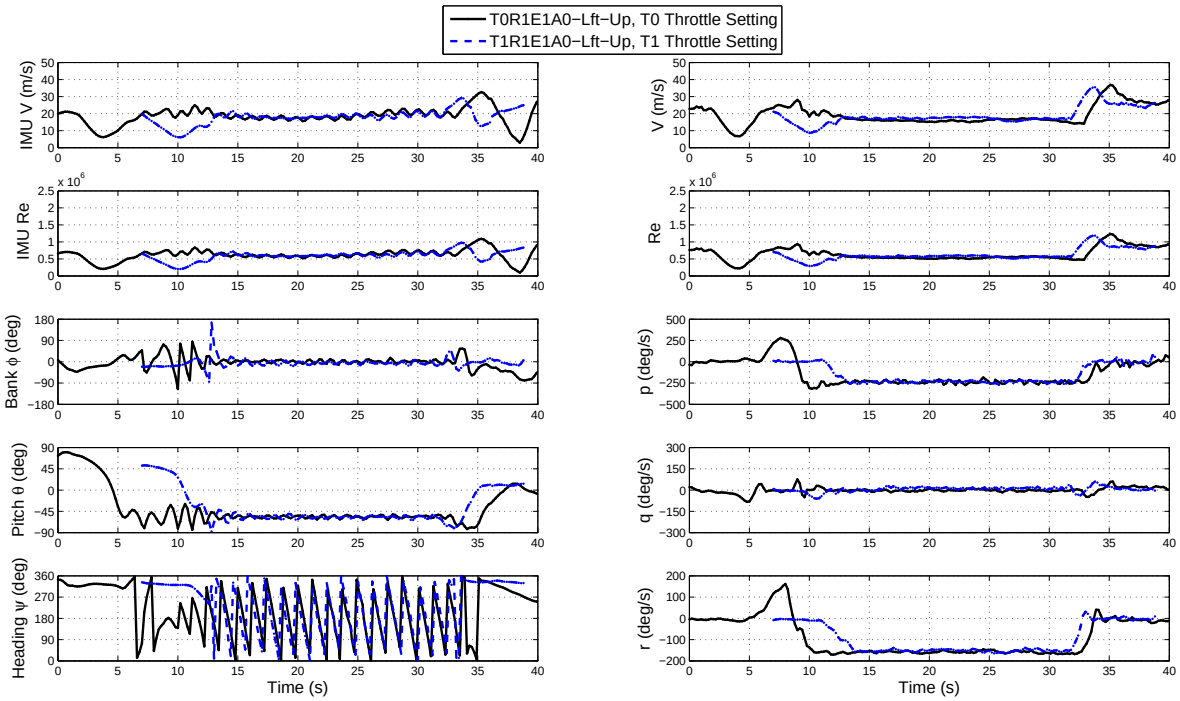

Figure 3.20: Effect of throttle setting: T0R1E1A0-Lft-Up and T1R1E1A0-Lft-Up spins performed on the same flight.

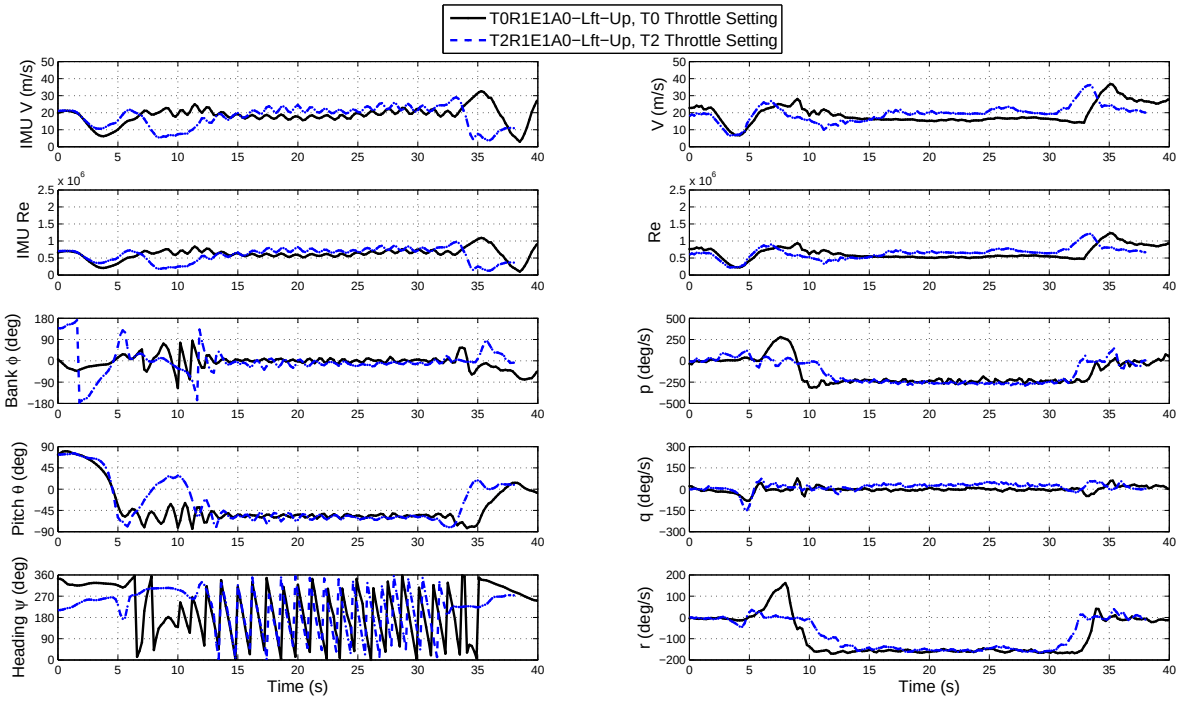

Figure 3.21: Effect of throttle setting: T0R1E1A0-Lft-Up and T2R1E1A0-Lft-Up spins performed on the same flight.

bank and pitch values. This stabilization of the spin, in contrast to the aileron neutral case, may be attributable to an increased dynamic pressure q over the ailerons, which extend quite far inboard on the wing, and would, presumably,

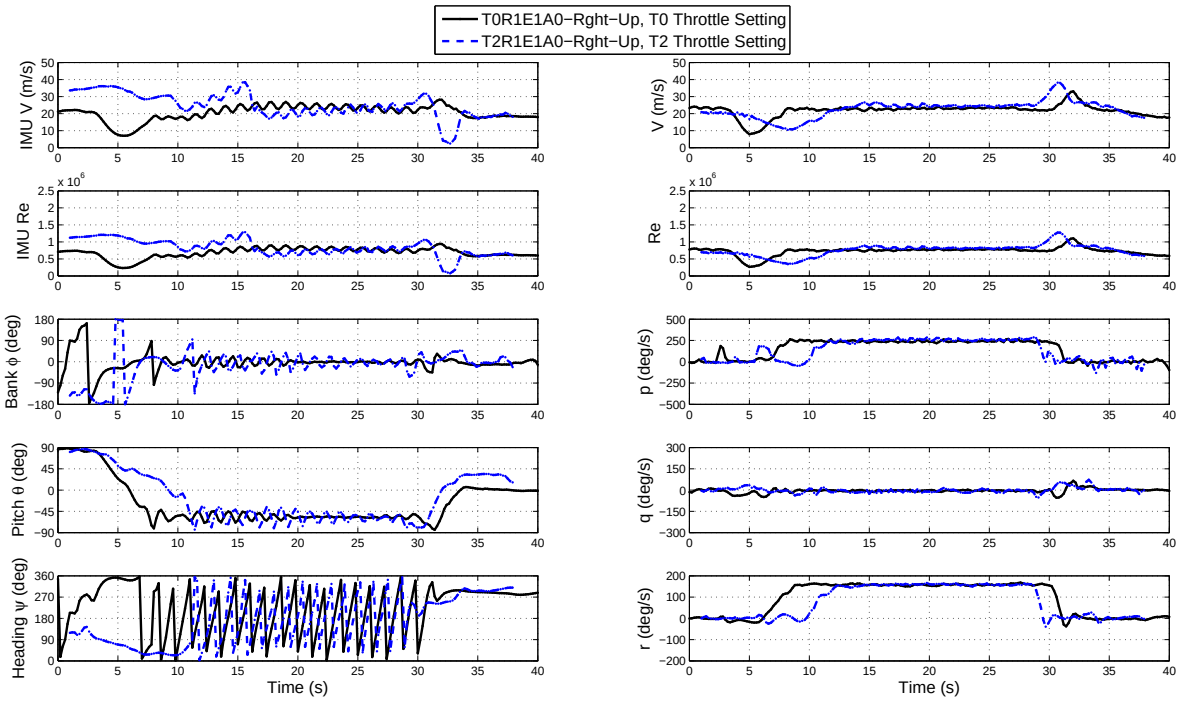

Figure 3.22: Effect of throttle setting: T0R1E1A0-Rght-Up and T2R1E1A0-Rght-Up spins performed on the same flight.

have a portion located within the propeller slipstream. The case of the right spin, as shown in Fig. 3.24, also demonstrates this decreased magnitude of oscillation in the bank and pitch spin values. Once again, the propeller effects appear to have minimal influence, as the left spin recovery is slightly slowed, and the right spin recovery is slightly accelerated.

A significant motor RPM effect was observed for a left spin with opposite ailerons, as shown in Fig. 3.25. When the throttle setting was increased from "T0" to "T1" (see Table 3.4), the recovery time increased from approximately 2 to 4 s. It required 2.5 turns of the aircraft before the yawing and rolling ceased. Recoveries from all spins were initiated by removing all of the control inputs and then initiating a gentle motor-idle ("T0") pullout with the wings level. The purpose of this pullout procedure was to keep the load factor experienced by the airplane as low as possible. The aggravated spin was reported to take 1–1.5 turns before a recovery could be initiated. The increase in throttle, from "T0" to "T1," required an additional 2.5 turns before the initiation of the recovery could be performed. In this instance, the increased q over the ailerons, which was caused by the propeller slipstream, provided significantly more inboard control authority. Further, this increased aileron control authority placed the aircraft in a flatter and less-recoverable spin, with $\theta = -39.8$ deg for the opposite aileron spins, compared with -57.3 deg and -61.3 deg for the neutral and pro-spin ailerons spins, respectively.

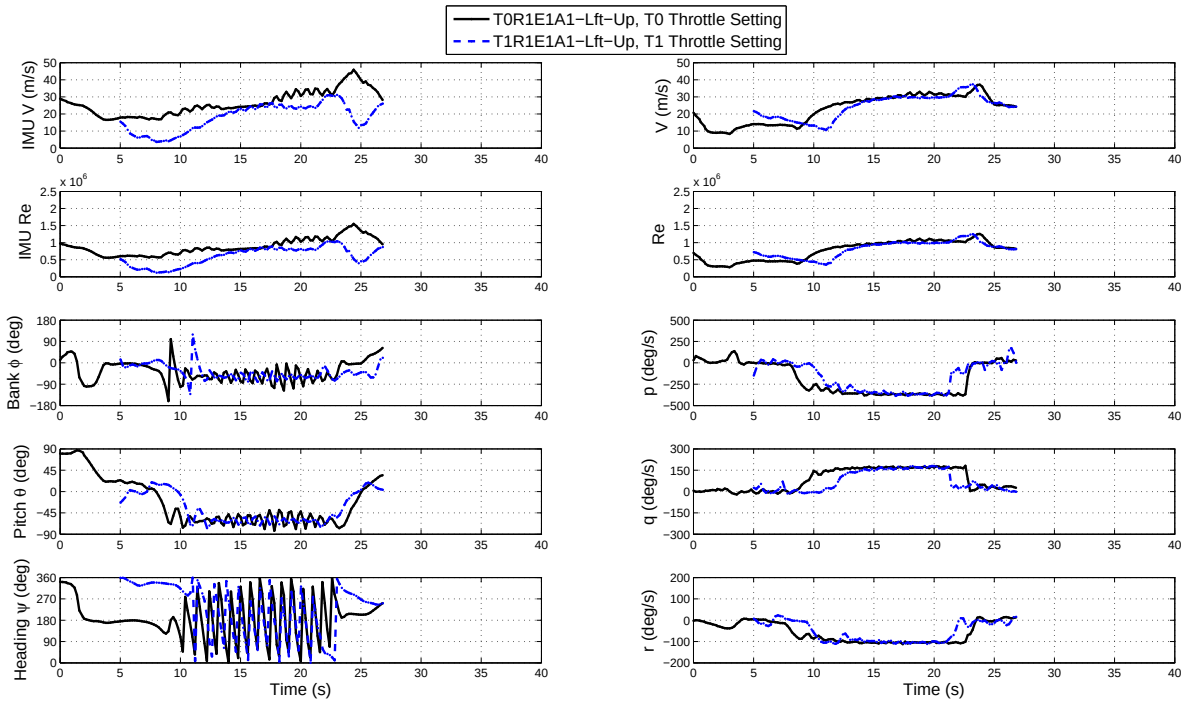

Figure 3.23: Effect of throttle setting with pro-spin ailerons: T0R1E1A1-Lft-Up and T1R1E1A1-Lft-Up spins performed on the same flight.

3.5.8 Effect of Ventral Fins 1, 2, and 3

Figure 3.26 compares T0R1E1A1-Lft-Up spins with and without Ventral Fin 1 installed. A drawing of the four fins and their installed location on the aircraft is presented in Fig. 3.2(b). No significant differences are apparent in Fig. 3.26. Table 3.6 shows that the yaw rate was reduced from -129.3 to -104.0 deg/s, and the spin parameter decreased in magnitude to -0.10. Extending Fin 1 forward yielded Fin 2, and the results of the installation of Fin 2 are presented in Fig. 3.27. The spin parameter values for the T0R1E1A1-Lft-Up-(Fin 1) and T0R1E1A1-Lft-Up-(Fin 2) spins are the same. Two spins from Table 3.6 revealed no significant differences, aside from a slight increase in the descent rate and Reynolds number.

Fin 3 was the same length as Fin 1, but it was 1-in taller. A comparison of the T0R1E1A1-Lft-Up and T0R1E1A1-Lft-Up-(Fin 3) spins is shown in Fig. 3.28. A more rapid recovery from the spin roll and yaw rates was evidenced in Fig 3.28. The Reynolds number in the spin was increased, and consequently, the spin parameter was decreased in magnitude from -0.08 to -0.07. The pitch angle was decreased in magnitude from -53.8 to -48.3 deg. The magnitudes of the pitch and bank oscillations were significantly increased with the addition of Fin 3, showing that the spin was less stable. Offering further insight on the Fin 3 installation is Fig. 3.29, which shows the differences created by installing Fin 3 for a left pro-spin aileron spin with a "T1" throttle setting. The addition of motor power significantly increases the magnitude of the bank and pitch oscillations. Again, the recovery from the yaw rate is increased through

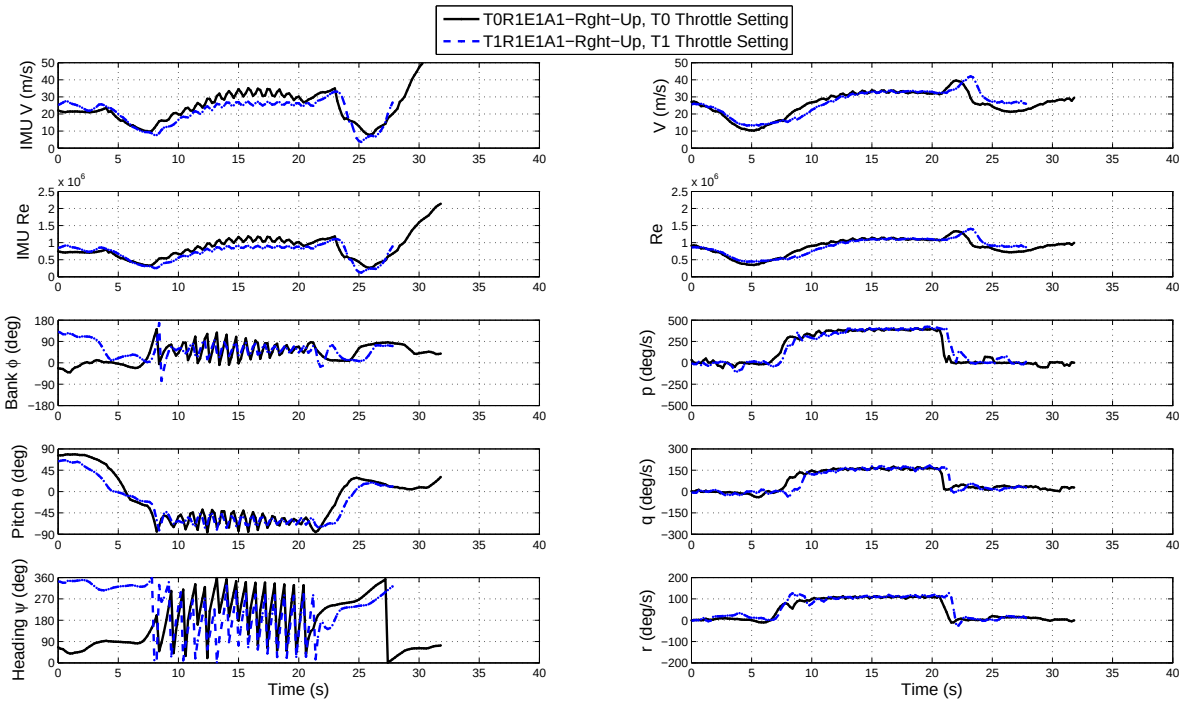

Figure 3.24: Effect of throttle setting with pro-spin ailerons: T0R1E1A1-Rght-Up and T1R1E1A1-Rght-Up spins performed on the same flight.

the addition of Fin 3. A slight increase in the pitch rate, and a slight decrease in the bank rate, was also observed. A small increase in the descent rate to 30.1 m/s was observed in Table 3.6, with no significant change in the magnitude of the spin parameter.

The final investigation examined the effects of Fin 3 in an aileron neutral spin (T0R1E1A0-Lft-Up), as shown in Fig. 3.30. Again, a clear increase in the rate of recovery of the yaw and bank rates is observed with Fin 3. The yaw rate and spin parameter of the developed spin were slightly decreased for the Fin 3 case, to $r = -145.8$ deg/s and $\omega = -1.10$, respectively. Additionally, the change in pitch from the developed spin to one from which a recovery pullout could be initiated was much quicker when Fin 3 was installed.

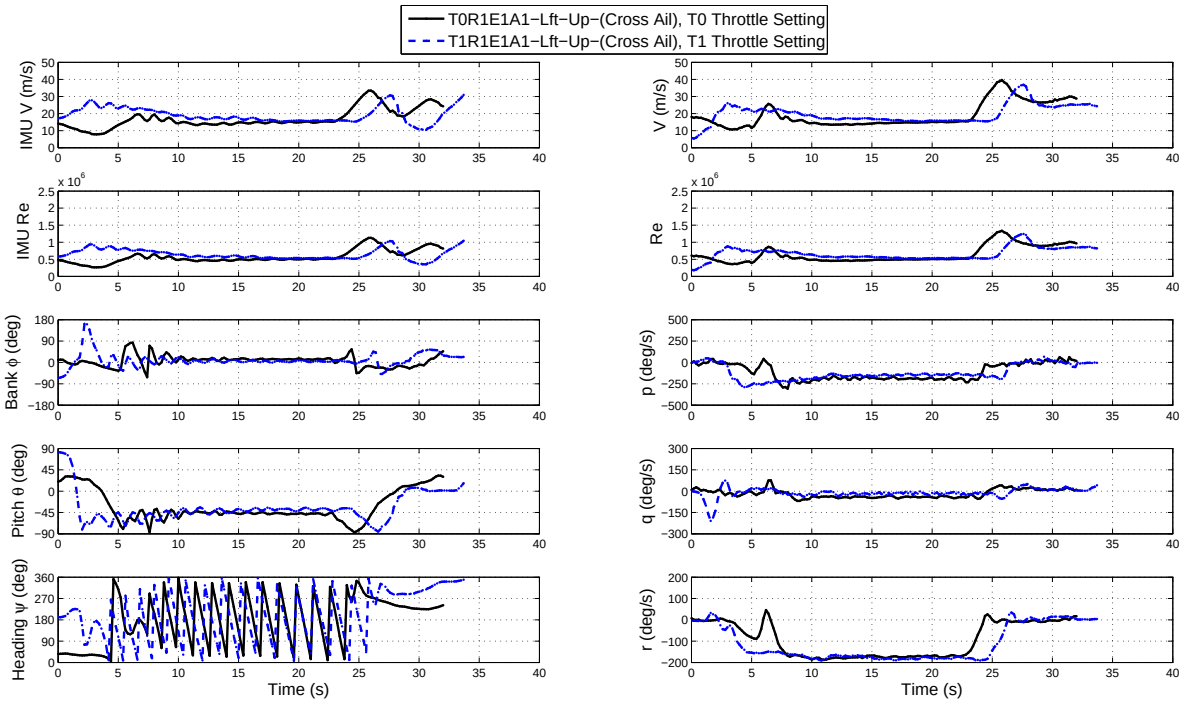

Figure 3.25: Effect of throttle setting with anti-spin ailerons: T0R1E1A1-Lft-Up-(cross ail) and T1R1E1A1-Lft-Up-(cross ail) spins performed on two different days.

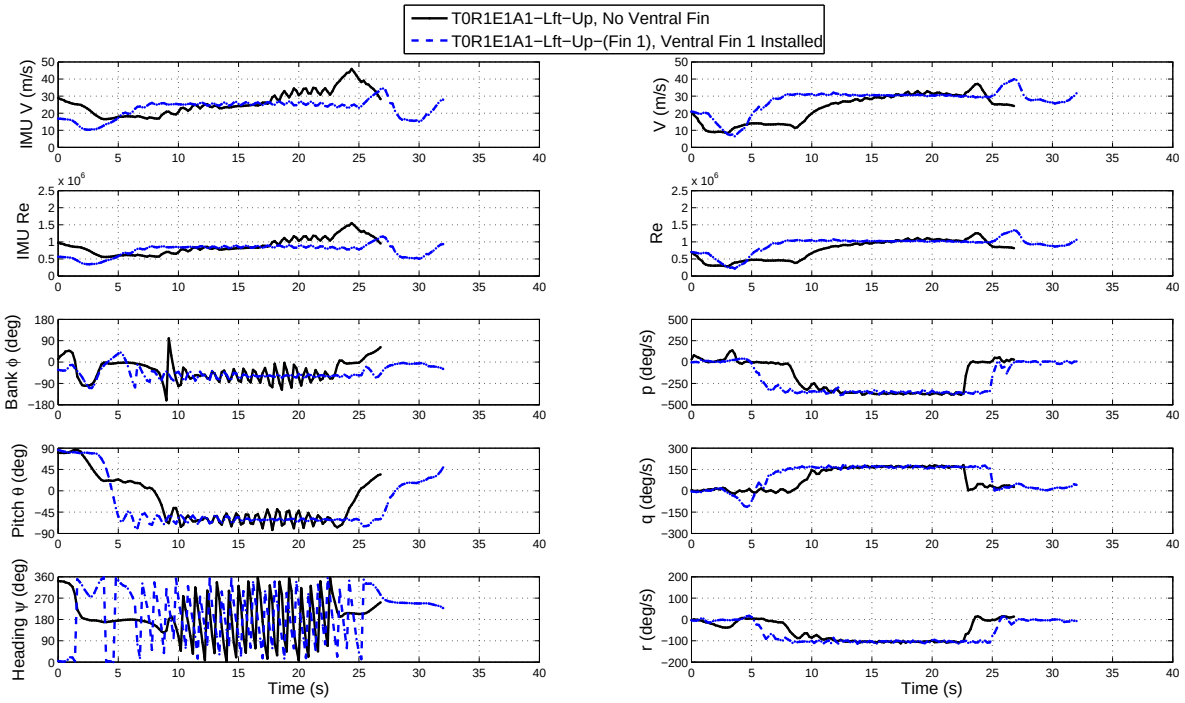

Figure 3.26: Effect of Ventral Fin 1: T0R1E1A1-Lft-Up and T0R1E1A1-Lft-Up-(Fin 1) spins performed on two different days.

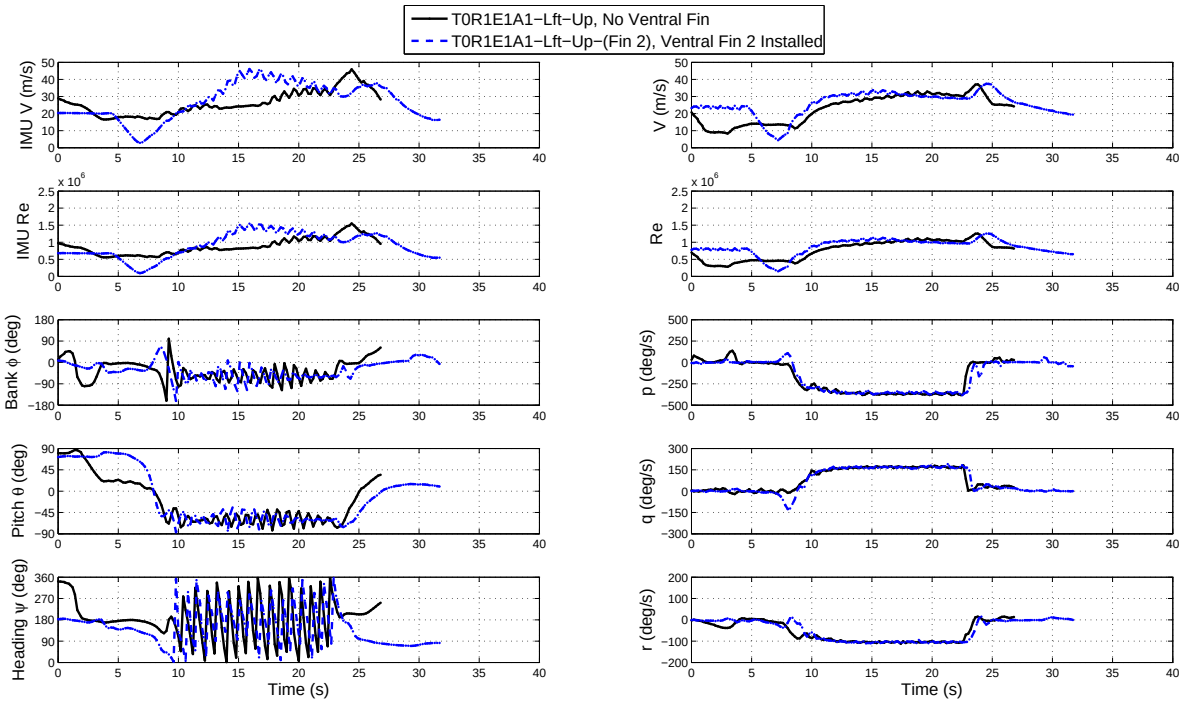

Figure 3.27: Effect of Ventral Fin 2: T0R1E1A1-Lft-Up and T0R1E1A1-Lft-Up-(Fin 2) spins performed on two different days.

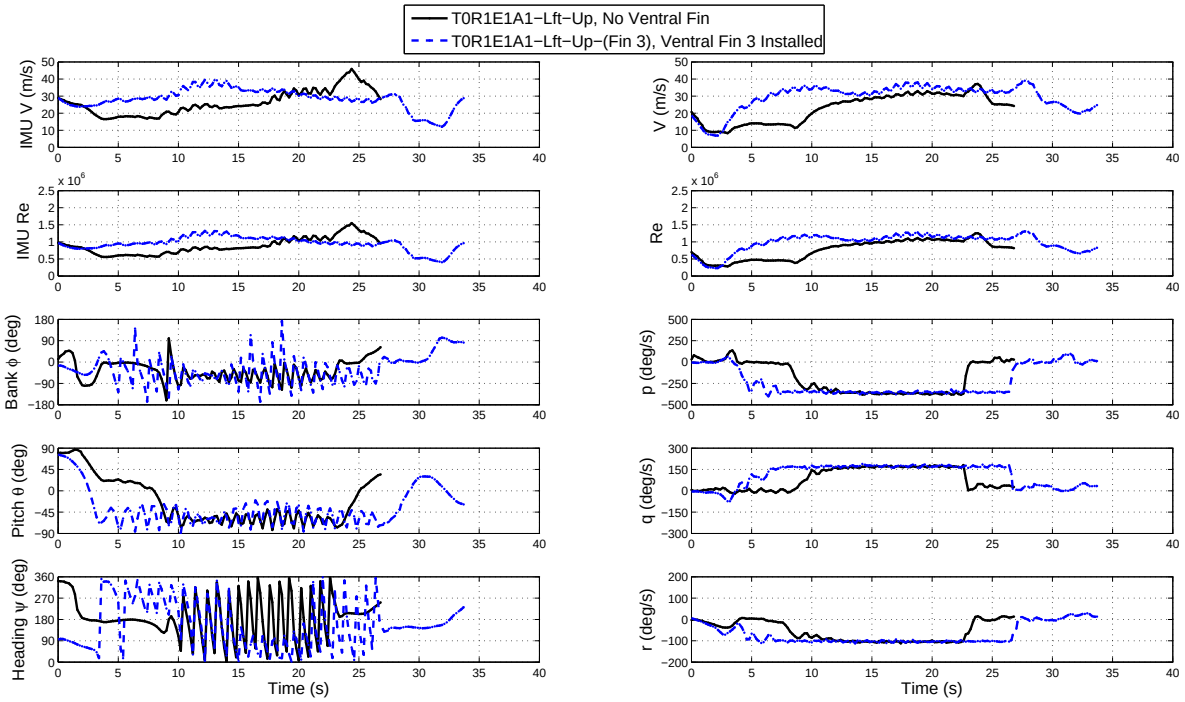

Figure 3.28: Effect of Ventral Fin 3: T0R1E1A1-Lft-Up and T0R1E1A1-Lft-Up-(Fin 3) spins performed on two different days.

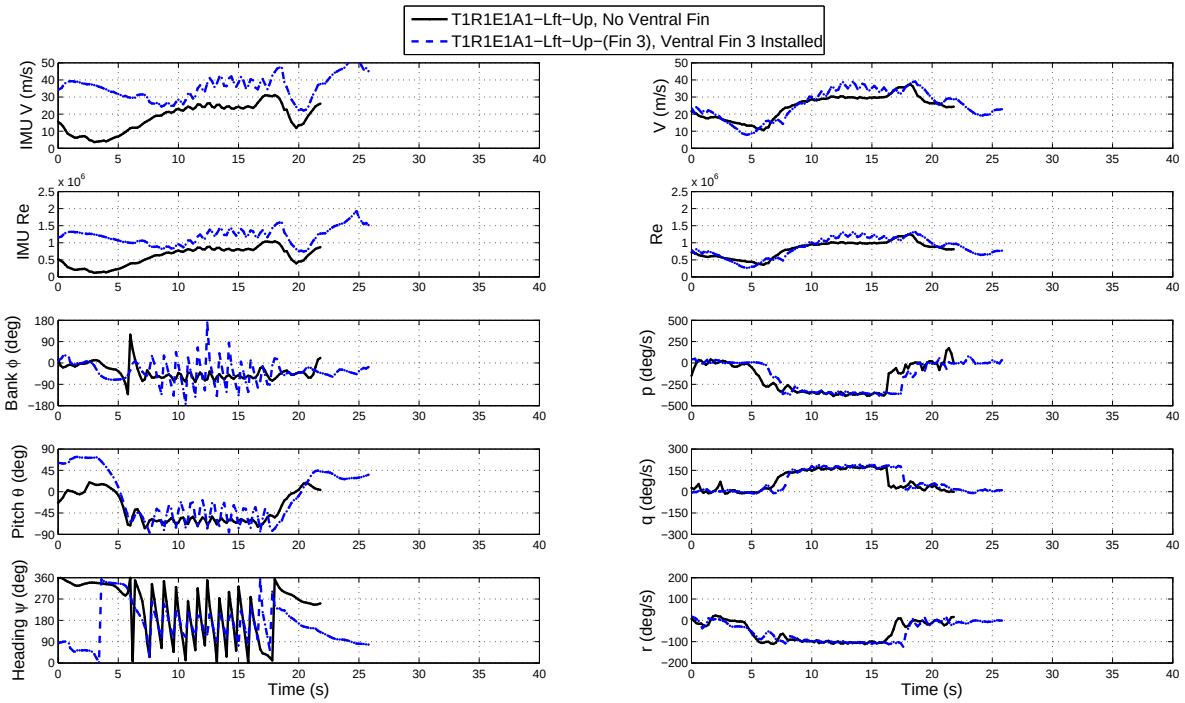

Figure 3.29: Effect of Ventral Fin 3 with non-zero throttle: T1R1E1A1-Lft-Up and T1R1E1A1-Lft-Up-(Fin 3) spins performed on two different days.

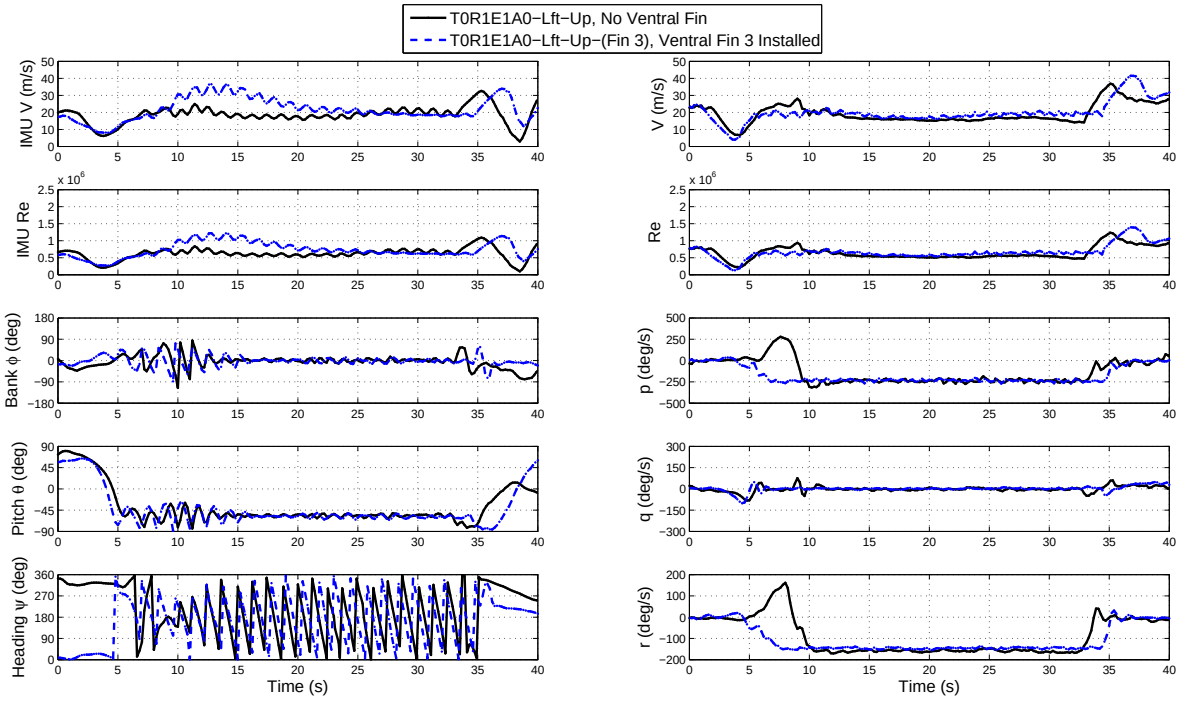

Figure 3.30: Effect of Ventral Fin 3 with neutral ailerons: T0R1E1A0-Lft-Up and T0R1E1A0-Lft-Up-(Fin 3) spins performed on two different days.

3.6 Discussion of Ventral Fin Spin-Exit Observations

An interesting observation was noted for all installed ventral fins: they allowed the airplane to exit a spin when anti-spin ailerons were commanded. This ability to immediately exit a spin with anti-spin ailerons (while rudder and elevator commands were held) was observed on all test flights and for all ventral fins. The exiting of the spin through anti-spin ailerons contrasts with the no-ventral fin configuration of the airplane, which would only spin to the left with anti-spin ailerons. If anti-spin ailerons were commanded in a spin to the right, the airplane would exit the spin and enter a nose-down dive. This no-ventral fin configuration demonstrated the slowest recovery of any of the spins. It is hypothesized that when the aileron of the outboard (faster-moving) wing was deflected upward, the wake of that wing was deflected upward, and the ventral fin was no longer in the low dynamic pressure flow of the wing wake. This increase in the dynamic pressure q on the ventral fin then created an anti-spin yaw moment and allowed the airplane to exit the spin. As an example, in a left spin, the upward deflection of the right aileron would direct the wing wake further upward, which exposed the right side of the ventral fin to a higher-q flow. The impinging of this high-q flow on the ventral fin from the right side created a right yaw moment, which reduced the magnitude of the airplane yaw moment to the left. This, in turn, reduced the airplane yaw rate r, which reduced the degree to which the wings were unevenly stalled, and thus allowed the airplane to exit the spin.

3.7 Reduction of Flight Test Data for 6DOF Simulation Validation

In this section, the equations and methods used to extract aerodynamic data from the flight test data are presented. These aerodynamic data will be extracted from and compared to select Aero Testbed spins in Section 6.2. The methodology was initially validated against a known and complete data set, and a validation check was performed on a direct SpinSim spiral flight to verify that the post-processing codes reached the same answer as the Stengel code [73]. SpinSim is the force predicting code that was developed as part of this research, and it will be discussed in detail in Chapter 5. The integration of the forces and moments from SpinSim was performed by the Stengel code [73], using the six degree-of-freedom equations of motion, as covered in Section 6.1.

3.7.1 Method Validation Using Direct SpinSim Spiral Flight Data

The methodology used for extracting the aircraft velocities in the body-fixed frame, u, v, and w, the angle of attack α, and the sideslip angle β, is validated in this subsection using the direct data from a SpinSim spiral flight. In this spiral flight, the elevator was deflected 5 deg up, and the rudder was deflected 15 deg to the right. A plot of the SpinSim-generated x-y-z trajectory of this spiral flight is presented in Fig. 3.31.

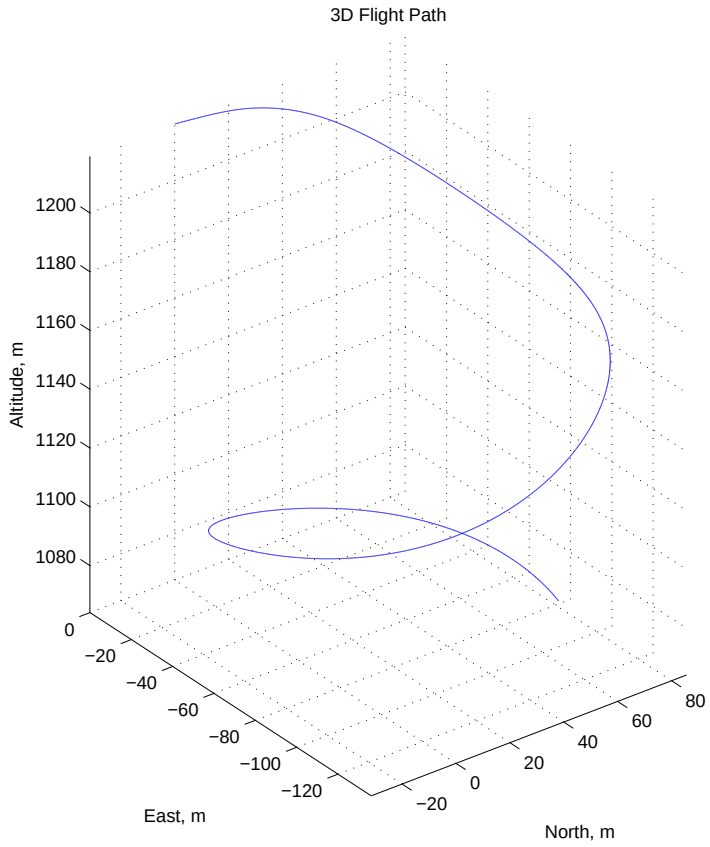

Figure 3.31: Trajectory of SpinSim-simulated righthand spiral of Aero Testbed with 5 deg up elevator deflection and 15 deg right rudder.

As seen in Fig. 3.31, the airplane begins the simulation flying due north at an approximate altitude of 1220 m, and it settles into a gentle descending spiral with a radius of just over 50 m. At the end of the 30-s simulation, the airplane is located at an altitude of approximately 1080 m, and it is on an easterly heading. The process to extract the aerodynamic data from the direct SpinSim data file, and eventually the IMU output of the Aero Testbed, requires that the earth-fixed velocity components, V_x, V_y, and V_z, be transformed into the u, v, and w velocity components in the aircraft-fixed reference frame. This transformation is achieved by using the Euler angles ϕ, θ, and ψ, although there was some initial suspicion as to the accuracy of the as-recorded Euler angles from the Aero Testbed IMU. This suspicion was caused by the electrical field of the motor, which was shown to interfere with the heading readings from the IMU.

Because of this suspicion as to the accuracy of the direct Euler angles, both the direct Euler angles and the integrated Euler angles based on the angular rates were compared. The angular rates p, q, and r were used directly from the IMU; thus, they were the angular rates in the IMU-fixed axis system. Assuming that the IMU principal axes were properly aligned with the aircraft principal axes, the angular rates of the IMU in the IMU-axes would be coincident with the angular rates of the airplane in the airplane-fixed axes. The potential for an installation error of the IMU on the airplane exists, and it will be investigated later in this section. By determining the Euler angles through both a direct and calculated method, a clearer view of any data inaccuracies may be observed. Using the direct IMU angular rates, and the initial values of the Euler angles, the following equations [74] were used to determine the rate of change of the Euler angles

$$\dot{\phi} = p + (q\sin\phi + r\cos\phi)\tan\theta \tag{3.7}$$

$$\dot{\theta} = q\cos\phi - r\sin\phi \tag{3.8}$$

$$\dot{\psi} = \frac{q\sin\phi + r\cos\phi}{\cos\theta} \tag{3.9}$$

Once $\dot{\phi}$, $\dot{\theta}$, and $\dot{\psi}$ were determined, the values could be integrated using standard integration techniques. The 4-step backward Adams-Bashforth method of Eqs. 3.3–3.6 was used to integrate the x-, y-, and z-locations, as well as the aircraft Euler angles. The results of that integration are presented in Fig. 3.32.

As seen in Fig. 3.32, the integrated and direct results for the aircraft Euler angles are coincident. Therefore, the methodology for integrating the angular rate is correct. Now that the aircraft Euler angles are known, the next step is to transform the velocities from the earth-fixed reference frame to the aircraft-fixed reference frame. For the sake of completeness, the aircraft velocities in the earth-fixed reference frame are plotted in Fig. 3.33.

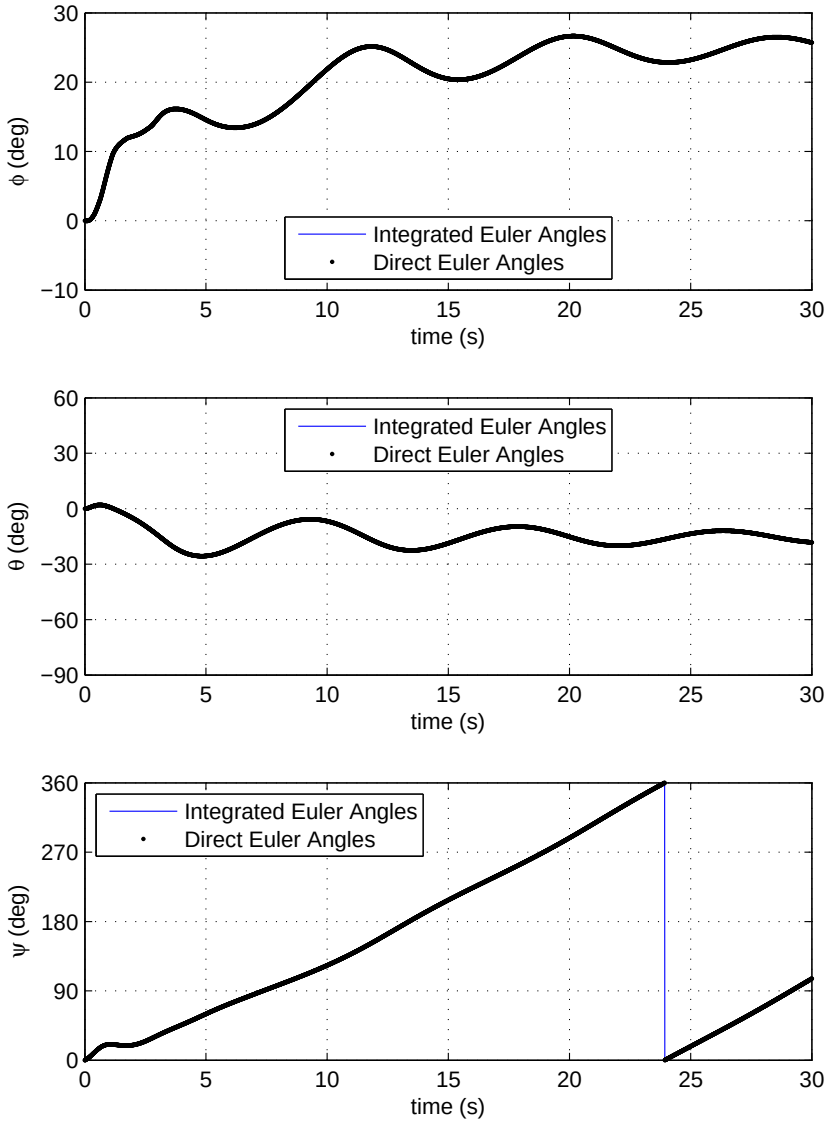

Figure 3.32: Plot of integrated and direct aircraft Euler angles for a righthand spiral flight.

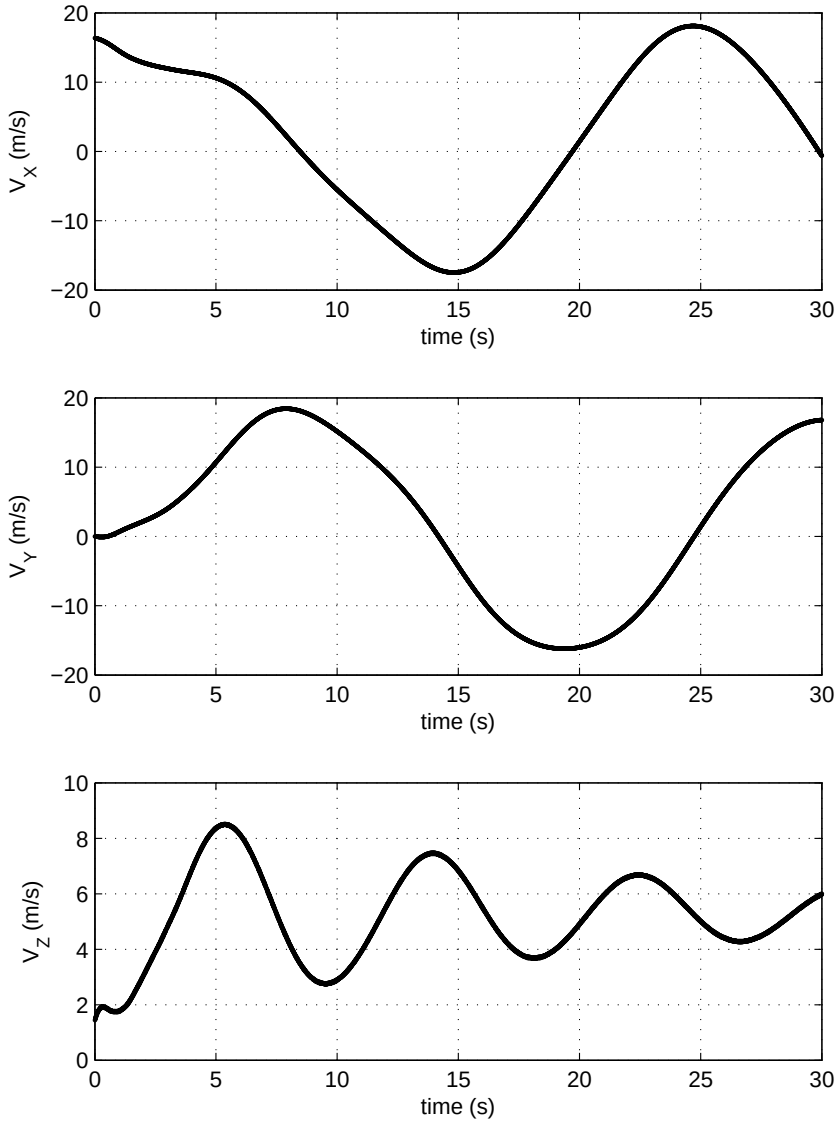

Figure 3.33: Plot of aircraft velocities in the earth-fixed reference frame for a righthand spiral flight.

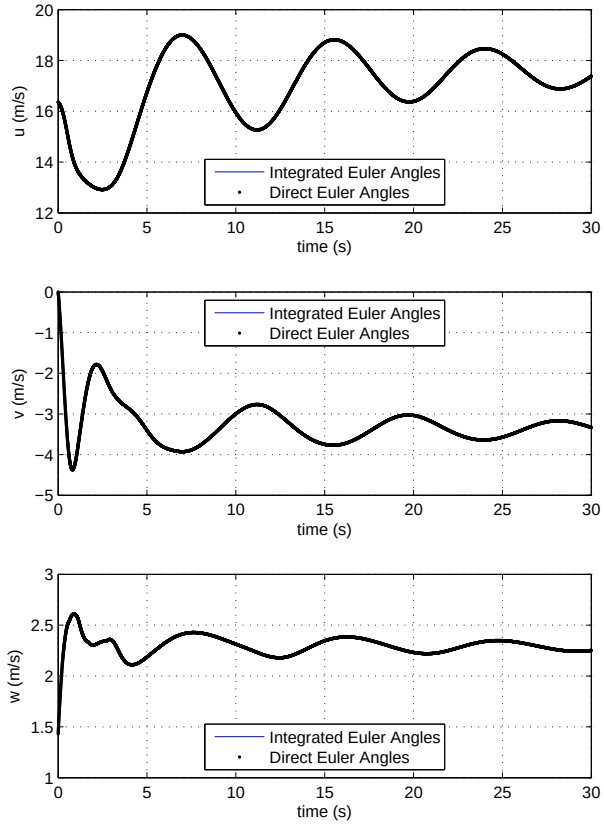

Figure 3.34: Plot of aircraft u, v, and w velocity components in the body-fixed reference frame for a righthand spiral.

To transform the velocities V_x, V_y, and V_z from the earth-fixed (inertial) to the aircraft-fixed (body) reference frame u, v, and w velocity components, the orthonormal transformation matrix $\mathbf{H}_I^B$ [74] is used

$$\mathbf{v}_{body} = \begin{bmatrix} u \\ v \\ w \end{bmatrix} = \mathbf{H}_I^B \mathbf{v}_{inertial} = \mathbf{H}_I^B \begin{bmatrix} V_X \\ V_Y \\ V_Z \end{bmatrix} \tag{3.10}$$

where

$$\mathbf{H}_I^B = \begin{bmatrix} \cos\theta\cos\psi & \cos\theta\sin\psi & -\sin\theta \\ -\cos\phi\sin\psi + \sin\phi\sin\theta\cos\psi & \cos\phi\cos\psi + \sin\phi\sin\theta\sin\psi & \sin\phi\cos\theta \\ \sin\phi\sin\psi + \cos\phi\sin\theta\cos\psi & -\sin\phi\cos\psi + \cos\phi\sin\theta\sin\psi & \cos\phi\cos\theta \end{bmatrix} \tag{3.11}$$

The results of applying this transformation are presented in Fig. 3.34, where the data set labeled “Integrated” uses the integrated Euler angles which are calculated from the method above. The data set labeled “Direct” uses the direct

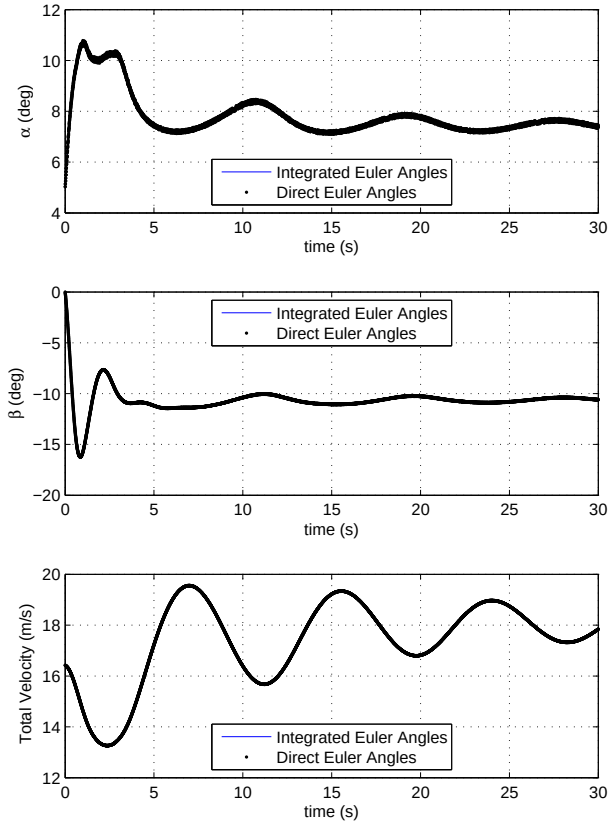

Figure 3.35: Plot of aircraft α, β, and V for a righthand spiral.

Euler angles from the SpinSim data file. As shown in Fig. 3.34, the u, v, and w velocity components in the body-fixed axes determined from the integrated and direct Euler angles are coincident.

Once the u, v, and w velocity components are calculated, the angle of attack α and sideslip angle β, as well as the total inertial velocity V, may be calculated using the following relationships [74]

$$\begin{bmatrix} \alpha \\ \beta \\ V \end{bmatrix} = \begin{bmatrix} \tan^{-1}(w/u) \\ \sin^{-1}(v/V) \\ \sqrt{u^2+v^2+w^2} \end{bmatrix} \tag{3.12}$$

Equation 3.12 was applied to the data of Fig. 3.34, and the calculated values of α, β and V are presented in Fig. 3.35.

The time histories of α, β, and V are coincident in Fig. 3.35; thus, the method described herein for extracting the aerodynamic angles is validated. Again, the data set labeled "Integrated" uses the integrated Euler angles, while "Direct" uses the direct Euler angles as output by SpinSim. Because the aerodynamic angles of Fig. 3.35 match exactly with those of the trusted data set calculated by the Stengel code [73], the methodology, transformation routines, and

integration schemes used to extract aerodynamic data from flight test data are validated. In the next section, this now-validated process will be applied to the flight test data for a "mush" flight, as recorded onboard the Aero Testbed by the XSens MTi-G IMU. Also, this process will be revisited later in Sections 6.2.1–6.2.4, specifically for the four spins selected for simulation in SpinSim.

3.7.2 Aero Testbed Gliding "Mush" Flight Data Results

In this section, the methodology and equations that were validated against the gentle SpinSim spiral of the previous section are applied to the data from a "mush" test flight of the Aero Testbed. To fly a "mush" flight, the aircraft was aligned with the runway at a high altitude, the motor power setting was reduced to zero, and an up-elevator command was gradually dialed in until the full, low deflection angle of 14 deg was reached. Once the full elevator deflection was reached, the up-elevator command was held. The pilot used minor aileron and rudder commands to keep the aircraft flying in a relatively straight line. The term "mush" is used in lieu of glide because the latter implies that the aircraft is trimmed in a low-drag configuration. A "mush" may also be thought of as a high-drag glide.

Figure 3.36 presents plots of the integrated and IMU-direct Euler angles from the Aero Testbed mush test flight. The integration methodology captures the shape and changes in the Euler angles, and a strong agreement is demonstrated for the roll angle ϕ. The pitch angle θ plot shows reasonable agreement, but when large changes in pitch occur, namely around $5 < t < 10$ s, and $t \approx 32$ s, the error between the direct and integrated data sets increases. Finally, the plot of the yaw angle ψ once again shows that it captures the minor changes in ψ. But, the plot of ψ demonstrates an ever-increasing error, causing the direct and integrated data sets to increasingly differ from one another as time passes.

If the Aero Testbed were in a high yaw rate condition, this growing error may be attributed to a growing integration error. A mush flight, however, is not characterized by high yaw rates or large changes in the yaw rate. This shows that the error is not due solely to integration, but it may be due at least in part to an error in the experimental setup. This error in the experimental setup would create a non-zero average offset on $\dot{\phi}$, which manifests itself as an artificially increasing ϕ. It is hypothesized that this $\dot{\phi}$ bias is due to a minor misalignment between the IMU principal axes and the airplane principal axes. To correct for the misalignment, an additional orthonormal transformation must be inserted into the process.

If the IMU and airplane are assumed to have their principal axes perfectly aligned, the airplane Euler angles in the earth-reference frame (ϕ, θ, ψ), and the angular rates in the body reference frame (p, q, r), can be used to determine the rate of change of the Euler angles with Eqs. 6.16–6.18. In the case of a minor misalignment between the IMU and the airplane, the results of Eqs. 6.16–6.18 no longer represent the Euler rates of the airplane but represent those of the IMU. To shift from the IMU Euler rates to the airplane Euler rates, an angular offset between the IMU and airplane must be assumed. From that assumed angular offset, the angular rates and body-fixed velocities can then be

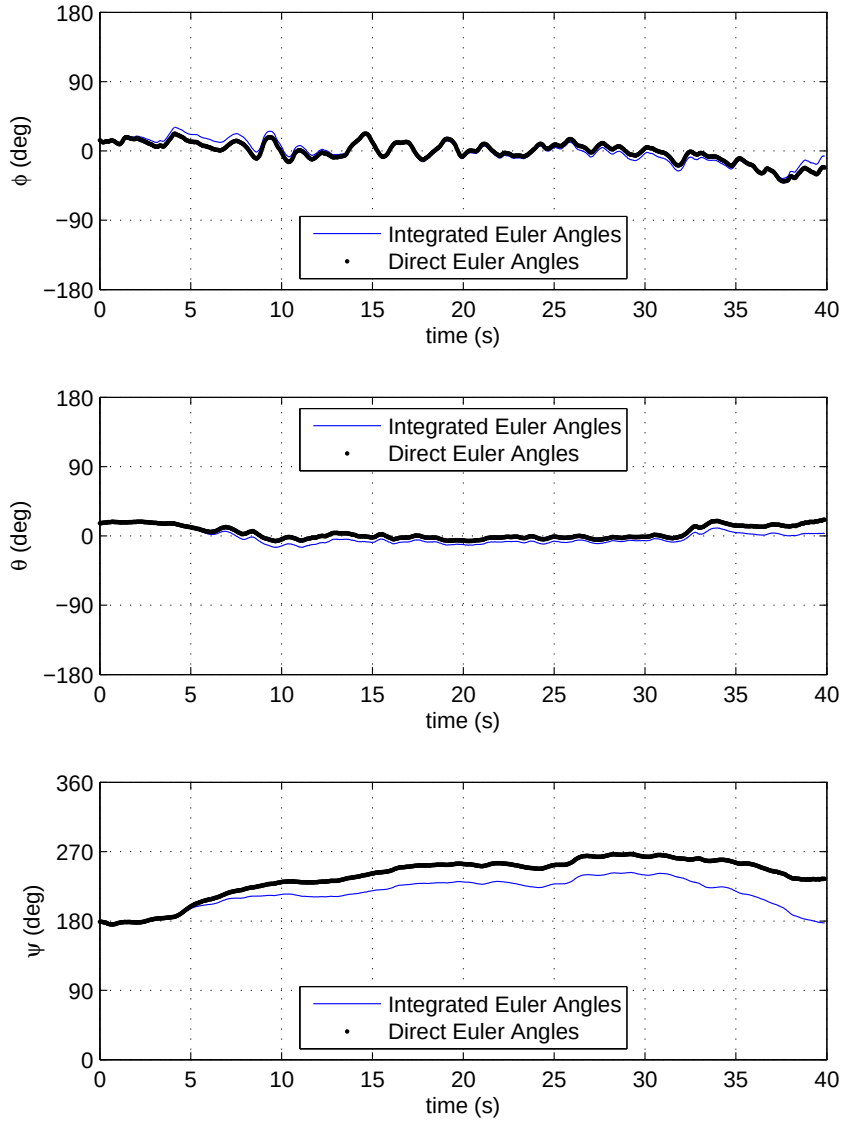

Figure 3.36: Plot of integrated and IMU direct Aero Testbed Euler angles for a mush flight.

calculated. In short, instead of performing one orthonormal transformation, two orthonormal transformations must be performed. The first set of Euler angles are those recorded by the IMU to move from the earth to the IMU-fixed axes, and the second set of Euler angles are an assumed set of angles quantifying the installation error of the IMU on the airplane that allows the information to be translated from the IMU-fixed to airplane-fixed axes.

All four combinations of adding offsets of ± 5 deg in θ and ψ were calculated with the additional orthonormal transformation procedure. The results of the calculated u, v, and w velocity components are presented in Fig 3.37.

Adding a positive offset to θ consistently worsened the agreement between the integrated and direct velocities, as shown in Figs. 3.37(b) and 3.37(d). On the other hand, subtracting an offset value from the IMU-direct value of θ improved the agreement of the velocities (Figs. 3.37(a) and 3.37(c)). These results show that there indeed was a pitch-axis installation error of the IMU that had the IMU pitched approximately 5 deg upward relative to the airplane body axes. This upward pitch error in the IMU seems likely, as the design of the installation hardware of the IMU positioned it affixed to an aft-hanging shelf by two bolts that were centered longitudinally on the IMU. If this shelf were not properly aligned with the aircraft axes, an installation error in θ would result, and under the force of gravity, any sag in the shelf would yield an IMU that is pitched up relative to the airplane body axes. Additionally, the bolt location on the IMU allowed the IMU a greater chance to be shifted in the pitch axis than in the yaw axis (see Fig. 3.3 for a photograph of the IMU installation). As regards the installation correction to ψ, the plots show that the best agreement between data sets is generated with a -5 deg correction to ψ (Fig. 3.37(c)). This better agreement implies that the IMU had an installation error of approximately 5 deg to the right in the yaw axis. This installation error in the yaw axis can easily be explained. The two mounting holes in the IMU housing had a slightly larger diameter than that of the bolts used to mount the IMU. The larger diameter of the holes, when compared with the bolt diameter, would allow for a small yaw misalignment between the IMU and airframe to occur easily. It is possible that this difficulty in measuring the Euler angles may be due to a combination of installation error in the yaw axis and the electromagnetic effects of the motor windmilling during the mush flight, as these flights were not operated with the motor brake active. Thus, a windmilling motor would be acting as a generator and creating an electromagnetic field, which would affect the IMU heading information.

Figure 3.38 presents the plots of the Euler angle rates of change for the mush flight, as calculated using Eqs. 6.16–6.18. This figure shows that during what is supposed to be the steady-state portion of the flight, $10 < t < 31$ s, $\dot{\psi}$ has a non-zero positive average offset, or bias. The rates of change of ϕ and θ do not demonstrate such an offset.

To present a complete set of data, Fig. 3.39 presents the x-, y-, and z-velocities in the earth frame of reference, V_x, V_y, and V_z, as recorded directly by the IMU for the Aero Testbed mush flight. As the other figures indicated, the $10 < t < 31$ s region generally defnes the steady-state regime of the mush. While the airplane maintained a reasonably-constant descent rate (V_z), the easterly velocity (V_y) increased in magnitude from 8 m/s for $10 < t < 15$ s to approximately 12 m/s, while the northerly velocity (V_x) decreased in magnitude from 11 m/s to 6 m/s after $t = 15$ s. These changes in the easterly and northerly velocities show that at $t = 15$ s, the airplane heading changed. This heading change may be due to rudder input or a change in the windfield.

Figure 3.40, which presents the calculated velocities in the aircraft-fixed axes, confirms that from $10 < t < 31$ s, the airplane maintained a relatively constant u velocity component of 13 m/s. The velocities based on the direct and integrated Euler angles agree well. A discrepancy is evident between the v- and w-velocities based on the direct and

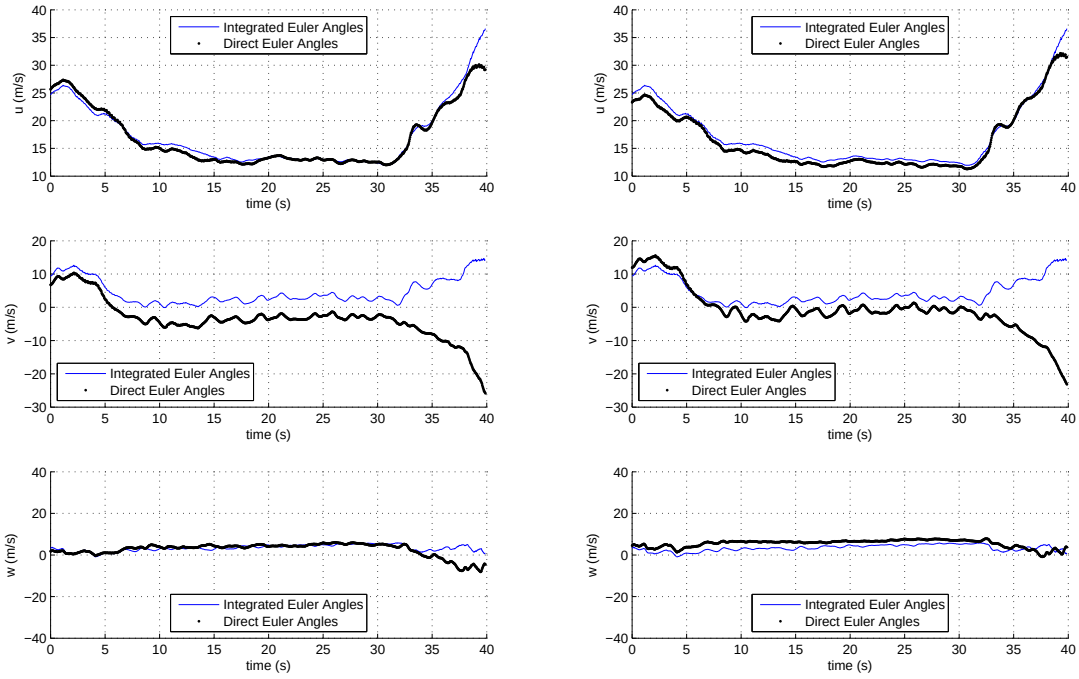

(a)

(b)

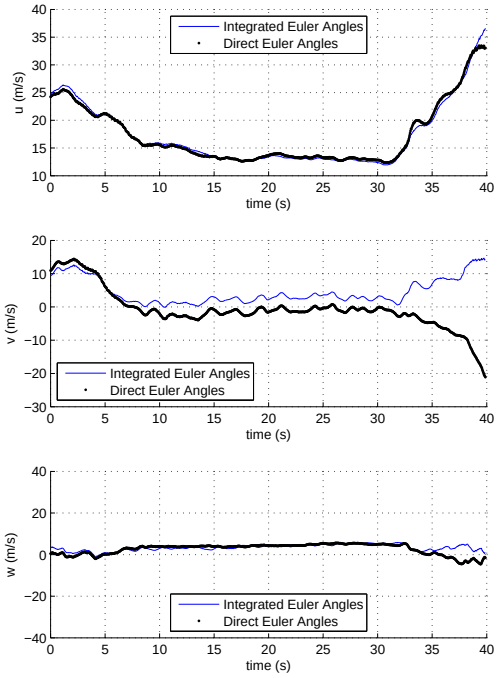

(c)

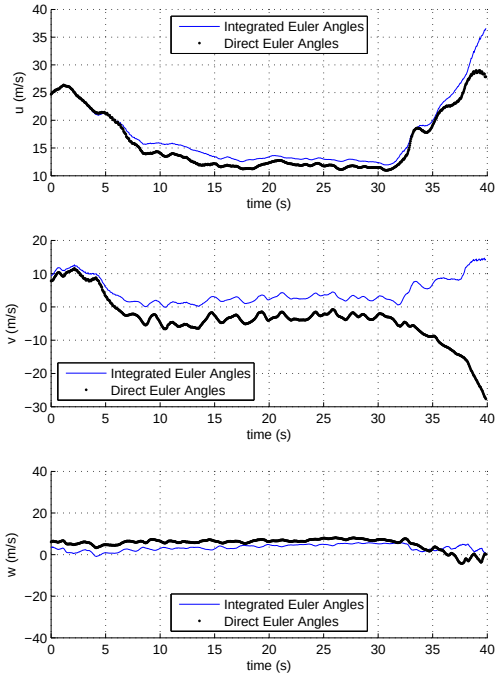

(d)

Figure 3.37: Results from assumed installation error corrections of a) $\theta - 5$ deg and $\psi + 5$ deg, b) $\theta + 5$ deg and $\psi - 5$ deg, c) $\theta - 5$ deg and $\psi - 5$ deg, d) $\theta + 5$ deg and $\psi + 5$ deg.

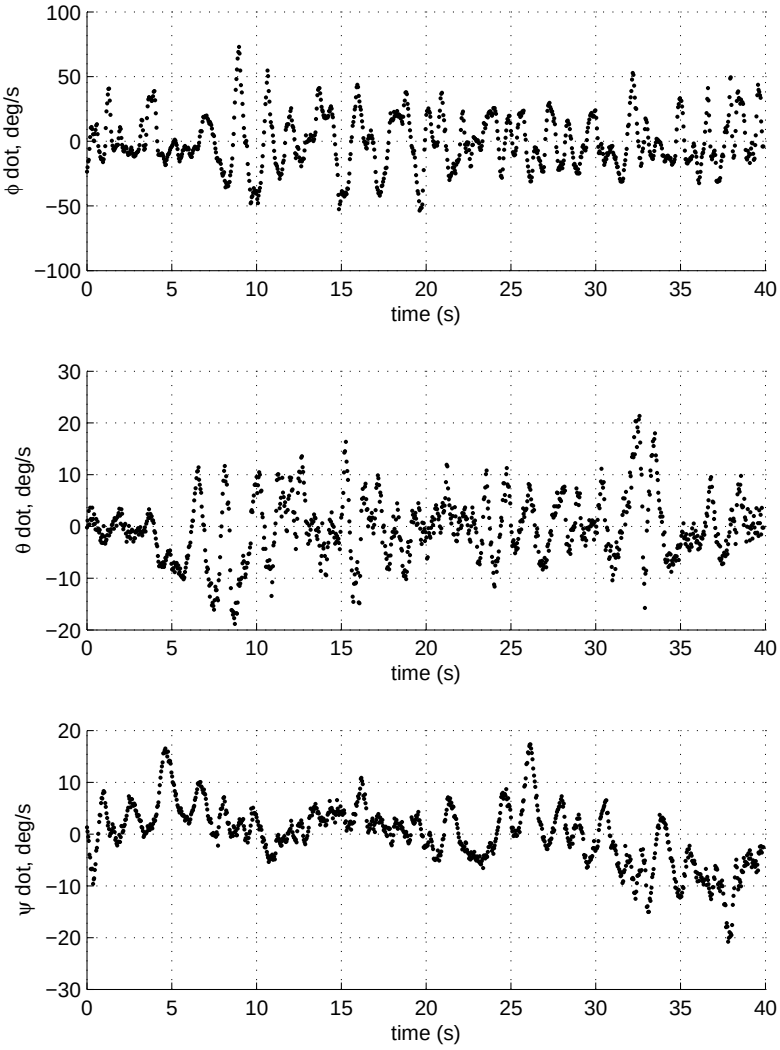

Figure 3.38: Plot of calculated Aero Testbed Euler angle rates for a mush flight.

integrated Euler angles, but in general, the airplane did not exhibit a large v velocity component and was descending at around 5 m/s (w) during the mush flight.

Based on the aircraft body-axis velocity components, Fig. 3.41 presents the α, β, and V values calculated for the mush flight. During the flight, α increases to around 20–25 deg despite differences in the two Euler angle sources. Further, a disagreement in β is observed between the direct and integrated values. These discrepancies are due to differences in θ and ψ between the direct and integrated Euler angles.

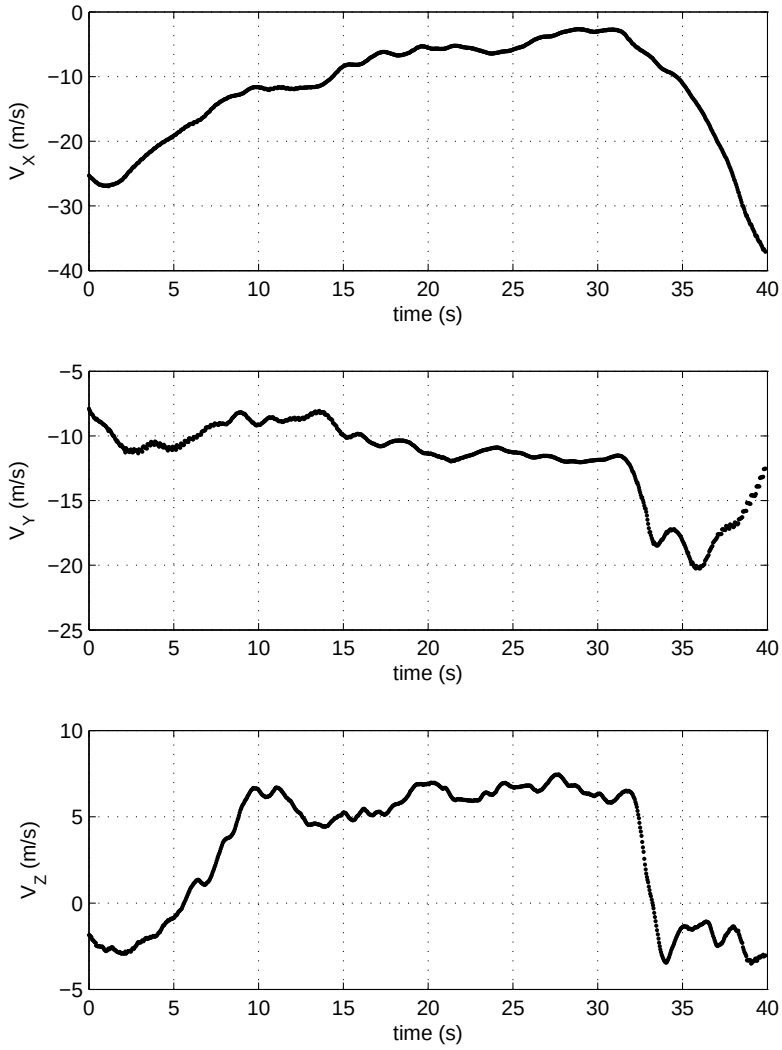

Figure 3.39: Plot of direct Aero Testbed velocities in the earth-fixed reference frame for a mush flight.

3.8 Summary of Flight Testing

In this section, the methodology and hardware that were used for conducting spin flight tests with the Extra 260 UIUC Aero Testbed aircraft were presented. The post-processing methods that were used to extract the helical trajectories of a spin were described, and the results were presented. As pilots are taught, adding anti-spin ailerons when in a spin increases the descent rate, which affords the pilot less time to recover. Various ventral fins were tested, and they were generally shown to improve the recovery characteristics of the airplane from spin. Further, data post-processing methods and equations were presented, and the methods were validated with simulation data and flight test data from

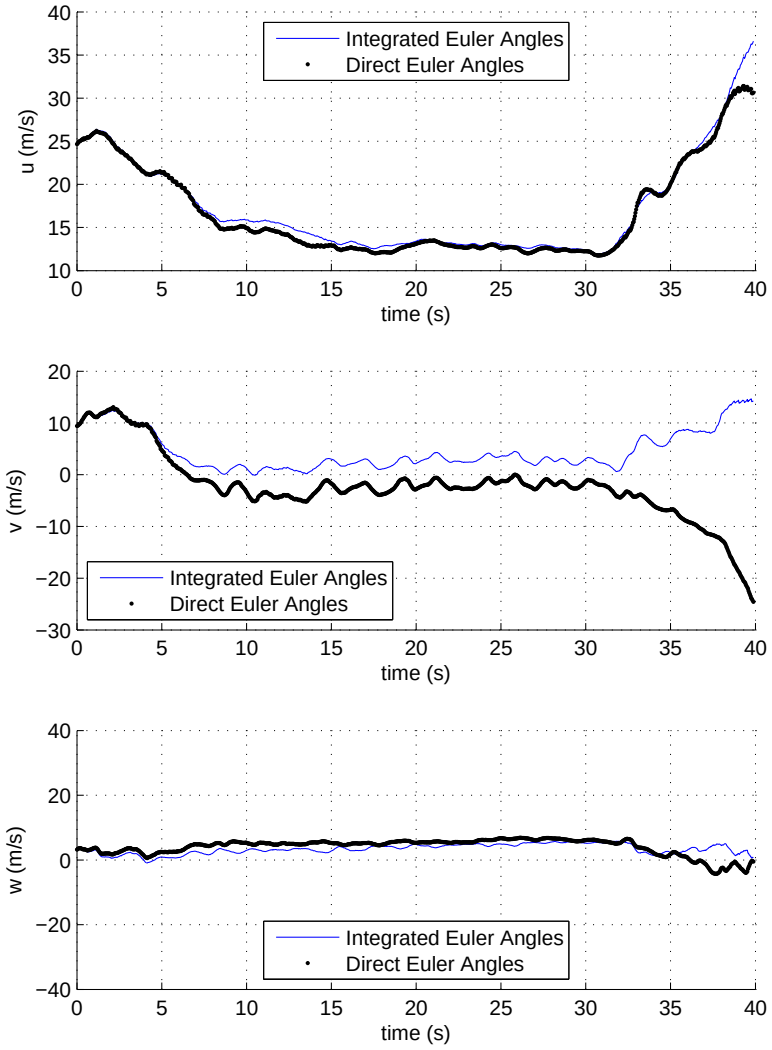

Figure 3.40: Plot of Aero Testbed u, v, and w velocity components in the body-fixed reference frame for a mush flight.

a "mush" flight. Post-processing of the flight test data to extract the aerodynamic angles α and β revealed a possible installation error of the IMU on the airplane, and a mathematical method to reduce that error was presented.

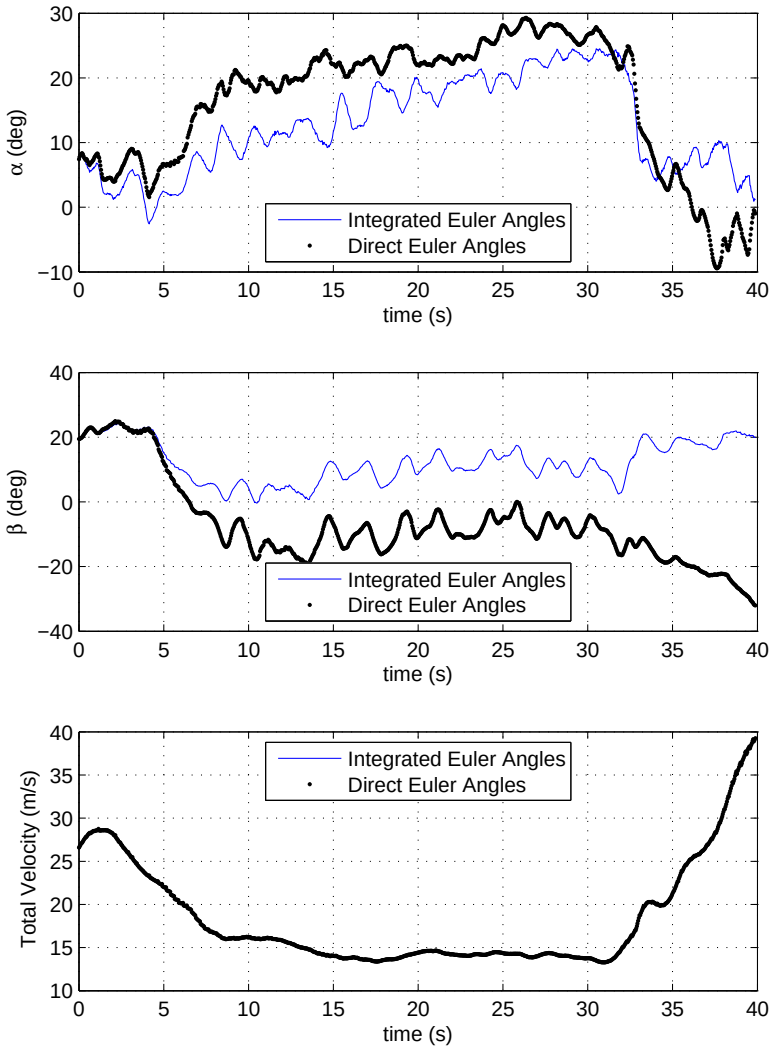

Figure 3.41: Plot of Aero Testbed α, β, and V for a mush flight.

Chapter 4

Wind Tunnel Testing

Another aspect of this research is the wind tunnel testing. Its purpose aim to parametrically identify the various effects of the Reynolds number, aspect ratio, and airfoil geometry on the relationship between the spin parameter ω and the normal force coefficient C_N for wings in spin with $R_s = 0$. These investigations support the larger objective of the present work, which is to validate an analytical model of the wing normal force of an airplane for use in simulating the aerodynamics of a stalled and spinning wing. This chapter is divided into four sections. The experimental setup is described in Section 4.1, and the wing test article properties are presented in Section 4.2. The experimental results are plotted and discussed in Section 4.3, and conclusions are presented in Section 4.4.

4.1 Experimental Setup

This section discusses the experimental setup, wind tunnel corrections used, motion control system, and data acquisition setup of these experiments. Aerodynamic tests of wings in spin were conducted in the University of Illinois at Urbana-Champaign low-speed low-turbulence subsonic wind tunnel, as shown in Fig. 4.1. The open-return tunnel has an inlet contraction ratio of 7.5:1, and the rectangular test section is 2.8×4.0 ft (0.853×1.22 m) and is 8 ft (2.44 m) long. The width of the test section increases by approximately 0.5 in (1.27 cm) to account for boundary layer growth at the test section sidewalls. To ensure good flow quality in the test section, one 4-in (10.2 cm) thick honeycomb and four anti-turbulence screens are located in the settling chamber. The empty-tunnel turbulence intensity is less than 0.1% for all operating conditions, which is sufficient for low Reynolds number airfoil measurements [75, 76]. The maximum empty-test-section speed is 235 ft/s (71.5 m/s), although the tunnel was operated at speeds up to only 35 ft/s (10.7 m/s) in the current research. The test section speed was set by a 125 hp (93.2 kW) AC motor driving a five-bladed fan controlled by an ABB ACS 800 low-voltage AC drive. The test-section speeds were measured with an MKS 220 1-torr differential pressure transducer, which was connected to static ports in the settling chamber and at the inlet of the test section. Ambient pressure was measured with a Setra Model 270 pressure transducer. The test section speed was computer-controlled to within 1% of the prescribed speed with these pressure transducers.

The normal force on the wing was determined through the use of the drag balance shown in Figs. 4.2–4.3, which pivoted on two sealed ball bearings and was constrained on the downstream side by a load cell [77, 78]. The propeller

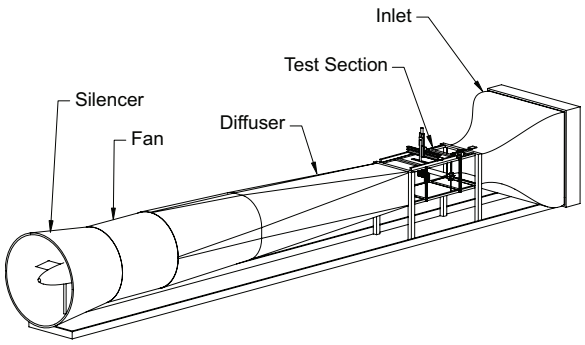

Figure 4.1: University of Illinois 2.8 × 4.0 ft low-speed low-turbulence wind tunnel.

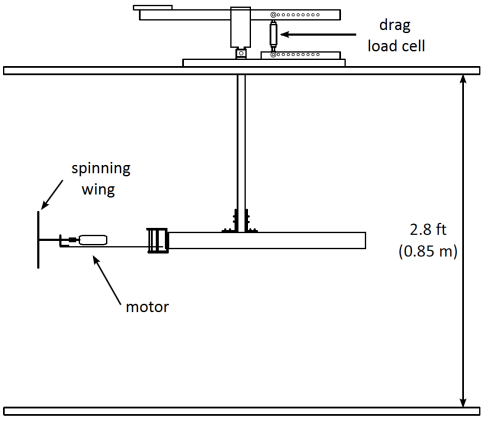

Figure 4.2: Experimental setup for drag force measurement (fairing not shown).

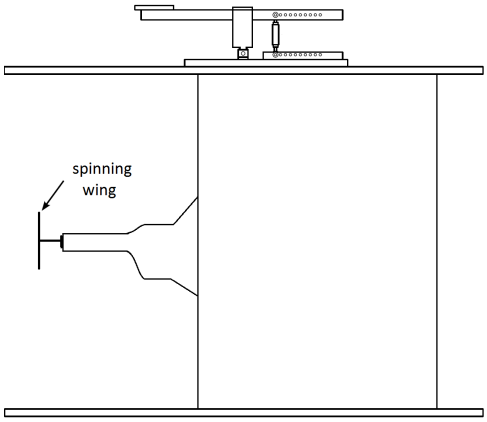

Figure 4.3: Spinning wing balance enclosed in fairing.

rig described in Ref. [79] was modified by reversing the streamwise orientation of the load cell and by replacing the flexures with ball bearings to account for the higher loads. An Interface SMT S-type load cell with a load capacity of 10 lb (44 N) was used to measure the drag force experienced by the rotating wing.

The drag load cell could be located at one of ten different locations in 0.5 in (1.27 cm) increments, ranging from 3.25 in (8.26 cm) to 7.75 in (19.69 cm) from the pivot point. These ten locations allowed the length of the moment arm to be changed to allow for the full measurement range of the load cell based on the measured drag. The weight and resulting force of the motor and sting structure maintained the load cell in tension for all test cases, ensuring that a condition where the load cell was loaded in compression, which could cause slipping of the load cell, was prevented. The normal force coefficient was determined from the drag of the spinning wing with the assumption that the net rotating lift component was small in comparison with the drag. Additionally, the in-plane force generated by the lift of the spinning wing (normal to the drag force) would zero out over a full rotation cycle of the wing. Thus, using $D \gg L$ yields

$$C_N \approx \frac{D}{qS_W} \sin\theta \tag{4.1}$$

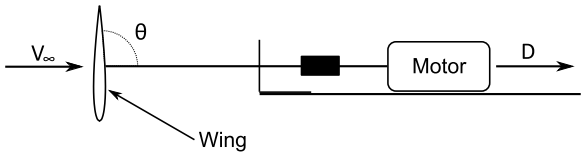

Figure 4.4: Diagram of experimental spinning wing setup showing the orientation of the freestream velocity, wing location, orientation of θ, motor location, and direction of D.

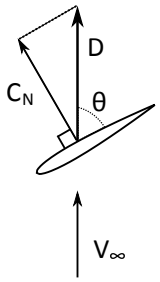

Figure 4.5: Diagram depicting relative orientations of V_∞, D, and C_N from Eq. 4.1.

where D is the drag force exerted on the spinning shaft, q is the dynamic pressure, S_W is the wing area, and θ is the pitch angle of the wing. Figure 4.4 depicts a detailed view of the spinning wing and motor of Fig. 4.2, with wing location, orientation of θ, motor location, and direction of the drag force labeled. Figure 4.5 depicts the relative orientations of V_∞, D, and C_N, based on θ, as used in Eq. 4.1. The Reynolds number of a wing in these tests was defined by the freestream velocity and mean aerodynamic chord, i.e.

$$Re = \frac{\rho V_\infty \bar{c}}{\mu} \tag{4.2}$$

where the viscosity μ was determined via Sutherland's law from the ambient temperature as measured by an Omega type-K static-temperature thermocouple.

A NACA 0025 symmetric fairing of chord length 24 in (0.61 m) was used to keep the motor sting, balance support arm, motor motion controller, and associated cabling out of the flow. This fairing, depicted in Fig. 4.6, spanned the entire test section from floor-to-ceiling in order to maintain a symmetric test section. The motor sting placed the rotating test specimen 17.75 in (44.45 cm) forward of the fairing leading edge — a sufficient distance forward to ensure that all wings in spin were over 1.7 wingspans upstream of the fairing. This forward placement of the wing in spin is based on the forward placement of a propeller, which must be located at least 1.5 propeller diameters upstream of the fairing in order to minimize the effects on the wake structure behind the rotating body [79].

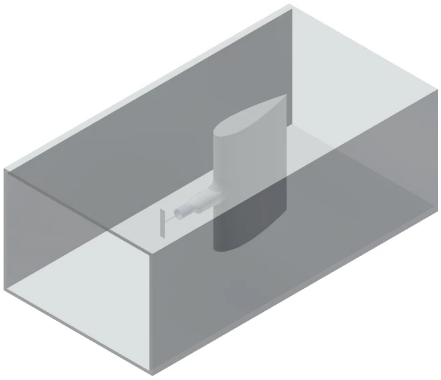

Figure 4.6: Isometric view of the fairing, sting, and spinning wing in the wind tunnel test section.

4.1.1 Wind Tunnel Corrections

Two wind tunnel corrections were used to correct the force data from testing the wings in spin. A velocity correction factor was used to account for the effect of a spinning wing in front of a fairing, and the Glauert [80, 81] propeller correction was used to correct drag measurements. Testing a spinning wing, or any aerodynamic test article, in front of a fairing, will result in the fluid velocity at the test article being lower than the measurement at the wind tunnel test section entrance because the test article lies on or in the vicinity of the stagnation streamline. Since the wings are tested on a sting in front of a fairing, the fluid velocity at the wing will be less than the velocity measured at the beginning of the test section. To account for this reduction in velocity, the ratio of the velocities defines a correction factor, that is

$$\frac{V_{c_{fairing}}}{V_\infty} = k_{fairing} \tag{4.3}$$

where the value of the factor $k_{fairing}$ [79, 81] was determined for each wing based on the wing dimensions and the distance upstream of the fairing. Since the fairing spanned the test section from the floor to ceiling, the fairing was modeled as an airfoil using source panels [79]. To satisfy the boundary condition of no cross flow at the tunnel side walls, reflections of the airfoil were included. The strength of each source panel and the flowfield surrounding the airfoil was then calculated using the method described in Anderson [82]. Using 100 sets of reflection pairs, the cross flow at the tunnel side walls was found to be less than $2 \times 10^{-6}\%$ of the freestream. The resulting 2D flowfield from the source panels was assumed to be the same along the span of the fairing. Wall effects were assumed to be negligible because the spinning wings were small compared with the tunnel test section dimensions. Equation 4.3 uses a weighted average of the velocities experienced by the entire area of the spinning wing based on the distance forward of the fairing and the wingspan to determine the single velocity reduction factor [79].

The Glauert [80, 81] correction for testing propellers in a closed wind tunnel test section was used to correct the spinning wing drag data. This velocity correction is used to correct for testing thrust-producing propellers in a closed test section, as constraining a thrust-producing propeller or a drag-producing wing in spin to a closed test section yields a difference from testing that article in free air. A spinning wing producing drag will have a wake region immediately downstream of the wing with a velocity lower than the nominal wind tunnel test section velocity. To maintain a constant mass flux of air (i.e., satisfy continuity), both upstream and downstream of the spinning wing, the region outside of the wake must be at a higher velocity than the freestream. Thus, the pressure outside of the wing wake would be lower than the pressure upstream of the spinning wing, and thus the drag measured is higher than what would be measured in free air for that same velocity. In other words, the drag measured would occur at a lower velocity in free air, and that lower velocity may be determined from

$$\frac{V_c}{V_\infty} = 1 - \frac{\tau\alpha}{2\sqrt{1+2\tau}} \tag{4.4}$$

where α is the ratio of the swept area of the spinning wing and the test section cross-sectional area, and

$$\tau = \frac{D}{\rho A V_\infty^2} \tag{4.5}$$

The correction given by Eq. 4.3 and the Glauert correction for testing a propeller in a closed test section (Eq. 4.4) were applied to all data, and the accuracy was verified based on calibration runs of non-rotating wings of varying $\mathcal{AR}$ compared with the C_D vs. $1/\mathcal{AR}$ data of Ref. [83].

4.1.2 Motion Control and Data Acquisition

The wings were rotated using a Faulhaber 3268G024BX4AES-4096 brushless DC servomotor, which was controlled by an MCBL 3006 AES-series motion controller connected via a RS232 cable to a computer running the Faulhaber Motion Manager 5.1 software. This motion control software allowed the motor rotational speed to be set and maintained at specific RPM values and monitored in realtime. The 3268 series DC servomotor has an operating range of 0 to 11,000 RPM, and it is capable of a maximum torque of 0.092 Nm. Shaft position information was measured by an absolute encoder and provided to the motion controller at a resolution of 4096 steps per revolution via a serial (SSI) interface. Power was supplied to the DC-servomotor by an NEC NG-150642-001 24-V 600-mA power supply that was connected to the controller.

All instrumentation voltages were channeled to a National Instruments PCI-6031E 16-bit analog-to-digital data acquisition (DAQ) board that was connected to a personal computer where the data were recorded. A LabVIEW program was used to record the drag, dynamic pressure, atmospheric pressure, and temperature at 3,000 Hz for a

Table 4.1: Aspect Ratio Study – Wing and Blade Information and Dimensions

Aspect Ratio	Raw Blade	Chord Length	Wingspan	Area
8.33	Align 325D 325 mm	1.25 in (3.2 cm)	10.4 in (26.4 cm)	13.0 in^2 (83.9 cm^2)
6.50	KBDD 325W 325 mm	1.37 in (3.5 cm)	8.91 in (22.6 cm)	12.2 in^2 (78.8 cm^2)
4.85	Revolution RVOB043000 430 mm	1.65 in (4.2 cm)	8.00 in (20.3 cm)	13.2 in^2 (85.2 cm^2)
3.85	KBDD 350W 350 mm	1.85 in (4.7 cm)	7.13 in (18.1 cm)	13.2 in^2 (85.1 cm^2)
2.55	Pro3D DY-6001 600 mm	2.20 in (5.6 cm)	5.61 in (14.2 cm)	12.3 in^2 (79.6 cm^2)

duration of 3 s. These experimental data were subsequently time averaged to yield one steady state value, which was returned to the computer. Each wind tunnel run was conducted at a constant freestream velocity, and the motor speed was varied to produce the desired range of spin parameter ω values. The motor speed was controlled to within 1% during the recording time period.

4.2 Wing Test Article Properties

Three types of wings were tested in this experiment including carbon fiber symmetric wings with a foam core, solid plastic flat bottom wings, and 3 mm plywood flat plate wings. All of the symmetric carbon fiber airfoils had a thickness-to-chord ratio of around 10%. These spinning wing test articles were made using a 3/16 in (4.76 mm) diameter steel shaft and symmetric radio-controlled helicopter blades. The test articles were linked to the 5 mm shaft of the motor with a 3/16 in to 5 mm bellows coupling to account for minor shaft misalignments. Holes were drilled in the wings to accept the shaft, which was mounted at pitch angles (θ) of 30, 60, and 90 deg (see Fig. 4.4 defining the pitch angle). The shaft was glued to the wing with epoxy so that its tip was flush with the forward-facing surface of the wing.

The dimensions and information for the five blades used in the study of wing aspect ratio effects are summarized in Table 4.1, which presents the $\mathcal{AR}$, chord length, wingspan, and area of each of the wings. Figure 4.7 presents a CAD rendering of the $\mathcal{AR} = 4.85$ wing test articles at 30, 60, and 90 deg orientations. The area of each wing was held as close as possible to 13 in^2 (84 cm^2) and resulted in a range of aspect ratios that included and expanded beyond values that would be seen on a typical general aviation aircraft. In the cases of the $\mathcal{AR} = 6.50$ and $\mathcal{AR} = 2.55$ wings, their area constraint was relaxed slightly in favor of maintaining a more evenly-spaced range of aspect ratios. It is for this reason that the areas of those two wings are slightly less than 13 in^2.

Additional tests were conducted on homogeneous, solid plastic blades, and on flat plate wings constructed from 3 mm plywood. Both of these wing styles were constructed in the same manner as the symmetric carbon fiber wings. The plastic blades were selected because their uniform density made them capable of higher rotation speeds, which allowed a greater range of ω values to be studied. Additionally, blades of similar chord lengths were available with

Table 4.2: Cross-Sectional Shape Study – Wing and Blade Information and Dimensions

Aspect Ratio	Raw Blade	Chord Length	Wingspan	Area
5.97	HDX VTS-109Y (flat-bottom)	1.35 in (3.4 cm)	8.06 in (20.5 cm)	10.9 in^2 (70.2 cm^2)
6.30	HDX VTS-108Y (symmetric)	1.14 in (2.9 cm)	7.19 in (18.3 cm)	8.19 in^2 (52.9 cm^2)
1.00	3mm plywood (flat plate)	3.63 in (9.2 cm)	3.63 in (9.21 cm)	13.1 in^2 (84.8 cm^2)
2.00	3mm plywood (flat plate)	2.50 in (6.4 cm)	5.00 in (12.7 cm)	12.5 in^2 (80.7 cm^2)
5.00	3mm plywood (flat plate)	1.50 in (3.8 cm)	7.50 in (19.1 cm)	11.3 in^2 (72.6 cm^2)
10.0	3mm plywood (flat plate)	1.19 in (3.0 cm)	11.9 in (30.2 cm)	14.1 in^2 (91.0 cm^2)

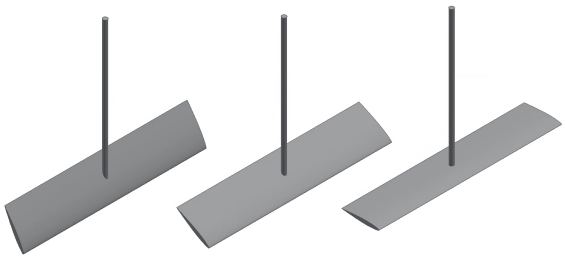

Figure 4.7: CAD rendering of the $\mathcal{AR} = 4.85$ wing of Table 4.1 at 30, 60, and 90 degree orientations, left to right.

symmetric and flat-bottom airfoils. These similar chord lengths allowed for the effects of the airfoil shape to be investigated. Table 4.2 presents information on these flat bottom airfoil and flat plate wings.

After each test article was assembled, it was statically balanced along the span. This static balancing was achieved through a combination of removing any preexisting counterweights from inside the wing and affixing small steel bolts and drops of epoxy into the foam core at the wing tip. For the 90 deg blades, the hole for the steel shaft was drilled at the 50% chord location because in a heavily-stalled situation the lift vector acts near that location. For the 30 and 60 deg blades, the shaft was located around the 35% to 40% chordline because of the fact that structural considerations were necessarily the primary driver of the hole drilling location. Initially, 30 and 60 deg test articles were fabricated with the hole located at the 50% chord location, but there was insufficient thickness to securely glue the shaft to the blades. These test articles were not used.

4.3 Results and Discussion

In this section, the experimental results of testing stalled spinning wings in a wind tunnel are presented. This section will parametrically establish the effect of Reynolds number, aspect ratio, airfoil geometry, and high spin parameter values.

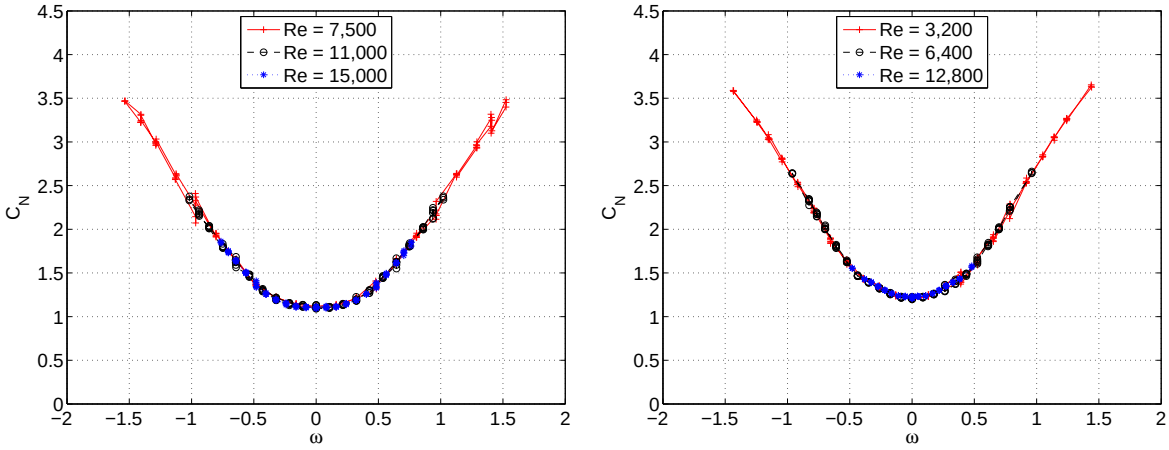

Figure 4.8: Plot of C_N versus ω for three different *Re* values at $\theta = 90$ deg for a symmetric wing with (a) $\mathcal{AR} = 6.50$, and (b) a flat plate with $\mathcal{AR} = 5.00$.

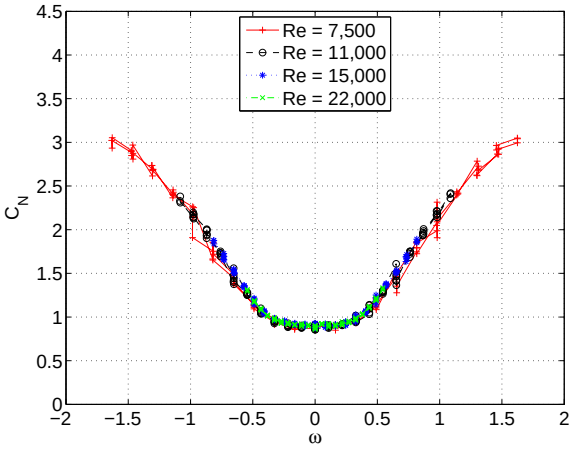

Figure 4.9: Plot of C_N versus ω for a symmetric wing at three different *Re* values at $\theta = 60$ deg for a wing with $\mathcal{AR} = 2.55$.

4.3.1 Reynolds Number Effects

The first investigation was performed to establish the effect of the Reynolds number on the aerodynamic flowfield of stalled spinning wings. It is well established that minimal Reynolds number effects exist on unswept non-yawing wings in the post-stall regime; however, the literature is devoid of any information on stalled wings in spin with regard to Reynolds number effects. To investigate whether or not Reynolds number effects exist on stalled wings in spin, a number of wings were tested at different Reynolds numbers.

Figure 4.8(a) presents C_N data for the $\mathcal{AR} = 6.50$ wing at $\theta = 90$ deg for three different freestream Reynolds numbers. By coplotting the data in this manner, it is established that no Reynolds number effects exist for a stalled spinning wing over the range of Reynolds numbers tested. This is a significant finding because the previous state of

the literature only addresses stalled, unspinning wings. These data demonstrate that the addition of rotation to a stalled wing does not add a Reynolds number dependency within the range of Reynolds numbers tested in this research. This lack of a Reynolds number dependency is further supported by Fig. 4.8(b), which presents data for the $\mathcal{AR} = 5.0$ flat-plate wing at $\theta = 90$ deg and at three different Reynolds numbers. Across the Reynolds number range, the C_N data follow the same ω^2 relationship with no offset or change in the rate of growth.

To further investigate Reynolds number effects at slightly higher Reynolds numbers, a low aspect ratio wing of $\mathcal{AR} = 2.55$ was tested at $\theta = 60$ deg. The data for this wing are presented in Fig. 4.9. As shown, no Reynolds number effects are apparent across a range of Reynolds number and pitch angles. The lack of Reynolds number effects shows that the 3D flow structures present in a stalled spinning wing are the same across the range of Reynolds numbers tested. For a constant maximum attainable rotation speed, an increased Reynolds number results in a decrease in the maximum attainable ω value. The benefit of testing at higher Reynolds numbers is an increased resolution in ω and decreased variation in the range of ω values that are close to zero. As shown in Fig. 4.9, the $Re = 22{,}000$ data points provide smooth and finely-spaced data centered around $\omega = 0$. These data do not differ from those of the lower Reynolds numbers.

It is also observed in Fig. 4.9 that the C_N–ω plot appears to exhibit a decreased C_N growth rate for $|\omega| > 1$, suggesting the presence of a maximum attainable C_N value. An investigation into high values of ω with a flat-bottom wing of $\mathcal{AR} = 5.97$ at $\theta = 90$ deg is presented later in Fig. 4.12(b). While the trend in Fig. 4.9 shows a decrease in growth rate for $|\omega| > 1$ and $C_N \approx 2.5$, the data of Fig. 4.12(b) shows a reduced growth rate for $|\omega| > 1.6$ and $C_N \approx 4$. These data show that the maximum attainable C_N may have an $\mathcal{AR}$ dependency, which will be explained later in Section 4.3.4. The majority of the tests were conducted in the $|\omega| < 1$ regime because it is within the expected range of a spinning aircraft. If an aircraft were to be spinning at $\omega = 3$, other considerations would become more important than the aerodynamics. It would become expected, for instance, that a structural limit on the wings, or a biological limit on the occupants, would have already been reached and exceeded in that spin regime.

4.3.2 Aspect Ratio Effects

To investigate the effects of the wing aspect ratio on C_N across the range of ω, the five wing planforms of Table 4.1 were tested at pitch angles of 30, 60, and 90 deg. Time-averaged data for the wing normal force of the five different aspect ratio wings were acquired over the approximate range of $-1 < \omega < 1$ at various Reynolds numbers. Data for $Re = 15{,}000$ are presented in Fig. 4.10 for pitch angles of 30, 60, and 90 deg. Data at $Re = 11{,}000$ are presented in Fig. 4.11 for the same pitch angles. As depicted in Figs. 4.10 and 4.11, C_N is generally proportional to the square of ω for all values of θ. Also evident in Figs. 4.10 and 4.11 is that as the wing pitch angle θ increases from 30 to 90 deg, the curves for the different $\mathcal{AR}$ wings exhibit smaller differences between one another and all increase in magnitude.

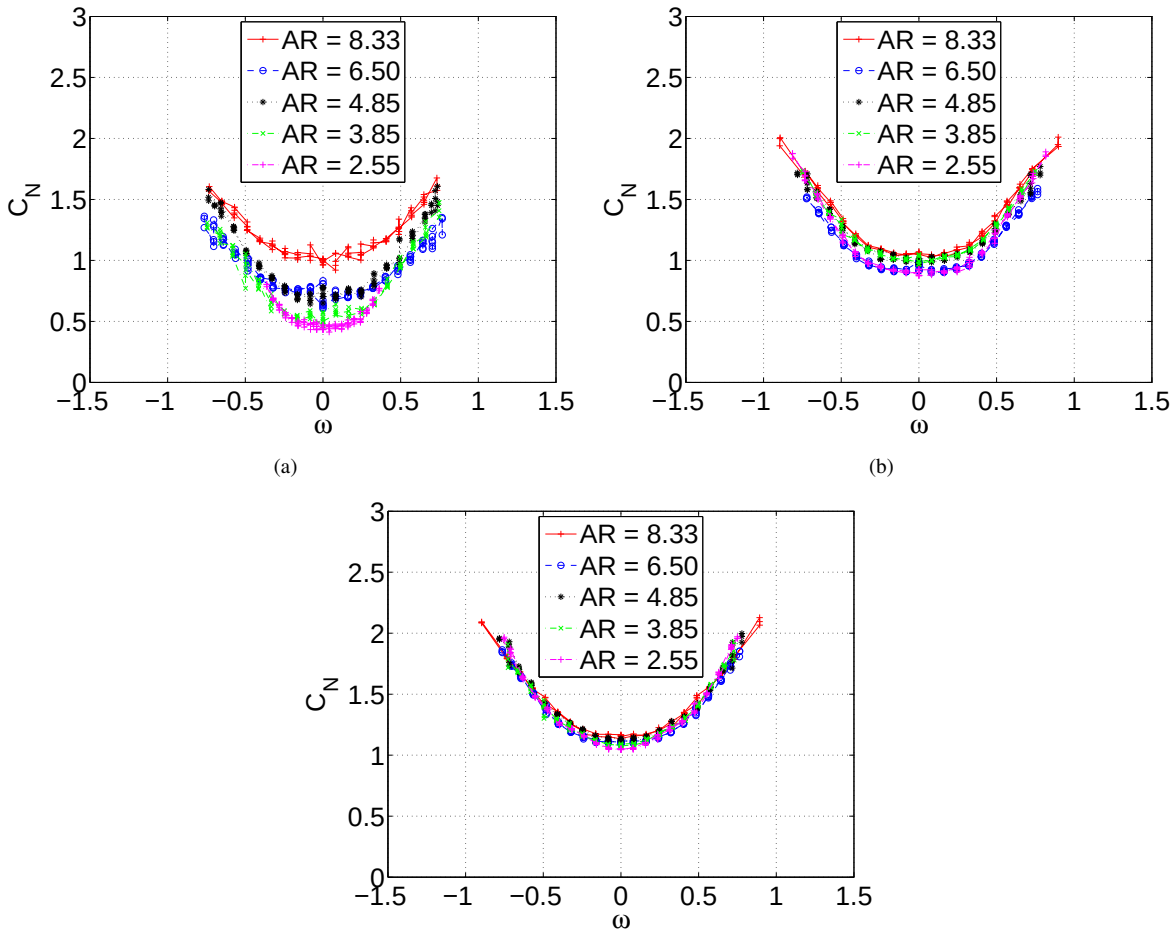

Figure 4.10: Plot of C_N versus ω for five different $\mathcal{AR}$ values for a symmetric wing at $Re = 15{,}000$ and (a) $\theta = 30$ deg, (b) $\theta = 60$ deg, and (c) $\theta = 90$ deg.

This increase in C_N is more prevalent for the lower $\mathcal{AR}$ wings. While the C_N value at $\omega = 0$ for the $\mathcal{AR} = 2.55$ wing increases by 0.62 from 0.43 in Fig. 4.10(a) to 1.05 in Fig. 4.10(c) as θ is increased from 30 to 90 deg, the C_N value of the $\mathcal{AR} = 8.33$ wing only increases by 0.18 from 0.99 to 1.17 for the same change in θ. Thus, the effect of aspect ratio, which is present to some degree at all θ values, is increased as the pitch angle θ is decreased. This increase in the effect of aspect ratio is because of the fact that, as the wing pitch angle is decreased, the wing is being operated in a condition closer to an unstalled state. Because the wing is nearer to an unstalled state, differences induced by aspect ratio, such as wing tip vortices, downwash, and the resulting change in performance, are more pronounced.

While all of the curves generally demonstrate a similar relationship between ω and C_N, it is of note that the C_N values for the $\mathcal{AR} = 2.55$ and 3.85 wings grow noticeably more rapid with ω than the higher aspect ratio wings for values of $|\omega| < 0.5$ and $\theta = 30$ deg, as shown in Fig. 4.10(a). In the case of a low aspect ratio wing at a moderate spin parameter, Coriolis forces dominate the centrifugal forces, the former of which tends to push the wake region off of the aft edge of the airfoil. This increased rate of C_N growth for the low aspect ratio wings is hypothesized to be

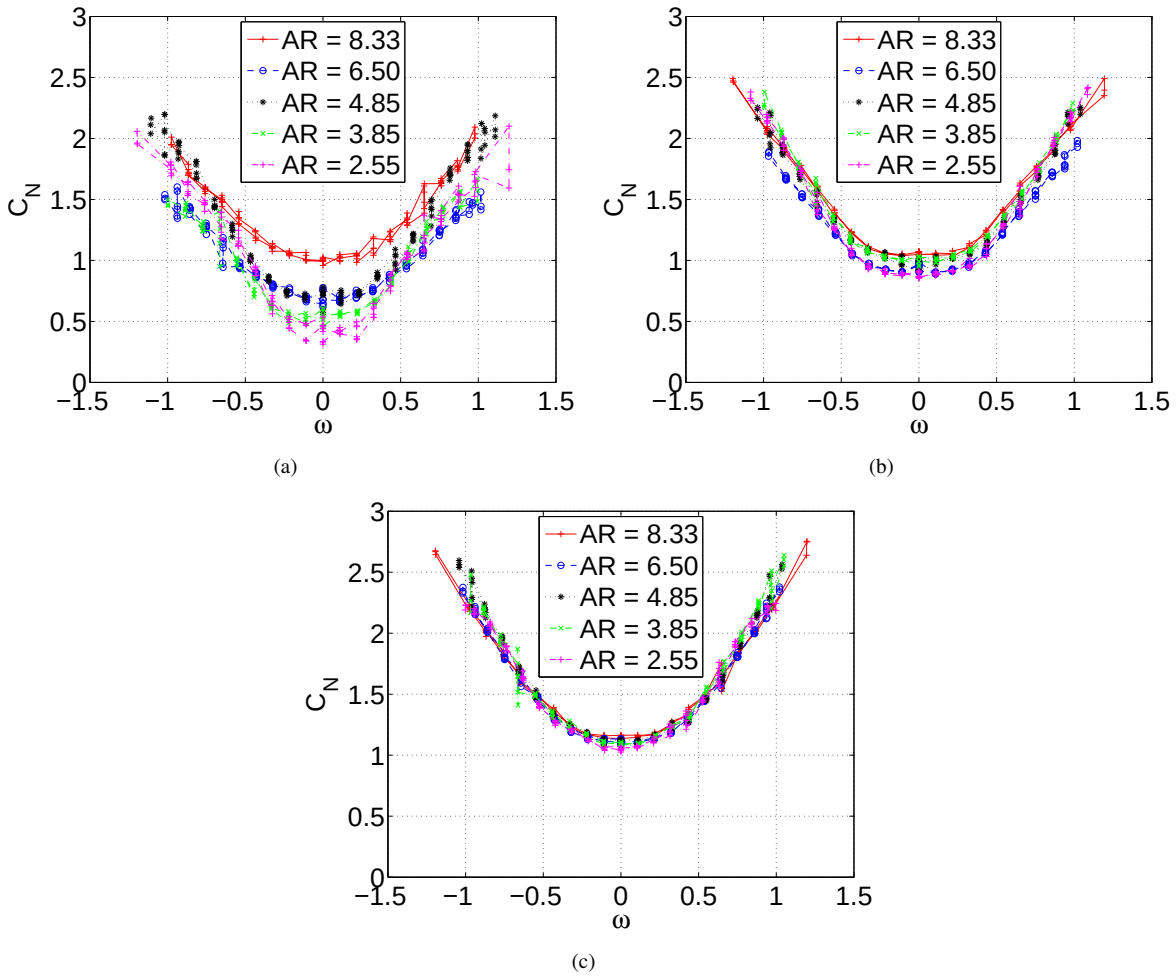

Figure 4.11: Plot of C_N versus ω for five different $\mathcal{AR}$ values for a symmetric wing at $Re = 11{,}000$ and (a) $\theta = 30$ deg, (b) $\theta = 60$ deg, and (c) $\theta = 90$ deg.

attributable to a leading edge vortex (LEV) structure serving as a channel for centrifugally-pumped fluid that forces part or all of the tip vortex structures outboard of the wing tip. By pushing any tip vortex structures outboard and away from the wing, the wake structure is able to be larger and unencumbered by any downwash-producing structures, which results in a more rapid growth of C_N. At lower aspect ratios, less of the spanwise flow is pushed off of the wing trailing edge. Consequently, more flow is available to push the tip structures outboard. This scenario agrees with the observations of Ref. [48] in which a strong leading edge vortex was observed to dominate the flow structures and to serve as a channel for pumping fluid outward along the span.

4.3.3 Airfoil Geometry Effects

Figure 4.12 presents C_N versus ω data for a symmetric airfoil wing with $\mathcal{AR} = 6.30$ and a flat-bottom airfoil wing of $\mathcal{AR} = 5.97$. While C_N values for the flat-bottom airfoil wing are slightly higher than those of the symmetric airfoil

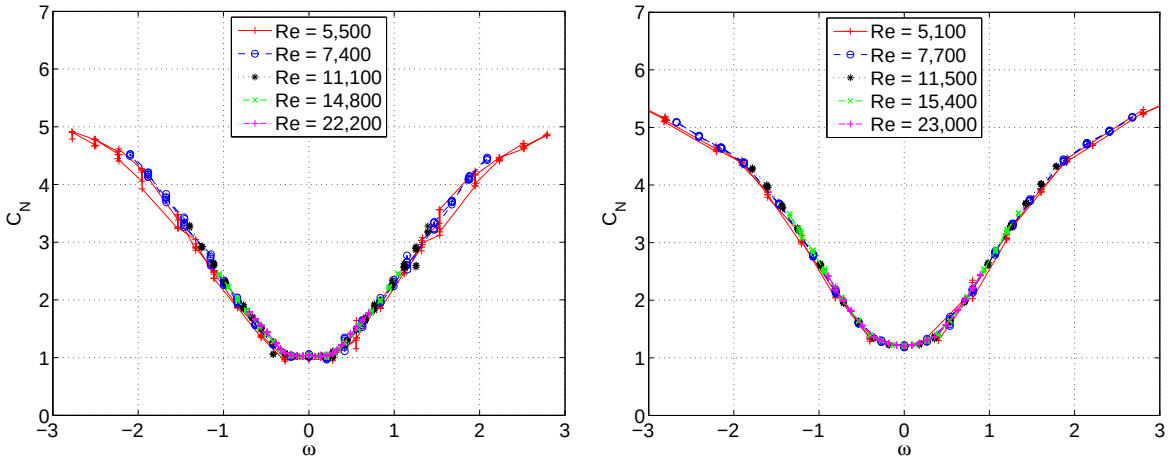

(a) (b)

Figure 4.12: Plot of C_N versus ω or five different *Re* values at $\theta = 90$ deg for (a) a symmetric wing with $\mathcal{AR} = 6.30$, and (b) a flat-bottom wing with $\mathcal{AR} = 5.97$.

wing, the shape of both curves follows the ω^2 relationship over the range of the spin parameter tested. The data from both wings indicate a reduction in the growth rate around $|\omega| \approx 1.6$, where the curve begins to flatten out. The data in Fig. 4.12 also confirm that, as expected, no significant qualitative differences exist between the stalled spinning wing testing of a flat plate versus a symmetric airfoil wing. Further, no quantitative difference is observed between flat-bottom and flat-plate wings of similar aspect ratios. This observation shows that it is only the flow-facing geometry that matters post-stall. The $\mathcal{AR} = 5.97$ flat-bottom wing of Fig. 4.12(b), and the flat-plate wing of Fig. 4.8(b), both have C_N values of around 1.25 for $\omega = 0$. The C_N curves of these two wings generally have similar values.

A quantitative difference exists, however, between the symmetric airfoil wings and the flat-bottom airfoil wings. In Fig. 4.13, the $\mathcal{AR} = 5.00$ flat plate wing at $\theta = 90$ deg has $C_N = 1.25$ at $\omega = 0$, while for the $\mathcal{AR} = 4.85$ symmetric wing of Fig. 4.10(c), $C_N = 1.13$ at $\omega = 0$. This difference in C_N is due to the fact that the flat-plate and flat-bottom wings act as a bluff body, while the symmetric wing acts more like a body with some degree of roundedness on its flow-facing side. This explanation is supported by experimental data for a wing with a flat-bottom airfoil and $\mathcal{AR} = 5.97$, as shown in Fig. 4.12(b). These values align more closely with the flat-plate airfoil C_N values than the symmetric airfoil C_N values.

The C_N value at $\omega = 0$ is slightly higher than that of the $\mathcal{AR} = 4.85$ symmetric airfoil wing data presented earlier in this section. This slightly higher C_N is to be expected because, in the $\theta = 90$ deg case, the flow sees a flat wall for the flat plate case but an ever-so-slightly streamlined shape for the symmetric wing case. The main conclusion from Fig. 4.8(b) is that no major differences or changes in the general shape of the C_N versus ω curve are observed as compared with a symmetric wing with a flat-plate wing.

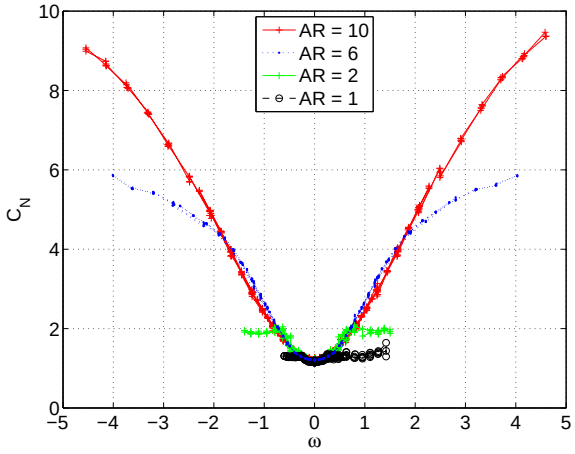

Figure 4.13: Plot of C_N versus ω for flat-bottomed wings of four different $\mathcal{AR}$ values and $\theta = 90$ deg at various Re values.

4.3.4 High Spin Parameter Effects

Data for flat-plate wings of aspect ratios 1, 2, and 10, and a flat-bottom wing of aspect ratio 6, over the range of ω values $-5 < \omega < 5$ at $\theta = 90$ deg, are presented in Fig. 4.13. As expected, for low spin parameter values, the C_N data for all wings follows the ω^2 relationship. Interestingly, data for the $\mathcal{AR} = 1$ wing show that a maximum attainable, or plateau, C_N value of approximately 1.3 is reached for $|\omega| > 0.25$. In the case of the $\mathcal{AR} = 2$ wing, C_N reaches a plateau value of approximately 1.9 for $|\omega| > 0.8$. The $\mathcal{AR} = 6$ flat-bottom wing shows that a decrease in the rate of growth occurs around $|\omega| = 1.6$ and $C_N \approx 4$. This decreasing rate of growth shows that a C_N plateau value is approached. When the wing aspect ratio is increased to 10 (see Fig. 4.13), this decreasing rate of growth occurs at $|\omega| \approx 3$ and $C_N \approx 6.6$, although once again spin parameter values large enough to reach the C_N plateau value were not attained.

The data of Fig. 4.13 clearly show evidence that a C_N plateau is present in a stalled spinning wing and this C_N plateau is aspect-ratio dependent. At that plateau point, further increasing the rotational rate of the wing will not affect C_N. As the wing aspect ratio increases, the C_N plateau value, and the ω value at which that value is attained, both increase. For low aspect ratio wings, the increase in C_N is attributable to the presence of a leading edge vortex in which the vortex core produces spanwise flow supplied by Ekman-like pumping [48]. It is stressed that the local Rossby number is responsible for leading edge vortex stability. This dimensionless parameter is a measure of the ratio of the interial and centrifugal forces to the Coriolis force. Lentink and Dickinson [48] suggest a simplification of this parameter as the ratio of the wing semispan to the MAC. Even on an $\mathcal{AR} = 10$ wing, for instance, the inner 30% of the wing would experience a $Ro < 3$ irrespective of the Ro of the wing. As the wing aspect ratio increases, the influence of the leading edge vortex decreases. Thus, the influence of the entire trapped wake region behind the wing extending from the leading edge to the trailing edge, which also experiences centrifugal pumping, is increased. As the spin parameter and aspect ratio are increased, the Coriolis force is increasingly able to push the wake structure

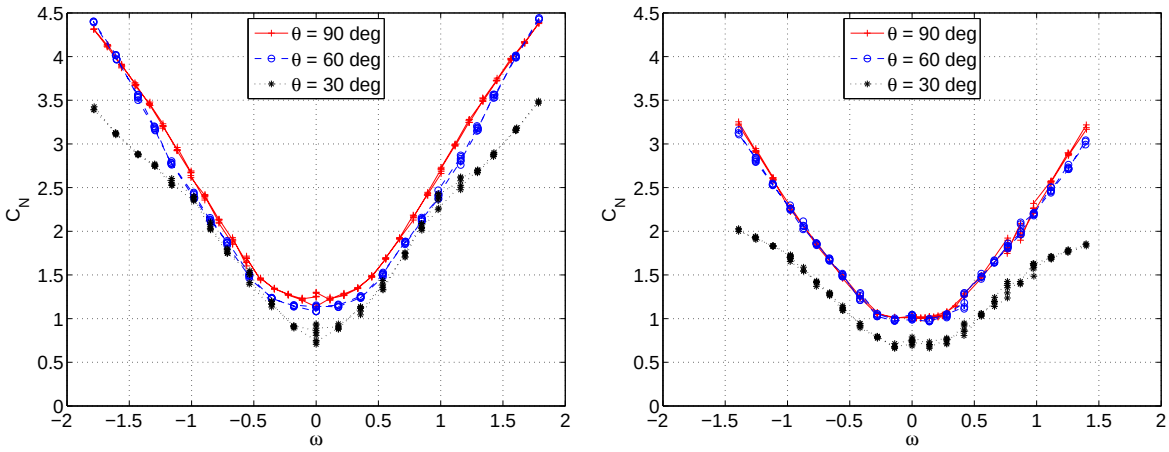

Figure 4.14: Plot of C_N versus ω for three different θ values at $Re = 11{,}000$ for (a) a flat-bottom wing, and (b) a symmetric wing.

and its radially-pumped fluid toward the trailing edge of the wing, thereby reducing the centrifugal pumping effects. For high values of ω, the outer portions of the wing are at lower angles of attack, thus reducing the size of the trapped wake structure. Consequently, there is further acceleration of the spanwise flow. This acceleration of the spanwise flow reduces the effect of the Coriolis force, which is trying to push the wake structure off of the back of the wing. At some point, however, the wake is pushed off of the wing trailing edge, and no further increase in C_N due to centrifugal pumping is possible. Additionally, as the rotational rate is further increased, the wing starts to unstall, beginning at the tips. It is at this point that the C_N–ω curve flattens out. At low aspect ratios and high values of ω, the drag-producing wake no longer takes the shape of the wing. Instead, it is thought to exist as a hemiellipsoid-shaped wake with the two shorter axes equal to the span of the wing, and the third, and longer axis extends downstream [84]. Once the wake takes on the hemiellipsoid shape, its size and thus the drag produced by the spinning wing does not change as ω is further increased. This rotation rate-invariant wake shape, which is experienced beyond a certain threshold, explains the C_N plateau observed in Fig. 4.13 for the aspect ratio 1 and 2 wings.

4.3.5 Airfoil and High Spin Parameter Effects

The effects of airfoil shape at high values of ω are presented in Fig. 4.14 at $Re = 11{,}000$ and θ values of 30, 60, and 90 deg for a flat-bottom and symmetric wing. The flat-bottom wing exhibits higher C_N values overall when compared with the symmetric wing for a given spin parameter at all θ values. Interestingly, the flat-bottom wing at $\theta = 30$ deg exhibits a significantly smaller drop-off relative to the 60 and 90 deg wings than the $\theta = 30$ deg symmetric wing.

At a spin parameter of unity, the $\theta = 30$ deg flat-bottom wing of Fig. 4.14(a) has a C_N slightly less than 2.5, and the $\theta = 60$ deg C_N value is just above 2.5. In contrast, the symmetric wing of Fig. 4.14(b) at $\omega = 1$ and $\theta = 30$ deg

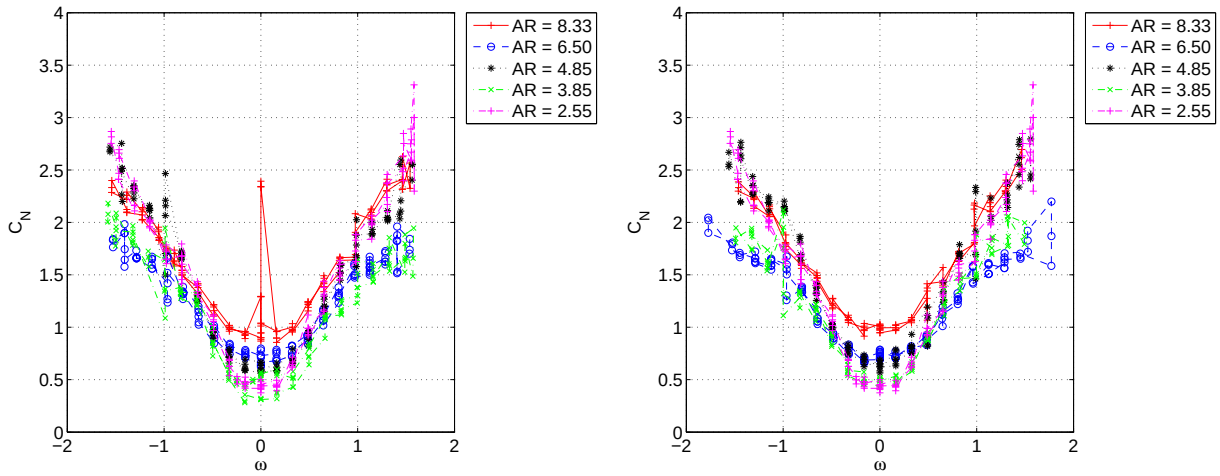

Figure 4.15: Plot of C_N versus ω for five different $\mathcal{AR}$ values at $Re = 7{,}500$ and $\theta = 30$ deg for (a) early tests, and (b) later tests.

has $C_N = 1.5$, while the $\theta = 60$ deg $C_N = 2.25$. These data demonstrate that a flat-bottom wing has a slightly larger C_N value for a given ω than a symmetric wing. Also, the decrease in C_N, due to reducing θ, is less pronounced on the flat-bottom wings. This increased performance of the lower-θ flat-bottom wing is hypothesized to be attributable, in part, to the presence of vortex lift. The sharper leading edge of the flat-bottom wing is thought to shed a more stable and stronger leading edge vortex. This stronger leading edge vortex helps to keep the flow attached and serves as a channel for a portion of the spanwise flow, thus helping to reduce the decrease in C_N compared with a symmetric, blunt-nosed wing, which would be characterized by a weaker leading edge vortex.

4.3.6 Experiments for Re = 7,500

Figures 4.15(a) and 4.15(b) present C_N versus ω data for the five different $\mathcal{AR}$ wings at $Re = 7{,}500$ and $\theta = 30$ deg for early and late wind tunnel test runs, respectively. The high C_N value for the $\mathcal{AR} = 8.33$ wing at $\omega = 0$ is an erroneous data point. In this case, the wing was oriented perpendicular to the top-to-bottom fairing in the wind tunnel. Thus, the wing was subjected to the higher-velocity air traveling around the blockage created by the symmetric fairing. After a few initial runs were recorded, the orientation of the blade for the $\omega = 0$ case was no longer random. The orientation was set to be parallel to the symmetric fairing (i.e., oriented vertically in the wind tunnel). This procedure removed any inaccurate data points, and the lack of points that do not match the expected C_N vs. ω curve is demonstrated in Fig. 4.15(b), among others, which includes only data with the controlled $\omega = 0$ wing orientation.

Figures 4.16(a) and 4.16(b) present $Re = 7{,}500$ results at $\theta = 60$ deg. Figures 4.17(a) and 4.17(b) present C_N versus ω data at the same Re and $\theta = 90$ deg. C_N demonstrates a relationship proportional to ω^2. At $\theta = 30$ deg, the five C_N curves appear to have different vertical shifts. The $\mathcal{AR} = 8.33$ wing has $C_N \approx 0.85$ at $\omega = 0$, while the

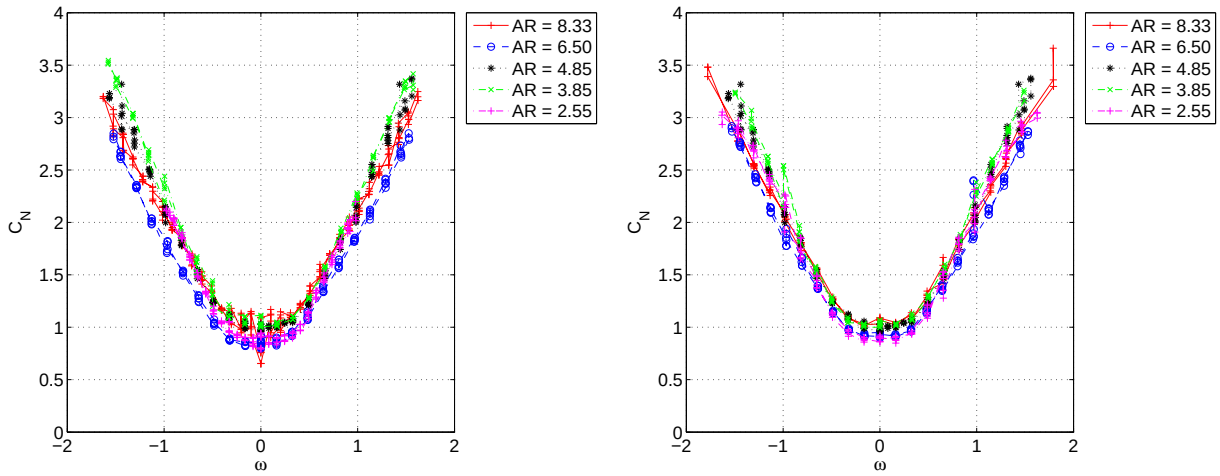

Figure 4.16: Plot of C_N versus ω for five different $\mathcal{AR}$ values at $Re = 7{,}500$ and $\theta = 60$ deg for (a) early tests, and (b) later tests.

$\mathcal{AR} = 2.55$ wing has $C_N \approx 0.4$ at $\omega = 0$. This vertical offset in C_N appears to be reasonably constant over the range of ω values, i.e., the shape of the curves is similar, but the vertical location is not. For the $\mathcal{AR} = 8.33$ wing at $\omega = 0$ and $\theta = 60$ deg (Figs. 4.16(a) and 4.16(b)), C_N is approximately 0.8. Meanwhile, for the $\mathcal{AR} = 2.55$ wing at the same conditions, C_N is approximately 0.75. This smaller difference between C_N values shows that the effect of $\mathcal{AR}$ on the C_N values decreases as θ increases. This decreased effect of $\mathcal{AR}$ as θ increases is reaffirmed by the narrower spread of the five curves of Figs. 4.16(a) and 4.16(b), when compared with Figs. 4.15(a) and 4.15(b).

The aforementioned observed trends are continued in Figs. 4.17(a) and 4.17(b). Almost no variation due to $\mathcal{AR}$ is evident, and the C_N values at $\omega = 0$, for all of the wings, increase to approximately 0.95. Of interest in the 90 deg case is that a maximum achievable C_N value appears to have been attained for the two lower $\mathcal{AR}$ wings. The $\mathcal{AR} = 2.55$ wing appears to have reached a maximum C_N value of 1.75 at $|\omega| > 1$, and the $\mathcal{AR} = 3.85$ wing appears to have reached a maximum C_N value of 2.5 at $\omega = 1.75$.

4.3.7 Additional Experiments for Re = 11,000 and Re = 15,000

In this section, the early wind tunnel experimental tests at $Re = 11{,}000$ and $Re = 15{,}000$ are presented at $\theta = 30$, 60, and 90 deg in Figs 4.18–4.23, respectively. Minor discrepancies encountered during early test cases may be evident, especially when compared with the later runs at those same Reynolds numbers, which were presented earlier in this section. Specifically, Figs. 4.19 and 4.22 show large deviations in the measured C_N at $\omega = 0$. These deviations at $\omega = 0$ are due to the previously mentioned orientation control of the blade, which was instituted only after a few early tunnel runs were completed. In general, all of the trends observed in the later tests were evident in these earlier-run plots, and the ω^2 relationship between C_N and ω is clearly evident. At some of the more-extreme values of ω, the

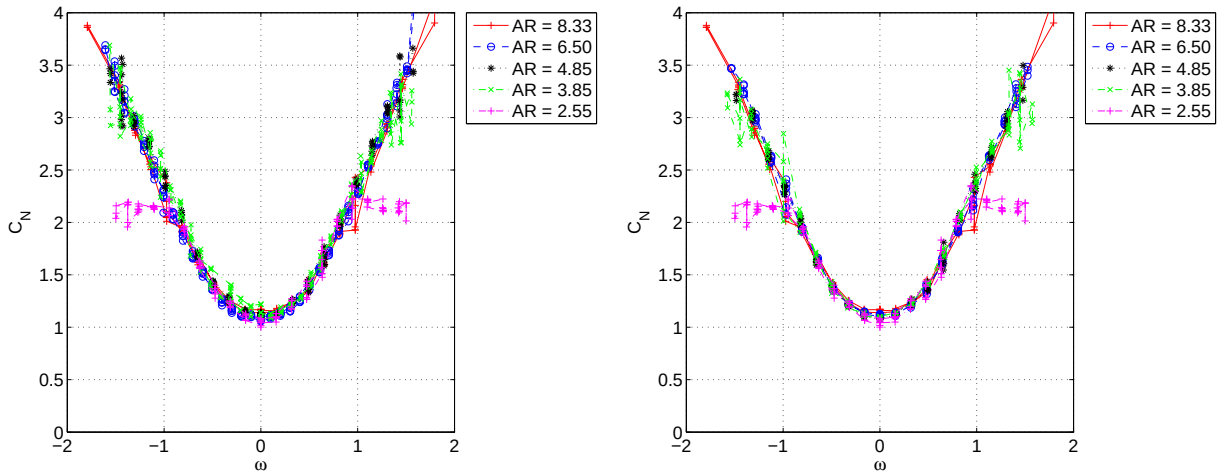

Figure 4.17: Plot of C_N versus ω for five different $\mathcal{AR}$ values at $Re = 7{,}500$ and $\theta = 90$ deg for (a) early tests, and (b) later tests.

effects of some oscillations, which yield a slightly wider range of C_N values for a given ω, are evident. The wider spread in the measured C_N may be observed in Figs. 4.20 and 4.22, among others.

4.3.8 Experiments for Re = 22,000

In this section, plots of C_N versus ω are presented for all five wings of different aspect ratios at three different pitch angles. Figures 4.24, 4.25, and 4.26 present plots of the all five wings at $Re = 22{,}000$ and $\theta = 30$, 60, and 90 deg, respectively.

As is to be expected from an increased Reynolds number, the data curves are smoother than the lower-Re curves, and they show minimal variation in C_N. These smoother curves are attributable to a higher load range with less fluctuation as recorded by the drag-measuring load cell. The improved data quality does come at a price, however; the range of ω values over which the tests could be conducted was reduced. Because of vibrational limits on the wind tunnel test articles, RPM values of over 400 could not be achieved. Despite the reduced range of achievable ω values, the same trends observed at the lower Reynolds numbers (and thus wider ranges of ω) are depicted.

4.3.9 Tests of Two Approximate GA Aircraft Wing Planforms

Figures 4.27 and 4.28 present plots of C_N versus ω at $\theta = 90$ deg for the scaled approximate planforms of the wings of a Piper Cherokee and a Cessna 172, respectively. An illustration of the approximate Piper Cherokee wing planform is presented in Fig. 4.29; similarly, the approximate Cessna 172 wing planform is presented in Fig. 4.30. The dimensions of these wings are summarized in Table. 4.3.

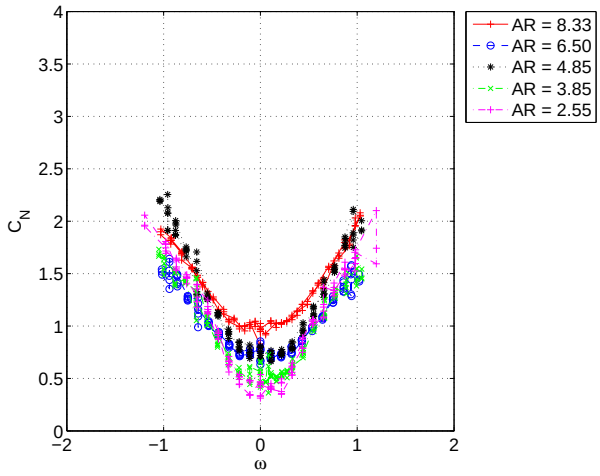

Figure 4.18: Plot of C_N versus ω for five different $\mathcal{AR}$ values at $Re = 11{,}000$ and $\theta = 30$ deg.

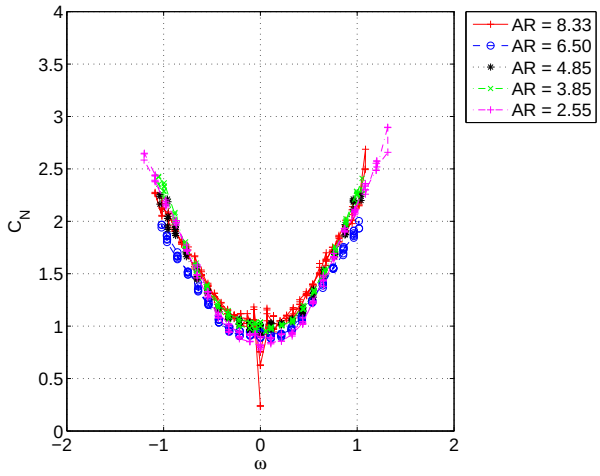

Figure 4.19: Plot of C_N versus ω for five different $\mathcal{AR}$ values at $Re = 11{,}000$ and $\theta = 60$ deg.

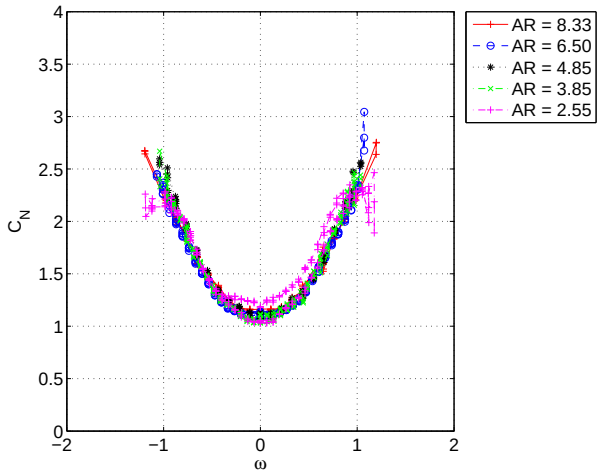

Figure 4.20: Plot of C_N versus ω for five different $\mathcal{AR}$ values at $Re = 11{,}000$ and $\theta = 90$ deg.

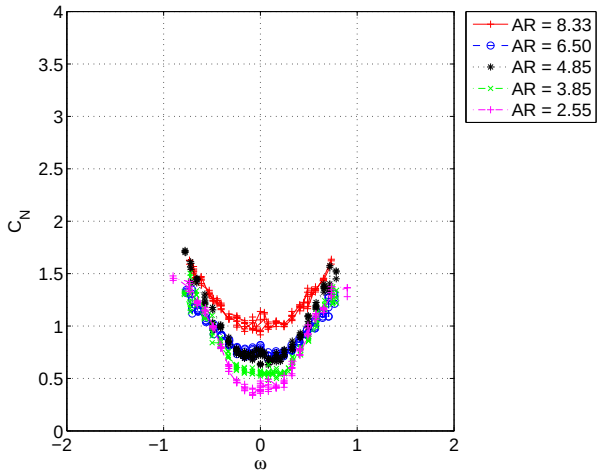

Figure 4.21: Plot of C_N versus ω for five different $\mathcal{AR}$ values at $Re = 15{,}000$ and $\theta = 30$ deg.

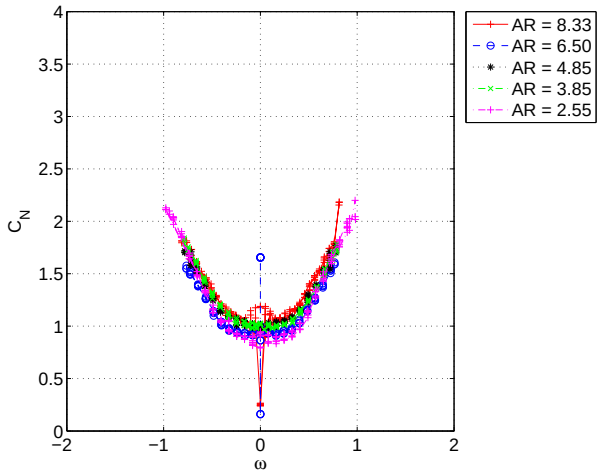

Figure 4.22: Plot of C_N versus ω for five different $\mathcal{AR}$ values at $Re = 15{,}000$ and $\theta = 60$ deg.

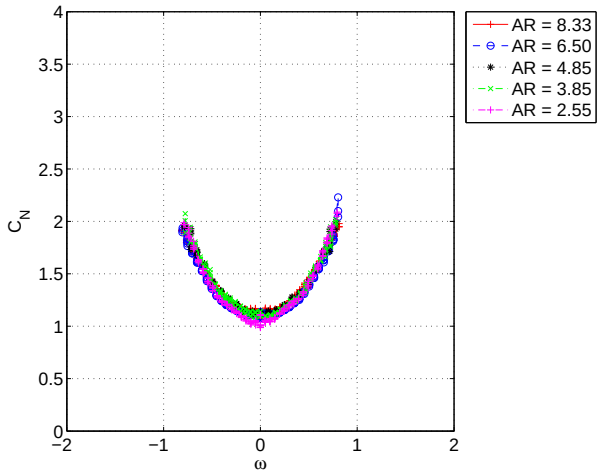

Figure 4.23: Plot of C_N versus ω for five different $\mathcal{AR}$ values at $Re = 15{,}000$ and $\theta = 90$ deg.

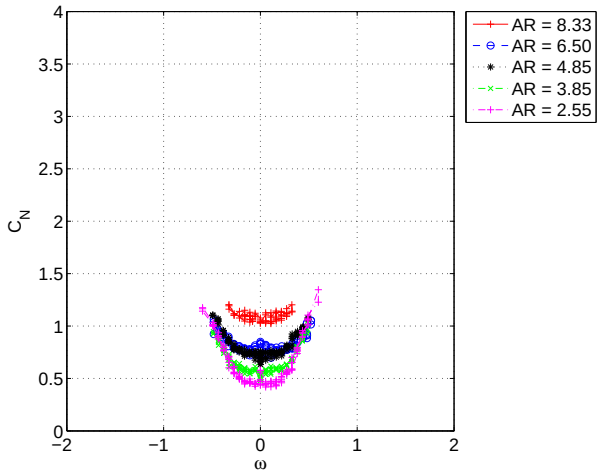

Figure 4.24: Plot of C_N versus ω for five different $\mathcal{AR}$ values at $Re = 22{,}000$ and $\theta = 30$ deg.

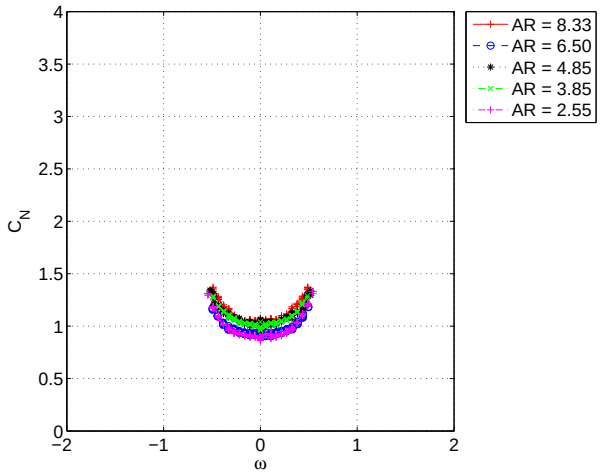

Figure 4.25: Plot of C_N versus ω for five different $\mathcal{AR}$ values at $Re = 22{,}000$ and $\theta = 60$ deg.

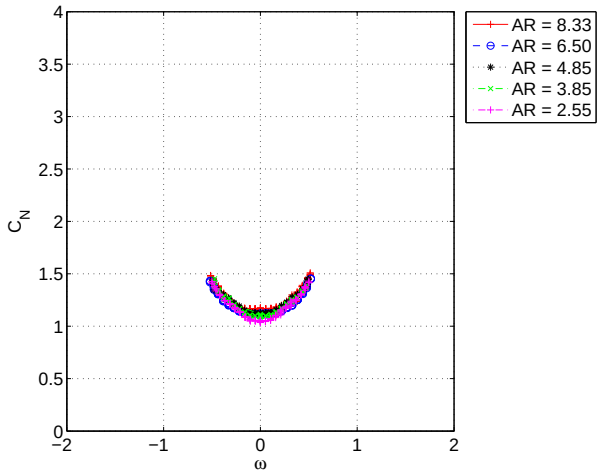

Figure 4.26: Plot of C_N versus ω for five different $\mathcal{AR}$ values at $Re = 22{,}000$ and $\theta = 90$ deg.

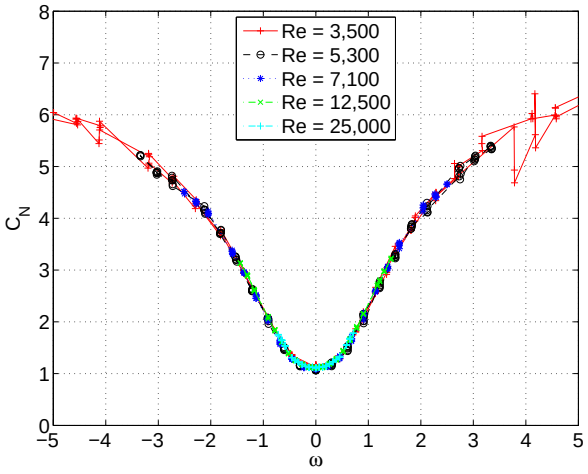

Figure 4.27: Plot of C_N versus ω for an approximate Piper Archer wing planform at five different Re values at $\theta =$ 90 deg.

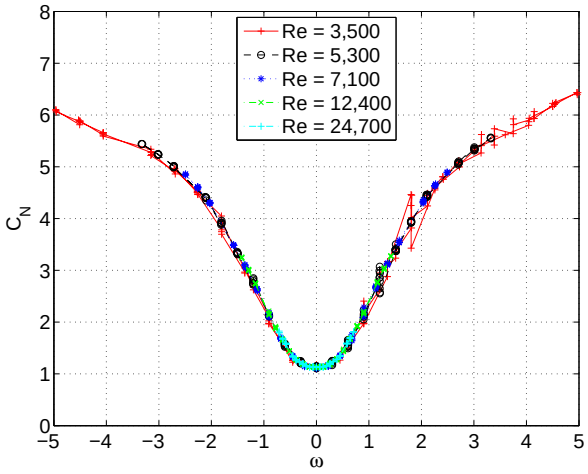

Figure 4.28: Plot of C_N versus ω for an approximate Cessna 172 wing planform at five different Re values at $\theta =$ 90 deg.

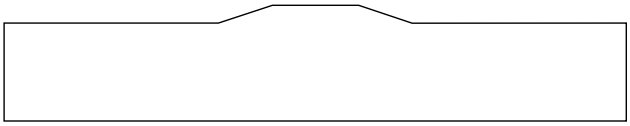

Figure 4.29: Illustration of approximate Piper Cherokee wing planform as tested in this study (leading edge on top).

Figure 4.30: Illustration of approximate Cessna 172 wing planform as tested in this study (leading edge on top).

Table 4.3: Approximate General Aviation Wing Planform Study – Wing Information and Dimensions

Aspect Ratio	Wing Planform (Material)	Chord Length	Wingspan	Area
6.7	Cessna 172 (3mm plywood)	1.30 (3.31 cm)	8.63 (21.9 cm)	11.2 (72.3 cm^2)
6.6	Piper Cherokee (3 mm plywood)	1.31 (3.34 cm)	8.69 (22.1 cm)	11.4 (72.9 cm^2)

These wing planforms were constructed of the same 3 mm birch plywood from which the flat-plate test articles were constructed. Because of their construction, the wings could be spun at RPM values of up to 800 before reaching the vibrational limit. The approximate Cessna 172 wing planform has an aspect ratio of 6.7 and the approximate Piper Cherokee wing planform has $\mathcal{AR} = 6.6$. Despite their minor planform shape differences, as shown in Figs. 4.29 and 4.30, the two wings behaved similarly. The C_N curve exhibits the previously-observed ω^2 relationship, until approximately $|\omega| = 2$ at $C_N \approx 4$, where the reduction in growth rate as described earlier in this chapter is encountered. The wide variations in C_N of Fig. 4.27, around $\omega = 4$, are due to vibrations, which occurred at that point in the test. These two figures demonstrate that, even with minor changes to the planform shape, for a similar aspect ratio, the same ω^2 relationship is evident, and the reduction in growth rate remains unaffected.

4.3.10 Experiments for Flat Plates of Varying Aspect Ratio

Figures 4.31–4.34 present plots of C_N versus ω at multiple Reynolds numbers for flat-plate wings of aspect ratio 1, 2, 5, and 10, respectively. The data of these plots have already been coplotted in Fig. 4.13 earlier in this chapter. Regardless, the data sets are presented here individually to allow future work to use them for validation, if necessary. These plots demonstrate that, also as discussed before, as the aspect ratio is reduced, the plateau value of C_N is achieved earlier and at a lower value when compared with wings of higher aspect ratio. This reduction in the plateau value of C_N with aspect ratio is hypothesized to be due to the wake degrading from one that is trapped and follows the shape of the wing, to a hemiellipsoid-shaped wake with semi-minor axes equal to the span of the wing. From the point at which this hemiellipsoid-shaped wake is fully developed, centrifugal pumping is no longer increased by an increase in ω and remains constant. As a result of the centrifugal pumping, which remains constant beyond a certain ω threshold, C_N no longer increases with an increase in ω.

4.4 Summary of Wind Tunnel Testing

In this section, the effects of various parameters on the normal force coefficient of wings in spin were investigated. Well-developed methods for testing propeller performance were modified and adapted to research stalled spinning wings in a horizontal wind tunnel. The effects of Reynolds number, aspect ratio, airfoil geometry, and the spin parameter on the normal force coefficient C_N are summarized. For the regime tested, the Reynolds number was shown to have no effect. An increase in the aspect ratio of a wing was shown to progressively increase the C_N value as the wing

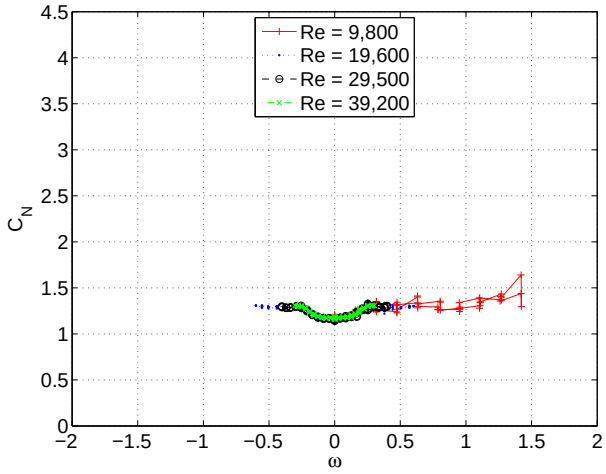

Figure 4.31: Plot of C_N versus ω for an $\mathcal{AR} = 1$ flat plate at four different Re values at $\theta = 90$ deg.

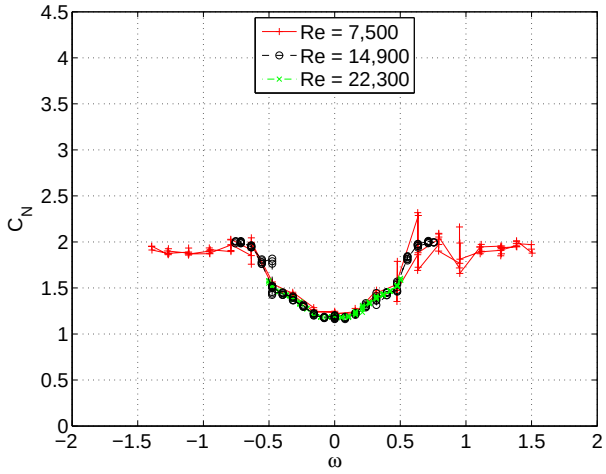

Figure 4.32: Plot of C_N versus ω for an $\mathcal{AR} = 2$ flat plate at three different Re values at $\theta = 90$ deg.

pitch angle θ was decreased. This increase in the C_N value with increasing $\mathcal{AR}$ and decreasing θ, was hypothesized to be due to a decrease in the tip vortex effects of the higher aspect ratio wings as the wings approached an unstalled state. Flat-bottom and flat-plate wings were found to have slightly larger values of C_N than a symmetric airfoil for all values of ω, but no significant difference between a flat-bottom and flat-plate wing was observed. The slightly-larger C_N values of wings with a flat bottom were attributed to the flow-facing side, which acted more similarly to a flat plate than to a streamlined surface, and to a stronger leading edge vortex shed by the sharp leading edge, which is common to both the flat-plate and flat-bottom wings.

For high values of ω, well beyond those that would be expected for an airplane in a stall/spin situation, the data show that a maximum attainable C_N plateau value exists, and that this value increases as the wing aspect ratio is increased. This value is limited by the ability of lower local angles of attack, which are created by high spin parameter values, to reduce the size of the wake structure and further accelerate the spanwise flow, thus reducing the ability of

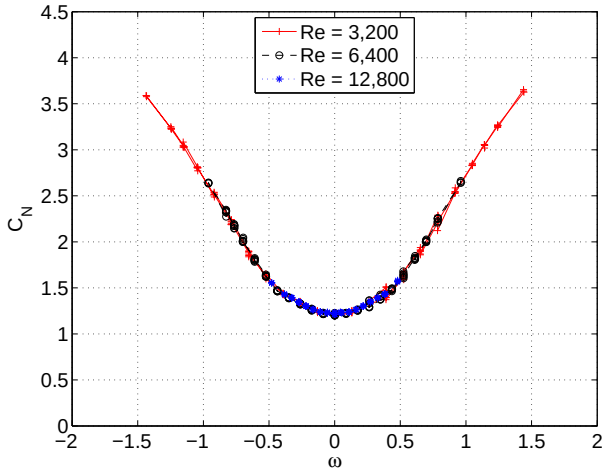

Figure 4.33: Plot of C_N versus ω for an $\mathcal{AR} = 5$ flat plate at three different Re values at $\theta = 90$ deg.

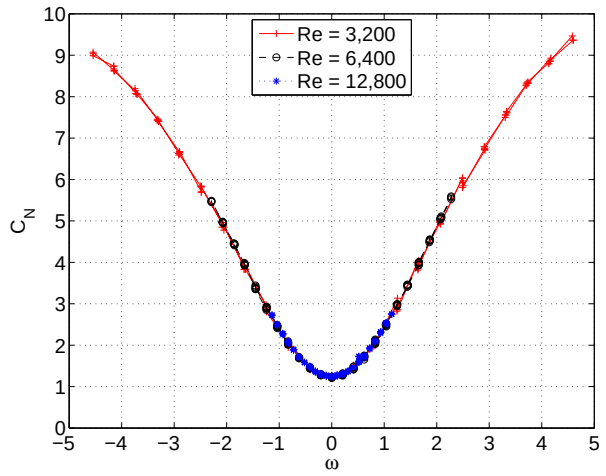

Figure 4.34: Plot of C_N versus ω for an $\mathcal{AR} = 10$ flat plate at three different Re values at $\theta = 90$ deg.

the Coriolis forces to push the spanwise flow off of the wing trailing edge. When the lower local angles of attack are unable to prevent loss of the wake structure, a maximum C_N value is reached. This C_N plateau was reached for wings of $\mathcal{AR} = 1$ and $\mathcal{AR} = 2$. At these low-aspect ratio conditions, the increased normal force is attributable primarily to centrifugal pumping in the leading edge vortex core, as opposed to higher aspect ratio wings, where the majority of the centrifugal pumping is experienced in the trapped wake structure.

These wind tunnel data are used to validate the analytic model in Chapter 5 of a wing in a stall/spin situation, where the trapped wake structure of the wing tends to drive the roll rate and normal force of a full-airplane configuration. These experimental data can also be used by other researchers to aid in the development of simulations and modeling of aircraft that are well beyond the normal flight envelope.

Chapter 5

Force Modeling Methodology of SpinSim

This section describes the force modeling methodology employed in this research. This methodology was used to generate a final force prediction code, which is geared toward predicting the forces on an airplane in a stall/spin situation. The force prediction code, which includes a first-principles based analytic correction for a wing in spin, is, thus, appropriately referred to as SpinSim. Indeed, this force prediction code is used to simulate selected flight test data from Chapter 3 and is validated with the wind tunnel data from Chapter 4.

5.1 Introduction

A force modeling methodology is proposed to account for the forces and moments on an aircraft in spin. The forces on the aircraft are modeled by the component buildup method, where the aircraft is divided into four major components: wing, fuselage, horizontal tail, and vertical tail. Using the strip theory, the wing is discretized into 40 segments. Aerodynamic data lookup tables are generated based on the wing airfoil, the fuselage shape, and the planform shapes and aspect ratios of the horizontal and vertical stabilizers. Further, lookup tables are interpolated over a range of angles of attack, from -180 to 180 deg. To determine the downwash distribution over the wing, an iterative scheme is used with an initial downwash distribution that is initialized, iterated upon until convergence, and then applied to the local α values. This iteration of the downwash distribution is continued until the difference between subsequent downwash distributions is reduced below a determined threshold value.

5.2 Basis for the Theory Behind the Proposed Analytical Model

The theory and assumptions adopted in the development and derivation of this analytical model are supported by the existing literature. Both McCormick [46] and Clarkson et al. [85] suggested that the flow and forces rotate with the stalled wing. McCormick noted the presence of a centrifugal pumping effect that created a spanwise pressure gradient. The method of the current model differs from the assumptions of McCormick with regard to the radial ejection of fluid at the wing tip, which has been experimentally observed by Carr et al. [50] through their PIV studies as shown in Fig. 5.1. Complex vortex structures were observed initially near the wing tip, but after the stalled wing yawed more

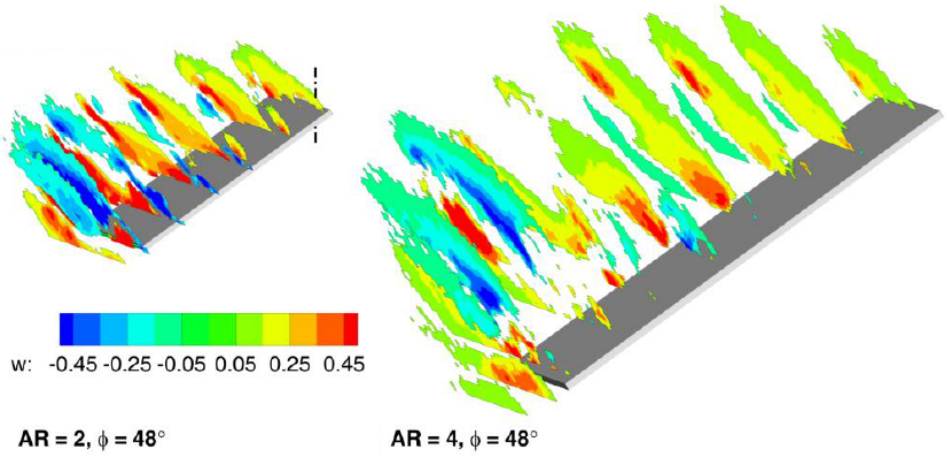

Figure 5.1: Plot of spanwise flow velocity w on rotating flat plate wings of $\mathcal{AR} = 2$ and 4 at $\alpha = 48$ deg (Carr [50]).

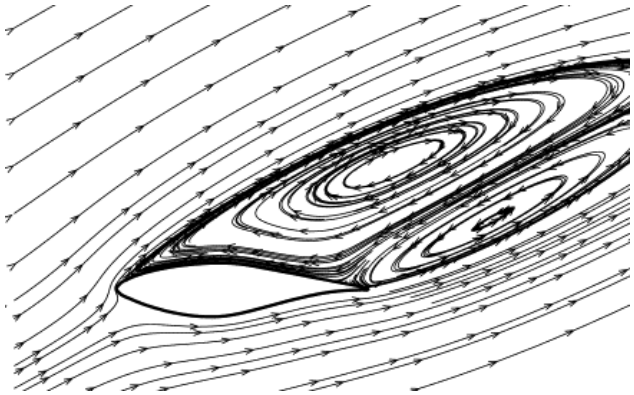

Figure 5.2: Plot of streamlines for a wind turbine airfoil at $\alpha \approx 25$ deg (Hu [89]).

than 40 deg, the complex vortex structures broke down and became entirely separated [50]. The concept of the flow moving with the wing, and being ejected at the tip, is therefore verified by the existing literature.

Also, depicted in Fig. 5.1 is how the shape of the stalled, radially flowing region is a semi-ellipse, which is reasonably consistent from root to tip. This area of flow increases in size with spanwise location. Similar results were observed in the studies of Garmann [49, 86] and Bross [87]. Arie and Rouse's 1956 JFM paper [88] confirms that the flow behind a non-rotating plate normal to a flow "was roughly elliptical in form," and "the streamlines ... approximate [to] those of ... flow past with an ellipse or a Rankine oval [which is much easier to model with sources and sinks] of comparable dimensions" [88]. Figure 5.2 taken from Hu [89] also shows that the region behind a stalled airfoil, in this case a thick wind turbine airfoil, is similar in shape to a semi-ellipse. Additionally, analysis of data from a 1959 report by Fail et al. [90] provides insight into the size of the bubble behind wings of varying $\mathcal{AR}$ values when normal to the flow. Data from Ref. [90] are presented in Table 5.1.

As shown in Table 5.1, the ratio of the bubble length to the chord length varies between less than 3 and slightly more than 7. A peak value for this ratio is shown for wings of an aspect ratio of 10. Returning to Fig. 5.1, it is noted

Table 5.1: Drag and Bubble Dimensions of Varying Aspect Ratio Flat Plates Normal to the Flow (Data from Ref. [90])

Aspect Ratio	Chord Length (in)	Span (in)	C_D	Bubble Length (in)	Bubble Length / Chord Length
1	5.00	5.00	1.14	14.8	2.96
2	3.54	7.07	1.15	14.3	4.04
5	2.24	11.20	1.22	12.3	5.49
10	1.58	15.80	1.27	11.3	7.15
20	1.12	22.35	1.50	4.8	4.29
∞	1.24	∞	1.86	3.5	2.82

that as the flow moves radially outward, both the size of the structure grows and, in general, the velocity increases. Thus, the scaling function, which accounts for the entrainment of additional fluid beyond the 2D drag case, is justified. If no additional fluid were entrained, the increased cross-sectional area would result in a reduction of the fluid velocity as it travels radially outward and toward the wing tip. In this case, however, the fluid is accelerated outward both by centrifugal forces and by the increase in the amount of fluid within the trapped wake. Another significant fallout of the velocity and size of the stalled region growing toward the wing tip is the observation by McCormick [46] that, with both wings fully stalled, the radial pressure gradient should have no effect on the rolling moment [46]. The model presented in this study adheres to this observation, as the largest forces will be experienced at the wing tips because of the high velocity and $\dot{m}$ of the stalled region. Those wing tip forces will drive the total configuration C_l, thus masking any differences due to the local airfoil α but not affecting the rolling moment.

While a significant part of MAV, flying insect, and flapping wing research focuses on the presence of an attached LEV and structures, where the LEV, trailing edge vortex, and tip vortex eventually connect into a large loop vortex [49], it is proposed that this first-order approximation of the forces on a stalled spinning wing not use such coherent structures in the explanation or estimation of the force. The PIV studies of Ref. [50] and the numerical simulations of Garmann [49] both noted that beyond a small yaw angle, these structures separate from the surface of the wing and exist in the wake. No studies were found in the literature that considered a wing yawed beyond a yaw angle $\psi = 360$ deg. Nevertheless, an in-person discussion with Dr. Garmann [91] revealed that he could envision these vorticial structures as fully shed after multiple rotations of a plunging stalled wing, and the wing would exhibit more of a bluff body behavior. The bluff body studies of Fail [90] and Arie [88] are, thus, justifiable. Further justification for this methodology is that both the centrifugal and pressure forces outside of the LEV core were found to be responsible for the large regions of outboard flow above the wing [49]. In a plunging flow, as in the case of an aircraft in spin, the LEV, if present, may eventually be pushed from the surface of the wing. Nevertheless, the centrifugal and pressure forces will still be present even in the absence of the LEV. The question as to whether a LEV is present, at all, is raised because in the papers of Carr, Garmann, and others, a half-wing was tested in spin, and the LEV began from the inboard corner [49]; in the case of a spinning full wing, no inboard corner is present.

Another study by Garmann et al. [86] investigated rotating wings pitched 30 and 15 deg from perpendicular to the axis of rotation and noted that there was still an LEV present with its outboard flow, but the LEV was weakened. Bross et al. [87] conducted PIV experiments on a rotating wing with a plunging flow, as would be experienced by an airplane in a stall/spin, and found that as the advance ratio J (where $J = 1/\omega$) increases from zero, the presence of the root vortex is no longer detectable. Thus, no large-scale loop structure is present [87]. Bross postulates that either this structure was convected outside of the field of view by the advancing flow, or that it simply does not exist [87]. Bross noted that this same observation was made by Carr [50], for their $\mathcal{AR} = 2$ wing, and that for nonzero values of J, the concentration of spanwise flow extends over a larger region of the plate than for the $J = 0$ case [87].

Considering the field of wind turbines, Lindenburg [52] presented a model for the "rotational augmentation" that results in wind turbines in stall generating more power and thrust than predicted by 2D aerodynamic coefficients. This rotational augmentation model is based on observations of a strong increase in the aerodynamic coefficients near the stalled blade root and a reduction in the aerodynamic coefficients near the tip [52]. The analytical method presented in this research, however, predicts a significant increase in the aerodynamic coefficients near the tip. This difference is hypothesized to exist because of the significant difference in the aspect ratio of GA aircraft wings compared with horizontal axis wind turbine (HAWT) blades. General aviation (GA) wings have aspect ratio values of around 6.5, while HAWT blades have aspect ratio values of around 20 [92, 93]. As a result, the Coriolis forces are more significant on HAWTs than in the case of a GA-style wing. Thus, much of the radial flow exits at the trailing edge of a HAWT blade before it reaches the tip. The increased influence of Coriolis forces, combined with the root twist, and generally aerodynamically inferior root section airfoils of a wind turbine, explain why a strong increase in the coefficients is observed at the root of a HAWT, or a rotating propeller, in the case of Himmelskamp [55]. Meanwhile, for a GA aircraft, a large increase of the tip coefficients, and a minimal effect on C_l is observed and predicted by this model. Tangler and Selig [51] provide further evidence for the significant differences between HAWT blades and a spinning low-$\mathcal{AR}$ GA aircraft wing. In their 1997 paper [51], these researchers state that in the case of HAWTs, potential normal force increases would have the potential to greatly exceed 30%. Experimental spin data regularly demonstrate normal force increases on the order of 100%, which is significantly higher than those for HAWTs. Thus, it is supported that this model for GA-type planforms predicts a large increase in the tip C_N due to spin. Notably, the wind turbine literature observes coefficient increases at the root and little change at the tip.

5.3 Analytical Spin Correction and Wing Model

A number of experiments, including the wind tunnel tests of Chapter 4 of this work, show that the normal force coefficient on stalled spinning wings is well in excess of the two-dimensional flat-plate drag coefficient of $C_d \approx 2$ [94]. Because of this 2D-to-3D difference, a stalled spinning wing cannot be analyzed based on two-dimensional aerody-

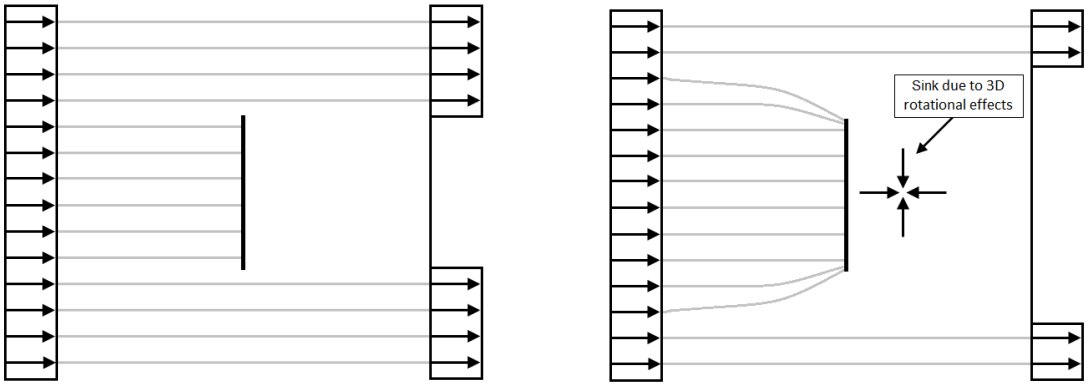

Figure 5.3: Illustration of a 2D flat plate (a) without, and (b) with the influence of rotational effects present.

namics and strip theory alone. Significant three-dimensional effects, which account for the additional normal force, exist in such a situation. The analytical methodology described herein is used to generate a new model for predicting those important three-dimensional effects.

Viewing and analyzing the three-dimensional problem from a two-dimensional point of view, an increase in C_d beyond a value of 2 necessitates the removal of additional momentum from the flow, when compared with the baseline two-dimensional case. To remove this additional momentum from the flow, a two-dimensional slice of a stalled spinning wing must entrain more of the flow than it would in a non-rotating case. The most logical way to account for entraining the additional flow, and thus increase the amount of momentum removed from a flow, is to introduce a sink downstream of the flat plate, as depicted in Fig. 5.3. The entrainment of additional flow by the sink, and thus the removal of more momentum from the flow than in a non-rotating two-dimensional flat plate case, is what allows the wing C_N to increase beyond the infinite flat plate C_d value of 2.

Modeling the increase in the normal force coefficient C_N as the yaw rate Ω increases begins by defining the mass of flow in the wake of the stalled wing. This flow travels and rotates with the wing, and it is ejected at the wing tip after the rotational motion of the wing accelerates it. This trapped flow is assumed to lie within a semi-ellipse, whose unscaled dimensions are depicted in Fig 5.4(a) in terms of the local wing chord, $c_{W,i}$ with an area defined by

$$A_{ellipse} = \frac{\pi}{2} r_1 r_2 \tag{5.1}$$

where r_1 and r_2 are the semi-major and semi-minor axes, respectively. With a semi-major axis $r_1 = 3.25 c_{W,i}$, and a semi-minor axis $r_2 = c_{W,i}/2$, Eq. 5.1 becomes

$$A_{wake,i} = \frac{\pi}{2} (3.25 c_{W,i})(c_{W,i}/2) w_1(\alpha_i) \tag{5.2}$$

where $c_{W,i}$ is the local wing chord at the i^{th} discretized wing section, and $w_1(\alpha_i)$ is the weighting function of Fig. 5.4(b), adding an α-dependency to the calculation by scaling the area of the local semi-ellipse. The weighting function $w_1(\alpha_i)$ is defined by

$$w_1(\alpha_i) = \sin\alpha_i \tag{5.3}$$

where α_i is the local angle of attack of the i^{th} wing slice. This weighting function is necessary because experimental data indicate a significant effect of varying the pitch angle θ of a spinning airplane. A variation in the local α across the wing would fall out from a variation in the aircraft pitch θ relative to the oncoming flow. This weighting function is not limited to only the post-stall regime bounded by $\alpha_{P,1}$ and $\alpha_{N,2}$, the beginning and end α values that define the stall regime, as defined by Selig [95]. This application of $w_1(\alpha_i)$ beyond the post-stall regime is done because, even when the yawing wing is not stalled, it is still reasonable to assume that some amount, albeit small, of spanwise flow exists because of rotational motion. In fact, spanwise flow was observed computationally on a spinning flat plate at $\theta = 15$ deg [86]. A simplification of Eq. 5.2 yields

$$A_{wake,i} = \frac{13\pi}{16} c_{W,i}^2 w_1(\alpha_i) \tag{5.4}$$

and using $A_{wake,i}$, the mass of each individual slice of the wake is

$$m_{wake,i} = A_{wake,i}\rho\Delta y \tag{5.5}$$

where ρ is the density of the air and Δy is the thickness of each strip.

At this point in the derivation of the methodology, a simplifying assumption regarding the entrainment of additional fluid into the wake, is introduced. The literature suggests that Coriolis forces decrease the area of the wake as the radial location increases [52]. On the contrary, however, as discussed above, it is proposed here that additional fluid would be entrained along the span of the wing because of the lower pressure of the wing wake and the aforementioned three-dimensional sink effect of Fig. 5.3. To produce a reduced-form equation able to capture the first-order effects that are important for design, the additional entrainment of flow into the wake behind the wing was initially assumed to result in a linear increase in the original fluid mass of each slice. Thus, the fluid mass of each slice as originally predicted by Eq. 5.5 was scaled by a factor of 1 to 2.5 as one moves outward radially from the wing centerline ($y = 0$) to the wing tips ($y = \pm b/2$). Thus, the mass of the flow in each wing slice becomes

$$m_{wake,scaled,i} = A_{wake,i}\rho w_2(y)\Delta y \tag{5.6}$$

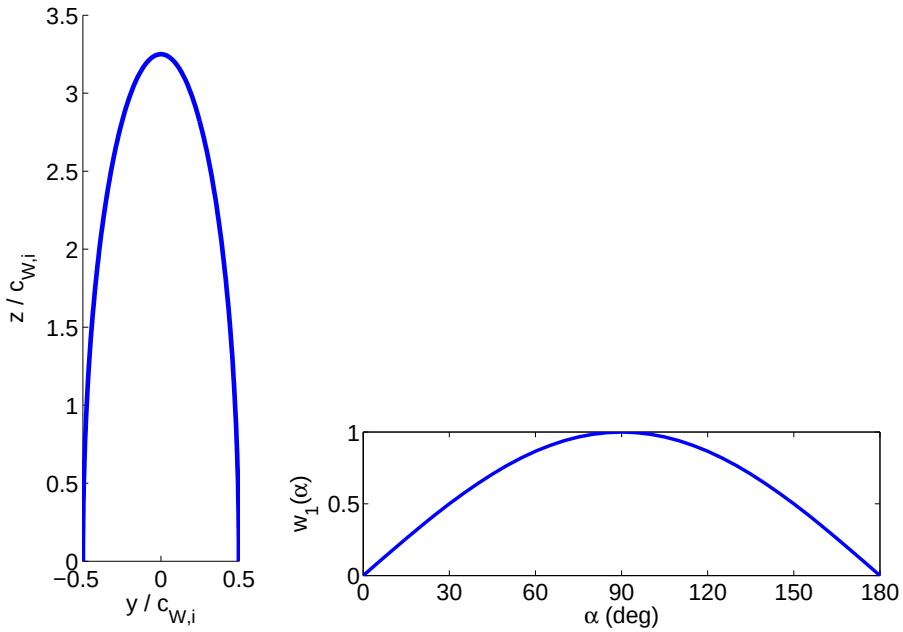

Figure 5.4: Plots of the (a) semi-ellipse of trapped flow behind a wing section with flow at $\alpha = 90$ deg, bottom to top, and (b) weighting function $w_1(i)$ used for ΔC_N in Eq. 5.3.

where $w_2(y)$ is a piecewise linear weighting function originally with the points $(y, w_2(y)) = (-b/2, 2.5)$, $(0,1)$, and $(b/2, 2.5)$. The entrainment function $w_2(y)$ accounts for the entrainment of additional flow into the trapped stalled wake downstream of the stalled wing, because of the local angular velocity. The reason that $w_2(0) = 1$ at the wing centerline is because the angular velocity of the wing section is zero at that point, because $r = 0$ at the center of rotation. Thus, no additional entrainment because of rotation at the centerline section exists.

After additional wind tunnel tests were conducted, greater understanding was met regarding this entrainment factor and the effect that the wing aspect ratio had on the amount of fluid entrainment into the trapped wake. It was found, for instance, that, as the wing aspect ratio increased, the force data from the spinning wing showed that more fluid was being entrained into the wing wake. As a result, the original linear scaling from 100% to 250% of the initial $w_2(y)$ weighting function was updated to account for this aspect ratio dependency through an empirical entrainment factor. The wing normal force experimental data were averaged, and the RMS error of the computational model was minimized by varying the amount of fluid assumed to be entrained. The results of this analysis are depicted in Fig. 5.5, which plots the entrainment factor $w_2(y)$ distribution (originally set to a constant 2.5 at the wing tips) at five different aspect ratios, as supported by the experimental wind tunnel data of Chapter 4.

As shown in Fig. 5.5, the amount of fluid that must be entrained into the trapped wake increases with the wing aspect ratio. While the $\mathcal{AR} = 2.55$ wing only entrained 22% more fluid than predicted by ellipse based on the local α, the amount of fluid within the wake of the $\mathcal{AR} = 8.33$ wing was calculated to be 400% of what would be predicted

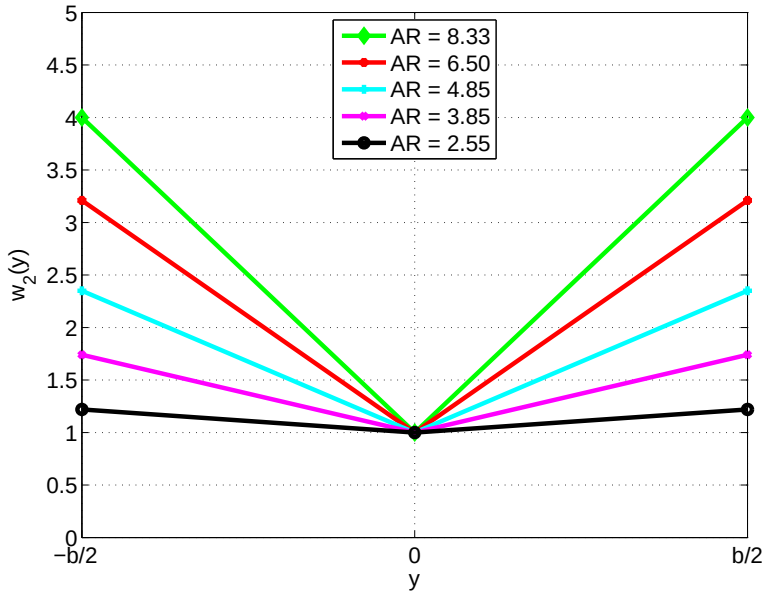

Figure 5.5: Plot of entrainment factor weighting function $w_2(y)$ versus normalized wing spanwise y location for five different aspect ratios.

solely by the local α, local chord length, and the resulting semi-ellipse. In this manner, the scaling function, $w_2(y)$, was improved by using data from the second round of wind tunnel tests. Plots of the curve fit using the updated aspect ratio-dependent $w_2(y)$ may be found in Sec. 5.9.1. It is hypothesized that the increase in the value of $w_2(\pm b/2)$ is not quite linearly related to the aspect ratio because, as the aspect ratio increases, there is an increased ability for the wake to entrain additional flow, but there is also more time for the Coriolis forces to push part of the fluid from the wake off of the trailing edge of the wing. As the aspect ratio increases beyond approximately six, the effect of the Coriolis forces begins to dominate the centrifugal forces that drive the flow entrainment, and the slope of the wing tip w_2 value vs. $\mathcal{AR}$ decreases. Figure 5.6 depicts the relationship of the wing tip value of $w_2(y)$ versus the wing aspect ratio.

While the wing tip value of $w_2(y)$ is not purely a linear function of the wing aspect ratio, $w_2(y)$ is still assumed to increase in a piecewise linear manner from unity at the wing midspan to the value of $w_2(\pm b/2)$ specified in Fig 5.6 at the wing tips in the manner shown in Fig 5.5. It is necessary to reiterate that the fluid mass ejected at the tip is not 400% of the amount of fluid in the wake at the wing midspan, but it is 400% (or whichever wing tip value of $w_2(\pm b/2)$ is appropriate for the wing aspect ratio) of the mass predicted by the wake dimensions and local α at the wing tip.

One mechanism that may drive the wake flow entrainment as captured by the empirical entrainment factor $w_2(y)$ is the horseshoe vortex structure present in the wake of a stalled spinning wing. This vortex structure consists of a stable LEV, TV (trailing vortex), and TEV (trailing edge vortex) [50, 96]. Carr et al. [50] observed that the LEV is conical in shape and grows with the wing span. Additionally, it was observed that as the wing aspect ratio increases, the horseshoe vortex structure grows in size [50] relative to the chord length. In some cases, the LEV forms an arch-like

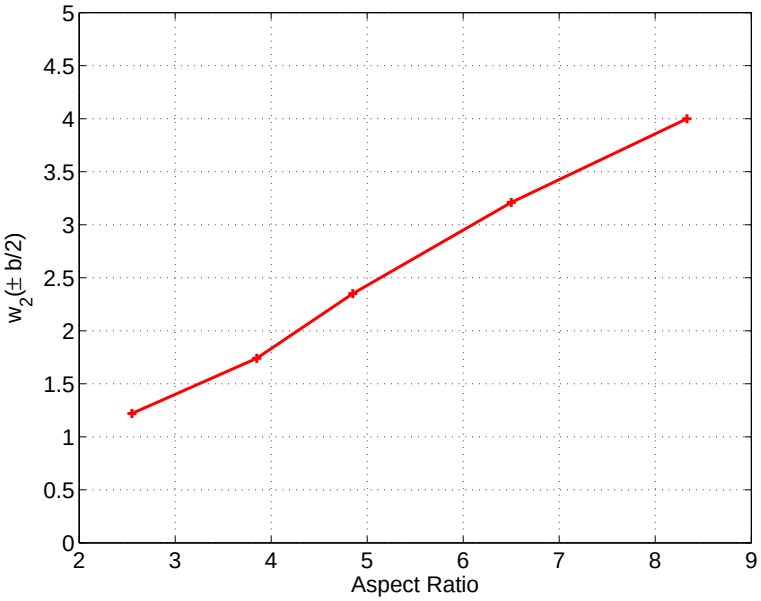

Figure 5.6: Plot of entrainment factor at wing tip versus wing aspect ratio, as determined by minimizing the RMS error between computational and experimental data.

structure and a second LEV begins at the wing leading edge at a non-zero spanwise location [50]. Maxworthy [97] notes that the varying vortex strength along the wing (i.e., the LEV grows stronger as the spanwise location increases) and the centrifugal forces drive the spanwise flow. A stronger LEV would be able to entrain more flow, and the studies of Refs. [49, 50, 97] have observed that the LEV grows in size and increases in strength with the spanwise loction. It is this increasingly stronger and larger vortex structure that may drive the entrainment of flow into the wake, a phenomenon that is accounted for numerically by the empirical entrainment factor $w_2(y)$.

The acceleration of the fluid inside each spanwise wake slice i, due to rotation, is defined by

$$a_i = \Omega^2 y \tag{5.7}$$

where Ω is the yaw rate, and y is the radial location from the wing centerline of $y = 0$. The established theory of sources and sinks specifies that the amount of fluid in the stalled wake increases as the radial location moves outboard, since additional fluid is being entrained. Using $F = ma$, and combining Eqs. 5.6 and 5.7, yields

$$\Delta C_N = \sum_{i=1}^{n} \frac{13\pi\rho\Omega^2}{16} c_{W,i}^2 w_1(\alpha_i) w_2(y) y \Delta y \tag{5.8}$$

where n is the number of wing panels, $c_{W,i}$ is the local wing chord, $w_1(\alpha)$ is the scaling function of Eq. 5.3, $w_2(y)$ is the empirical entrainment factor weighting function of Fig. 5.5, and y is the radial distance from the wing semispan of

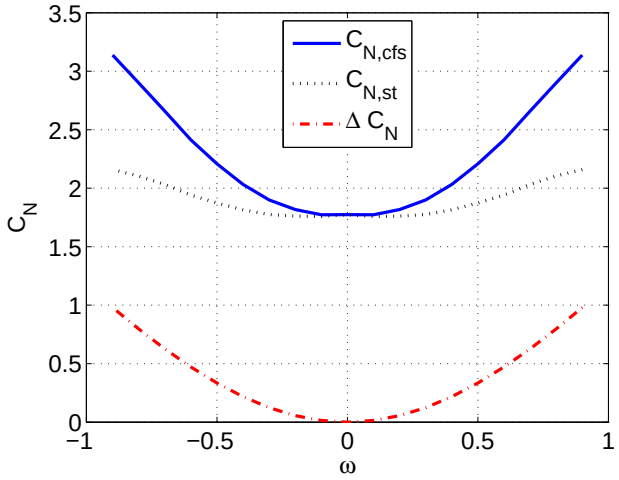

Figure 5.7: Plot of buildup of C_N corrected for spin based on C_N from strip theory ($C_{N,st}$) and ΔC_N from centrifugal pumping components.

each slice of width Δy. Significantly, if one were to extract a specific equation or value from this dissertation, Eq. 5.8 would be that equation.

It should be noted that Eq. 5.8 is additive to the strip theory-determined forces on the wing, and it is equal to zero when the airplane has a zero yaw rate. Figure 5.7 provides an example of the relationship between ΔC_N because of spinning, C_N as calculated by standard strip theory, and the C_N value of a wing corrected for spin for the case of $\alpha = 70$ deg. Figure 5.7 may also be compared on a qualitative basis to Figs. 1.2(a) and 1.2(b) from Chapter 1, which provided the initial motivation for this dissertation work.

Presented in equation form, Fig. 5.7 is described by the relationship

$$C_{N,cfs} = C_{N,st} + \Delta C_N \tag{5.9}$$

where ΔC_N is the additional normal force due to the centrifugal pumping of Eq. 5.8, $C_{N,st}$ is the wing normal force coefficient as calculated by standard strip theory, and $C_{N,cfs}$ is the wing normal force coefficient corrected for spin. The aforementioned correction due to spin does affect the pitching moment, and the magnitude of the change in the pitching moment due to the additional ΔC_N is given by

$$\Delta C_m = \Delta C_N (x_{cg} - x_{c/2}) \tag{5.10}$$

where ΔC_N is defined by Eq. 5.8, and x_{cg} and $x_{c/2}$ are the centerline locations of the c.g. and wing half chord, respectively. The force from centrifugal pumping is applied at the half chord location because that is the location at which the resultant force on a heavily stalled airfoil at 90 deg acts.

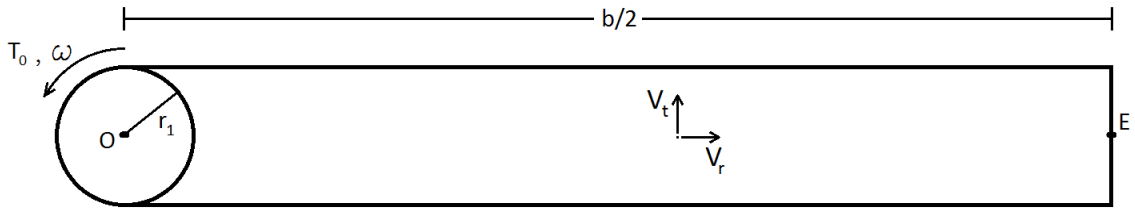

Figure 5.8: Illustration of the classic sprinkler problem modified for this research.

The final correction due to spin consists of an anti-spin yaw moment, which is caused by the work required to provide the radially-pumped flow with its rotational velocity. This correction is based on the classic "sprinkler problem," where the task is to determine the rotational velocity of a frictionless lawn sprinkler given the fluid mass flow rate and the angle at which the fluid is ejected at the tip. Adapted to the field of stall/spin, the problem becomes one where, given a specified rotational rate and mass flow rate, how might the torque that is required to radially accelerate the volume of fluid within the wing wake (i.e., a maintaining torque) be calculated. This maintaining torque would be manifested in a developed stall/spin situation as an anti-spin yaw moment, but it would not be a main driver of the yaw moment. The side forces from the fuselage and vertical tail would be the main drivers of the yaw moment, as well as the drag differential between the left and right wings.

For a one-dimensional, non-deformable control volume, and based on the parameters of Fig. 5.8, it can be shown that:

$$\sum M_o = T_O = \sum(\mathbf{r}\times\mathbf{V})_{out}\dot{m}_{out} - \sum(\mathbf{r}\times\mathbf{V})_{in}\dot{m}_{in} = \int_{CS}(\bar{r}\times\bar{V})\rho(\bar{V}\cdot\bar{n})dA \tag{5.11}$$

Because the force acts radially through point O, the equation for the torque required to maintain the angular rate of ω, T_o, simplifies to

$$T_o = (\bar{r}_E\times\bar{V}_E)\dot{m}_E - (\bar{r}_o\times\bar{V}_o)\dot{m}_o \tag{5.12}$$

Using Eq. 5.6, the relationship between $\dot{m}_E$ and $\dot{m}_o$, the mass flow rates at the wing tip and wing root, respectively, may be defined as

$$\dot{m}_E = \frac{w_2(b/2)}{w_2(0)}\dot{m}_o \tag{5.13}$$

Applying the cross product to Eq. 5.12, noting $V = \omega r$ and $r_E = b/2$, and taking the radius of the fluid source to be r_1 yields the final expression for the maintaining torque, which is manifested as ΔC_n

$$\Delta C_n = \dot{m}_o \omega \left[\frac{w_2(b)}{w_2(b/2)} (b/2)^2 - r_1 \right]^2 \tag{5.14}$$

It should again be noted that this contribution to the yawing moment coefficient is small and does not drive the aircraft yawing moment. The fuselage and the effectiveness and level of flow shielding presented by the horizontal stabilizer on the vertical stabilizer primarily drive the change in aircraft C_n in a spin. Additionally, the uneven drag distribution on a stall wing in spin may present a strong pro-spin or anti-spin yaw moment.

To use airfoil data in a wing post-stall case, the 3D post-stall correction of Selig [95] is employed. To calculate the standard aerodynamic forces on a wing in the post-stall regime, a modification of the Lindenburg [83] 90 deg drag coefficient ($C_{d,90}$) is used, as shown in Eq 5.15 [95]

$$C_{d,90} = 2.21 - 0.41[1 - exp(17/\mathcal{R})] \tag{5.15}$$

where the wing $\mathcal{R}$ is used instead of the effective aspect ratio $\mathcal{R}_{eff}$ of [83]. The value of $C_{d,90}$ from Eq. 5.15 is normalized to supply the scaling factor k_{c_d} [95], where

$$k_{C_d} = C_{d,90}/2.2 \tag{5.16}$$

This scaling factor k_{C_d} is used to calculate the lift, drag, and quarter chord moment coefficients through the following three equations [95]

$$C_{l,\text{corrected}} = C_l[1 - w(1 - k_{C_d})] \tag{5.17}$$

$$C_{d,\text{corrected}} = C_d[1 - w(1 - k_{C_d})] \tag{5.18}$$

$$C_{m,c/4,\text{corrected}} = C_{m,c/4}[1 - w(1 - k_{C_d})] \tag{5.19}$$

where w is the weighting function defined by [95]

$$w = \cos\left[\pi \left(\frac{\alpha - \alpha_{P,1}}{\alpha_{N,2} - \alpha_{P,1}} \right) - \frac{\pi}{2}\right] \tag{5.20}$$

and $\alpha_{P,1}$ and $\alpha_{N,2}$ define the beginning and end range, respectively, over which the post-stall correction is applied.

5.4 Wing Aerodynamic Data and Development

The wing airfoil was based on a 10% thick symmetric airfoil. Data and general trends for an airfoil with no control surface deflection were taken from Refs. [95, 98–102]. Candidate lift and drag coefficient distributions over the range $-180 \leq \alpha \leq 180$ deg were developed. To determine the effects of the control surface deflection on the aerodynamics of the airfoil, the methodology of McCormick [43] was used for the unstalled region. Because flap effectiveness is inherently nonlinear, an empirical factor η is proposed by McCormick to account for the effects of separated flow. Thus, the increment in C_l in the unstalled region is [43]

$$C_l = C_{l_\alpha}\left(\alpha + \tau\eta\delta_f\right) \tag{5.21}$$

where the flap effectiveness factor τ is defined by

$$\tau = \frac{\theta_f - \sin\theta_f}{\pi} \tag{5.22}$$

and

$$\theta_f = \cos^{-1}\left(\frac{2c_f}{c} - 1\right) \tag{5.23}$$

where c_f/c is the ratio of the flap chord to the wing chord, and δ_f is the flap deflection angle. The control surface was treated as a plain flap, which determined the empirical factor η as a function of δ_f. A plot of the empirical correction factor η is presented in Fig. 5.9.

All control surfaces on the Aero Testbed were modeled as plain flaps. Flap deflection angle δ_f values of 15, 30, and 50 deg yielded η values of 0.77, 0.53, and 0.40, respectively. Using these values of η, coefficient distributions over the linear range of α values were generated for deflection angles of -50, -30, -15, 0, 15, 30, and 50 deg. From Eq. 5.21, the change in C_l due to the deflection of a flap is

$$\Delta C_l = C_{l_\alpha}\tau\eta\delta_f \tag{5.24}$$

On account of the fact that a flapped airfoil, or in the case of this simulation, an airfoil with a deflected control surface, will stall at a lower angle of attack than the airfoil with the flap or control surface not deflected, the expected increase in $C_{l_{max}}$ is less than the increase in C_l below stall. An empirical relationship for this reduced increment to $C_{l_{max}}$ is given by McCormick [43] and presented in Fig. 5.10. The wing airfoil of the Aero Testbed was modeled for $c_f/c = 0.28$, while the horizontal and vertical stabilizers were modeled for $c_f/c = 0.50$.

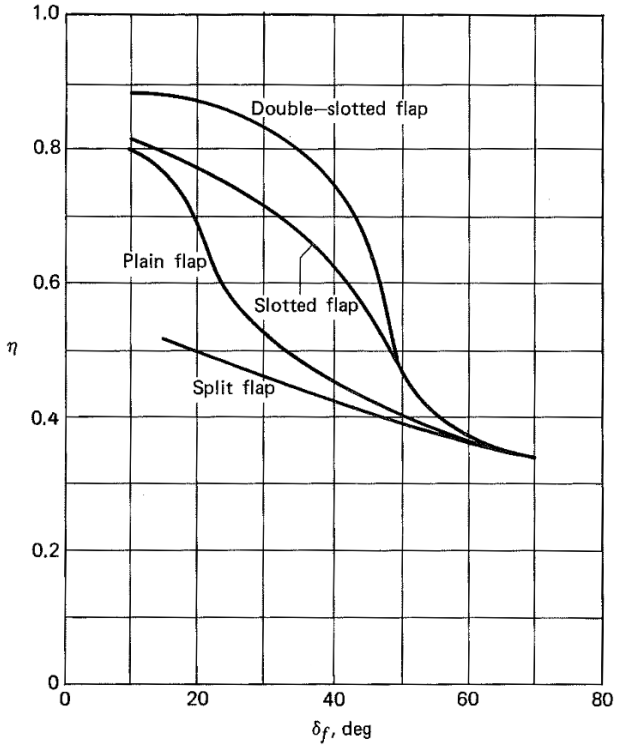

Figure 5.9: Plot of correction factor η versus flap deflection angle δ_f (McCormick [43]).

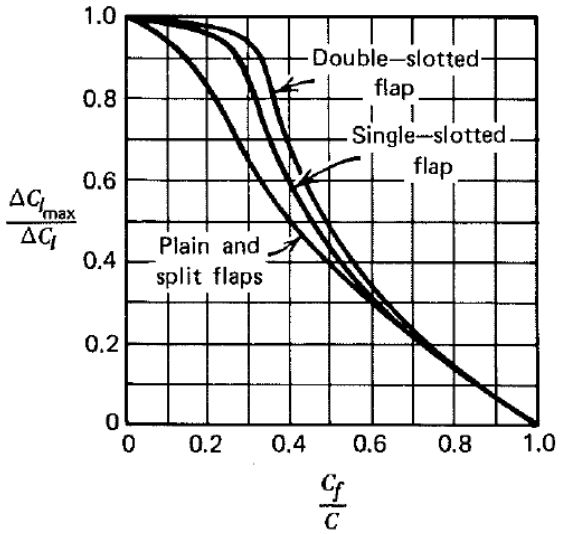

Figure 5.10: $C_{l_{max}}$ increment ratio as a function of c_f/c (McCormick [43]).

Drag distributions over the linear range of α values were generated based on the zero-deflection data and observations in the trends of experimental data sets with deflected flaps. The shape of the peaks in the stalled region generally did not change, but instead, they experienced vertical and horizontal shifts corresponding to the flap deflection angle

and c_f/c ratios. Additionally, McCormick [43] provided some guidance when determining the drag due to a flap or control surface deflection, defining the increment in the wing drag coefficient for a plain (and split flap) as

$$\Delta C_D = 1.7(c_f/c)^{1.38}(S_f/S)\sin^2\delta_f \tag{5.25}$$

To determine the pitching moment due to a deflected control surface in the unstalled region, the following relationship from McCormick [43] was used

$$\frac{\Delta C_{m_{1/4}}}{\Delta C_l} = \frac{2\sin\theta_f - \sin 2\theta_f}{8(\pi - \theta_f + \sin\theta_f)} \tag{5.26}$$

where θ_f is the flap effectiveness factor, as previously defined in Eq. 5.23. Moment coefficients in the high α regime were determined, using the assumption that at $\alpha = 90$ deg, the lift and drag forces act through the 50% effective chord length. This 50% location is in contrast with an unstalled airfoil, where the reference point is at the quarter chord. Additionally, in the regime of $\alpha \approx \pm 180$ deg, where C_l is once again linearly related to α, the flow can be assumed to have reattached, and thus, the lift and drag are taken to act at a reference point located at the 75% effective chord length in this regime. To account for the shift from the quarter chord, to the 50% chord, to the 75% chord, the location at which the forces act was linearly interpolated based on the angle of attack beginning around stall and ending at reattachment. The reattachment location was approximately defined by the edges of the linear regime centered around $\alpha = \pm 180$ deg. This process, developed independently as part of this research, was nearly identical to the process outlined in the paper by Montgomerie [103] for extending the angle of attack range to ± 180 deg. The final moment distribution was achieved by blending the unstalled region, acting at the quarter chord, and whose ΔC_M because of flap deflection is defined by Eq. 5.26, with the distribution of the stalled regions to yield a smooth curve.

Validation of the above process was performed by using C_L and C_D data from Koeing [104] to calculate the moment coefficient and comparing that calculated moment to experimental moment data from the same data set. A plot of the C_L and C_D, calculated and experimental $C_{M,c/4}$, and the estimated x_{cp}/c and x_{cp}/c, as calculated from the experimental data, all versus α for an estimated $\mathcal{AR} = 2.5$ tail surface, is presented in Fig. 5.11.

As shown in Fig. 5.11, beyond ± 30 deg, the x_{cp} at which the lift and drag are applied is moved aft to $x_{cp} = 0.5$ at 90 deg and $x_{cp}/c = 0.75$ in the reattached region around $\alpha = 180$ deg. This assumption is reasonable as the calculated and experimental $C_{M,c/4}$ values show excellent agreement over the applicable range of this method, which was devised as part of this research. While $x_{cp}/c = 0.50$ at $\theta = 90$ deg is known, and x_{cp}/c in the reattached region around $\alpha = \pm 180$ deg is supported through thin airfoil theory, some thoughts should be presented as to why the center of pressure moves aft as α increases from stall to 180 deg. This simple method was devised to connect three known points, and the justification comes from the stagnation point moving aft on the airfoil as α is increased. Since in the high-α regime, the majority of the force normal to the wing comes from drag forces, it is fitting that those forces

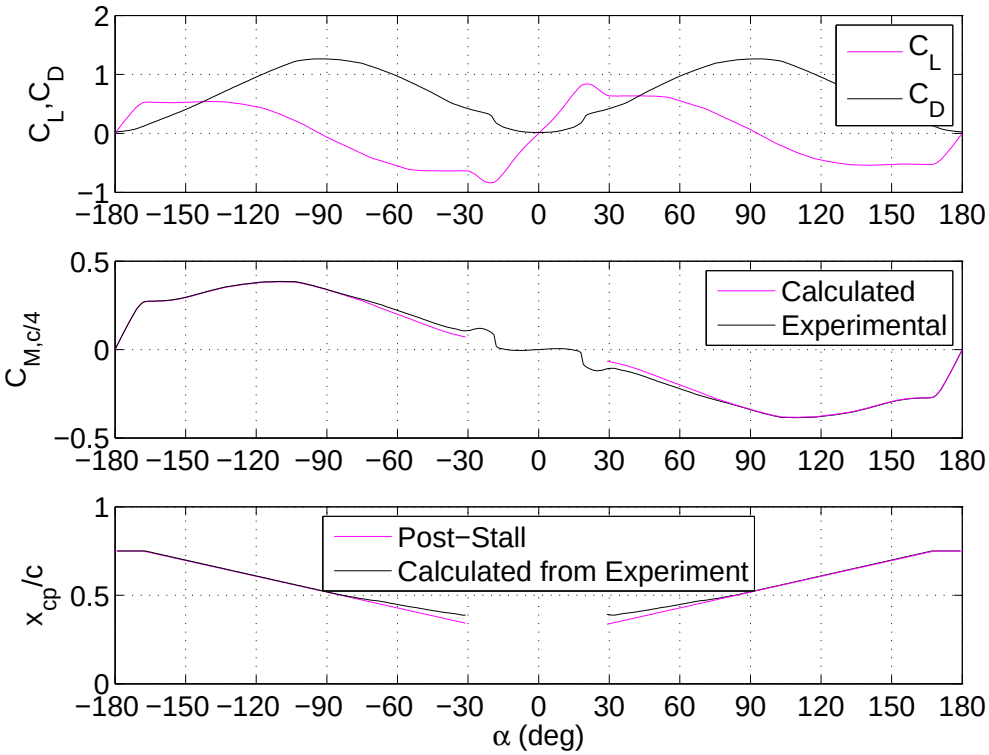

Figure 5.11: Plot of experimental C_L and C_D data, calculated and experimental $C_{M,c/4}$ data, and the x_{cp}/c location used for determining the moment, all as a function of α.

are assumed to act around that point which is known to shift aft. While the shift fore and aft from the 50% chord location at 90 deg may or may not necessarily be linear, a linear interpolation of the location through which the lift and drag forces was shown in Fig. 5.11 to produce a good fit to experimental data, and a linear fit was used by Montgomerie [103]. At the bottom of Fig. 5.11, the "Calculated from Experiment" curve was created. This curve uses the experimental data of Koenig [104] for the lift, drag, and moment coefficients to back out the moment arm. As shown in Fig. 5.11, the linear approximation matches quite well with the experimentally calculated location of x_{cp}/c. While the experimentally-calculated $x_{cp}/c = 0.39$ at 30 deg, the linear interpolation calculated the moments based on $x_{cp}/c = 0.34$ at 30 deg. For $|\alpha| > 80$ deg, the linearly-interpolated and experimentally-determined x_{cp}/c values are indistinguishable and increase linearly with α. Three additional validation plots, which are similar to Fig. 5.11, are also presented.

The first of these additional validation plots, Figure 5.12, presents a plot of the airfoil C_l and C_d data of Sheldahl and Klimas [98], calculated and experimental $C_{m,c/4}$ data, and the estimated x_{cp}, all versus α. Because of the waviness of the $C_{m,c/4}$ values, the $C_{m,c/4}$ data were not used to calculate x_{cp}/c values. The overall trend, however, of the experimental and calculated C_m values, matches. Additional validation was performed on the Koenig $\mathcal{AR} = 2$ data set, and Fig. 5.13 presents a plot of the horizontal stabilizer C_L and C_D data of Koenig [104]. Calculated and experimental

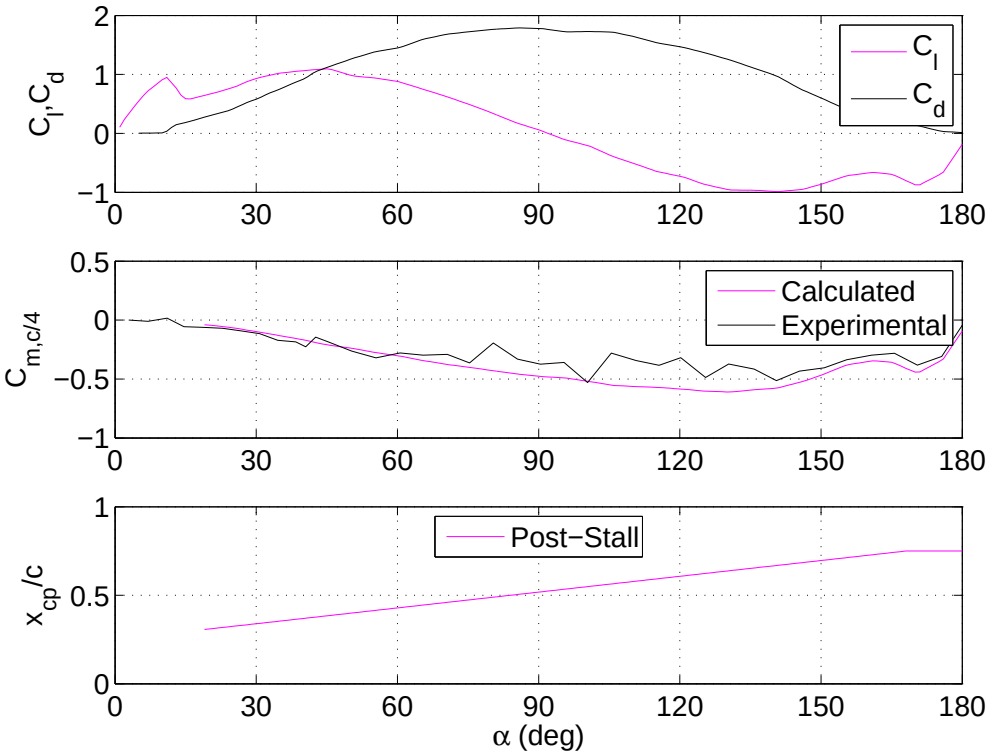

Figure 5.12: Plot of experimental C_l and C_d airfoil data from Sheldahl and Klimas [98], calculated and experimental $C_{m,c/4}$ data, and the x_{cp} location used for determining the moment, all as a function of α.

$C_{M,c/4}$ data, and the estimated x_{cp}, all versus α, are also shown. Finally, Fig. 5.14 presents the same information for a horizontal tail surface of $\mathcal{AR} = 6$. As shown in all Figs. 5.11–5.14, the assumption of a linear interpolation of the x_{cp}/c location from stall until the reattachment of flow near $\alpha = \pm 180$ deg is reasonable. The curves show strong agreement between calculated and experimental moment data, as well as with backing out the x_{cp}/c location using lift, drag, and moment data.

Returning to the effective chord length, in the case of a zero control surface deflection, the effective chord length is equal to the chord length. Yet, in the case of a deflected control surface, the effective chord length, measured as the x-distance between the leading edge and the trailing edge, will be less than the chord length of the undeflected airfoil. To calculate the effective chord length as a function of the control surface deflection angle δ_f and the control surface chord ratio c_f/c, the following equation is used

$$c_{eff} = \left[\left(1 - \frac{c_f}{c}\right) + \left(\frac{c_f}{c}\cos\delta_f\right)\right] c \tag{5.27}$$

Figure 5.15 presents a diagram denoting the difference between the chord length c and the effective chord length with deflected control surfaces c_{eff}. Once the effective chord length is determined, the moment at the wing quarter

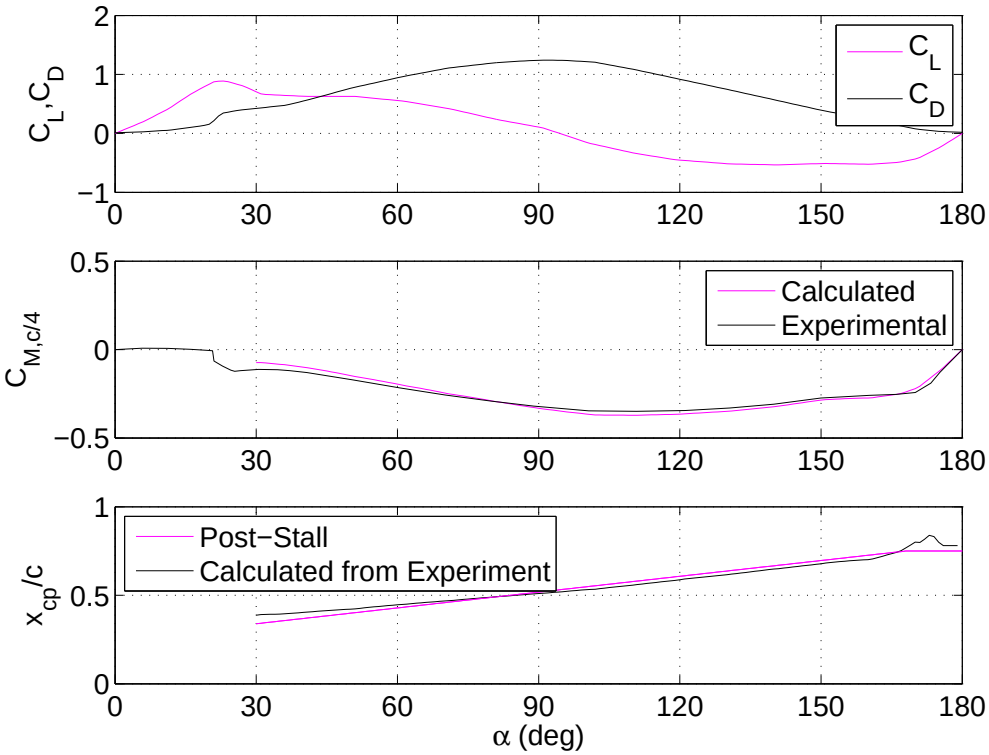

Figure 5.13: Plot of experimental C_L and C_D data from Koenig [104] for an $\mathcal{AR} = 2$ tail surface, calculated and experimental $C_{M,c/4}$ data, and the x_{cp} location used for determining the moment, all as a function of α.

chord for $\alpha = 90$ deg is calculated by multiplying the resultant force by the moment arm between the 50% effective chord location and the quarter chord of the base airfoil as calculated by

$$x_{eff} = \frac{c_{eff}}{2} - \frac{c}{4} \tag{5.28}$$

A plot of the root airfoil section of the Extra 260 Aero Testbed aircraft is presented in Fig. 5.16. The final aerodynamic lookup tables that were developed for the wing airfoil C_l, C_d, and $C_{m,c/4}$ distributions are presented in Figs. 5.17, 5.18, and 5.19 for various control surface deflections. For completeness, a plot of the lift-to-drag ratio C_l/C_d of the airfoil is presented in Fig. 5.20. To obtain coefficients for intermediate deflections of the ailerons in the force prediction code, a standard linear interpolation between the two closest distributions was performed.

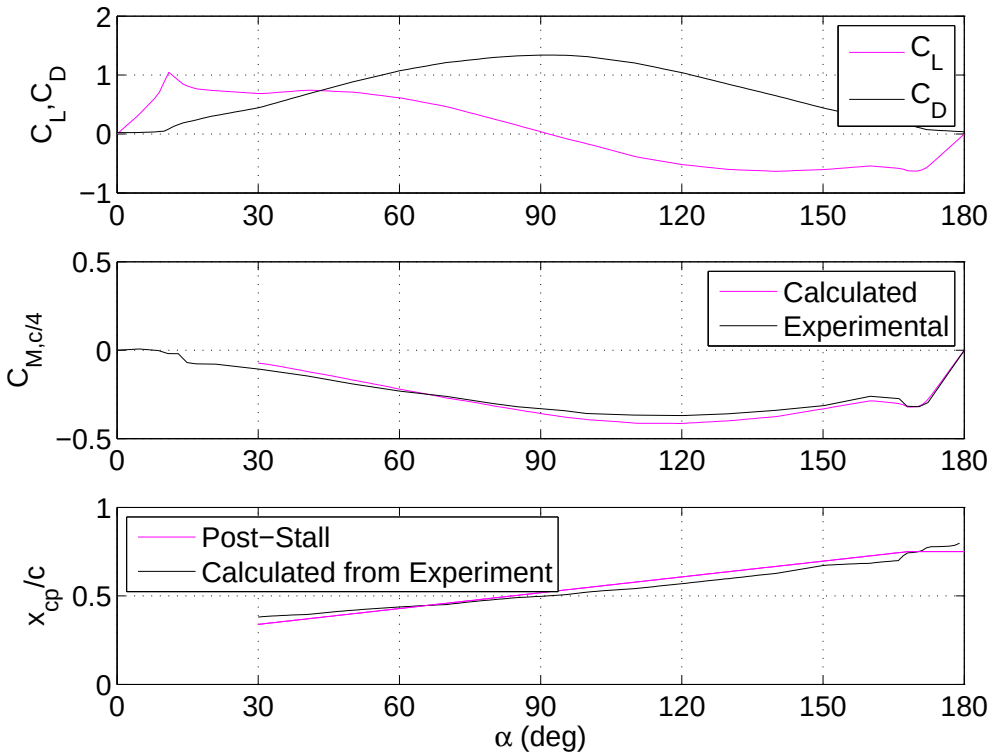

Figure 5.14: Plot of experimental C_L and C_D data from Koenig [104] for an $\mathcal{AR} = 6$ tail surface, calculated and experimental $C_{M,c/4}$ data, and the x_{cp} location used for determining the moment, all as a function of α.

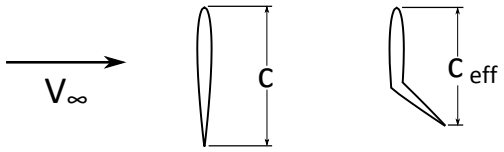

Figure 5.15: Comparison of undeflected airfoil chord length c and the effective chord length c_{eff} of an airfoil with deflected control surfaces.

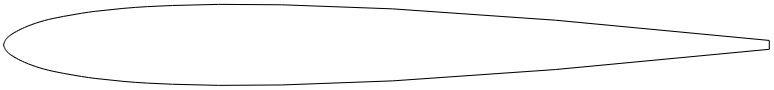

Figure 5.16: Root airfoil section of the Extra 260 Aero Testbed aircraft.

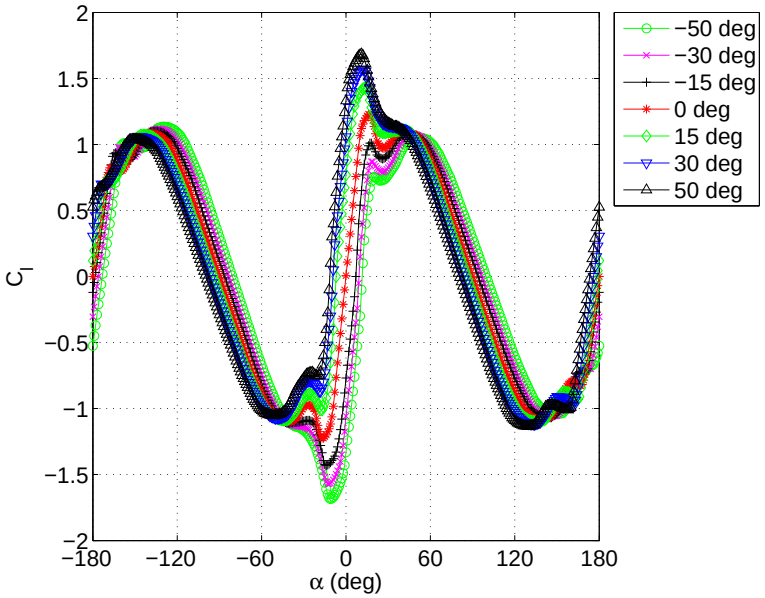

Figure 5.17: C_l lookup table data used for wing airfoil over the range $-180 \leq \alpha \leq 180$ deg.

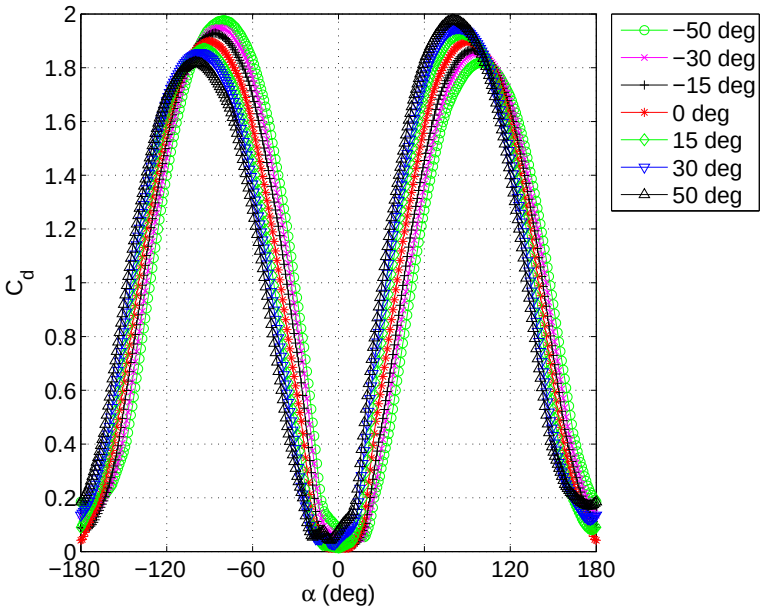

Figure 5.18: C_d lookup table data used for wing airfoil over the range $-180 \leq \alpha \leq 180$ deg.

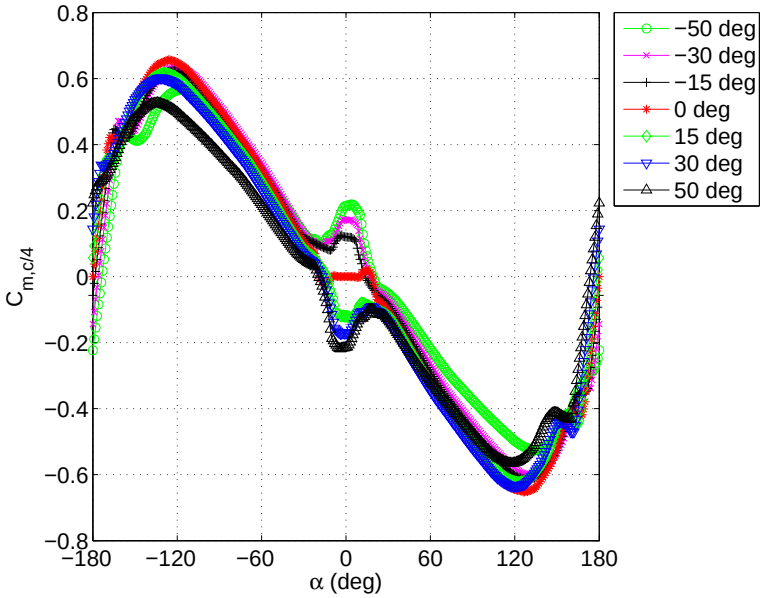

Figure 5.19: $C_{m,c/4}$ lookup table data used for wing airfoil over the range $-180 \leq \alpha \leq 180$ deg.

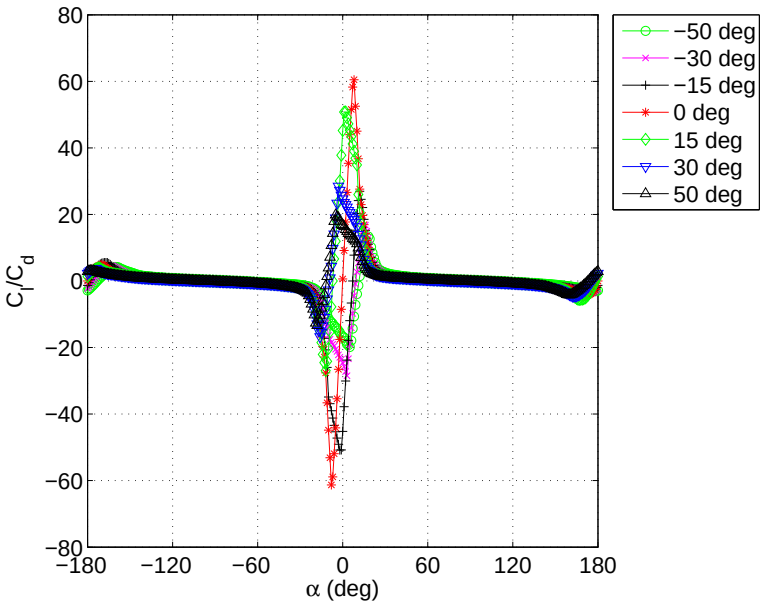

Figure 5.20: Plot of C_l/C_d for wing airfoil over the range $-180 \leq \alpha \leq 180$ deg.

In order to use the lookup tables, the u, v, and w velocity components at each location on the wing must be calculated. These values are based on the motion of the aircraft c.g., the x-y-z distance from the c.g. to the airfoil section quarter chord, and the angular rates p, q, and r of the airplane. The local x-velocity of each section of the wing in the aircraft frame of reference is computed by

$$u_{wing,i} = u_{body,cg} + \left(q_{body,cg} z_{c/4_{wing,i},cg}\right) - \left(r_{body,cg} y_{c/4_{wing,i},cg}\right) \tag{5.29}$$

where $[u,v,w]_{body,cg}$ is the velocity component vector of the c.g. in the aircraft reference frame, $[p,q,r]_{body,cg}$ are the angular rates of the airplane, and $[x,y,z]_{c/4_{wing,i}}$ is the vector from the airplane c.g. to the i^{th} wing panel quarter chord, positive to the right. The local wing y-velocity in the aircraft body axis is calculated by:

$$v_{wing,i} = v_{body,cg} + \left(r_{body,cg} x_{c/4_{wing,i},cg}\right) - \left(p_{body,cg} z_{c/4_{wing,i},cg}\right) \tag{5.30}$$

Finally, the wing z-velocity in the aircraft body axis is calculated by:

$$w_{wing,i} = w_{body,cg} + \left(p_{body,cg} y_{c/4_{wing,i},cg}\right) - \left(q_{body,cg} x_{c/4_{wing,i},cg}\right) \tag{5.31}$$

Based on $[u,v,w]_{wing,i}$ the local lift, drag, and moment coefficients were calculated using a strip analysis procedure. An iterative process was used to calculate the downwash and local α and iterate upon their effects on one another. Once the difference between successive iterations fell below a specified threshold, the solution for the downwash and local α was considered as converged. The difference between successive downwash iterations was calculated with:

$$difference = \sum \sqrt{\left(\Gamma_{new,i} - \Gamma_{old,i}\right)^2} \tag{5.32}$$

where $\Gamma_{new,i}$ is the new Γ-value at the i^{th} wing section, and $\Gamma_{old,i}$ is the previous Γ-value at the i^{th} wing section. It should be noted that while full downwash calculations (including Γ and w_i) are performed at each timestep and applied in the unstalled regime, the induced z-velocity of downwash is scaled down from its calculated value, beginning at $\alpha = 30$ deg down to zero times the calculated value at $\alpha = 90$ deg. This scaling down to zero at $\alpha = 90$ deg is performed because there is no downwash on a flow-normal plate. Also, the planar straight wake assumption was used with no narrowing of the wake as it traveled downstream. Assumptions made in regard to the zero-dihedral angle wing z-location are that the c.g. and wing are located at the same z-coordinate, and that any vertical deflection to the wing is small.

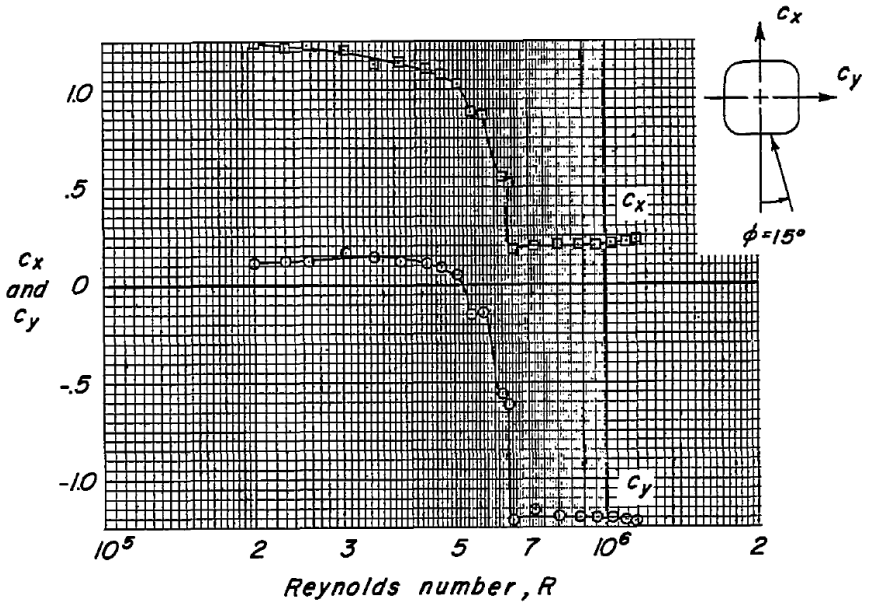

Figure 5.21: Illustration of the convention used to define C_x, C_y, and ϕ for the aft fuselage lookup tables (Polhamus [25]).

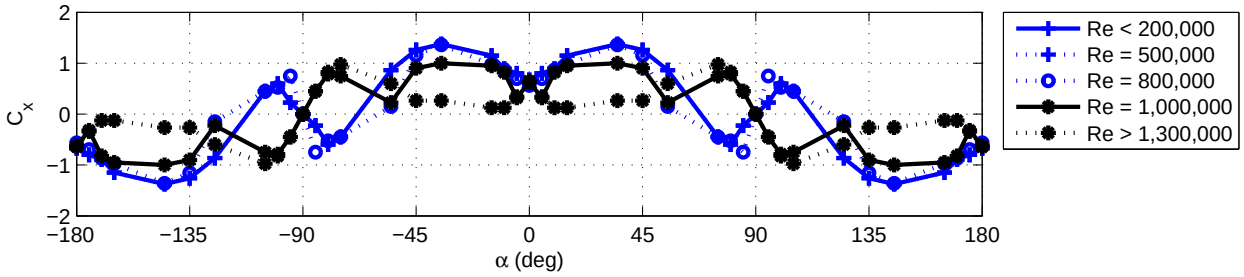

Figure 5.22: C_x lookup table data used for aft fuselage over the range $-180 \leq \alpha \leq 180$ deg.

5.5 Fuselage

The aft fuselage forces are also calculated via lookup tables. In this case, the raw data are based on those of Polhamus [25]. In contrast to the case of the wing, where rotational effects are significant and included, rotational effects on the fuselage are not included. This exclusion of rotational effects is in agreement with the approaches and findings of Refs. [24, 47, 85]. These data were recorded in a body-fixed axis system, and Fig. 5.21 presents an example of the raw data from which the data of Figs. 5.22 and 5.23 were derived. Figures 5.22 and 5.23 present the data from Ref. [25] for multiple Reynolds numbers, and they show how above a critical *Re* value, the aft fuselage forces can switch from an anti-spin to a pro-spin direction. To generate the plots of Figs. 5.22–5.25, the ϕ term of Fig. 5.21, which was bounded by $0 \leq \phi \leq 90$ deg, was extended to the range $-180 \leq \alpha \leq 180$ deg.

After early simulation runs, new lookup tables were generated for the forward fuselage of the airplane. In general, the aft fuselage of the type of aircraft modeled is rectangular, with the longer axis oriented vertically. The sections

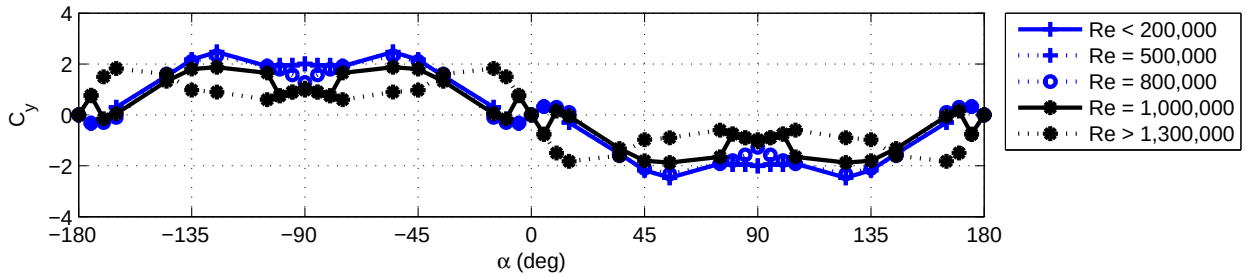

Figure 5.23: C_y lookup table data used for aft fuselage over the range $-180 \leq \alpha \leq 180$ deg.

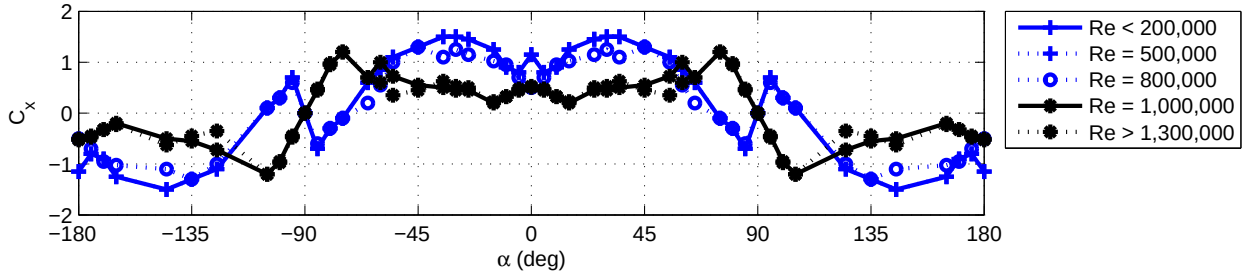

Figure 5.24: C_x lookup table data used for forward fuselage over the range $-180 \leq \alpha \leq 180$ deg.

are taller than they are wide because the fuselage fairs down from the airplane cabin, which is located above the fuselage. The forward fuselage of the airplane, on the other hand, is generally closer in cross-section to a square than a rectangle. This square shape exists mainly because of the fact that this section of the aircraft contains the motor or engine of the aircraft. As was the case for the aft fuselage, the data of Polhamus [25] was used to model the front fuselage cross-sections. On account of the more-square cross-section, the Polhamus square and rectangular data were averaged. Figures 5.24 and 5.25 present the C_x and C_y coefficients for a square cross-section with rounded corners over the range $-180 \leq \alpha \leq 180$ deg.

The x-, y-, and z-velocities at each section of the fuselage were calculated using

$$u_{fuselage,i} = u_{body,cg} + \left(q_{body,cg} z_{fuse_i,cg}\right) - \left(r_{body,cg} y_{fuse_i,cg}\right) \tag{5.33}$$

$$v_{fuselage,i} = v_{body,cg} + \left(r_{body,cg} x_{fuse_i,cg}\right) - \left(p_{body,cg} z_{fuse_i,cg}\right) \tag{5.34}$$

$$w_{fuselage,i} = w_{body,cg} + \left(p_{body,cg} y_{fuse_i,cg}\right) - \left(q_{body,cg} x_{fuse_i,cg}\right) \tag{5.35}$$

where $[x,y,z]_{fuse_i,cg}$ are the x, y, and z distances from the i^{th} fuselage section to the airplane c.g. An additional feature added to SpinSim was the ability to switch fuselage force calculation methods. Because the fuselage is located along the aircraft centerline, $y_{fuse_i,cg} = 0$ for the fuselage. In addition to the aforementioned Polhamus-data based method, a second method, based on NASA rotary balance data sets [40] for fuselage-only configurations (i.e., an airplane with

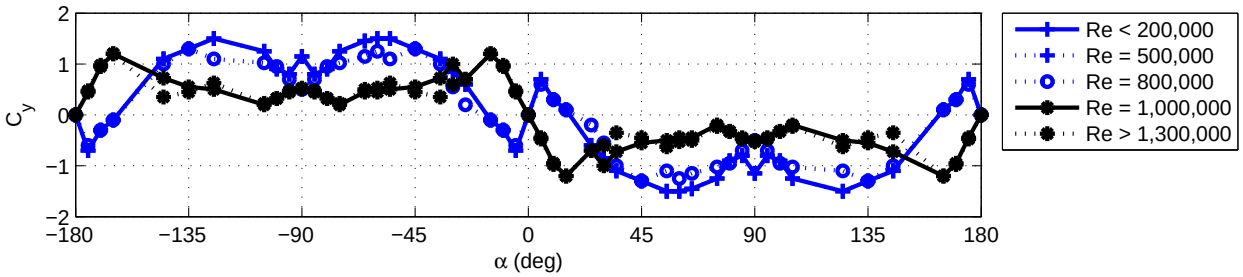

Figure 5.25: C_y lookup table data used for forward fuselage over the range $-180 \leq \alpha \leq 180$ deg.

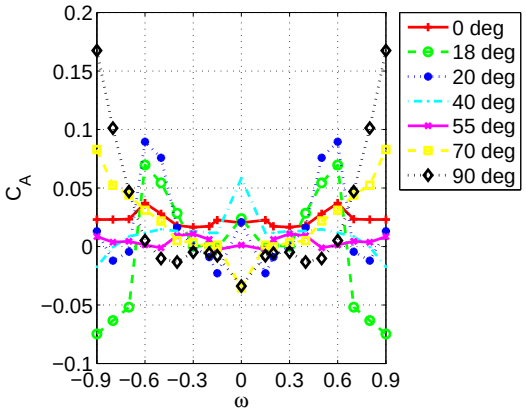

Figure 5.26: C_A lookup table data used for full fuselage over the range $-0.9 < \omega < 0.9$ at seven values of α.

wing, vertical stabilizer, and horizontal stabilizer removed), is also available within the code. SpinSim users are able to switch between the two methodologies. The lookup tables for the fuselage C_A, C_Y, C_N, C_m, and C_n are presented in Figs. 5.26–5.30, respectively. No tables for the roll moment coefficient C_l were created because the fuselage contribution to airplane roll is negligible when compared with the moments from the other components. Moreover, the rotary balance data were indistinguishable from that of a straight line.

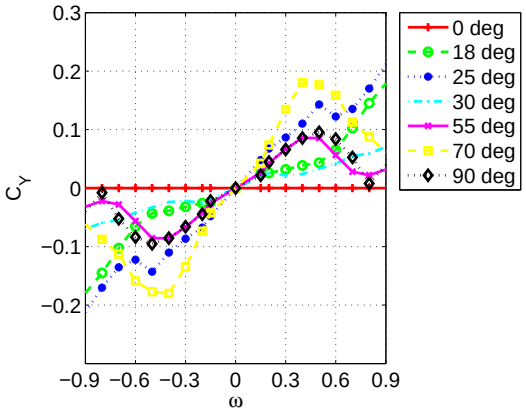

Figure 5.27: C_Y lookup table data used for full fuselage over the range $-0.9 < \omega < 0.9$ at seven values of α.

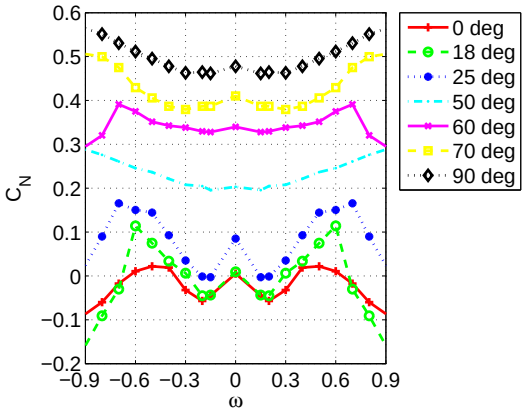

Figure 5.28: C_N lookup table data used for full fuselage over the range $-0.9 < \omega < 0.9$ at seven values of α.

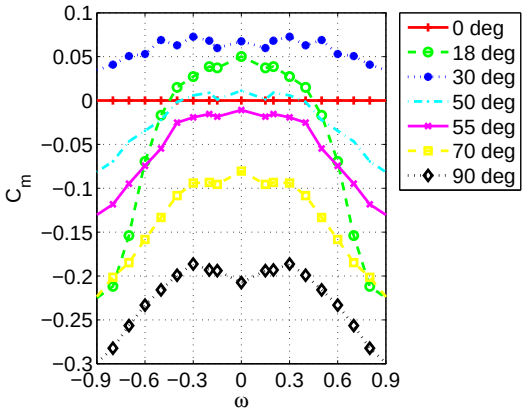

Figure 5.29: C_m lookup table data used for full fuselage over the range $-0.9 < \omega < 0.9$ at seven values of α.

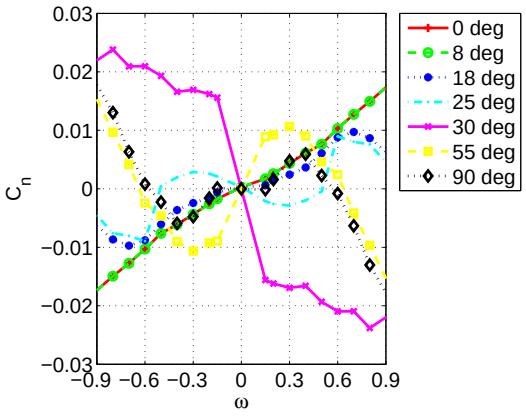

Figure 5.30: C_n lookup table data used for full fuselage over the range $-0.9 < \omega < 0.9$ at seven values of α.

5.6 Vertical Tail

The vertical tail is treated as a single element. A shielding term is incorporated to account for its residing in the wake of the horizontal tail at high α values, as demonstrated qualitatively numerous times in the literature, and quantitatively in Ref. [60]. Lookup table aerodynamic data for the undeflected vertical stabilizer was taken from Ref. [104], which provided data for semispan wings of $\mathcal{AR} = 2.0$ and 3.0 using the NACA 64A010 airfoil, $\lambda = 2$, and a sweep angle of 7 deg. These data were then averaged to approximate the $\mathcal{AR} = 2.5$ vertical stabilizer of the Aero Testbed. The same process and equations, which were used to create the airfoil data with deflected control surfaces, were also used to generate the deflection data for the vertical stabilizer, which has $c_f/c = 0.5$. Figures 5.31, 5.32, and 5.33 present the C_L, C_D, and $C_{M,c/4}$ values, respectively, which were used in the aerodynamic lookup tables for the vertical stabilizer. For completeness, Fig. 5.34 presents the lift-to-drag ratio of the vertical stabilizer over the full $-180 \leq \alpha \leq 180$ deg range.

The local flow at the vertical stabilizer $[u,v,w]_{vstab}$ was calculated using

$$u_{vstab} = u_{body,cg} + \left(q_{body,cg} z_{MAC_{vstab},cg}\right) - \left(r_{body,cg} y_{MAC_{vstab},cg}\right) \tag{5.36}$$

$$v_{vstab} = v_{body,cg} + \left(r_{body,cg} x_{MAC_{vstab},cg}\right) - \left(p_{body,cg} z_{MAC_{vstab},cg}\right) \tag{5.37}$$

$$w_{vstab} = w_{body,cg} + \left(p_{body,cg} y_{MAC_{vstab},cg}\right) - \left(q_{body,cg} x_{MAC_{vstab},cg}\right) \tag{5.38}$$

where $[x,y,z]_{MAC_{vstab},cg}$ are the x, y, and z distances from the vertical stabilizer MAC quarter chord to the airplane c.g. Because the vertical stabilizer is located on the aircraft centerline, $y_{MAC_{vstab},cg} = 0$ for the vertical stabilizer. A

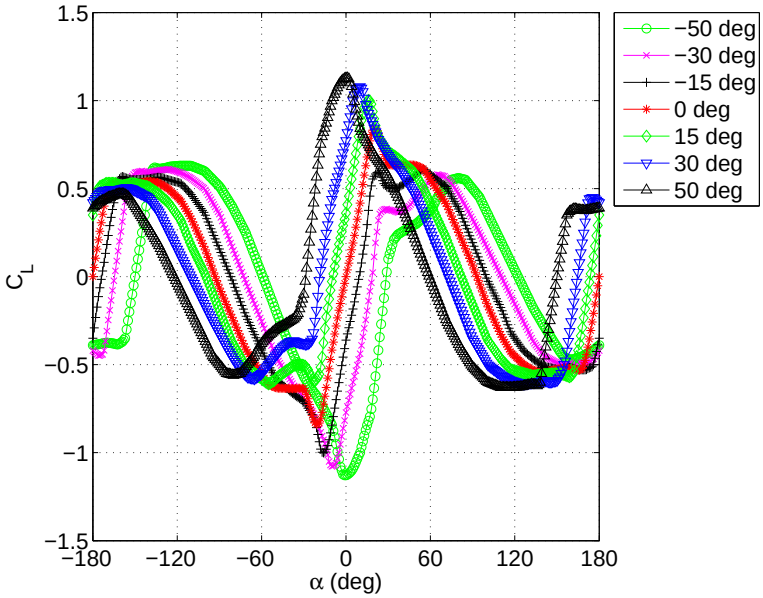

Figure 5.31: C_L lookup table data used for the vertical stabilizer over the range $-180 \leq \alpha \leq 180$ deg.

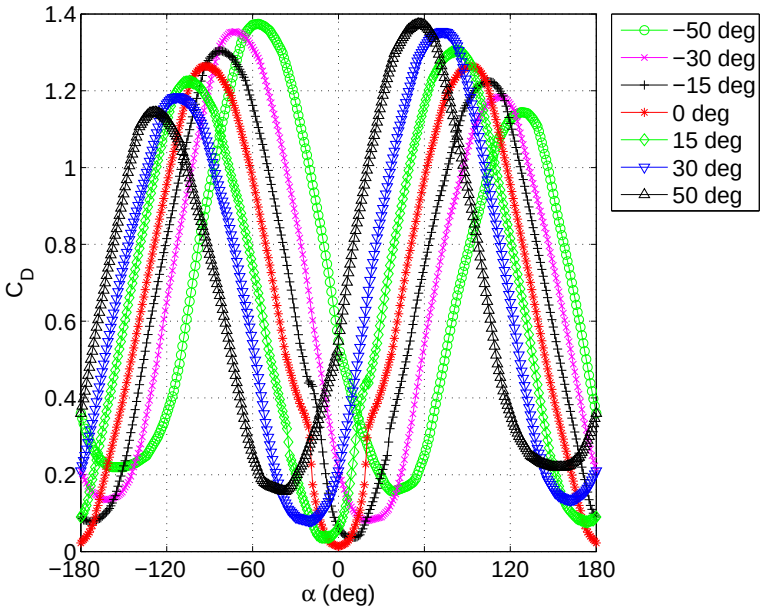

Figure 5.32: C_D lookup table data used for the vertical stabilizer over the range $-180 \leq \alpha \leq 180$ deg.

shielding term, due to the presence of the horizontal stabilizer, exists. The methodology used for shielding of the vertical stabilizer is described in detail in Section 5.8.

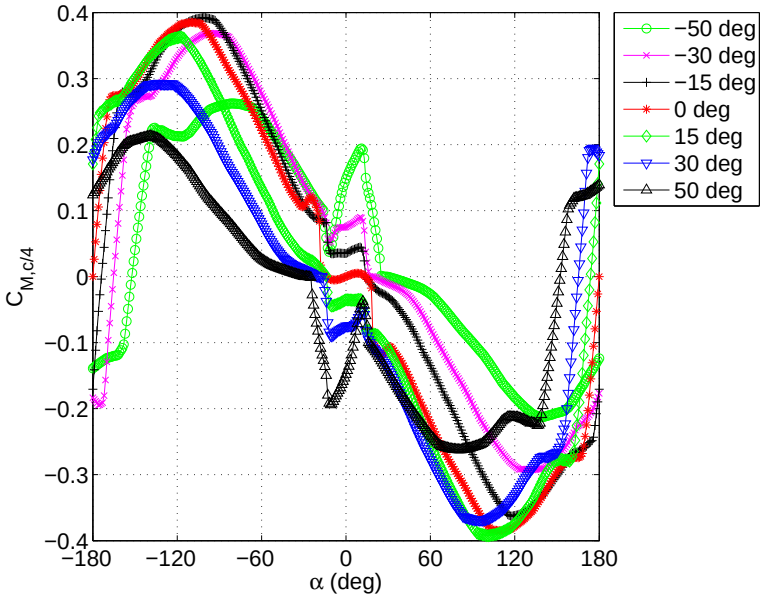

Figure 5.33: $C_{M,c/4}$ lookup table data used for the vertical stabilizer over the range $-180 \leq \alpha \leq 180$ deg.

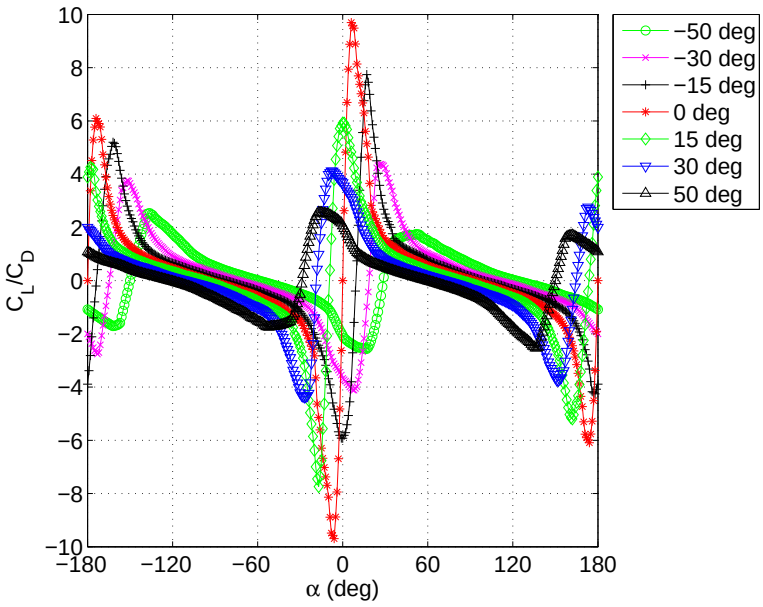

Figure 5.34: Plot of C_L/C_D for the vertical stabilizer over the range $-180 \leq \alpha \leq 180$ deg.

5.7 Horizontal Tail

The horizontal tail is treated as a single element surface based on the approach of Selig [95]. Lookup tables are based on data and the results of Refs. [95, 98, 105, 106]. Specifically, the lookup table data was taken from Ref. [104], which provided aerodynamic data for an $\mathcal{AR} = 4.5$ symmetric horizontal tail. The Aero Testbed horizontal tail has $\mathcal{AR} = 4.9$, and the aspect ratio of the NASA rotary balance models was approximately 4.5. When the C_L values were compared

with the $\mathcal{AR} = 2.5$ averaged data, as described in Section 5.6, and the raw experimental $\mathcal{AR} = 4.5$ data of Ref. [104], the values were nearly coincident. Since the c_f/c ratios are the same for both the horizontal and vertical tails, the same C_L data is used. The ratio of the drag values between the two data sets was approximately 1.05 because of the increase in $\mathcal{AR}$. Thus, all drag values were scaled accordingly to generate the horizontal stabilizer C_D data. To generate the moment coefficient, the calculated moments from the vertical stabilizer were multiplied by $[1 + 0.05\sin(\alpha)]$ in order to account for the same C_L values, but C_D values that were 5% greater. Figures 5.35, 5.36, and 5.37 present the lookup table data used for the horizontal tail.

The local flow at the horizontal stabilizer $[u, v, w]_{hstab}$ was calculated by

$$u_{hstab} = u_{body,cg} + \left(q_{body,cg} z_{MAC_{hstab},cg}\right) - \left(r_{body,cg} y_{MAC_{hstab},cg}\right) \tag{5.39}$$

$$v_{hstab} = v_{body,cg} + \left(r_{body,cg} x_{MAC_{hstab},cg}\right) - \left(p_{body,cg} z_{MAC_{hstab},cg}\right) \tag{5.40}$$

$$w_{hstab} = w_{body,cg} + \left(p_{body,cg} y_{MAC_{hstab},cg}\right) - \left(q_{body,cg} x_{MAC_{hstab},cg}\right) \tag{5.41}$$

where $[x, y, z]_{MAC_{hstab},cg}$ are the x, y, and z distances from the horizontal stabilizer MAC quarter chord to the airplane c.g. Because of the symmetry of the horizontal stabilizers, the left and right horizontal stabilizers will have negative and positive values of $y_{MAC_{hstab},cg}$, respectively.

While the data lookup tables for the zero control surface deflection were based on the experimental data of Koenig [104], the control surface-deflected data tables were synthesized based on the methodology and equations of McCormick [43], as described in the airfoil data section. Figures 5.35, 5.36, and 5.37 depict the aerodynamic lookup data tables of C_L, C_D, and $C_{M,c/4}$, which were developed for the horizontal stabilizer aerodynamic force calculation routines. Figure 5.38 presents the lift-to-drag ratio of the horizontal stabilizer over the full $-180 \leq \alpha \leq 180$ deg range.

5.8 Shielding Methodology for Vertical Stabilizer and Aft Fuselage

When an aircraft is in a normal, pre-stall, and low-rate flight regime, it is known that the horizontal tail is subjected to downwash from the wing. When an aircraft is in a high-α flight regime, the vertical tail may be located in the wake of the stalled wing. Consequently, when in the high-α, high-angular rate regime of a stall/spin, shielding exists among the tail surfaces. For example, if an airplane is in a 90-deg stall, and it has a tail with a low horizontal stabilizer, the vertical stabilizer would lie within the wake of the horizontal stabilizer. In this instance, the vertical stabilizer would not produce any appreciable control authority or forces. This wake is sometimes referred to as the "flow shadow" [95], and its effects are not limited to those of the horizontal tail on the vertical tail. Reviewing and inspecting NASA rotary balance data sets verifies this concept.

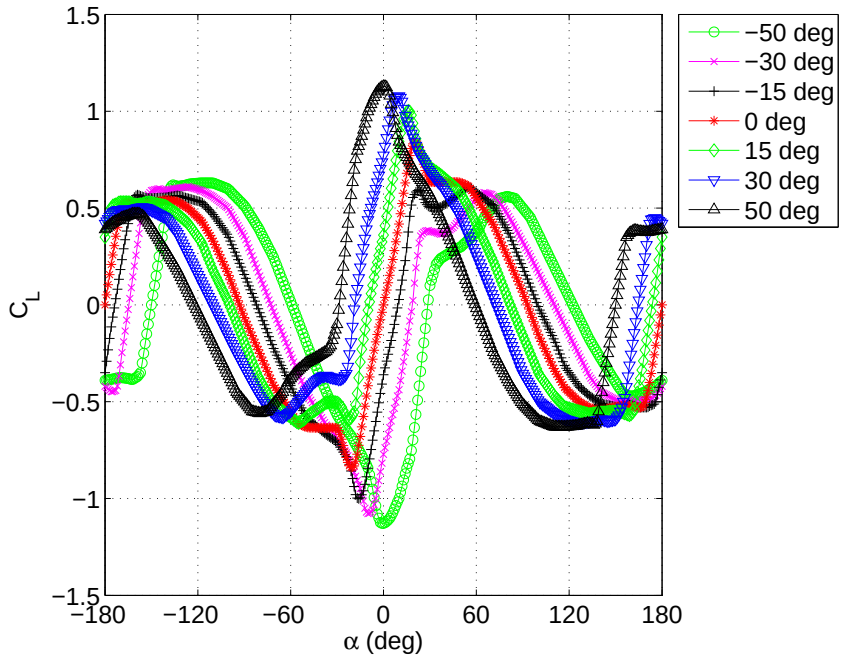

Figure 5.35: C_L lookup table data used for the horizontal stabilizer over the range $-180 \leq \alpha \leq 180$ deg.

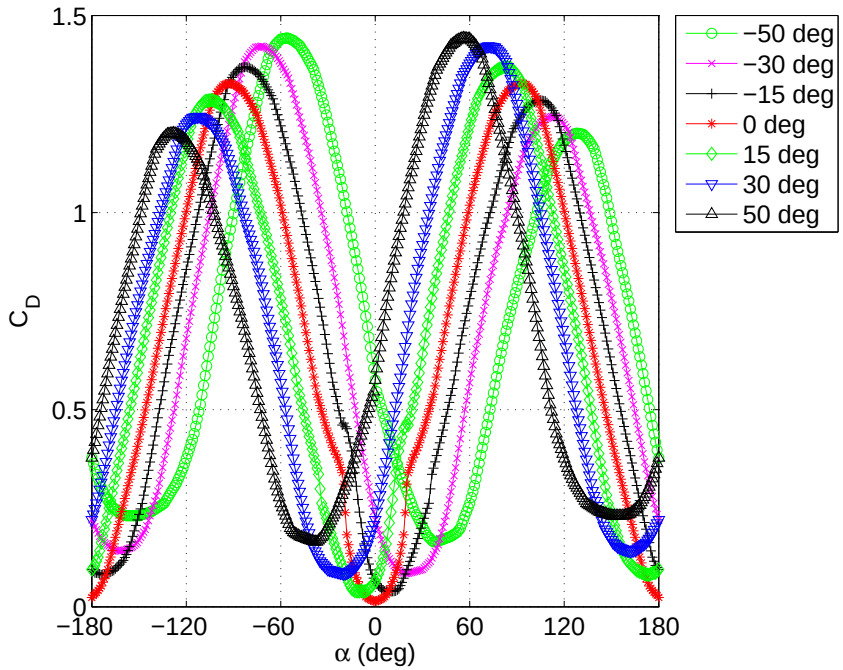

Figure 5.36: C_D lookup table data used for the horizontal stabilizer over the range $-180 \leq \alpha \leq 180$ deg.

The plethora of NASA rotary balance data sets provides a great resource for adjusting the shielding of components by the wing and the horizontal stabilizer. For example, the fuselage-only data have a small variation in yaw coefficient as the spin parameter increases. Adding the wing increases the yaw moment coefficient because the wing contributes

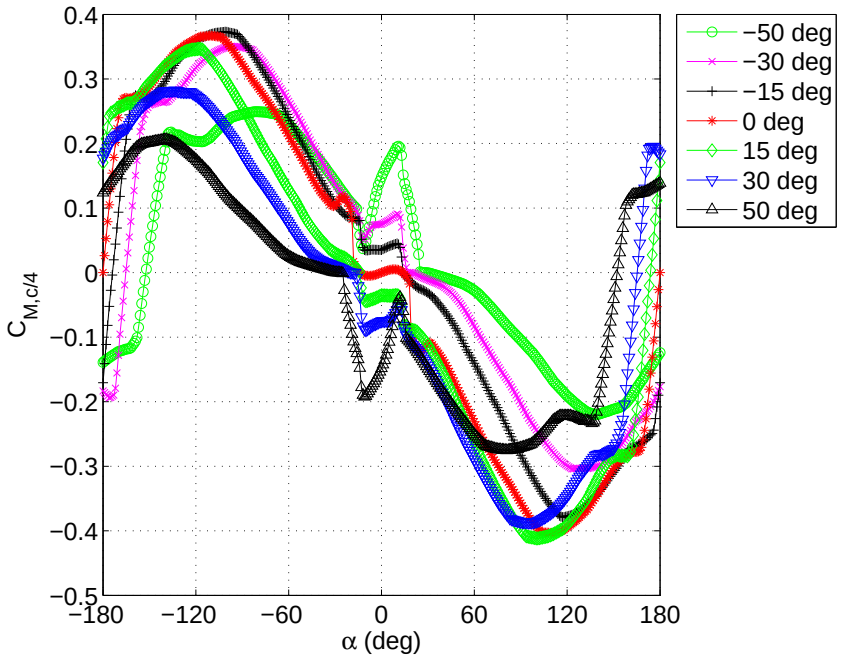

Figure 5.37: $C_{M,c/4}$ lookup table data used for the horizontal stabilizer over the range $-180 \leq \alpha \leq 180$ deg.

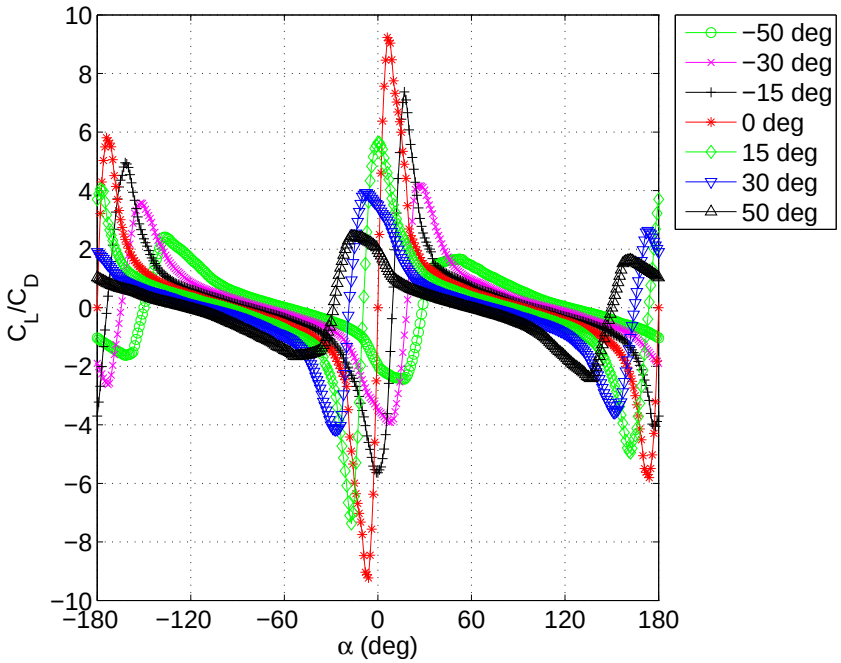

Figure 5.38: Plot of C_L/C_D for the horizontal stabilizer over the range $-180 \leq \alpha \leq 180$ deg.

its yaw moment to the body. The addition of the wing also shifts the peak yaw moment coefficients to lower spin parameter values, showing that at $\omega \approx 0.5$, a degree of fuselage shielding, is present. Without the wing, the yaw moment coefficient changes slope at $|\omega| \approx 0.4$, while with the wing, the slope changes at $|\omega| \approx 0.15$.

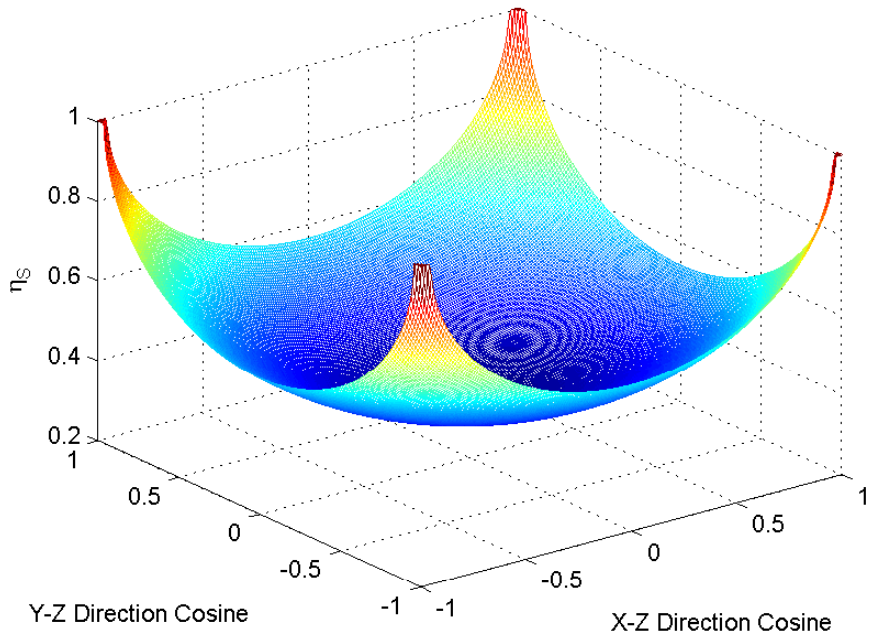

Figure 5.39: Flow shadow map used to model the vertical stabilizer of the Extra 260 Aero Testbed aircraft.

In contrast to using a shielded area method, as suggested by the definition of the Tail Damping Power Factor from early NASA spin studies, the dynamic pressure scaling method of Selig [95] was used, as defined by

$$\eta_S = \frac{V_{R,local}}{V_{R,total}} \tag{5.42}$$

where $V_{R,local}$ is the flow velocity experienced by the vertical stabilizer, and $V_{R,total}$ is the local flow condition, as determined by the airplane velocity and angular rates.

For the reasons described above, two different flow shadow maps were initially used to model the shielding of the vertical stabilizer by the horizontal stabilizer, as well as the shielding of the aft fuselage by the wing wake. Later investigations showed that a flow shadow map was not necessary for the fuselage. The dynamic pressure of the fuselage remained unscaled, but the SpinSim code retained the capability to easily add a scaling function, if necessary, for future spin simulation investigations. Figure 5.39 presents the flow shadow map used to model the Aero Testbed in SpinSim. Equation 5.43 defines the vertical stabilizer flow shadow map of η_S by

$$\eta_S = 1 - \sqrt{0.65 - 0.21u_1^2 - 0.232v_1^2} \tag{5.43}$$

where

$$u_1 = \cos\left(\arctan\frac{w}{u}\right) \tag{5.44}$$

and

$$v_1 = \cos\left(\arctan\frac{w}{v}\right) \tag{5.45}$$

The value η_S can vary from zero (stagnant local flow) to 1 (no shielding present) [95]. In the case of the vertical stabilizer, low direction cosines (large angles near 90 deg) in the x-z and y-z directions yield η_S values approaching the function minimum. Large directional cosines, which correspond to small angles, have η_S values closer or equal to unity, which corresponds to no shielding of the freestream flow. This shielding method differs slightly from what Selig [95] proposed, in that the unit velocity vector projection onto the hemispherical surface methodology is not used. Thus, the flow shadow shapes are not necessarily located at the end of a unit vector. Based on a y-z flow direction cosine u_1 and an x-z flow direction cosine v_1, a single unique η value exists. High y-z direction cosines correspond to a high sideslip condition or a high yaw rate. Additional tail shielding inputs include a reduction in q on the horizontal stabilizer that is shielded by the vertical stabilizer, as well as the aft fuselage, because of yaw (i.e., the leeward horizontal stabilizer). In a positive yaw rate case, the right horizontal stabilizer is partially shielded by the vertical stabilizer. In a negative yaw rate case, the left horizontal stabilizer encounters a reduced q. This concept has an effect on the airplane roll moment in the developing spin regime. The other tail shielding input is the changing of the moment arm upon which the vertical stabilizer force acts, which primarily affects the rolling moment in a developed spin. As the vertical stabilizer is increasingly shielded by the conventional tail (i.e., an empennage with the horizontal stabilizer located at the bottom of the vertical tail), the unshielded portion of the vertical stabilizer is increasingly near the top. Thus, it is reasonable that as the effectiveness of the vertical stabilizer is reduced because of shielding by the horizontal stabilizer, and the magnitude of the side force and yaw moment is reduced by the lower q, the vertical moment arm, upon which the side force acts to contribute to the airplane rolling moment, increases. This increase in the vertical moment arm of the vertical stabilizer helps to reduce the degree to which the roll moment of the vertical stabilizer decreases as the shielding of the stabilizer increases.

5.9 Modeling Results

The general theory behind an analytical model is typically validated with the presentation of experimental results. The figures in this section compare the computational results of the current model to experimental data sets from the wind tunnel tests of Chapter 4. The general conclusion from these figures is that the current model is able to model

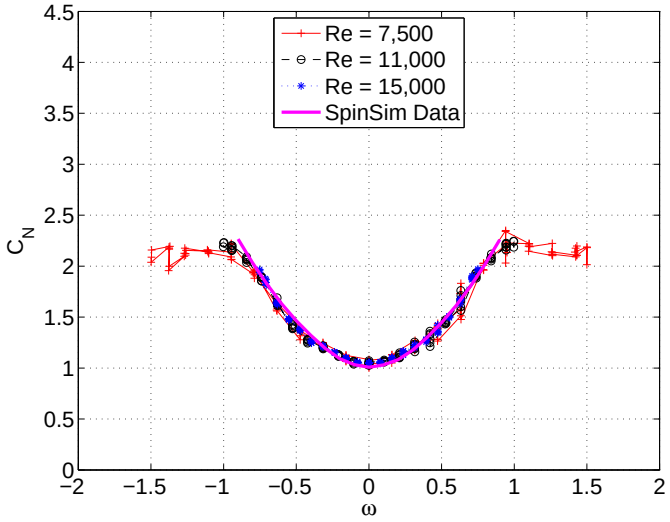

Figure 5.40: Plot of C_N versus ω for the $\mathcal{AR} = 2.55$ wing of Table 4.1 at three experimentally-measured *Re* values compared with analytically-modeled results using SpinSim.

the experimentally measured increase in C_N across a wide range of ω and θ values. The figures demonstrate that wings with different planforms (namely different values of $\mathcal{AR}$) exhibit different growth rates with respect to ω, and the current model is able to capture those different growth rates. This ability to capture the different aspect ratio-dependent growth rates is attributable to the incorporation of the empirical entrainment factor into the ΔC_N correction equation of Eq. 5.8.

5.9.1 SpinSim Simulation of Wing-Only Wind Tunnel Tests

In this section, plots are presented for the SpinSim simulations of the actual wind tunnel test articles, whose testing was documented in Chapter 4. Figure 5.40 presents a comparison of wind tunnel C_N experimental data at three Reynolds numbers for the $\mathcal{AR} = 2.55$ spinning wing test article compared with the SpinSim simulation of that same wing. The SpinSim simulation is performed over the range $-0.9 < \omega < 0.9$, as that is the range of ω values found in the NASA rotary balance data sets. This range is also the range over which the empirical entrainment factor $w_2(y)$ was calculated.

As depicted in Fig. 5.40, excellent agreement between SpinSim and the experimental results is demonstrated. The increase in C_N from a stationary wing is accurately captured over the range of $-0.75 < \omega < 0.75$, at which point the rate of growth of C_N decreases, and it rapidly levels off. This rate of growth decrease and leveling-off, at such a low magnitude of ω, is due to the low aspect ratio of the wing. Equation 5.8 does not capture its effect nor does strip theory. Figures 5.41–5.44 present similar coplotting of experimental wind tunnel and SpinSim computational results for wing test articles of aspect ratios 3.85, 4.85, 6.50, and 8.33, respectively.

As demonstrated in Figs. 5.41–5.44, there is an excellent agreement between SpinSim simulations and experimental wind tunnel test data. The C_N vs. ω curves of the wind tunnel data and simulations are nearly coincident.

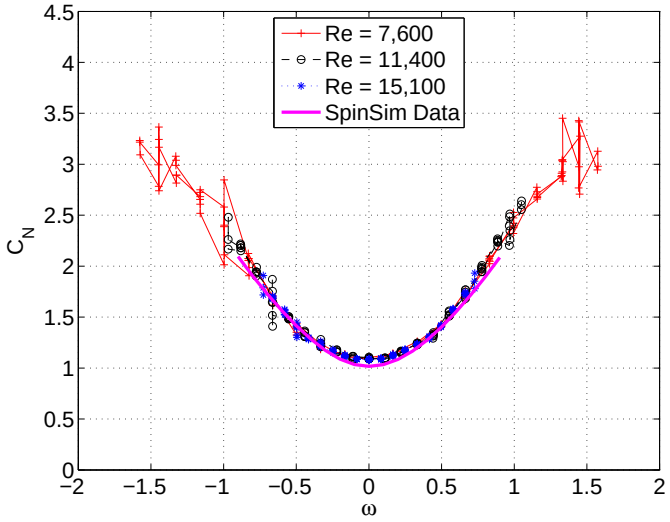

Figure 5.41: Plot of C_N versus ω for the $\mathcal{AR} = 3.85$ wing of Table 4.1 at three experimentally-measured *Re* values compared with analytically-modeled results using SpinSim.

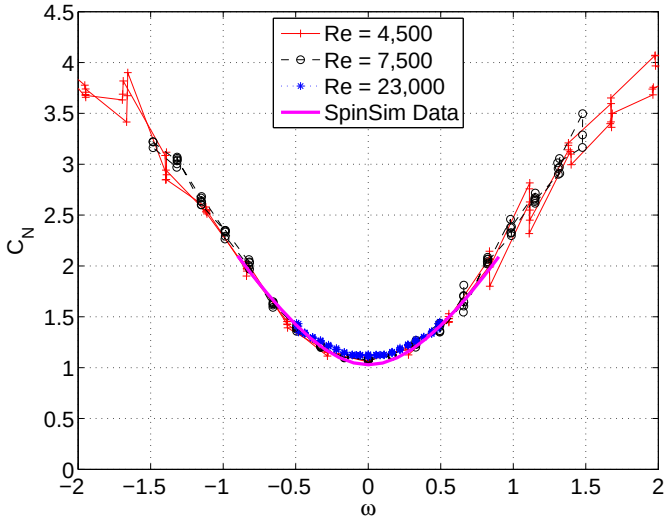

Figure 5.42: Plot of C_N versus ω for the $\mathcal{AR} = 4.85$ wing of Table 4.1 at three experimentally-measured *Re* values compared with analytically-modeled results using SpinSim.

While minor differences between the simulation and experimental C_N data exist, and with a maximum difference of approximately 0.08 between experimental and simulation occurring for the $\mathcal{AR} = 4.85$ wing at $\omega = 0$, these differences are small. Further, they do not preclude the SpinSim modeling methodology from capturing the large-scale trend of the C_N growth due to changes in ω. This excellent agreement is due to the addition of the empirical entrainment factor (as opposed to the initial constant wing tip value of $w_2(\pm b/2) = 2.5$). This excellent agreement is also achieved as the tests are for wing-only configurations, where no wing-body interactions are present.

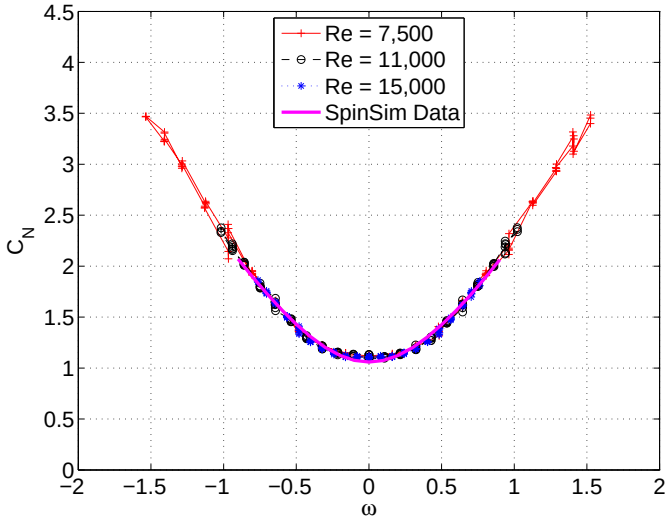

Figure 5.43: Plot of C_N versus ω for the $\mathcal{AR} = 6.50$ wing of Table 4.1 at three experimentally-measured *Re* values compared with analytically-modeled results using SpinSim.

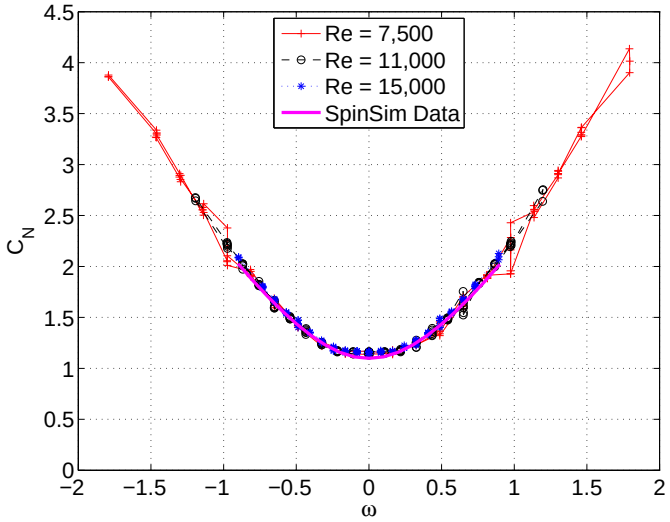

Figure 5.44: Plot of C_N versus ω for the $\mathcal{AR} = 8.33$ wing of Table 4.1 at three experimentally-measured *Re* values compared with analytically-modeled results using SpinSim.

5.9.2 Full Airplane C_N Comparisons

The results of adding Eq. 5.8 to a strip theory-based force simulator of a spinning low-wing single-engine GA airplane with $\mathcal{AR} = 5.9$ and $\lambda = 1$ are presented in Fig. 5.45. Those results are compared with the experimental data of Ref. [38]. Strong agreement between the analytical model and experimental results is obtained for all four values of θ. While the analytical curves are symmetric about the *y*-axis, some variation is observed in the curves of the experimental data. This variation is due to inaccuracies and inconsistencies between the test runs. A gull-wing effect is slightly evident in the results. This gull-wing effect is characterized by a slight increase in analytical results for C_N from $\omega = 0$ until

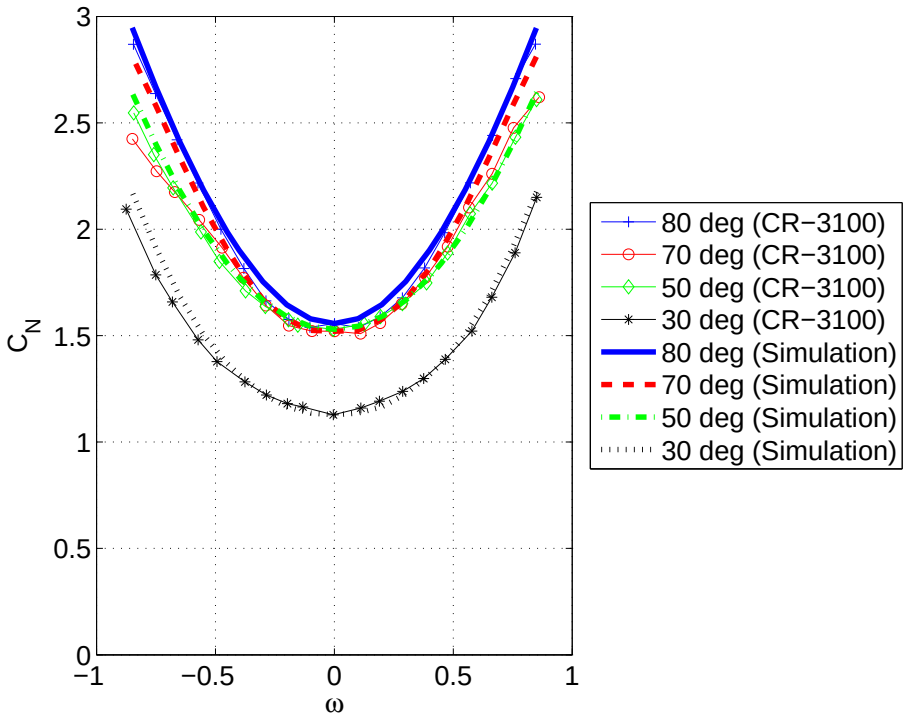

Figure 5.45: Plot of C_N versus ω for $R_s = 0$ at four analytically-modeled θ values compared with the rotary balance data of the low-wing general aviation full-airplane configuration of Ref. [38] with $\mathcal{AR} = 5.9$ and $\lambda = 1$.

$|\omega| = 0.1$, a decrease in C_N through $|\omega| = 0.2$, and an increase in C_N over the remaining range of ω. This gull-wing effect of the experimental results is somewhat more prominent at $\theta = 80$, 70, and 50 deg, for values of $|\omega| \leq 0.2$.

Results of a validation test of the analytical simulation method of this research, against the tapered wing of Ref. [37] with $\lambda = 0.5$ and $\mathcal{AR} = 6.21$, are presented in Fig. 5.46. Similarly strong agreement and general features of Fig. 5.45 are present in Fig. 5.46, although the taper ratio of the wing is different. This difference in the wing taper ratio results in a slower C_N growth rate with increasing $|\omega|$. The gull-wing effect is manifested experimentally for θ values of 70 and 55 deg, for values of $|\omega| \leq 0.2$. While a good fit to the growth rate of the experimental data is observed at high values of θ, the simulations of C_N at $\theta = 30$ deg grow slightly more rapidly than the experimental data. Again, this is not an artifact of the spin correction to C_N of Eq. 5.8, rather, it is an artifact of the strip theory-based calculations, which are not the subject of this research.

When comparing Figs. 5.45 and 5.46, it may be observed that the C_N values generally grow at a much higher rate in the former figure and result in a taller and narrower parabola shape. This more rapid growth, as a function of ω, is accounted for by the differences in the aircraft wing planform, namely the taper ratio λ, and the lack of taper in the wing of Fig. 5.45. The regions of the wing experiencing the highest local velocity and q are located furthest outboard. In the case of the tapered wing of Fig. 5.46, the outboard regions of the wing have smaller chord lengths. Therefore, they produce a smaller amount of lift. As λ increases towards unity, the outboard wing sections contribute a larger

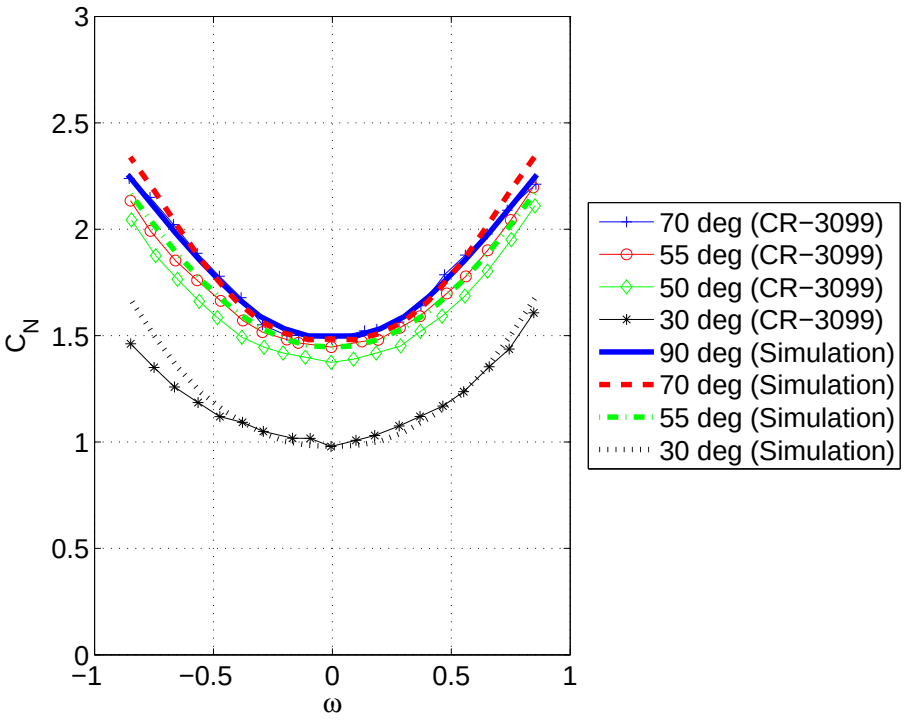

Figure 5.46: Plot of C_N versus ω for $R_s = 0$ at four analytically-modeled θ values compared with the rotary balance data of the low-wing single-engine trainer full-airplane configuration of Ref. [37] with $\mathcal{AR} = 6.21$ and $\lambda = 0.5$.

portion of the total C_N. Thus, the parabola-like C_N vs. ω curve will grow at a more rapid rate as λ approaches unity. A similar effect of an increased rate of growth is also observed for a decreasing $\mathcal{AR}$ value, as discussed previously in Chapter 4.

Figures 5.47–5.54 present plots of the normal force coefficient C_N, versus the spin parameter ω, for an additional eight rotary balance data sets. These plots compare the values, which are calculated by using the proposed methodology to experimental rotary balance data sets, and demonstrate satisfactory agreement between the simulation and experimental data. These plots demonstrate that, as wing parameters, such as twist and taper change the shape of the C_N vs. ω curve, the SpinSim force calculation methodology is able to capture and accurately simulate those effects. For all eight of these figures with four curves modeled in each, large disagreements are only seen in two of the 24 curves. Figure 5.52 shows disagreement between the NASA experimental data set and SpinSim simulation at $\theta = 30$ deg for values of $|\omega| > 0.5$. Figure 5.51 exhibits minor disagreement between the experimental data set and simulation, which is also at $\theta = 30$ deg over the range $-0.5 < \omega < 0.5$. Notably, these simulations of C_N are for a full-airplane configuration. Thus, any discrepancies, especially in the case of Fig. 5.51, may be due to components of the airplane other than the wing, namely the fuselage. As described in the literature, whether a fuselage has a flat or rounded bottom can have a significant effect on the spin characteristics, and, consequently, the body-normal forces of an airplane.

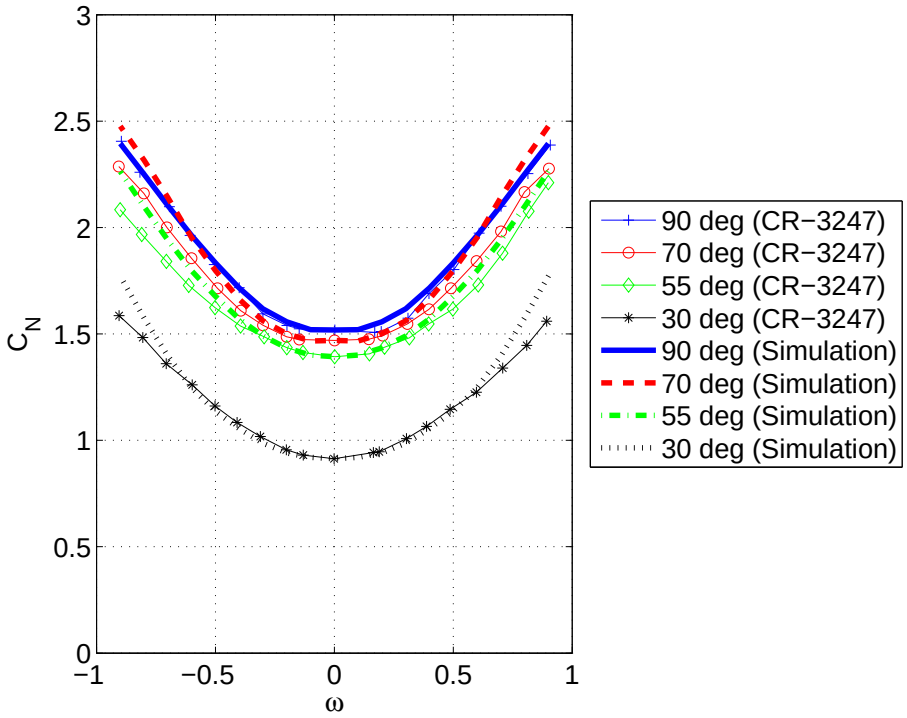

Figure 5.47: Plot of C_N versus ω for $R_s = 0$ at four analytically-modeled θ values compared with the rotary balance data of the low-wing general aviation full-airplane configuration of Ref. [31] with $\mathcal{AR} = 7.24$ and $\lambda = 0.67$.

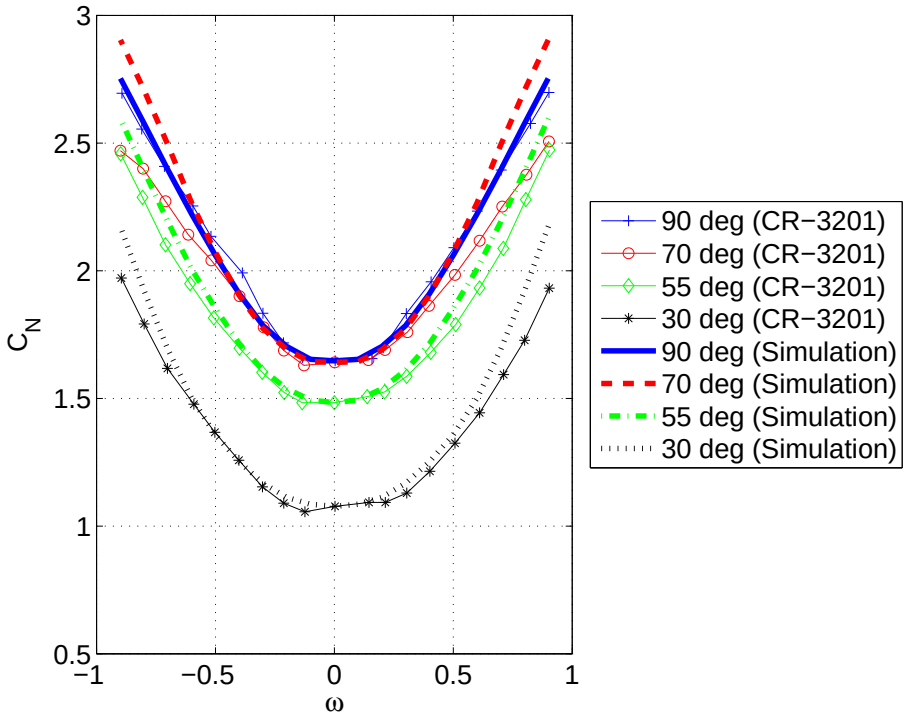

Figure 5.48: Plot of C_N versus ω for $R_s = 0$ at four analytically-modeled θ values compared with the rotary balance data of the high-wing general aviation full-airplane configuration of Ref. [41] with $\mathcal{AR} = 7.4$ and $\lambda = 1$.

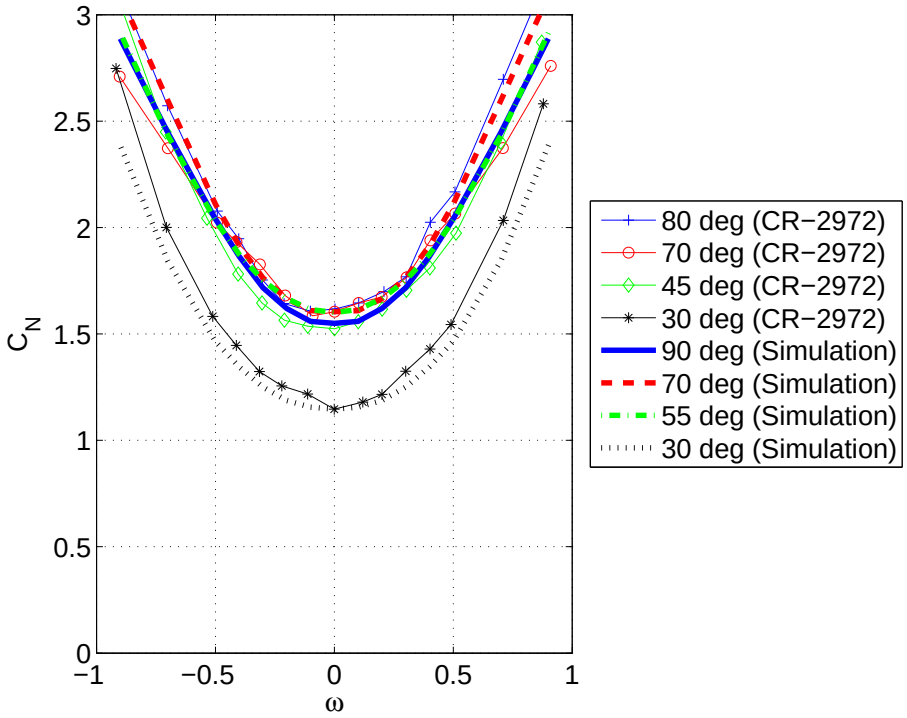

Figure 5.49: Plot of C_N versus ω for $R_s = 0$ at four analytically-modeled θ values compared with the rotary balance data of the low-wing general aviation full-airplane configuration of Ref. [33] with $\mathcal{AR} = 5.9$ and $\lambda = 1$.

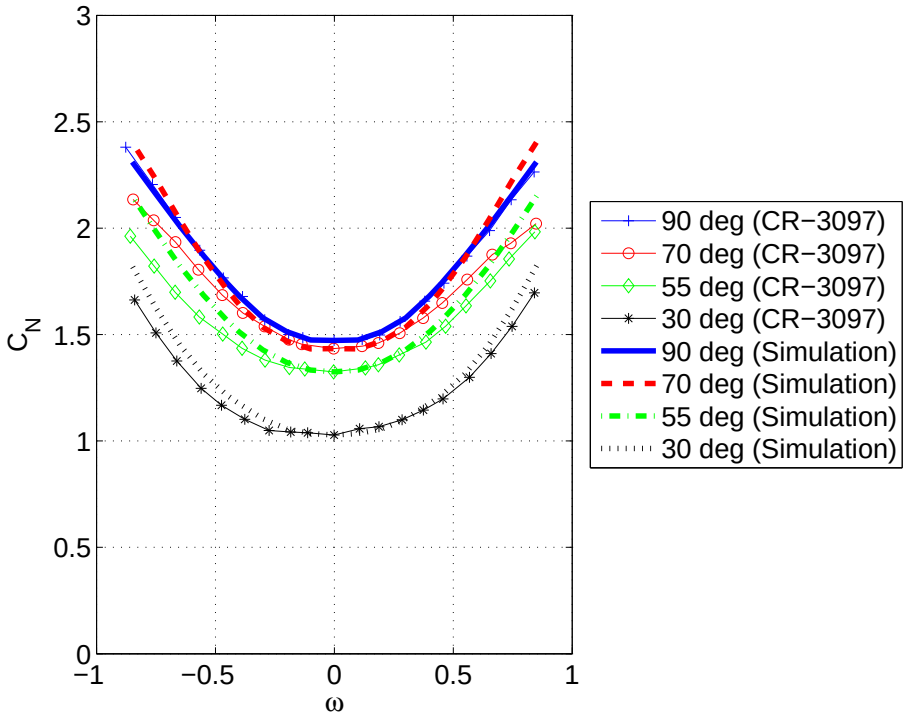

Figure 5.50: Plot of C_N versus ω for $R_s = 0$ at four analytically-modeled θ values compared with the rotary balance data of the high-wing general aviation full-airplane configuration of Ref. [36] with $\mathcal{AR} = 7.37$ and $\lambda = 0.70$.

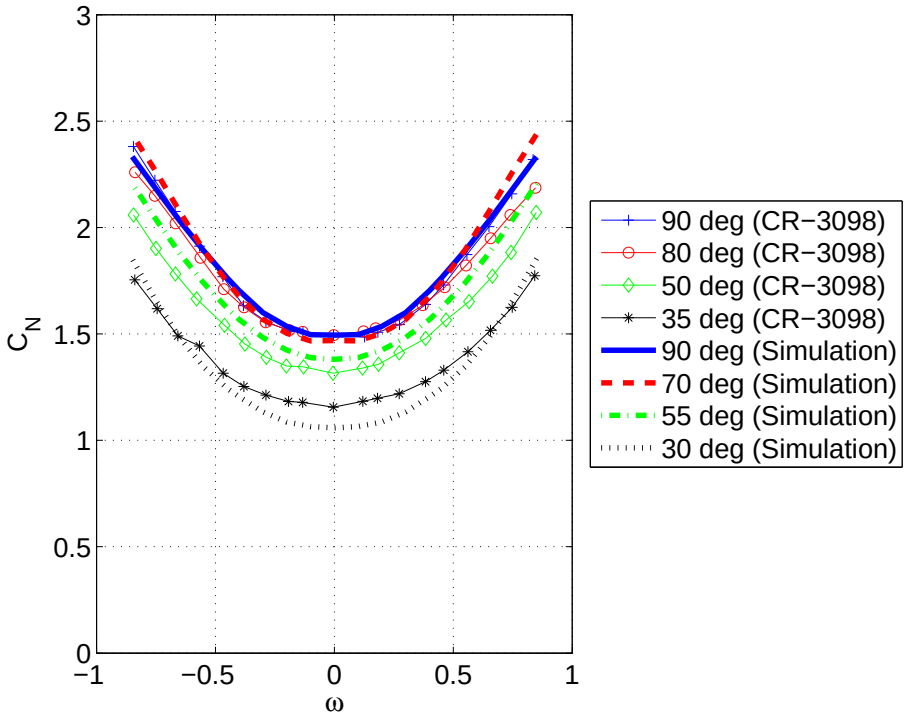

Figure 5.51: Plot of C_N versus ω for $R_s = 0$ at four analytically-modeled θ values compared with the rotary balance data of the low-wing general aviation full-airplane configuration of Ref. [42] with $\mathcal{AR} = 7.37$ and $\lambda = 0.70$.

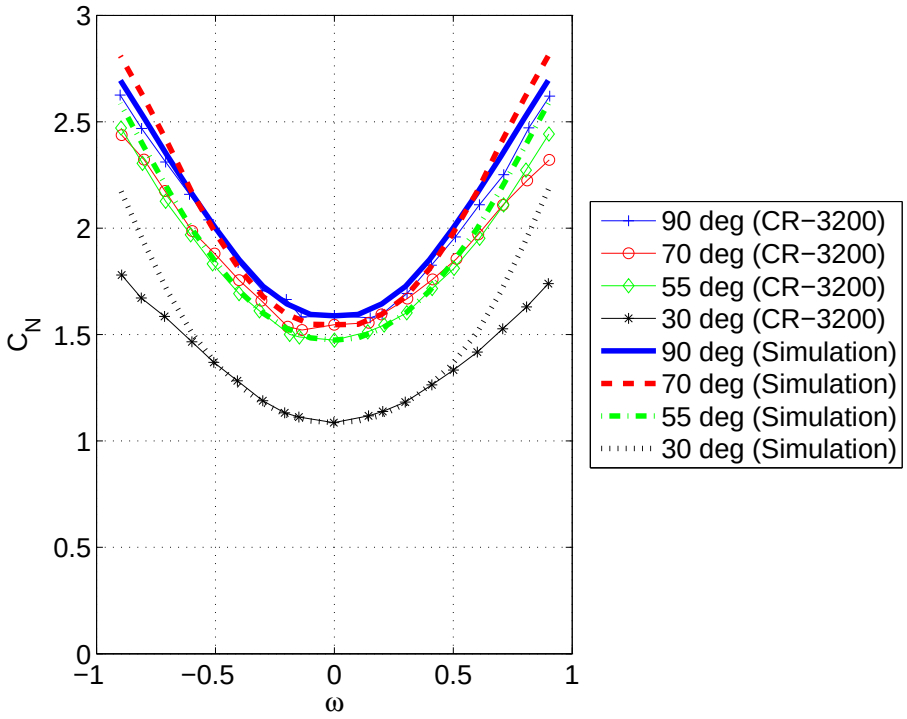

Figure 5.52: Plot of C_N versus ω for $R_s = 0$ at four analytically-modeled θ values compared with the rotary balance data of the low-wing general aviation full-airplane configuration of Ref. [40] with $\mathcal{AR} = 7.4$ and $\lambda = 1$.

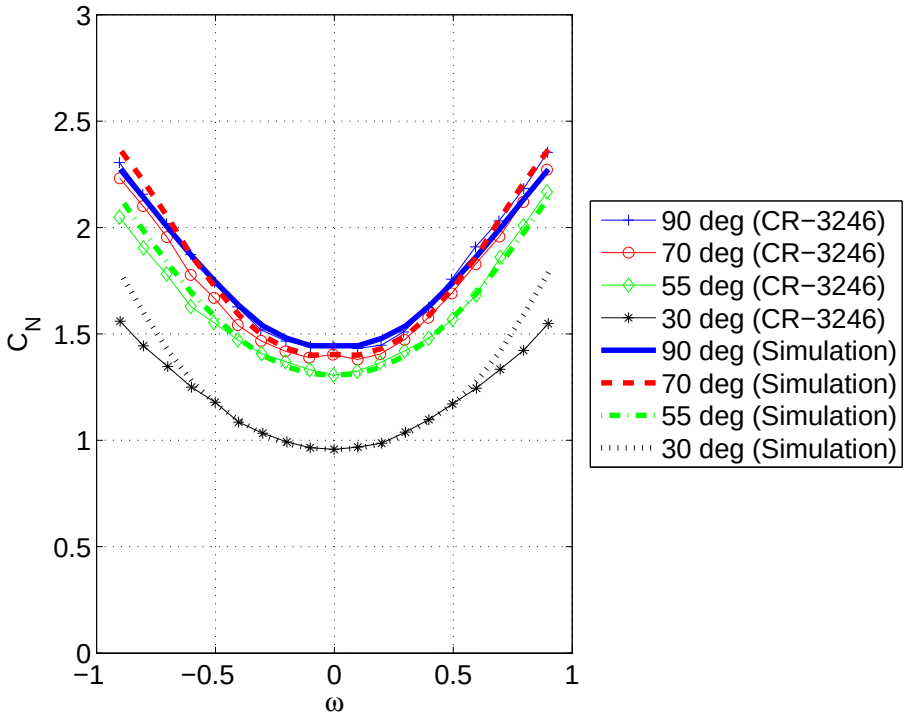

Figure 5.53: Plot of C_N versus ω for $R_s = 0$ at four analytically-modeled θ values compared with the rotary balance data of the low-wing general aviation full-airplane configuration of Ref. [30] with $\mathcal{AR} = 7.24$ and $\lambda = 0.67$.

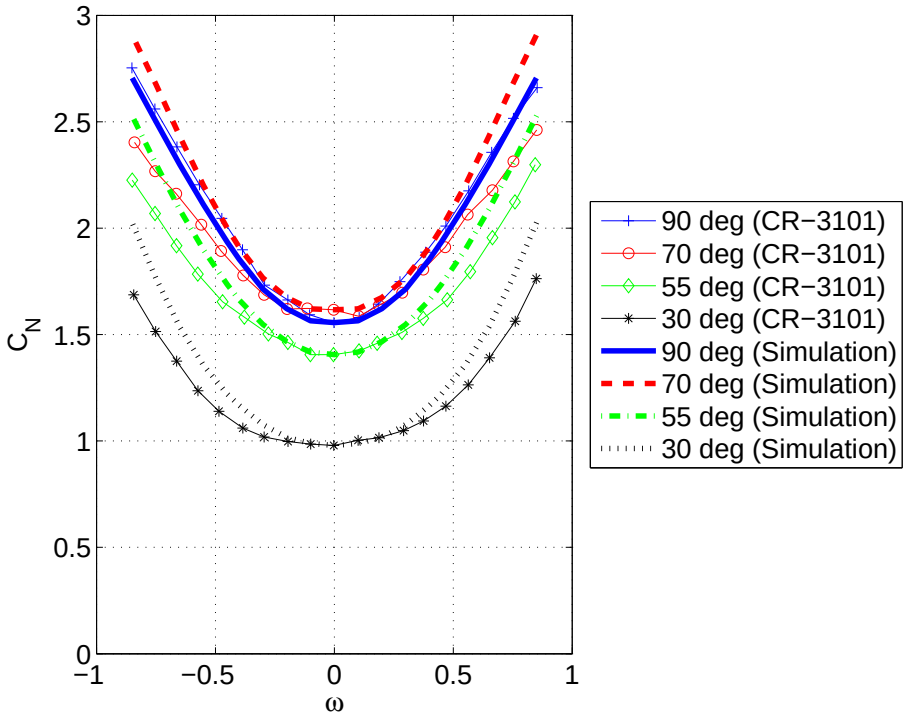

Figure 5.54: Plot of C_N versus ω for $R_s = 0$ at four analytically-modeled θ values compared with the rotary balance data of the high-wing general aviation full-airplane configuration of Ref. [39] with $\mathcal{AR} = 5.9$ and $\lambda = 1$.

5.9.3 Comparison of Proposed Analytical Wing Model to Current State of the Art

In this section, results are presented for the SpinSim simulations of the increase in the normal force coefficient C_N of the ten NASA rotary balance data sets, over the α range of $30 < \alpha < 90$ deg, and spin parameter values of $-0.9 \leq \omega \leq 0.9$. These simulated values are compared with those predicted by the method of McCormick [46] in Eq. 1.3, and the root mean square (RMS) error between simulation and experimental data set values is calculated. The RMS error is defined by

$$RMS = \sqrt{\frac{\sum_{i=1}^{n} (\bar{y}_i - y_i)^2}{n}} \tag{5.46}$$

where $\bar{y}_i$ is the experimental value for C_N, y_i is the analytically-modeled ΔC_N value, and n is the number of data points in the compared data sets. Figures 5.55 and 5.56 present comparisons of the RMS error across ten experimental data sets of a strip theory-based force calculator using Eq. 5.8 to correct for rotational effects, and a force calculator using Eq. 1.2 [46] to correct for rotational effects. The first approach, labeled "Simulation," corrects the strip theory-based force calculator with Eq. 5.8 (i.e., SpinSim is used as-is to calculate the force), the proposed analytical methodology derived in this research, and will, henceforth, be referred to as the current model. The second approach, labeled "Literature," corrects the strip theory force calculator of SpinSim with Eq. 1.2 (instead of using Eq. 5.8), which represents the current state of the art, and it will be referred to as the McCormick model. These results are compared over the full ω range of $-0.9 \leq \omega \leq 0.9$ and the high-ω range of $|\omega| > 0.5$. This high-ω range is important because improving the fidelity of force models at high magnitudes of ω can allow for the expansion of the range over which spins may be accurately modeled. This expanded modeling range may, consequently, reduce the range over which potentially dangerous full-scale flight tests or expensive dynamically-scaled spin tunnel tests must be performed.

Predictions from the current model at $\theta = 30$ deg were not as accurate as those from the McCormick model, exhibiting higher RMS error values when the aircraft of Ref. [33] was simulated (Fig. 5.55a). The fact that SpinSim only had higher RMS error values at $\theta = 30$ deg is a significant result, because prior to the addition of the empirical entrainment factor, the as-is SpinSim code had higher RMS error values at three of the four pitch angles, and it demonstrated only a slightly lower RMS error for $\theta = 90$ deg. This finding was to be expected, however, as the McCormick model was devised to provide a stall/spin correction to a strip-theory simulation of, and validated only against, the experimental data of Ref. [33].

Lower RMS error values were demonstrated by the current model for all of the other nine data sets, and at all four angles of attack, for both the full and limited ranges of ω. In summary, the current model of Eq. 5.8 produced lower RMS error values than the McCormick model of Eq. 1.2 for 78 out of the 80 total cases. This demonstrates an across-the-board improvement over the current state of the art and was only possible with the addition of the wind tunnel

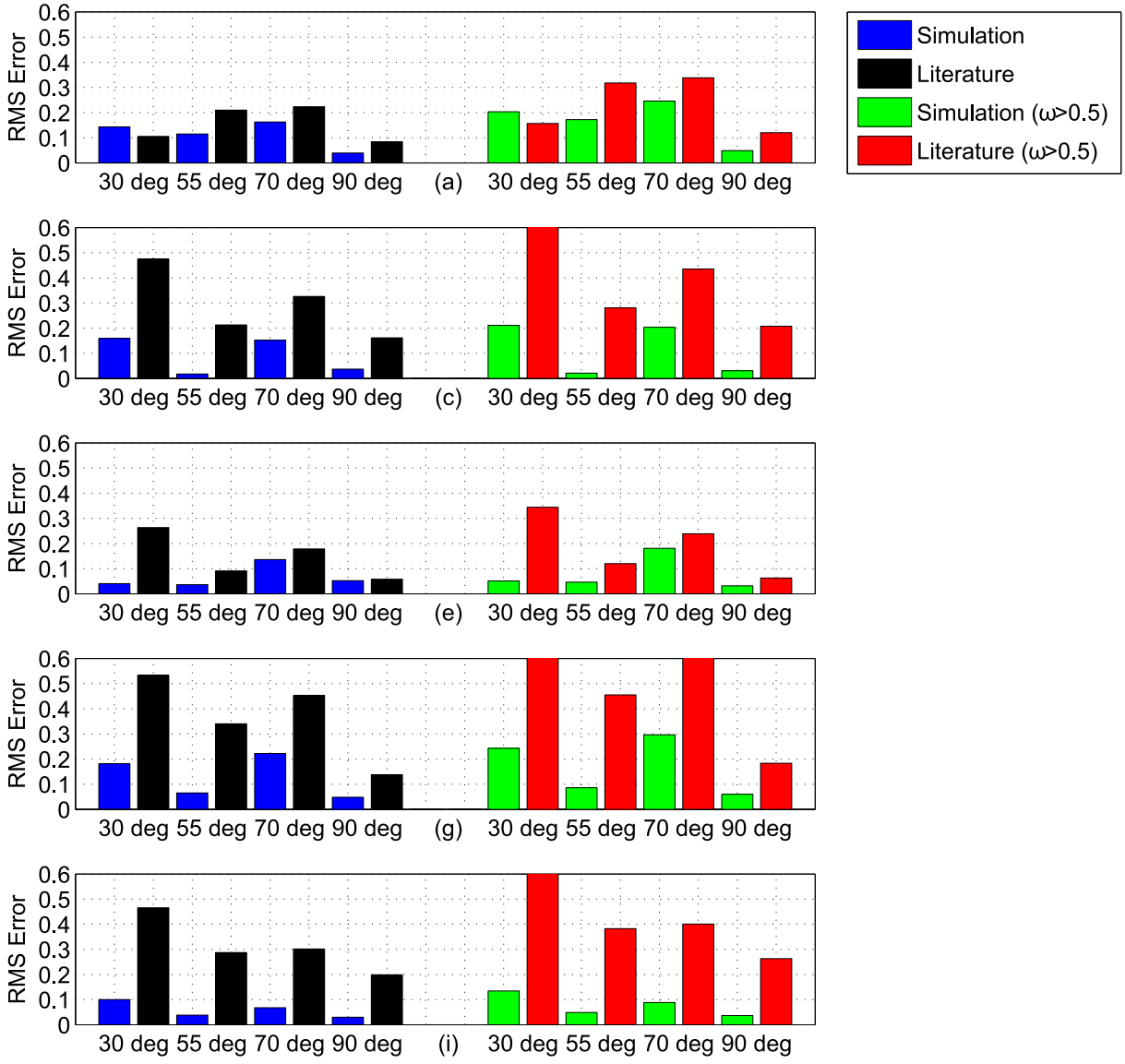

Figure 5.55: Comparison of RMS error values of SpinSim C_N correction (Eq. 5.8) and the current state of the art (Eq. 1.2) in predicting C_N over the five experimental rotary balance data sets of (a) CR-2972, (c) CR-3098, (e) CR-3100, (g) CR-3200, and (i) CR-3246.

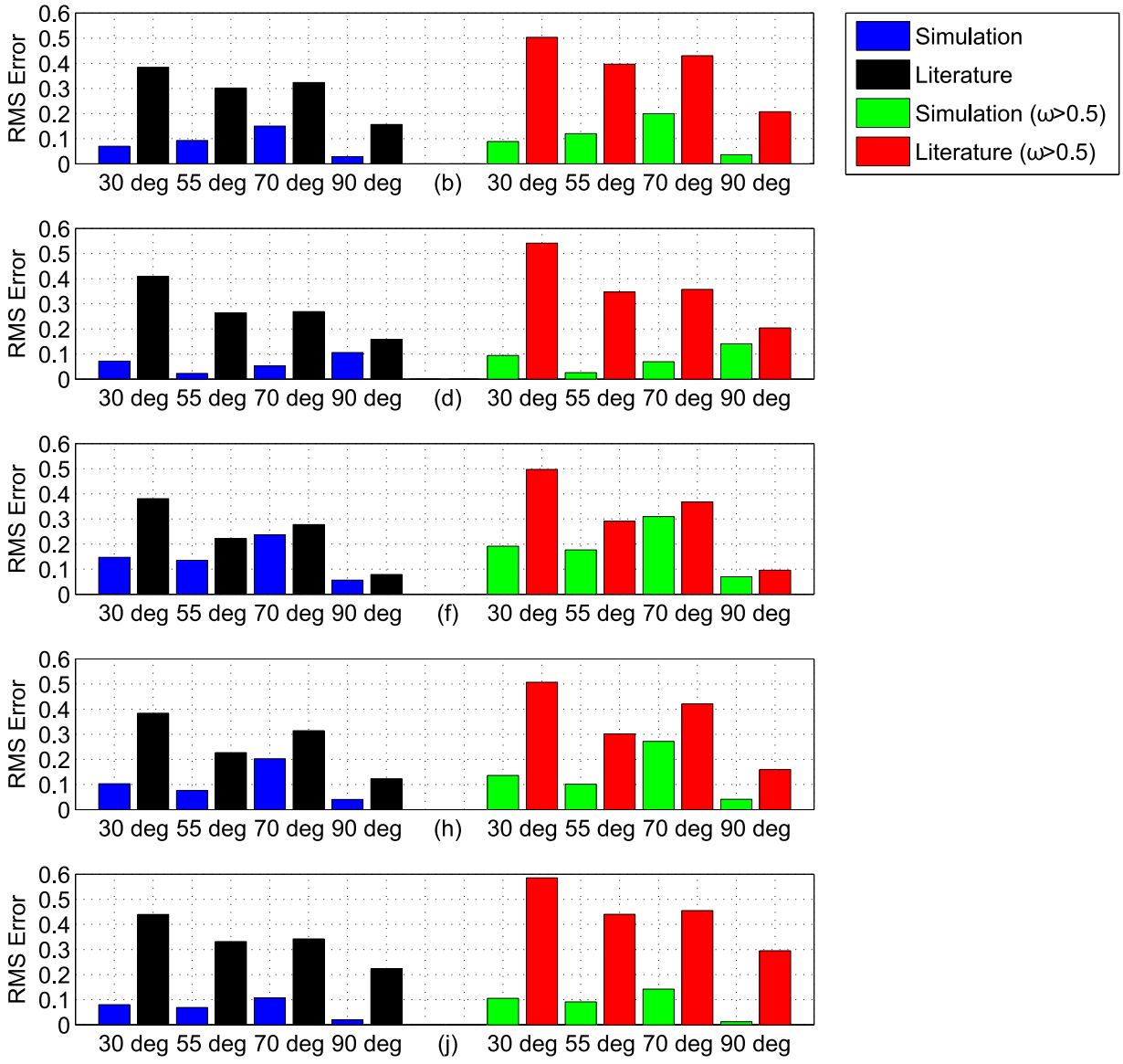

Figure 5.56: Comparison of RMS error values of SpinSim C_N correction (Eq. 5.8) and the current state of the art (Eq. 1.2) in predicting C_N over the five experimental rotary balance data sets of (b) CR-3097, (d) CR-3099, (f) CR-3101, (h) CR-3201, and (j) CR-3247.

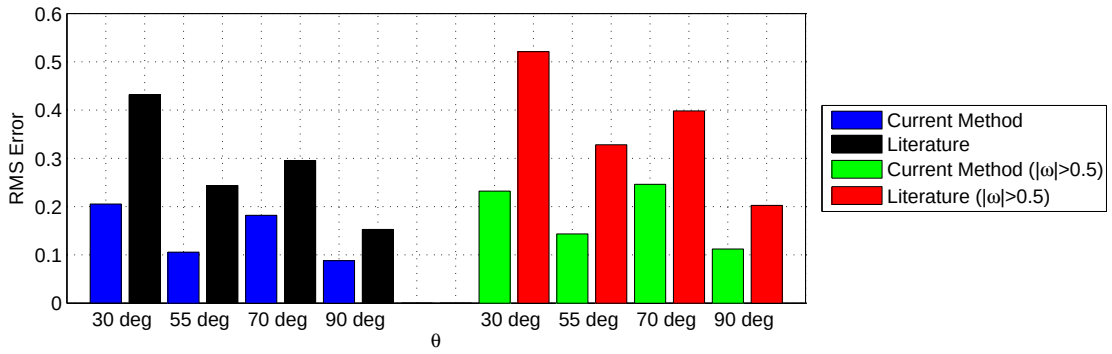

Figure 5.57: Comparison of average RMS error values of SpinSim C_N correction (Eq. 5.8) and the current state of the art (Eq. 1.2) across all ten experimental rotary balance data sets.

test-validated empirical entrainment factor. Prior to the incorporation of this factor, Eq. 5.8 outperformed Eq. 1.2 at all four angles of attack for only four of the ten data sets and for only 32 of the 40 total cases for the $|\omega| > 0.5$ regime.

The fact that the results of Eq. 5.8 have a nearly complete advantage over the current state of the art, and that they maintain this advantage for the higher values of $|\omega| > 0.5$, shows that the increased accuracy of the current model at more-extreme ω values may allow it to be used both to improve current spin models and to expand the boundaries of stall/spin situations which may be accurately simulated. This increased accuracy, in turn, may be used to create more-accurate loss-of-control or unusual-attitude simulators, or to expand the envelope over which simulators maintain a minimum level of accuracy. More-accurate simulations create the potential for lives to be saved, and for pilots to be better trained for unusual flight situations, such as a loss-of-control. To summarize the improved performance of Eq. 5.8 over Eq. 1.2, Fig. 5.57 presents a comparison of the 10-data-set averages of the RMS error values of the current model to those of the McCormick model. Over the full $-0.9 \leq \omega \leq 0.9$ and limited $|\omega| > 0.5$ ranges, the average RMS error values of the current model are significantly lower at all four angles of attack. These results demonstrate a significant improvement over the current state of the art.

Further research could contribute to a greater understanding of whether this model would be applicable only to GA-configured aircraft, or if it may potentially show promise in the modeling of transport category aircraft with swept wings, such as the Boeing 737 or Airbus A330. The potential for application of this methodology to analyses involving flapping-wing flight and hovering flight of micro air vehicles and insects may also exist. As it was demonstrated above, applying concepts developed from low Reynolds number rotational experiments ($Re \approx 3{,}000$) to the $Re \approx 100{,}000$ regime resulted in good agreement with experimental data. It, therefore, seems plausible that the methodology validated against experimental rotary balance data may be somewhat applicable to the low Re regime, from which the justification of the underlying general concepts emerged.

5.9.4 Comparison of Calculated Airplane Coefficients to Experimental Data

In this section, the plots of a simulation of the airplane model of Ref. [40] are presented, using the component breakdown method, as described earlier. Equation 5.8 is used to correct the wing normal force due to a heavily-stalled spinning wing. Overall, strong agreement of the simulations with the experimental data is demonstrated. Figure 5.58 presents a comparison of the simulation results, with rotary balance experimental data for the normal force coefficient, C_N. Figure 5.59 presents the axial force coefficient, C_A. Figure 5.60 presents the side force coefficient, C_Y. Moment coefficients comparisons are presented in Figs. 5.61, 5.62, and 5.63 for the roll, pitch, and yaw moment coefficients, respectively. The three force and three moment coefficients are

$$C_X = \frac{F_X}{qS} \tag{5.47}$$

$$C_Y = \frac{F_Y}{qS} \tag{5.48}$$

$$C_Z = \frac{F_Z}{qS} \tag{5.49}$$

$$C_l = \frac{L}{qSb} \tag{5.50}$$

$$C_m = \frac{M}{qS\bar{c}} \tag{5.51}$$

$$C_n = \frac{N}{qSb} \tag{5.52}$$

where q is the dynamic pressure, S is the wing reference area, b is the wingspan, $\bar{c}$ is the wing mean aerodynamic chord, F_X, F_Y, and F_Z denote the forces in the aircraft principal axes, and L, M, and N denote the roll, pitch, and yaw moments. Because the NASA data sets present forces in terms of C_A and C_N instead of C_X and C_Z, respectively, the following relationships are noted:

$$C_A = -C_X \tag{5.53}$$

$$C_N = -C_Z \tag{5.54}$$

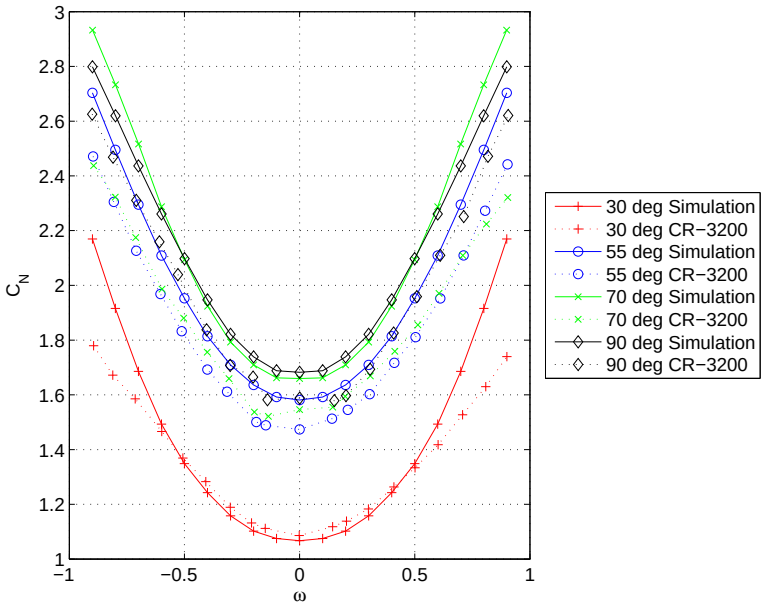

Figure 5.58: Comparison of component breakdown simulation corrected with proposed centrifugal pumping model used to correct wing forces to the experimental data set of Ref. [40] for the aircraft normal force coefficient C_N.

In Fig. 5.58, at $\theta = 30$ deg, the C_N prediction is admittedly less accurate at high values of $|\omega|$. Nevertheless, it agrees well with the data over the range of $|\omega| < 0.5$. This $|\omega| < 0.5$ regime is the regime in which an actual airplane in a stall/spin situation would reside. For example, the highly-aerobatic Aero Testbed aircraft (see Chapter 3) was able to achieve a maximum spin parameter of $\omega = 0.71$, in a forced spin, with the majority of the flight test spin parameters located over the range $0.10 < \omega < 0.25$. At $\theta = 55$, 70, and 90 deg, the predictions are much more accurate, even as $|\omega|$ approaches unity.

The agreement between the experiment and simulation was not great for the axial force coefficient, C_A, as shown in Fig 5.59. In general, the experimental data demonstrated higher C_A values for lower θ values and a minimal dependence on ω. For these reasons, it is suggested that any 6DOF simulation would source the axial force coefficients from a lookup table of experimental values. Compared with the other five coefficients, there are no general trends with ω apparent in the experimental data. Additionally, there are significant discrepancies in the experimental data sets for spin parameter values of opposite signs. Importantly, the force prediction code predicted axial force coefficients that lie within the order of magnitude of the experimental data, and they follow generally similar trends.

Unlike the poor agreement between the analytical model results and the experimental data for C_A, the agreement between the analytically-modeled and experimental data for the side force coefficient C_Y was good, as shown in Fig. 5.60. It should be noted that these experimental data sets were asymmetric, and they did not pass through the origin. While all of the other experimental data sets demonstrated some form of symmetry about $\omega = 0$, the experimental data set for C_Y did not. This lack of symmetry immediately reduced the accuracy with which it may be

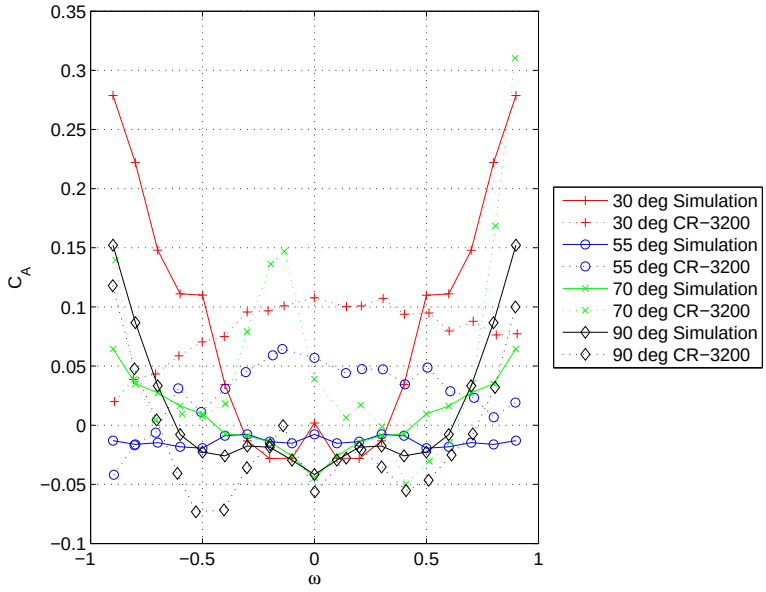

Figure 5.59: Comparison of component breakdown simulation corrected with proposed centrifugal pumping model used to correct wing forces to the experimental data set of Ref. [40] for the aircraft axial force coefficient C_A.

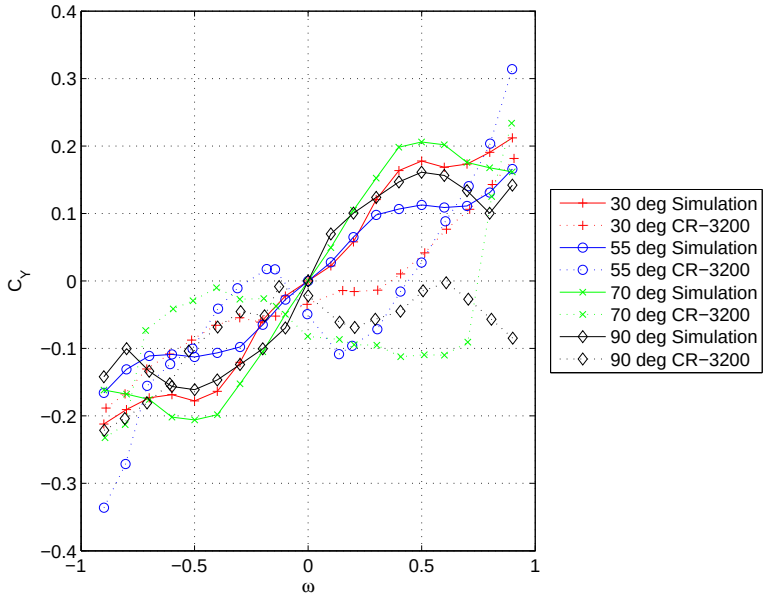

Figure 5.60: Comparison of component breakdown simulation corrected with proposed centrifugal pumping model used to correct wing forces to the experimental data set of Ref. [40] for the aircraft side force coefficient C_Y.

accurately modeled. The analytical model captures the general trend of the experimental data, especially if the $\omega < 0$ experimental data is rotated about the origin $(0,0)$ and is used to replace the $\omega > 0$ experimental data.

Strong agreement is observed between the analytical simulation and experimental data in Fig. 5.61. Such agreement is not surprising as the rolling moment coefficient of a spinning aircraft is driven primarily by the forces on the wing. In both the experimental and analytically-modeled data sets, the largest rolling moment occurred at $\theta = 30$ deg

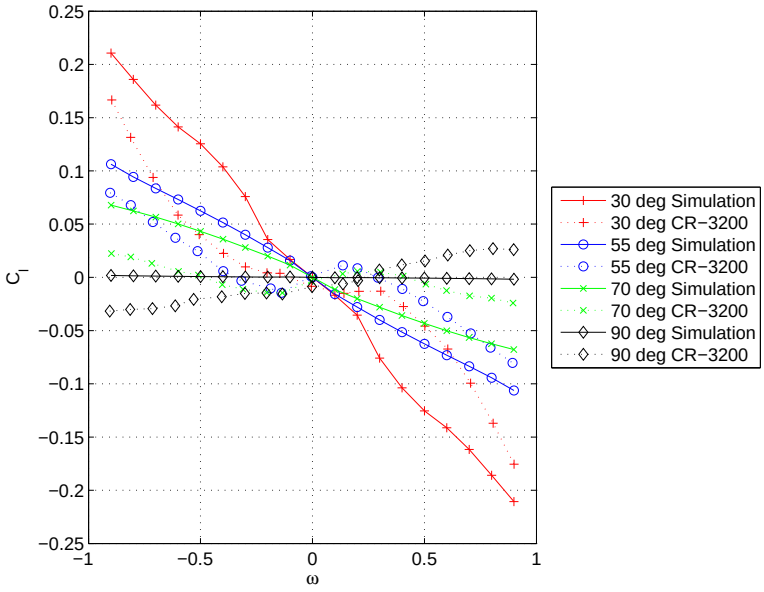

Figure 5.61: Comparison of component breakdown simulation corrected with proposed centrifugal pumping model used to correct wing forces to the experimental data set of Ref. [40] for the aircraft roll moment coefficient C_l.

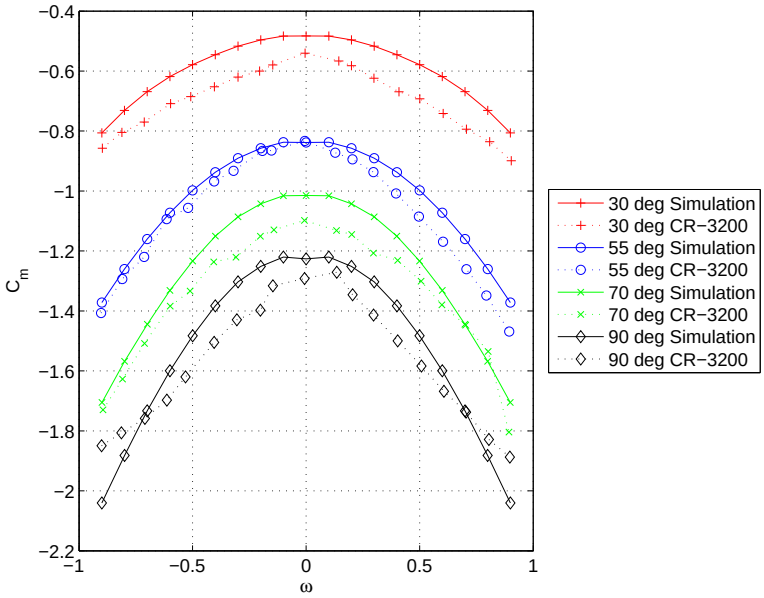

Figure 5.62: Comparison of component breakdown simulation corrected with proposed centrifugal pumping model used to correct wing forces to the experimental data set of Ref. [40] for the aircraft pitch moment coefficient C_m.

and high values of ω. As θ increased through 55 and 70 deg, the C_l versus ω curves flattened out. At $\theta = 90$ deg however, the rolling moment coefficient reversed its trend. For high negative values of ω, C_l was positive at $\theta = 30$, 55, and 70 deg. C_l became negative for $\theta = 90$ deg. The analytical model developed as part of this research was nearly able to capture this important detail.

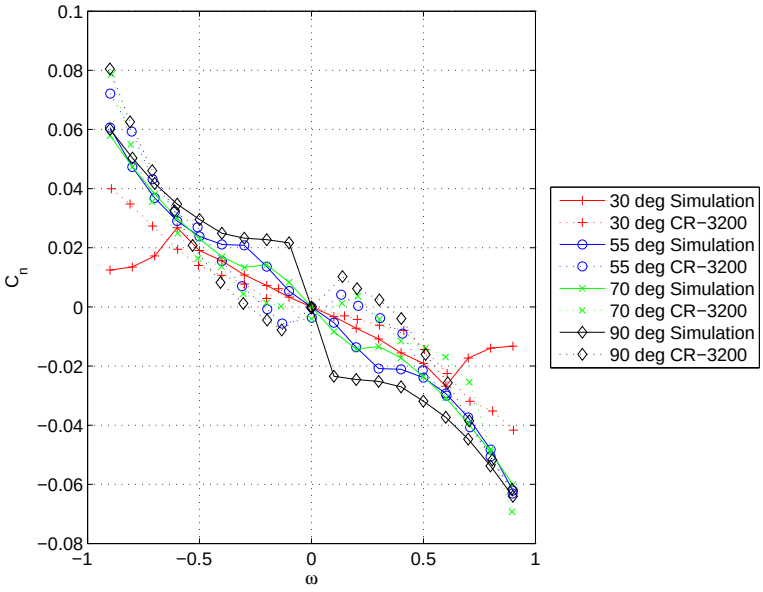

Figure 5.63: Comparison of component breakdown simulation corrected with proposed centrifugal pumping model used to correct wing forces to the experimental data set of Ref. [40] for the aircraft yaw moment coefficient C_n.

The simulation results for the pitch moment coefficient C_m agree well with the experimental data, as shown in Fig. 5.62. The vertical separation between the $\theta = 30$ deg and $\theta = 90$ deg cases match those of the experimental data. The curves follow a similar general shape and trend. This general shape and trend is characterized by a growth rate in the negative direction. The negative growth rate is proportional to ω^2, and it increases as θ increases. The curves of C_m shift downward as θ is increased, with the $\omega = 0$ value of C_N equal to -0.5 for $\theta = 30$ deg. The $\omega = 0$ value of C_N is approximately equal to -1.22 at $\theta = 90$ deg. The aft fuselage and horizontal stabilizer primarily drive the pitching moment, C_l. At lower angles of attack, a shielding term is applied to the horizontal stabilizer to reflect its presence in the wake of the wing.

Figure 5.63 presents a plot of the analytically-modeled and experimental data points for the aircraft yaw moment coefficient C_n and once again, satisfactory agreement is demonstrated in the general trends between the experimental and analytically-modeled data. In general, the C_n values appear to increase proportionally to ω^2 with slightly larger values observed as θ increases from 30 to 90 deg. As ω increases in the negative direction, C_n increases in the positive direction. For large positive values of ω, C_n is characterized by large negative numbers. In terms of the analytically-modeled values, the curves for $\theta = 90$, 70, and 55 deg are similar. The $\theta = 30$ deg curve, however, differs from the rest of the curves at high $|\omega|$ values. It carries values approximately equal to the other three θ values for $|\omega| < 0.6$. Overall, however, the curves accurately model the general trends and are of the correct magnitude.

5.10 Summary of SpinSim Force Modeling Methodology

In this section, the techniques and equations that were used to develop the SpinSim force modeling methodology were presented. Additionally, the methods used for generating aerodynamic data over the full $-180 \leq \alpha \leq 180$ deg range were presented and validated. A novel strip theory correction method, which was based on centrifugal pumping and wing tip ejection of the trapped flow was presented. Further, the correction method assumptions were supported based on the previous literature from a wide range of fields. Significantly, when this strip theory correction method was incorporated into the force prediction code of SpinSim, a nearly across-the-board improvement over the state of the art was demonstrated for the simulation of rotary balance data sets. An empirical entrainment factor, which is a function of the wing aspect ratio, was presented and shown to improve the accuracy of the correction method.

Chapter 6

Six Degree of Freedom (6DOF) SpinSim Simulations

After validating SpinSim, the force prediction code (described in Chapter 5) with the NASA rotary balance data sets, a six-degree of freedom (6DOF) integration code was used to generate 3D trajectories for an aircraft in spin from the predicted forces. This chapter introduces the equations of motion (EOMs), and it describes select modifications, which were made to the integration routines because of the uniquenesses of spinning flight. Also, this chapter presents a number of parametric studies, which are used to evaluate the robustness of the simulations. The chapter concludes with comparisons of SpinSim-generated spin simulations of the Aero Testbed to spin flight test data generated as part of this research.

6.1 Aircraft Equations of Motion

At each timestep, based on the orientation and motion of the aircraft, the force prediction code of SpinSim output all three force coefficients in the body axis (C_X, C_Y, C_Z) and all three moment coefficients in the body axis (C_l, C_m, C_n). The forces and moments were calculated by multiplying each coefficient by the dynamic pressure as follows, [40]

$$F_x = \frac{1}{2}\rho V^2 S C_X \tag{6.1}$$

$$F_y = \frac{1}{2}\rho V^2 S C_Y \tag{6.2}$$

$$F_z = \frac{1}{2}\rho V^2 S C_Z \tag{6.3}$$

$$L = \frac{1}{2}\rho V^2 S b C_l \tag{6.4}$$

$$M = \frac{1}{2}\rho V^2 S \bar{c} C_m \tag{6.5}$$

$$N = \frac{1}{2}\rho V^2 SbC_n \tag{6.6}$$

where ρ is the air density, V is the aircraft inertial velocity, S is the wing reference area, b is the wingspan, and $\bar{c}$ is the wing mean aerodynamic chord.

These forces and moments were then output to the 6DOF integrator of Stengel [73], and the airplane motion was determined using the following equations of motion for the rate of change of translational velocity in the body-fixed axes [74],

$$\dot{u} = \frac{F_x}{m} - g\sin\theta + rv - qw \tag{6.7}$$

$$\dot{v} = \frac{F_y}{m} + g\sin\phi\cos\theta - ru + pw \tag{6.8}$$

$$\dot{w} = \frac{F_z}{m} + g\cos\phi\cos\theta + qu - pv \tag{6.9}$$

where m is the airplane mass, g is the gravitational constant, ϕ, θ, and ψ are the aircraft Euler angles, p, q, and r are the aircraft body-axis angular rates, and u, v, and w are the aircraft body-axis velocity components. The following EOMs were used to determine the rate of change of angular velocity in the body-fixed axes [74]

$$\dot{p} = \frac{I_{zz}L + I_{xz}N - (I_{xz}(I_{yy} - I_{xx} - I_{zz})p + ({I_{xz}}^2 + I_{zz}(I_{zz} - I_{yy}))r)q}{I_{xx}I_{zz} - {I_{xz}}^2} \tag{6.10}$$

$$\dot{q} = \frac{M - (I_{xx} - I_{zz})pr - I_{xz}(p^2 - r^2)}{I_{yy}} \tag{6.11}$$

$$\dot{r} = \frac{I_{xz}L + I_{xx}N - (I_{xz}(I_{yy} - I_{xx} - I_{zz})r + ({I_{xz}}^2 + I_{xx}(I_{xx} - I_{yy}))p)q}{I_{xx}I_{zz} - {I_{xz}}^2} \tag{6.12}$$

where I represents the aircraft moments of inertia. The rigid body equations of motion for rate of change of translational position are defined in the earth-fixed x-, y-, and z-axes by [74]

$$\dot{x} = (\cos\theta\cos\psi)u + (-\cos\phi\sin\psi + \sin\phi\sin\theta\cos\psi)v + (\sin\phi\sin\psi + \cos\phi\sin\theta\cos\psi)w \tag{6.13}$$

$$\dot{y} = (\cos\theta\sin\psi)u + (\cos\phi\cos\psi + \sin\phi\sin\theta\sin\psi)v + (-\sin\phi\cos\psi + \cos\phi\sin\theta\sin\psi)w \tag{6.14}$$

$$\dot{z} = (-\sin\theta)u + (\sin\phi\cos\theta)v + (\cos\phi\cos\theta)w \tag{6.15}$$

while the rate of change of angular position in the earth-fixed axes equations are [74]

$$\dot{\phi} = p + (q\sin\phi + r\cos\phi)\tan\theta \tag{6.16}$$

$$\dot{\theta} = q\cos\phi - r\sin\phi \tag{6.17}$$

$$\dot{\psi} = \frac{(q\sin\phi + r\cos\phi)}{\cos\theta} \tag{6.18}$$

For clarity, the Euler angles define the orientation of the airplane, and, thus, of its body-fixed axes, in the earth frame of reference. The angles ϕ, θ, and ψ correspond to the roll, pitch, and yaw rotations of the aircraft, as shown in Fig. 6.1 [107]. Based on Eqs. 6.13–6.15, the orthonormal transformation for vector components from the earth-fixed inertial frame to the body-fixed frame was calculated using the transformation matrix below [74]:

$$\mathbf{H}_I^B = \begin{bmatrix} \cos\theta\cos\psi & \cos\theta\sin\psi & -\sin\theta \\ -\cos\phi\sin\psi + \sin\phi\sin\theta\cos\psi & \cos\phi\cos\psi + \sin\phi\sin\theta\sin\psi & \sin\phi\cos\theta \\ \sin\phi\sin\psi + \cos\phi\sin\theta\cos\psi & -\sin\phi\cos\psi + \cos\phi\sin\theta\sin\psi & \cos\phi\cos\theta \end{bmatrix} \tag{6.19}$$

6.1.1 Select Corrections Made to 6DOF Integrating Code

Three significant modifications to the 6DOF integrator were necessary to properly plot the spin simulation results. First, and most importantly, was the calculation of the airplane yaw angle ψ. In its original state, the 6DOF integrator was capable only of calculating ψ values between 0 and 90 deg (0 and π/2 rad). This calculation limitation of ψ existed because the code determined the angle through a simple inverse cosine function, which was limited to only the first quadrant. A four-quadrant cosine function was necessarily implemented to correctly determine the aircraft ψ value from its x- and y-velocities. Figure 6.2 depicts the modifications that were made to the code to define the angle

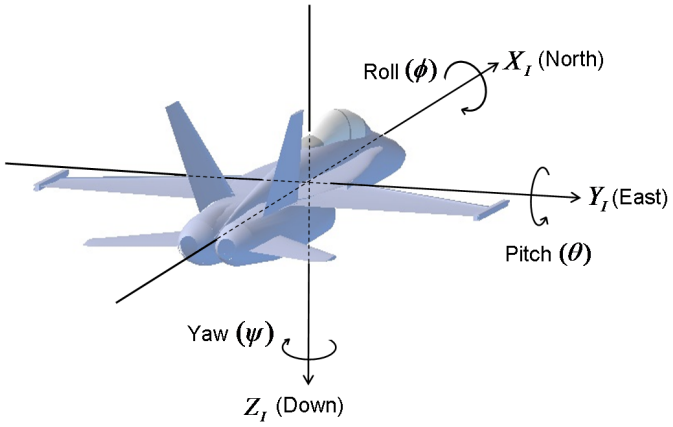

Figure 6.1: Graphic depicting the Euler angles of an aircraft (CH Robotics [107]).

```
if vEarth(1,i) < 0 && vEarth(2,i) > 0 % Quadrant II, added 11/15/2015
    Xir         =   pi() - asin(vEarth(2,i) / sqrt((vEarth(1,i))^2 + (vEarth(2,i))^2));
elseif vEarth(1,i) < 0 && vEarth(2,i) < 0 % Quadrant III, added 11/15/2015
    Xir         =   pi() - asin(vEarth(2,i) / sqrt((vEarth(1,i))^2 + (vEarth(2,i))^2));
elseif vEarth(1,i) > 0 && vEarth(2,i) < 0 % Quadrant IV, added 11/15/2015
    Xir         =   2* pi() + asin(vEarth(2,i) / sqrt((vEarth(1,i))^2 + (vEarth(2,i))^2));
else % x>0 and y>0 case, Quadrant I
    Xir         =   asin(vEarth(2,i) / sqrt((vEarth(1,i))^2 + (vEarth(2,i))^2)); %Original Stengel Line
end
```

Figure 6.2: Screenshot of modified code for defining ψ.

ψ. Figure 6.3 shows what the plot of ψ looked like prior to the necessary modifications. Similarly, the angle of attack was originally limited to ± 90 deg, and it was expanded to handle the full range of $-180 \leq \alpha \leq 180$ deg.

The lines of code used to plot the yaw angle in the earth-fixed axis system also required a modification that was more easily implemented. Prior to modifications, the plotted earth-relative yaw angle ψ value increased unboundedly. The original code was modified in MATLAB to plot the remainder of the yaw angle in degrees divided by 360, instead of the unprocessed yaw angle. Through this process, and other small modifications, the plot of ψ was successfully limited to the range of $-180 \leq \psi \leq 180$ deg. Similar modifications were made to limit θ and ϕ to the regime bounded by ± 180 deg.

On account of the fact that the 6DOF integrator was originally built around an airplane dynamics model that used stability derivatives, the transformations of the forces and moments were necessarily modified. This modification was necessary, particularly because a stability derivative-based model generally outputs the forces in terms of C_L and C_D. While the forces and moments from the previous dynamics model output aerodynamic values, such as C_L and C_D, SpinSim output forces and moments in the body-fixed coordinate system. Thus, the 6DOF integrating routine needed to be modified to accept the body forces and moments from SpinSim instead of aerodynamic coefficients.

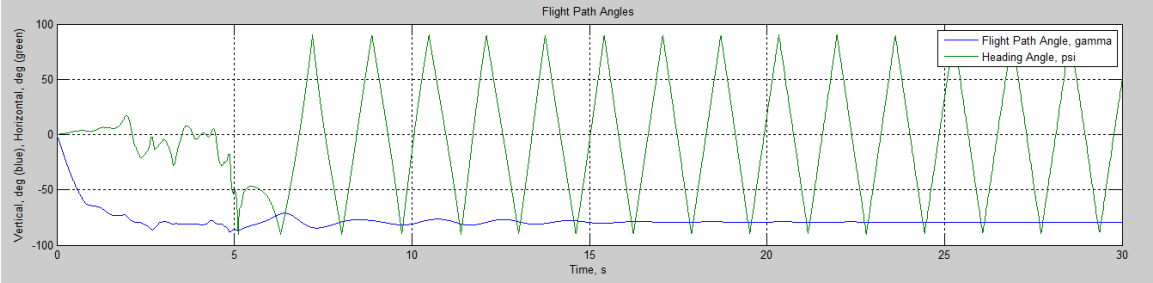

Figure 6.3: Plot of ψ prior to necessary modifications.

A final modification of mention is that an option to use a non-built-in 4^{th} order Runge-Kutta (RK4) integration routine was added to the 6DOF integration routines. This addition was performed in order to produce data, more specifically 3D trajectories, that had evenly-spaced and user-specifiable timesteps. The default integration routine used for the 6DOF EOM integrator was the built-in MATLAB function *ode*45, which self-adjusts the timestep based on the specified integration tolerances and the rigid-body motions and rotations. No functionality exists in the *ode*45 function to control the timestep size.

The classical Runge-Kutta method is defined by the initial value problem:

$$\dot{y} = f(t,y) \tag{6.20}$$

$$y(t_0) = y_0 \tag{6.21}$$

where t is the time and y is the value being integrated. With a step size $h > 0$

$$y_{n+1} = y_n + \frac{h}{6}(k_1 + 2k_2 + 2k_3 + k_4) \tag{6.22}$$

$$t_{n+1} = t_n + h \tag{6.23}$$

where

$$k_1 = f(t_n, y_n) \tag{6.24}$$

$$k_2 = f\left(t_n + \frac{h}{2}, y_n + \frac{h}{2}k_1\right) \tag{6.25}$$

$$k_3 = f\left(t_n + \frac{h}{2}, y_n + \frac{h}{2}k_2\right) \tag{6.26}$$

$$k_4 = f(t_n + h, y_n + hk_3) \tag{6.27}$$

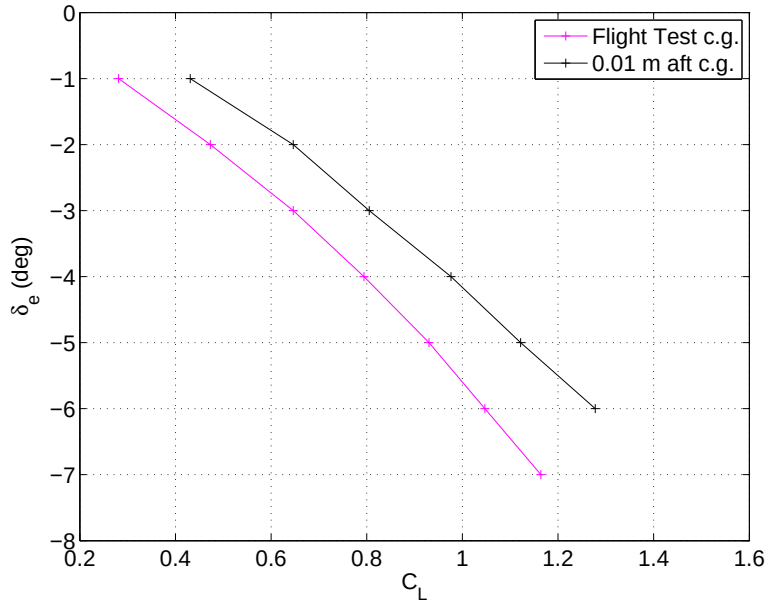

Figure 6.4: Plot of δ_e versus trim C_L from SpinSim for flight test c.g. location, and a c.g. location moved 0.055 m aft.

This RK4 method was used for generating 3D trajectories simulated at 300 Hz in order to allow for an easy coplotting of the simulation results and flight test results. This section does not provide an exhaustive list of the myriad changes that were performed to successfully integrate SpinSim with a 6DOF EOM integrator, but it does chronicle some of the modifications that were performed. These modifications may be of use to researchers attempting later to integrate force prediction codes into existing integration codes.

6.1.2 Elevator Deflection Trimmed Flight Trade Studies

To serve as validation of the airplane behavior in the 6DOF simulation, the SpinSim computational model of the Aero Testbed Extra 260 was tested to examine the effects of a range of elevator deflection angles on a trimmed flight. Specifically, the curves of elevator deflection, δ_e, versus the trimmed airplane velocity, V_{trim}, and the C_L at which the airplane trimmed, were generated over a range of elevator deflection angles. The trends of the curves were examined. To verify the correct modeling of the airplane, the effects on trimmed flight from shifting the c.g. aft were also investigated. Figures 6.4 and 6.5 present plots of the SpinSim-generated results for elevator deflection versus trim C_L, and V_{trim}, for two c.g. locations. The c.g. location of the first set of simulations is the location at which Aero Testbed test flights were conducted. It is labeled "Flight Test c.g." A second c.g. location for the simulations was specified, 0.01 meters aft of the flight-tested c.g. but still forward of the neutral point (h_n); this second c.g. location is labeled "0.01 m aft c.g."

As expected for an airplane with the c.g. forward of the neutral point, shifting the c.g. rearward reduces the slope of the δ_e vs. C_L plot. Both simulation data sets correctly follow a generally-linear trend for δ_e vs. C_L. In the case of

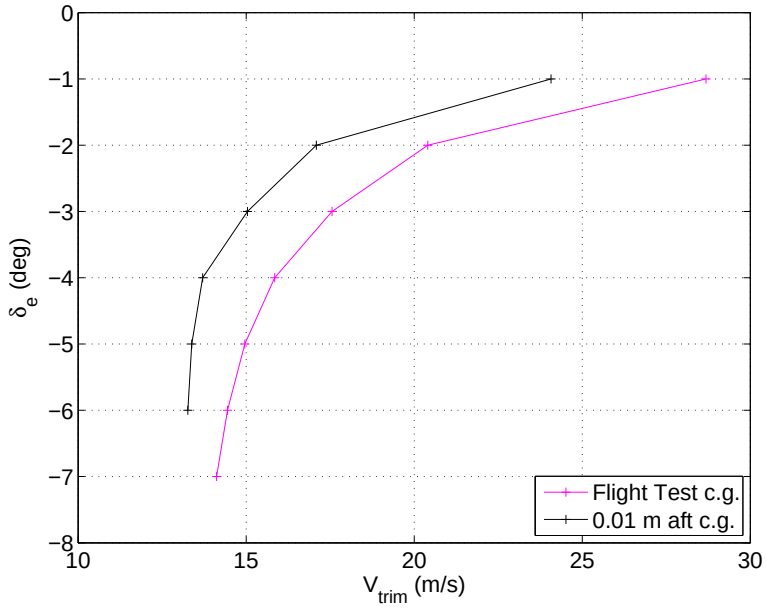

Figure 6.5: Plot of δ_e versus trim V_{trim} from SpinSim for flight test c.g. location, and a c.g. location moved 0.055 m aft.

δ_e vs. V_{trim}, the plot correctly demonstrates that as the airplane c.g. moves aft and closer to the neutral point, the data curve moves in the direction of the origin (i.e., for a given elevator deflection angle an aft c.g. shift toward the neutral point results in a lower V_{trim}). Another way to describe the trend in Fig. 6.4 is that to maintain a constant V_{trim}, the elevator deflection angle must be reduced if the c.g. location is moved aft toward the neutral point.

6.1.3 Integration Tolerance Parametric Studies

The original Stengel integration code [73] had absolute and relative integration tolerances of 10^{-7}, which sometimes resulted in long runtimes. A convergence study was performed to determine a suitable balance between computational run time and simulation accuracy. A change was made to the integration tolerances of the built-in *ode*45 function, from a value of 10^{-7} to 10^{-4}. The new absolute and relative integration tolerance value of 10^{-4} significantly reduced the run time without any major impact on the simulation results. Figure 6.6 presents comparison plots of the body u, v, and w velocity components. Figure 6.7 presents comparison plots of the angular rates for the tolerance values of 10^{-7} and 10^{-4} from a SpinSim simulation of the Aero Testbed in a spin to the left with pro-spin ailerons.

The trajectory and angular rate plots of Figs. 6.6 and 6.7 demonstrate that no significant changes arose from changing the integration tolerance from 10^{-7} to 10^{-4}. This change in the tolerance value from 10^{-7} to 10^{-4} did, however, result in a significant reduction in the computational time required for a spin simulation. Most importantly, the simulations predicted and converged to the same developed spin values. The inertial velocity and inertial rate plots of the SpinSim simulation with integration tolerance values of 10^{-4} and 10^{-7} of a left, low, pro-spin aileron spin are

nearly indistinguishable. In both cases, the simulations converge to u, v, and w velocity components of approximately 20, -4, and 6.5 m/s, respectively, within approximately 6 s. In regard to the angular rates, both simulations converge within about 5 s to p, q, and r inertial rates of -325, 125, and -100 deg/s, respectively.

Figure 6.8 presents trajectory comparisons for SpinSim simulations with integration tolerances of 10^{-7} and 10^{-4}. This comparison of the trajectories shows that changing the integration tolerance to 10^{-4} causes no discernable change to the trajectory, and it does not affect the spin radius. The spin radius is the most-important parameter of the trajectory, and it is approximately 0.5 m in both simulations. This value of the spin radius compares well with the 0.6 m experimental value of Table 3.6 for the T0R1E1A0-Lft-Up spin cases.

Figure 6.9 presents angular orientation comparisons for SpinSim simulations with integration tolerances of 10^{-7} and 10^{-4}. Again, only minor differences are evident between the angular rates of the two integration tolerances. The top plots with the 10^{-7} tolerance parameter show oscillations of the roll angle ϕ, and pitch angle θ, which are smaller than those of the 10^{-4} tolerance parameter simulation, which is located at the bottom of Fig. 6.9. Moreover, these differences are small, and they do not have a significant effect on the trajectory of the airplane. As regards the roll angle ϕ, the small oscillations for the 10^{-7} tolerance case persist until $t \approx 9$ s, but by $t \approx 13$ s, the oscillations of the 10^{-4} tolerance case disappear.

Figure 6.10 presents velocity, Mach number, and q comparisons for SpinSim simulations with integration tolerances of 10^{-7} and 10^{-4}. Again, only minimal differences may be observed. Both simulations predict an air-relative speed around 22 m/s, a Mach number of 0.06, and a dynamic pressure q of 250 N/m^2.

Figure 6.11 presents aerodynamic and flight path angle comparisons of SpinSim simulations with integration tolerances of 10^{-7} and 10^{-4}. These plots of the orientation angles show strong agreement with one another, as evidenced by the fact that there are nearly no differences between the plots. The only discernable difference between the results from the two different tolerance parameters is that the small oscillations in α and β persist until $t \approx 7$ s for the 10^{-7} tolerance case, while the oscillations are no longer seen by $t \approx 10$ s for the 10^{-4} tolerance case. As regards the flight path angle γ, the small oscillations for the 10^{-7} tolerance case persist until $t \approx 6$ s, but by $t \approx 9$ s, the oscillations of the 10^{-4} tolerance case disappear. As Figs. 6.6–6.11 show, increasing the integration tolerance parameter from 10^{-7} to 10^{-4} has only a minor effect on the simulation results, but it saves computational time.

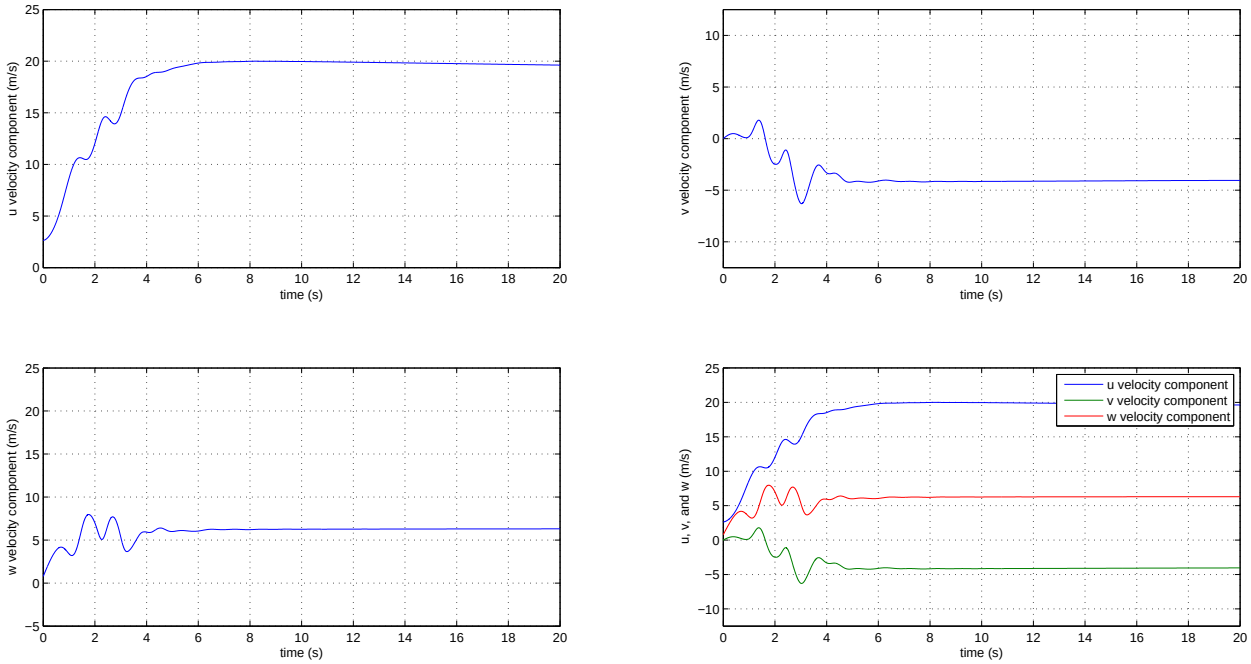

(a) Body inertial velocities at integration tolerance of 10^{-7}

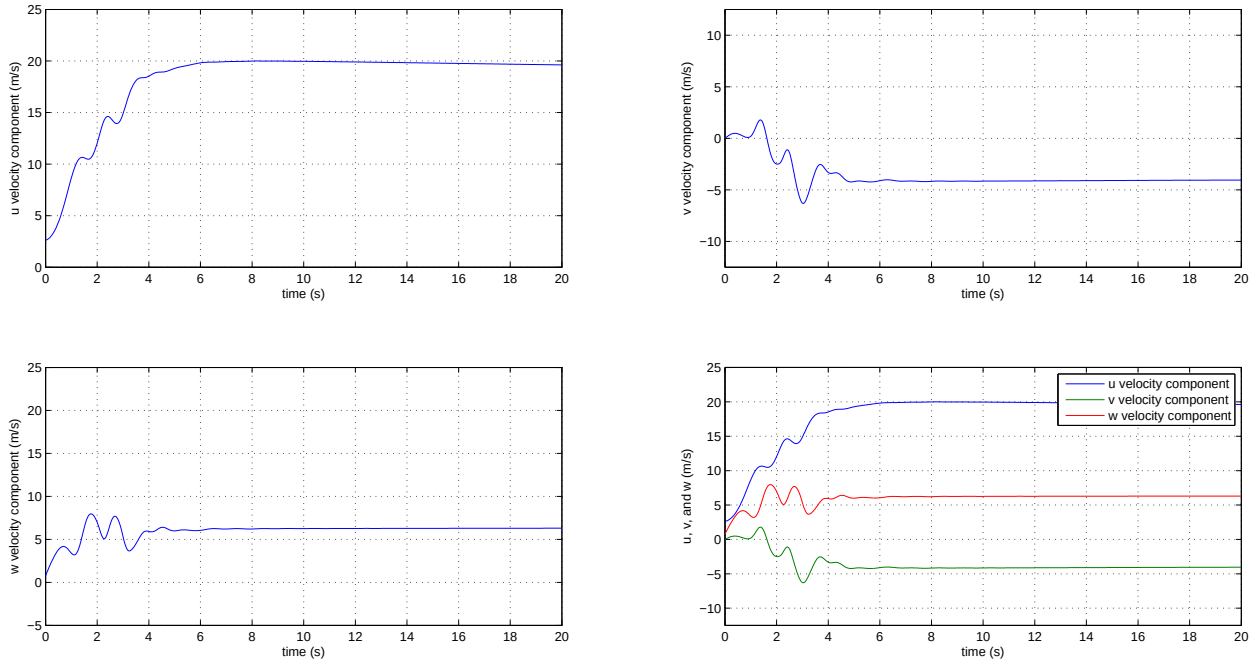

(b) Body inertial velocities at integration tolerance of 10^{-4}

Figure 6.6: Comparison of u, v, and w velocity components for SpinSim simulation of the Aero Testbed in a left spin with pro-spin ailerons and integration tolerances of 10^{-7} and 10^{-4}.

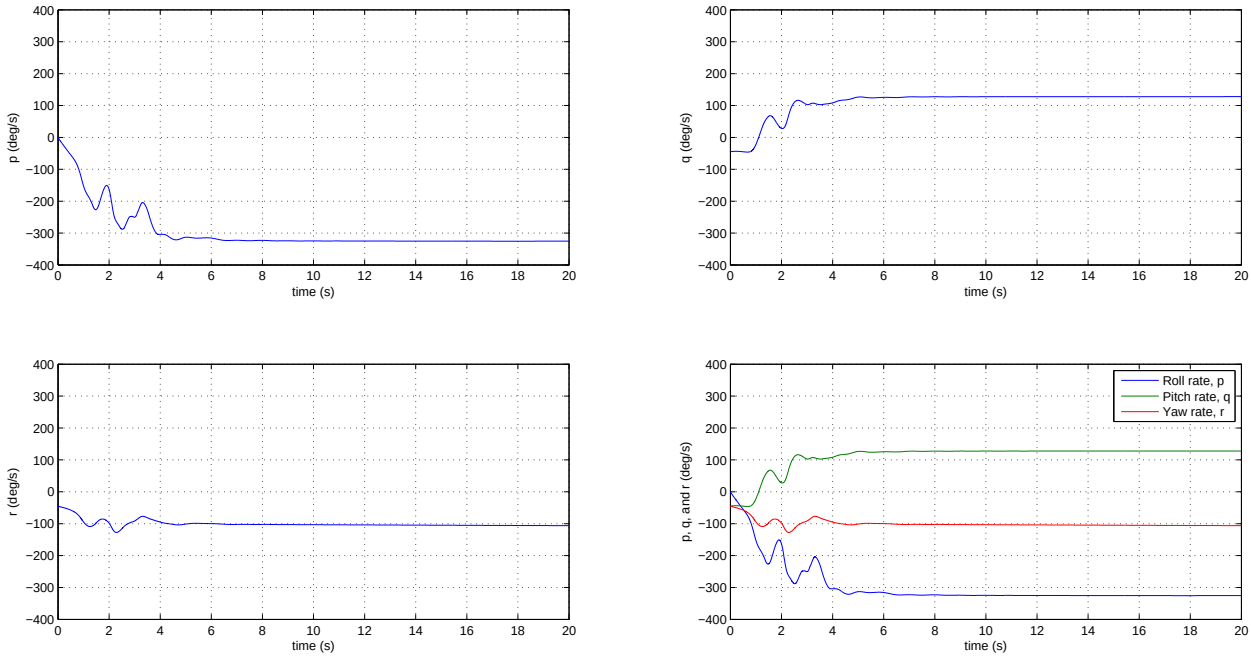

(a) Angular Rates at integration tolerance of 10^{-7}

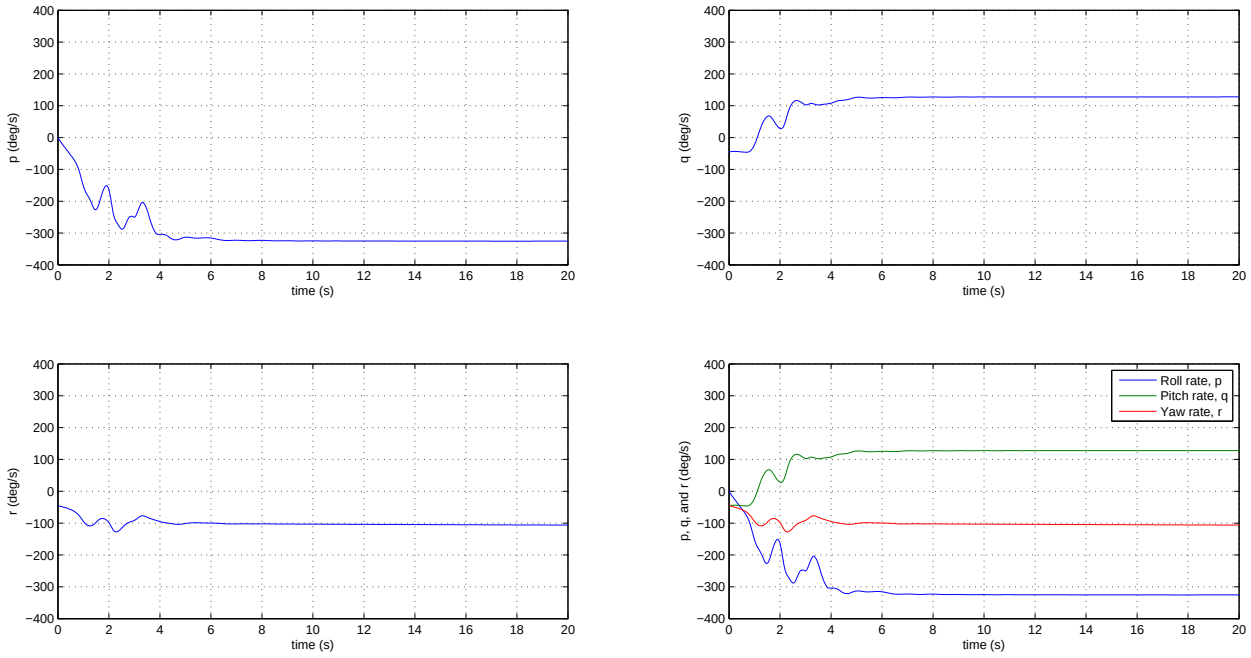

(b) Angular Rates at integration tolerance of 10^{-4}

Figure 6.7: Comparison of p, q, and r angular rates for SpinSim simulation of the Aero Testbed in a left spin with pro-spin ailerons and integration tolerances of 10^{-7} and 10^{-4}.

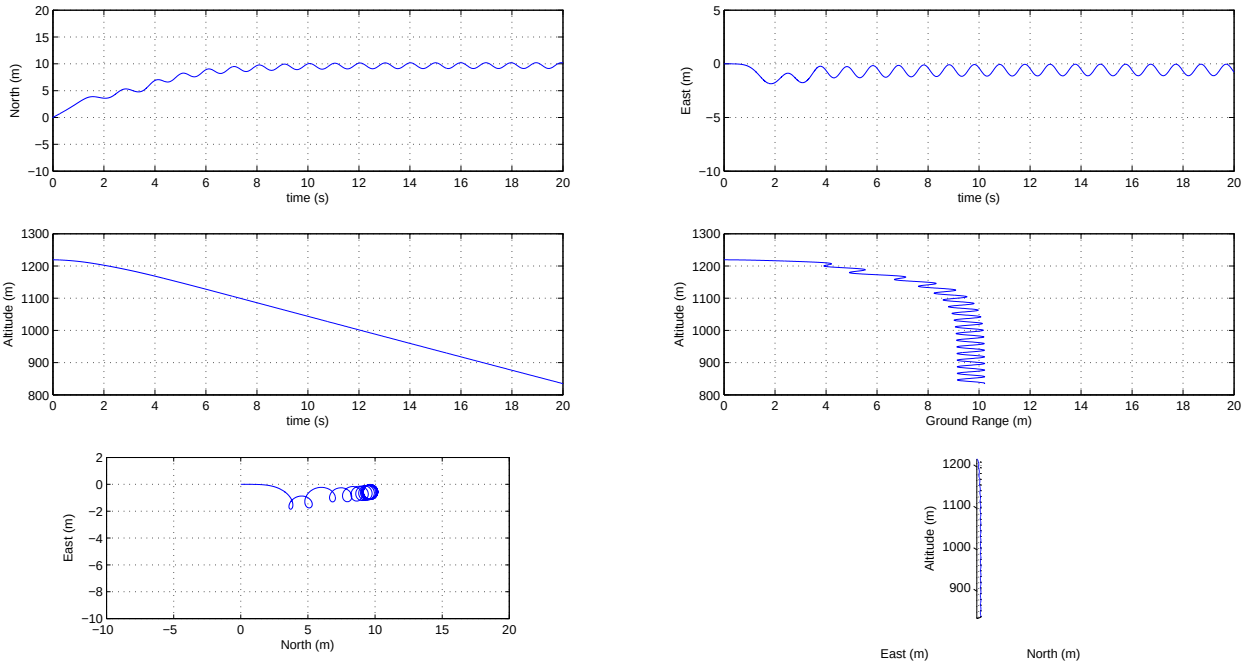

(a) Trajectory at integration tolerance of 10^{-7}

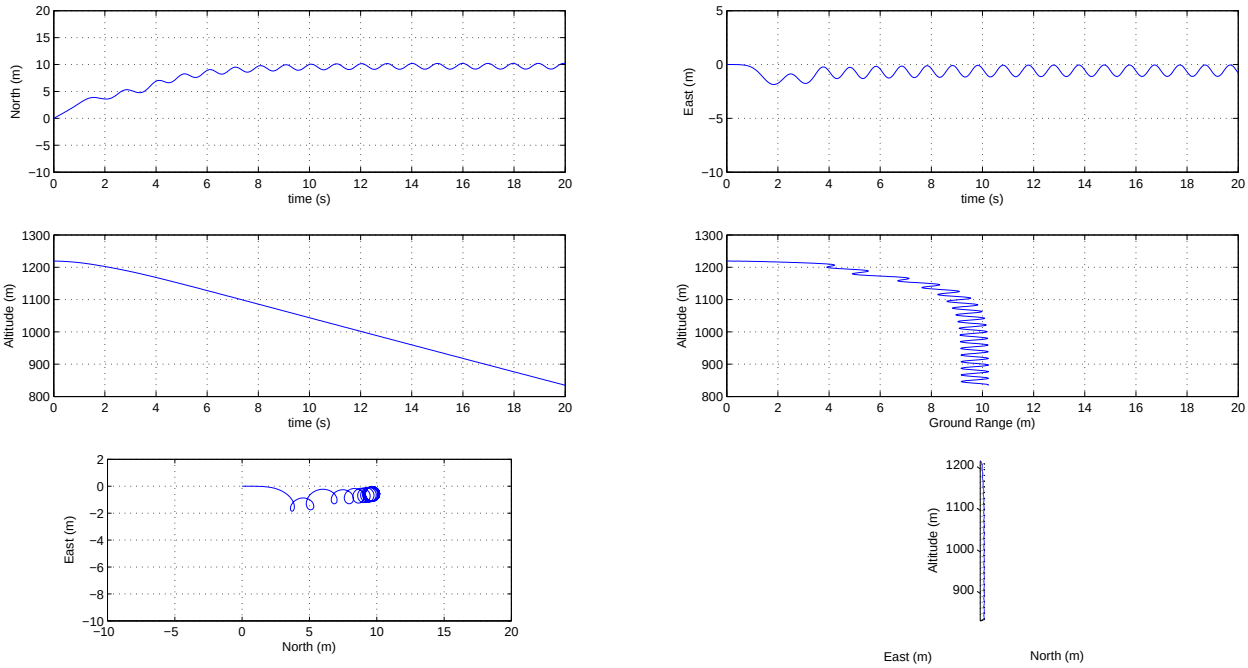

(b) Trajectory at integration tolerance of 10^{-4}

Figure 6.8: Comparison of trajectories for SpinSim simulation of the Aero Testbed in a left spin with pro-spin ailerons and integration tolerances of 10^{-7} and 10^{-4}.

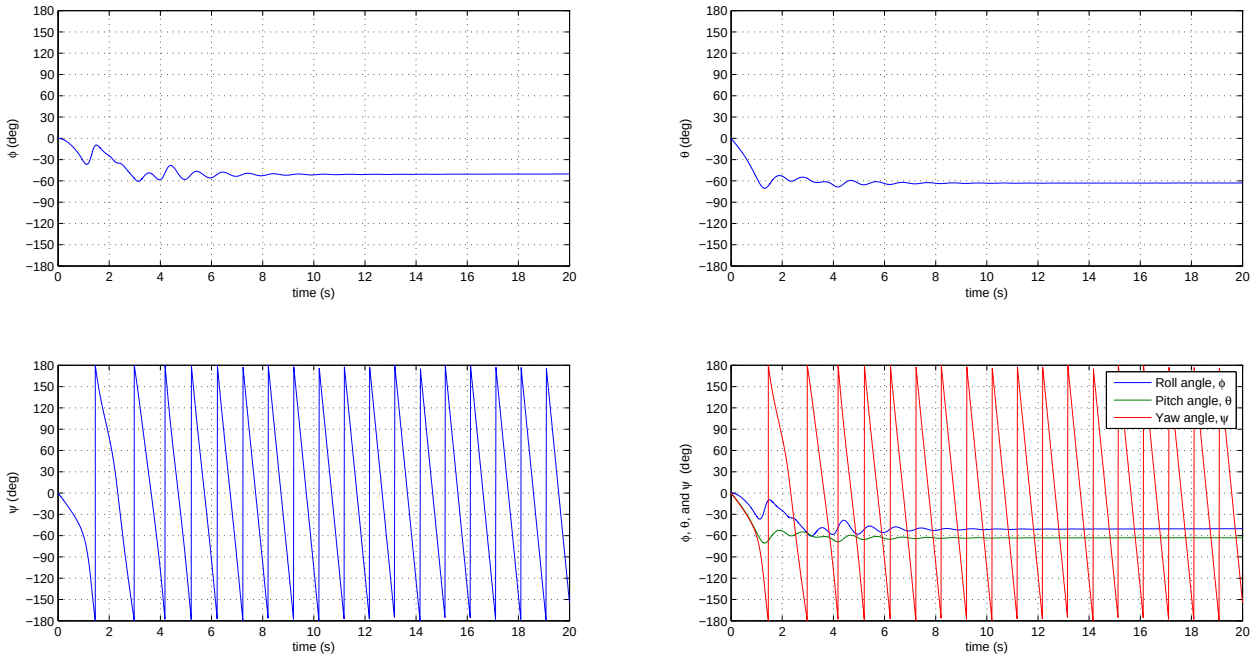

(a) Angular orientations at integration tolerance of 10^{-7}

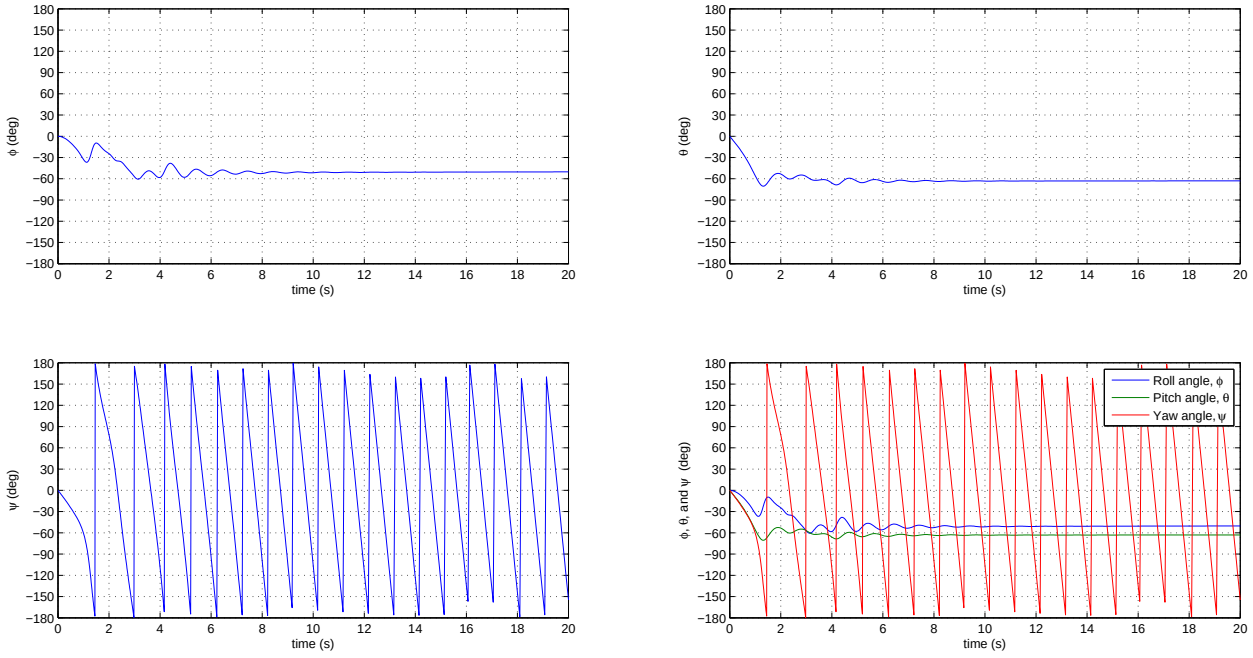

(b) Angular orientations at integration tolerance of 10^{-4}

Figure 6.9: Comparison of ϕ, θ, and ψ Euler angles for SpinSim simulation of the Aero Testbed in a left spin with pro-spin ailerons and integration tolerances of 10^{-7} and 10^{-4}.

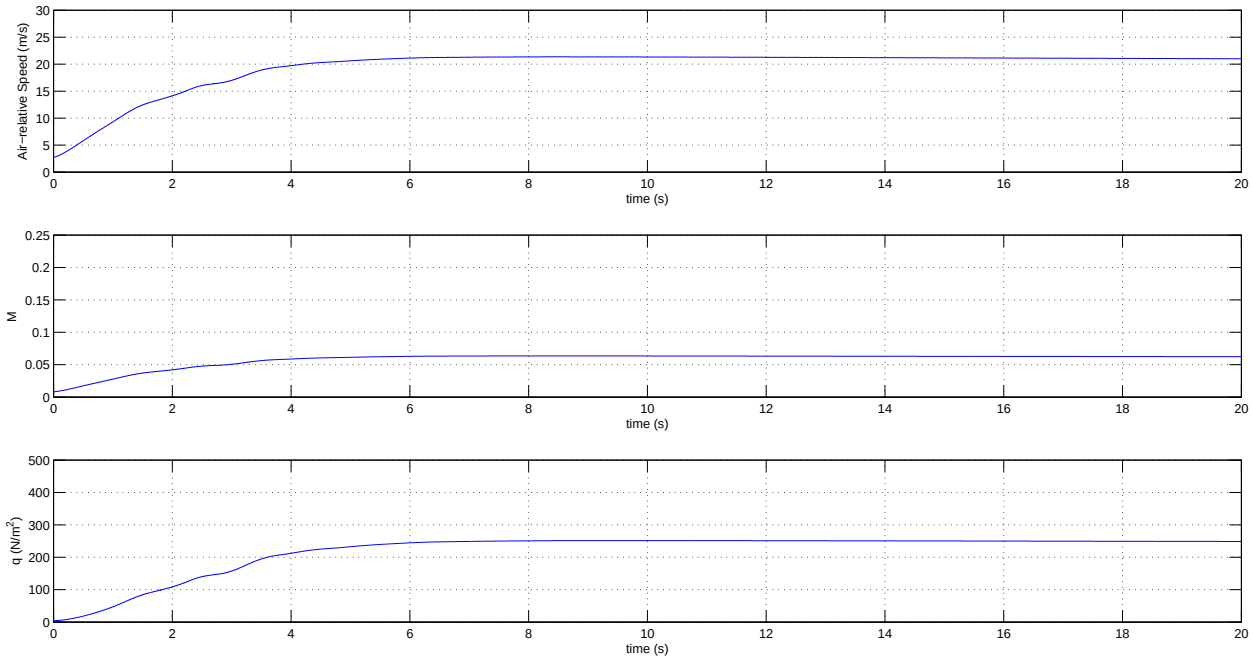

(a) Velocity and q at integration tolerance of 10^{-7}

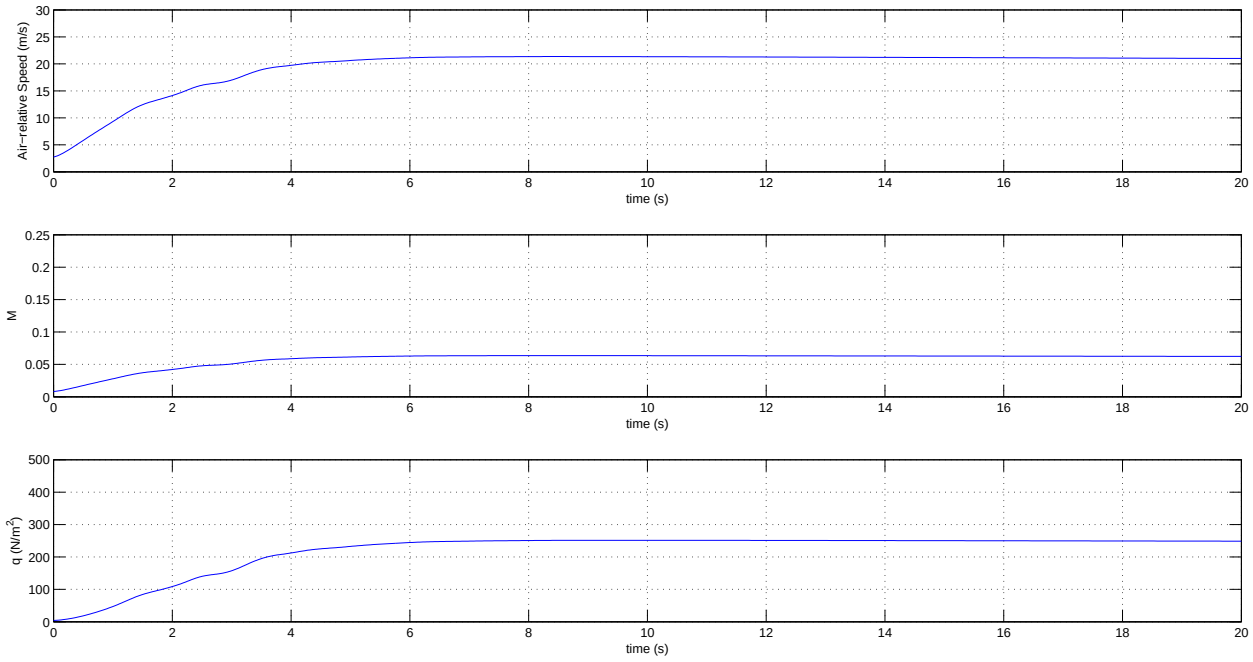

(b) Velocity and q at integration tolerance of 10^{-4}

Figure 6.10: Comparison of airspeed, Mach number, and q for SpinSim simulation of the Aero Testbed in a left spin with pro-spin ailerons and integration tolerances of 10^{-7} and 10^{-4}.

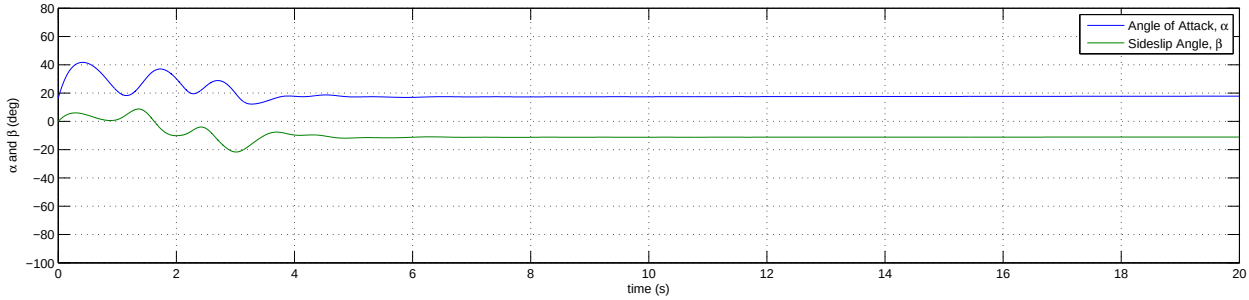

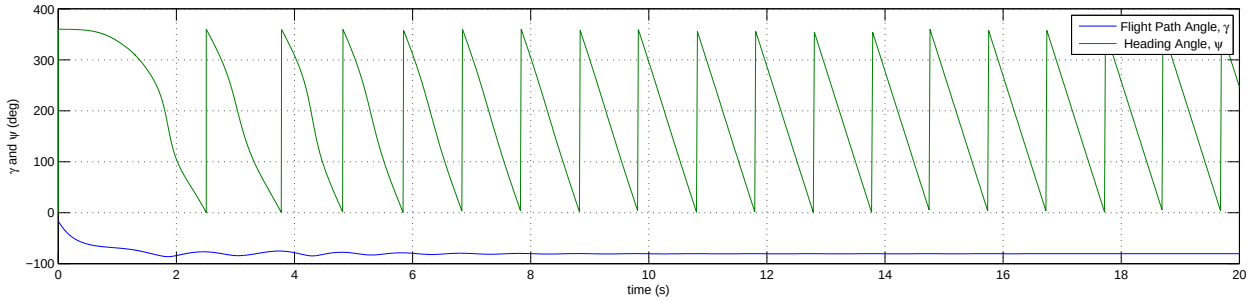

(a) Aerodynamic and flight path angles at integration tolerance of 10^{-7}

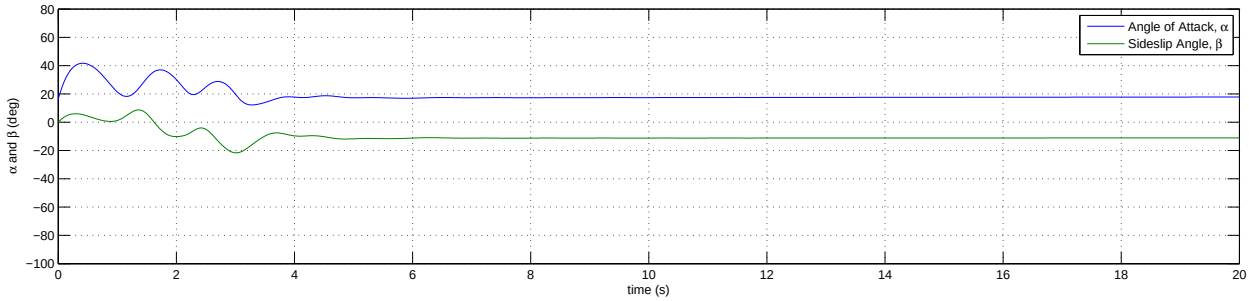

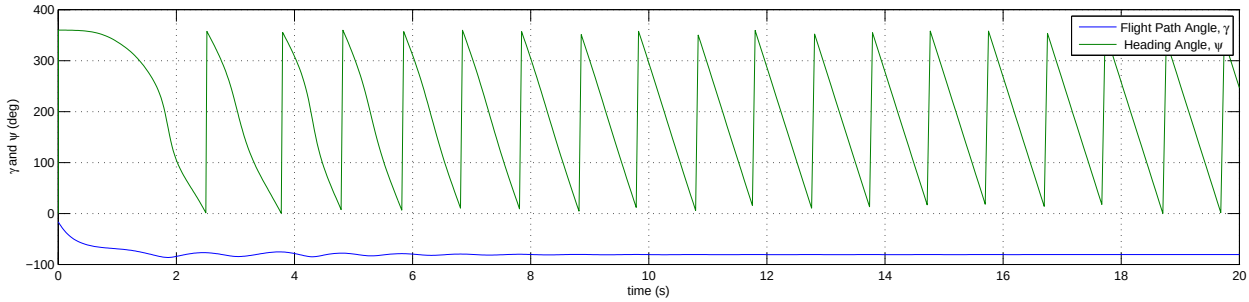

(b) Aerodynamic and flight path angles at integration tolerance of 10^{-4}

Figure 6.11: Comparison of airspeed, Mach number, and q for SpinSim simulation of the Aero Testbed in a left spin with pro-spin ailerons and integration tolerances of 10^{-7} and 10^{-4}.

6.1.4 Integration Methodology Parameter Study

As mentioned earlier in this chapter, to generate simulations at 300 Hz, a 4^{th} order Runge-Kutta routine was implemented because the built-in MATLAB *ode*45 function had only a self-adjusting timestep. The effects on the simulation of this different integration routine were investigated, and no major differences were observed. Figures 6.12 and 6.13 show that at an absolute and relative tolerance of 10^{-4}, the value of all simulations used for analysis, no discernable differences exist between the RK4 routine, operating at 300 Hz, and the built-in MATLAB *ode*45 function for the u, v, and w velocity components, or for the angular rates p, q, and r. Both simulations presented in this subsection are for a low deflection angle spin to the left with the ailerons deflected in a pro-spin manner at 22 deg, and both simulations are initialized with a yaw rate of -45 deg/s. The simulation using the built-in MATLAB *ode*45 function is labeled as "MATLAB *ode*45," and the 4^{th} order Runge-Kutta scheme with manually-adjustable timestep produced the results labeled "RK4." Figure 6.14 presents trajectory comparisons for SpinSim simulations using the built-in MATLAB *ode*45 function and the external RK4 integration routine. As with the previous two figures, these plots indicate that no differences in the results are evident.

There were no discernable changes observed by using the RK4 function, compared with the *ode*45 function. The RK4 function operated at 300 Hz was used for the trajectory coplots to produce airplane x-y-z coordinate points with even temporal spacing. All simulations where angular rates are shown are performed with the built-in MATLAB *ode*45 function. Meanwhile, all simulations coplotted with Aero Testbed experimental flight test data are performed with the RK4 function at 300 Hz.

Figure 6.15 presents angular orientation comparisons for SpinSim simulations using the built-in MATLAB *ode*45 function and the external RK4 integration routine. As with Fig. 6.14, no significant differences are evident. A difference between the two simulations is observed in the plots of the yaw angle ψ. Looking at the peaks in the yaw angle ψ, which are the result of bounding the yaw angle by $-360 \leq \psi \leq 360$ deg, the peak values appear uneven in the *ode*45 plot. Meanwhile, the peak values appear to be nearly uniform for the 300 Hz RK4 plot. This uniformity in the RK4 ψ peak values is due to the RK4 method integrating at a smaller and constant timestep. Because of the smaller-sized timesteps of the RK4 method, the plotted maximum and minimum values of ψ are closer to ± 360 deg. It is the uneven timesteps of the *ode*45 integration that produce uneven peaks in that simulation. The fact that those maximum and minimum values are farther from ± 360 deg is due to the larger timesteps (i.e., lower-resolution simulation) of the *ode*45 simulation at a tolerance parameter of 10^{-4}.

Figure 6.16 presents airspeed and q comparisons for SpinSim simulations, using the built-in MATLAB *ode*45 function and the external RK4 integration routine. Again, no significant differences between the results from the two integration routines are evident in the plots of airspeed and q. The values of V and q are predicted to be 22 m/s and 250 N/m^2, respectively. Figure 6.17 presents aerodynamic and flight path angle comparisons for SpinSim simulations,

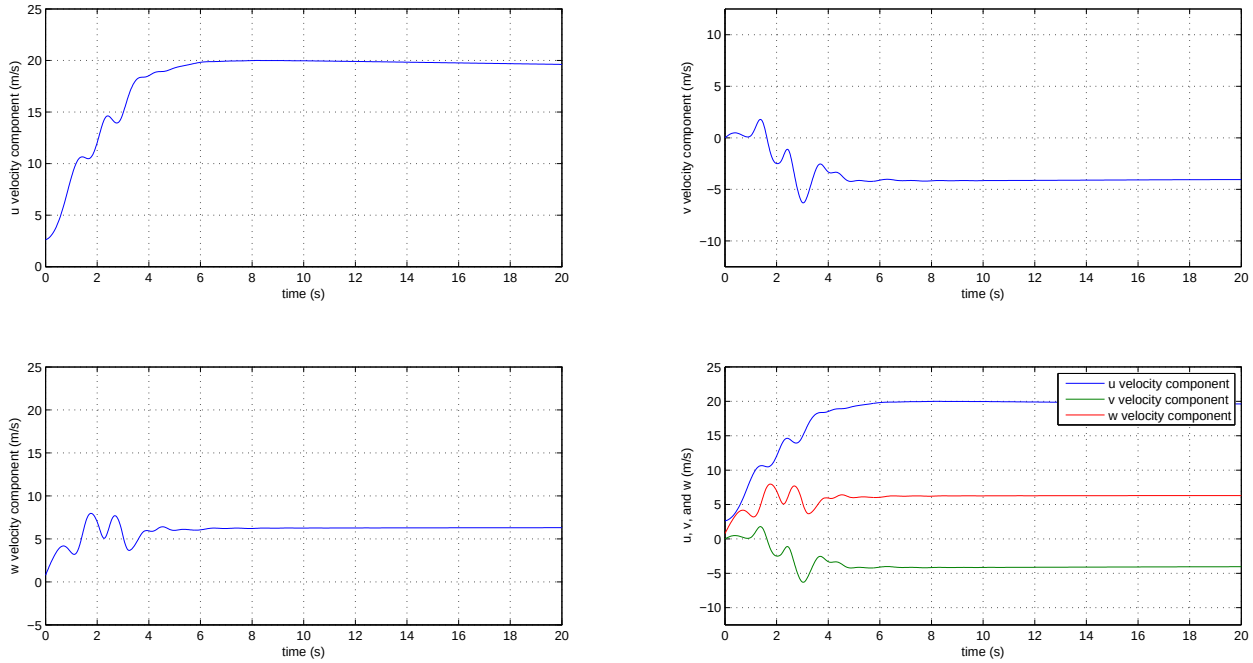

(a) Body inertial velocities of MATLAB *ode*45 routine

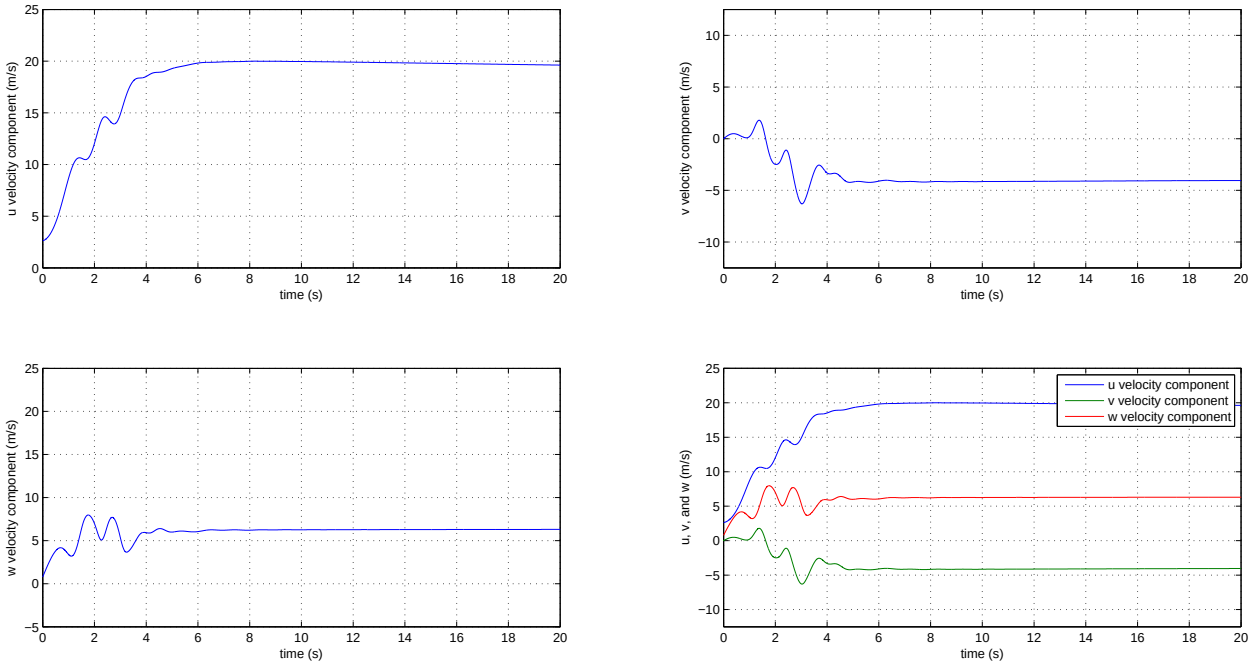

(b) Body inertial velocities of RK4 routine

Figure 6.12: Comparison of u, v, and w velocity components for SpinSim simulation of the Aero Testbed in a left spin with pro-spin ailerons and *ode*45 and RK4 integration routines.

using the *ode*45 function and the RK4 integration routine. These plots indicate that no differences in the results are evident, aside from the uneven peak and minimum values of ψ, as discussed previously with regard to Fig. 6.15. Both simulations predict steady spin values for α and β of just under 20 deg and -10 deg, respectively.

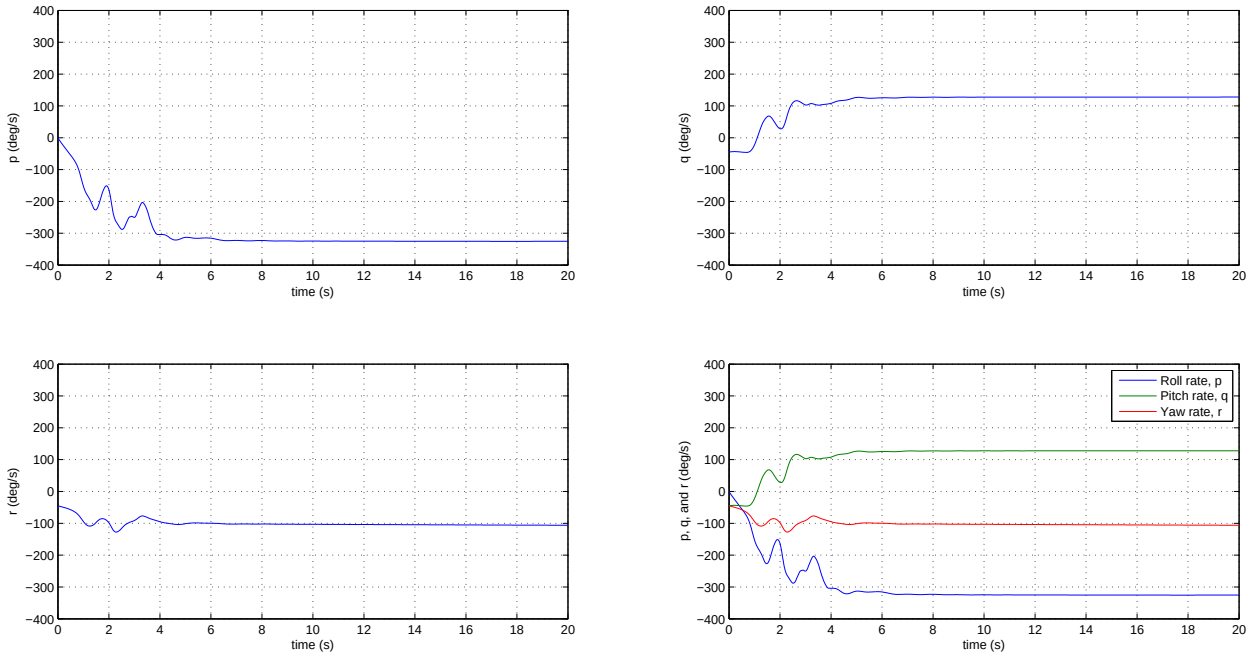

(a) Angular rates of MATLAB *ode*45 routine

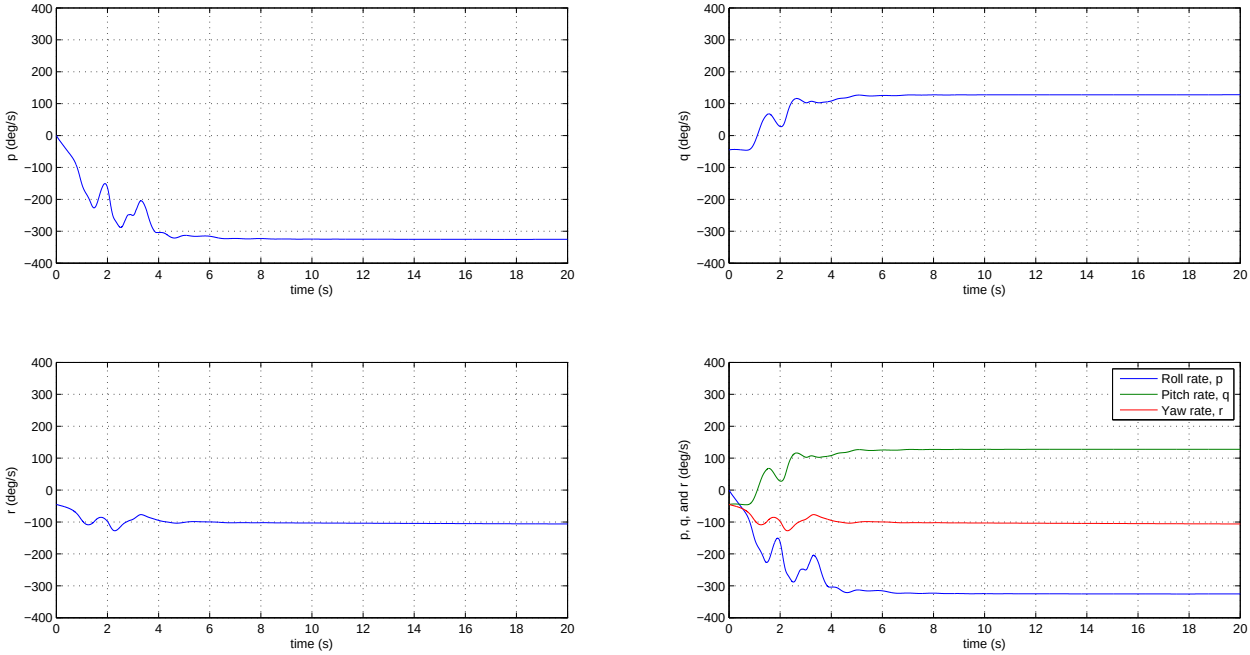

(b) Angular rates of RK4 routine

Figure 6.13: Comparison of p, q, and r angular rates for SpinSim simulation of the Aero Testbed in a left spin with pro-spin ailerons and *ode*45 and RK4 integration routines.

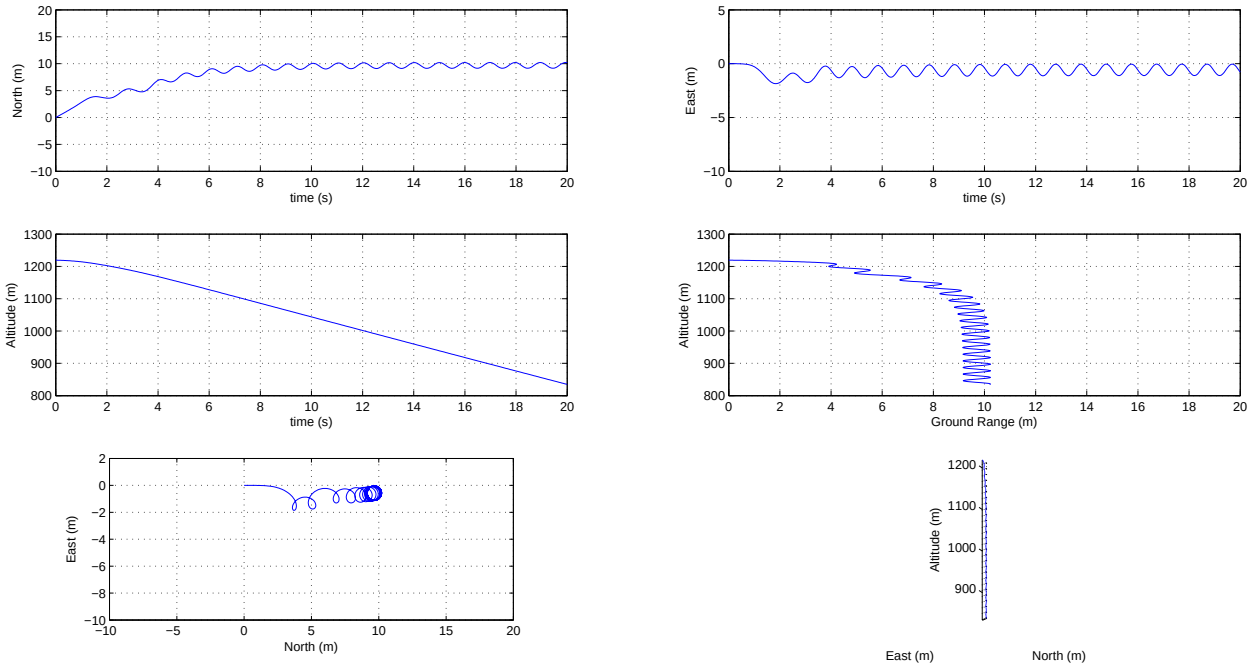

(a) Trajectory using MATLAB *ode*45 integration scheme

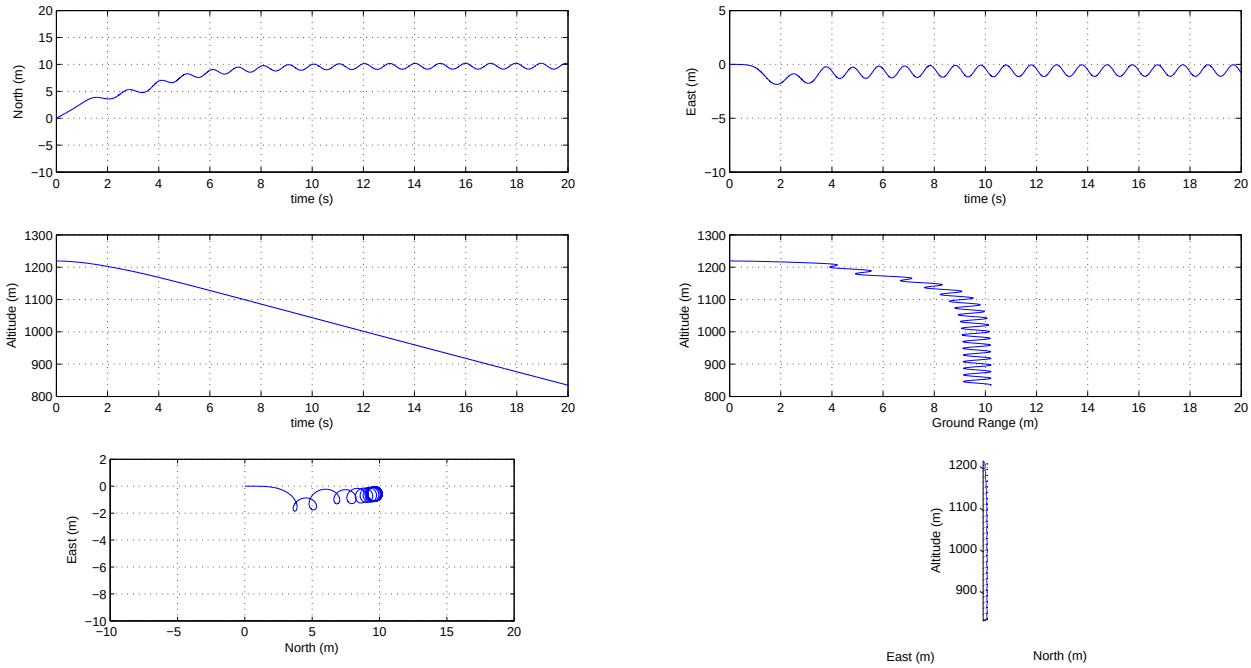

(b) Trajectory using RK4 integration scheme

Figure 6.14: Comparison of trajectories for SpinSim simulation of the Aero Testbed in a left spin with pro-spin ailerons and *ode*45 and RK4 integration routines.

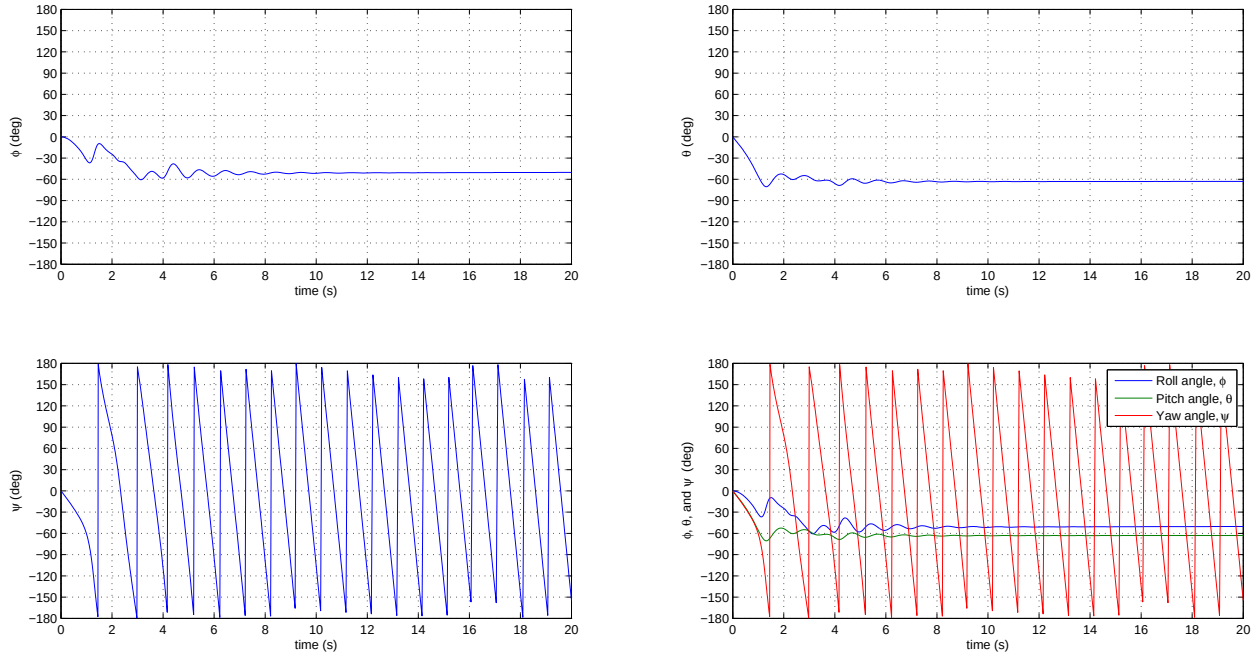

(a) Angular orientations using MATLAB *ode*45 integration scheme

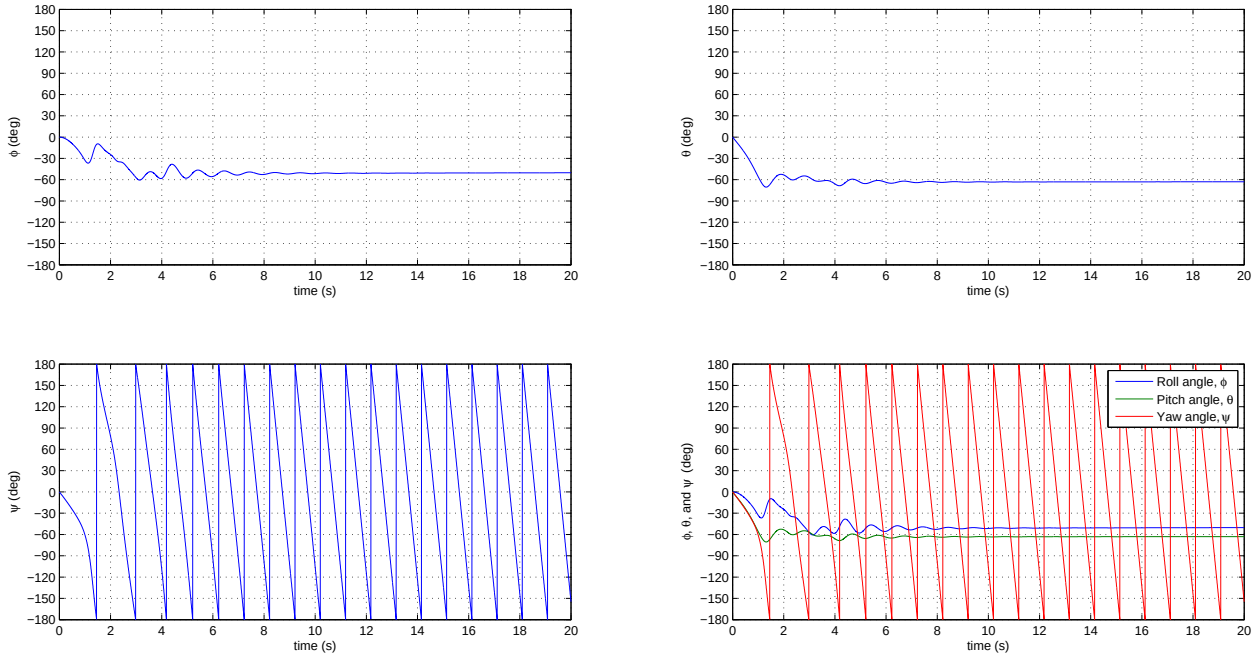

(b) Angular orientations using RK4 integration scheme

Figure 6.15: Comparison of ϕ, θ, and ψ Euler angles for SpinSim simulation of the Aero Testbed in a left spin with pro-spin ailerons and *ode*45 and RK4 integration routines.

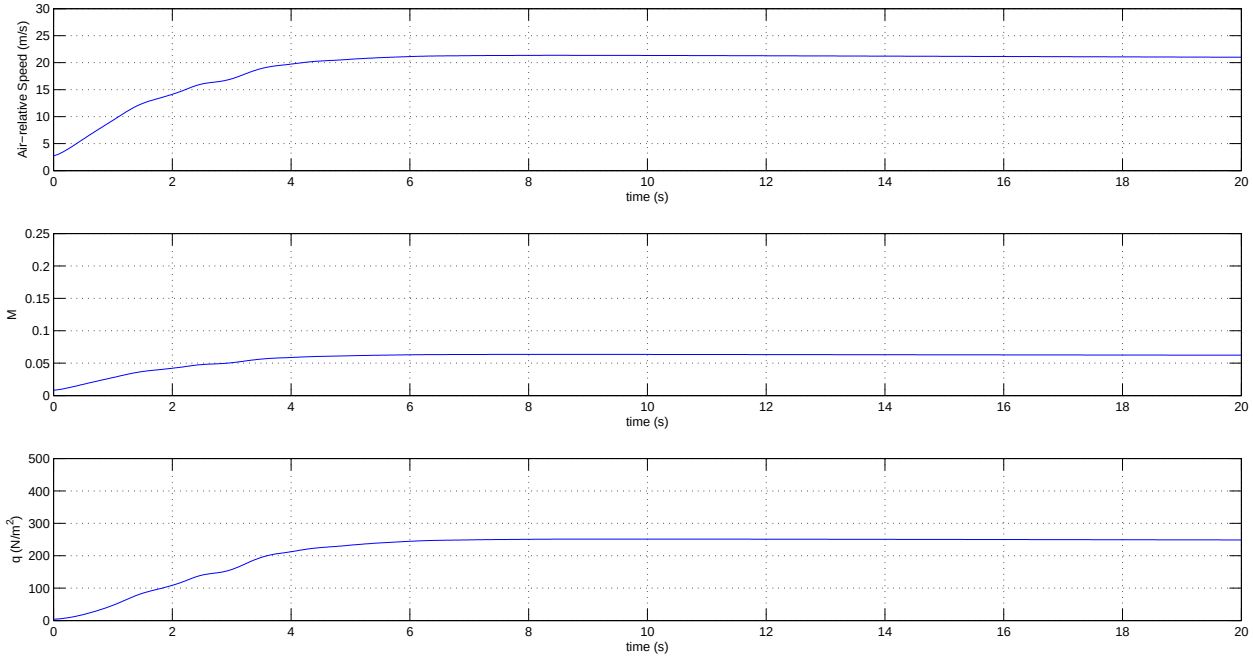

(a) Velocity and q using MATLAB *ode*45 integration scheme

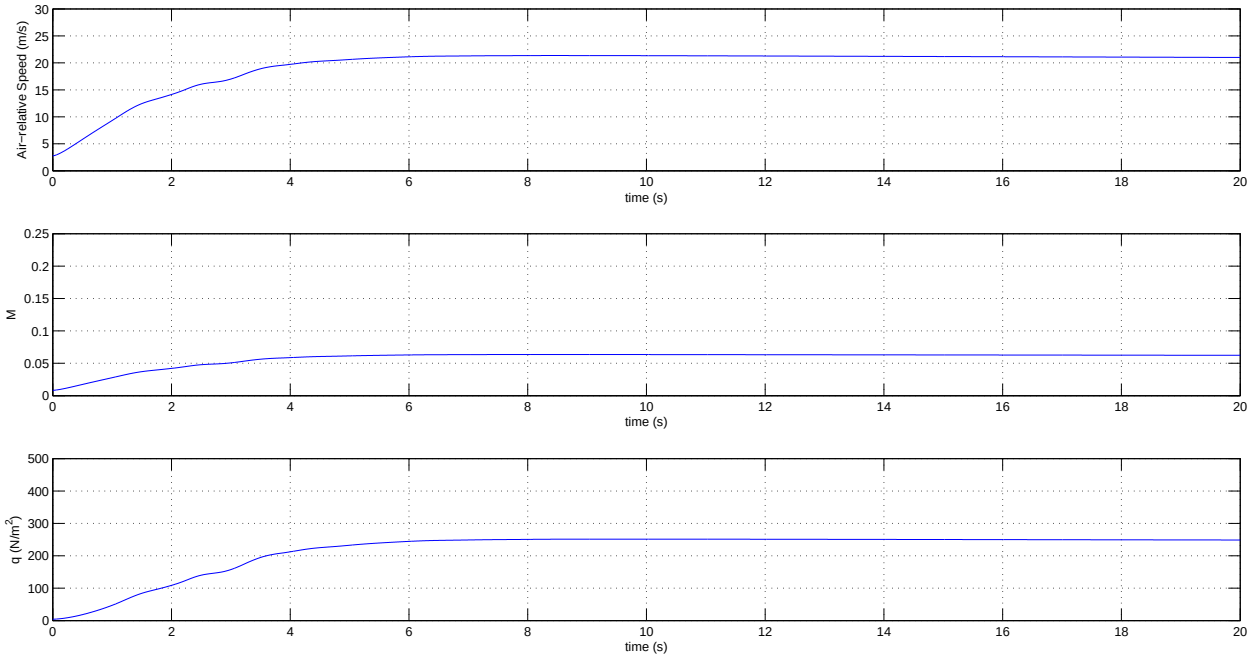

(b) Velocity and q using RK4 integration scheme

Figure 6.16: Comparison of airspeed, Mach number, and q for SpinSim simulation of the Aero Testbed in a left spin with pro-spin ailerons and *ode*45 and RK4 integration routines.

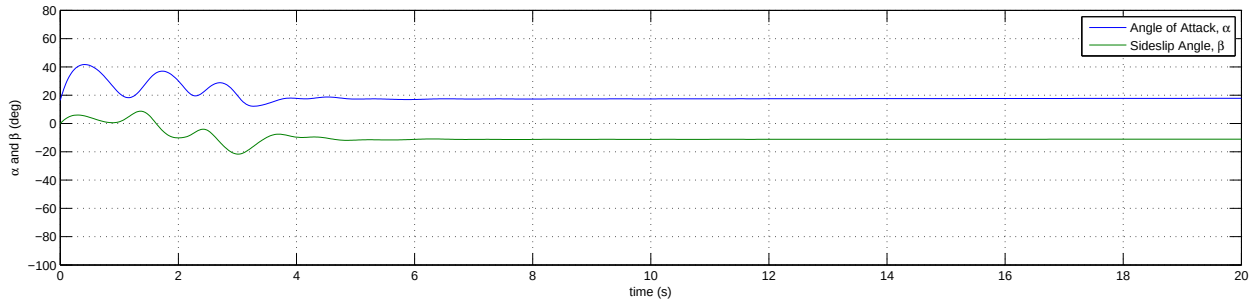

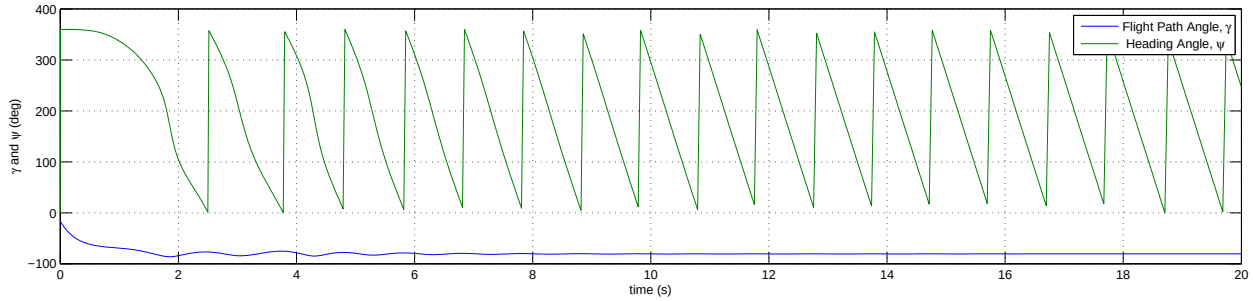

(a) Aerodynamic and flight path angles using MATLAB *ode*45 integration scheme

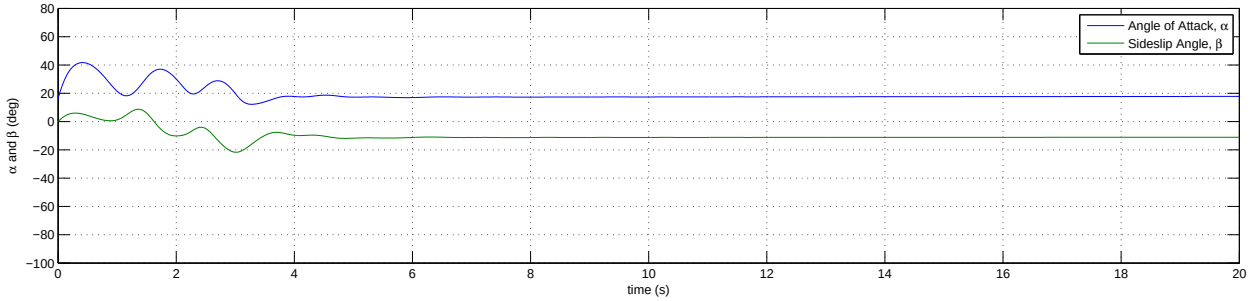

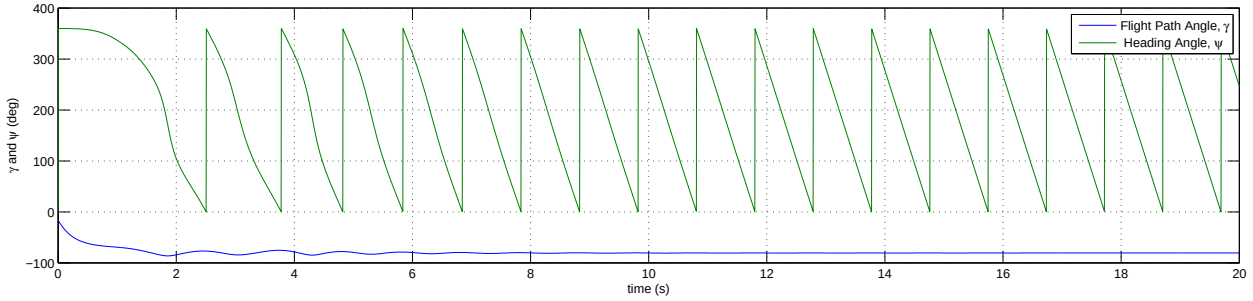

(b) Aerodynamic and flight path angles using RK4 integration scheme

Figure 6.17: Comparison of airspeed, Mach number, and q for SpinSim simulation of the Aero Testbed in a left spin with pro-spin ailerons and *ode*45 and RK4 integration routines.

6.1.5 Demonstration of Initial Condition Insensitivity

While spin modes are not entirely initial condition specific, this section presents some non-exhaustive studies of initial condition sensitivity. The plots in this section show that even with different initial conditions, the SpinSim simulation eventually converges on the same spin mode. In the first study, the baseline initial conditions of roll and yaw rates p and r of -45 deg/s are changed, such that the initial yaw rate r is increased in magnitude to -90 deg/s. The initial roll rate p remains unchanged at -45 deg/s. A comparison of the two spin simulation results is presented in Figs. 6.18 and 6.19, which present the body inertial velocities and angular rates, respectively.

When comparing the simulations for the two different initial conditions, the most important observation is that both simulations converge on the same spin modes, with the u, v, and w velocity components approximately equal to 20, -4, and 6.5 m/s, respectively. The angular rates p, q, and r, to which the two simulations converged, are also indistinguishable. Additionally, in both cases the steady-spin values are achieved after approximately 6 s. Greater changes to the w velocity component, in the incipient stage of the spin, were observed for the $r = -45$ deg/s initial condition simulation when compared with the simulation with $r = -90$ deg/s. In regard to the u and v velocity components, greater changes were observed for the $r = -90$ deg/s initial condition when compared with the $r = -45$ deg/s initial condition. These simulation characteristics are supported by the fact that the increased initial yaw rate r would create a larger positive overshoot of the steady-state v velocity component value, as illustrated in Fig. 6.18. The greater initial yaw rate r gives the airplane more rotational energy. This extra rotational energy must be dissipated between the u and v velocity components until the steady-state spin is achieved. This increase in the yaw rate r also results in a higher average q on the wing, which would explain the smaller variations in the w velocity component.

Similar observations can be made for the p, q, and r angular rate time history plots of Fig. 6.19. Smaller oscillations prior to achieving the steady state spin are observed for the roll and pitch rates of the $r = -45$ deg/s initial condition simulation. Again, this is the case because the airplane has less initial angular momentum in the baseline case, which results in smaller aerodynamic forces. The smaller changes in the yaw rate for the $r = -90$ deg/s initial condition are accounted for by the fact that the initial condition is much closer to the steady-spin condition of $r \approx -100$ deg/s when compared with the $r = -45$ deg/s initial condition.

Figure 6.20 presents trajectory comparisons for SpinSim simulations where the initial condition yaw rate r was changed from -45 deg/s to -90 deg/s. Minor differences are evident as a result of doubling the magnitude of the initial yaw rate r. These minor differences include the fact that the developed spin is located approximately 1 m farther from the simulation start point than the $r = -45$ deg/s initial condition case. The higher initial yaw rate r also results in the spin developing slightly further east. This more-easterly location of the developed spin appears to be a result of the airplane following an initial helical trajectory with a larger radius and rolling over earlier. This larger radius and quicker rolling-over can be directly attributed to the increased initial yaw rate, which increases the degree

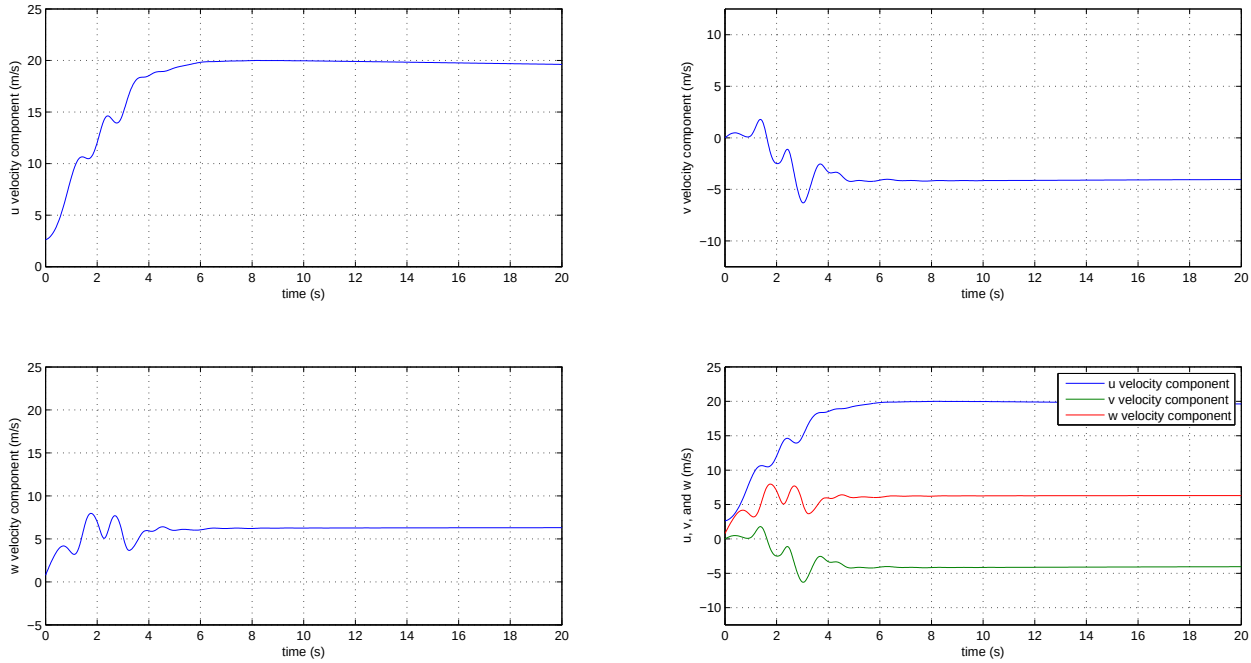

(a) Body inertial velocities of baseline with $p = r = -45$ deg/s initial condition

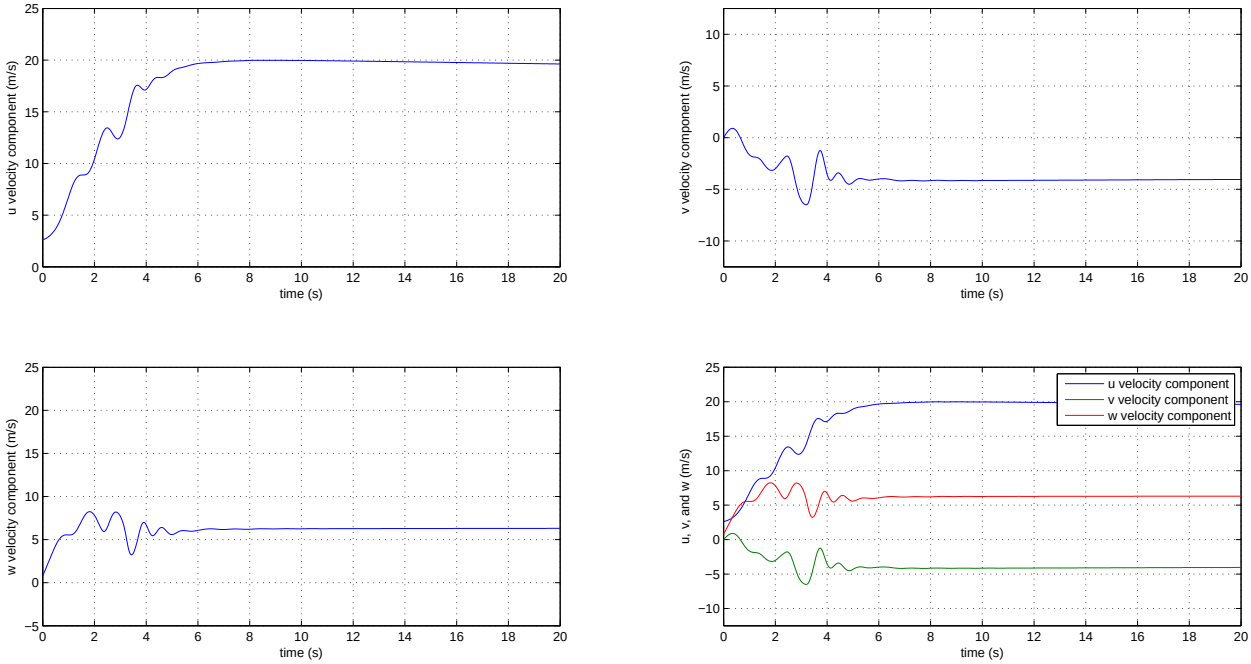

(b) Body inertial velocities of parameter study with $r = -90$ deg/s initial condition

Figure 6.18: Comparison of u, v, and w velocity components for SpinSim simulation of the Aero Testbed in a left spin with pro-spin ailerons for baseline spin and $r = -90$ deg/s initial condition.

of unevenness of stall to the wings. The change in the east location between the two initial conditions is also minor, and it appears to be on the order of approximately 1 m. Most importantly, the developed spin radius is unchanged by the different initial conditions, with $R_s \approx 0.5$ m irrespective of the initial yaw rate.

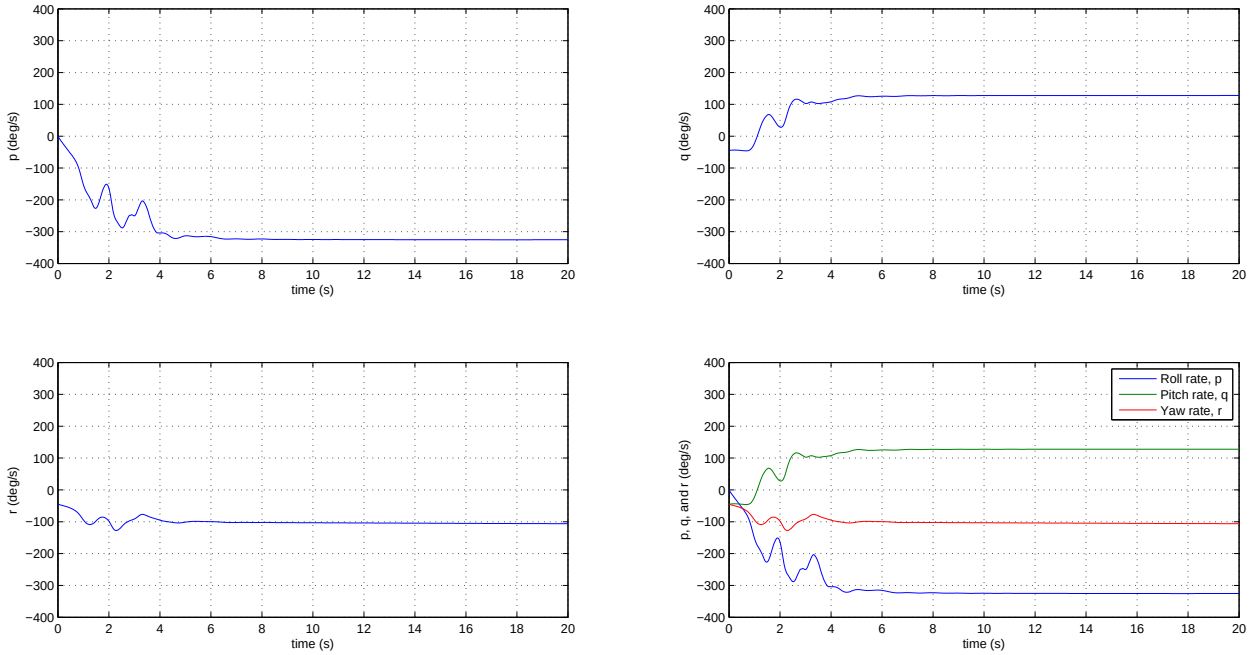

(a) Angular rates of baseline with $p = r = -45$ deg/s initial condition

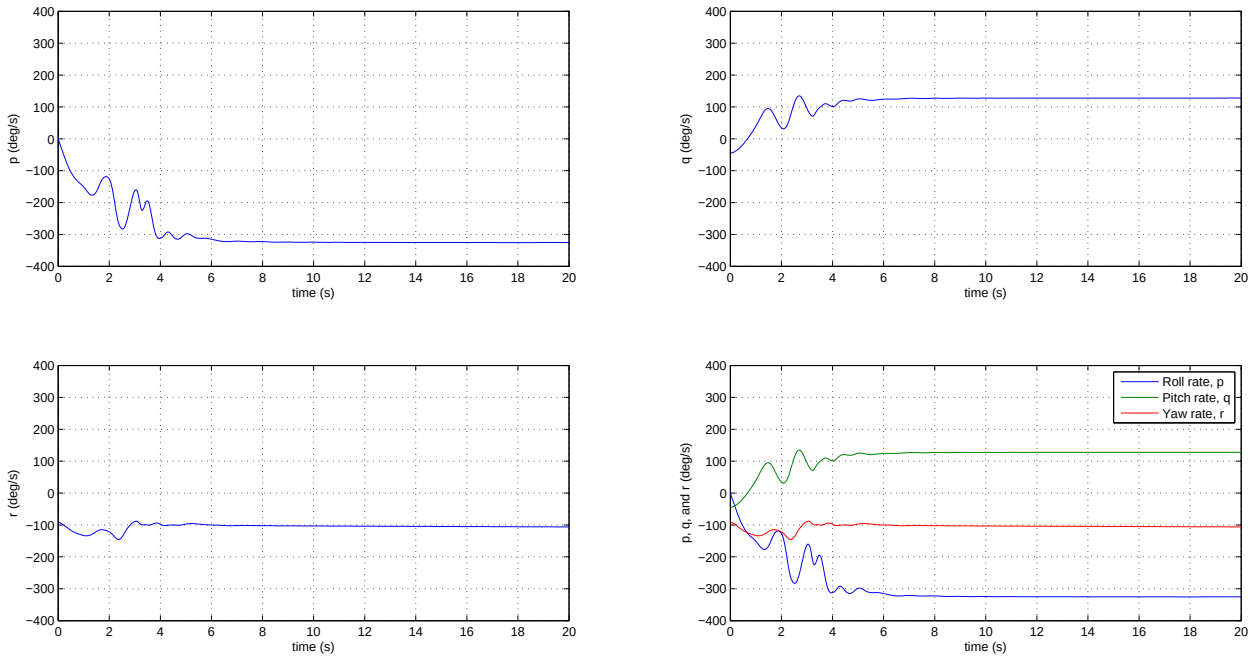

(b) Angular rates of parameter study with $r = -90$ deg/s initial condition

Figure 6.19: Comparison of p, q, and r angular rates for SpinSim simulation of the Aero Testbed in a left spin with pro-spin ailerons for baseline spin and $r = -90$ deg/s initial condition.

Figure 6.21 presents angular orientation comparisons for SpinSim simulations where the initial condition yaw rate was changed from -45 deg/s to -90 deg/s. No major differences are evident, aside from the slope of the yaw angle ψ vs. time plot being steeper for the $r = -90$ deg/s initial condition case when compared with the $r = -45$ deg/s case.

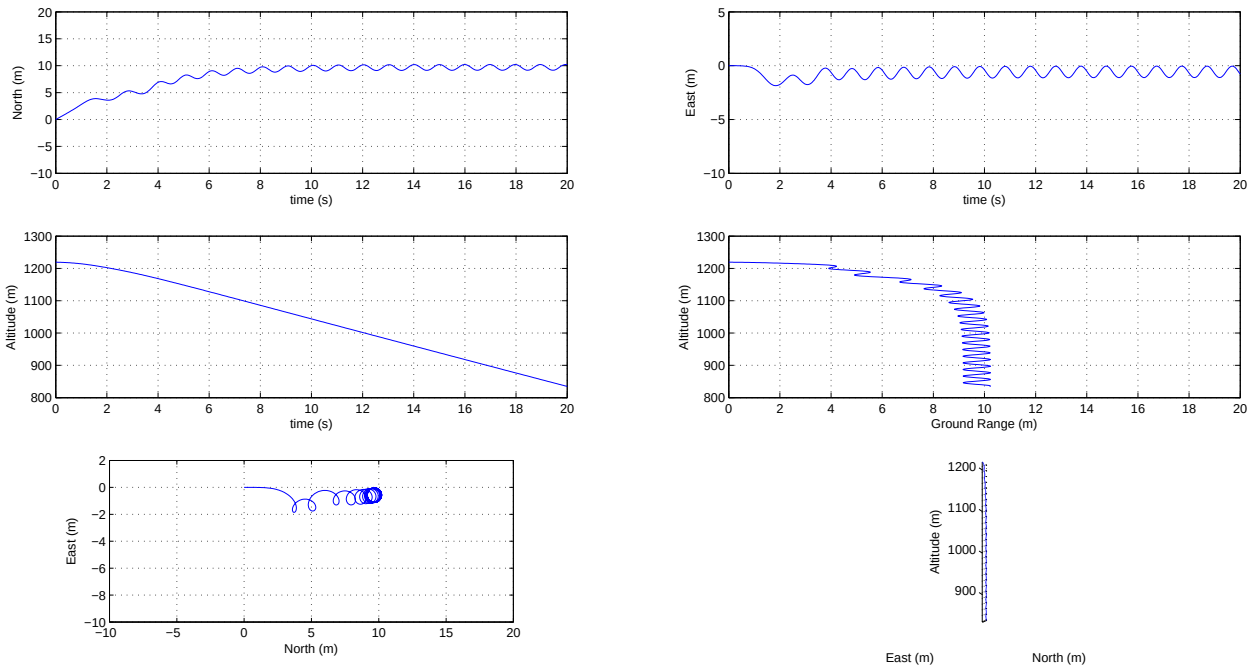

(a) Baseline trajectory with $p = r = -45$ deg/s initial condition

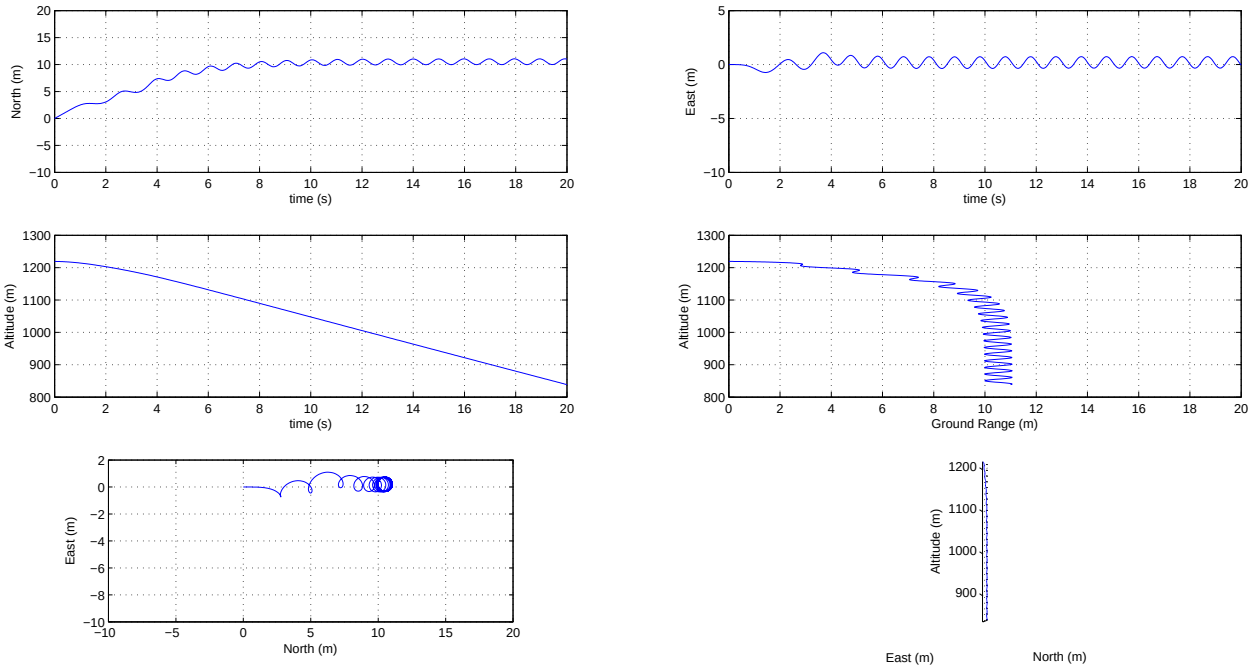

(b) Parametric study trajectory with $r = -90$ deg/s initial condition

Figure 6.20: Comparison of trajectories for SpinSim simulation of the Aero Testbed in a left spin with pro-spin ailerons for baseline spin and $r = -90$ deg/s initial condition.

Minor differences are present in the time histories of ϕ and θ, but these are attributable to the different initial yaw rate.

All values are nearly identical beyond $t = 7$ s.

The velocity and q comparisons for SpinSim simulations with initial yaw rates of $r = -45$ deg/s and $r = -90$ deg/s are presented in Fig. 6.22. As expected, the final motion of the two simulations converges on the same values. The increase in the initial yaw rate results in the air-relative speed V and q increasing to the steady-spin values at a slightly slower rate than the $r = -45$ deg/s initial condition case. This slower convergence toward the steady-spin velocity can be attributed to a larger amount of the airplane momentum being lost at the beginning of the simulation. This larger loss of momentum is due to the higher v velocity component, and the resulting increase in the sideslip angle β, which puts the airplane in a higher-drag orientation relative to the freestream.

Comparisons of the aerodynamic angles of the SpinSim simulations with $r = -45$ deg/s and $r = -90$ deg/s are presented in Fig. 6.23. This figure supports the hypothesis of the previous paragraph. When the initial yaw rate r is increased in magnitude from -45 deg/s to -90 deg/s, the airplane, indeed, encounters a larger maximum value of slideslip angle β. For the $r = -45$ deg/s case, an initial peak value of $\beta \approx 6$ deg is achieved by $t \approx 0.3$ s. The sideslip angle β later reaches $\beta = 8.7$ deg at $t \approx 1.4$ s. In the $r = -90$ deg/s case, an initial peak β valueof 11.8 deg is reached at $t = 0.27$ s. The fact that the airplane reaches a maximum of $\alpha \approx 50$ deg at $t = 0.55$ s for the initial $r = -90$ deg/s simulation, while the $r = -45$ deg/s simulation shows a maximum of $\alpha = 41.7$ deg, further explains this slower increase in velocity toward the steady-spin condition. The higher peak in α of the $r = -90$ deg/s initial condition also puts the airplane in a higher-drag orientation to the freestream. It is these higher peak values of α and β that together place the airplane in a higher-drag orientation relative to the freestream. This situation explains why the $r = -90$ deg/s simulation is slightly slower to accelerate toward the steady state spin velocity of just under 22 m/s.

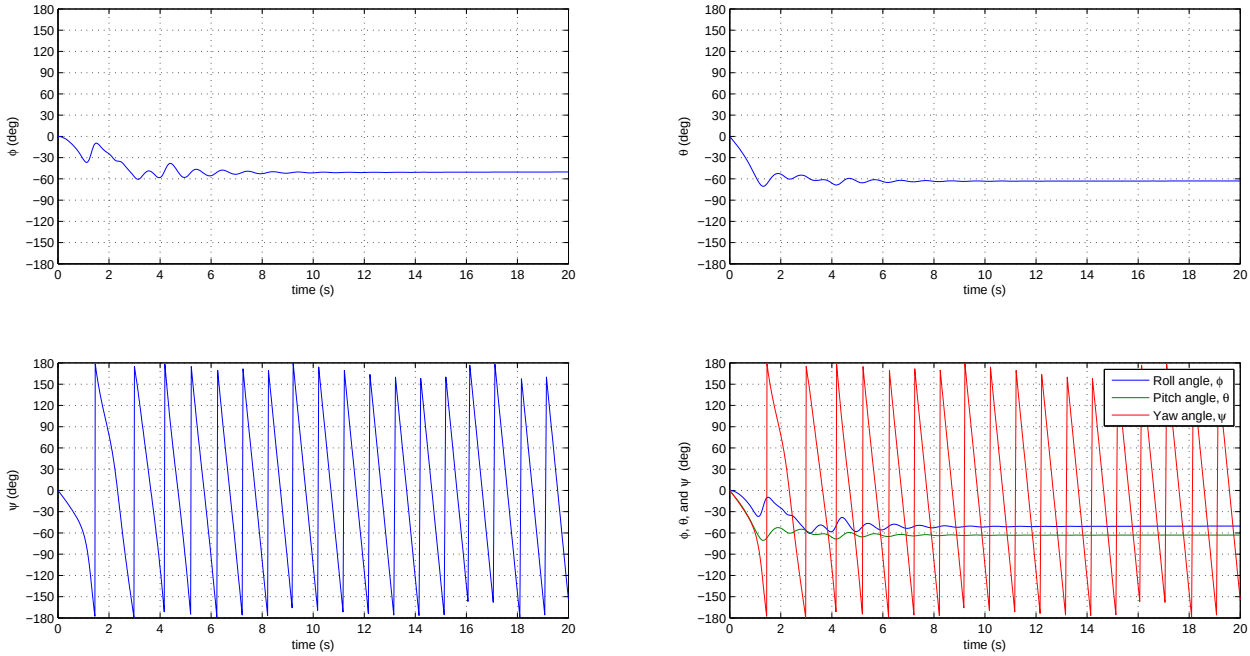

(a) Baseline angular orientations with $p = r = -45$ deg/s initial condition

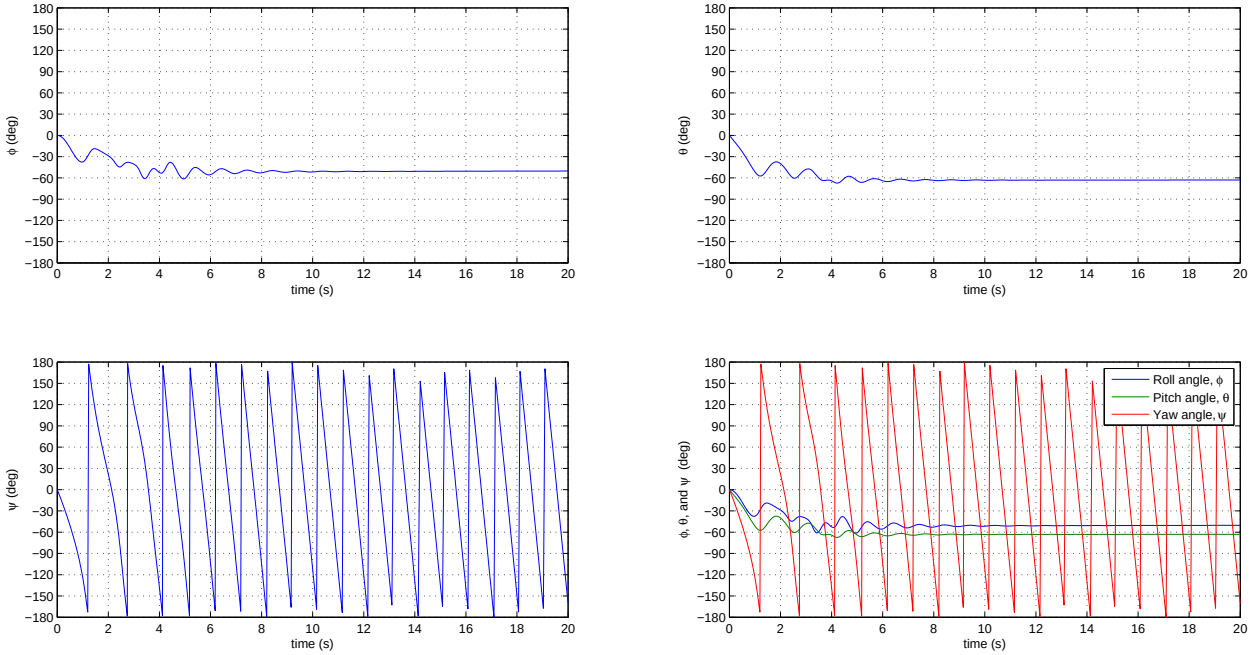

(b) Parametric study angular orientations with $r = -90$ deg/s initial condition

Figure 6.21: Comparison of ϕ, θ, and ψ Euler angles for SpinSim simulation of the Aero Testbed in a left spin with pro-spin ailerons for baseline spin and $r = -90$ deg/s initial condition.

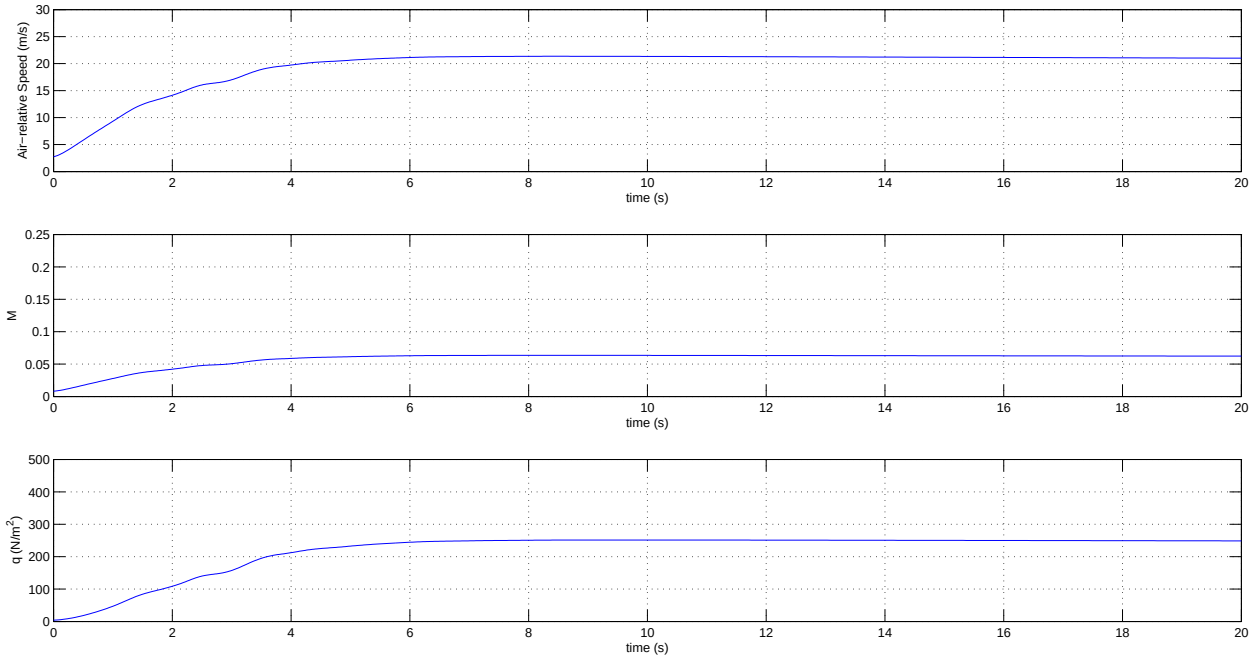

(a) Baseline velocity and q with $p = r = -45$ deg/s initial condition

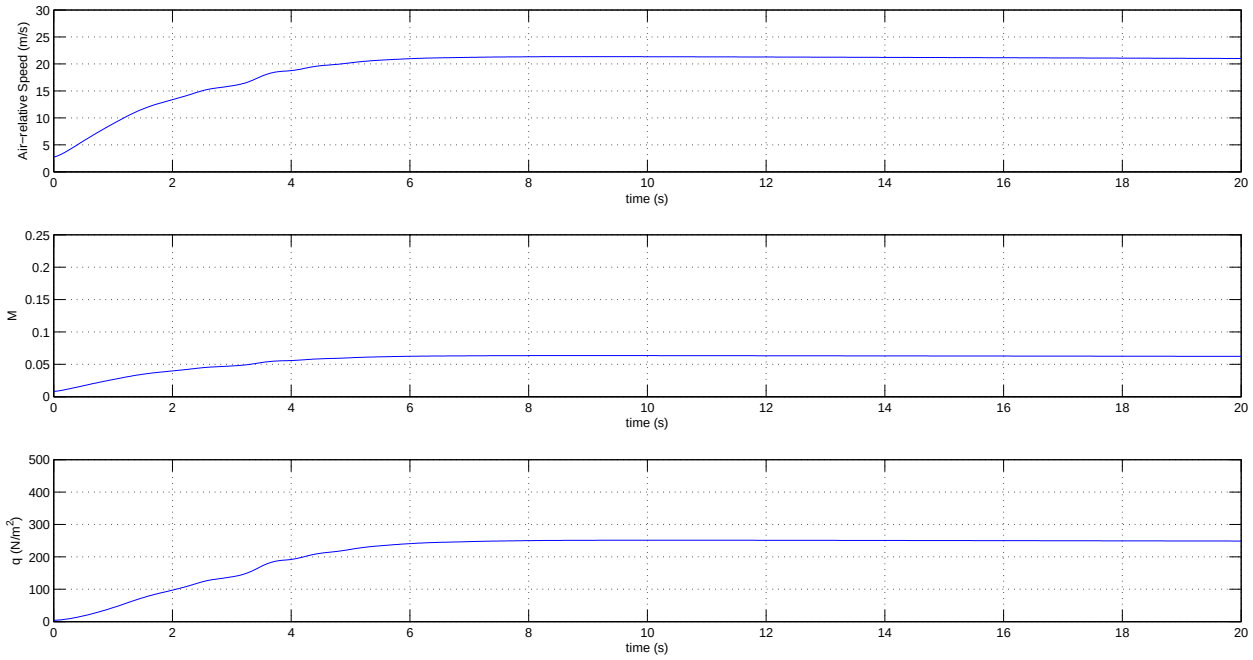

(b) Parametric study velocity and q with $r = -90$ deg/s initial condition

Figure 6.22: Comparison of airspeed, Mach number, and q for SpinSim simulation of the Aero Testbed in a left spin with pro-spin ailerons for baseline spin and $r = -90$ deg/s initial condition.

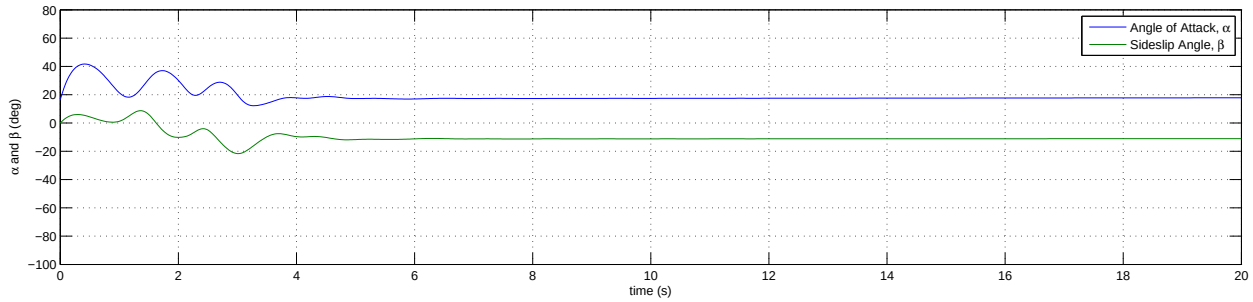

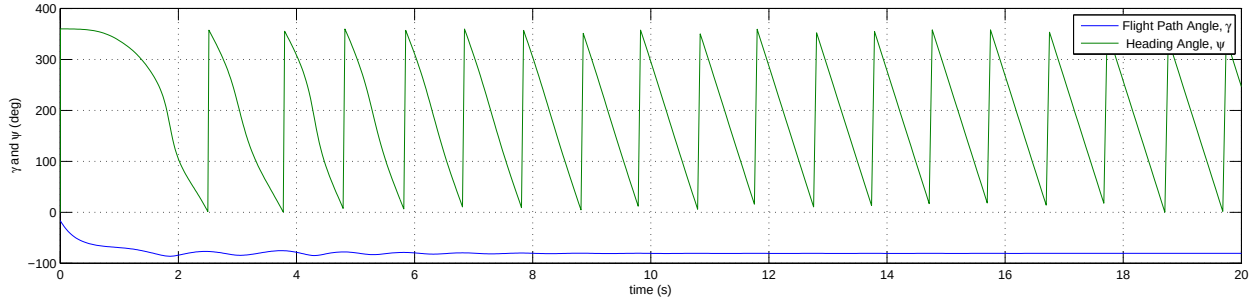

(a) Baseline aerodynamic and flight path angles with $p = r = -45$ deg/s initial condition

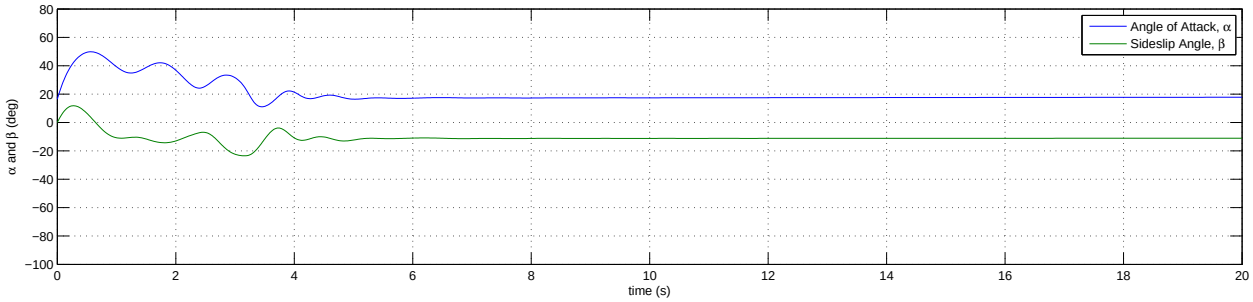

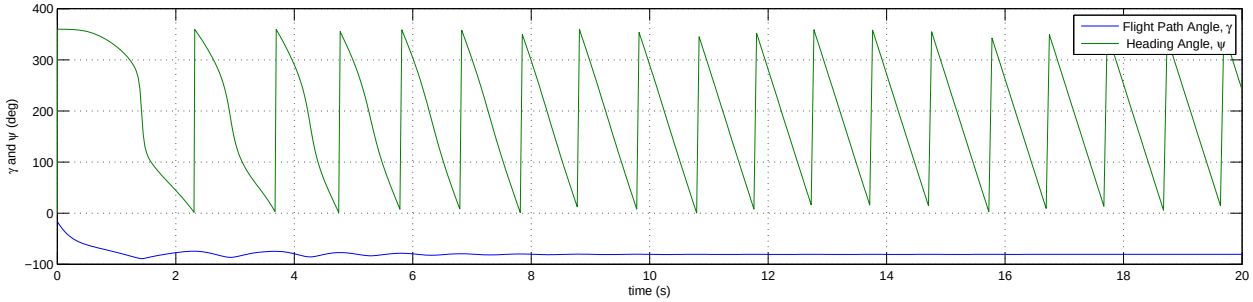

(b) Parametric study aerodynamic and flight path angles with $r = -90$ deg/s initial condition

Figure 6.23: Comparison of aerodynamic and flight path angles for SpinSim simulation of the Aero Testbed in a left spin with pro-spin ailerons for baseline spin and $r = -90$ deg/s initial condition.

An additional initial condition sensitivity parameter study was conducted where the airplane angle of attack was increased from $\alpha = 16.4$ deg to $\alpha = 32.8$ deg at the same r-value of $r = -90$ deg/s. This increase in the angle of attack ensured that the initial conditions positioned the airplane at an orientation where the wing was unevenly stalled, which is a necessary condition for entering a spin. Figure 6.24 presents comparisons of the body inertial velocities from the two simulations. Figure 6.25 presents a comparison of the angular rate time histories of the two simulations with different initial values of α and r.

Consistent with the theme of these parametric studies, and although minor differences are observed between the simulations during the spin entry phase, which is defined by $0 < t < 6$ s, both the simulation with an initial $\alpha = 16.4$ deg and the simulation with an initial $\alpha = 32.8$ deg, nevertheless, converge upon the same steady spin mode. In Fig. 6.24, the plots of the u velocity component are nearly the same. Meanwhile, the plots of the v and w velocity components depict some differences in the pre-spin oscillations until $t \approx 6$ s. For $t \geq 6$ s, both simulations converged on the same steady spin parameter values. As expected, the p, q, and r angular rate time histories are slightly different at the beginning. It may be observed clearly in Fig. 6.25 that initializing the simulation with $r = -90$ deg/s allows for the simulation to converge more quickly toward its developed spin yaw rate of approximately -100 deg/s.

Figure 6.26 presents trajectory comparisons for SpinSim simulations where the initial condition yaw rate r was changed from -45 deg/s to -90 deg/s and α was increased from 16.4 to 32.8 deg. The higher-α initial condition results in a developed spin that is achieved at a northerly ground range that is 0.3 m closer to the starting point than the lower-α and lower-r initial condition. Further, it is approximately 1.2 m further east. The trends for the next three figures (Figs. 6.27–6.29) mirror those of the increased-r initial conditions. The larger α_{max} and earlier peak in β, as shown in Fig. 6.23, remain for the $r = -90$ deg/s initial condition when the initial α is increased from 16.4 to 32.8 deg.

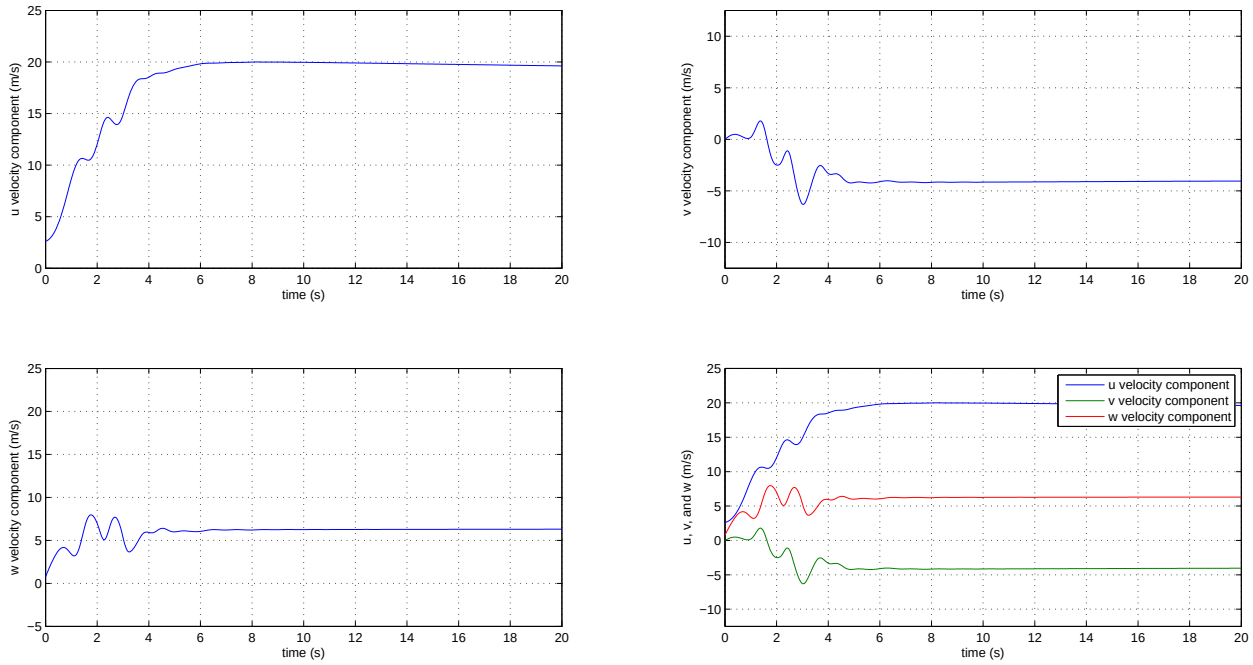

(a) Body inertial velocities of baseline with initial conditions of $p = r = -45$ deg/s and $\alpha = 16.4$ deg

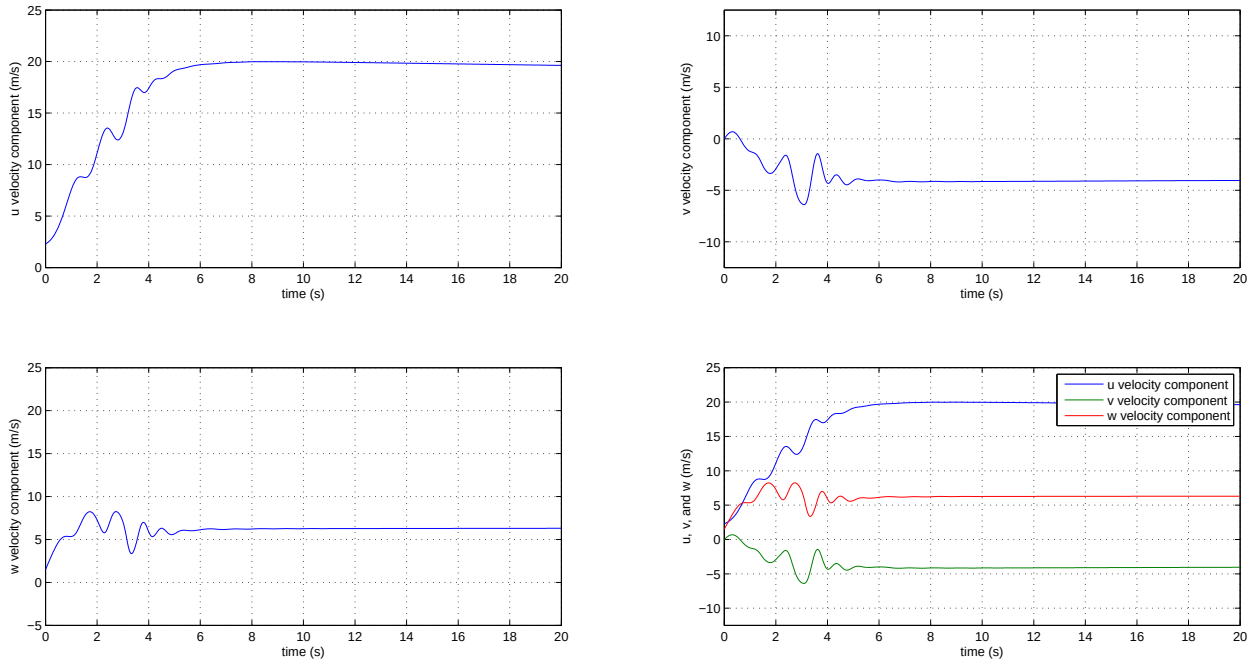

(b) Body inertial velocities of parameter study with initial conditions of $r = -90$ deg/s and $\alpha = 32.8$ deg

Figure 6.24: Comparison of u, v, and w velocity components for SpinSim simulation of the Aero Testbed in a left spin with pro-spin ailerons for baseline spin and $r = -90$ deg/s and $\alpha = 32.8$ deg initial condition.

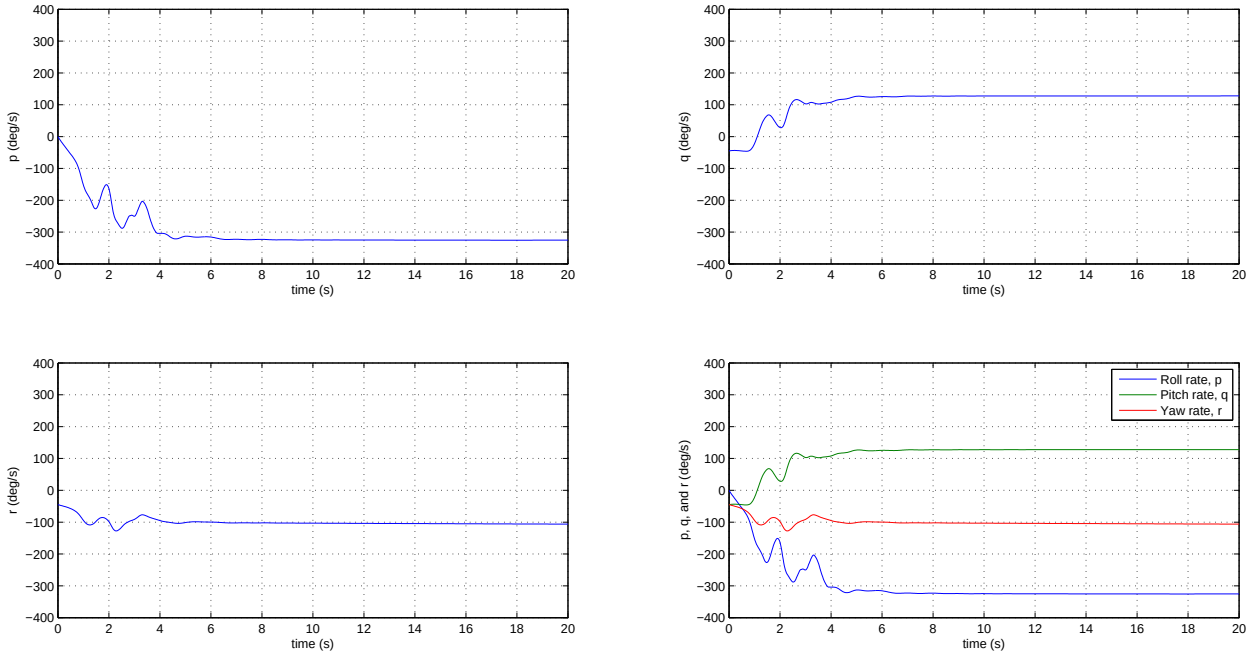

(a) Angular rates of baseline with initial conditions of $p = r = -45$ deg/s and $\alpha = 16.4$ deg

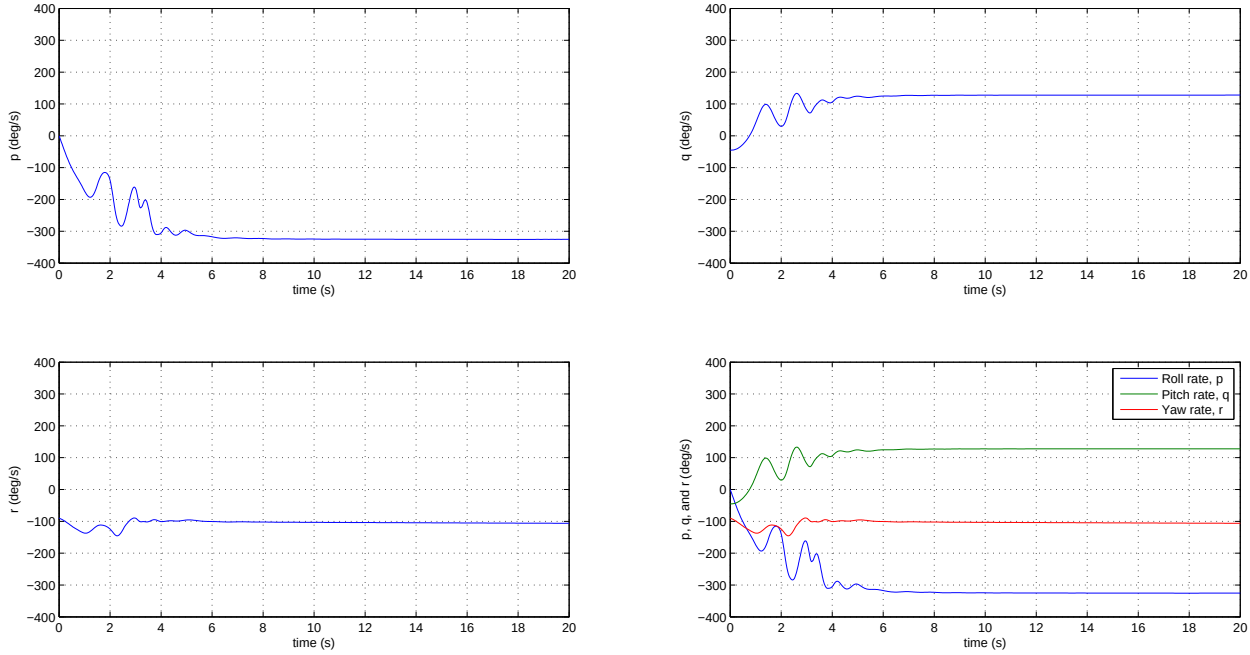

(b) Angular rates of parameter study with initial conditions of $r = -90$ deg/s and $\alpha = 32.8$ deg

Figure 6.25: Comparison of p, q, and r angular rates for SpinSim simulation of the Aero Testbed in a left spin with pro-spin ailerons for baseline spin and $r = -90$ deg/s and $\alpha = 32.8$ deg initial condition.

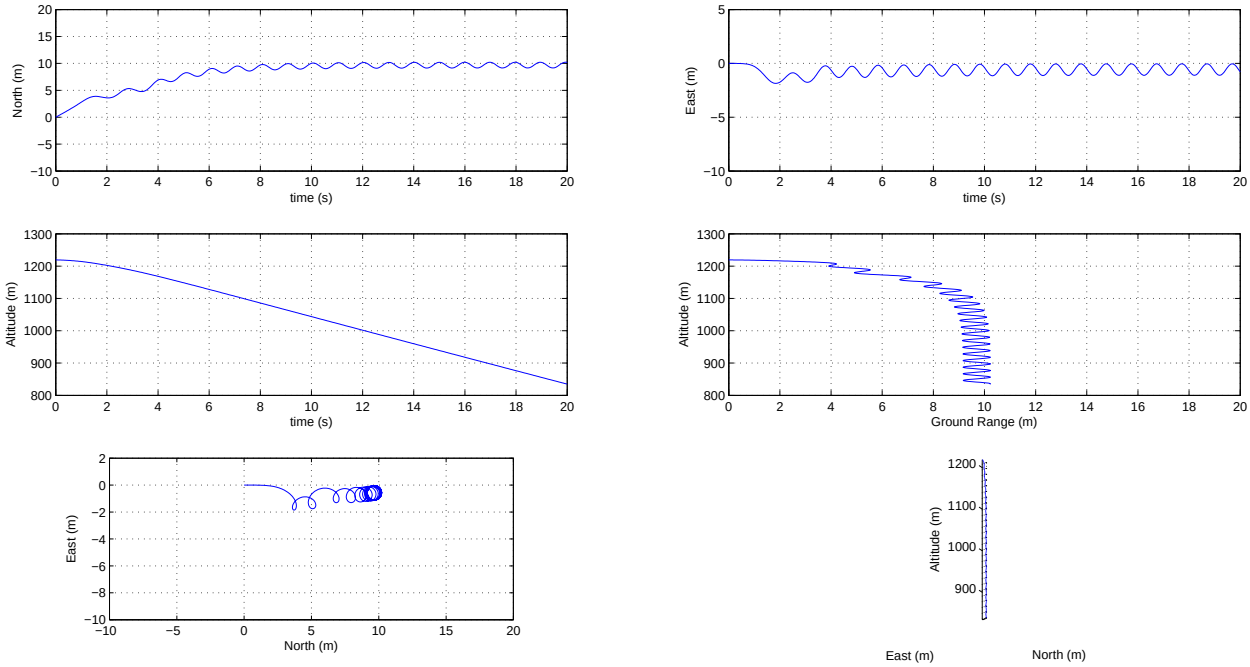

(a) Baseline trajectory with initial conditions of $p = r = -45$ deg/s and $\alpha = 16.4$ deg

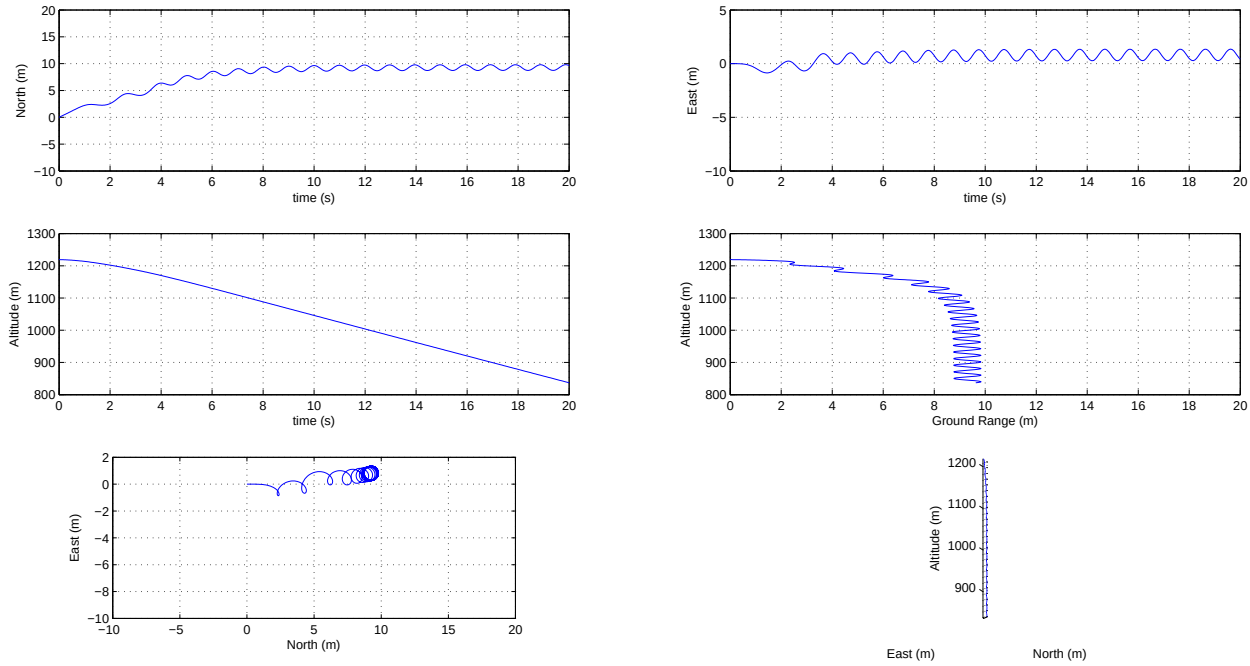

(b) Parametric study trajectory with initial conditions of $r = -90$ deg/s and $\alpha = 32.8$ deg

Figure 6.26: Comparison of trajectories for SpinSim simulation of the Aero Testbed in a left spin with pro-spin ailerons for baseline spin and $r = -90$ deg/s and $\alpha = 32.8$ deg initial condition.

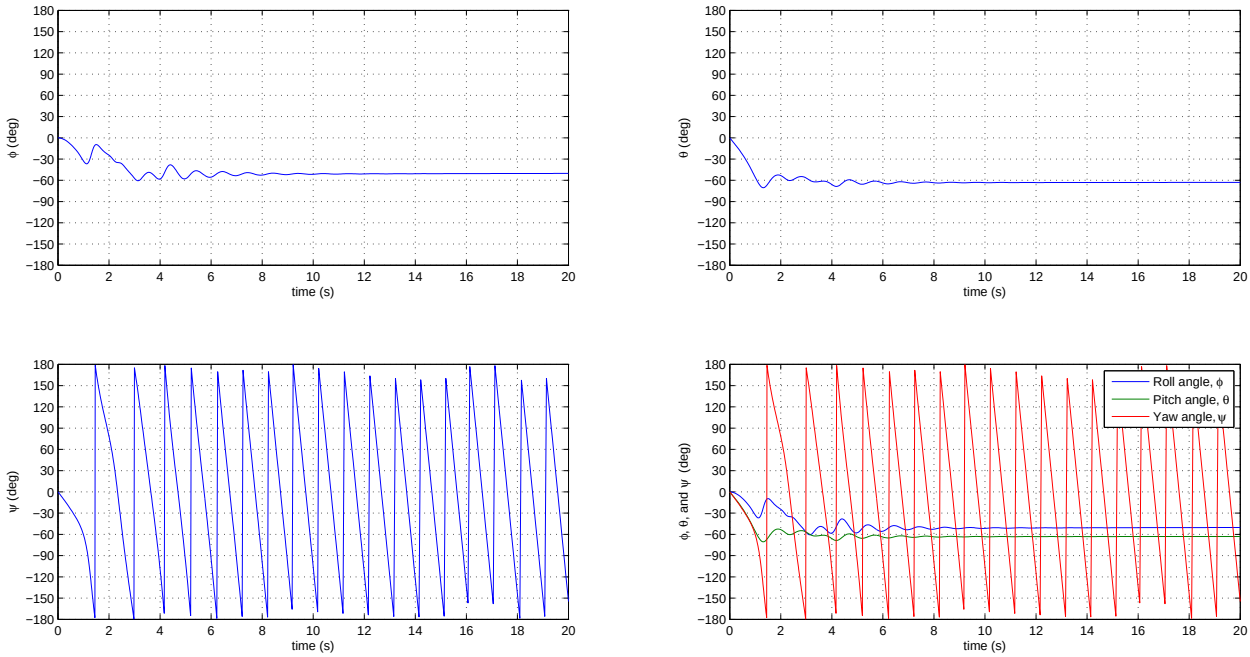

(a) Baseline angular orientations with initial conditions of $r = -45$ deg/s and $\alpha = 16.4$ deg

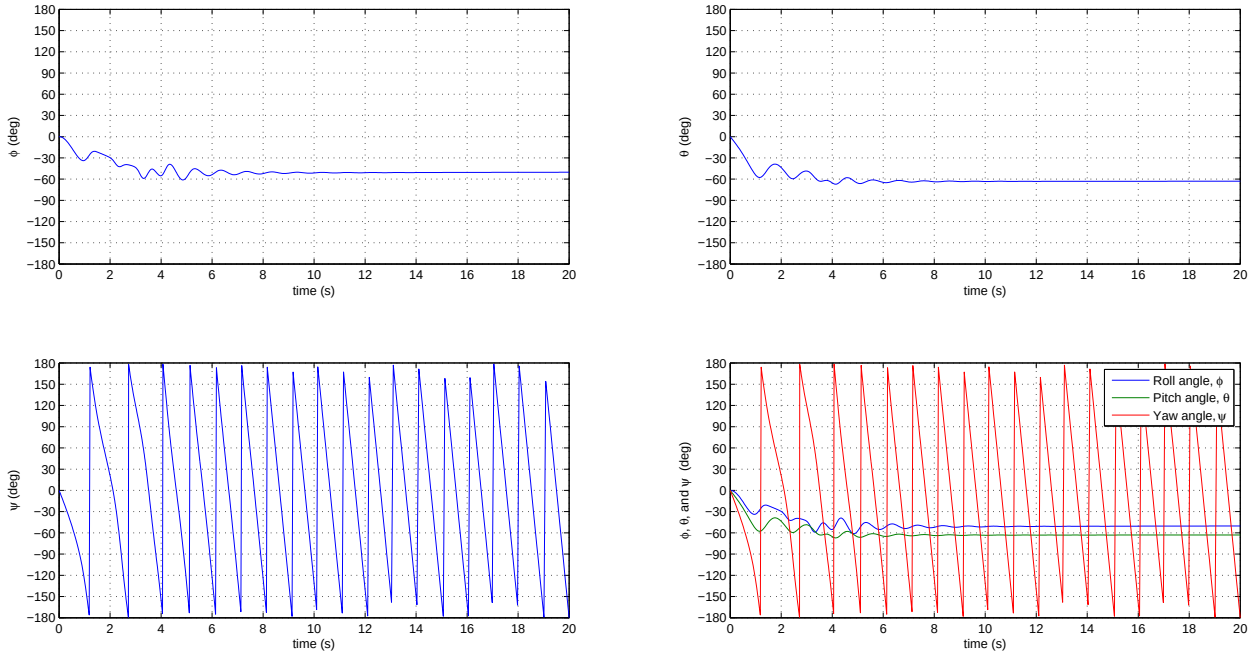

(b) Parametric study angular orientations with initial conditions of $r = -90$ deg/s and $\alpha = 32.8$ deg

Figure 6.27: Comparison of ϕ, θ, and ψ Euler angles for SpinSim simulation of the Aero Testbed in a left spin with pro-spin ailerons for baseline spin and $r = -90$ deg/s and $\alpha = 32.8$ deg initial condition.

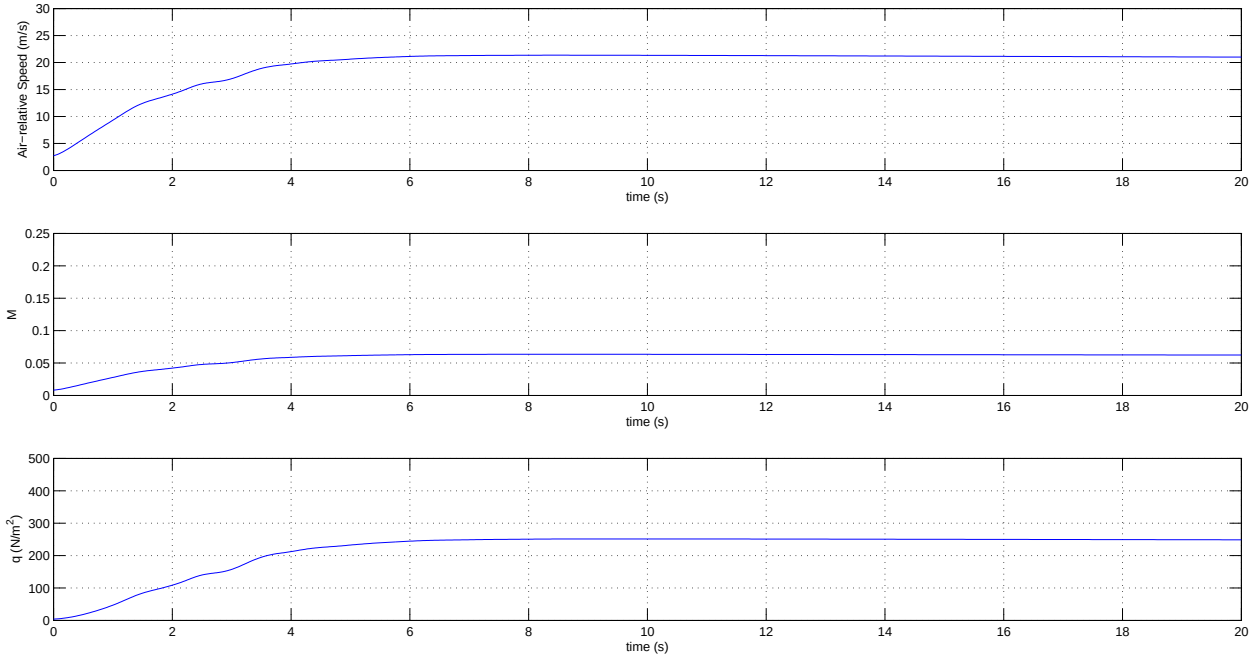

(a) Baseline velocity and q with initial conditions of $r = -45$ deg/s and $\alpha = 16.4$ deg

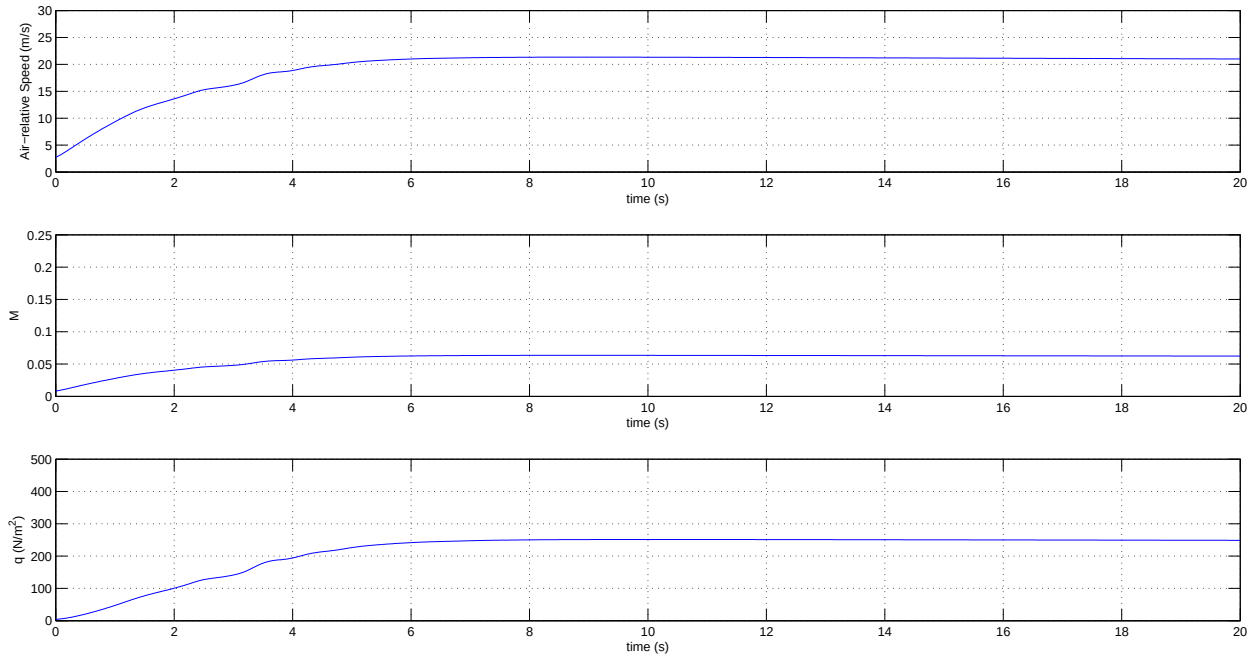

(b) Parametric study velocity and q with initial conditions of $r = -90$ deg/s and $\alpha = 32.8$ deg

Figure 6.28: Comparison of airspeed, Mach number, and q for SpinSim simulation of the Aero Testbed in a left spin with pro-spin ailerons for baseline spin and $r = -90$ deg/s and $\alpha = 32.8$ deg initial condition.

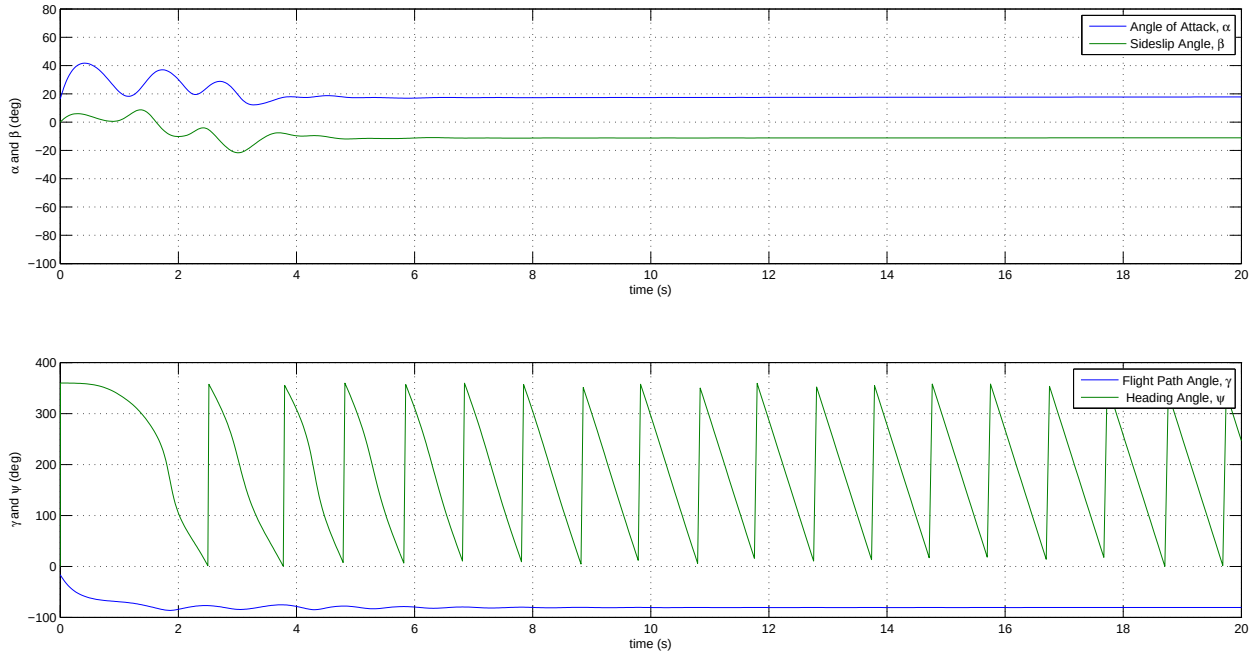

(a) Baseline aerodynamic and flight path angles with initial conditions of $r = -45$ deg/s and $\alpha = 16.4$ deg

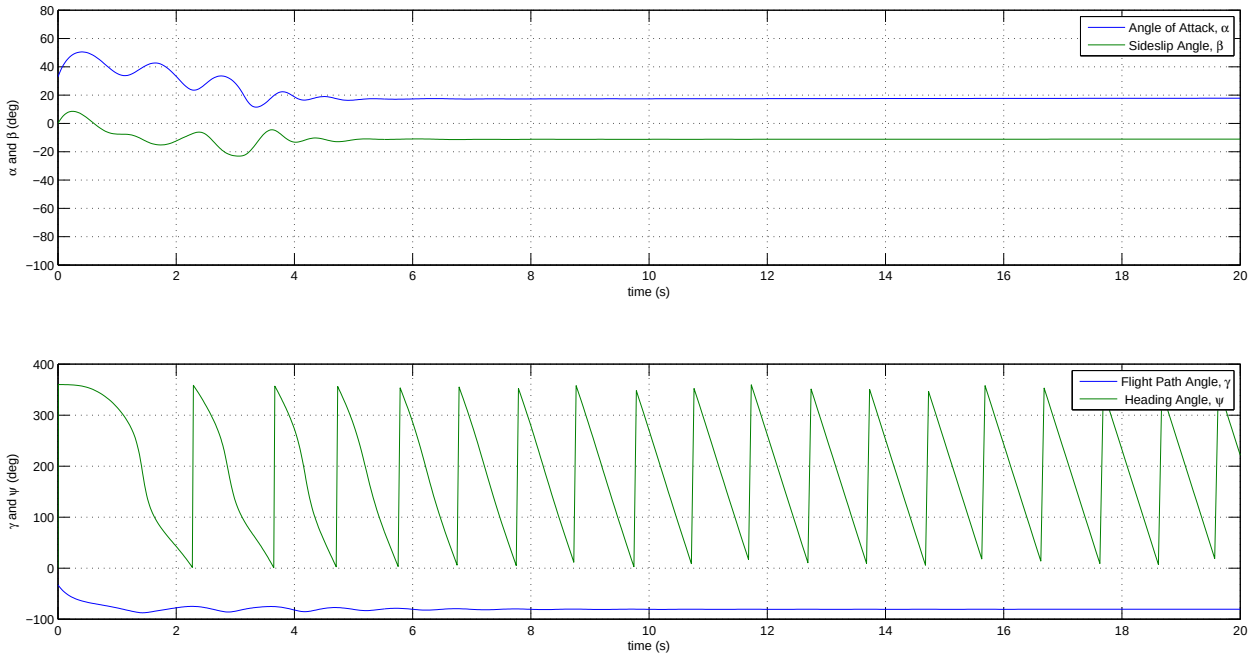

(b) Parametric study aerodynamic and flight path angles with initial conditions of $r = -90$ deg/s and $\alpha = 32.8$ deg

Figure 6.29: Comparison of aerodynamic and flight path angles for SpinSim simulation of the Aero Testbed in a left spin with pro-spin ailerons for baseline spin and $r = -90$ deg/s and $\alpha = 32.8$ deg initial condition.

Table 6.1: Control Surface Deflection Combinations of Spin Cases A, B, C, and D

Spin Name	Rudder (deg)	Elevator (deg)	Aileron (deg)	Spin Name in Table 3.6
Case A	−29	14	0	T0R1E1A0-Lft-Up
Case B	−29	14	−22	T0R1E1A1-Lft-Up
Case C	−40	46	0	T0R2E2A0-Lft-Up
Case D	−40	46	−34	T0R2E2A2-Lft-Up

6.2 Comparison of SpinSim 6DOF Simulations and Aero Testbed Extra 260 Flight Test Results

In this section, flight test experimental data are compared with SpinSim simulations of four different Aero Testbed spins. These cases include low and high control surface deflection angles as well as neutral and pro-spin aileron deflections. Table 6.1 summarizes the control surface combinations of the four test cases, which are named "Case A," "Case B," "Case C," and "Case D" and correlates them to the spins of Table 3.6.

As shown in Table 6.1, Cases A and C are characterized by neutral aileron deflections. Cases B and D are characterized by pro-spin aileron deflections. Cases A and B are spins that are performed with the low control surface deflection angles, and Cases C and D are spins that are performed with the high, or aerobatic, control surface deflection angles. All spins are performed to the left, as shown by the negative values of rudder deflection. All spins are performed upright as evidenced by the positive elevator deflection angle values.

6.2.1 Aero Testbed Results: Case A

In this section, the flight test results for the Case A spin are presented. Figure 6.30 presents the integrated Euler angles for this spin and the direct output from the IMU. These integrated and direct Euler angle values were calculated using the equations presented, as well as the method which was validated in Section 3.7.1 (for a simulated spiral flight) and Section 3.7.2 (for a "mush" test flight). As concluded in those sections, the direct IMU data provides reasonable and supportable Euler angle values for the spin. The data of Fig. 6.30 show that the roll angle ϕ is approximately zero, and $\theta \approx -50$ deg. These values for ϕ and θ are reasonable values, and onboard video recording corroborates these data. As expected, the yaw angle ψ is constantly increasing in the negative direction. It is the plotting routine that constrains the heading to be bounded by $0 \leq \psi \leq 360$ deg. In sharp contrast to the direct IMU data, the Euler angles derived through integration of the angular rates are unreliable in the spin, and they do not exhibit a general trend. As mentioned previously in Section 3.7.2, this unreliability of the integrated Euler angles may be due to a number of factors. The two most likely factors are a minor installation error and electromagnetic effects from a windmilling propeller. The fact that the integrated Euler angles match prior to the onset of the spin, and that they follow similar trends to the direct data after the spin has been exited, further demonstrates that the integration methodology is sound.

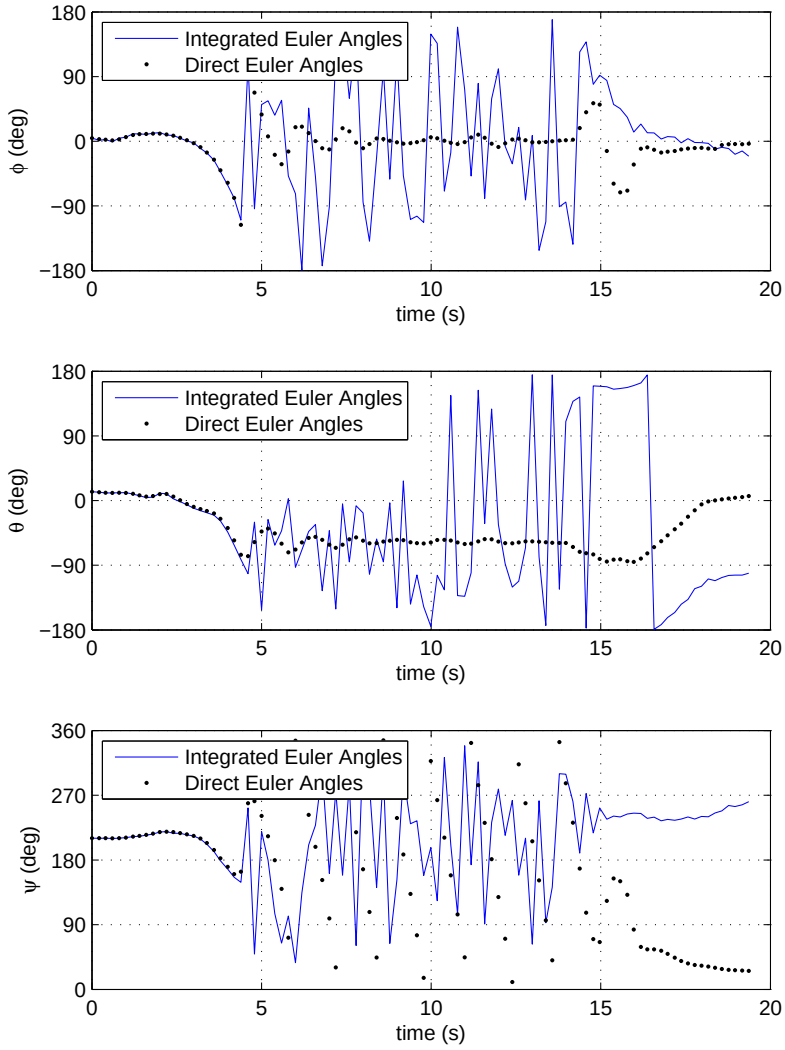

Figure 6.30: Plot of integrated and IMU direct Aero Testbed Euler angles for a Case A spin.

Figure 6.31 presents plots of the velocities in the earth-fixed coordinate system. As expected, during the spin, V_x and V_y oscillate as the airplane follows a helical path. The descent velocity, V_z, remains relatively constant in the spin with a value of 16.5 m/s.

Figure 6.32 presents plots of the u, v, and w velocity components in the aircraft-fixed axis system. Two data sets are presented: the solid blue line represents the velocities which are calculated from the integrated Euler angles, and the black dots represent the velocities which are calculated from the direct IMU Euler angle output. As expected, the untrustworthy integrated Euler angle data produced erroneous velocity component values. The direct IMU Euler angles produced reasonable values that exhibited small but regular oscillations. As regards the u velocity component,

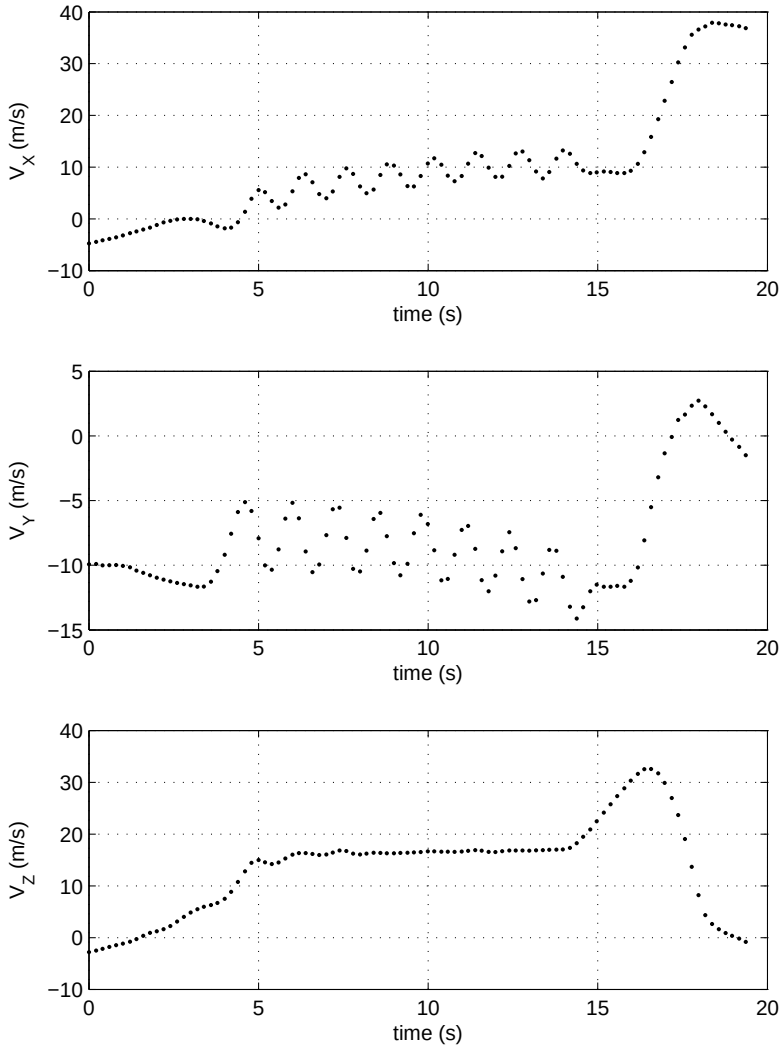

Figure 6.31: Plot of direct Aero Testbed velocities in the earth-fixed reference frame for a Case A spin.

the developed spin portion of the data set oscillated between 5 and 20 m/s. The v velocity component oscillated with an amplitude of approximately 35 m/s and a slight positive offset of approximately 2.5 m/s. Moreover, the w velocity component oscillated between 0 and 20 m/s. These oscillations are introduced into the data by the oscillations of V_x and V_y, which are correct because of the circular motion of the aircraft c.g. in the earth-fixed x-y plane. Because of the low recording frequency of 5 Hz during these Aero Testbed tests, large oscillations in the u and v velocity components were introduced into the data plots. It is hypothesized that data recorded at a higher frequency would cause the oscillations to be significantly reduced in magnitude, thus producing better results. These results are useful

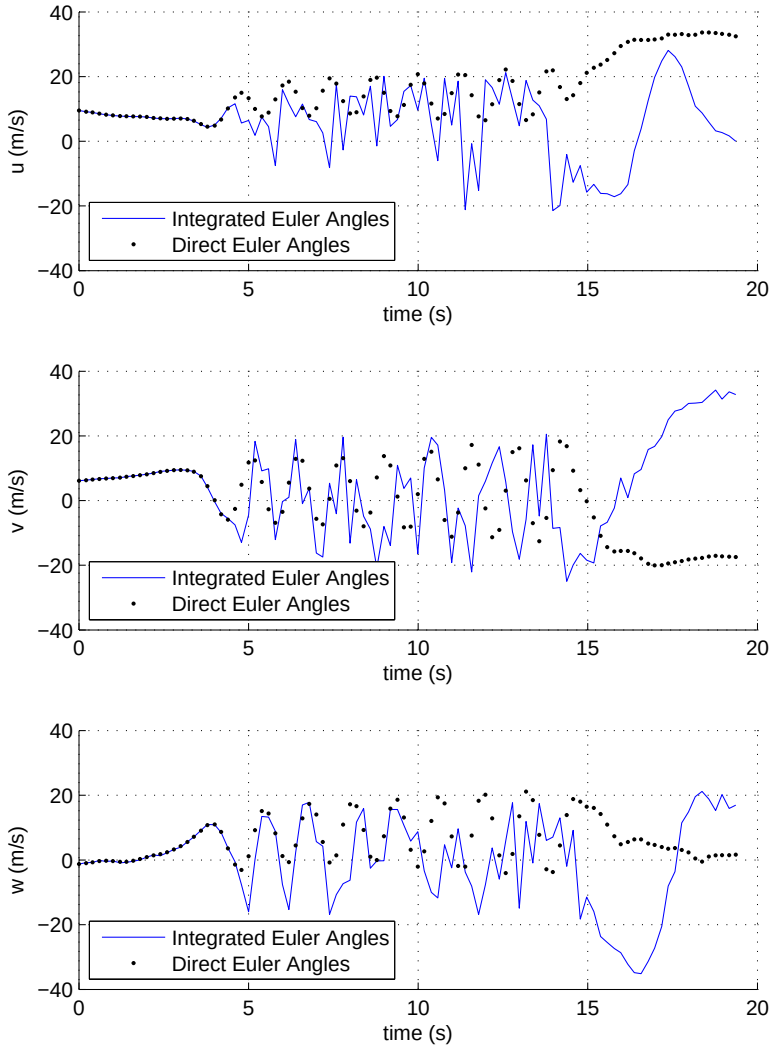

Figure 6.32: Plot of Aero Testbed u, v, and w velocity components in the body-fixed reference frame for a Case A spin.

however, as it can be reasonably assumed that the steady-state values for the u and v velocity components lie along or near to the center of the oscillations.

The aerodynamic angles α and β of the Case A spin are presented in Fig. 6.33 along with the aircraft total velocity V. The oscillations are present, but once again, the steady-state values may be assumed to lie near to the center of the regular oscillations. Using this information, the Case A spin is characterized by $\alpha \approx 40$ deg and a β value slightly larger than zero. These values are determined from the minimum and maximum values of the oscillation in α, from 0 to 80 deg and β, from -30 to 40 deg. The average aircraft total velocity increases linearly throughout the spin, from

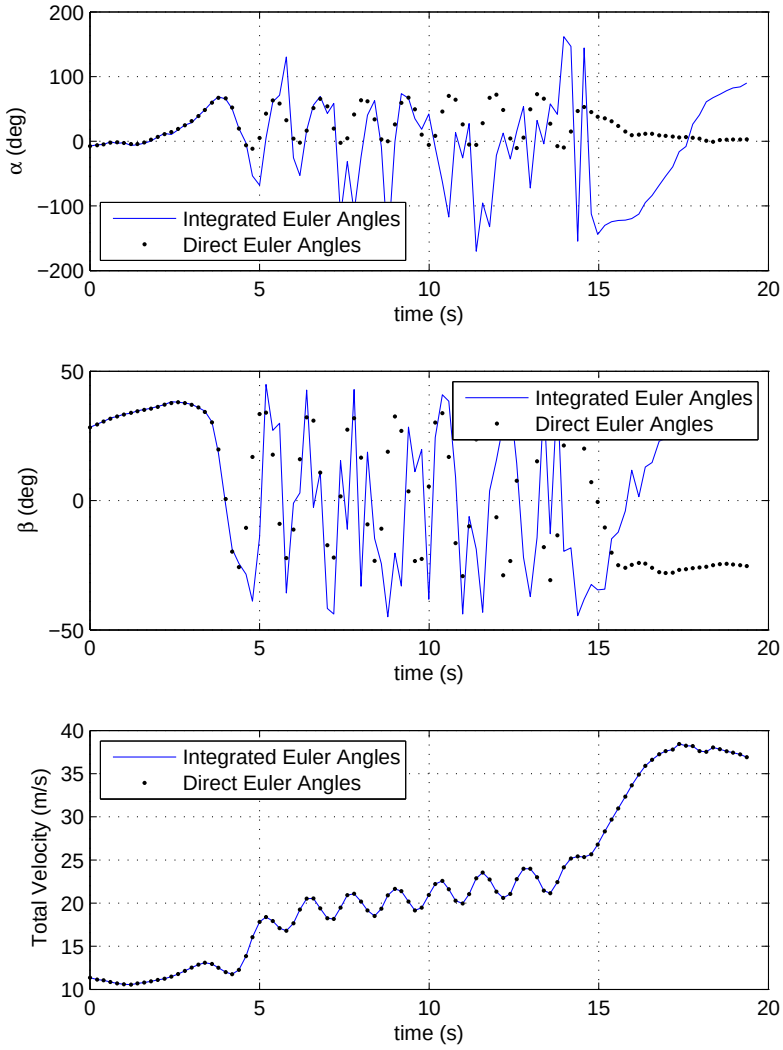

Figure 6.33: Plot of Aero Testbed α, β, and V for a Case A spin.

approximately 17.5 m/s at the beginning, to 22.5 m/s immediately prior to the spin exit. While the oscillations in α and β are rather large at 75 deg each, higher frequency data would reduce the magnitude of these oscillations and would allow for a more accurate representation of the aerodynamics to be deduced.

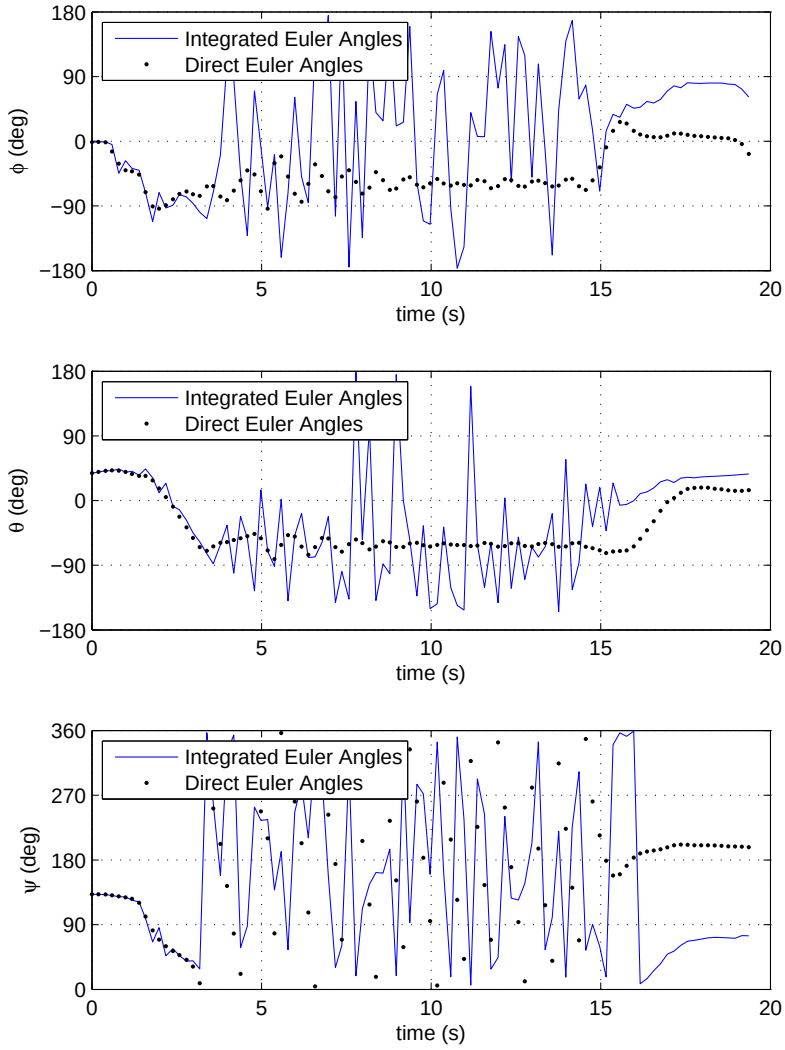

Figure 6.34: Plot of integrated and IMU direct Aero Testbed Euler angles for a Case B spin.

6.2.2 Aero Testbed Results: Case B

In this section, a Case B spin from the Aero Testbed flight test data is investigated. Figure 6.34 presents a plot of the Euler angles for this spin. The data derived from the integrated Euler angles are unreliable during the duration of the spin. While the Case A spin with neutral ailerons had a bank angle $\psi \approx 0$, the addition of the pro-spin ailerons of Case B changes the bank angle to $\phi \approx -50$ deg. The pitch angle remains similar to Case A with a slight increase in magnitude to -60 deg, and the heading angle ψ increases in the negative direction as expected with a left spin.

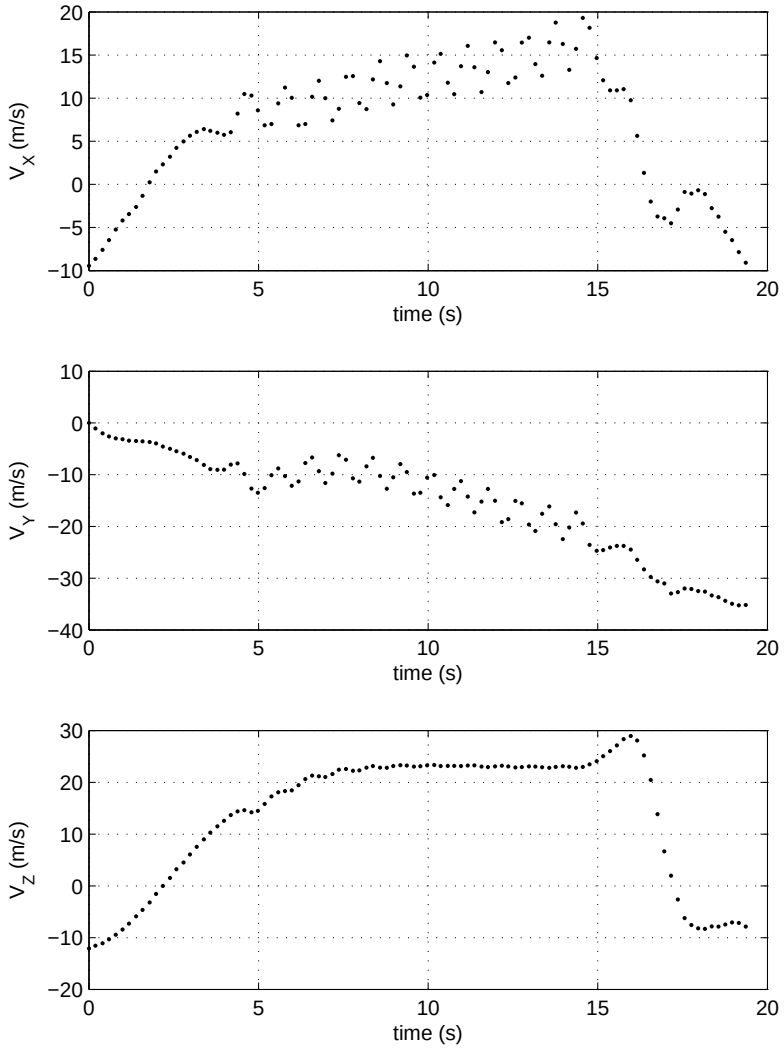

Figure 6.35: Plot of direct Aero Testbed velocities in the earth-fixed reference frame for a Case B spin.

The aircraft velocities in the earth-fixed axis system are presented in Fig 6.35. Oscillations in the x- and y-velocities are again present, and the descent velocity is increased relative to the Case A spin from 16.5 m/s to 24 m/s. These data show that if in a spin, adding pro-spin ailerons exacerbates the spin and significantly increases the descent velocity of the airplane. Interestingly, despite the constant Euler angles, the northerly velocity V_x and easterly velocity V_y are shown to increase in a linear fashion as time passes. Because the angular rates and Euler angles remain constant during this spin, these increases in the x-y velocities are most likely caused by an increase in the windfield velocity. The nearly-constant nature of the descent rate V_z further supports this hypothesis, namely that the aircraft aerodynamics

remain constant throughout the spin, while the airmass within which the airplane is traveling is increasing in velocity because of a wind gust.

Figure 6.36 presents the u, v, and w velocities in the aircraft-fixed axes for the Case B spin. While the data derived from the integrated and direct IMU Euler angles agree well until $t = 3.5$ s, once the airplane enters the spin, the integrated Euler angle-based velocities do not show a pattern and do not provide useful information. The u velocity component based on the direct Euler angles oscillates between 10 and 30 m/s and is centered at around $u = 20$ m/s. Meanwhile, the v velocity component oscillates around $v = -5$ m/s with an ever-increasing magnitude that begins with oscillations between -20 and 10 deg and expands to a range of -30 to 20 deg by the end of the spin. This ever-increasing magnitude is a characteristic also shared by the oscillations of the w velocity component which begins its oscillations over a range of -5 to 20 deg.

The aerodynamic angles α and β derived from the IMU data are presented in Fig. 6.37. The angle of attack, α, based on the direct IMU Euler angles, oscillates over a range of -40 and 80 deg and is centered around $\alpha \approx 20$ deg. Further, β shows an average value of around -20 deg. The sideslip angle β oscillates between -40 and 30 deg. Again, the aerodynamic angles derived from the integrated Euler angles provide no useful information or trends. The aircraft total velocity increases from 20 m/s, at the beginning of the spin, to approximately 35 m/s by the end of the spin. This increase is due, at least in part, to an increase in the windfield velocity as the airplane descended.

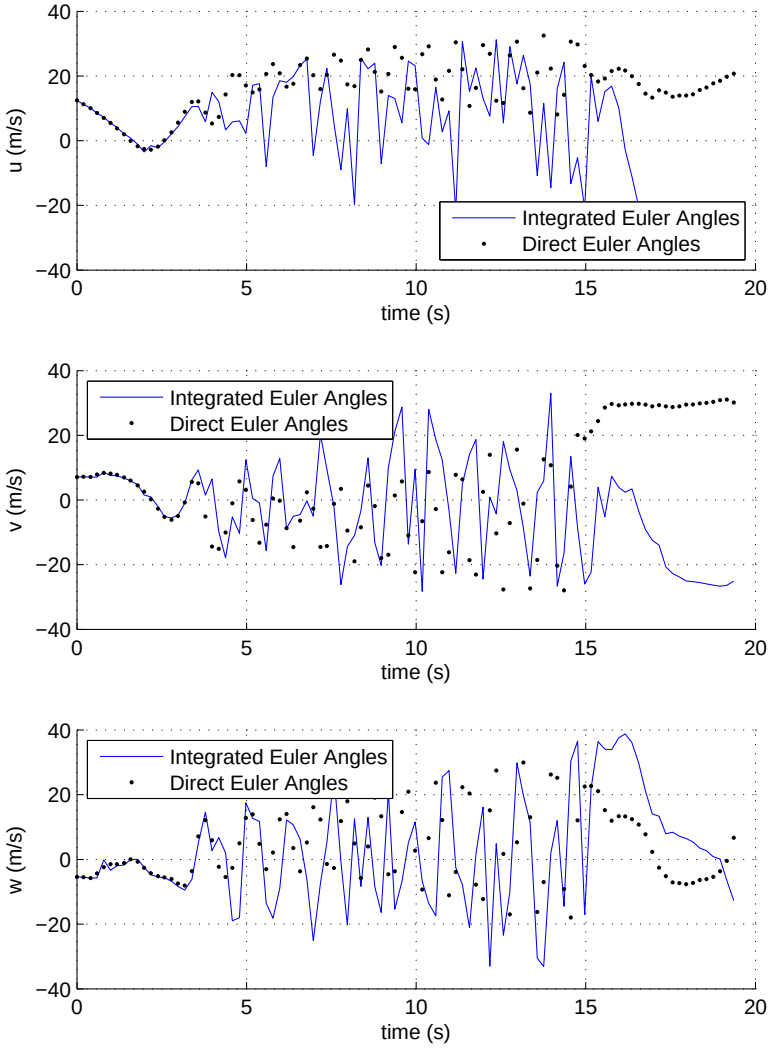

Figure 6.36: Plot of Aero Testbed u, v, and w velocity components in the body-fixed reference frame for a Case B spin.

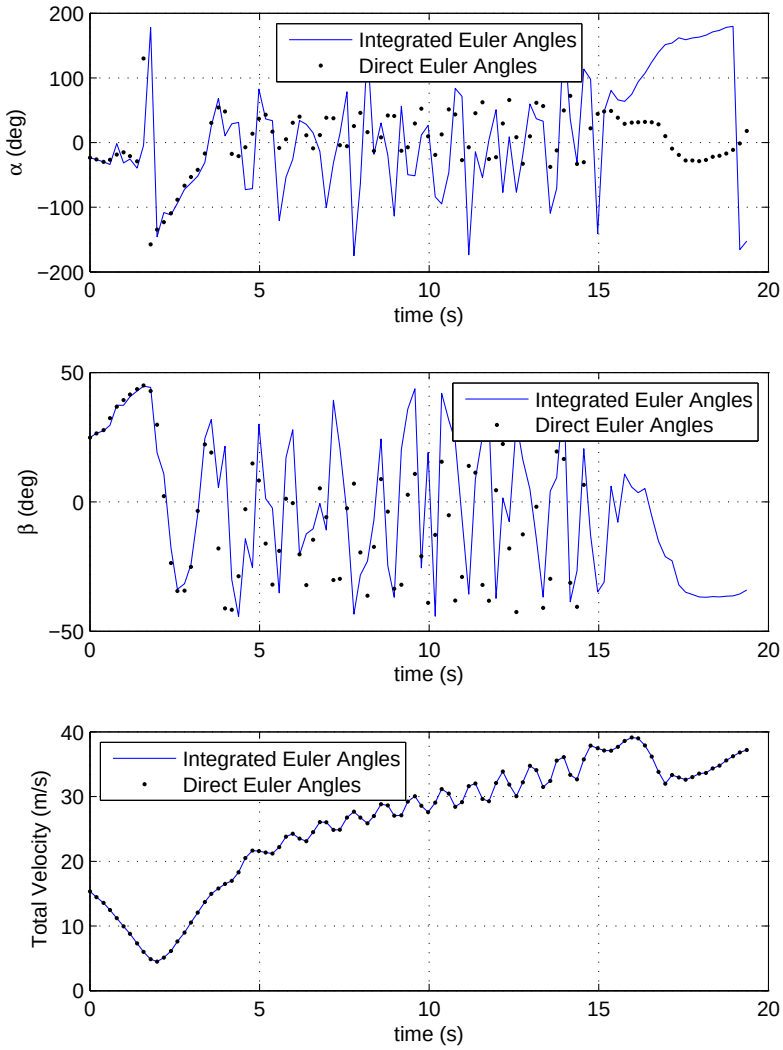

Figure 6.37: Plot of Aero Testbed α, β, and V for a Case B spin.

6.2.3 Aero Testbed Results: Case C

In this section, the Case C spin is studied. This spin is characterized by a rudder deflection of -40 deg and a 46-degree up-elevator control surface deflection. Figure 6.38 presents the direct and integrated Euler angles for this spin. As was previously the case, the data derived from the integrated Euler angles are unreliable during the spin. The direct IMU Euler angles show a slightly negative roll angle ϕ that converges to approximately -15 deg, a pitch angle θ of approximately -50 deg, and a heading angle ψ that decreases at a constant rate, bounded by 0 and 360 deg.

The direct velocities in the earth-fixed axis system recorded by the IMU are presented in Fig. 6.39. This spin had a descent rate V_z of around 15 m/s that is slightly less than the low deflection angle spin with neutral ailerons. This observation of a reduced V_z is supportable, as the higher deflection angles of this Case C spin place the airplane in a higher-drag configuration. This higher-drag configuration causes the airplane to descend at a slower rate. While V_x shows an oscillation of amplitude 5 m/s around an average value of 3.6 m/s, the easterly velocity V_y oscillates with a similar amplitude. It follows, however, a decreasing average value that begins at 2 m/s and ends at -5 m/s. Because the orientation (Euler angles) and angular rates of the airplane remained constant during the spin, this change in the easterly velocity V_y is most probably due to the airplane encountering a westerly gust of wind at the beginning of the spin with a magnitude of 7 m/s.

Figure 6.40 presents the u, v, and w velocity components in the body-fixed axis system. While the values derived from the integrated Euler angles are of no use, the values of u, v, and w based on the direct IMU Euler angles provide some insight as to the aerodynamics of this spin. The u velocity component oscillates in the latter stages of the spin with a magnitude of 7.5 m/s around an average velocity of 10 m/s, and the v velocity component oscillates with a magnitude of just over 13 m/s with a slightly positive average velocity. The w velocity component trend mirrors that of the axial velocity, oscillating around an average of 9 m/s with a magnitude of 10 m/s. From these data, it may be deduced that the actual values of u, v, and w are close to the averages about which the data oscillate; these values are approximately 10, 1, and 9 m/s, respectively.

Based on the aircraft u, v, and w velocity components, the aerodynamic angles α and β are calculated and presented in Fig. 6.41. Ignoring the data derived from the integrated Euler angle values, the data derived from the direct Euler angle IMU output show that the flight test α value oscillates between 0 and 75 deg, and that β oscillates between -30 and 30 deg for the Case C spin. The total velocity, V, of the airplane varies slightly from just under 20 m/s to an average of 16 m/s at the end of the spin. This decrease in V is expected, as in a previous plot it was shown that V_y decreased after the beginning of the spin. This result was most probably due to the presence of a wind gust during the beginning of the spin (the wind removal routine was designed to remove a constant windfield, not an accelerating windfield).

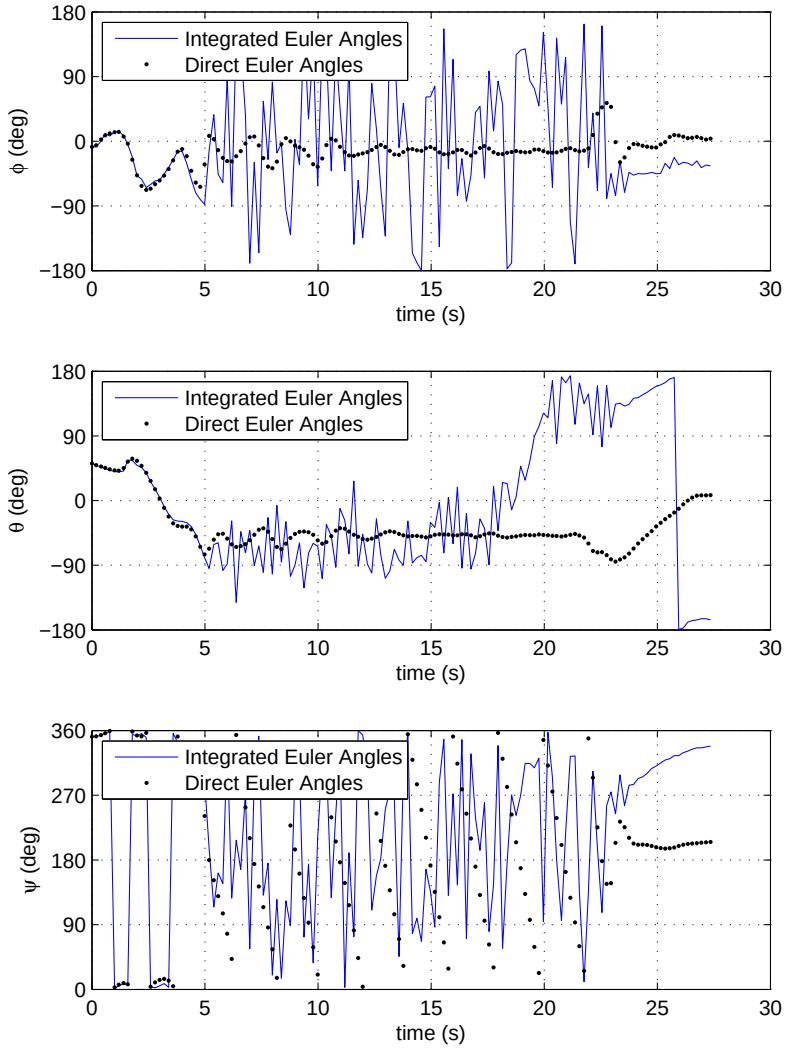

Figure 6.38: Plot of integrated and IMU direct Aero Testbed Euler angles for a Case C spin.

6.2.4 Aero Testbed Results: Case D

Adding pro-spin ailerons to the aerobatic deflection angle spin of Case C produced the fourth and final spin studied in detail. In the Case D spin, the rudder is deflected -40 deg, the elevator 46 deg, and the ailerons -34 deg, commanding a yaw and roll to the left. Figure 6.42 presents the direct and integrated Euler angles from the flight tests of this spin. Because of the highly-dynamic motions of this spin, the Euler angles demonstrate large and regular oscillations. This behavior contrasts with the other three spins of Cases A, B, and C, which are characterized by reasonably steady motion, and thus, reasonably constant Euler angles. The bank angle ϕ oscillates between -100 deg and 20 deg.

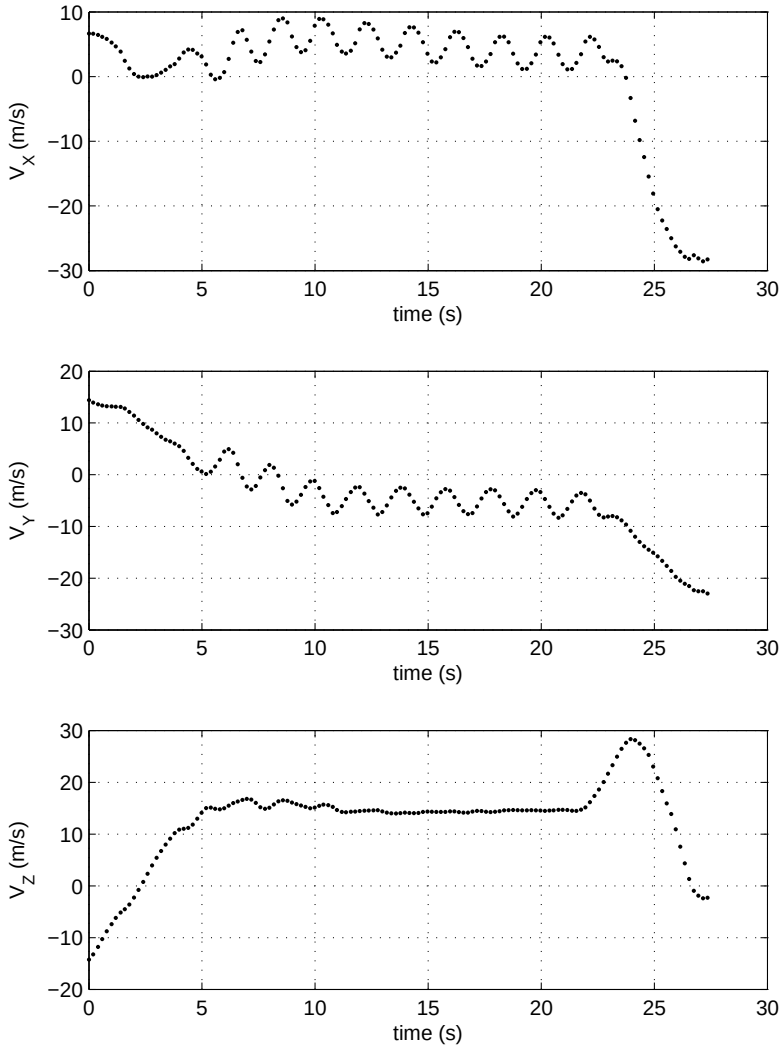

Figure 6.39: Plot of direct Aero Testbed velocities in the earth-fixed reference frame for a Case C spin.

Meanwhile, the pitch angle θ varies between -80 deg and zero. The non-constant yaw rate ψ is shown in Fig. 6.42 by the more-closely spaced black dots, which tend to occur in groups of five. Given a recording rate of 5 Hz, this shows that the airplane takes a 1-second "pause" to the motion in yaw during the dynamic motion of the spin. One such closely-spaced group of ψ values is seen around $t = 22$ s for $130 > \psi > 0$ deg.

The velocities V_x, V_y, and V_z in the earth-fixed axis system are presented in Fig. 6.43. During the second two-thirds of the spin, the northerly velocity V_x varies centered about zero. In the first third of the spin, it oscillates around a velocity of -5 m/s. Because none of the other angular rates of the spin change during this time, this change in the northerly velocity may be attributable to the airplane entering a different windfield, which was observed to be the

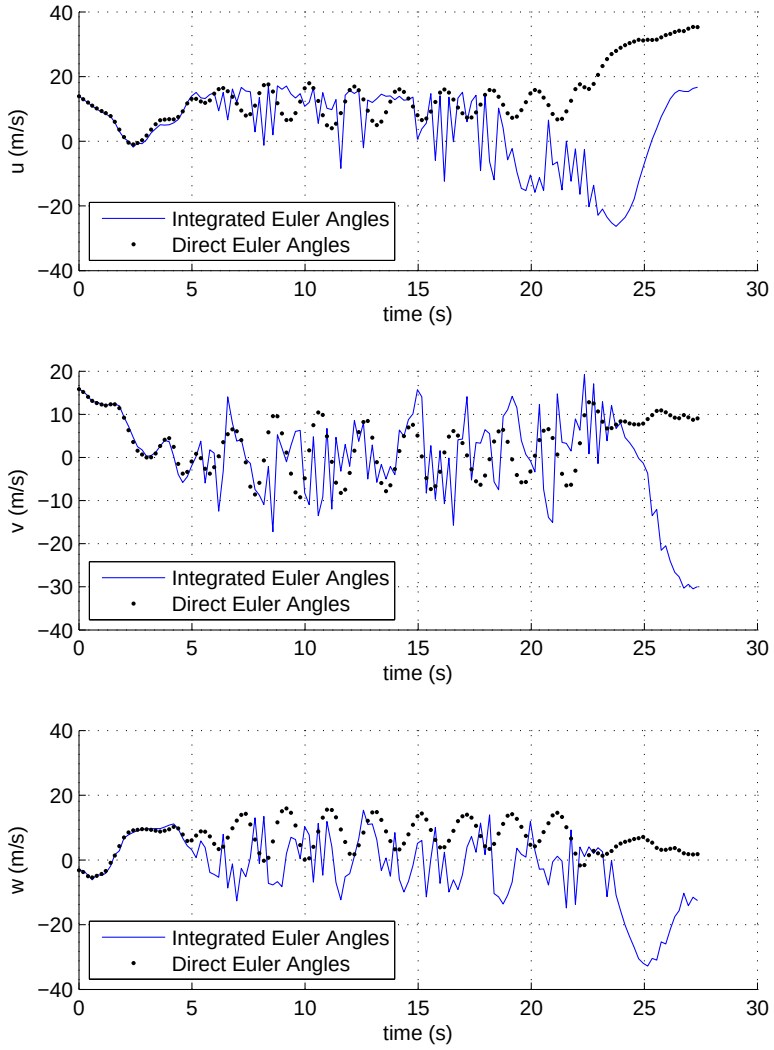

Figure 6.40: Plot of Aero Testbed u, v, and w velocity components in the body-fixed reference frame for a Case C spin.

case during a number of spins. While the easterly velocity V_y maintains an average value of -2.5 m/s throughout the spin, a large increase in magnitude to almost -10 m/s is encountered right around the time that the northerly velocity V_x changes, further supporting the hypothesis that the airplane entered a different windfield. As is to be expected, any possible windfield effects do not significantly affect the descent velocity V_z, which oscillates in a regular pattern centered on approximately 13.5 m/s. This spin is unique among the four studied in detail in that it is the only one not characterized by a nearly constant descent rate. This regularly-varying descent rate is caused by the highly-dynamic and non-constant oscillations of this aerobatic control surface deflection angle spin with pro-spin ailerons.

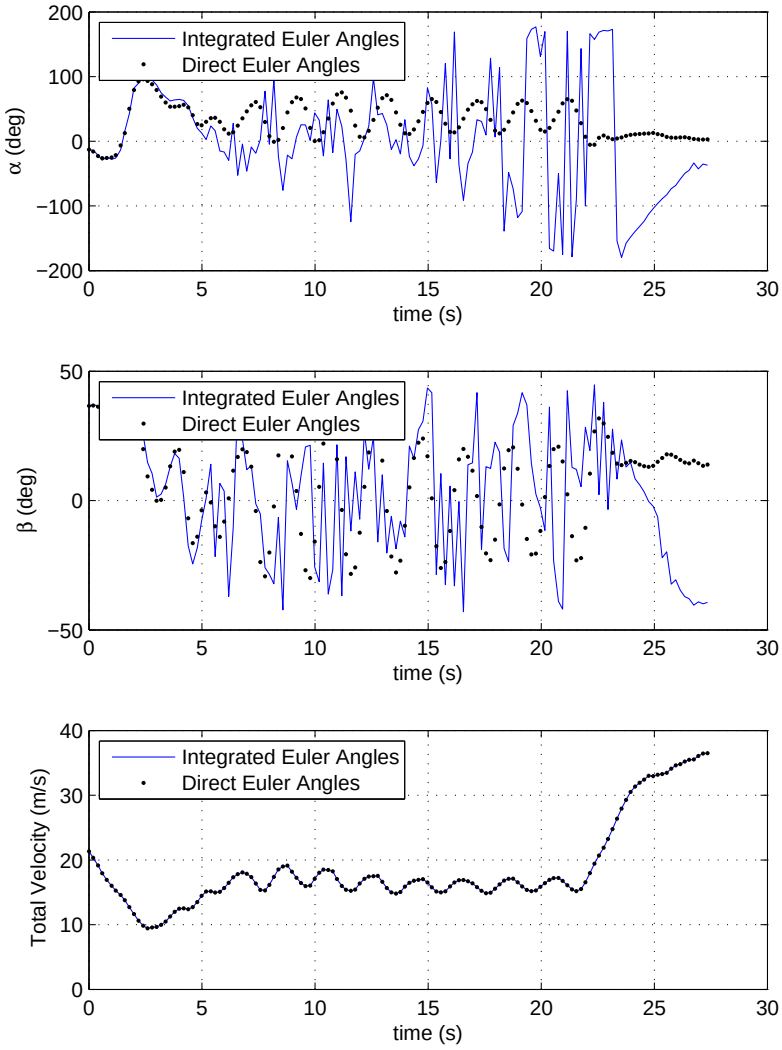

Figure 6.41: Plot of Aero Testbed α, β, and V for a Case C spin.

In Fig. 6.44, the Aero Testbed u, v, and w velocity component time histories are presented for the Case D spin. Consistently, the data derived from the integrated Euler angles demonstrate sharp variations, and there is no apparent trend once the spin is entered. Data derived from the direct IMU Euler angles show oscillations, with the u velocity component varying regularly between 17 m/s and just above 0 m/s. The v velocity component varies between -15 m/s and 10 m/s, and the w velocity component varies between -5 m/s and 14 m/s. The oscillations in w are due, in part, to the real oscillations in V_z. Some of the oscillatory behavior, however, is introduced because of the low recording rate of the IMU. This conclusion, regarding the oscillations in w being caused by a low recording rate, is supported by the fact that the other three spins had relatively constant values of V_z, but exhibited small oscillations in w.

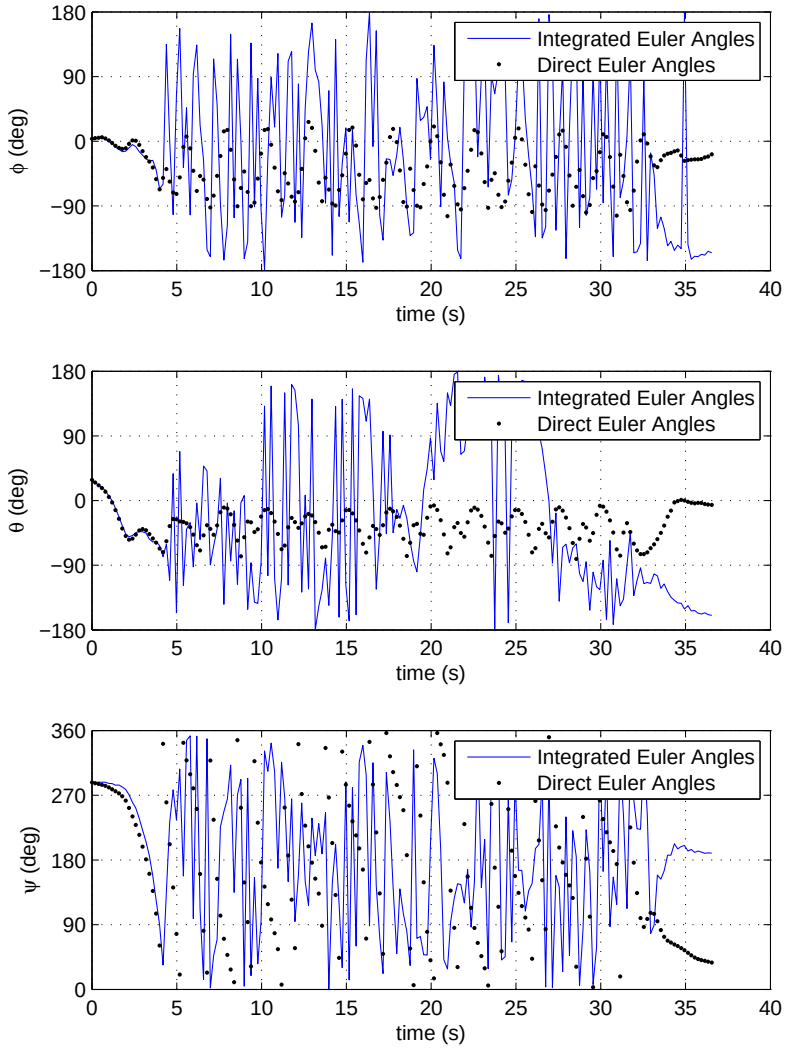

Figure 6.42: Plot of integrated and direct Aero Testbed Euler angles for a Case D spin.

Figure 6.45 presents the calculated α and β values for the Case D spin. While a somewhat regular oscillation is evident in the α data derived from the direct IMU orientation angles, the β values do not show a regular pattern. There appears to be a higher prevalence of data points for negative values of β, suggesting that β is negative in this spin. This conclusion agrees with the SpinSim simulation results (to be presented later in this chapter). The α values appear to oscillate around a mean value of 40 deg. In regard to the aircraft total velocity, an irregular oscillation around $V = 15$ m/s is shown. As expected, this control combination produces the spin with the lowest total velocity V, which is attributable to the high drag associated with elevator, rudder, and aileron deflections of -46, 40, and -34 deg, respectively.

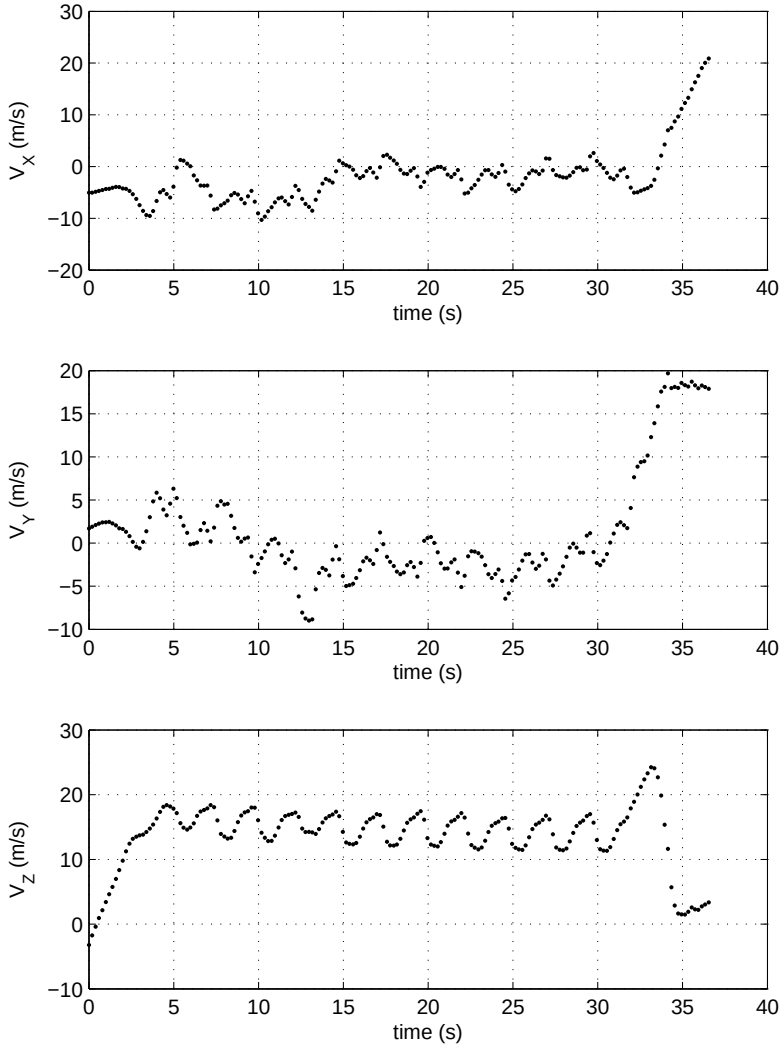

Figure 6.43: Plot of IMU direct Aero Testbed velocities in the earth-fixed reference frame for a Case D spin.

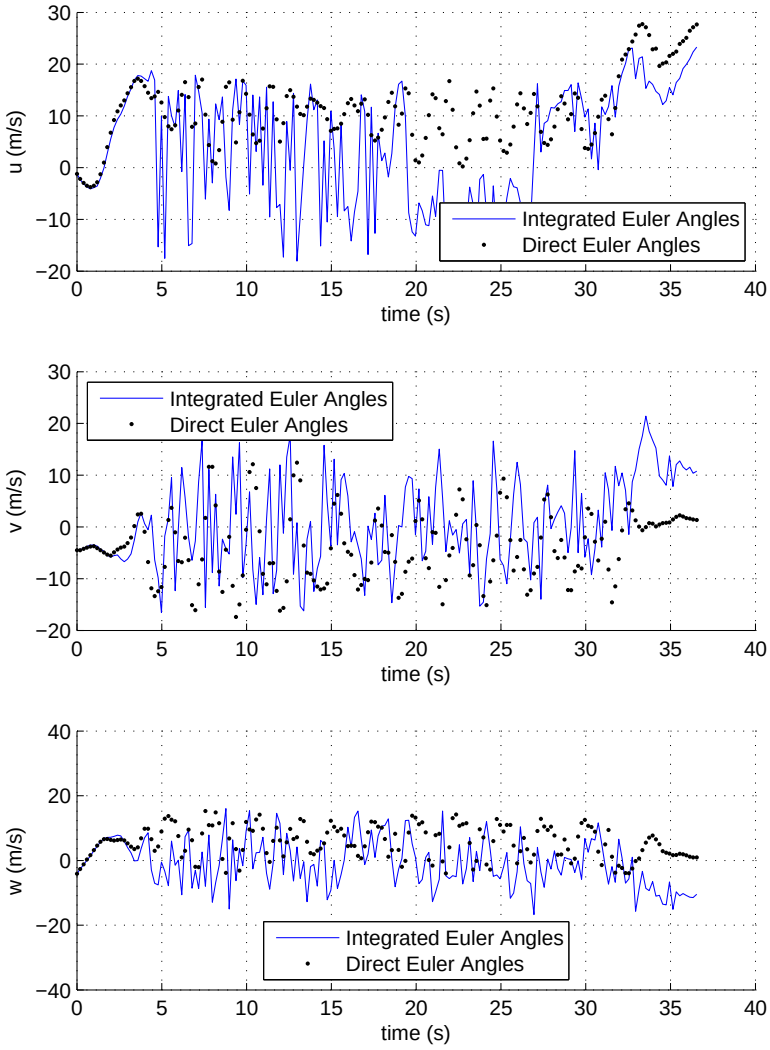

Figure 6.44: Plot of Aero Testbed u, v, and w velocity components in the body-fixed reference frame for a Case D spin.

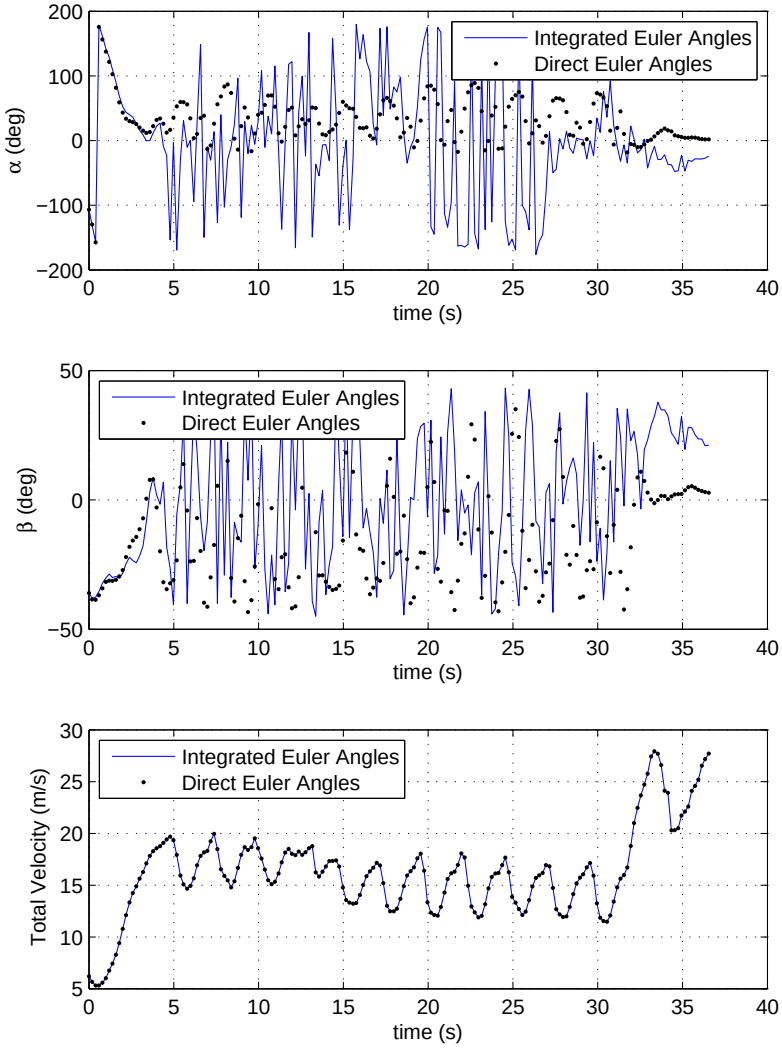

Figure 6.45: Plot of Aero Testbed α, β, and V for a Case D spin.

6.2.5 SpinSim Flight Simulations and Total Angular Velocity Parameter

In the following sections, comparisons of SpinSim flight simulations with Aero Testbed flight test experiments are presented. For reference, all SpinSim simulations are integrated using the RK4 integration routine at a frequency of 300 Hz. Time histories of the altitude, descent rate, spin parameter, airplane angular rates p, q, and r, and trajectory are presented. In addition to the individual angular rates (p, q, and r), the total angular velocity of the airplane is also presented, as defined by [108]

$$\Omega = \sqrt{p^2 + q^2 + r^2} \tag{6.28}$$

where p, q, and r are the roll, pitch, and yaw rates, respectively.

The total angular velocity parameter of Eq. 6.28 is of use. On account of how the Euler angles are defined, a singularity is approached as the x-axis of a sensor (longitudinal axis of the Aero Testbed) approaches a pitch angle of ± 90 deg [61]. This phenomenon is called "gimbal lock." Gimbal lock occurs because when the body pitch is near ± 90 deg, motion in the yaw and roll axes causes the aircraft, and thus the sensor, to move in the same way. As a result of the inability to distinguish between roll and yaw, an orientation sensor or AHRS using Euler angles is unable to provide reliable measurements near a pitch angle of ± 90 deg [107]. While the XSens MTi-G IMU, as used in the Aero Testbed [21], has orientation output configuration options for using quaternions or rotation matrices to define the vehicle orientation, the Euler angles output mode, also known as "XKF-6G Scenario Aerospace," was used. This output mode was used because it provided data in the most useful, easily visualized, and aerospace-relevant format. The direct output of the Euler angles mode provided orientation data directly as the roll, pitch, and yaw or heading angle. Using Ω, as it is defined in Eq. 6.28, ensures that the total angular velocity would still correctly reflect the sum of the angular motions of the airplane in the case of gimbal lock. Thus, some degree of reliable information is still available regarding the angular velocity of the airplane with which flight simulations may be validated.

6.2.6 SpinSim Results: Case A

Figure 6.46 presents a comparison of the simulation and experiment altitude, descent rate, and spin parameter values for a Case A spin. Strong agreement is demonstrated with regard to the descent rate values. The simulation predicts a descent rate of 15.3 m/s, and the flight test shows a 16.5 m/s descent rate. This agreement is also exhibited by both time history plots of the airplane altitude, which decrease linearly at similar rates. The agreement of the simulated and flight test spin parameter values is not as good, however. The flight test spin parameter was calculated to be approximately -0.2 with a minor oscillation present of period ≈ 1.75 s, while the simulated spin parameter ω was almost 0.05 higher with an oscillatory period of just over 1 s.

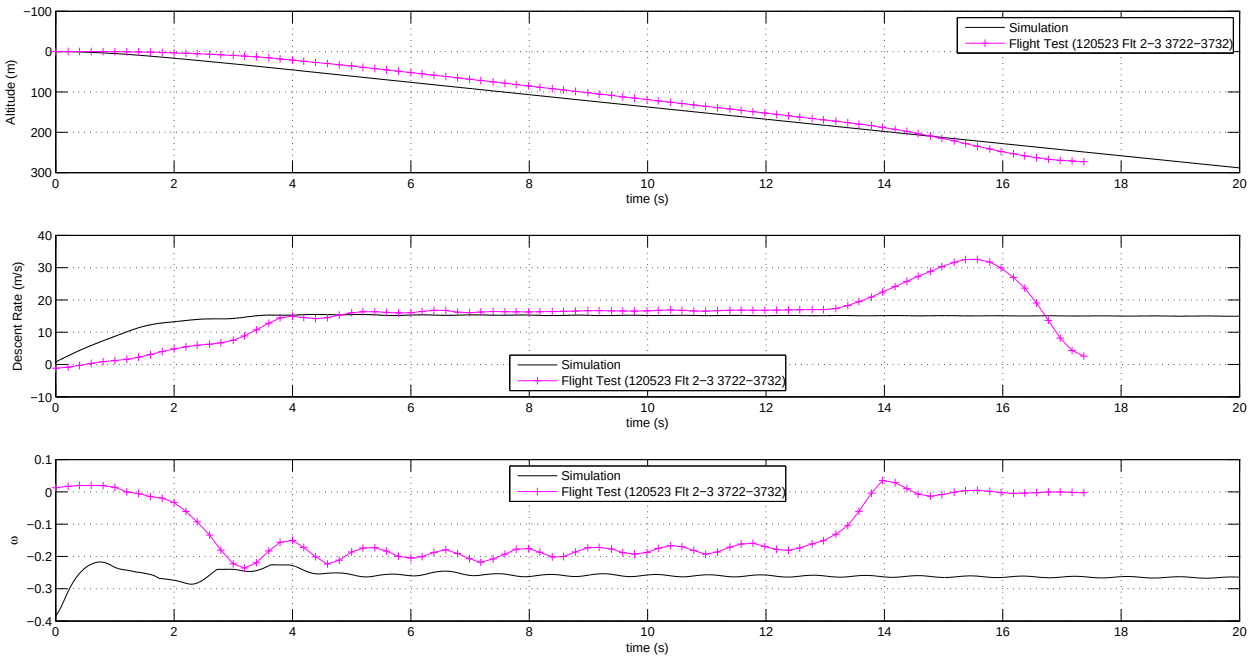

Figure 6.46: Comparison plots of altitude, descent rate, and spin parameter of a Case A spin for Aero Testbed flight test and SpinSim simulation.

A comparison of the Case A SpinSim spin simulation and experimental flight test angular rates is presented in Fig. 6.47. A strong agreement is demonstrated for all three angular rates. The SpinSim yaw rate averages around -195 deg/s, which compares well with the flight test average of approximately -229 deg/s. Moreover, the oscillations in both data sets are similar, having an amplitude of around 20 deg/s. The pitch rate for both the simulation and flight test was centered on zero, and some difference was observed for the yaw rates. An average r value of -170 deg/s was observed for the simulation, and an average of -155 deg/s was observed for the flight test. The average total angular velocity, Ω, for the Aero Testbed flight test was around 275 deg/s. Meanwhile, SpinSim predicted a value centered on 260 deg/s, demonstrating excellent agreement.

A detailed trajectory comparison, between simulation and experiment, with the airplane orientation plotted is presented in Fig. 6.48. According to Fig. 6.48, the data sets have similar descent rates and similar spin radii. The SpinSim simulation produces a spin radius of $R_s \approx 0.55$ m, and the flight test spin radius from Table 3.6 for the T0R1E1A0-Lft-Up spin is nearly the same at around 0.60 m. The reason that the experimental spin is not perfectly vertical is that the winds during the spin flight test were not uniform and constant. Thus, in the past three figures, an accurate simulation of a lefthand spin with neutral ailerons was presented. For reference, Figs. 6.49–6.54 present data from the same simulation, without experimental data coplotted. Significantly, the α and β values of 40 deg and 10 deg calculated in the simulation of Fig 6.54 are very near to the center of the oscillations of the α and β values calculated from flight test in Fig. 6.33, which shows strong agreement between the SpinSim simulation and the Aero Testbed flight test data. Strong agreement is also shown in regard to the body inertial velocities. The u, v, and w

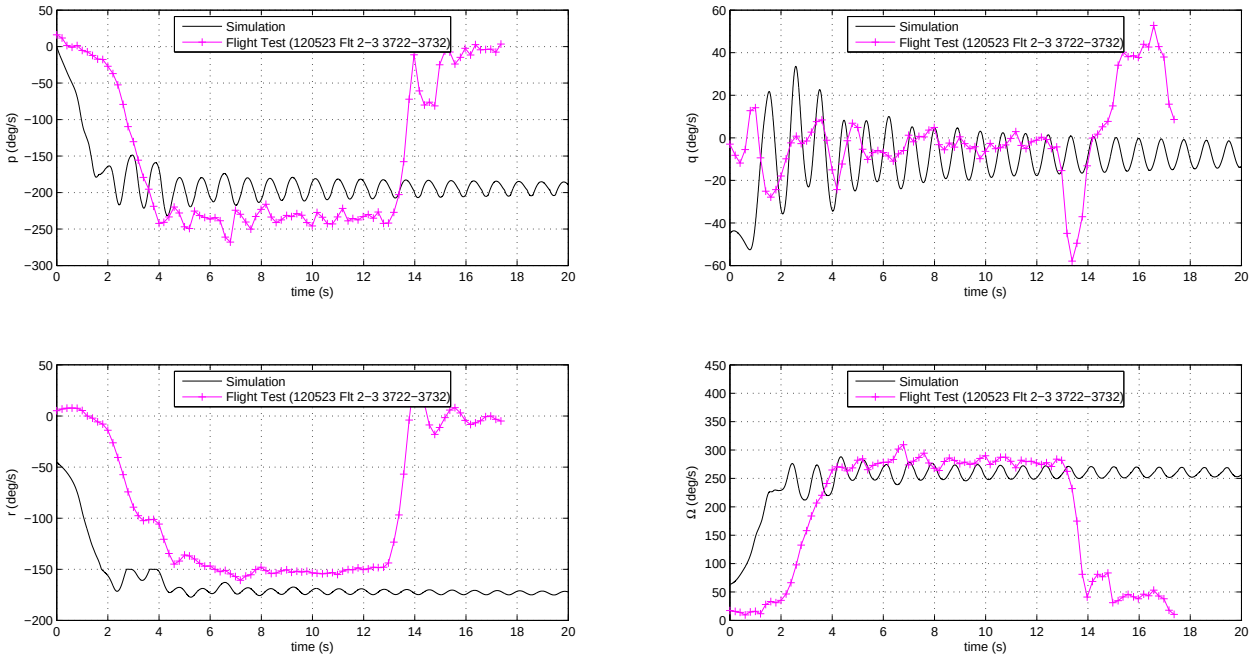

Figure 6.47: Comparison plots of angular rates of a Case A spin for Aero Testbed flight test and SpinSim simulation.

velocity components of aprroximately 12, 10, and 10 m/s, respectively, from the simulation lie near the center of the oscillations of the flight test data of Fig. 6.32.

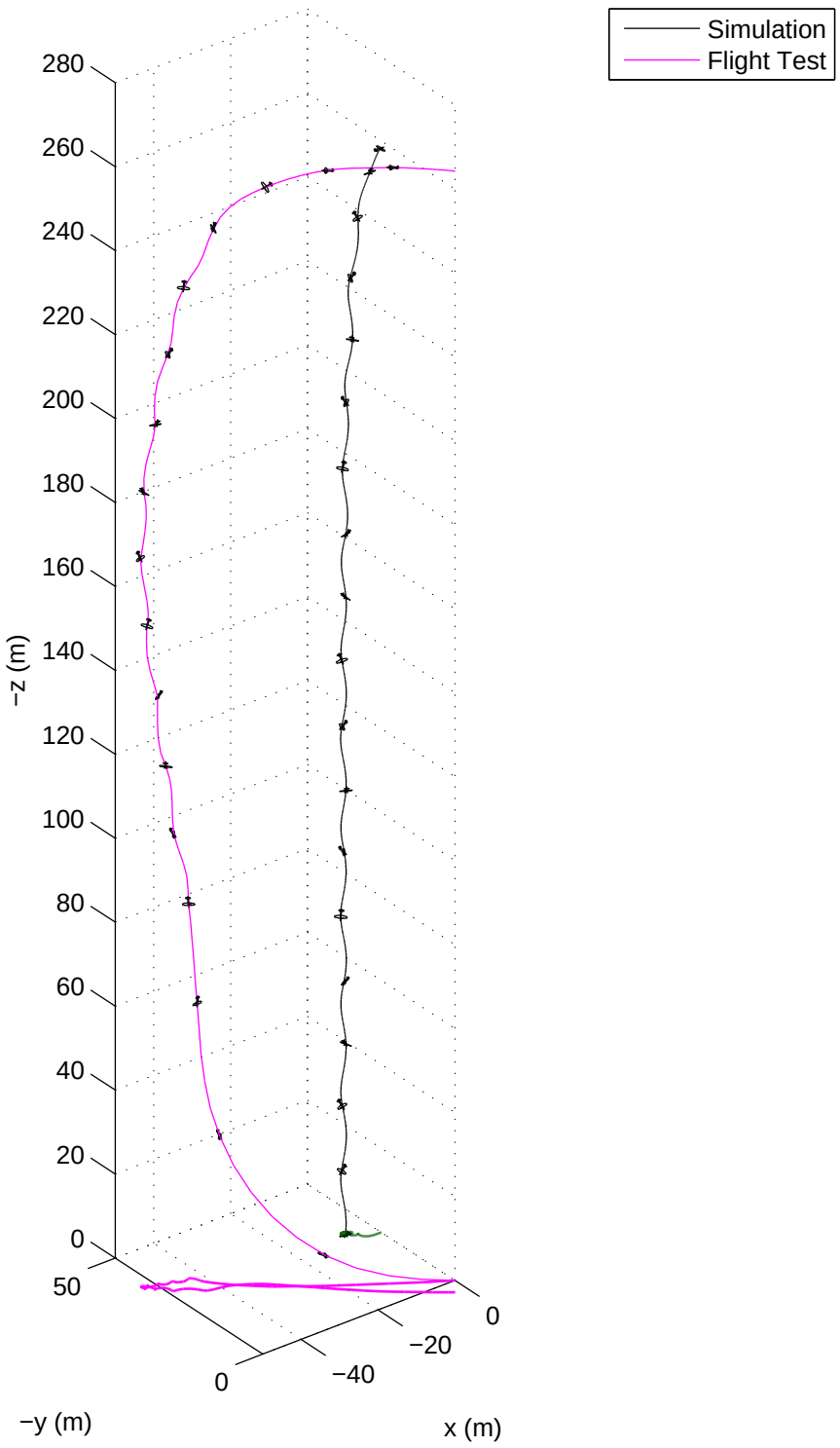

Figure 6.48: Comparison plots of Case A spin trajectories with airplane plotted every second at a 1:1 scale for Aero Testbed flight test and SpinSim simulation.

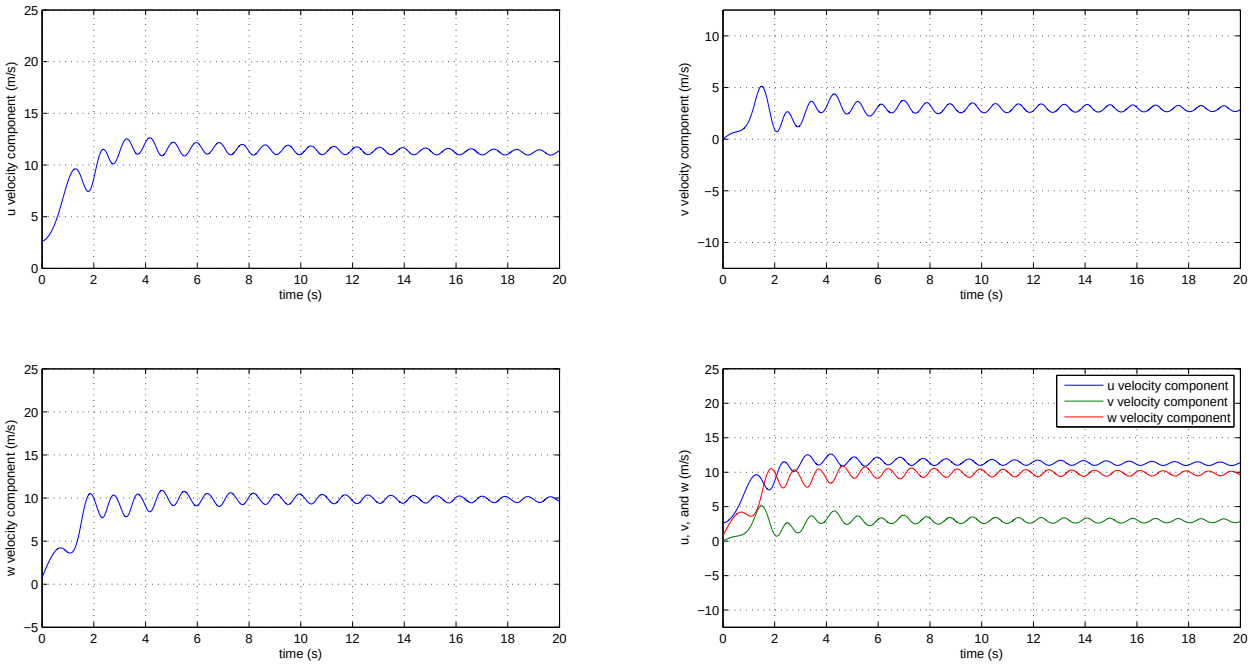

Figure 6.49: Body inertial velocities of SpinSim simulation of the Aero Testbed in a Case A spin.

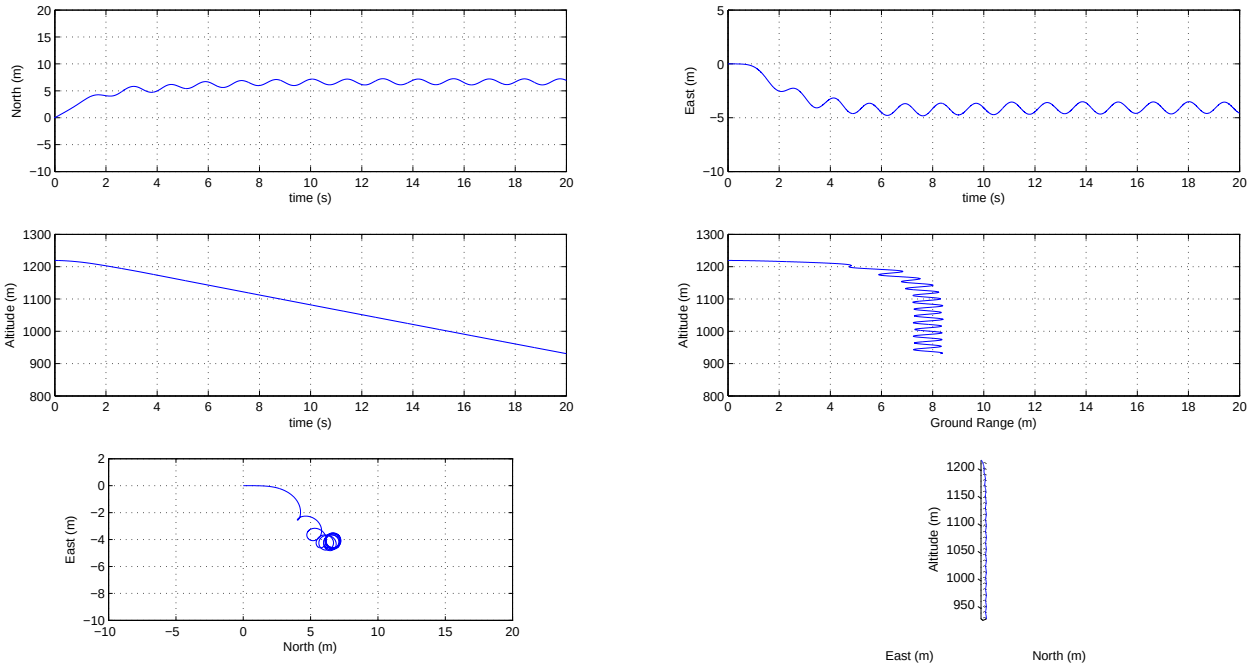

Figure 6.50: Trajectory of SpinSim simulation of the Aero Testbed in a Case A spin.

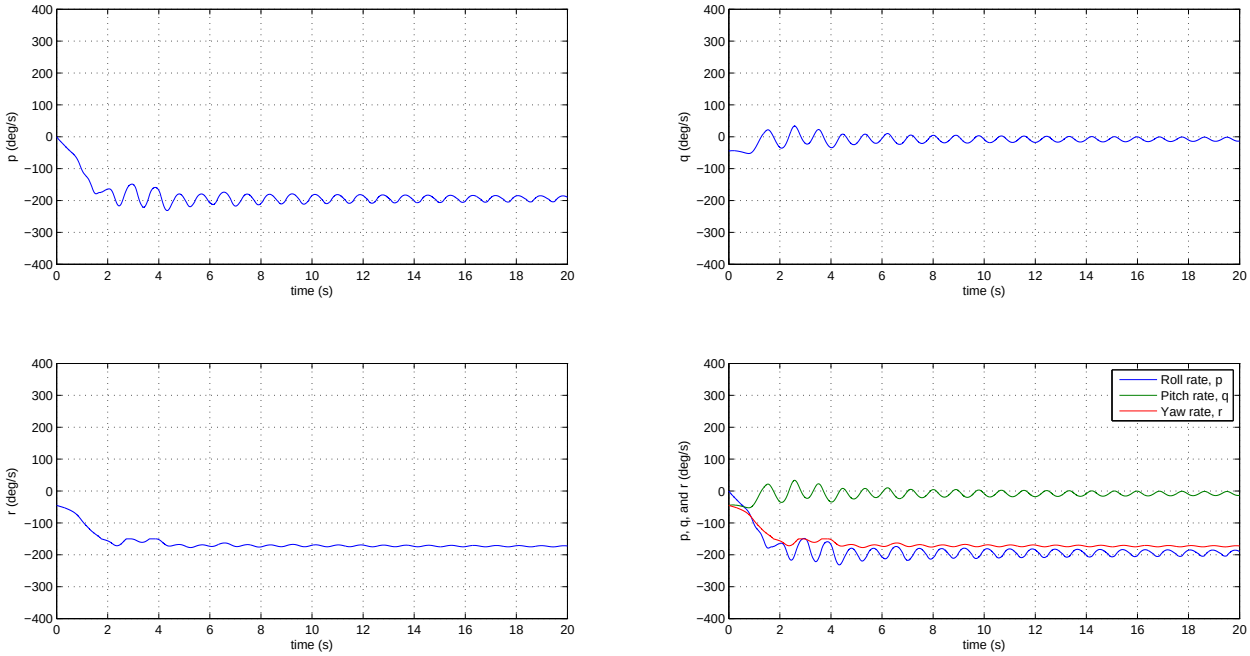

Figure 6.51: Angular rates of SpinSim simulation of the Aero Testbed in a Case A spin.

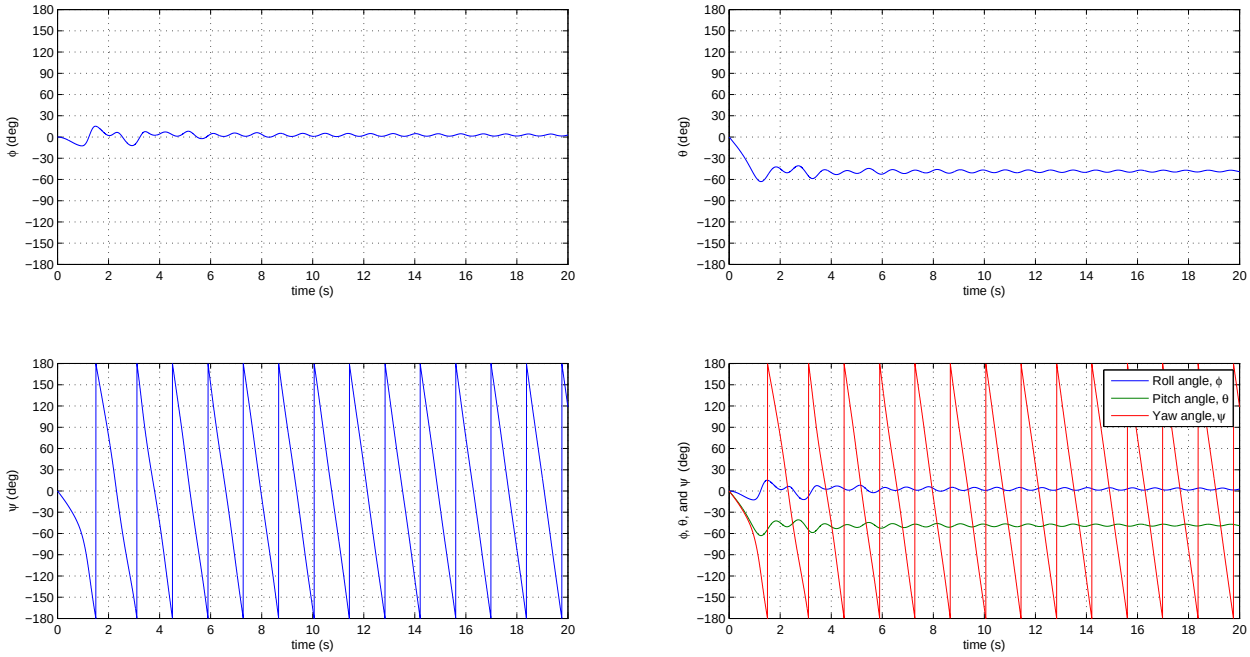

Figure 6.52: Angular orientation of SpinSim simulation of the Aero Testbed in a Case A spin.

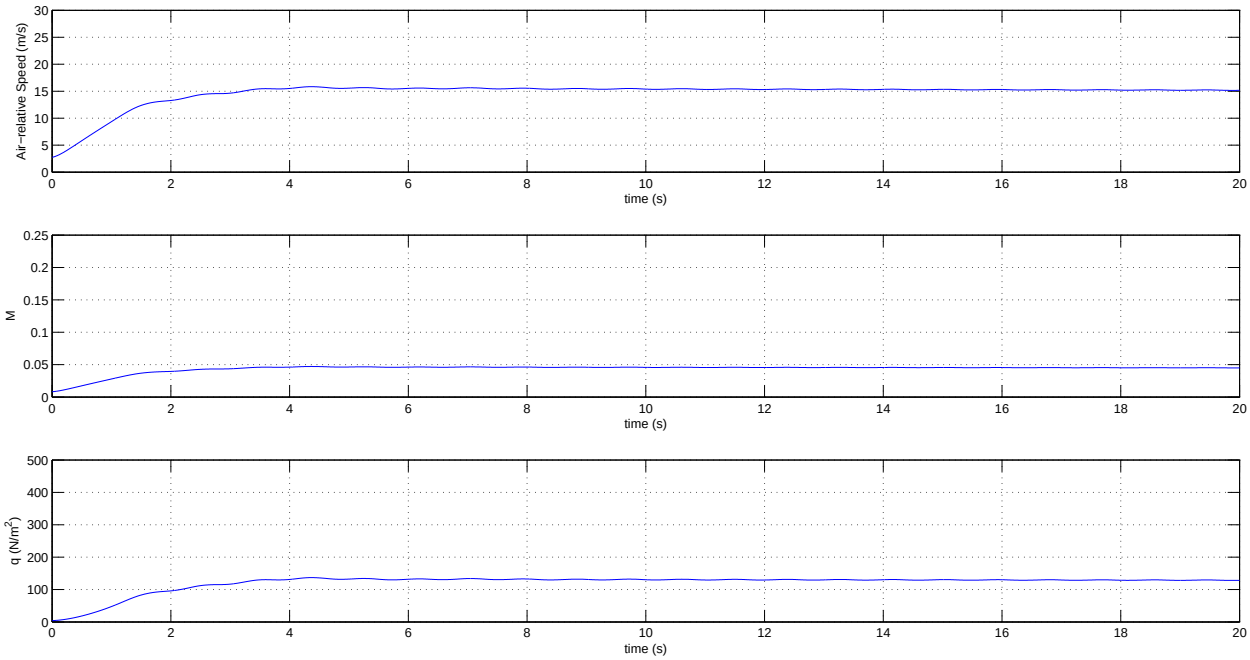

Figure 6.53: Airspeed, Mach number, and q of SpinSim simulation of the Aero Testbed in a Case A spin.

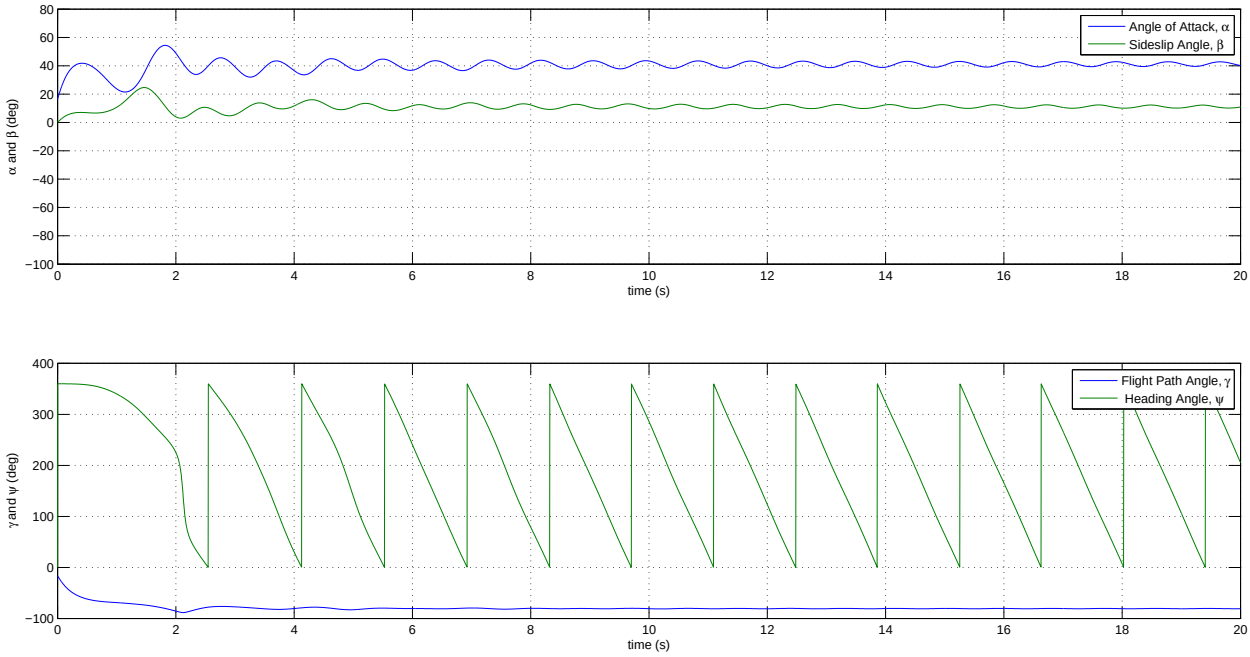

Figure 6.54: Aerodynamic and flight path angles of SpinSim simulation of the Aero Testbed in a Case A spin.

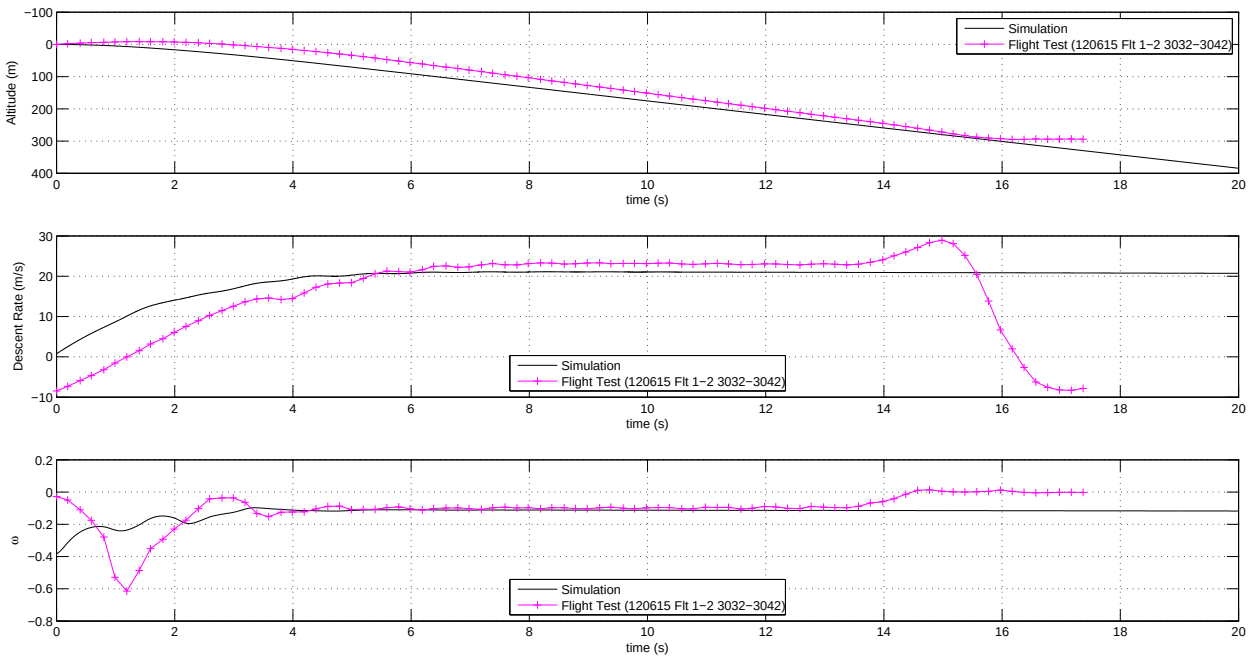

Figure 6.55: Comparison plots of altitude, descent rate, and spin parameter of a Case B spin for Aero Testbed flight test and SpinSim simulation.

6.2.7 SpinSim Results: Case B

Figure 6.55 presents a simulation and experiment coplot of the altitude, descent rate, and spin parameter for a Case B spin. Again, solid agreement between simulation and experiment is demonstrated for this spin. The altitudes both decrease linearly and at similar descent rates. In this spin, the SpinSim simulation predicts a descent rate of approximately 21 m/s. Meanwhile, the flight test data set exhibited a descent rate of just under 23 m/s throughout the spin. The spin parameter values also match exactly with both SpinSim and the experiment, converging to $\omega \approx -0.10$.

Figure 6.56 compares the angular rates of the simulation and experimental flight test spins. While a slight difference in roll rate is present, the yaw rates match nearly exactly. The SpinSim simulation converges on a roll rate of almost -325 deg/s and the flight test data centered around a roll rate of $p = -357$ deg/s. The simulation and flight test yaw rates showed excellent agreement, where $r = -105$ deg/s and $r = -104.9$ deg/s were the developed spin yaw rates from the simulation and flight test data sets, respectively. Good agreement is evident in the pitch rates of the simulation and flight test, which had values of $q = 128$ deg/s and $q \approx 160$ deg/s, respectively.

The detailed 3D spin trajectory, with airplane orientations coplotted, is presented in Fig. 6.57 for the Case B spin. The trajectories align well in terms of descent rate and spin radius. This strong agreement, between the descent rate and spin radius, demonstrates the accuracy of the SpinSim spin simulation. For this spin, the simulation predicts $R_s \approx 0.5$ m, which agrees well with the experimental result of approximately 0.5 m from Table 3.6 for the T0R1E1A1-Lft-Up spin, as shown in Fig. 6.57. For reference, Figs. 6.58–6.63 present the SpinSim 6DOF output for this spin. The

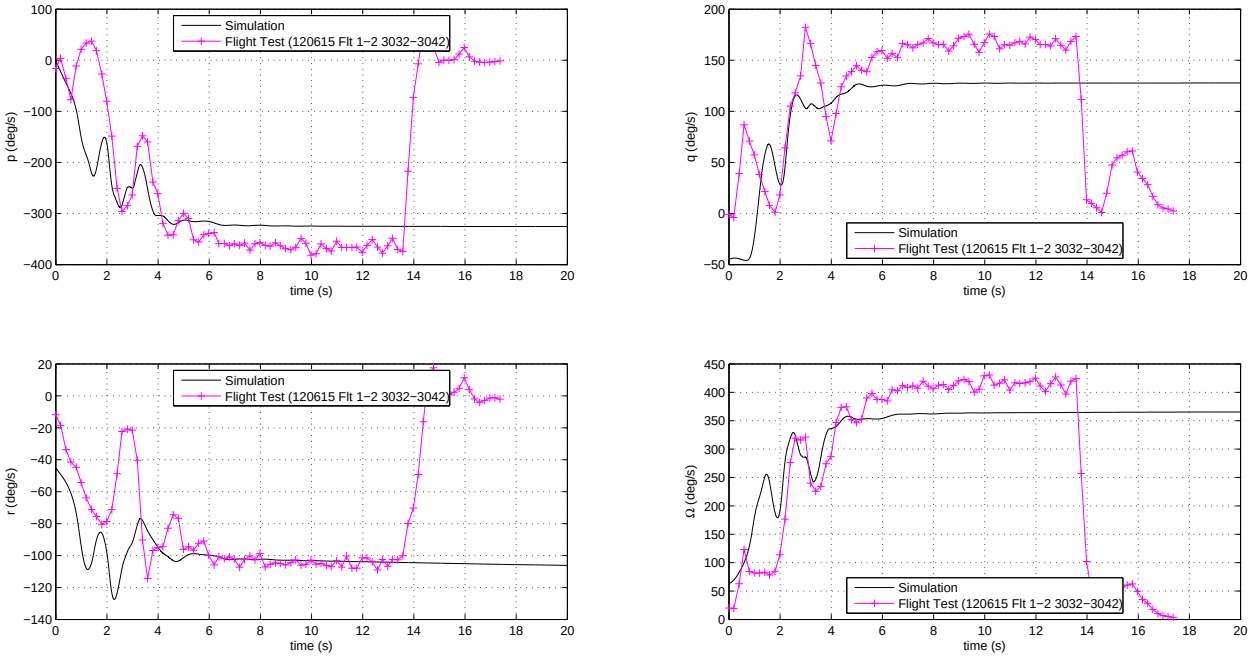

Figure 6.56: Comparison plots of angular rates of a Case B spin for Aero Testbed flight test and SpinSim simulation.

steady spin values for the *u*, *v*, and *w* velocity components of 20, -4, and 7 m/s are located very near to the center of the oscillations of the flight test values shown in Fig. 6.36. The steady spin values of $\alpha \approx 20$ deg and $\beta \approx -10$ deg from the SpinSim simulation of Fig 6.63 are very near to the center of the oscillations of the α and β values calculated from flight test data in Fig. 6.37. This result shows very strong agreement between the aerodynamic angle predictions of SpinSim when compared with the values extracted from Aero Testbed flight test data.

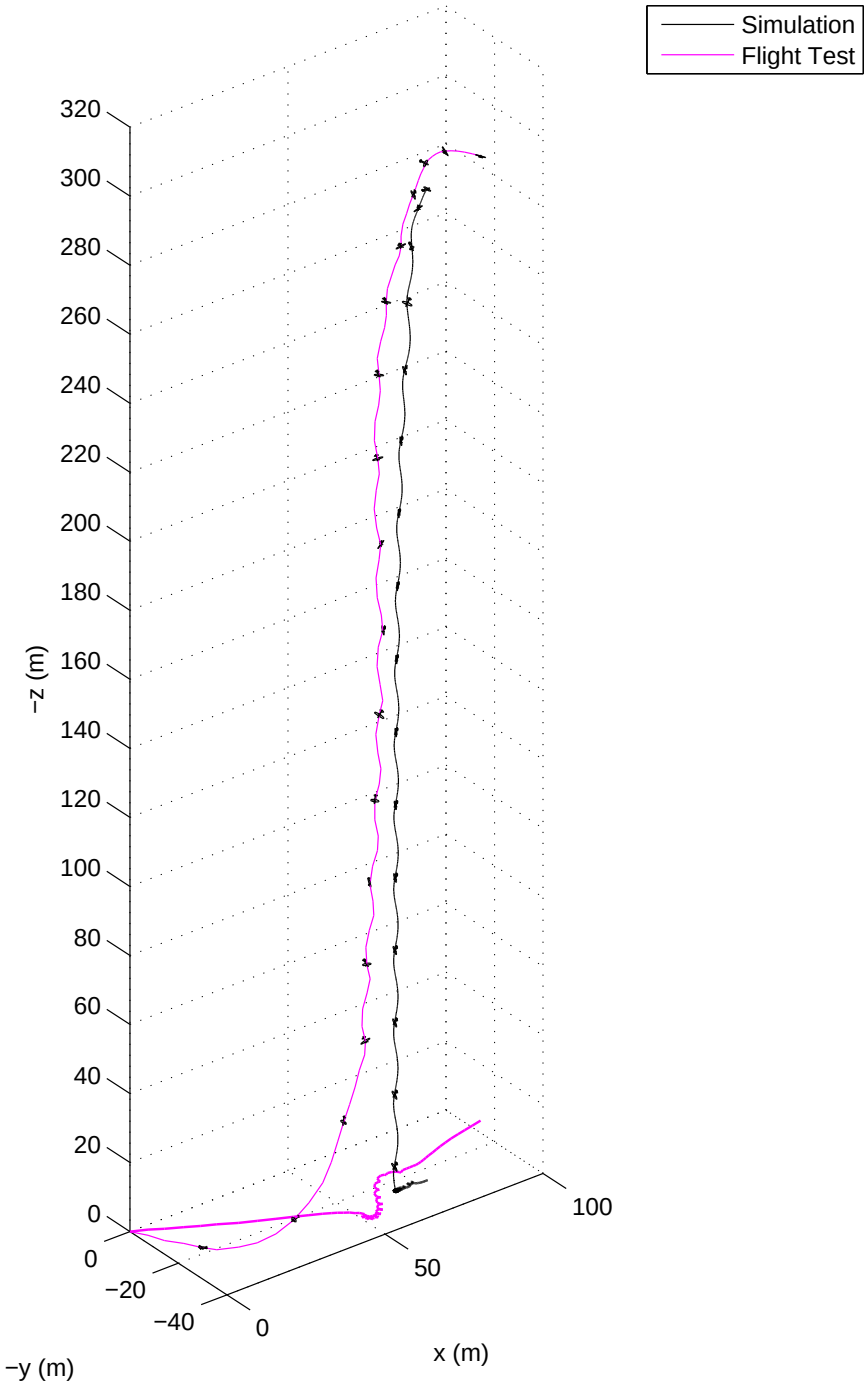

Figure 6.57: Comparison plots of Case B spin trajectories with airplane plotted every second at a 1:1 scale for Aero Testbed flight test and SpinSim simulation.

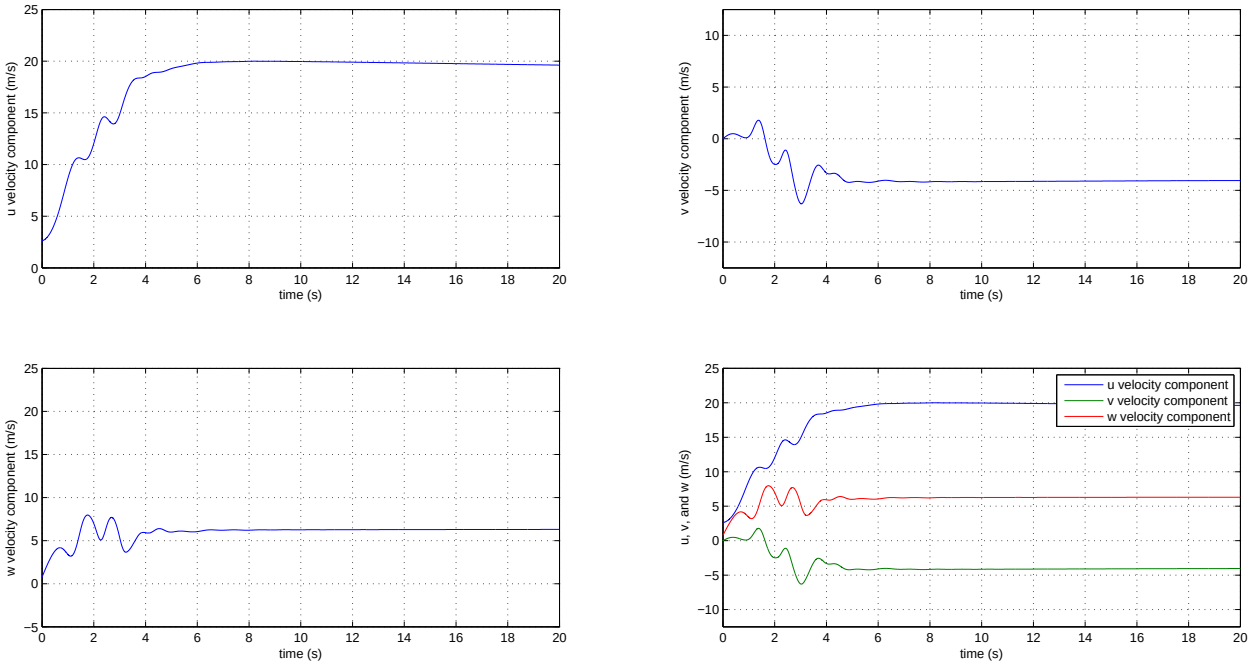

Figure 6.58: Body inertial velocities of SpinSim simulation of the Aero Testbed in a Case B spin.

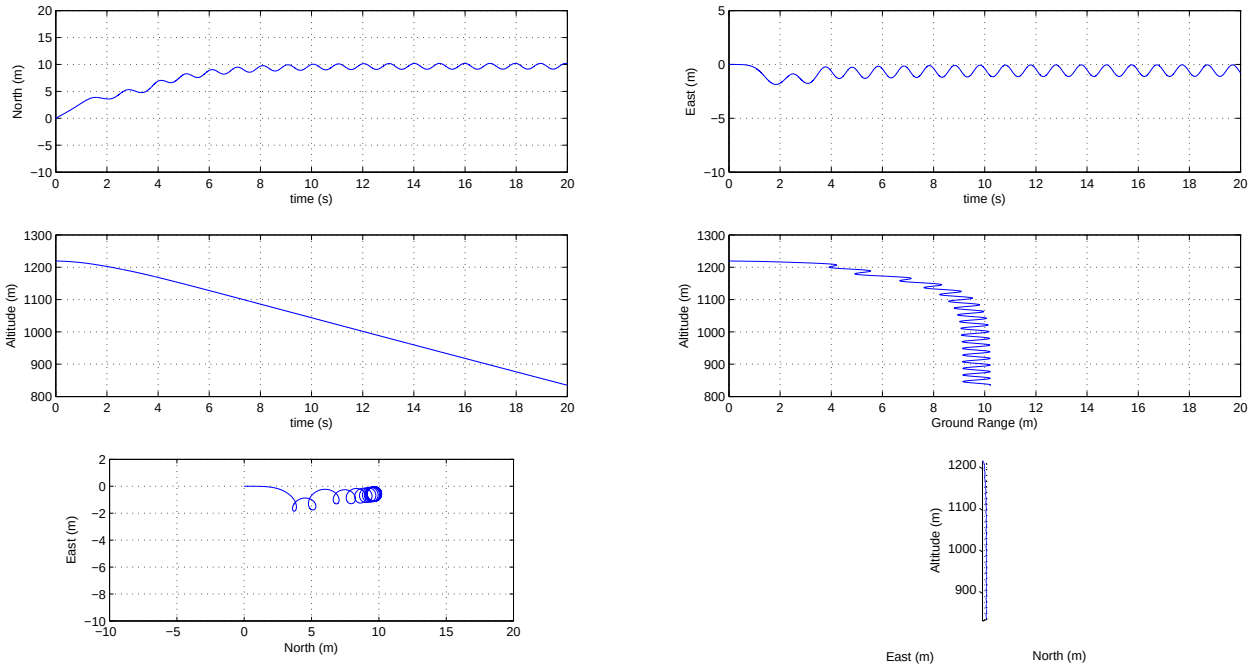

Figure 6.59: Trajectory of SpinSim simulation of the Aero Testbed in a Case B spin.

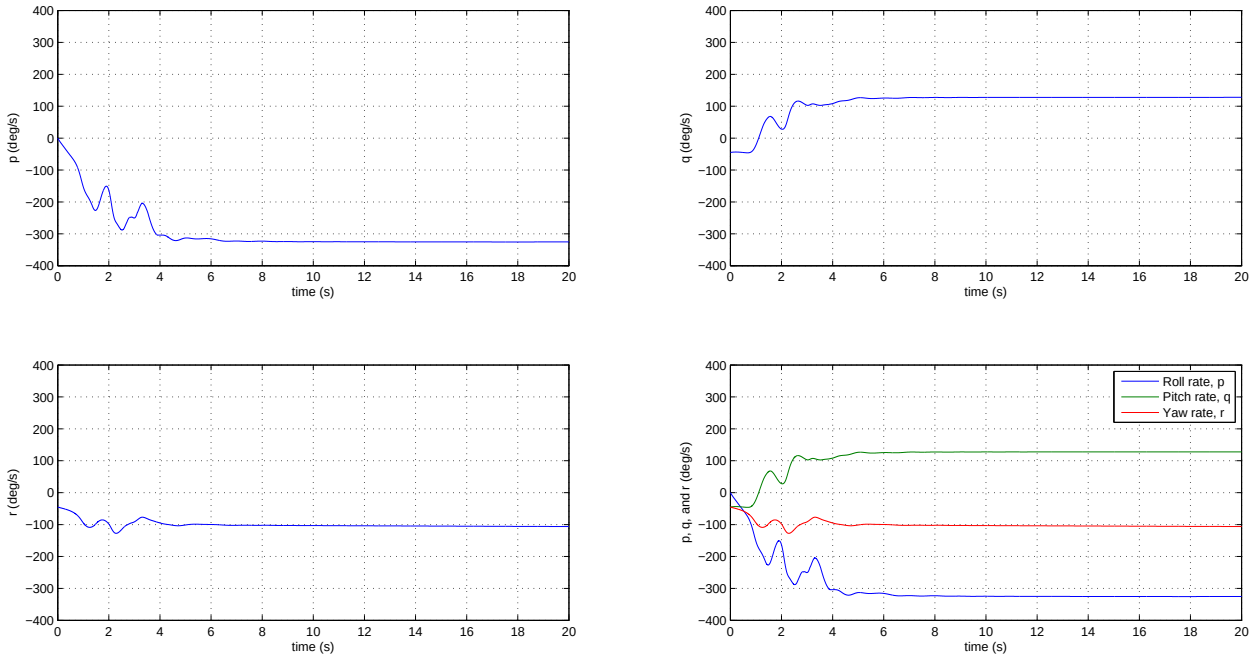

Figure 6.60: Angular rates of SpinSim simulation of the Aero Testbed in a Case B spin.

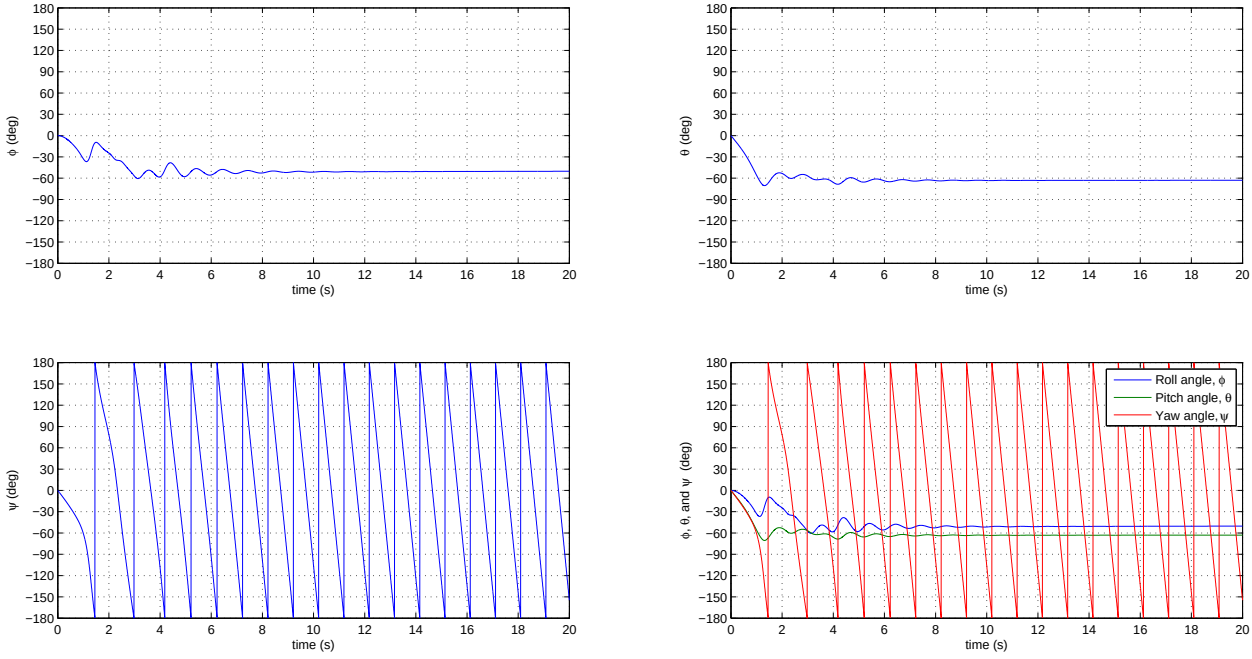

Figure 6.61: Angular orientation of SpinSim simulation of the Aero Testbed in a Case B spin.

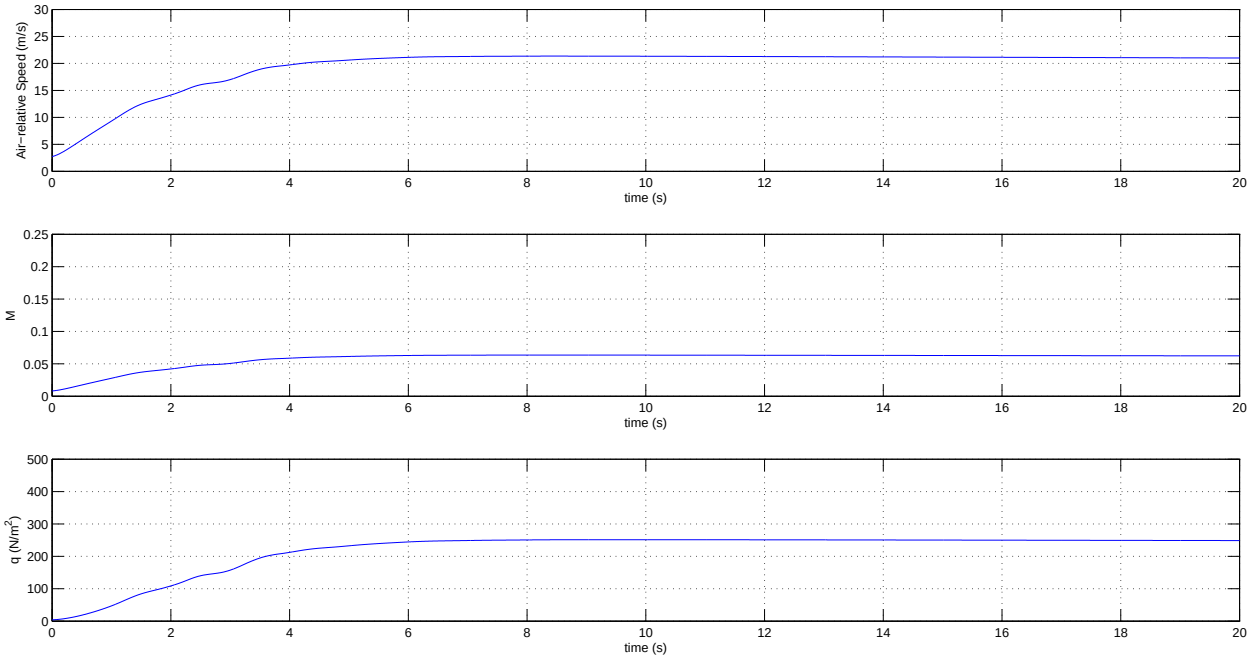

Figure 6.62: Airspeed, Mach number, and q of SpinSim simulation of the Aero Testbed in a Case B spin.

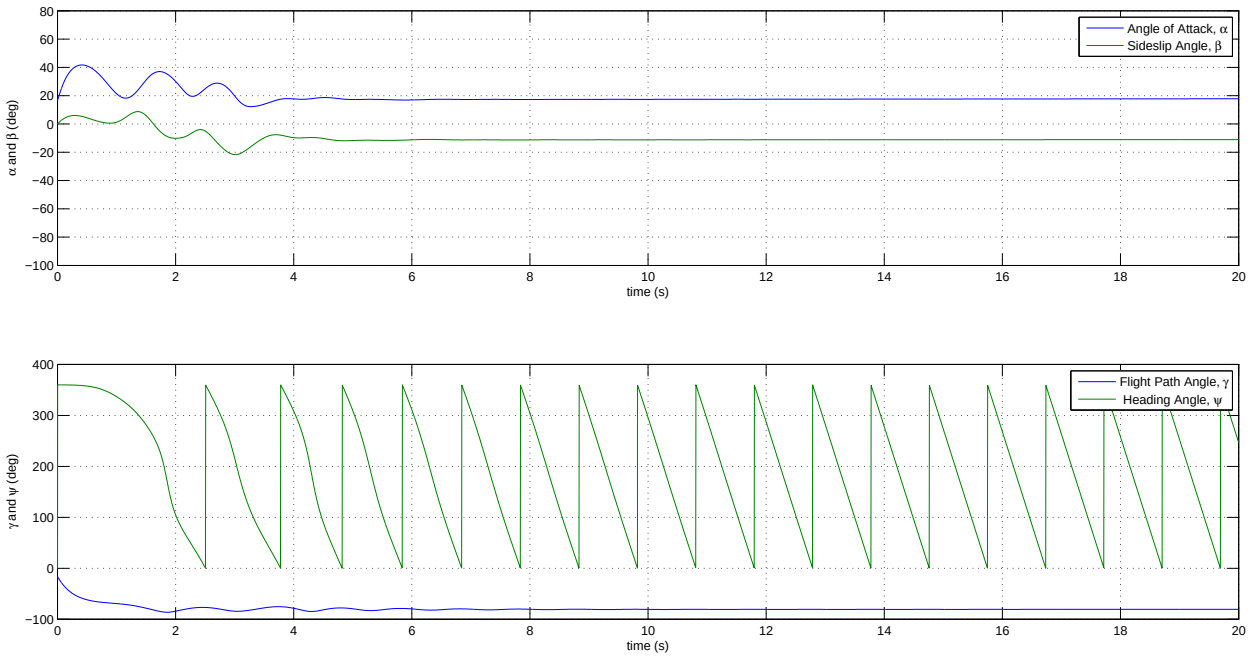

Figure 6.63: Aerodynamic and flight path angles of SpinSim simulation of the Aero Testbed in a Case B spin.

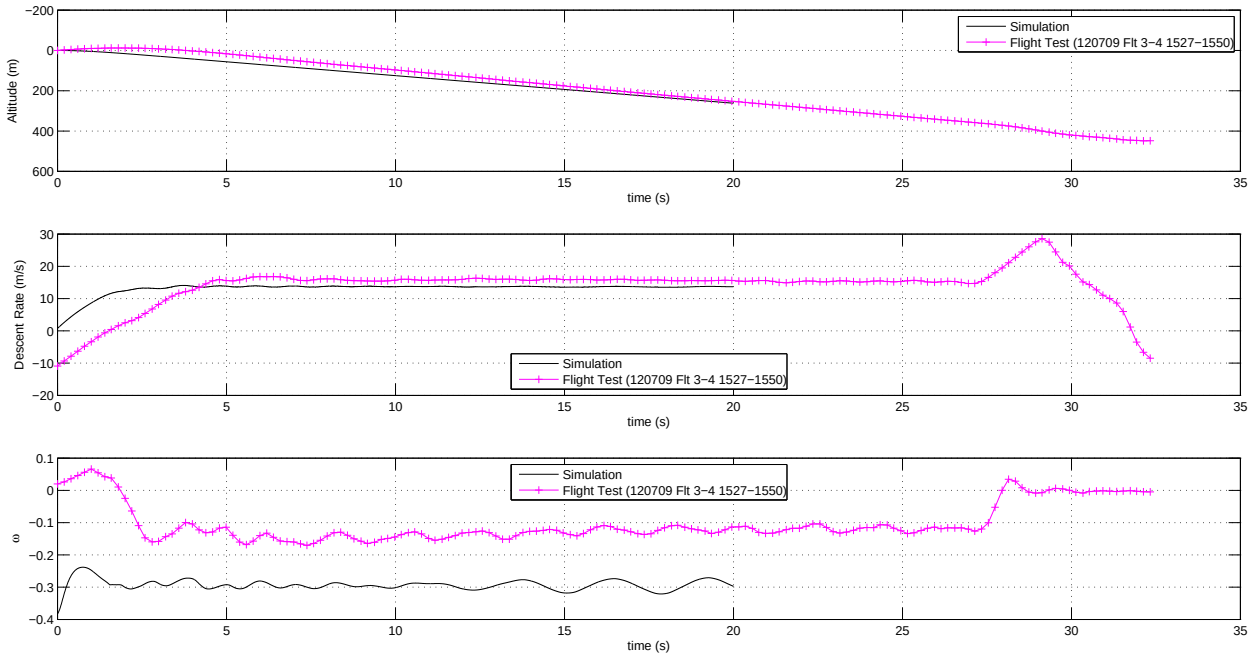

Figure 6.64: Comparison plots of altitude, descent rate, and spin parameter of a Case C spin for Aero Testbed flight test and SpinSim simulation.

6.2.8 SpinSim Results: Case C

Figure 6.64 presents a comparison plot of the simulated and experimental altitude time history, descent rate, and spin parameter values for a Case C spin. Strong agreement in the descent rate is demonstrated for this spin, but the spin parameter ω values do not agree as well. The altitudes both decrease linearly and at similar descent rates. The SpinSim simulation predicts a descent rate of 13.8 m/s. Meanwhile, the flight test data set exhibited a descent rate of around 15.47 m/s during the spin. These values are significantly lower than those of the non-aerobatic deflection spins (of the Case A and B spins) because the high-angle control surface deflections significantly increase the axial drag on the airplane. The spin parameter values do not match that well, with SpinSim predicting values oscillating between $\omega \approx -0.30$ and $\omega \approx -0.25$, and the experiment oscillating between $\omega \approx -0.17$ and $\omega \approx -0.11$.

Figure 6.65 compares the angular rates of the simulation and experimental flight test spins. This figure explains the ω discrepancies of Fig. 6.64. Good agreement, in regard to the roll rate p of the simulation and flight test, is demonstrated with the average roll rates being nearly coincident around -150 deg/s. The yaw and pitch rates, however, exhibit differences. The fact that the roll rates match well, which characterize a motion driven primarily by the wing, indicate that the wing force model is well-tuned. The fact that SpinSim overpredicts the yaw rate causes the prediction of the total angular velocity Ω to also be overpredicted. Curiously, a regular motion in the simulated spin is predicted with an approximate period of 2.55 s. While the Case C spin did not exhibit such behavior, when pro-spin ailerons were commanded (Case D) during Aero Testbed flight tests, a long-period oscillation was observed.

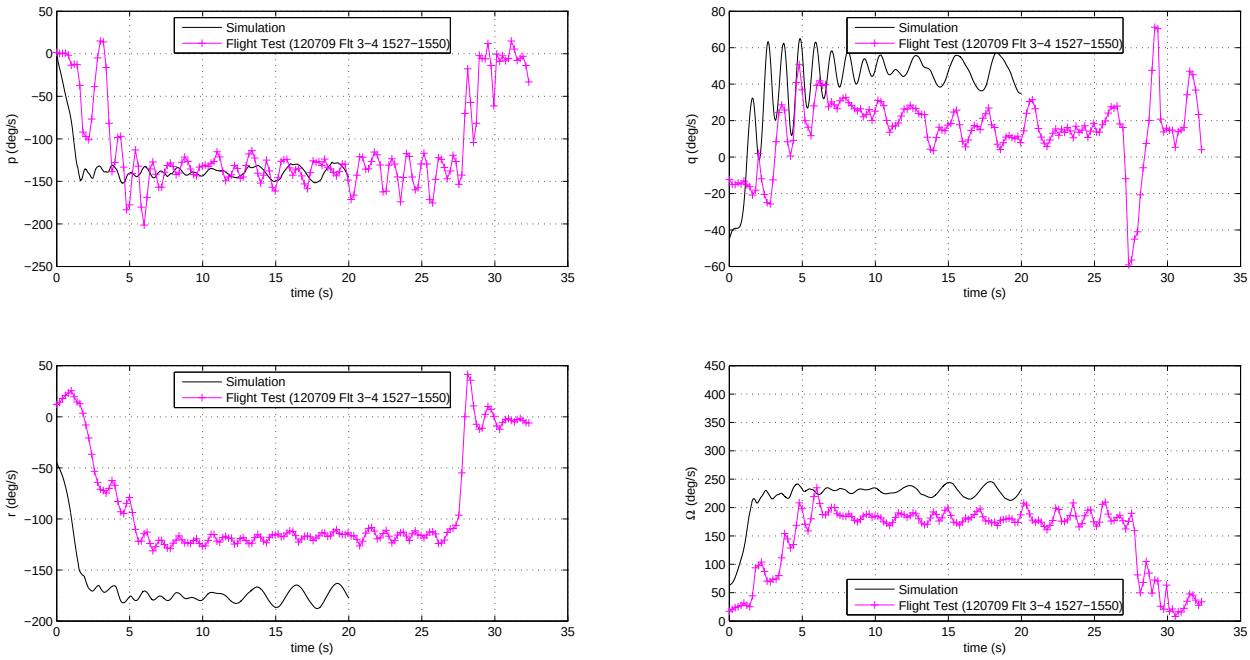

Figure 6.65: Comparison plots of angular rates of a Case C spin for Aero Testbed flight test and SpinSim simulation.

Regardless, this long-period oscillation predicted by SpinSim is incorrect. It suggests that future work could be directed toward understanding the aerodynamics of the control surfaces and their interactions with one another at these extreme aerobatic deflection angles.

As an aside, it is this long-period motion that was observed during the flight tests for the Case D spin that is the reason why no simulations were initially attempted for that spin. The experimental flight test data indicate that there are significant dynamic stall-like effects, occurring in the Case D spin, and those are beyond the scope of the capabilities of SpinSim. Modeling the dynamic stall-like effects could prove to be an interesting and rewarding direction in which future work may be directed.

Figure 6.66 presents the detailed 3D spin trajectory with airplane orientations coplotted for the Case C spin. Again, the trajectories align well, in terms of descent rate and spin radius. This strong agreement, between simulation and flight test, demonstrates the accuracy of the SpinSim spin simulation, despite the previously-described yaw rate and pitch rate oscillatory issues. The approximate spin radius predicted is $R_s \approx 0.75$ m and this value agrees well with the experimentally-measured value of 0.86 m from Table 3.6 for the T0R2E2A0-Lft-Up spin. For reference, Figures 6.67–6.72 present the balance of the SpinSim-generated output for the Case C spin. As shown in Fig. 6.67, the steady-state simulation u, v, and w velocity component values are approximately 9, -2, and 10 m/s; these values lie very near to the center of the oscillations in the experimental values of Fig. 6.40. Additionally, the center of the oscillations of the α and β values calculated from flight test in Fig. 6.41 is very near to the SpinSim-predicted α and β values of 50 deg and

-5 deg, respectively, in Fig 6.72. Significantly, this result shows strong agreement between the aerodynamic angles predicted by SpinSim and those extracted from flight test data.

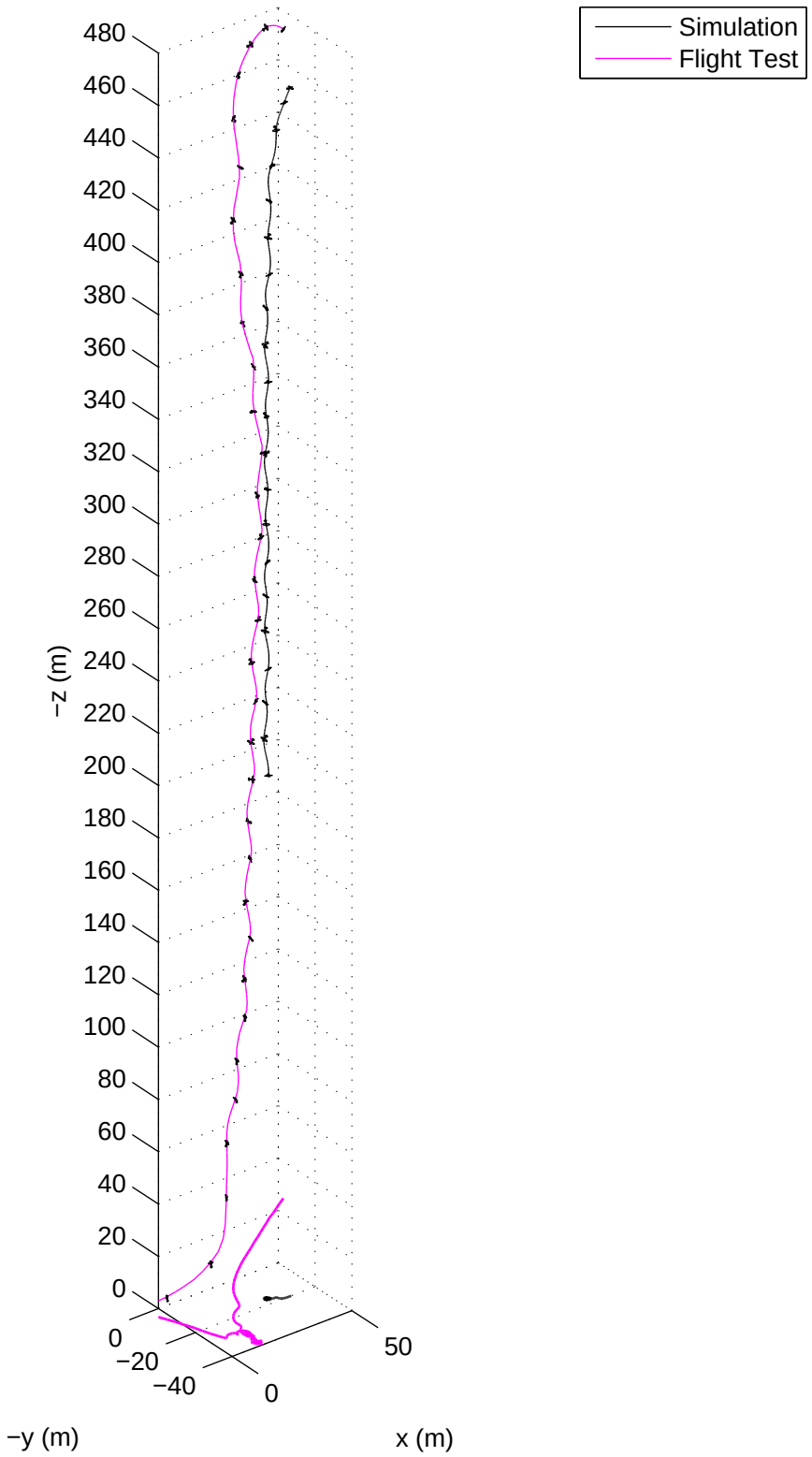

Figure 6.66: Comparison plots of Case C spin trajectories with airplane plotted every second at a 1:1 scale for Aero Testbed flight test and SpinSim simulation.

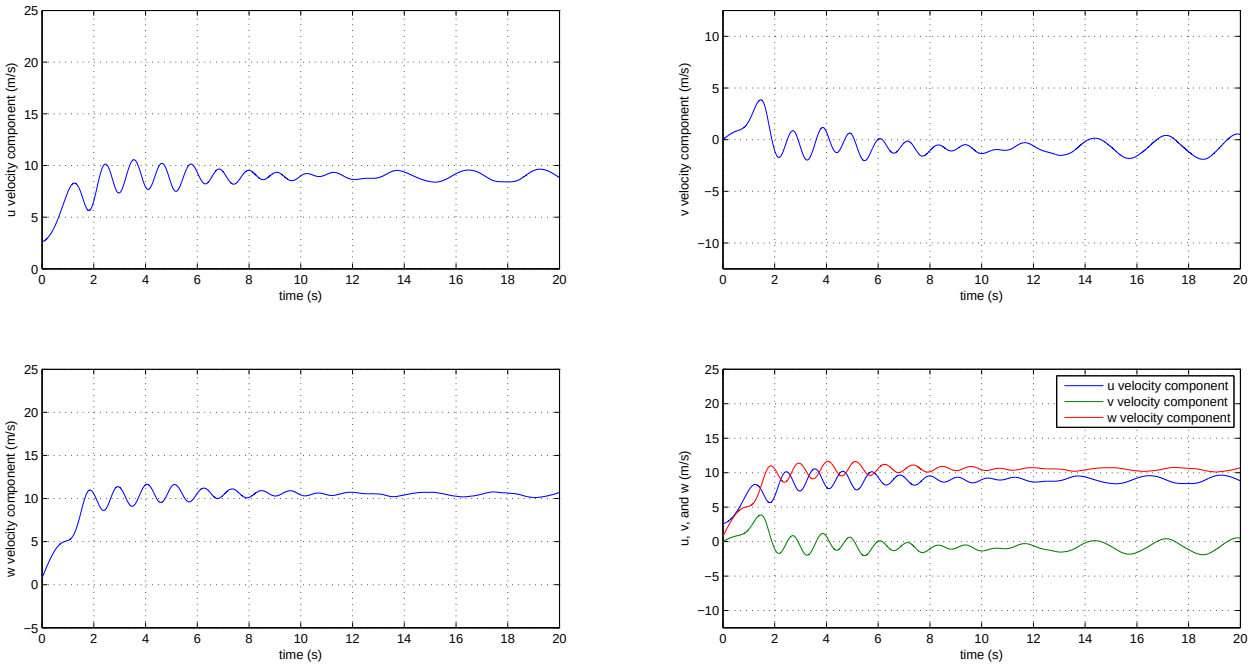

Figure 6.67: Body inertial velocities of SpinSim simulation of the Aero Testbed in a Case C spin.

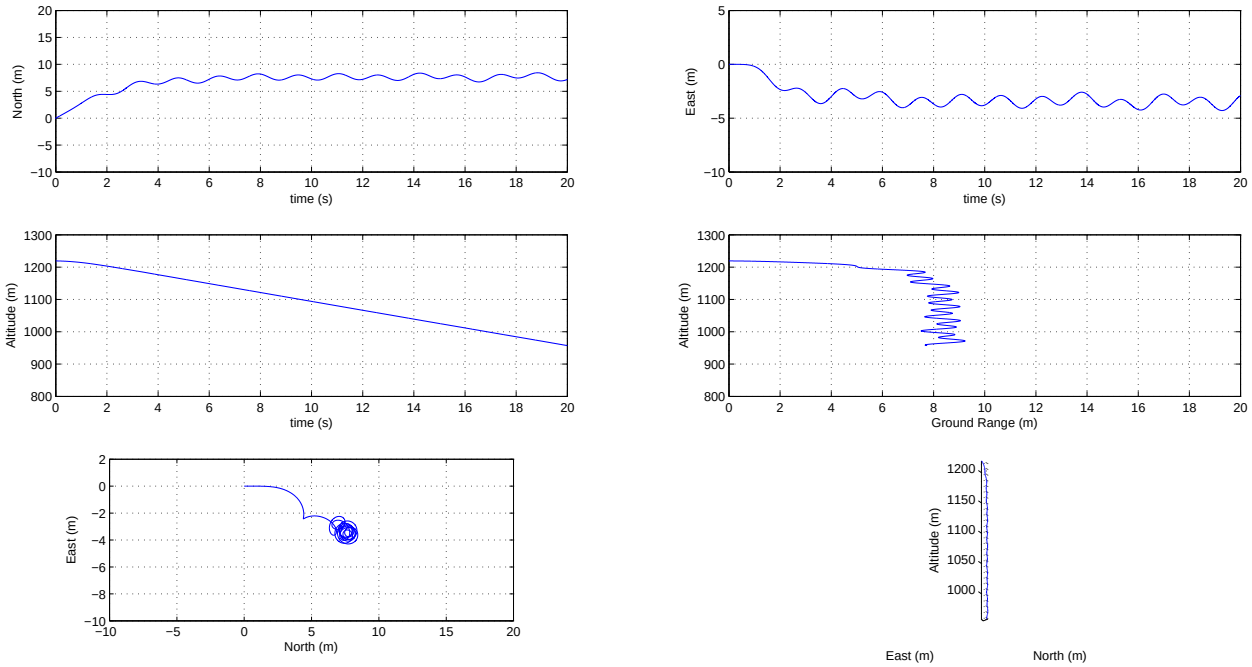

Figure 6.68: Trajectory of SpinSim simulation of the Aero Testbed in a Case C spin.

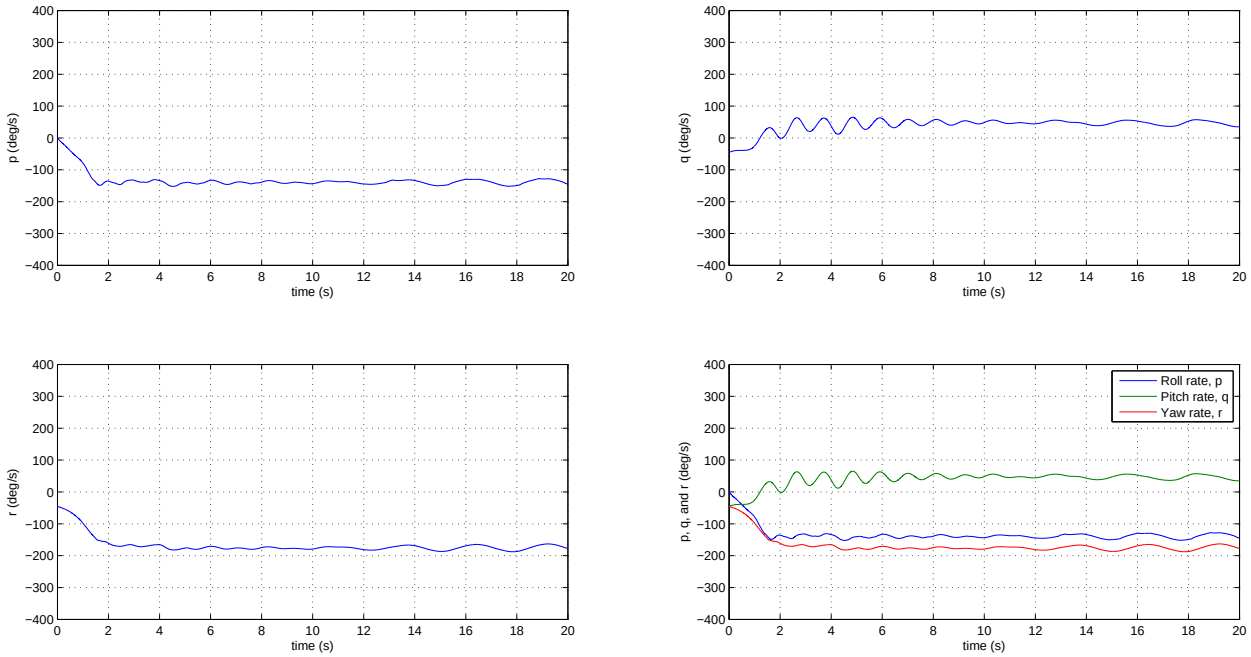

Figure 6.69: Angular rates of SpinSim simulation of the Aero Testbed in a Case C spin.

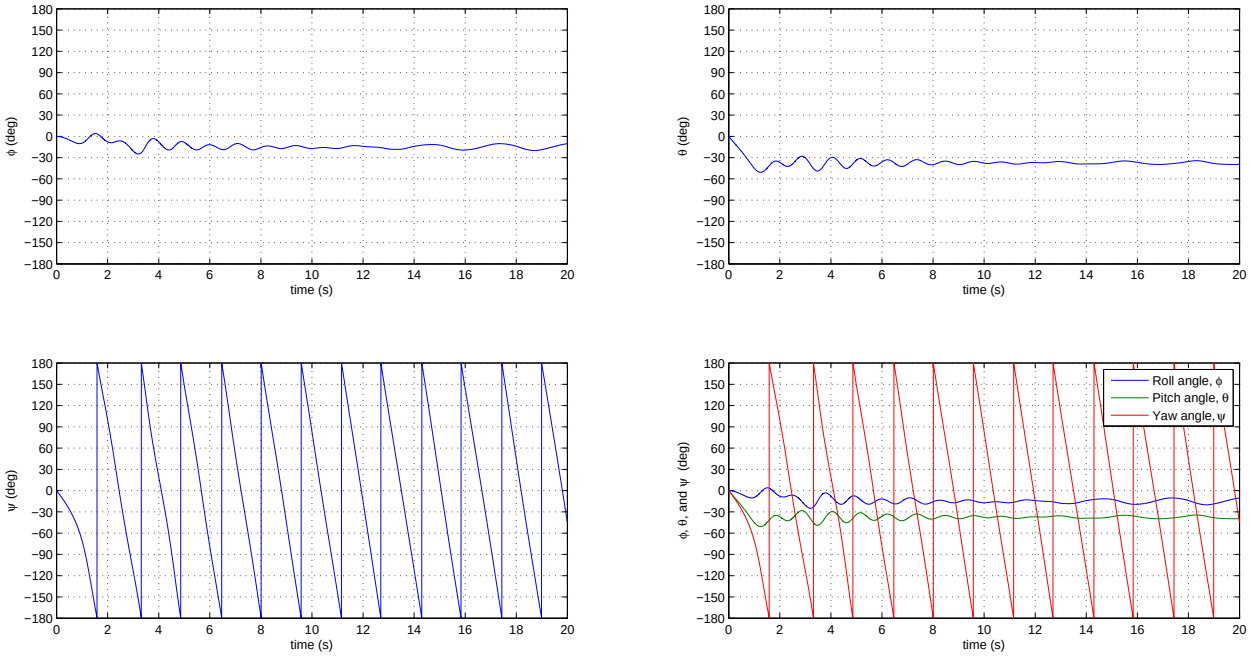

Figure 6.70: Angular orientation of SpinSim simulation of the Aero Testbed in a Case C spin.

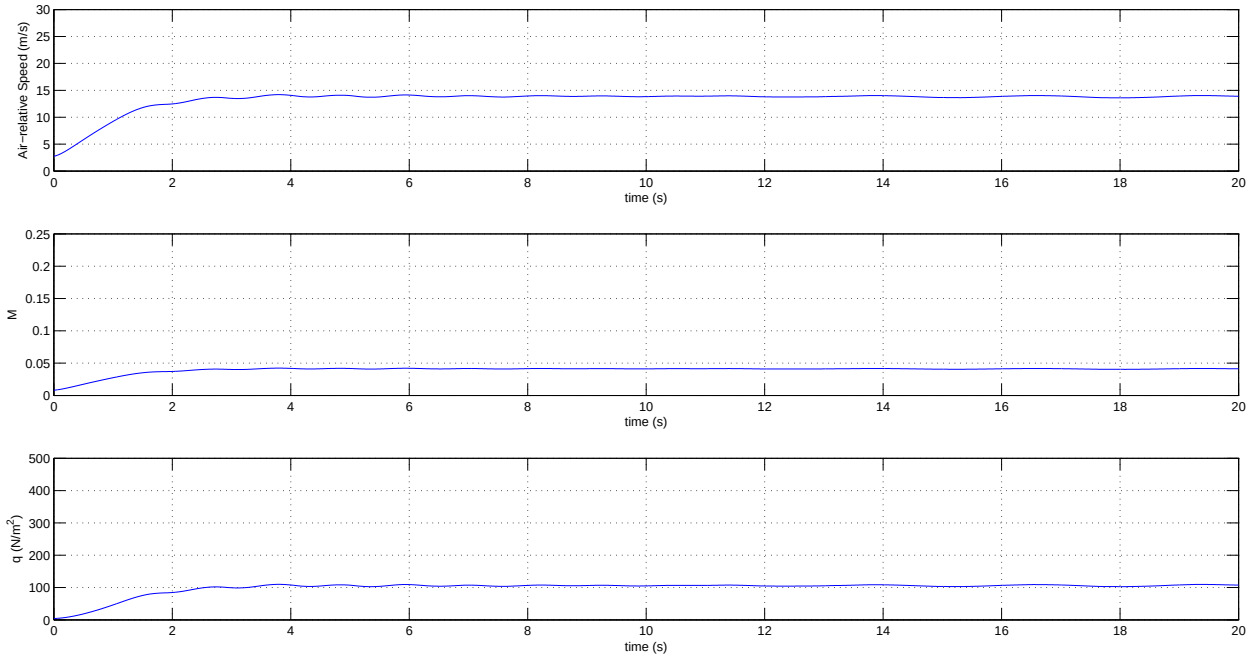

Figure 6.71: Airspeed, Mach number, and q of SpinSim simulation of the Aero Testbed in a Case C spin.

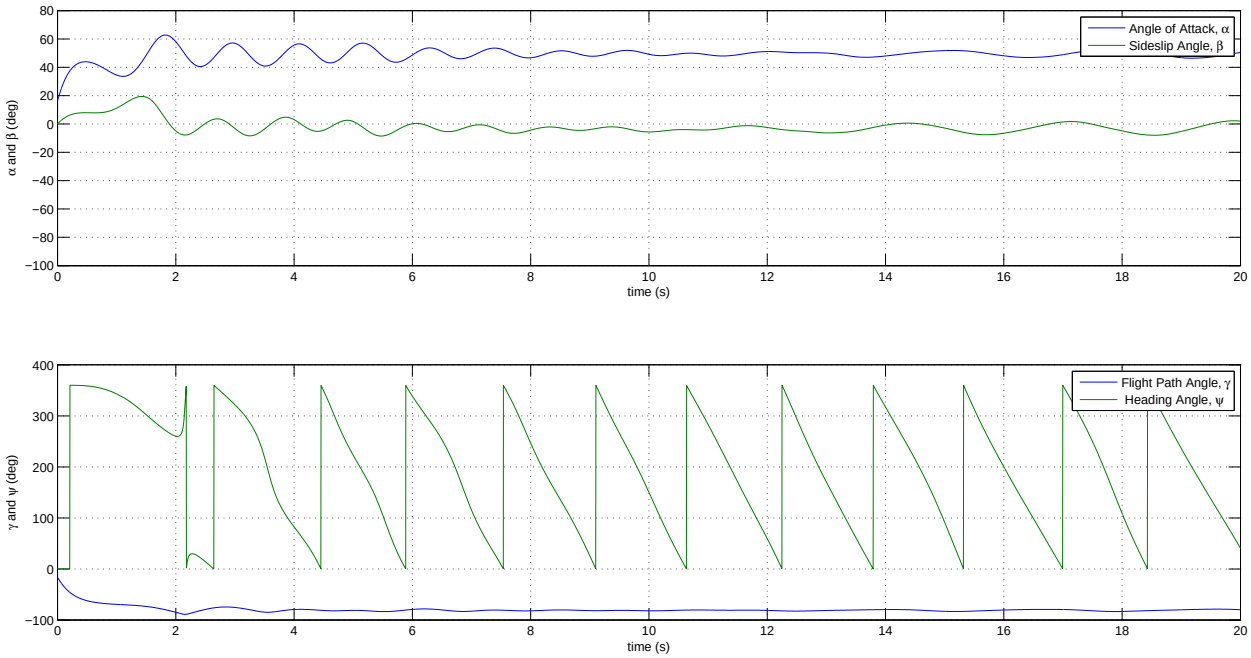

Figure 6.72: Aerodynamic and flight path angles of SpinSim simulation of the Aero Testbed in a Case C spin.

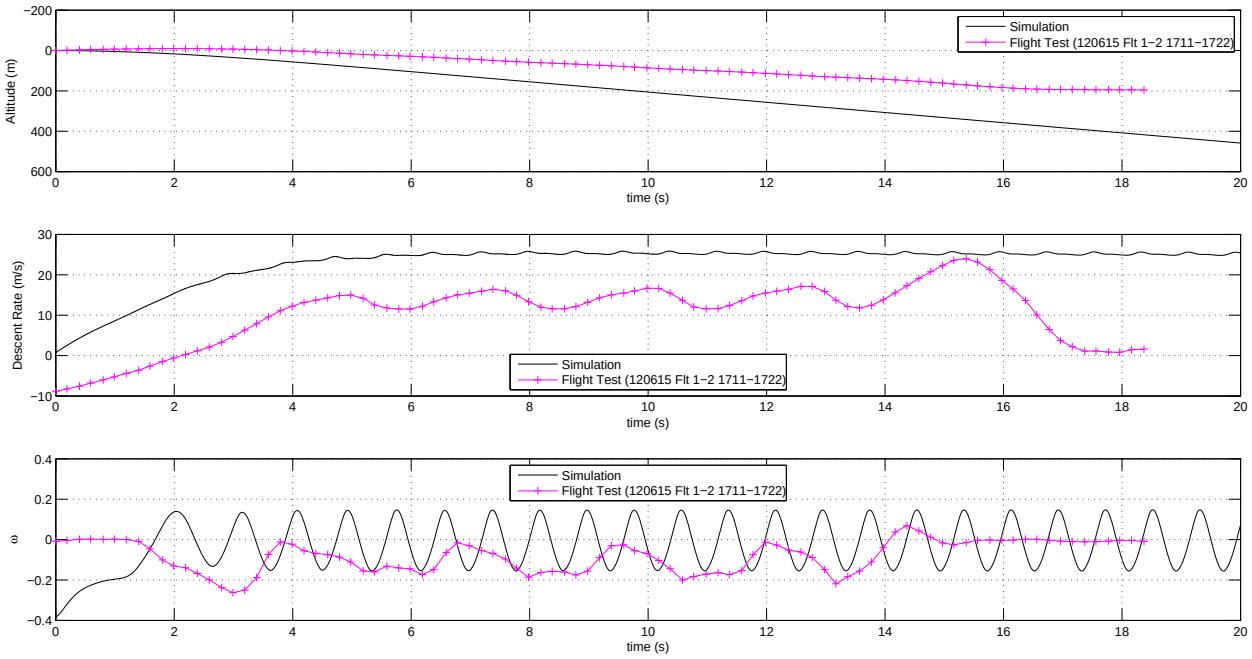

Figure 6.73: Comparison plots of altitude, descent rate, and spin parameter of a Case D spin for Aero Testbed flight test and SpinSim simulation.

6.2.9 SpinSim Results: Case D

The fourth and final spin presented in this section is the Case D spin. As previously depicted in Fig. 3.17, this spin in flight test was unsteady and highly-oscillatory in nature. These characteristics were verified by both onboard video and the IMU. The oscillations were equal, opposite, and repeatable for left and right spins. For completeness, this spin was simulated in SpinSim. Although, it must be stressed that SpinSim does not have any dynamic stall-like terms. Figure 6.73 presents a comparison of the altitude descended, descent rate, and spin parameters for the Case D spin, as simulated by SpinSim, and as recorded during Aero Testbed flight tests.

Unlike all of the other spins, the flight test data for this spin does not show a linear decrease in altitude, nor does the data exhibit a constant descent rate. The descent rate plot for this spin indicates that the descent rate oscillates between 11.6 and 16.6 m/s with an approximate period of $t = 2.8$ s. SpinSim predicts a somewhat-constant descent rate of 25 m/s, which is admittedly not a great result. The reason for this discrepancy, as shown in Fig. 6.79, is that in the simulation, the aircraft is predicted to be at a roll angle θ centered around 90 deg. In flight test, however, the spins were nearly flat with $\theta \approx 0$. An airplane descending at a bank angle of 90 deg, sometimes known as a knife-edge maneuver, is clearly in a lower-drag configuration relative to the freestream than an airplane in a nearly-flat spin. Because the knife-edge orientation of the SpinSim simulation is a lower-drag configuration than the experiment, the descent rate as predicted by SpinSim is greater than that of the flight test experiments.

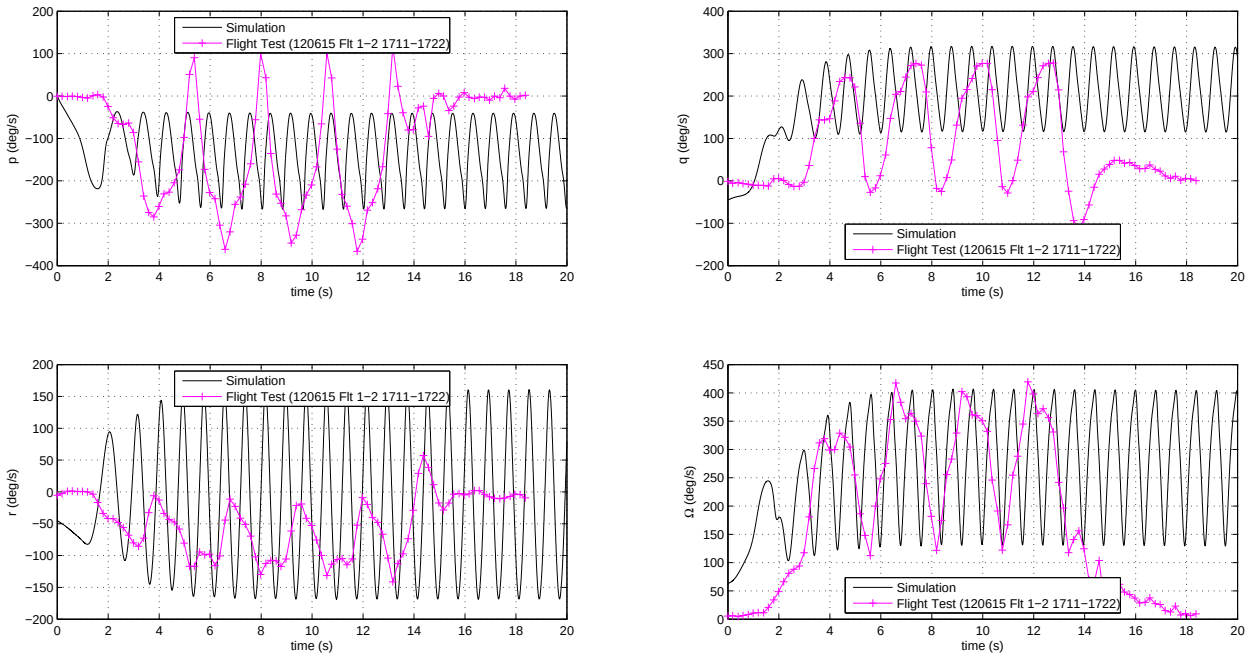

Figure 6.74: Comparison plots of angular rates of a Case D spin for Aero Testbed flight test and SpinSim simulation.

Agreement between simulation and flight test data for the spin parameter is somewhat closer than for the descent rate. While the flight test values oscillated between $\omega = -0.03$ and $\omega = -0.185$, SpinSim predicted a spin parameter that oscillated between $\omega = -0.15$ and $\omega = 0.14$. Notably, the flight test oscillations had a period of approximately 2.8 s and were not a pure sin function. SpinSim, however, predicted what appears to be a purely-sinusoidal oscillation with a period of about 0.8 s.

Figure 6.74 compares the spin angular rates from flight test with the simulation results of SpinSim. While SpinSim predicts a roll rate that oscillates rapidly between -60 and -260 deg/s, the flight test data, in contrast, show a roll rate that oscillates quite slowly between -350 deg/s and 100 deg/s. This slow change in the flight test roll rate clearly demonstrates that dynamic effects are present in the Case D spin because pro-spin ailerons were constantly commanded during this spin at a deflection of -34 deg. These dynamic effects are also depicted in the pitch rate time history, where flight test values varied between -27 deg/s and 276.5 deg/s with an approximate period of 2.8 s. Again, SpinSim did not capture this oscillatory behavior becuase of its dynamic nature, and instead, it predicted a rapidly-oscillating pitch rate q between 116 and 315 deg/s. The yaw rate r time history exhibited similar behavior; flight test values for r were between 0 and -140 deg/s. SpinSim-predicted yaw rates were within the range $-160 < r < 160$ deg/s. Despite these large differences in the behavior of the inertial rates, the total angular velocity Ω of the flight test and simulation matched reasonably well with an average value of 270 deg/s and similar magnitude of oscillation of 280 deg/s. Of course, the periods of the oscillations were vastly different, leaving room for future work that could be directed toward incorporating dynamic stall factors into the aerobatic deflection angle spin simulations.

Figure 6.75 presents the detailed 3D spin trajectory with airplane orientations coplotted for Case D spin. Although the descent rates do not align well, some agreement is present in regard to the spin radii. While SpinSim predicts $R_s \approx 1$ m, the flight test data exhibit an approximate spin radius of 0.8 m as shown in Table 3.6 for the T0R2E2A2-Lft-Up spin. Given the discrepancies in the angular rates, and the periodicity of the oscillatory motions, it is quite surprising that the spin radii show such reasonable agreement. For reference, Figures 6.76–6.81 present the balance of the SpinSim-generated output for the lefthand, high deflection angle, pro-spin aileron spin of Case D. The calculated α values of Fig. 6.81 oscillated between approximately zero and 15 deg, while the flight test α values of Fig. 6.45 oscillated around a mean of 30 to 50 deg. In Fig. 6.81, the calculated β values oscillated between -80 and -40 deg. Meanwhile, the β value data from flight test is inconclusive, as shown in Fig. 6.45, because of the highly-dynamic nature of the spin.

6.3 Summary of 6DOF SpinSim Spin Simulations

In this section, the simulation results, as generated by SpinSim, were presented for four select spins with different combinations of control surface deflections and deflection angles. The equations of motion were presented, and a number of parametric studies on SpinSim-generated spins were shown. The use of different integration tolerance parameters, different airplane initial conditions, and different integration schemes were shown to not have a significant effect on the steady-spin parameters to which the simulations converged. Spin simulations were compared against spin flight test data, and their accuracy was demonstrated. Significantly, angular rates, spin radii, and airplane velocity were shown to have strong agreement in some cases. Generally, the results were more accurate for spins with low control surface deflection angles, but even the high control surface deflection angle spins were simulated with some degree of accuracy. Comparisons of simulation and flight test data for the Case D spin were inconclusive. This result is expected, as the flight test spins were highly-oscillatory in nature and dominated by unsteady dynamic effects. Finally, and significantly, strong agreement between SpinSim simulations and Aero Testbed flight test data was shown in regard to the aerodynamic angles α and β for the Case A, Case B, and Case C spins.

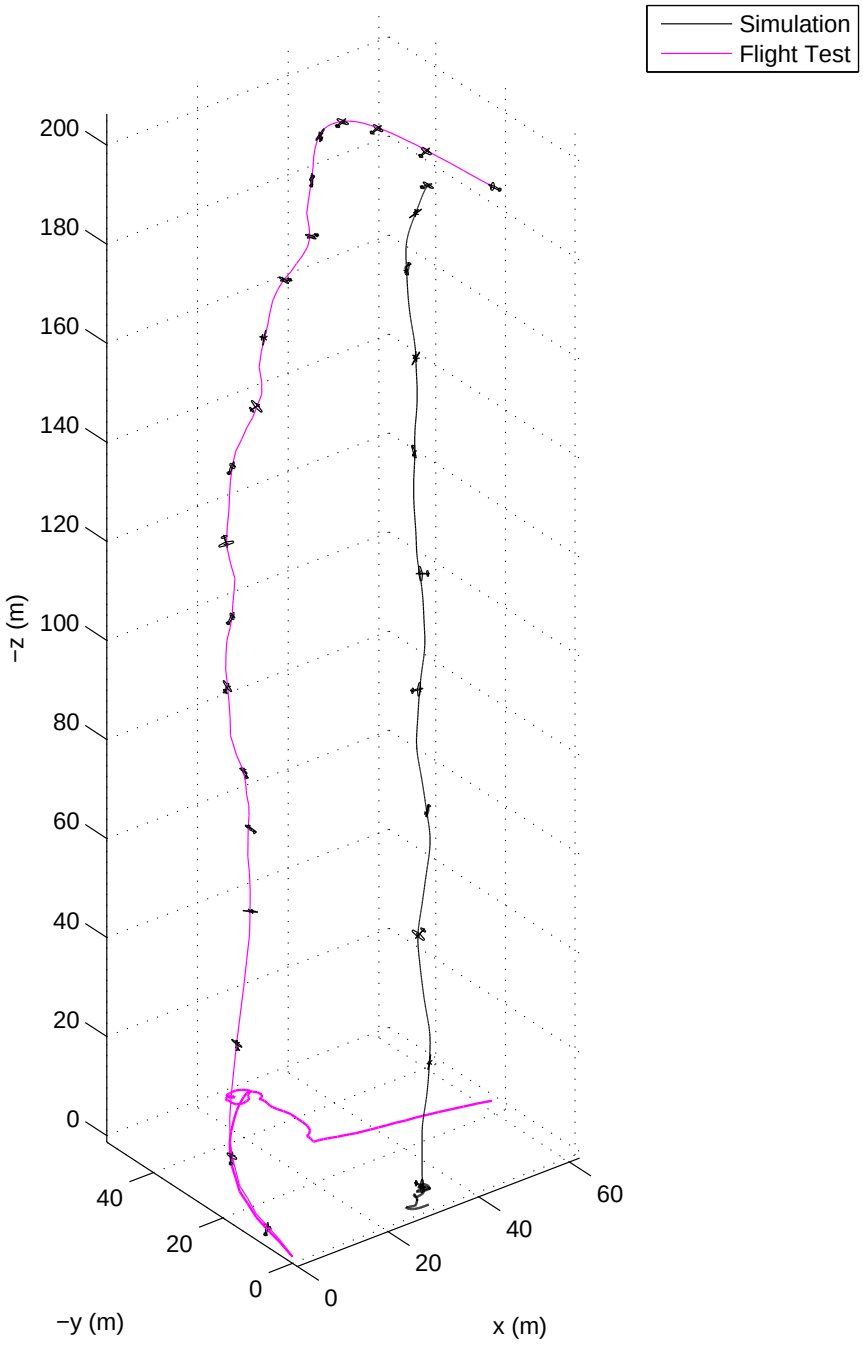

Figure 6.75: Comparison plots of a Case D spin trajectories with airplane plotted every second at a 1:1 scale for Aero Testbed flight test and SpinSim simulation.

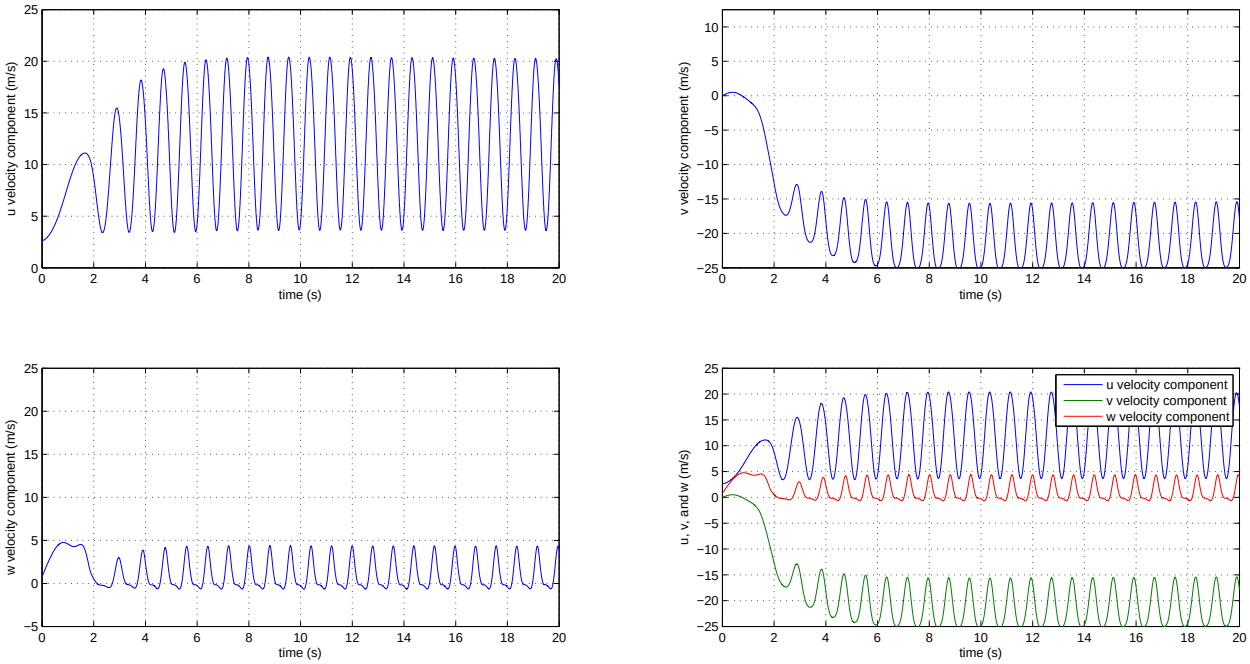

Figure 6.76: Body inertial velocities of SpinSim simulation of the Aero Testbed in a Case D spin.

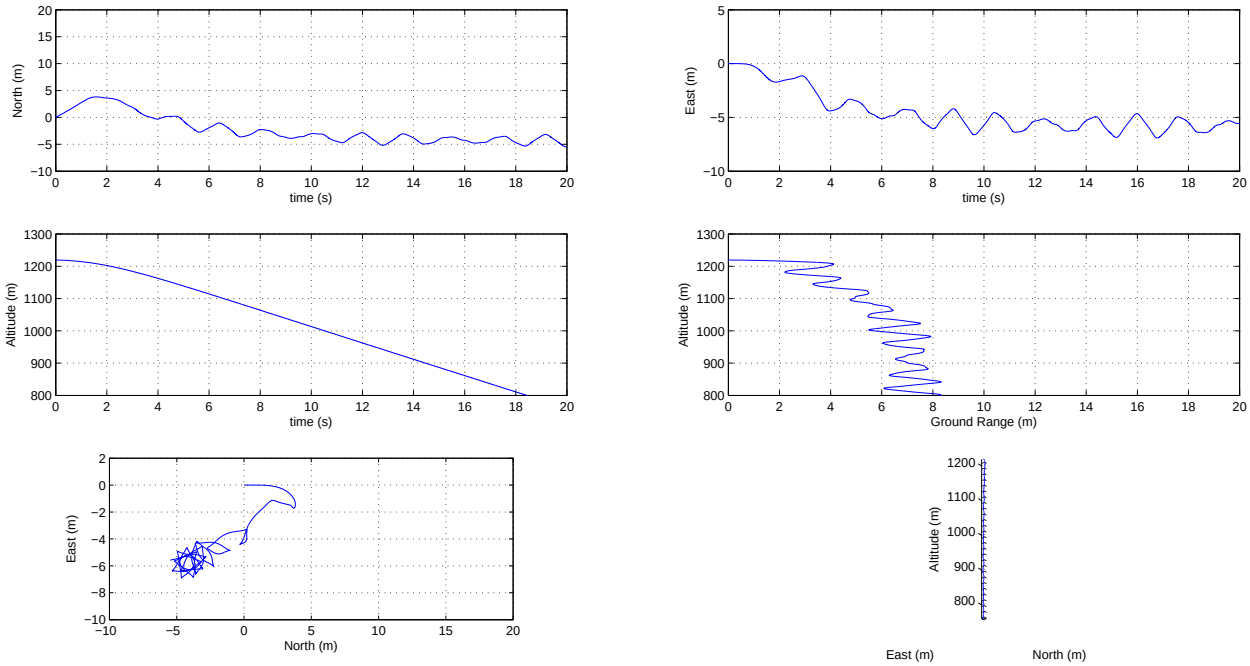

Figure 6.77: Trajectory of SpinSim simulation of the Aero Testbed in a Case D spin.

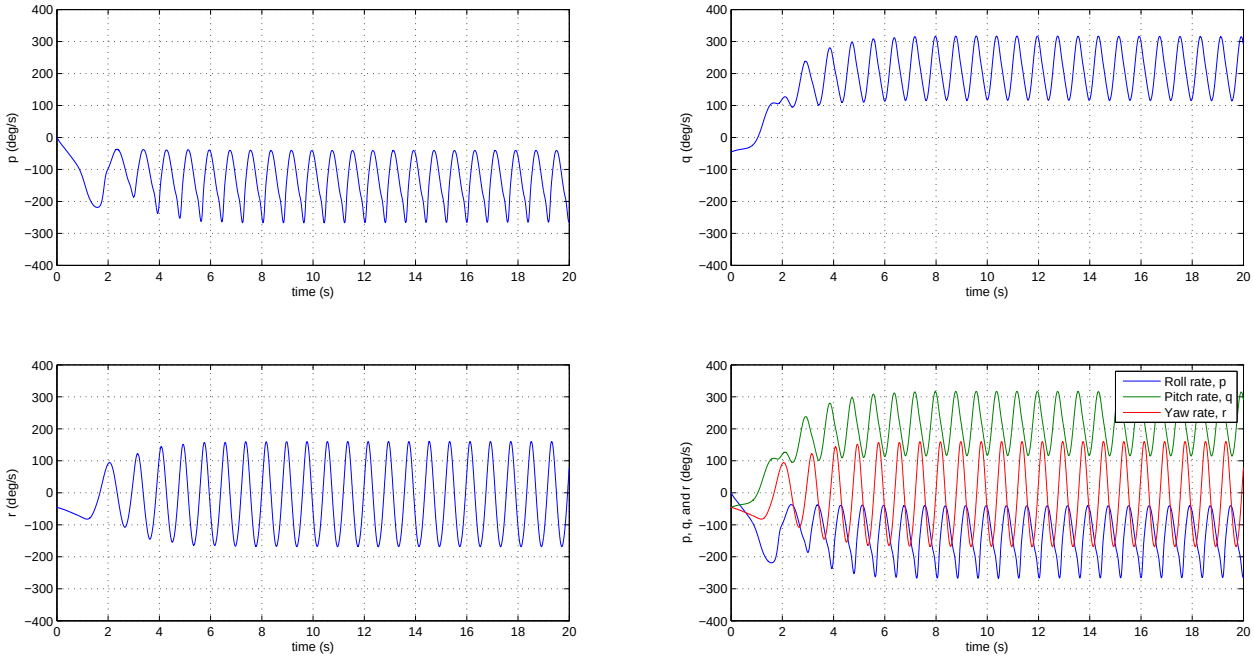

Figure 6.78: Angular rates of SpinSim simulation of the Aero Testbed in a Case D spin.

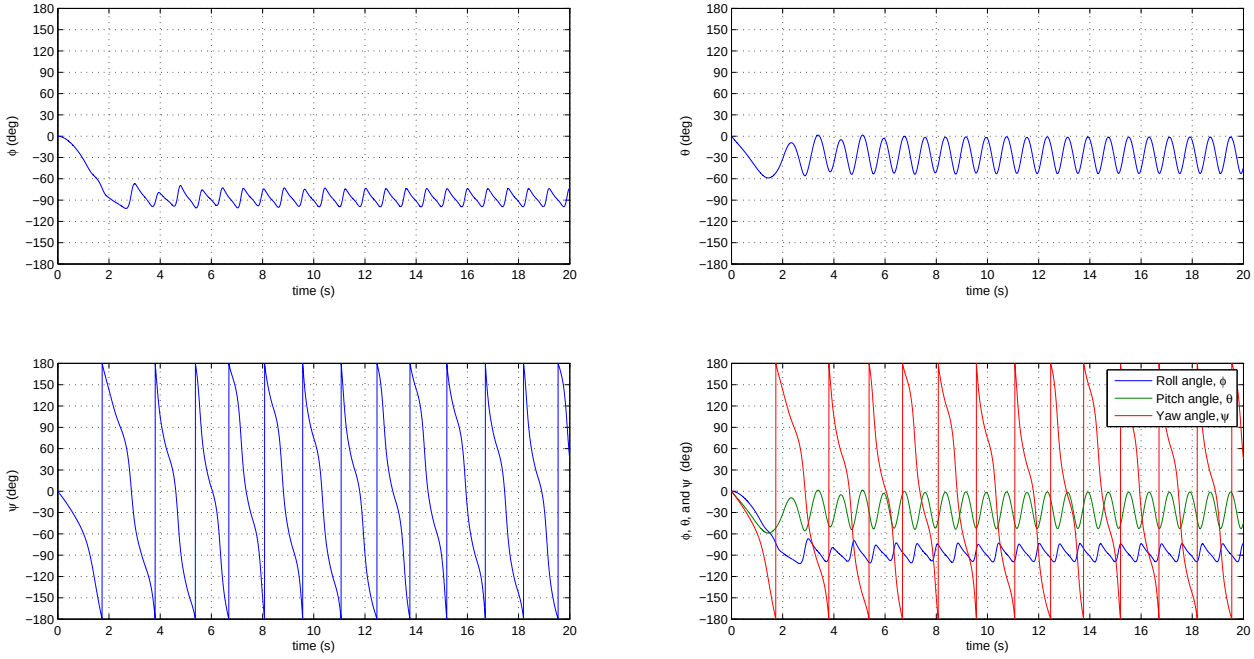

Figure 6.79: Angular orientation of SpinSim simulation of the Aero Testbed in a Case D spin.

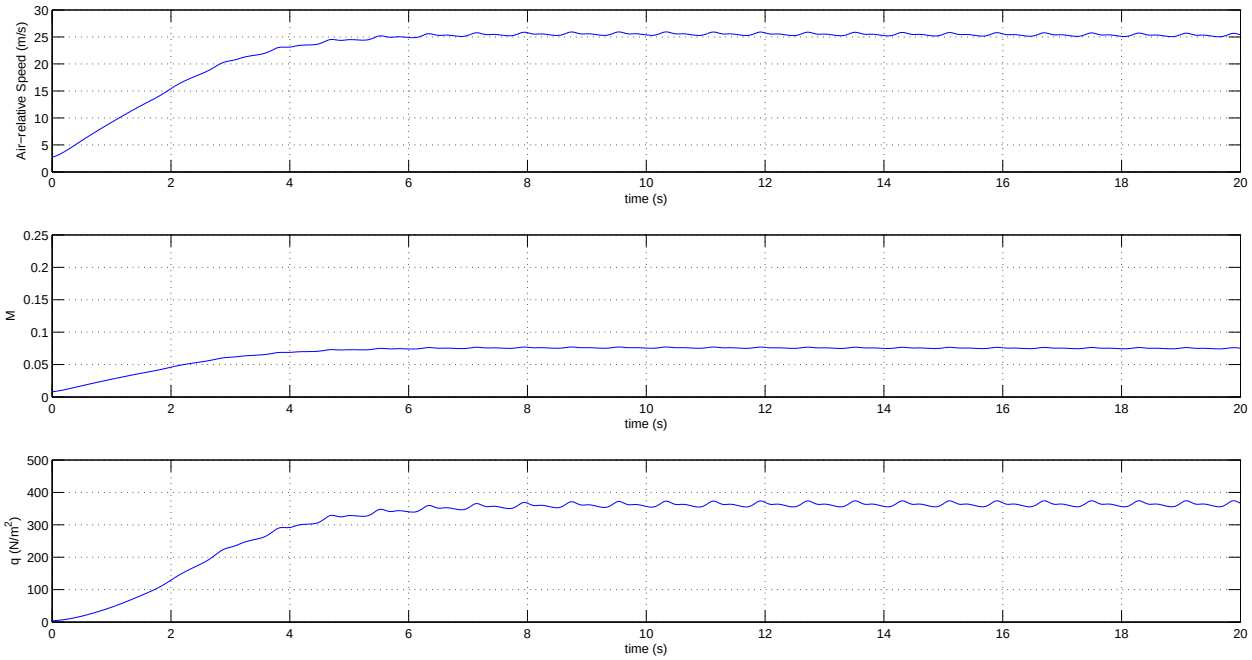

Figure 6.80: Airspeed, Mach number, and q of SpinSim simulation of the Aero Testbed in a Case D spin.

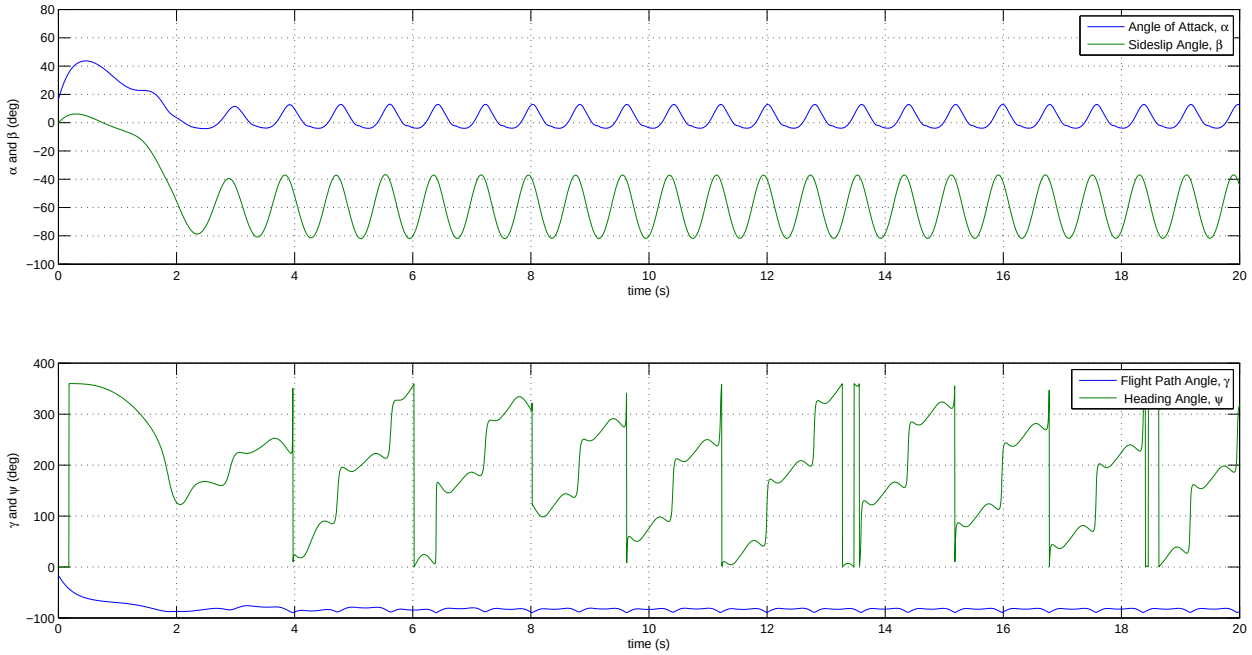

Figure 6.81: Aerodynamic and flight path angles of SpinSim simulation of the Aero Testbed in a Case D spin.

Chapter 7

Conclusions and Recommendations

This dissertation presented an in-depth and multi-faceted investigation of the aerodynamics of airplanes in stall/spin flight regimes. First, an introduction to the aerodynamics of spins was presented. The importance of the study of stall/spin aerodynamics and simulation was discussed, as well as the renewed interest in the topic. Moreoever, this research has the significant ability to save lives. The limitations of strip theory for predicting wing forces in spin were presented, and previous work to correct strip theory for spin was summarized. A discussion of the experimental and computational methods used to investigate spin aerodynamics was presented, and conclusions and results were discussed. The results presented, for instance, include the effect of ventral fins in flight test, the effect of aspect ratio on flow entrainment in wind tunnel tests, and the methods by which these data were used to develop and validate the new SpinSim force prediction code and post-stall centrifugal pumping methodology. Finally, the results of using a six-degree-of-freedom (6DOF) integration code to simulate spins, using the force prediction and novel centrifugal pumping methodology, which were developed as part of this research, were presented. The agreement of the simulations with flight test results was demonstrated and discussed. Further conclusions and insights from this project, as well as recommendations, will be presented in this chapter.

7.1 Conclusions

In this dissertation, a 6DOF simulation of an aircraft in a stall/spin was successfully accomplished. This achievement required a three-pronged approach. For the first task, flight tests were conducted to generate 3D spin trajectories to study the effects of ventral fins on spin qualities and to generate 3D spin trajectory information, against which an analytical model would be validated. The second task involved the creation of a force calculation code, SpinSim, which calculated the forces on an airplane in the full $-180 \leq \alpha \leq 180$ deg regime, and it was based on a component breakdown method. To correctly calculate the wing normal force, a first-principles based correction was devised. This correction was based on wake geometry and the centrifugal pumping of fluid outward in the trapped wake. The third task involved the validation of this first-principles correction equation, which was completed through the wind tunnel testing of various wings in spin. These wind tunnel data were then used to adjust and validate the spin correction equation within SpinSim.

7.1.1 Flight Testing

This dissertation demonstrates the configuration of a large-scale RC aircraft testbed specifically for stall/spin research and data acquisition. An onboard IMU system was configured to record angular rates, orientation, acceleration, and position information. These data, in conjunction with a passive cockpit-view video recording system, allowed for a detailed database of spin information to be created. The accuracy of the IMU direct position information was successfully increased through a numerical integration of the as-recorded velocities. Only then was the expected helical trajectory of a spin observed. This helical shape was initially hidden by the inherent errors of civilian GPS and its low resolution when compared with the magnitude of the spin radius. The repeatability of spin results through day-to-day variations in winds aloft, pressure, and temperature was demonstrated.

In conjunction with the configuration of the data acquisition hardware, a series of MATLAB programs was developed as part of this research effort to reduce, analyze, integrate, and effectively display the flight test data. These MATLAB programs are considered as a necessary and useful addition for future flight test investigations, and they allow for flight test data to be rapidly analyzed in the field. A highly efficient, safe, repeatable, and viable spin testing method was devised and was demonstrated. This spin testing method produced a large number of spins without incident.

It was observed that, as pilots are taught, when in a spin, adding anti-spin ailerons aggravates the spin, which makes it harder to recover from a spin. In the instance of the airplane without a ventral fin, exiting a right spin when a left roll is commanded is an airframe-specific occurrence and no generalization may be made from this situation. Also, as pilots are taught, commanding a pro-spin aileron deflection should not be performed in a spin. As demonstrated in both left and right spins, adding pro-spin ailerons significantly increases the descent rate, which leaves a pilot less time to recover from a spin. Finally, an idle throttle setting is optimal for spin recovery. The Aero Testbed recovered from the spin motions more slowly as power was added.

Four ventral fins were designed to increase the vertical tail area, and the area beneath the horizontal stabilizer. Their beneficial effects on the spin recovery characteristics were verified. These fins were designed specifically for this research to successfully allow for the rapid reconfiguration of the airframe while at the field in order to maintain an efficient flight test schedule. The experimental tests verified that ventral fins are effective for improving an airframe design for spin. In this case, a ventral fin aided in the recovery from a spin. No conclusive information was garnered from the ventral fins for spin entry, but based on the high α values, it would seem logical that a ventral fin would, indeed, make it more difficult for an aircraft to enter a spin. One especially important aspect of what was accomplished with the Aero Testbed, as specifically configured for spin research, was that all of these data were generated: (a) without putting a human pilot at risk, (b) without requiring an expensive dynamically-scaled aircraft, and (c) with an RC aircraft flown outdoors, and not in a specially-designed vertical spin tunnel facility.

7.1.2 Wind Tunnel Testing

Wind tunnel tests reaffirmed NASA results that the normal force on a stalled spinning wing is proportional to the spin parameter squared. Well-developed methods for testing propeller performance were modified and adapted to research stalled spinning wings in a horizontal wind tunnel. The effects of the Reynolds number, aspect ratio, airfoil geometry, and spin parameter on the normal force coefficient C_N were summarized. For the regime tested, the Reynolds number was shown to have no effect. Meanwhile, an increase in the aspect ratio of a wing was shown to progressively increase the C_N value as the wing pitch angle θ was decreased. This occurrence was hypothesized to be due to a decrease in the tip vortex effects of the higher aspect ratio wings as the wings approached an unstalled state. Flat-bottom and flat-plate wings were found to have slightly larger values of C_N than a symmetric airfoil for all values of ω, but little significant difference between a flat-bottom and flat-plate wing was observed. The slightly-larger C_N values of wings with a flat bottom were attributed to the flow-facing side acting more similar to a flat plate than a streamlined surface, and to a stronger leading edge vortex being shed by the sharp leading edge, which is common to the flat-plate and flat-bottom wings.

For high values of ω, well beyond those that would be expected for an airplane in a stall/spin situation, the data show that a maximum attainable C_N plateau value exists. Moreover, the data show that this value increases as the wing aspect ratio is increased. This value is limited by the ability of lower local angles of attack, which are created by high spin parameter values, to reduce the size of the wake structure and further accelerate the spanwise flow, thus reducing the ability of the Coriolis forces to push the spanwise flow off of the wing trailing edge. When the lower local angles of attack are unable to prevent loss of the wake structure, a maximum C_N value would be reached. Indeed, this C_N plateau was reached for wings of $\mathcal{AR} = 1$ and $\mathcal{AR} = 2$. Further, at these low-aspect ratio conditions, the increased normal force was hypothesized to be due primarily to centrifugal pumping in the leading edge vortex core, as opposed to higher aspect ratio wings, where the majority of the centrifugal pumping is experienced in the trapped wake structure.

These data may be used to validate analytical models of a wing in a stall/spin situation, which tends to drive the roll rate and normal force of a full-airplane configuration. These experimental data may thus aid in the development of simulations of aircraft that are well beyond the normal flight envelope, an area that has received recent regulatory attention. The experimental methodology, which was derived from existing propeller testing methods, shows promise for application to normal force measurements in a conventional wind tunnel on a spinning full-airplane (or at least fuselage-present) configuration, as long as the model is properly balanced. Demonstrating that these tests may be conducted successfully in a conventional wind tunnel, as opposed to in a vertical wind tunnel, should help to make the acquisition of similar data much easier, as it requires less-specialized equipment.

7.1.3 Analytical Modeling and Simulations

For the analytical and simulations aspects of this research, a first principles-based estimation of the change in normal force on a stalled spinning wing was proposed. Further, the proposed estimation was demonstrated to match with extensive experimental data, including wind tunnel testing. The conclusive part of the present work, this normal force model, demonstrated significantly improved agreement with experimental data when compared with the current state of the art. This normal force model also demonstrated that it allows for wing simulations to agree well with the wind tunnel test data of this research. Finally, when this normal force model was incorporated into a force prediction code, it successfully allowed for accurate simulations of airplane spins to be performed. In short, this research generated experimental spin data, and it employed that data to produce a significantly improved and validated analytical correction model for a stalled spinning wing. This correction model, in turn, may be used to help better design GA aircraft for spin, an effort, which will help to prevent accidents and save lives. This analytical model has been shown to fit a number of varying planforms, to account for the effects of taper ratio, and to generate consistently lower RMS error values compared with the current state of the art (when used as a strip-theory correcting model).

In conclusion, this dissertation advanced the state of the art in the field of stall/spin, and any improvements in aircraft stall/spin behavior have the potential to save many lives. Flight tests and wind tunnel tests were conducted, and a new force prediction code — SpinSim — included the novel and improved first-principles based analytical model for correcting static airfoil data to the condition of a stalled spinning wing. This code was used to generate 6DOF simulations of an airplane in spin that matched well with flight test data in regard to angular rates and the aerodynamic angles α and β.

7.2 Recommendations

While the present work represents a significant contribution to the research of stall/spin, and specifically to simulating the aerodynamics of stalled wings in spin, there remain areas in which further work would help to achieve a better understanding, and, thus, improve the ability to simulate the complex aerodynamics of stalled spinning flows. The recommendations for future research include the following:

- Performing an examination of the benefits and drawbacks of running the MTi-G IMU on the Aero Testbed in quaternion mode. While quaternion mode would eliminate the potential issue of gimbal lock, difficulties in correctly translating the data into the aerodynamic-oriented Euler angles may remain. Since spin repeatability was demonstrated, data sets from identical spin configurations could be compared, especially between the two different recording modes of the IMU, in order to quantify the differences in the results, if any. The issue of gimbal lock may be a non-issue for spins, as the θ values were not very near to $\theta = -90$ deg. Resolving the

potential gimbal lock issue may be beneficial in that it would allow the Aero Testbed to perform and record maneuvers with $\theta = \pm 90$ deg, such as a vertical climb or a descending spiral. As mentioned, a slight angular offset, between the IMU and aircraft principal axes, due to installation error, would cause the non-zero offset (bias), which was observed in the $\dot{\phi}$ data for an otherwise non-yawing flight. Quantifying this installation error should improve the accuracy of the recorded Euler angles and angular rates. This installation error quantification could be designed into the analysis and integration codes to improve their integrated results. Another possible cause of, at least, the heading discrepancy in ψ could be the windmilling motor. The addition of a magnetometer would allow for a quantification of the error due to electromagnetic effects. Recording data at a higher frequency, which is already being done on later iterations of testbed aircraft in the Applied Aerodynamics Research Group, should also serve to reduce the oscillations in the post-processed data.

- In regard to the wind tunnel tests, a helpful investigation would involve performing flow visualization on the tests of wings in spin. Injecting smoke immediately downstream of the wing centerline in spin would help to more-definitively identify the shape of the trapped wake and how it behaves as the spin parameter is increased. A logical expansion of this flow visualization, which admittedly may prove quite challenging, would be to introduce a seeded flow to the wake in order to perform PIV and/or PLIF imaging techniques to determine the velocity field within the wake. These data would help to define the size and structure of the wake and possibly the flowfield within, both qualitatively and quantitatively. It may also provide qualitative insight into the differences in tip effects on wings of different aspect ratios.

- Another logical follow-up project to the wind tunnel testing would be to test wings with dihedral, twist, and sweep. Being able to quantify the effects of these wing parameters on the spin aerodynamics would allow for a wider range of wings to be simulated more-accurately in spin. Indeed, it may uncover some rather interesting and unique results, especially in the case of swept wings. Performing these tests might allow a modified correction, or perhaps a different correction, to be developed for swept wings, such as those found on commercial transport-category aircraft or for low aspect ratio delta-type wings, such as those found on fighter aircraft or MAVs.

- A final follow-up to the wind tunnel testing would be to test full-airplane configurations using the methods of this dissertation, which were applied to testing spinning wings. The difficulty would be to properly balance the model. Nevertheless, the effects of various treatments, such as ventral fins, wing fences, drooped leading edges, and tail configuration changes could be rapidly investigated, and their changes on the forces and moments in a spin could be quantified. One major barrier to this testing would be the Reynolds number effects that would be encountered when attempting to extrapolate experimental data from small test models to full-scale airplanes.

- Further work is needed to understand the effects of large control surface deflection angles. While SpinSim was able to quite accurately simulate the low-deflection angle spins of Cases A and B, which would be seen on general aviation aircraft, its accuracy was decreased for the high-deflection-angle spins of Cases C and D. It is hypothesized that there exist some 3D effects and interactions, especially in the tail section, which are unique to the extreme deflection angles and are not currently captured by SpinSim. Even conducting wind tunnel tests on the individual components may not fully answer this question, as the c_f/c and δ_e values used in this research were not at the extreme edges of the empirical relationships of the literature. An example of the complex high-deflection angle aerodynamics is the oscillating spin encountered during flight test experiments for the Case D spin. In that spin, there appeared also to be some significant dynamic effects in addition to the 3D effects due to high deflection angles. Clearly, modeling extreme deflection angles requires additional corrections or interaction factors, and it is not currently or readily achievable with the data at hand. Nevertheless, the data were acquired for these spins, and some insight into the potential aerodynamic interactions was presented. Thus, some of the initial and important work for simulating these highly-dynamic spins is already completed, and the initial path paved. Adding dynamic effects and quantifying the unique high deflection angle component interactions could further improve upon SpinSim.

- A final interesting path of study would be to source or acquire full-scale general aviation aircraft spin data and attempt to simulate a full-scale airplane with SpinSim. At least one full-scale data set may be found in the literature, although it is for a Harvard Mk IV trainer aircraft. The Harvard Mk IV is not a general aviation aircraft, but, similar to many general aviation aircraft, it is a low-wing, single-engine, propeller-driven aircraft. These spin data for the Harvard are presented in AIAA-2004-4815 Flight Manoeuvre and Spin Characteristics of the Harvard 4: Application to Human Factors Flight Research, by Brown, Dillon, and Erdos.

References

[1] Zimmerman, C. H., "Preliminary Tests in the NACA Free-Spinning Wind Tunnel," NACA Report 557, 1937.

[2] Soule, H. A. and Scudder, N. F., "A Method of Flight Measurement of Spins," NACA Report 377, 1931.

[3] Stephens, A. V., "Recent Research on Spinning," *Royal Aircraft Society Journal*, Vol. 37, No. 275, 1933, pp. 944–955.

[4] AOPA Air Safety Foundation, "Joseph T. Nall Reports (1997-2010)," http://www.aopa.org/asf/publications/nall.html, Accessed January 2012.

[5] Federal Aviation Administration, "14 CFR Part 121: Qualification, Service, and Use of Crewmembers and Aircraft Dispatchers; Final Rule," *Federal Register*, Vol. 78, No. 218, 2013.

[6] Federal Aviation Administration, "14 CFR Part 60: Flight Simulation Training Device Qualification Standards for Extended Envelope and Adverse Weather Event Training Tasks; Proposed Rule," *Federal Register*, Vol. 79, No. 132, 2014.

[7] Bowman, J. S., "Summary of Spin Technology as Related to Light General-Aviation Airplanes," NASA TN D-6575, December 1971.

[8] Ward, D. T. and Strganac, T. W., *Introduction to Flight Test Engineering*, Kendall/Hunt Publishing Company, 2001.

[9] *Airplane Flying Handbook*, No. FAA-H-8083-3A, U.S. Department of Transportation: Federal Aviation Administration Flight Standards Service, 2004.

[10] Hreha, M. A. and Lutze, F. H., "A Dynamic Model for Aircraft Poststall Departure," AIAA Paper 83-0367, 1983.

[11] Murch, A., *Aerodynamic Modeling of Post-Stall and Spin Dynamics of Large Transport Airplanes*, M.S. Thesis, Georgia Institute of Technology, Atlanta, GA, August, 2007.

[12] Shaw, G. H., Cunningham, K., Foster, J. V., Fremaux, C. M., Stewart, E. C., Wilborn, J. E., Gato, W., and Pratt, D. W., "Wind-Tunnel Investigation of Commercial Transport Aircraft at Extreme Flight Conditions," SAE Paper 2002-01-2912, November 2002.

[13] Foster, J. V., Cunningham, K., Fremaux, C. M., Shah, G. H., Stewart, E. C., Rivers, R. A., Wilborn, J. E., and Gato, W., "Dynamics Modeling and Simulation of Large Transport Airpoanes in Upset Conditions," AIAA Paper 2005-5933, August 2005.

[14] Murch, A. M. and Foster, J. V., "Recent NASA Research on Aerodynamic Modeling of Post-Stall and Spin Dynamics of Large Transport Airplanes," AIAA Paper 2007-0463, January 2007.

[15] Nagati, M. G., "Stall/Spin/Flight Simulation," U.S. Department of Transportation: Federal Aviation Administration Technical Center DOT/FAA/CT-88/28, 1989.

[16] Bihrle, W., "Correlation Study of Theoretical and Experimental Results for Spin Tests of a 1/10-Scale Radio Control Model," NASA CR-144995, July 1976.

[17] Martin, C. A. and Hill, S. D., "Prediction of Aircraft Spin Recovery," AIAA Paper 89-3363, 1989.

[18] Bazzocchi, E., "Stall Behavior and Spin Estimation Method by Use of Rotating Balance Measurements," AGARD Conference Proceedings AGARD-CP-199, June 1975.

[19] Tischler, M. B. and Barlow, J. B., "Determination of the Spin and Recovery Characteristics of a General Aviation Design," *Journal of Aircraft*, Vol. 18, No. 4, 1981, pp. 238–244.

[20] Bowman, J. S., Burk, S. M., Stough, H. P., and Patton, J. M., "Correlation of Model and Airplane Spin Characteristics for a Low-Wing General Aviation Research Airplane," AIAA Paper 78-1477, August 1978.

[21] Ragheb, A. M., Dantsker, O. D., and Selig, M. S., "Stall/Spin Flight Testing with a Subscale Aerobatic Aircraft," AIAA Paper 2013-2806, 31st AIAA Applied Aerodynamics Conference, San Diego, CA, 2013.

[22] Lutze, F. H. and Lluch, D., "Simulation of Stall, Spin, and Recovery of a General Aviation Aircraft," AIAA Paper 96-3409, 1996.

[23] Feistel, T. W. and Anderson, S. B., "Alleviation of Spin-Entry Tendencies through Localization of Wing-Flow Separation," *Journal of Aircraft*, Vol. 18, No. 2, 1981, pp. 69–75.

[24] Pamadi, B. N. and Taylor, L. W., "Estimation of Aerodynamic Forces and Moments on a Steadily Spinning Airplane," *Journal of Aircraft*, Vol. 21, No. 12, 1984, pp. 943–954.

[25] Polhamus, E. C., "Effect of Flow Incidence and Reynolds Number on Low-Speed Aerodynamic Characteristics of Several Noncircular Cylinders with Applications to Directional Stability and Spinning," NASA TN 4156, January 1958.

[26] Adams, W. M., "Analytic Prediction of Airplane Equilibrium Spin Characteristics," NASA Technical Paper TN D-6926, November 1972.

[27] Sobie, B., "Flightglobal Pro - PICTURE: Flight gets first look at redesigned SkyCatcher," http://www.flightglobal.com/news/articles/picture-flight-gets-first-look-at-redesigned-skycatcher-322034/, Accessed October 2012.

[28] Sobie, B., "Flight International - OSHKOSH 2009: PICTURES: VIDEO: Cessna unveils revised SkyCatcher ," http://www.flightglobal.com/news/articles/oshkosh-2009-pictures-video-cessna-unveils-revised-skycatcher-330157/, Accessed October 2012.

[29] Hoff, R. I. and Gratton, G. B., "Spin Induced Aerodynamic Flow Conditions on Full-Scale Aeroplane Wing and Horizontal Tail Surfaces," *Aeronautical Journal*, Vol. 117, No. 1198, 2013, pp. 1207–1231.

[30] Ralston, J. N., "Rotary Balance Data for a Typical Single-Engine General Aviation Design for an Angle-of-Attack Range of 8 to 90 deg: I - Influence of Airplane Components for Model D," NASA CR-3246, 1983.

[31] Barnhart, B., "Rotary Balance Data for a Typical Single-Engine General Aviation Design for an Angle-of-Attack Range of 8 to 90 deg: II - Influence of Horizontal Tail Location for Model D," NASA CR-3247, 1982.

[32] Bihrle, W., Barnhart, B., and Pantason, P., "Static Aerodynamic Characteristics of a Typical Single-Engine Low-Wing General Aviation Design for an Angle-of-Attack Range of -8 deg to 90 deg," NASA CR-2971, 1978.

[33] Bihrle, W., Hultberg, R. A., and Mulcay, W., "Rotary Balance Data for a Typical Single-Engine Low-Wing General Aviation Design for an Angle-of-Attack Range of 30 to 90 deg," NASA CR-2972, 1978.

[34] Mulcay, W. and Chu, J., "Rotary Balance Data for a Single-Engine Agricultural Airplane Configuration for an Angle-of-Attack Range of 8 to 90 deg," NASA CR-3311, 1980.

[35] Barnhart, B., "F-15 Rotary Balance Data for an Angle-of-Attack Range of 8 to 90 deg," NASA CR-3478, 1982.

[36] Bihrle, W. and Hultberg, R. S., "Rotary Balance Data for a Typical Single-Engine General Aviation Design for an Angle-of-Attack Range of 8 to 90 deg: I - High-Wing Model B," NASA CR-3097, 1979.

[37] Pantason, P. and Dickens, W., "Rotary Balance Data for a Single-Engine Trainer Design for an Angle-of-Attack Range of 8 to 90 deg," NASA CR-3099, 1979.

[38] Hultberg, R. S. and Mulcay, W., "Rotary Balance Data for a Typical Single-Engine General Aviation Design for an Angle-of-Attack Range of 8 to 90 deg: I - Low-Wing Model A," NASA CR-3100, 1980.

[39] Mulcay, W. and Rose, R. A., "Rotary Balance Data for a Typical Single-Engine General Aviation Design for an Angle-of-Attack Range of 8 to 90 deg: II - High-Wing Model A," NASA CR-3101, 1979.

[40] Mulcay, W. and Rose, R. A., "Rotary Balance Data for a Typical Single-Engine General Aviation Design for an Angle-of-Attack Range of 8 to 90 deg: I - Low-Wing Model C," NASA CR-3200, 1980.

[41] Hultberg, R. S., Chu, J., and Dickens, W. L., "Rotary Balance Data for a Typical Single-Engine General Aviation Design for an Angle-of-Attack Range of 8 to 90 deg: II - High-Wing Model C," NASA CR-3201, 1980.

[42] Bihrle, W. and Hultberg, R. S., "Rotary Balance Data for a Typical Single-Engine General Aviation Design for an Angle-of-Attack Range of 8 to 90 deg: II - Low-Wing Model B," NASA CR-3098, 1979.

[43] McCormick, B. W., *Aerodynamics, Aeronautics, and Flight Mechanics*, 2nd ed., John Wiley & Sons, Inc., New York, 1995, pp. 577–579.

[44] Ragheb, M. and Ragheb, A. M., *Wind Turbines Theory - The Betz Equation and Optimal Rotor Tip Speed Ratio, Fundamental and Advanced Topics in Wind Power*, InTech, 2011.

[45] Pomeroy, B. W. and Uhlig, D. V., "Boomerang Flight Tests," AIAA Paper 2014-3127, June 2014.

[46] McCormick, B. W., "The Prediction of Normal Force and Rolling Moment Coefficients for a Spinning Wing," NASA CR-165680, February 1981.

[47] Pamadi, B. N. and Taylor, L. W., "Semiempirical Method for Prediction of Aerodynamic Forces and Moments on a Steadily Spinning Light Airplane," NASA TM 4009, 1987.

[48] Lentink, D. and Dickinson, M. H., "Rotational Accelerations Stabilize Leading Edge Vortices on Revolving Fly Wings," *The Journal of Experimental Biology*, Vol. 212, No. 16, 2009, pp. 2705–2719.

[49] Garmann, D. J. and Visbal, M. R., "Dynamics of Revolving Wings for Various Aspect Ratios," *Journal of Fluid Mechanics*, Vol. 748, 2014, pp. 932–956.

[50] Carr, Z., Chen, C., and Ringuette, M. J., "The Effect of Aspect Ratio on the Three-Dimensional Vortex Formation of Rotating Flat-Plate Wings," AIAA Paper 2013-0912, 50th AIAA Aerospace Sciences Meeting, Nashville, TN, 2012.

[51] Tangler, J. L. and Selig, M. S., "An Evaluation of an Empirical Model for Stall Delay due to Rotation for HAWTS," *National Renewable Energy Laboratory, Golden, CO, NREL/CP-440-23258, Presented at Windpower '97, Austin, TX*, June 1997.

[52] Lindenburg, C., "Modelling of Rotational Augmentation Based on Engineering Considerations and Measurements," Energy Research Center of the Netherlands, ECN-RX-04-131, Petten, The Netherlands, European Wind Energy Conference, London, England, November, 2004.

[53] Dwyer, H. A. and McCroskey, W. J., "Crossflow and Unsteady Boundary-Layer Effects on Rotating Blades," *AIAA Journal*, Vol. 9, No. 8, 1971, pp. 1498–1504.

[54] Du, Z. and Selig, M. S., "A 3-D Stall-Delay Model for Horizontal Axis Wind Turbine Performance Prediction," AIAA Paper 98-0021, August 1998.

[55] Himmelskamp, H., *Profile Investigations of a Rotating Airscrew*, PhD. Thesis, MAP Volkenrode Reports and Translation No. 832, September, 1947.

[56] Tangler, J. L., "Insight into Wind Turbine Stall and Post-Stall Aerodynamics," *Wind Energy*, Vol. 7, No. 3, 2004, pp. 247–260.

[57] Dantsker, O. D., Johnson, M. J., Selig, M. S., and Bretl, T. W., "Development of the UIUC Aero Testbed: A Large-Scale Unmanned Electric Aerobatic Aircraft for Aerodynamics Research," AIAA Paper 2013-2807, June 2013.

[58] Hangar 9, "35% Extra 260 ARF: Hangar 9," http://www.hangar-9.com/products/default.aspx?prodid=han1000, Accessed March 2012.

[59] Neihouse, A. I., Lichtenstein, J. H., and Pepoon, P. W., "Tail-Design Requirements for Satisfactory Spin Recovery," NASA Technical Note TN 1045, April 1946.

[60] Bowman, J. S., Hultberg, R. S., and Martin, C. A., "Measurements of Pressures on the Tail and Aft Fuselage of an Airplane Model During Rotary Motions at Spin Altitudes," NASA Technical Paper TP-2939, November 1989.

[61] Xsens Technologies B.V., "MTi-G User Manual and Technical Documentation, Rev. G," *Xsens Technologies B.V.*, 2009.

[62] Eagle Tree Systems, "User Manual for the Seagull Wireless Dashboard Telemetry and Data Recorder Systems: Pro, Flight, Glide, Boat," *Eagle Tree Systems LLC*, Revision 4.3.

[63] Eleodis Electronic Components Distributor, "Miniature Amplified Pressure Sensors Specification Sheet," *Allsensors.com*, 2012.

[64] Sukumar, P. P. and Selig, M. S., "Dynamic Soaring of Sailplanes over Open Fields," *Journal of Aircraft*, Vol. 50, No. 5, 2013, pp. 1420–1430.

[65] Stull, R., *An Introduction to Boundary Layer Meteorology*, Atmospheric and Oceanographic Sciences Library, Vol. 13, Springer, 2009.

[66] Lambert, J. D., *Numerical Methods for Ordinary Differential Systems: The Initial Value Problem*, John Wiley and Sons, 2000.

[67] "FS One, Precision RC Flight Simulator," Version 2, Software Developed by InertiaSoft, Champaign, IL, 2013.

[68] 14 C.F.R., Part 91, §91.126, "Federal Aviation Regulations / Aeronautical Information Manual (FAR/AIM)," 2013.

[69] Liebeck, R., "Personal Communication," at 31st AIAA Applied Aerodynamics Conference, June 25, 2013.

[70] Burk, S. M., Bowman, J. S., and White, W. L., "Spin-Tunnel Investigation of the Spinning Characteristics of Typical Single-Engine General Aviation Airplane Designs," NASA TP-1009, December 1977.

[71] Beaurain, L., "General Study of Light Plane Spin, Aft Fuselage Geometry, Part 1," NASA Technical Translation TTF-17,446, 1977.

[72] Bihrle, W. and Bowman, J. S., "Influence of Wing, Fuselage, and Tail Design on Rotational Flow Aerodynamics Beyond Maximum Lift," *Journal of Aircraft*, Vol. 18, No. 11, 1981, pp. 920–925.

[73] Stengel, R. F., "Appendix B. Mathematical Models and Six-Degree-of-Freedom Simulation of Two Business Jet Aircraft Supplement for Flight Dynamics, a book by Robert F. Stengel," http://www.princeton.edu/ stengel/FDcodeB.html, Accessed January 2013.

[74] Stengel, R. F., *Flight Dynamics*, 2nd ed., Princeton University Press, Princeton, NJ, 2004, pp. 240–244.

[75] Selig, M. S. and McGranahan, B. D., "Wind Tunnel Aerodynamic Tests of Six Airfoils for Use on Small Wind Turbines," National Renewable Energy Laboratory, Technical Report NREL/SR-500-34515, Golden, CO, 2004.

[76] Khodadoust, A., "An Experimental Study of the Flowfield on a Semispan Rectangular Wing with a Simulated Glaze Ice Accretion," Ph.D. Thesis, University of Illinois at Urbana-Champaign, Department of Aeronautical and Astronautical Engineering, Urbana, IL, 1993.

[77] Ragheb, A. M. and Selig, M. S., "Wind Tunnel Testing of Wings in Spin," AIAA Paper 2016-1073, 54th AIAA Aerospace Sciences Meeting, San Diego, CA, 2016.

[78] Brandt, J. B. and Selig, M. S., "Propeller Performace at Low Reynolds Numbers," AIAA Paper 2011-1255, 49th AIAA Aerospace Sciences Meeting, Orlando, FL, 2011.

[79] Deters, R. W., Ananda, G. K., and Selig, M. S., "Reynolds Number Effects on the Performance of Small-Scale Propellers," AIAA Paper 2014-2151, 32nd AIAA Applied Aerodynamics Conference, Atlanta, GA, 2014.

[80] Glauert, H., "Wind Tunnel Interference on Wings, Bodies and Airscrews," Aeronautical Research Committee, R&M No. 1566, 1933.

[81] Barlow, J. B., Rae, W. H., Jr., and Pope, A., *Low-Speed Wind Tunnel Testing*, 3rd ed., John Wiley & Sons, Inc., New York, 1999, pp. 433–435.

[82] Anderson, J. D., Jr., *Fundamentals of Aerodynamics*, 2nd ed., McGraw-Hill, Inc., New York, 1991.

[83] Lindenburg, C., "Stall Coefficients," Energy Research Center of the Netherlands, ECN-RX-01-004, Petten, The Netherlands, IEA Symposium on the Aerodynamics of Wind Turbines, National Renewable Energy Laboratory, Golden, CO, December, 2000.

[84] Vassberg, J., "Personal Communication," at 54th AIAA Aerospace Sciences Meeting, January 7, 2016.

[85] Clarkson, M. H., Malcolm, G. N., and Chapman, G. T., "Experimental Determination of Post-Stall Rotary Derivatives for Airplane-Like Configurations at Several Reynolds Numbers," AIAA Paper 75-171, January 1975.

[86] Garmann, D. J., Visbal, M. R., and Orkwis, P. D., "Three Dimensional Flow Structure and Aerodynamic Loading on a Revolving Wing," *Experiments in Fluids*, Vol. 25, No. 3, 2013.

[87] Bross, M., Ozen, C. A., and Rockwell, D., "Flow Structure on a Rotating Wing: Effect of Steady Incident Flow," *Physics of Fluids*, Vol. 25, No. 8, 2013, 081901.

[88] Arie, M. and Rouse, H., "Experiments on Two-Dimensional Flow Over a Normal Wall," *Journal of Fluid Mechanics*, Vol. 1, No. 2, 1956, pp. 129–141.

[89] Hu, D., Hua, O., and Du, Z., "A Study on Stall-Delay for Horizontal Axis Wind Turbine," *Renewable Energy*, Vol. 31, No. 6, 2005, pp. 821–836.

[90] Fail, R., Lawford, J. A., and Eyre, R. C. W., "Low-Speed Experiments on the Wake Characteristics of Flat Plates normal to an Air Stream," Aeronautical Research Council Reports and Memoranda 3120, 1959.

[91] Garmann, D., "Personal Communication," during UIUC Aerospace Engineering Department visit, November 17, 2014.

[92] Jamieson, P., *Innovation in Wind Turbine Design*, John Wiley & Sons, New York, NY, 1st ed., 2011.

[93] Jonkman, J., Butterfield, S., Musial, W., and Scott, G., "Definition of a 5-MW Reference Wind Turbine for Offshore System Development," National Renewable Energy Laboratory, Technical Report NREL/TP-500-38060, February 2009.

[94] Fage, A. and Johansen, F. C., "On the Flow of Air Behind an Inclined Flat Plate of Infinite Span," *Proc. R. Soc. Lond.*, Vol. 116, No. 773, 1927, pp. 170–197.

[95] Selig, M. S., "Real-Time Flight Simulation of Highly Maneuverable Unmanned Aerial Vehicles," *Journal of Aircraft*, Vol. 51, No. 6, 2014, pp. 1705–1725.

[96] Poelma, C., Dickson, W. B., and Dickinson, M. H., "Time-Resolved Reconstruction of the Full Velocity Field Around a Dynamically-Scaled Flapping Wing," *Experiments in Fluids*, Vol. 41, 2006, pp. 213–225.

[97] Maxworthy, T., "The Formation and Maintenance of a Leading-Edge Vortex During the Forward Motion of an Animal Wing," *Journal of Fluid Mechanics*, Vol. 587, 2007, pp. 471–475.

[98] Sheldahl, R. E. and Klimas, P. C., "Aerodynamic Characteristics of Seven Symmetrical Airfoil Sections Through 180-Degree Angle of Attack for Use in Aerodynamic Analysis of Vertical Axis Wind Turbines," Sandia National Laboratories Energy Report SAND80-2114, 1981.

[99] Ostowari, C. and Naik, D., "Post Stall Studies of Untwisted Varying Aspect Ratio Blades with an NACA 4415 Airfoil Section - Part I," *Wind Engineering*, Vol. 8, No. 3, 1984, pp. 176–194.

[100] Ostowari, C. and Naik, D., "Post Stall Studies of Untwisted Varying Aspect Ratio Blades with NACA 44XX Series Airfoil Sections - Part II," *Wind Engineering*, Vol. 9, No. 3, 1985, pp. 149–164.

[101] Kerwin, J. E., Mandel, P., and Lewis, S. D., "An Experimental Study of a Series of Flapped Rudders," *Journal of Ship Research*, Vol. 16, No. 4, 1972, pp. 221–239.

[102] Johnson, H. S. and Hagerman, J. R., "Wind-Tunnel Investigation at Low Speed of an Unswept Untapered Semispan Wing of Aspect Ratio 3.13 Equipment With Various 25-Percent-Chord Plain Flaps," NASA TN 2080, April 1950.

[103] Montgomerie, B., "Methods for Root Effects, Tip Effects and Extending the Angle of Attack Range to $\pm$180, with Application to Aerodynamics for Blades on Wind Turbines and Propellers," Swedish Defense Research Agency (Totalförsvarets Forskningsinstitut - FOI), Scientific Report FOI-R–1305-SE, Stockholm, Sweden, 2004.

[104] Koenig, D. G., "Low-Speed Tests of Semispan-Wing Models at Angles of Attack from 0 deg to 180 deg," NASA Memorandum 2-27-59A, 1959.

[105] Dods, J. B., "Wind-Tunnel Investigation of Horizontal Tails: IV - Unswept Plan Form of Aspect Ratio 2 and a Two-Dimensional Model," NACA Research Memorandum A8J21, 1948.

[106] Bates, W. R., "Collection and Analysis of Wind-Tunnel Data on the Characteristics of Isolated Tail Surfaces With and Without End Plates," NACA Technical Note 1291, 1947.

[107] Robotics, C., "CH Robotics: Understanding Euler Angles," http://www.chrobotics.com/library/understanding-euler-angles, Accessed January 2016.

[108] Stough, H. P., DiCarlo, D. J., and Patton, J. M., "Flight Investigation of Stall, Spin, and Recovery Characteristics of a Low-Wing, Single-Engine, T-Tail Light Airplane," NASA TP-2427, May 1985.